

IMFTF2024



International Multiphase Flow Technology Forum 2024 Abstract Collection (IMFTF2024)

July 2-5, 2024
Dali Yueyun Accord Resort Hotel, Dali China



目录

Plenary speech 11

Recent progress in thermochemical multiphase reacting flow 11

The influence of flow on the production of low-carbon hydrogen 12

FB mineral processing from fundamental to application 13

Modeling and simulation of gas-particle fluidized beds with heat and mass transfer for the development of low carbon engineering applications 14

Pseudo-boiling in supercritical pressures: theory, experiment and applications 15

Electrical capacitance tomography for multiphase flow measurement 16

Abnormal gravity scaling behavior and bubble dynamics in nucleate pool boiling with low heat flux: what have we learned from vg BOILING-CSS 17

Modelling of multiphase reacting flows and industry applications 18

Topic1- Multiphase reactive flow: model development and industrial applications 19

CPFD simulation of a continuous tapered fluidized bed reactor for U3O8 hydrogen reduction 19

Drag and Heat transfer coefficients for prolate ellipsoids in low-Mach number variable-density flow in the absence of buoyancy 20

CFD-DEM modelling of absorber sphere pneumatic conveying and erosive wear 21

The research of Separation and Resistance Characteristics of Horizontal Corrugated Plates 23

Fast Predicting Spatiotemporal Distributions of Fluidized Bed Pyrolysis for Biomass Using Convolutional Neural Networks 24

Numerical Investigation into the Gasification of Industrial Organic Waste in Entrained-Bed Reactors Utilizing Detailed Chemical Kinetic Mechanisms 26

A Novel Intrusive Reduced-order Model for the Parametric Prediction of Bubbling Fluidized Beds 29

The investigation of CO_2–H_2O flow corrosion mechanism on the surface of mild carbon steel 31

CFD Study of Hydrogen Injection in Blast Furnaces: Tuyere Co-injection of Hydrogen and Coal 34

Gas-solid flow in bubbling fluidized beds 36

A novel hybrid CFD-DEM method for high-fidelity modelling of cross scale particulate-fluid flow 38

Field-resolved Surrogate Model for an Arbitrarily Spinning Particle Based on Parameterized Physics-informed Neural Networks (P-PINNs) 40

CFD-DEM modeling of thermochemical heat storage in the framework of GPU 41

CFD and Experimental Study of Hydrodynamics in Pulsed Fluidized Beds: A Preliminary Investigation 44

Numerical simulation of the soot generation during a single biomass particle combustion 46

Coupling a neural network-inspired kinetics model and coarse-grained DEM-CFD for a fluidized bed plastic pyrolizer simulation 50

Topic 2-I-Multiphase flow: innovations and low-carbon engineering applications 51

Multiphase flow challenges in industrial-scale conversion of biomasses and wastes 51

Clathrate Hydrates in Porous Media: Application to Low-carbon Fuels in Clean Energy Transition 52

CFD investigation of the structural effects of internal gas intake on powder conveying performance in fuel supply systems for aerospace engines 53

Multiscale investigation of fluidized bed reactors for thermochemical conversion of biomass 54

Dynamically structured flow patterns in vibrated gas-fluidized beds 55

A novel circulating fluidized bed process for low-carbon alkane dehydrogenation 58

Impact of electrolyte circulation on HTO in alkaline water electrolysis 59

Numerical studies on the controlled thermocapillary migration of sessile droplet 60

Three-dimensional full-loop simulation of gas-solid flow characteristics in chemical looping combustion system 62

Fluidization engineering design based on gas-solid structural model 63

Experimental and simulation study of flow and mass transfer performance of annular microchannel enhanced by spiral-wound wires 65

Development of Fluidization Technology for Thermochemical Energy Storage Application 67

Scale-up mechanism of spout fluidized bed by multiple spout channels 68

An Improved Numerical Simulation of Porous Particle Flows Based on A New Drag Correlation Considering the Permeability 70

Kinetic, products formation, and mechanism analysis for the pyrolysis of Ethylene-co-vinyl acetate 72

Study on the oxidation mechanism of asphaltene in supercritical water by ReaxFF molecular dynamics simulation 74

Parallel Session III: Topic3-Fundamentals of dispersed multiphase flow 77

Study in multiple successive collisions between a flow-driven prolate spheroidal particle and a plane wall 77

Behavior of suspension cohesive particles in Rayleigh- Bénard turbulence 79

Electrospray cooling characteristics and the heat transfer enhancement mechanism 82

Dynamics of Taylor bubble formation and evolution in a 100μm width microchannel with an acute symmetrical inlet geometry 85

Drag coefficient for micron-sized sphere particle in high-speed flow based on symbolic regression 87

Experimental and numerical investigations on the process of the gas-particle jet in supersonic crossflow 89

Numerical Simulation of Transient Heat Transfer within Rotating drum via Smoothed Particle Hydrodynamics 91

Particle Shape-Induced Settling Segregation 95

Effects of complex discrete particles on granular and multiphase flows 97

Influence of Secondary Flow Induced by Riblets on the Particle Distribution and Transport in Wall Turbulence 98

Research on Initial Stage Behavior of Liquid Film Formation during Bubble Collision using Direct Numerical Simulation 99

Effect of fluid-inertial torque on the orientation of tiny spheroidal particles in turbulent channel flow 111

Particle transport in turbulent square duct flows with a free surface 113

Direct numerical simulation of particle deposition in sedimentary pipes 115

Modelling of droplet multiple breakage accounting for entire energy spectrum bottleneck effect and eddy-droplet discrepancy 118

Sinking behavior of submillimeter microplastic fibers in still water and rising bubbly flow 123

Parallel Session IV: Topic 8-Multiphase flow measurement and industrial applications 124

An Improved Semi-Resolved CFD-DEM Model 124

Visual experiments and OpenFOAM modelling for gas-liquid bubbling flow and mass transfer process 127

Research on Mass Flow Measurement Model Based on averaging-velocity tube vortex street flow sensor 130

Research on Dynamic Measurement System of Gas Liquid Interface Based on Deep Learning 133

Optimizing Electrical Capacitance Tomography Images by ISTA-Net Algorithm Based on Dynamic Simulation of Gas-Oil Two-Phase Flow 136

Erosion of Sediment beds Using Impinging Jets: Application to Nuclear Waste Mixing 137

Investigation of Ice Crystal Morphology, Size Distribution and Concentration in Icing Wind Tunnel via HACPI 139

Online Measurement of Particulate Matter Concentration in Dilute Liquid-Solid Two-Phase Flow 141

Investigation of fluidized bed wetting and drying process by process tomography combined with acoustic sensor 143

Study on the characteristics of fine particle removal using surfactant-assisted spray 144

Study on Measurement of Gas-Liquid Two-Phase Stratified Flow 146

Measurement of polydisperse solid-liquid suspensions using positron emission particle tracking 149

Removal of fine seaweed from wastewater by means of cylindrical swirl flow and vibration 151

Coupling Simulation of Holdup and Dielectric Constant Distribution in Electrical Capacitance Tomography 153

Experimental study on the variation of microbubble size in a long vertical pipe 155

A real-time magnetic induction tomography system using differential coils printed by flex circuit boards 157

Parallel Session V-1: Topic 9- Phase change heat and mass transfer 159

Breakup Dynamics of Droplets of Complex Fluids 159

Stall Mechanism of Supercritical Carbon Dioxide Centrifugal Compressor with Vaneless Diffuser 161

Enhanced Condensation Droplet Growth and Shedding Performances under Electrowetting-on-Dielectric (EWOD) 162

Shadowgraphy for the liquid film dynamics in spray cooling under normal and reduced gravity 165

Experimental investigation of the evaporation characteristics of R1336mzz(Z) droplet at elevated temperature and pressure 167

Abnormal Gravity Scaling Behaviour and Bubble Dynamics in Low Heat Flux Nucleate Pool Boiling: What Have We Learned from vgBOILING-CSS 173

Experimental study on flow instability characteristics of supercritical-pressure R134a in a heated tube 174

Investigation on flow boiling heat transfer characteristics in parallel microchannels based on temperature sensitive paint 176

Topology Optimization Design of Natural Convection Heat Transfer Fins 180

Parallel Session V-2: Topic 10-Multiphase flow applications: electrostatics and bio-medical engineering 181

Numerical simulation of hemodynamics and spry cooling for the personalized laser dermatosis 181

A DEM study on effect of electrostatic interactions on granular flow behaviours during rotating 182

Experimental investigation of fractional laser's optimization effect for Q-switched laser skin thermotherapy 184

Electrostatic discharge properties of charged powders in the silo 186

Efficient Optimization of a Novel Dry Powder Inhaler Design Using Computational Fluid and Particle Dynamics 187

Experimental investigation on cavitation bubbles produced by laser-induced plasma in water 189

Two-phase flashing cryogen spray cooling: a skin pre-cooling technique assisting laser dermatology 191

Parallel Session VI: Topic11-Multi-scale modeling of multiphase flow 193

Multiscale kinetic theory for heterogeneous granular and gas-solid flows 193

Modeling of two-phase turbulence and mass transfer in bubble column reactors 194

Research on influence of periodic magnetic field on photothermal evaporation of ferromagnetic nanofluid droplets 195

Dynamic simulation of the funicular liquid bridge evolution in the separation process among three particles 198

Parameter Optimization of Gas-solid Two-phase Flow in a Plasma Melting Furnace 201

Research on characteristics of the external and internal flow coupling of supercavitating vehicle 202

Particle-resolved CFD modeling of the transfer performance in gas-solid fixed beds 204

Multiscale discrete–continuum simulation of granular flow 208

Soft coarse-grained particle model for particle-fluid systems 210

Numerical study on the flow field about steam condensation in the suppression pool by multi-hole spargers 212

Simulation of gas-solid two-phase flows with two-fluid model and data-driven closures 214

Nucleation and Growth of Au Nanocrystals during Aerosol Synthesis 216

Complex non-Newtonian droplet generation and flow pattern evolution in geometrical confined microfluidic cross-junctions 218

Study on Regulation of Drying Process of Non-spherical Wet Particles 221

Parallel Session VII: Topic 2-II- Multiphase flow：innovations and low-carbon engineering applications 223

Multi-Fidelity Optimization of Geological CO_2 Sequestration with Brine Extraction using Coarse Grid Network Model 223

Solid-solid stress model for the gas-fluidization of binary mixtures based on Inertial number 227

Novel design of baffled Micro-fluidized beds and its hydrodynamic behavior investigations: experiment and numerical simulation 229

Enhanced hydrogen production in novel reactor based on porous micro-structure flowing 232

A coarse-grained MP-PIC model for bubbling fluidization simulation 234

Fast pyrolysis of large biomass particles in a diameter transformed fluidized bed reactor 236

A reactor concept for water-gas shift with in-situ CO2-mineralization 238

CFD-DEM simulation of particle mixing and cycling characteristics in liquid-containing gas-solid fluidized bed reactor and spatial-temporal scales analysis 240

Euler-Lagrange simulations of large-scale reactive particle-laden flows 243

Hydrogen production from methanol by liquid phase discharge 245

Methodology of measuring parameters for particles based on their settled state 248

Numerical and experimental investigation of a fluidized bed intensified with volatiles distributors for biomass chemical looping combustion 249

Improving ethylene selectivity in MTO process by regulating the arrangement of coke in SAPO-34 molecular sieve crystals 250

Numerical simulation of particle erosion coupled with flue gas desulphurization in the spouted bed 253

Three-dimensional Numerical Investigation of Flow Past a Porous Spherical particle 254

Parallel Session VIII: Topic 4: Multiphase flows in heat exchangers 256

Thermal performance investigation of soil heat storage wall in solar greenhouse in severe cold regions 256

Thermal Performance of a helical channel printed circuit plate heat exchanger 258

Thermal performance of a novel battery thermal management system combining phase change material and air-cooled technologies 260

Machine learning prediction for thermal-hydraulic parameters of propane condensation flow in a PCHE straight channel 262

The experimental study on frictional pressure drop characteristics of two-phase fluids flow across the spiral tube bundles 263

Molecular dynamics study on the heat transfer properties of organic fluid based on deep learning potential 265

Numerical study on propane condensation in airfoil-enhanced PCHE for S-LNG vaporization 273

Numerical model and experimental verifications on turbulent CO_2 flow in supercritical and trans-critical regions inside a long thin circulation loop 274

Numerical Simulation on Direct Contact Condensation Heat Transfer characteristics in Steam-Water Film 276

Identification of Flow Patterns in an Opaque Condenser Tube by Distributed Fiber Bragg Gratings 280

Effects of heat flux, pressure, and surfactant concentration on pool boiling of water using expanding-channeled surface 281

Research on the Influence of Ocean Conditions on the Film-Forming Characteristics of Jet Ejector Condensers 283

Experimental investigations on water film flow inside the jet-type condenser 284

Parallel Session IX: Topic 5: Measurement methods and techniques in multiphase flow 288

External Field Intensified Particle Preparation and Machine Learning Assisted Flow Pattern Recognition 288

Effects of submicron particle layers on microparticle impact dynamics 290

The dynamic characteristics of impulse waves generated by landslides containing erratic boulders 291

Mixing of Highly Viscous Fluids: Flow Visualization and Intensification 292

Secondary Droplets Measurement during A Single Droplet Impacting on Heated Surfaces 297

Refractive Index Matching and Inertial Measurement Unit Particle Tracking Techniques for Application in Particle-Liquid Mixture Flow 299

Image quality evaluation of EIT sensors on dynamic multiphase flows with coupling field simulation 301

A learning-based volumetric reconstruction method for light field PIV 303

Application of Stacking Ensemble Learning in the Measurement of Suspended Sediment Particle Size Distribution 305

Two-phase stereo-PIV techniques for gas-liquid two-phase flow 308

An experimental investigation on characteristics of liquid film thickness of gas-liquid Taylor flow in rectangular microchannel 310

Study on the liquid-solid two-phase flow phenomenon and stress distribution characteristics in a batch slag-discharge lock hopper 312

Experimental and simulation studies based on an improved drag model 315

Parallel Session X: Topic 6-Multiphase flow in oil ang gas development and conversion 317

Multi-scale flow and transport dynamics in porous media 317

Estimation of CO_2-Oil Minimum Miscibility Pressure based on Integrated Machine Learning approach 319

Evolution characteristics of CO_2 plume and trapping under heterogeneous capillary pressure and geochemical reactions during injection and post-injection 320

Experimental study of monitoring fluid migration in CO_2 reservoir by fiber optic strain sensing 323

Study on the influence of heterogeneity of porous media on CO_2 immiscible displacement in pore scale 329

Pore-scale study of mineral dissolution-precipitation during saline aquifer storage 330

A Study on the Structural Characteristics and Transport Properties of Porous Media based on Fractal Geometry and Deep Learning 332

Dynamic behavior of the oil-air interface in a hard disk drive' spindle under centrifugal force or axial shock 334

Study on Characteristics of Hydrate-based CO_2 Sequestration in Marine Sediments 337

An improved model for heavy oil-water eccentric core annular flow in a horizontal pipe 339

Investigation into pore-scale multiphase reactive heat and mass transfer mechanisms during methane hydrate dissociation 342

Wettability effect on the two-phase flow-induced vibration in response to a micro-scale ⊥-shaped pipe 343

Influence of the operation pressure on gas-liquid two-phase severe slugging flow in a pipeline-riser system 344

SuperDEM-CFD modeling of fluidization of spherical and cylindrical particles binary mixtures and experiment validation 346

Parallel Session XI: Topic 7- Multiphase flows in thermal management and thermal energy storage 347

Effects of particle's surface properties and aggregation modes on heterogeneous condensational growth of droplets on particle surfaces 347

Effect of large material compliance on water skipping physics of deformable spheres 348

Explorations of scaled-up spout fluidized beds in heat exchange of thermochemical particles 349

Design and simulation of transpiration cooling combined with Solid-Solid PCM at leading edge of hypersonic vehicles 350

Fluid Flow and Heat Transfer in Microchannels with Porous Bio-Inspired Fish Scale Structures 354

Numerical investigation on the supercritical startup of cryogenic loop heat pipe for space application 356

Polymeric Flocculation of Multiphase Nuclear Waste Suspensions 358

Numerical investigation on center-dispersed microchannel liquid-cooling plates for battery thermal management 360

Pore-Scale Numerical Modelling of Multiphase Flow in Chemical Flooding of Oil Reservoir 361

Solid particles as solar receiver and thermal energy storage media: flow behaviour and heat transfer characteristics 362

Research on Steam Mass Flow Measurement Based on a Novel Vortex Flowmeter with Annubar Tube 364

Numerical study on surface coating of phase change materials based on coaxial technology 365

Parallel Session XII: Topic12-Multiphase flow: Complex granular flows: new progress in numerical simulations and rheological models 367

A modified kinetic theory for the grain phase in dense liquid-particle mixture flow 367

Boundary Conditions Alter Inhomogeneity and Stress Fluctuations in Shear-Thickening Suspensions 370

CFD-DEM modeling and investigation of the heat transfer behaviors in a fluidized bed containing rod-like particles 372

Study on the effects and mechanisms of vibration insert to the discharging process in silos 373

Particle kinetics with sintering force under high temperature 374

Unjamming and yielding of intruder-deformation-driven dense granular materials 376

The restitution coefficient and critical sticking velocity of small particles: simulation and experiment 377

Intermittent Jamming of Cohesive Particle Flow in FT4 Rheometer 379

Length-scale-based rheology for dense granular suspensions 381

A new numerical method for dynamic resuspension of particles 382

Machine Learning Based Surrogate Models for Efficient Particulate Flow Simulation 384

Interface-resolved simulations of particles in active nematics 386

A combined DEM and Positron Emission Particle Tracking (PEPT) study on continuous blending 387

Poster Session 389

Filtration performance of a granular bed filter in a coupled separator 389

Performance evaluation of a wet air oxidation reactor with external circulation for high-chemical oxygen demand wastewater treatment 390

Optimization of process parameters in an entrained flow gasifier 393

Temperature Regulation of Polyethylene Composite Materials 394

Explosion-driven fragmentation of particle shells 396

Spontaneous transfer of droplets across a microfluidic liquid-liquid interface 397

The response of droplet traffic to a perturbation of flow resistance at the arms of a micro-T-junction 399

Explosion-driven expansion instability study of granular media 405

Research on the Distribution of Residual Oil during the Ultra-High Water-Cut stage of Bottom Water Reservoir and the Enhancing Oil Recovery Methods 407

A Review on the flow modification technology of multiphase flow systems using electric fields 408

Study on the behavior characteristics of the oil leakage from submarine pipeline 409

Experimental study on static immersion cooling of large-scale lithium-ion battery 412

Optimization of the battery thermal management system with phase change materials, aerogel and cold plates 415

Imaging Hydrogen Bubble Distribution and Flow through Granular Material with X-Ray Computed Tomography 417

Hydrodynamics and mass transfer in a planar bubbly cyclone 419

A structural optimization method for conductivity array liquid film sensor 422

Droplet shape acquisition by its light scattering pattern assisted with deep learning 424

A new ultrasonic attenuation model based on gas-liquid two-phase flow 426

Experimental and modeling study on liquid film thickness of horizontal gas-liquid annular flow using ultrasonic method 428

Friction nanogenerator based on solid-liquid contact initiation principle 430

Simulation study of synthetic jets for enhanced jet breakup in liquid-liquid systems 433

Particle movement mode effect on electrostatics 434

Numerical simulation of fuel droplet breakup and dispersion cross-scale behavior.....437
Numerical Simulation of Cut Tobacco Flow in a Fluidized Bed.....438
Numerical simulation of particle behavior under two-phase impinging jet erosion.....441
Charged multiphase flow-based suppression of fugitive dust and application.....444

Plenary speech

Recent progress in thermochemical multiphase reacting flow

Jin Hui, Guo Liejin
Xi'an Jiaotong University

Thermochemical process, such as combustion and gasification produces the greatest amount of power and chemical sources, however, exiting coal thermochemical process occurs in gas environment and inevitably causes environmental pollution and emits huge amount of CO2 emission. Supercritical water gasification is a promising thermochemical process, and provides a homogeneous and rapid environment for coal conversion to produce pure H2 and CO2, then realizes the multi-goals of clean, efficient and low carbon together. Nevertheless, supercritical reacting flow refers to a complicated process, and cannot be regulated by a single operating parameter, hence the carbon gasification efficiency is low in some experiments without reaction regulation. Therefore, we recover the method of optimal matching of substance and energy in supercritical water reacting flow. The multiphase flow characteristics are well arranged to provide suitable substance and energy for each reaction to regulate the reaction pathway and rate. 1)Inter-facial heat and mass transfer rules between transcritical water and particle are revealed and trancritical water injection flow pattern distribution characteristics are proposed to realized the rapid heating of coal particle, which achieves side reaction inhibition. 2)Trans-scale reaction kinetic model is proposed, then rate-controlling step and reaction enhancement method is put forward, which achieves main reaction enhancement. 3)The method for optimal matching of substance/energy production and consumption by multi-reactions so as to reduce the process irreversibility, which achieves multi-reaction coordination. Through the above efforts, the complete gasification temperature is decreased below 670℃, to ensure the technological and economical feasibility, paving the way for technology industrialization.

The influence of flow on the production of low-carbon hydrogen

Raffaella Ocone
Heriot-Watt University (United Kingdom)

FB mineral processing from fundamental to application

Zhu Qingshan
Institute of Process Engineering, Chinese Academy of Sciences

China has large reserves of low grade minerals, which are difficult to be beneficiated by conventional processes, and are currently not able to be utilized. It is therefore often needed to transform ores from difficult-processed phases and structures to more easily processed phases and structures, normally through chemical processes like roasting via oxidation, reduction, etc. Fluidized bed (FB) reactors have been proven to be the most efficient reactors for mineral roasting. In the present presentation, fluidized bed roasting practices of our group will be introduced.

Over the past decade, several fundamental aspects related to FB mineral roasting have been explored, like the influence of roasting conditions on the phase and structure change, process intensification via FB configuration and internals, adjustment of means residence time (MRT) for the coarse and fine particles, optimization of FB scale-up through CFD simulations, etc., have been systematically investigated. Several key technologies, like powder preheating via cyclones, feeding/discharging non-mechanical valves, sensible heat recovery for high temperature roasted powders, etc. have also been developed. Moreover, our practices on engineering implementation of fluidized bed mineral roasting will also be introduced, including oxidative-reductive roasting of Panzhihua ilmenite for the production of synthetic rutile, magnetizing roasting of low grade iron ores for iron ore beneficiation, direct reduction of iron ore concentrate for the development of non-blast furnace ironmaking technology, calcination of aluminum hydroxide to produce 50-70% -Al2O3, reduction of low grade pyrolusite for MnSO4 production, calcination of phosphogypsum, magnetizing roasting of iron-manganese mixing ore, etc. Several pilot and commercial scale plants have been established with cooperation of various companies, e.g. 200 kt/a reduction plant has been successfully put in operation for over 8 years for the reduction of low grade pyrolusite in Yunn province, China.

Modeling and simulation of gas-particle fluidized beds with heat and mass transfer for the development of low carbon engineering applications

Olivier Simonin
Université de Toulouse / CNRS (France)

Gas-particle fluidized beds have exceptional characteristics in terms of transport and mixing, contact between a dispersed phase and a reactive gaseous medium, thermal inertia and wall transfer. This makes them highly relevant to the energy industry, particularly for the development of innovative processes that meet the challenges of the energy transition, such as biomass gasification or chemical looping combustion plants, fluidized bed solar receivers, hydrogen combustion or heat storage on particles. Unsteady three-dimensional numerical simulation of these flows, on a pilot or industrial scale, is increasingly emerging as a key tool for supporting the development of new processes. However, its development continues to pose numerous modeling problems due to the wide range of scales encountered and the many multi-physical couplings involved and to the difficulty to carry out detailed experiments.

Over the last twenty years or so, high-performance computing has made it possible to develop a multi-scale approach for the modeling and simulation of gas-solid fluidized beds based on:

- fully resolved" microscopic simulations of ensembles of particles up to several thousand, modelling local interactions and transfers with the fluid for very simple flow configurations;
- mesoscopic CFD-DEM simulations of ensembles of particles up to several million, capturing the collective effects of particles interactions with the fluid and the walls, for flow configuration close to laboratory experiments;
- macroscopic N-Euler simulations of the statistical properties of the set of particles, such as number density, average velocity and kinetic energy of the random motion, for pilot or industrial flow configurations.

Detailed analysis of the results of the microscopic and mesoscopic simulations makes it possible, on the one hand, to improve understanding and modelling of local phenomena and, on the other hand, to inform and validate the closure models developed as part of the statistical approaches associated with the Eulerian equations governing the macroscopic quantities.

The presentation will present recent developments and results obtained in the frame of the multiscale approach focusing on some key closure problems for the prediction of fluidized beds for low-carbon engineering applications such as chemical looping combustion and fluidized bed solar receiver. In particular, the presentation will focus on: the dynamic and thermal boundary conditions between particles and walls, the coupling between hydrodynamic and heterogeneous/homogeneous reactions in gas-solid multiphase flows and the development of filtered macroscopic approaches for the simulation at industrial scale on feasible mesh sizes.

Pseudo-boiling in supercritical pressures: theory, experiment and applications

Xu Jinliang
North China Electric Power University

Heat transfer in supercritical pressures is a nature phenomenon and widely occurs in power generation system, geothermal system and materials fabrication process. Classically, supercritical heat transfer is treated in the single-phase fluid framework without bubbles, droplets and vapor-liquid interfaces. Because the experiments are obviously against the single-phase fluid theory in supercritical pressures, the term of pseudo-boiling was reported in 1960s-1970s, referring to that when heat is applied to supercritical fluid, bubble-like and vapor-film-like features appear and wall temperature peaks occur, similar to boiling in subcritical pressures. Here, I report the progress of pseudo-boiling theory, experiment and applications made in our laboratory.

We established a multi-phase framework in supercritical pressures, including three regimes of liquid-like (LL), two-phase-like (TPL) and vapor-like (VL) regimes. Contrary to one saturation temperature in subcritical pressures, two phase transition temperatures: the onset of pseudo-boiling temperature (T-), and the termination of pseudo-boiling temperature (T+), are determined by the molecular dynamics (MD) simulation, matching those determined by the thermodynamics approach. Thermophysical properties of LL and VL phases are evaluated using T- and T+, respectively. In the TPL regime, a set of non-dimensional parameters are proposed to reflect the interactions of mass, momentum and energy between LL and VL phases. The pseudo-vapor mass quality (x) is newly defined to characterize the vapor mass content in the mixture. Our multi-phase theory successfully explains the unconventional phenomena in supercritical pressures. It is found that the measured heat transfer coefficients in the TPL regime ($0<x<1$) significantly deviated from those based on the single-phase fluid theory, but can be predicted by the multi-phase theory. Our MD simulations also detected the chaotic behavior of phase distributions in supercritical domain.

We established an experiment system to study the multi-phase feature of supercritical fluid with the wire heating. Using a direct photographic technique based on the light refractive principle, we analyse the brighter/darker pattern in a varied-density field. The vapor–liquid interface is quantified using the grey extraction method. Our results show that beyond the limit of natural convection (NC), the evaporation-like (EL) mode, the transition from EL to boiling-like (BL) mode, and the BL mode are directly observed, supporting the multi-phase theory. The small-perturbation theory is developed to indicate that pseudo-boiling is caused by the spatio-temporal gradient induced instability. Our work elaborately explores common and uncommon features between supercritical pseudo-boiling and subcritical boiling, and uncovers the secret of two modes of pseudo-boiling. We further explore the pseudo-boiling contribution ratio qb/q, where qb is the boiling heat flux and q is the applied heat flux. Covering a wide experiment range, it is found that qb/q varies in a range from 0.19 to 0.65, indicating that the pseudo-boiling effect is significant. Inverse boiling curves are found in supercritical pressures with respect to those in subcritical pressures. Finally, we discuss the applications of the pseudo-boiling theory for industry applications, including the development of non-dimensional parameters to predict normal heat transfer and heat transfer deteriorations, as well as the numerical works based on the multi-phase framework for the analysis of bubbles/droplets formation during the transient operation of advanced power generation systems.

Electrical capacitance tomography for multiphase flow measurement

Yang Wuqiang
University of Manchester (United Kingdom)

Among various industrial tomography modalities, electrical capacitance tomography (ECT) is the most mature and has been used for many challenging applications, in particular for multiphase flow measurement. ECT is based on measuring very small capacitance from a multi-electrode sensor and reconstructing the permittivity distribution in a cross section of an industrial process. Because of very small capacitance to be measured and the "soft-field" nature, ECT does present challenges in capacitance measurement and solving the inverse problem. The latest AC-based ECT system can generate online images at 100 frames per second with a signal-to-noise ratio (SNR) of 70 dB. During this talk, ECT principle will be discussed, including image reconstruction algorithms. The AC-based ECT system will be introduced, including hardware design and its performance. Examples of industrial applications include gas/solids pneumatic conveying, gas/oil/water flow measurement, and imaging gas/solids fluidised beds for pharmaceutical manufacturing, clean coal combustion and methanal-to-olefin conversion. Future developments will also be highlighted. It is likely that a live demonstration how an ECT system works is given during the talk.

Abnormal gravity scaling behavior and bubble dynamics in nucleate pool boiling with low heat flux: what have we learned from vg BOILING-CSS

Zhao Jianfu
Institute of Mechanics, Chinese Academy of Sciences

Boiling is one of the most effective methods of heat transfer, which is employed widely in component cooling and in various energy conversion systems in normal gravity on the ground, and will be a potential candidate with significant advantages such as compactness, light weight, high efficiency for space applications in microgravity environment. Due to large difference between the densities of the liquid and its vapour, bubble dynamics, flow structures and heat transfer performances of boiling in different gravity conditions exhibit distinct difference. The applicability of common-used correlations, e.g. the Rohsenow correlation for nucleate pool boiling, diminishes quickly to reduced gravity conditions. The fundamental reason is that gravity appeared in those correlations is only a dimensional constant rather than a controllable independent variable. To meet the application requirements of multiple scenarios with different gravity levels in space missions, it is necessary to conduct in-depth research on the influence of gravity on heat transfer and bubble dynamics in boiling phenomenon. With the help of simulated gravity environment provided by the Variable Gravity Science Rack (VGR) in Wentian Lab Module of the China Space Station (CSS), a project vg BOILING-CSS, one of the first batch of two scientific experiment tasks utilizing VGR, was proposed to study heat transfer and bubble dynamics during pool boiling in a wide range of gravity levels from 2g to the background microgravity environment of CSS. The experimental facility of vg BOILING-CSS, including an electronic control box, an experimental box, a connecting cable and a ventilation pipe, was sent to CSS by the cargo spacecraft Tianzhou-5 on November 12, 2022, and was installed by the astronaut crew of Shenzhou-15 on a centrifugal of VGR on December 12, 2022. After successful in-orbit performance testing on December 15, 2022, four stages of space scientific experiments have been conducted in the past period of time. An abnormal gravity scaling behaviour, namely an enhancement rather than deterioration of the heat transfer with the decreasing gravity, has been discovered in the nucleate pool boiling region with low heat flux. The largest diameter of growing isolated bubble attached on the heating surface is found to be inversely proportional to gravity and proportional to the 0.3-power of the superheating. The present lecture will provide a summary on the preliminary findings obtained from the project vg BOILING-CSS.

Modelling of multiphase reacting flows and industry applications

Shen Yansong
University of New South Wales (Australia)

Process design and control play a significant role in modern industries. Most processes and reactors are very complex, as they usually involve not only multiphase flows but also heat and mass transfers related to chemical reactions and their interactions – the so-called reacting flow. The operation must be optimised in order to be competitive and sustainable, particularly under more and more demanding economic and environmental conditions. This will need continuous innovative research and development. Computer simulation and modelling, supported by online data and experiments, have emerged as an indispensable adjunct to the traditional modes of investigation for the design, control and optimisation of processes, reactors, and devices. Several case studies, including hydrogen generation, storage and use in the net zero steel industry, are presented in this talk to demonstrate that the modelling works are indeed helpful in understanding fundamentals and optimising & developing new, cleaner and more efficient technologies towards net zero industry innovations with measurable outcomes and profits.

Topic1- Multiphase reactive flow: model development and industrial applications

CPFD simulation of a continuous tapered fluidized bed reactor for U3O8 hydrogen reduction

Shuyue Li [1], Yongmin Zhang [1], Huan Wang [1,2*]

1 State Key Laboratory of Heavy Oil Processing, China University of Petroleum-Beijing, Beijing 102249, PR China

2 CNNC No. 7 Research and Design Institute Co., Ltd., Taiyuan 030012, PR China

Abstract

Fluidized beds have been widely employed in several critical stages of dry natural uranium conversion processes. However, poor de-fluidization phenomena and low reaction conversion are frequently encountered in these systems due to the high-density particles. This work employs the CPFD method, coupled with chemical reactions, to perform a long-duration numerical simulation of U_3O_8 reduction reactor. The model considers gas-solid flows, turbulence, heat and mass transfer, and heterogeneous reactions, among others. Numerical results show that under conditions of an 80% excess of hydrogen gas, despite the fluidization velocity being significantly higher than the minimum fluidization velocity of the particles, the fluidization state is poor, with most regions remaining in a non-fluidized state. Severe gas bypassing phenomena are observed at the walls, leading to a low bed expansion rate. The average residence time of particles at the solid outlet is consistently equivalent to half of the total operational time of the reactor, indicating a highly uniform mixing of particles within the bed. Within the limited computation time, the conversion rate of products at the solid outlet continue to increase. Based on the available growth trend and through extrapolation using a fitting formula, it is inferred that a qualified solid product (97 wt.% UO_2) could be obtained after around 13 hours of continuous operation of the studied apparatus. Based on the results, it is recommended that future efforts should focus on optimizing the structure and operational conditions of the reactor to enhance fluidization and improve product conversion.

Drag and Heat transfer coefficients for prolate ellipsoids in low-Mach number variable-density flow in the absence of buoyancy

Yong Chen
Wuhan University of Technology, Wuhan, Chin

Abstract

Low-Mach number variable-density flows are ubiquitous in nature and industry, e.g. sedimentation of volcanic plume, solid particle solar receiver, biomass gasification, and hydrogen production by chemical looping combustion. The numerical simulation of such flows relies critically on the availability of closure relationships for the hydrodynamic coefficients (i.e. drag, lift and torque correlations) and Nusselt number to model correctly momentum and heat transfer. For particles in incompressible flow a range of hydrodynamic coefficients[1-3] and Nusselt number[4-5] correlations have been proposed. However, very few works have been devoted to derive hydrodynamic coefficients and Nusselt number correlations for axisymmetric nonspherical particles in low-Mach number variable-density flow.

In this work, the lattice Boltzmann method with immersed moving boundary conditions will be used to calculate the drag coefficient and Nusselt number for prolate ellipsoids over a wide range of Reynolds numbers ($\boldsymbol{Re \leq 100}$), aspect ratios ($\boldsymbol{1.25 \leq Ar \leq 4}$) and Boussinesq parameters ($\boldsymbol{\gamma \leq 2}$, relative particle-fluid temperature difference), respectively. Correlations for drag and Nusselt number will be developed based on the simulation data. The new correlations can help to improve the accuracy of Euler-Lagrangian simulations of low-Mach number variable-density flow comprising prolate ellipsoids.

Keywords: Low-Mach number variable-density flow; Drag coefficient; Nusselt number; Prolate ellipsoid.

References

[1] Ke, C., Shu, S., Zhang, H., Yuan, H., Yang, D. (2018). On the drag coefficient and averaged Nusselt number of an ellipsoidal particle in a fluid. Powder Technology, 325, 134-144.
[2] Fröhlich, K., Matthias, M., Schröder, W. (2020). Correlations for inclined prolates based on highly resolved simulations. Journal of Fluid Mechanics, 901, A5.
[3] Chen, Y., Jiang, P., Xiong, T., Wei, W., Fang, Z., Wang, B. (2021). Drag and heat transfer coefficients for axisymmetric nonspherical particles: A LBM study. Chemical Engineering Journal, 424, 130391.
[4] Ganguli, S., Lele, S.K. (2019). Drag of a heated sphere at low Reynolds numbers in the absence of buoyancy. Journal of Fluid Mechanics, 869, 264-291.
[5] Kiwitt, T., Fröhlich, K., Meinke, M., Schröder, W. (2022). Nusselt correlation for ellipsoidal particles. International Journal of Multiphase Flow, 149, 103941.

CFD-DEM modelling of absorber sphere pneumatic conveying and erosive wear

Lianyong Zhou[a], Tianjin Li[b], Yongzhi Zhao[a,*]
[a] Zhejiang University, Hangzhou, China [b] Tsinghua University, Beijing, China

Abstract
As a second shutdown system for the High-temperature Gas-cooled Reactor (HTGR), the absorber sphere shutdown system is of significant importance to the safe operation of HTGR. Therefore, an in-depth study on the core process of absorber sphere shutdown system, i.e., absorber sphere pneumatic conveying is an urgent need for the development of fourth-generation nuclear energy technology in China. This study simulated the three critical processes, i.e., stable conveying, conveying interruption, and conveying restart using an improved CFD-DEM method that releases the limit of fluid grid size on CFD-DEM simulation. (i) Particle acceleration and flow rate characteristics during the stable conveying, (ii) particle falling and packing characteristics in the riser after conveying interruption, and (iii) the initial fluidization and restart pressure drop characteristics after conveying restart were analyzed quantitatively. The results demonstrated that (i) the acceleration height occupied 15% of the riser height and the mass flow rate of particles increased linearly with the inlet velocity; (ii) the packing height is independent of the inlet velocity and most of the packing particles are falling particles for dense pneumatic conveying; (iii) the gas velocities required for initial fluidization and particle entering the riser were also independent of the target inlet velocity. Furthermore, the erosive wear of the absorber sphere feeder, riser and container was calculated using an impact energy erosion model (IEEM). The spatial distribution and the influence factors of erosive wear were analyzed.

Keywords: CFD-DEM, Gas-solid flow, Absorber sphere, Pneumatic conveying, Erosive wear

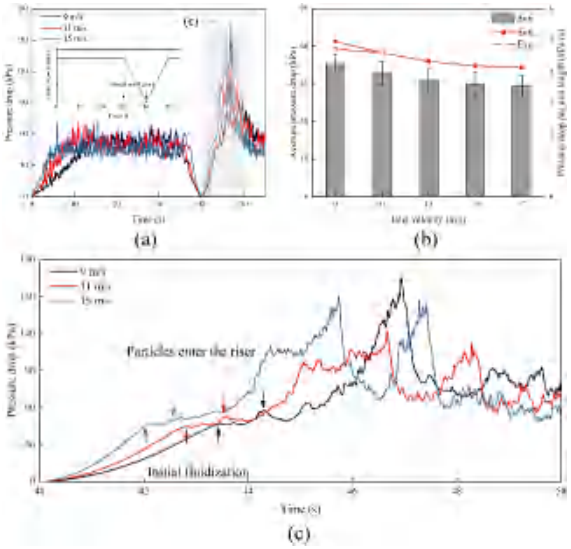


Figure 1 – Pressure drop of riser inlet

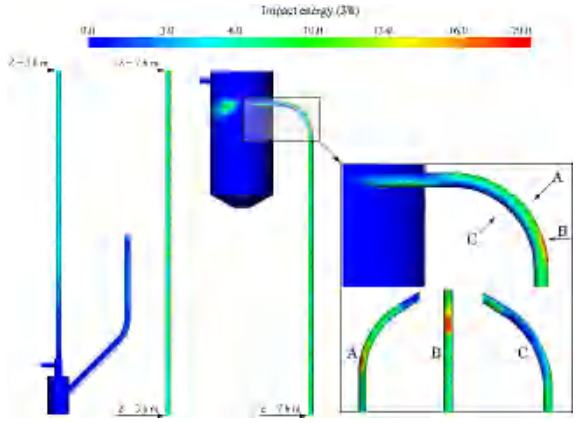


Figure 2 – Erosive wear of conveying system

References

[1] L. Zhou, T. Li, H. Ma, Z. Liu, Y. Dong, Y. Zhao. Development and verification of an unresolved CFD-DEM method applicable to different-sized grids, Powder Technology 432 (2024) 119127.

[2] L. Zhou, T. Li, Z. Liu, H. Ma, C. Xu, Y. Dong, Y. Zhao. An impact energy erosion model with an energy allocation rule for the discrete element method. Wear 540-541(2024) 205233.

The research of Separation and Resistance Characteristics of Horizontal Corrugated Plates

ZiWei Zhang[1],ChuanChang Dong[1],ZhaoMing Meng[1,*]

1 Heilongjiang Provincial Key Laboratory of Nuclear Power System & Equipment, Harbin Engineering University, Harbin 150001, China

Abstract

The research utilized the software ICEM for mesh generation, the software Fluent for numerical simulation and the discrete-phase model to describe the motion of the droplet particles in order to obtain more accurate results for horizontal Corrugated Plates in the startup separator. The research performed the numerical simulation of the gas-liquid two-phase flow within the corrugated plates through Realizable k-ε model and wall film model based on discrete-phase model to explore the influencing factors of the the separation efficiency of the corrugated plates and obtained the empirical equation of separation efficiency and resistance characteristics of corrugated plates. Results showed that the factors affecting the separation efficiency of the corrugated plates in the steam-water separator include droplet diameter, airflow velocity and inlet humidity et al. As the velocity of the vapor-fluid increases, the separation efficiency is improved correspondingly and the droplet particles are more easily separated with larger sizes. However, under a constant state of steam flow velocity and droplet particle diameter, as the steam humidity increases, the separation efficiency improves initially and followed by a decline. From above, the empirical equation of separation efficiency and resistance characteristics of corrugated plates were derived.

Key Words: Corrugated plate; Droplet diameter; Separation efficiency; Empirical formula; Resistance characteristics

Fast Predicting Spatiotemporal Distributions of Fluidized Bed Pyrolysis for Biomass Using Convolutional Neural Networks

Qingang Xiong[1], Hanbin Zhong[2]
1. South China University of Technology, Guangzhou, China;
2. Xi'an Shiyou University, Xi'an, China

Abstract
A deep learning (DL) model centered on convolutional neural networks was developed based on CFD results to efficiently predict spatiotemporal distributions of quantities of each phase in a bubbling fluidized bed for biomass fast pyrolysis. Input of the DL model is a sequence of spatiotemporal distributions, and only an initial input is required to generate continuous outputs. The model was optimized by adjusting four typical parameters, i.e., length of input sequence, number of neurons, learning rate, and prediction step size. Accuracy of short-term prediction (10 frames) and stability of long-term prediction (1000 frames) were analyzed, as well as the relationship between time-averaged distributions and prediction length. It was found that with satisfactory accuracy, several orders of magnitude increase in prediction efficiency can be realized.

Keywords: Bubbling fluidized bed, CFD, Deep learning, Convolutional neural network, Spatiotemporal distributions

Introduction

Bubbling fluidized-bed biomass fast pyrolysis is a crucial technology for carbon neutrality and sustainability, and computational fluid dynamics (CFD) is one of the promising approaches to investigate and optimize bubbling fluidized-bed biomass fast pyrolysis. However, traditional CFD is still computationally costly for bubbling fluidized-bed biomass fast pyrolysis, especially for spatiotemporal transport-reaction behaviors which are critical to clarify intrinsic characteristics and optimize operations. To address this issue, this work proposed a DL model based on CNN for the fast predicting of spatiotemporal distributions during biomass fast pyrolysis in a bubbling fluidized bed.

Methodology and Results

CFD data of bubbling fluidized-bed biomass fast pyrolysis[1] were used as the training set for CNN to develop a DL model to predict spatiotemporal distributions of quantities. Firstly, the processes of data acquisition and DL model development were discussed. After DL model evaluation, its application in predictions of spatiotemporal distributions of quantities in bubbling fluidized-bed biomass fast pyrolysis was presented. The model's results undergo meticulous analysis, including the accuracy of short-term predictions (10 frames) and the stability of long-term predictions (1000 frames), as well as the relationship between time-averaged distributions and prediction length. Finally, the proposed model was extended to predict five other distributions, the mass fraction of tar, gas, biomass, char, and the volume fraction of bio-mixture. The results indicate that length of input sequence is the parameter that has the greatest influence for phases and species.

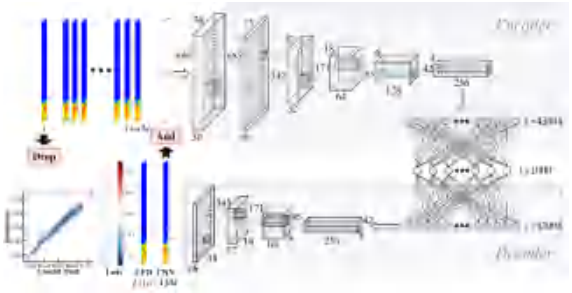


Figure 3 – Flowchart of DL method

References

[1] H. Zhong, Z. Wei, Y. Man, S. Pan, J. Zhang, B. Niu, X. Yu, Y. Ouyang, Q. Xiong, Prediction of instantaneous yield of bio-oil in fluidized biomass pyrolysis using long short-term memory network based on computational fluid dynamics data, Journal of Cleaner Production 391 (2023) 136192.

Numerical Investigation into the Gasification of Industrial Organic Waste in Entrained-Bed Reactors Utilizing Detailed Chemical Kinetic Mechanisms

Huiyang Bi, Bin Yang
Zhejiang University, Hangzhou, China

Abstract
Organic hazardous waste is inevitable in the chemical industrial production processes, and its reasonable disposal is particularly important nowadays. This work used methanol as a typical low calorific value industrial organic hazardous waste, and studied its gasification conversion characteristics by constructing methods and models for numerical calculation. The results showed that the optimized operation condition for its gasification when the atomization particle size of the liquid droplets was controlled within 100-300 μm, the oxygen-fuel ratio located in 0.6-0.8, and the moisture content is near 10 wt%. This work provided reasonable operation conditions for similar low calorific value waste disposal.

Keywords: Numerical simulation, Waste management, Gasification, Optimization

Introduction

In the chemical industrial production process, large amounts of organic hazardous wastes are inevitably produced, and their harmless disposal and resource utilization are of great significance. As a representative of liquid organic wastes, waste methanol has the characteristics of high toxicity, low calorific value, high latent heat of vaporization, and contains water and other organic matters. Its direct incineration further aggravates CO_2 emissions, and its low calorific value feature is disadvantageous to incineration process. However, by converting it into syngas through partial oxidation, high value-added chemicals can be produced through industrial chain to recycle hydrocarbon resources [1]. The gasification process includes multi-phase mixing and reactions in the gasifier, and their flow field distribution characteristics transformation rules of substances and product characteristics can be observed through CFD methods during the reaction processes [2].

Since the properties of organic waste liquid are significantly different from traditional coal-water slurry, a numerical model based on Texaco entrained-bed gasifier for gasification conversion of organic hazardous waste, represented by waste methanol, to synthesis gas was established to investigate the conversion process and product properties for operation conditions optimization.

Methodology

Based on the actual industrial used gasifier by an enterprise in Zhejiang Province, the effects of operation conditions on the gasification of typical materials were explored. ICEM software was used to divide the geometry of the gasifier into a hexahedral structured mesh. Basic govern equations were used to describe the reaction process, and the Realizable k-ε turbulence model was used to describe the turbulent characteristics of the fluid flow [3]. The Redlich-Kwong equation was used to describe the gas compressibility and P-1 model was used to describe the radiation heat transfer due to the high temperature and pressure in the gasifier. The discrete phase model was used to describe the atomization of inlet materials at the nozzle, and a reaction mechanism optimized by U. Burke et. al. was used for the calculation [4].

Results

Grid independence verification

The independence of the number of grids on the calculation results should be firstly determined. When the number of grids increased from 8k to 195k, the deviation of the prediction results compared to 398k decreased from a maximum of 8.9% to less than 0.8%, and further increasing

the number of grids had little impact on the results. Therefore, 195k was considered as the number of independent grid number.

Effect of oxygen-fuel ratio on gasification

The temperature of the gasifier body continued to increase as the oxygen-fuel ratio (OR) increased. When OR was increased from 0.3 to 0.6, injected methanol can be evaporated and converted to syngas, and the average gasifier temperature increased from 541 K to 1370 K with the highest H_2 and CO concentration of 63%. However, when OR further increased to 1.0, a more complete oxidative combustion occurred with an average temperature of 2192 K with H_2 and CO concentration decreased to 36%.

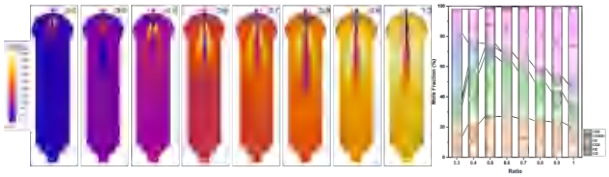


Figure 1 - Effect of oxygen-fuel ratio on temperature and syngas concentration.

For multi-channel nozzles with central and external annulus, the oxygen flow ratio of the central and external annular channels were adjusted from 1:1 to 1:25. The results showed that the difference of the outlet syngas content was less than 3%, indicating that its proportion had little impact on the gasification results.

Effect of atomized particle size on gasification

When the droplet size was larger than 1000 μm, the heat transfer rate was low, causing incomplete vaporization and localized deep oxidation with high exotherm. Complete gasification and conversion can be achieved when the droplet size was smaller than 500um. When the particle size was less than 300 μm, the length of the flame zone was reduced by 75.7% to 0.53 m, and further reducing the particle size had no significant impact on the product results. When the particle size reached 10 μm, a flame zone of 2942 K was formed only 0.19 m away from the nozzle, while particle size of 100 μm was 0.73 m, indicating that a too small particle size was detrimental to the life of the nozzle.

Effect of moisture content on gasification

The impact of both moisture and OR was investigated on the gasification due to changes in calorific value of the inlet material.

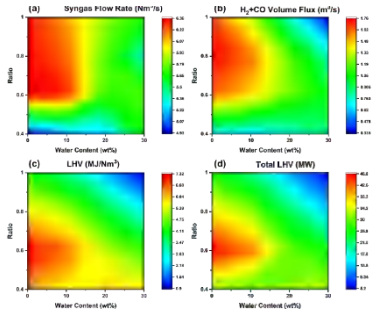


Figure 2 - (a)Flow rate, (b)H_2+CO flux, (c)LHV, and (d)Total LHV of the syngas product.

Regarding the outlet syngas characteristics, the gas flow rate ranged from a minimum of 4.93 Nm^3/s at OR=0.4 and MC (moisture content) =0 wt% to a maximum of 6.36 Nm^3/s at OR=0.6 and MC=10 wt%. The overall flow rate showed a trend of first increasing and then decreasing. But for the CO and H_2 flow rate, the flow rate ranged from 0.34 Nm^3/s at OR=1.0 and MC=30 wt%, to a maximum of 1.76 Nm^3/s at OR=0.8 and MC=10 wt%. The volume averaged LHV distribution of syngas was similar to CO and H_2 flow rate, which was 0.9 MJ/Nm^3 at OR=1.0 and MC=30 wt% for the lowest and 7.32 MJ/Nm^3 at OR=0.6 and MC=10 wt% for the highest. The total LHV also showd consistent characteristics, with a peak near the middle of the area,

which was related to the effective gas component flow rate.

Conclusions

This work established a numerical simulation method for the gasification conversion of low calorific value organic hazardous waste represented by methanol, and investigated the distribution of syngas production and reaction characteristics of operating conditions.

The results show that good gasification conversion of waste liquid can be achieved when OR was higher than 0.6 while the gas flow distribution in the nozzle had little impact on the reaction results. The atomized particle size of droplets had a significant impact on its gasification process, and the particle size should be controlled between 100-300um to ensure good conversion efficiency and reasonable flame position. When moisture content was near 10 wt% and OR ranged from 0.6 to 0.8, syngas with better fuel properties and larger CO and H_2 flow rates can be obtained.

This work provided reasonable research ideas and operating conditions for the gasification conversion and disposal of similar low calorific value water-containing organic hazardous waste.

References

[1] G. Tian, Q. Xia, Z. Wu, T. Fu, Ecological network analysis of industrial wastes metabolism based on input-output model for Jiangsu, Waste Management 143 (2022) 23-34.

[2] H. Sun, G Bao, S Yang, J. Hu, H. Wang, Numerical investigation of the reactive gas–solid characteristics in biomass fast pyrolysis of conical spouted reactor equipped with draft tube, AIChE Journal 69 (2023) 1-17.

[3] R. Shaheed, A. Mohammadian, K.G. Hossein, A comparison of standard k-ε and realizable k-ε turbulence models in curved and confluent channels, Environmental Fluid Mechanics 19 (2019) 543-568.

[4] U. Burke, W.K. Metcalfe, S.M. Burke, K.A. Heufer, P. Dagaut, H.J. Curran, A detailed chemical kinetic modeling, ignition delay time and jet-stirred reactor study of methanol oxidation, Combustion and Flame 165 (2016) 125-136.

A Novel Intrusive Reduced-order Model for the Parametric Prediction of Bubbling Fluidized Beds

Xiaofei Li, Shuai Wang, Kun Luo, Jianren Fan
Zhejiang University, Hangzhou, China

Abstract
A major application of numerical simulation in industrial processes is parametric simulation. However, simulating dense gas-solid flow in bubbling fluidized beds is computationally intensive. Conducting expensive numerical simulations for different parameters is uneconomical, necessitating the development of new high-speed simulation methods. In this study, a parameterized reduced-order model (ROM) for the dense gas-solid turbulent flow process is innovatively developed. The ROM decomposes the dense gas-solid flow into several main orthogonal spatial modes and their corresponding temporal coefficients using the proper orthogonal decomposition (POD) method. The Navier-Stokes equation is projected onto each spatial mode using the Galerkin method to efficiently solve the mode temporal coefficients. Notably, this method accounts for the pressure term at the ROM level, applies POD-Galerkin ROM to the parameterized solution process of dense gas-solid flow within a finite volume framework, and simultaneously couples the Reynolds-averaged turbulence model to achieve efficient and accurate solutions for dense gas-solid flow. The ROM proposed in this study holds great significance for parameter optimization in industrial applications.
Keywords: Reduced-order model, Fluidized bed, Proper orthogonal decomposition, Galerkin method, Two-fluid method

Introduction

Dense gas-solid flow is prevalent in energy and chemical production, presenting complex multi-physical coupling processes such as turbulent flow, heat transfer, and mass transfer [1]. Conducting high fidelity numerical simulations of this process is a time-consuming task, and it is urgent to develop fast simulation methods. In recent years, rapid parametric simulation through reduced-order model (ROM) has emerged as a promising alternative tool for various complex physical processes [2]. This paper presents a POD-Galerkin ROM for simulating turbulent flow in dense gas-solid systems. The ROM effectively reduces the dimensionality of the solution, leading to a significant enhancement in the computational efficiency of numerical simulations.

Methodology

The target variable undergoes proper orthogonal decomposition to derive its modal representation:

$$\widehat{\boldsymbol{W}}(\boldsymbol{x},\boldsymbol{t}) = \boldsymbol{W_0}(\boldsymbol{x}) + \sum_{\boldsymbol{k=1}}^{\boldsymbol{N_{POD}}} \boldsymbol{\alpha_k}(\boldsymbol{t}) \cdot \boldsymbol{\Phi_k}(\boldsymbol{x}) \qquad (1)$$

The ROM solver is constructed by incorporating the decomposed variables into the Navier-Stokes equation, followed by Galerkin projection and iterative solving.

Conclusions

The proposed POD-Galerkin ROM method exhibits high accuracy in simulating turbulent flow in dense gas-solid systems. It offers significantly improved efficiency compared to traditional CFD approaches.

Acknowledgements

We are grateful for the support from the National Natural Science Foundation of China (No. 51925603).

References

[1] S. Wang, K. Luo, J. Fan, CFD-DEM coupled with thermochemical sub-models for biomass gasification: Validation and sensitivity analysis, Chemical Engineering Science 217 (2020) 115550.
[2] L.-T. Zhu, X.-Z. Chen, B. Ouyang, W.-C. Yan, H. Lei, Z. Chen, Z.-H. Luo, Review of Machine Learning for Hydrodynamics, Transport, and Reactions in Multiphase Flows and Reactors, Ind. Eng. Chem. Res. 61 (2022) 9901–9949.

The investigation of CO_2−H_2O flow corrosion mechanism on the surface of mild carbon steel

Qichao Fang, Yanlin Zhao, Jun Yao
China University of Petroleum (Beijing), Beijing, China

Abstract
The flow corrosion mechanism of mild carbon steel in CO_2-H_2O was investigated using a two-dimensional finite element method. Corrosion calculations including chemical and electrochemical reactions were coupled with two-dimensional flow calculations to establish a flow corrosion mechanism model. The effects of temperature, pH, partial pressure of CO_2 and flow rate were deeply analysed. An interaction between corrosion mass transfer and flow is demonstrated, and the turbulence is a significant incentive for corrosion enhancement.

Keywords: Flow corrosion, Multi-field coupling, Mass transfer, Electrochemistry, Turbulence

Introduction

In oil and gas production, the associated CO_2 gas enters the pipeline and causes steel corrosion. And the loose, porous and inhomogeneous $FeCO_3$ corrosion products are insufficient to provide adequate protection to the pipeline matrix. [1] On the other hand, the flow tends to disrupt the amorphous $FeCO_3$ product film, significantly accelerating carbon steel corrosion and localised corrosion, [2] while particle wall impingement in solid-liquid two-phase flow directly destroys the product layer. [3] Although a one-dimensional CO_2 uniform corrosion prediction model has been developed. [4] However, its neglect of flow dynamics limits its accuracy. Therefore, an analysis and discussion on the CO_2-H_2O flow corrosion mechanism is conducted using a two-dimensional finite element mechanism model.

Methodology

Mathematical models of the chemical equilibrium such as Eq. (1) and electrochemical corrosion reactions on steel surfaces shown in Eq. (2) in fluid solutions are constructed. [5] The accurate two-dimensional flow field is obtained by solving the Navier-Stokes equations system and the low Reynolds k-ε turbulence model.

$$CO_{2(aq)} + H_2O_{(aq)} \Leftrightarrow H_2CO_{3(aq)} \quad (1)$$

$$Fe_{(s)} \rightarrow Fe^{2+}_{(aq)} + 2e^- \quad (2)$$

Subsequently, coupled with the Nernst-Planck equation of Eq. (3), the distributions of corrosion media such as H_2CO_3, H^+ and corrosion products like Fe^{2+} during transient flow corrosion under various conditions are solved. Thereby, the flow corrosion mechanism at different temperatures, pH and partial pressures are discussed, and the mass transfer law at different flow rates and local turbulence are analysed.

$$N_i = -D_i \nabla c_i + c_i u \quad (3)$$

Results and discussion

The relationship between corrosion rate and temperature for X65 mild steel at different pH values with a flow rate of 2 m/s is shown in Fig. 1. The simulation results are in good agreement with the experimental data. [4] As depicted in the figure, the corrosion rate increases with increasing temperature but decreases with increasing pH.

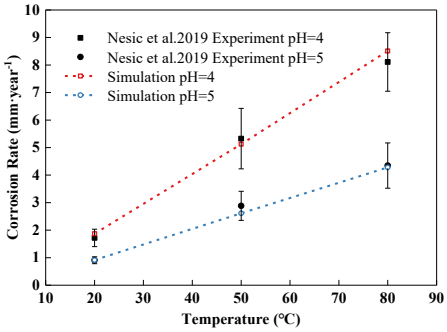


Figure 4 Variation of flow corrosion rate with temperature (pH=4,5; v=2.0 m/s, Pco_2=1 bar)

The CO_2 flow corrosion rates obtained from the simulation under different velocity conditions at 20°C, pH=4 and 5 are shown in Fig. 2. [6] The average corrosion rate on the steel surface increased with the increase of velocity. Based on this, the distribution of substance concentration on the steel surface at 50°C, pH=4, and 4m/s flow velocity was obtained as shown in Fig. 3. In the flow corrosion, the anodic Fe dissolution makes the Fe^{2+} concentration near the wall significantly higher than that in the mainstream area. H^+ acts as a reactant for the cathodic reduction reaction, and the concentration difference at the wall is less than zero.

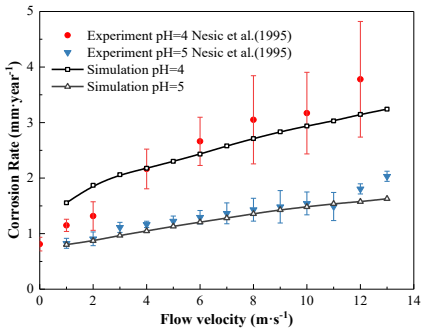


Figure 2 Flow corrosion rates of carbon steel at different velocities (pH=4,5, Pco_2=1 bar)

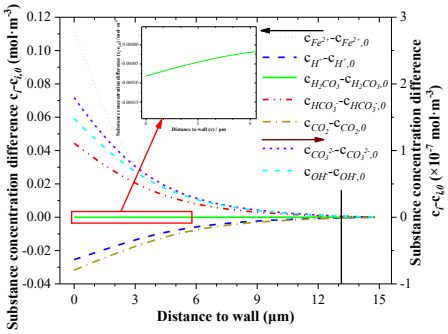


Figure 3 Substances concentration difference with the distance to the wall at 4 m/s (T= 50°C, pH=4)

Conclusions

The following results can be obtained from this two-dimensional finite element simulation study.

(1) The diffusion transfer rate of each substance in the boundary layer increase with temperature and so does the corrosion rate.

(2) The flow corrosion rate increases with decreasing pH. The pH directly affects the cathodic reaction of the flow corrosion and determines the strength of H_2CO_3 buffering in the corrosion.

(3) The results show that the H^+ reduction of corroded cathode is sensitive to the flow. CO_2-H_2O flow corrosion is found to occur in the diffusion boundary layer, and such corrosion

diffusion boundary layer decreases with increasing Reynolds number.

References

[1] D. Burkle, R. De Motte, W. Taleb, A. Kleppe, T. Comyn, S. M. Vargas, A. Neville, R. Barker, In situ SR-XRD study of $FeCO_3$ precipitation kinetics onto carbon steel in CO_2-containing environments: The influence of brine pH, Electrochimcal Acta 255 (2017) 127-144.

[2] Y.-S. Chol, M. Colahan, S. Nesic, Effect of Flow on the Corrosion Behavior of Pipeline Steel in Supercritical CO_2 Environments with Impurities, Corrosion 79 (2023) 497-508.

[3] Z. Wang, Y.-L. Zhao, M. Liu, H. Shen, Q. Fang, J. Yao, Investigation of the effects of small flow rate and particle impact on high temperature CO_2 corrosion of N80 steel, Corrosion Science 209 (2022) 110735.

[4] S. Nesic, A. Kahyarian, Y.-S. Chol, Implementation of a Comprehensive Mechanistic Prediction Model of Mild Steel Corrosion in Multiphase Oil and Gas Pipelines, CORROSION 75 (2019) 274-291.

[5] Q. Fang, Y.-L. Zhao, J. Wei, Z. Wang, J. Yao, Investigation of the Working Mechanism of CO_2–H_2O Flow Corrosion of Mild Carbon Steel, Industrial & Engineering Chemistry Research (2023).

[6] S. Nesic, G. T. Solvi, J. Enerhaug, Comparison of the rotating cylinder and pipe flow tests for flow-sensitive carbon dioxide corrosion. Corrosion 51 (1995) 773-787.

CFD Study of Hydrogen Injection in Blast Furnaces: Tuyere Co-injection of Hydrogen and Coal

Yiran Liu[1], Yansong Shen[2]
1 University of Western Australia, Perth, Australia
2 University of New South Wales, Sydney, Australia

Abstract
Hydrogen is a carbon-free clean energy and a potential fuel to mitigate CO_2 emission in ironmaking blast furnaces (BFs) where the co-injection of hydrogen/coal is one of the most promising and feasible technologies. In this article, a 3D steady-state industrial-scale CFD model is improved and used for investigating the co-injection of hydrogen/coal in BFs. The model involves gas–particle-solid flow, heat and mass transfer related to the chemical reactions of hydrogen, coal and coke. This model has been validated against the measurements in terms of gas distribution, temperature and burnout. Several injection schemes of the co-injection of hydrogen/coal are designed under the conditions of constant bosh gas volume. The typical in-furnace phenomena, including the interaction between hydrogen and coal, are described, and the effects of the hydrogen injection rate on the co-injection of hydrogen/coal are analysed. The simulation results indicate that hydrogen combustion enhances the devolatilization of coal, but hinders the volatiles combustion. It is found that, as the hydrogen rate increases, the raceway volume-averaged temperature increases and the raceway peak temperature increases and then decreases; both the raceway surface-averaged burnout and final burnout increase. Such different responses of them to hydrogen injection rates indicate the importance of 3D modelling study. In addition, the higher hydrogen injection rate increases the molar fraction of reducing gas components (H_2 and CO) in the coke bed. The model provides a cost-effective tool for the design, optimisation and industrialisation of the co-injection of H_2 and coal.

Keywords: Hydrogen, Coal, combustion, CFD

Introduction
H_2, a climate-friendly fuel with high energy content, shows promise in reducing carbon emissions in ironmaking. The blast furnace (BF), a major CO_2 emitter in the industry, traditionally uses carbon-based fuels. Hydrogen, sourced through water electrolysis powered by renewables, can replace carbon sources, offering a cleaner alternative. Co-injecting hydrogen and coal through tuyeres in BFs is a promising transition. However, research is in the early stages, and in this study, a 3D computational model has been developed to study in-furnace phenomena.

Methodology
The present model is developed for describing the physical and chemical processes of the co-injection of hydrogen/coal through tuyeres into the lower part of the BF, including the blowpipe, tuyere, lance, raceway and surrounding coke bed. This model is solved based on the framework of ANSYS-CFX 19.2. The key flow and thermochemical phenomena include (1) turbulent gas–particle flow; (2) H_2/H_2O reactions (hydrogen combustion, water–gas shift reaction); (3) coal combustion (devolatilisation, volatile matter combustion, char combustion and gasification); (4) coke combustion and gasification; (5) heat transfers in the considered gas–particle–coke bed.

Conclusions
The co-injection of hydrogen/coal in the BF is investigated using a 3D steady-state industrial-scale CFD model. This model features gas–particle–solid flow, heat and mass transfer with

detailed reactions, including H_2/H_2O-related reactions, and coal- and coke-related reactions. This model has been validated against the measurements in terms of gas distribution and burnout. Several injection schemes are designed under the conditions of fixed bosh gas volume.

Gas-solid flow in bubbling fluidized beds

Qiuya Tu[1], Zhiyang Ma[2], Haigang Wang[2], Lei Mei[1], Xiaosong Jiang[1]
[1]SPIC, Beijing, China
[2]Institute of Engineering Thermophysics, CAS, Beijing, China

Abstract

This study investigates the impact of gas-solid flow dynamics on bubbling fluidized beds, which comprise two primary components: the fluidized bed and the freeboard. The fluidized bed is a highly back-mixed reactor, while the freeboard is a plug flow reactor with refluxing solid particles. In the fluidized bed, there are three zones based on the bubble behavior, namely, bubble formation zone, bubble rising and merging zone, and bubble breakup zone. In each zone, the bubbles are mainly concentrated in the central region. The solid particles transfer heat mainly by conduction, but bubbles hinder direct contact with particles. Therefore, small bubbles are preferred. Moreover, bubble frequency is also closely related to the particle heat transfer.

Keywords: Bubbling fluidized bed, Bubble behavior, Gas-solid flow

Introduction

The characteristics of gas-solid flow are vital to the performance of a bubbling fluidized bed, a device extensively utilized across various industries. For example, in the pharmaceutical industry, the quality of pellets depends on the uniform mixing of ingredients and the coating or drying process in the fluidized beds. In the energy or chemical industry, the bubbling fluidized bed can function as an independent reactor or a component of a dual fluidized bed system, where the efficiency of combustion or gasification is determined by the dynamics of the gas-solid flow.

Methodology

Both CFD simulation and experimental measurements are employed to study the gas-solid flow dynamics in the bubbling fluidized beds across different applications. For example, in the dual fluidized beds, the bubble behaviors are detailed through CPFD simulation. The selected cross sectional particle volume fractions obtained from simulation and ECT measurement show that bubbles are concentrated in the middle region. In the particle drying fluidzed beds, 3D CFD simulations at certain moisture contents were performed. It is found that the simulated cross-sectional particle volume fraction shows core-annular structure and is verified by the on-line ECT measurement. An internal circulation is formed along the reactor height, with mass and heat transfer primarily occurring at the dryer's lower part and the contact region between the bubbles and the solid phase. As the particle moisture level decreases, the minimum fluidization velocity decreases, and the bubble rising velocity increases.

Conclusions

The gas-solids flow in bubbling fluidized beds plays a crucial role in reactor performance, influencing not only flow behaviors but also mass and heat transfer.

Acknowledgements

The authors would like to thank the National Natural Science Foundation of China (No. 52006222) for support.

References

[1] Q.Y Tu, Z. Luo, H. G. Wang, MP-PIC simulation of the gas-solid full-loop flow characteristics in a dual fluidized bed and validation with experimental data, Chemical Engineering Journal, 421(2021) 129835.

[2] Q.Y. Tu, Z.Y. Ma, H.G. Wang, Investigation of wet particle drying process in a fluidized bed dryer by CFD simulation and experimental measurement, Chemical Engineering Journal 452 (2023) 139200.

A novel hybrid CFD-DEM method for high-fidelity modelling of cross scale particulate-fluid flow

Zhouzun Xie, Yansong Shen
School of Chemical Engineering, University of New South Wales, Sydney, NSW 2052, Australia

Abstract
Cross-scale polydisperse particulate-fluid flows are widely practised yet their multi resolution simulations are not achieved due to the lack of reliable numerical methods. In this work, a novel hybrid CFD-DEM model is developed for the high-fidelity multi-resolution simulations of cross-scale polydisperse particulate-fluid flow systems, for the first time featuring no limit on the grid size to particle diameter ratio (lm/dp). This work provides a promising tool for the modelling of many cross scale particulate-fluid flow systems.

Keywords: Cross-scale particulate-fluid flow, CFD-DEM, fluid dynamics

Introduction

Cross-scale polydisperse particulate-fluid flow, existing in many chemical engineering applications, involves fluid flow with particles varying significantly in size (dcoarse/dfine of 10 to 103) (Figure 1). The size difference impacts flow hydrodynamics. Existing numerical models are limited by specific lm/dp ranges: high-resolution mesh (lm/dp < 0.1) for resolved CFD-DEM, lm/dp > 3 for unresolved methods, and 0.1 < lm/dp < 3 for semi-resolved methods. In this work, we developed a novel hybrid CFD-DEM model for the high-fidelity multi-resolution simulations of cross-scale polydisperse particulate-fluid flow systems, for the first time featuring no limit on the grid size to particle diameter ratio (lm/dp), by means of combining the features of unresolved, semi-resolved and resolved methods [1].

Methodology

Hybrid CFD-DEM model comprehensively integrates unresolved, semi-resolved and resolved sub-models. In this model, the FD based resolved sub-model is used to achieve the high-resolution of fluid flow around the CPs (lm/dp < 0.1); b) the unresolved sub-model is used to describe the interactions between FPs (lm/dp > 3) and fluid flow; c) the semi-resolved sub-model is used to describe the interactions between MPs (0.1 < lm/dp < 3) and fluid flow. The ability, applicability, and accuracy of the hybrid model are illustrated by three solid liquid cases.

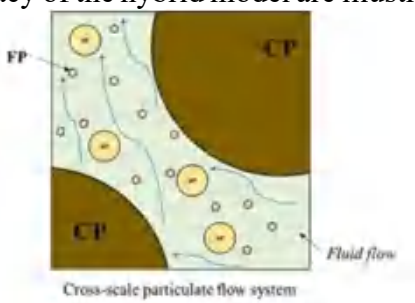


Figure 1 - The schematic of cross-scale particulate-fluid flow system

Conclusions

The hybrid CFD-DEM model is successfully developed and tested. The ability, applicability, and accuracy of the hybrid CFD DEM model are demonstrated by 1) single particle sedimentation in liquid, 2) two particles sedimentation in liquid, and 3) The fine glass particles transporting through the pores formed by the coarse particles. The computational cost is affordable. The new hybrid CFD-DEM model enables high-fidelity, multi-resolution

simulations of cross-scale particulate-fluid flow systems, eliminating limits on size ratios between particles and fluid mesh. This makes it an effective tool for modelling various cross scale particulate-fluid flows.

References

[1] Z. Xie, S. Wang, Y. Shen, A novel hybrid CFD-DEM method for high-fidelity multi resolution modelling of cross-scale particulate flow, Chemical Engineering Journal, 455 (2023) 140731.

Field-resolved Surrogate Model for an Arbitrarily Spinning Particle Based on Parameterized Physics-informed Neural Networks (P-PINNs)

Kai Liu[a,b], Kun Luo[a,b,*], Yuzhou Cheng[b], Anxiong Liu[b], Haochen Li[c], Jianren Fan[a,b], S. Balachandar[d]

[a] State Key Laboratory of Clean Energy Utilization, Zhejiang University, Hangzhou, Zhejiang 310027, China

[b] Shanghai Institute for Advanced Study of Zhejiang University, Shanghai 201203, China

[c] Department of Civil and Environmental Engineering, University of Tennessee, Knoxville, Tennessee 37996, USA

[d] Department of Mechanical & Aerospace Engineering, University of Florida, Gainesville, FL 32611, USA

Abstract

Modelling the drag and lift of rotating spheres is significant for predicting the particle behaviour in many multiphase flow simulations such as fluidized bed, sedimentation, and powder mixing. However, existing models can only deal with simple conditions where the axis of rotation must be perpendicular to the incoming flow velocity, while predicting more prevalent real conditions of spheres rotating around an arbitrary direction remains challenging. This study presents a parameterized physics-informed neural networks (P-PINNs) approach as an alternative to conventional computational fluid dynamics (CFD) in solving the parameterized flow fields of an arbitrarily spinning particle immersed in a uniform flow. Only one unsupervised training is needed to obtain the P-PINNs model. Given any inputs of the six non-dimensional variables: streamwise coordinate $x_* = x/D \in [-10,30]$, spanwise coordinate $y_* = y/D \in [-10,10]$, transverse coordinate $z_* = z/D \in [-10,10]$, Reynolds number $\mathrm{Re} = U_0 D/\upsilon \in [0,400]$, streamwise angular velocity $\Omega_{x*} = \Omega_x D/U_0 \in [-3,3]$, and spanwise angular velocity $\Omega_{y*} = \Omega_y D/U_0 \in [-3,3]$, the model outputs the 3D force and torque exerted on the sphere and also the velocity, pressure, and their spatial derivatives on the coordinates. Additional coordinates transformation and dimensionalization ensure this model applicable to handling a wide range of application scenarios. Rigorous validations against particle-resolved direct numerical simulations (PR-DNS) of 128 cases with varied Reynolds number, and angular velocity conditions prove that the P-PINNs model is comparably accurate in predicting all the above information of the flow field. A posteriori test of particle sedimenting in an upwelling uniform flow with imposed 3D initial rotation settings has also been performed to exhibit the model capability and the importance of computing the six degrees of freedom (6DOF) behaviour of the falling sphere. We have also utilized this P-PINNs model to investigate several detailed phenomena associated with an arbitrarily spinning sphere, including flow symmetry, secondary drag and lift, critical Reynolds number, flow bifurcation, and flow separation.

Keywords: Physics-informed neural networks, Parameterized machine learning, Six degrees of freedom motion, Particle-resolved simulations, Surrogate modelling

CFD-DEM modeling of thermochemical heat storage in the framework of GPU

Jiahui Yu, Shuai Wang, Kun Luo, Jianren Fan
Zhejiang University, Hangzhou, P. R. China

Abstract
Concentrated Solar Power (CSP) has garnered significant attention due to its ability to achieve high efficiencies and low carbon emissions. Conventional solar thermochemical heat storage based on indirect surface heating usually suffers from high heat losses and low solar-chemical efficiency. Understanding the fundamental principles governing gas-solid flow and thermochemical behavior is crucial for optimizing, designing, and controlling different types of thermochemical heat storage systems. The computational fluid dynamics-discrete element method (CFD-DEM) coupled with the Monte Carlo ray tracing (MCRT) method has emerged as a promising tool for achieving this objective, albeit with significant computational resource requirements. To address this challenge, we have developed a GPU-accelerated CFD-DEM reactive model that incorporates considering heat and mass transfer, chemical reaction, and irradiation ray tracing. The accuracy of the developed model has been thoroughly validated. The hydrodynamics and thermochemical characteristics in Calcium-Looping (CaL) process operating under several key operating parameters are numerically studied. Furthermore, we have demonstrated that the GPU-accelerated strategy offers significant speed-up performance and stability. This work presents a reliable and high-performance parallel calculation method for numerically investigating the high-efficiency direct solar thermochemical heat storage system.

Keywords: CFD-DEM, Thermochemical heat storage, Dense gas-solid reacting flow, Monte Carli ray tracing

Introduction

Concentrated Solar Power (CSP) has garnered significant attention due to its ability to achieve high efficiencies and low carbon emissions. However, early CSP systems suffer from intermittent and unstable problems because of seasons and weather. Conventional solar thermochemical heat storage based on indirect surface heating usually suffers from high heat losses and low solar-chemical efficiency. Thermal energy storage (TES) has become an imperative technique for current CSP systems due to its ability to overcome fluctuating energy supply issues and obtain a balance between energy demand and supply. Understanding the fundamental principles governing gas-solid flow and thermochemical behavior is crucial for optimizing, designing, and controlling different types of TES systems. The computational fluid dynamics-discrete element method (CFD-DEM) coupled with the Monte Carlo ray tracing (MCRT) method has emerged as a promising tool for achieving this objective [1]. Zheng et al. [2] built a CFD-DEM model considering irradiation ray tracing, granular flow, heat and mass transfer, and chemical reaction. However, both the CFD-DEM method and the MCRT method require significant computational resources which limit its application. To address this challenge, we have developed a GPU-accelerated CFD-DEM reactive model that incorporates considering heat and mass transfer, chemical reaction, and irradiation ray tracing.

Methodology

CFD-DEM framework

A GPU-accelerated CFD-DEM reactive model is developed for simulating dense gas-solid reacting flow. The gas phase is considered the continuum and solved through the volume-averaged governing equations [3]. In the DEM method, the solid phase is considered as the dispersed phase and particles can be tracked individually. The dynamics of particles can be calculated using Newton's law of motion [4]. The gas phase can be coupled with the solid phase

through the interphase exchange terms. The heat transfer sub-models are coupled with the CFD-DEM model. The particle is assumed to be isothermal without considering the temperature gradient inside the particle. The heat transfer of a particle can be classified into five modes: conduction, convection, radiation, reaction, and solar irradiation, as shown in Fig. 1. The energy conservation equation of ith particle is given as:

$$m_i C_{p,i} \frac{dT_{p,i}}{dt} = Q_{pp,i} + Q_{pgp,i} + Q_{gp,i} + Q_{rad,i} + \Delta H_{rs} + Q_{psolar} \quad (1)$$

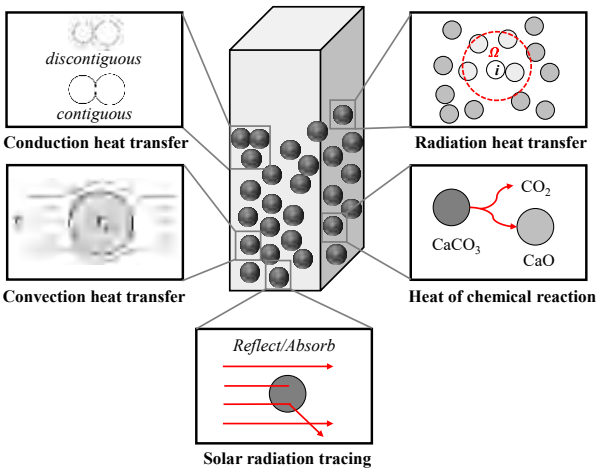


Figure 5 - Schematic of the volumetric fluidized bed with irradiation transport, granular flow, heat transfer, and chemical reaction.

The main chemical reaction considered in the current work is the revisable carbonation/calcination reaction to achieve the heat storage process:

$$CaCO_3(s) \rightleftharpoons CaO(s) + CO_2(g) \quad (2)$$

Compared to CPU, GPU can provide much higher instruction throughout and memory bandwidth [5]. The introduction of CUDA makes it possible to solve complex computing problems in a more efficient way than the CPU. The developed GPU-accelerated CFD-DEM reactive method has been proven to have great acceleration performance in our previous works [6, 7].

Solar irradiation transport simulation

The MCRT method is a random simulation method based on probability statistics and is widely used in concentrated solar research [8]. In this work, a GPU-accelerated MCRT approach is developed to evaluate the irradiative source throughout the entire particle system. Specifically, all particles are assumed as grey bodies. Light absorption and transport properties are independent of wavelengths. The initial energy of solar ray is represented by a weight value (W = 1) and decreases as being absorbed by particles. Each ray is traced until it escapes from the reactor or reaches a threshold value of its original weight value.

Conclusions

In this work, a GPU-accelerated CFD-DEM reactive model is developed and coupled with the MCRT method. The accuracy of the current model has been detail verified and the speed-up performance is assessed. Furthermore, the hydrodynamics and thermochemical characteristics in the thermochemical heat storage system are illustrated. This work presents a reliable and high-performance parallel calculation method for numerically investigating the high-efficiency direct solar thermochemical heat storage system.

Acknowledgments
We are grateful for the support from the National Natural Science Foundation of China (grant No. 51925603) and the Shanghai Pujiang Program (23PJ1412000).

References
[1] S. Bellan, N. Gokon, K. Matsubara, H.S. Cho, T. Kodama, Heat transfer analysis of 5kWth circulating fluidized bed reactor for solar gasification using concentrated Xe light radiation, Energy 160 (2018) 245-56.
[2] H. Zheng, X. Liu, Y. Xuan, C. Song, D. Liu, Q. Zhu, Z. Zhu, K. Gao, Y. Li, Y. Ding, Thermochemical heat storage performances of fluidized black CaCO3 pellets under direct concentrated solar irradiation, Renew. Energy 178 (2021) 1353-69.
[3] S. Wang, Y. Shen, CFD-DEM study of biomass gasification in a fluidized bed reactor: Effects of key operating parameters, Renew. Energy 159 (2020) 1146-64.
[4] R. Garg, J. Galvin, T. Li, S. Pannala, Open-source MFIX-DEM software for gas–solids flows: Part I—Verification studies, Powder Technol. 220 (2012) 122-37.
[5] Y. He, F. Muller, A. Hassanpour, A.E. Bayly, A CPU-GPU cross-platform coupled CFD-DEM approach for complex particle-fluid flows, Chem. Eng. Sci. 223 (2020) 115712.
[6] J. Yu, S. Wang, K. Luo, J. Fan, CFD-DEM modeling of dense gas-solid reacting flows in the framework of GPU, Chem. Eng. J. (2024) 149480.
[7] J. Yu, S. Wang, K. Luo, J. Fan, GPU-accelerated discrete element simulation of granular and gas-solid flows, Powder Technol. (2024) 119475.
[8] X. Chen, X. Xia, H. Liu, Y. Li, B. Liu, Heat transfer analysis of a volumetric solar receiver by coupling the solar radiation transport and internal heat transfer, Energy Conv. Manag. 114 (2016) 20-7.

CFD and Experimental Study of Hydrodynamics in Pulsed Fluidized Beds: A Preliminary Investigation

Mohamadali Mirzaei[a], Morten Pedersen[b], Varunkumar S[c], Hao Wu[a]
[a] Technical University of Denmark (DTU), Kongens Lyngby 2800, Denmark. [b] FLSmidth A/S, Valby 2500, Denmark . [c] Indian Institute of Technology Madras (IIT Madras), Chennai, India

Abstract
This study investigates the effect of pulsation on fluidized bed hydrodynamics, focusing on Computational Fluid Dynamics (CFD) simulations of Geldart A particle fluidization using the two-fluid model.

Keywords: CFD, Fluidized bed, Pulsation, Geldart A, Two-Fluid model

Introduction
The fluidization of Geldart C particles presents a significant challenge due to their cohesive nature, their tendency to form agglomerates, and their susceptibility to bed instabilities such as channeling and slugging. To address the difficulties associated with fluidizing such fine particles, flow pulsation techniques are utilized. However, the specific hydrodynamics of pulsed fluidized beds, particularly for fine Geldart C particles, remain underexplored. This study, therefore, aims to enhance our understanding of the hydrodynamics within pulsed fluidized beds, focusing specifically on Computational Fluid Dynamics (CFD) modeling. As a preliminary step in our investigation, we initially focused on Geldart A particles, which are more easily fluidized, to establish a foundational understanding before tackling the more complex fluidization dynamics of Geldart C particles.

Methodology
A lab-scale transparent cylindrical fluidized bed, equipped with pressure sensors and pulsed inlet flow streams (with adjustable frequency), was used to study fluidization dynamics. The focus was initially on Geldart A particles, examining the effects of pulsation frequencies to inform future research on more complex particle types. CFD analyses were conducted using the Eulerian-Eulerian approach with the Two-Fluid Model in Ansys Fluent, incorporating the Kinetic Theory of Granular Flow for particle collision simulations. The research anticipates refining these models to better represent the behaviour of more cohesive particles.

Results
Experimental findings align with literature, showing pulsation effectively reduces minimum fluidization velocity. However, the CFD model struggles to accurately replicate this effect, suggesting a need for model enhancement to capture the dynamics of fluidization under pulsation accurately.

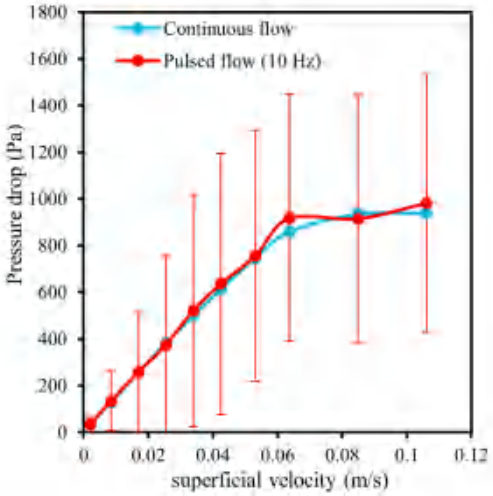


Figure 6. Minimum fluidization velocity obtained from the CFD model

Conclusions

The study confirms pulsation's role in reducing minimum fluidization velocity, highlighting a gap in current CFD models' ability to predict this phenomenon, even for relatively simple Geldart A particles. Future model improvements, particularly in drag and particle interaction modeling, are essential for accurately simulating more complex particle types.

Acknowledgements

This work is a collaboration among DTU, IIT Madras, and FLSmidth A/S, supported by Innovation Fund Denmark.

References

[1] M. Saidi, H. Basirat Tabrizi, and J. R. Grace, “A review on pulsed flow in gas-solid fluidized beds and spouted beds: Recent work and future outlook,” Advanced Powder Technology, vol. 30, no. 6, pp. 1121–1130

Numerical simulation of the soot generation during a single biomass particle combustion

Tao Chen, Zeying Zhao, Chenhao Yang, Zhiheng Liu, Wei Jiang, Youmin Hou
Wuhan University, Wuhan China

Abstract
Biomass thermochemical conversion is a promising technology in the area of renewable energy. The combustion of biomass is one of the high efficient utilization methods. However, the direct combustion of biomass particles, especially for large biomass particles, will generate pollutant emissions such as tar and soot which will reduce the conversion rate of the feedstock and deteriorate the conversion equipment. The current work develops a numerical algorithm to simulate the combustion and soot generation process of a single biomass particle. The evolution of the pyrolysis products including light gas and tar species during the combustion are analyzed. The flame structure and the soot generation process are also systematically studied.

Keywords: Biomass combustion, Single particle, Flame structure, Soot generation, Multiphase reaction flow simulation

Introduction

Soot formation during biomass combustion is a complex issue, which not only deteriorates the combustion efficiency but also poses threats to human health. In recent years, Trubetskaya et al. has done a lot of work on soot formation during the pyrolysis of biomass in drop tube furnaces [1]. It is found that the lignin content contributes the largest amount of soot formation compared with cellulose and hemicellulose. Deng et al. found similar trends for the soot formation during the basic biomass component pyrolysis [2]. Ferreiro et al also studied the soot formation during biomass gasification [3]. However, these experimental works are all carried out in drop tube furnaces. When it comes to larger reactors such as a wood stove, the soot formation becomes more complex [4]. Moreover, the soot formation process itself is also a complex issue that has not been fully understood, which usually follows a series of nucleation processes relating to not only physical but also chemical conversions.

In this paper, we aim at developing a simplified soot formation algorithm that is suitable for efficient prediction of soot formation during biomass combustion. The mathematical model and the numerical results are presented in Section 2. Finally, some conclusions are drawn in Section 3.

Methodology

Biomass combustion is a complex multidisciplinary problem, which includes the thermal conduction of the solid material, the flow field evolution, the pyrolysis and chemical reactions. Considering the fact that the biomass particle becomes a porous char material after devolatilization, it is modeled as a porous media and a virtual particle method is used to simulate the heating and the pyrolysis of the solid biomass particle. During the simulation, the biomass particle is discretized into a cluster of virtual particles. Together with the surrounding gas phase environment, the virtual particle cluster combusting in air is treated as a multiphase flow system. Table 1 presents the virtual particle heat transfer equation and the flow field governing equations.

Table 1. solid and gas phase governing equations.

	Governing equations
Solid phase	$\rho_s c_s \frac{\partial T_s}{\partial t} = hS'\left(T_g - T_s\right) + \frac{e_s S'}{4}\left(G - 4\sigma T_s^4\right) + Q$
Gas phase	$\frac{\partial}{\partial t}\left(\varepsilon_g \rho_g\right) + \nabla \cdot \left(\varepsilon_g \rho_g \boldsymbol{u}_g\right) = S_{p,m}$
	$\frac{\partial}{\partial t}\left(\varepsilon_g \rho_g \boldsymbol{u}_g\right) + \nabla \cdot \left(\varepsilon_g \rho_g \boldsymbol{u}_g \boldsymbol{u}_g\right) = -\nabla p + \nabla \cdot \left(\varepsilon_g \boldsymbol{\tau}_{eff}\right) + \varepsilon_g \rho_g \boldsymbol{g} + S_{p,mom}$
	$\frac{\partial}{\partial t}\left(\varepsilon_g \rho_g E\right) + \nabla \cdot \left(\varepsilon_g \boldsymbol{u}_g (\rho_g E + p)\right) = \nabla \cdot \left(\varepsilon_g \alpha_{eff} \nabla h_{sen}\right) + S_h + S_{p,h} + S_{rad}$
	$\frac{\partial}{\partial t}\left(\varepsilon_g \rho_g Y_i\right) + \nabla \cdot \left(\varepsilon_g \rho_g \boldsymbol{u}_g Y_i\right) = \nabla \cdot \left(\varepsilon_g \rho_g D_{eff} \nabla Y_i\right) + S_{p,Y_i} + S_{Y_i}$

Soot formation depends largely on tar and flow field evolutions during biomass combustion. Tar is a pyrolysis compound containing hundreds of chemical species such as benzene, naphthalene and so on. Under high-temperature conditions, some of the tar species will convert to hydrocarbon ring structures, so-called polycyclic aromatic hydrocarbons (PAH). With a complex nucleation process, the PAH is finally converted to soot particles. However, the current paper is not aimed at a detailed description of the tar and soot formation processes. Instead, the tar species are simplified as $C_6H_{6.2}O_{0.2}$ and soot precursor is modeled as C_2H_2. Table 2 shows the pyrolysis, the combustion and the soot formation reactions. The char combustion reactions are taken from our previous work [5]. For the simulation of soot evolution, a classical two-equation model is used [5].

Table 2. pyrolysis, gas phase combustion and soot formation reactions.

	Reactions
pyrolysis	$m_s = \sum \alpha_i m_s, \quad \sum \alpha_i = 1$ i = H_2O, H_2, CO, CO_2, $C_6H_{6.2}O_{0.2}$(tar), C_2H_2, char, and ash.
Combustion	$H_2+0.5O_2=H_2O$ $CO+0.5O_2=CO_2$ $C_2H_2+O_2=CO_2+H_2O$ $C_6H_{6.2}O_{0.2}+2.9O_2=6CO+3.1H_2$
Soot formation	$C_2H_2=2C+H_2$

Figure 1 shows the computational grid of the single particle combustion system. The diameter of the particle is 5mm. The temperature at the reactor wall is set to 1000 K. Figure 2 presents the flow field temperature at t=0s and 4s, respectively. The ignition process is clearly seen in Fig.2b, where the flame structure surrounds the biomass particle with the maximum flame temperature over 2000 K. During the combustion process, tar

and soot precursor are generated near the biomass particle, which quickly convert to micron-sized soot particles near the flame region. Figure 3 shows the soot mass fraction contour at t =4s. It is seen that the maximum soot mass fraction reaches over 0.1 and locate mainly in the leeward side of the particle.

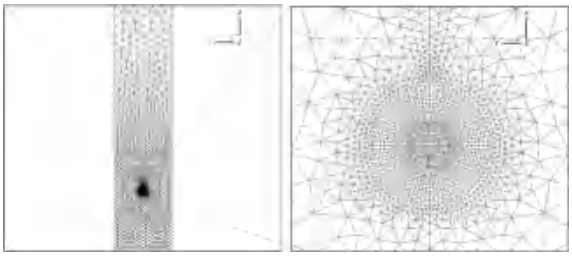


Figure 1 computational grid



(a)t=0s **(b)t=4s**

Figure 2 flow field temperature



(a)t=0s **(b)t=4s**

Figure 3 soot generation

Conclusions

In this work, a multiphase reaction flow algorithm is developed to simulate the soot generation process during the combustion of a single biomass particle. A two-equation soot formation model is integrated within an Eulerian-Lagrangian multiphase flow algorithm. The combustion process of a 5mm sized biomass particle is simulated. The maximum flame temperature is found to reach over 2000K and the corresponding soot mass fraction increases over 0.1 at t=4s. The current work explores the soot evolution during the combustion of a single biomass particle, which is difficult to measure in experiment. This provides an useful tool for the analysis and optimization of biomass combustion equipment.

Acknowledgements

The organizers would be grateful if you could follow this template in preparing your extended abstract. This work is financially supported by the National Nature Science Foundation of China (No. 52206206 and No. 52276160).

References

[1] A. Trubetskaya, M.T. Timko, K. Umeki, Prediction of fast pyrolysis products yields using lignocellulosic compounds and ash contents. Appl. Energy 257 (2020) 113897.
[2] C. Deng, S.B. Liaw, X. Gao, H. Wu, Differences in soot produced from rapid pyrolysis of

xylan, cellulose and lignin under pulverized-fuel conditions. Fuel 265 (2020) 116991.
[3] A.I. Ferreiro, R. Segurado, M. Costa, Modelling soot formation during biomass gasification. Renewable Sustainable Energy Rev. 134 (2020) 110380.
[4] E.D. Vicente, C.A. Alves. An overview of particulate emissions from residential biomass combustion. Atmos. Res. 199 (2018) 159-185.
[5] T. Chen, T. Li, J. Sjoblom, H. Strom. A reactor-scale CFD model of soot formation during high-temperature pyrolysis and gasification of biomass. Fuel 303 (2021) 121240.

Coupling a neural network-inspired kinetics model and coarse-grained DEM-CFD for a fluidized bed plastic pyrolizer simulation

Jiangfeng Shen, Xi Gao

Abstract

The understanding of complex fluidization behavior and pyrolysis reaction kinetics in plastic pyrolysis fluidized bed reactors is currently limited. There is an urgent need to develop accurate mathematical models capable of describing the complex multiphase reaction systems of plastic pyrolysis. This study developed a plastic pyrolysis kinetic model using the chemical reaction neural network (CRNN) and experimental data from a thermogravimetric analyzer (TGA) and Py-GC-MS measurement. Additionally, a comprehensive multiscale model was developed in the open-source MFiX code, combining detailed plastic pyrolysis kinetics, single particle modeling, and coarse-grained DEM-CFD simulations to investigate the fluidization and pyrolysis behavior of HDPE in a sand-assisted fluidized bed. To validate the proposed model, measurements were conducted in a fluidized bed pyrolyzer, including quantifying the segmented pressure drop along the bed height and determining the yield and composition of gas, oil, and wax products. Furthermore, various aspects such as particle mixing and segregation, axial distribution and residence time, Lacey index, and pyrolysis product analysis were investigated. The study provides experimental and theoretical foundations for designing multiphase fluidized bed reactors and advancing HDPE thermochemical conversion.

Topic 2-I-Multiphase flow: innovations and low-carbon engineering applications

Multiphase flow challenges in industrial-scale conversion of biomasses and wastes

Henrik Ström
Chalmers University of Technology, SE-412 96 Gothenburg, Sweden;
henrik.strom@chalmers.se

Abstract
Multiphase flow phenomena are of key importance in the scale-up of processes involving thermochemical conversion of biomasses and wastes. The present work provides an overview of important multiphase aspects in indirect gasification, focusing on both reactor design/retrofitting and raw-gas cleaning. Specific emphasis is put on in silico predictions of lateral solids dispersion in fluidized beds, self-cleaning heat exchangers design/control of packed-bed adsorbers.
Keywords: Fluidization, and Gasification, Computational Fluid Dynamics, Lattice Boltzmann Method, Reduced-Order Model

Overview
Indirect gasification is a technologically feasible approach to large-scale production of renewable fuels and chemicals from biomasses and wastes [1]. Multiphase phenomena are central to these processes, both in the gasifier itself (dual fluidized-bed system) as well as in the downstream processing equipment for heat extraction and gas cleaning (two-phase flow heat exchangers and packed-bed adsorption units). Accurate and efficient simulation models are essential in the successful design, scale-up and/or retrofitting of these thermochemical processes. At the same time, the many orders of magnitude difference between the molecular scales and the complete unit scale typically necessitates a multi-scale or hybrid approach to encompass all the relevant physics. This talk will start from the challenges involved in performing multi-scale analyses of large-scale biomass conversion systems and thereafter focus on the specifics of modelling and simulations of the multiphase flow phenomena involved. More specifically, the use of short sequences of computational fluid dynamics (CFD) simulations to accurately predict the effective lateral dispersion of momentum, heat and mass in bubbling fluidized beds will be discussed. It will be shown that different methods to obtain the effective dispersion from the same underlying two-fluid model data will produce predictions of varying accuracy (when compared against experiments) and that the length of the time series needed varies significantly.
Furthermore, the use of simulations based on the lattice-Boltzmann method (LBM) in analyses of self-cleaning heat exchangers and packed-bed adsorbers will be discussed. Here, LBM simulations reveal how the intricacies of small, motile condensed droplets can be leveraged to maintain heat transfer surfaces free from tar fouling.
It is also shown how the presence of condensate after adsorber regeneration modulates the flow properties relevant to transport and reaction within a packed bed, and routes towards in silico deduction of properties for more advanced reduced-order models are outlined.

Acknowledgements
The work presented has received financial support from the Swedish Energy Agency, the Swedish Research Council, and the Swedish Research Council Formas.

References
[1] H. Thunman, M. Seemann, T. Berdugo Vilches, J. Maric, D. Pallarès, H. Ström, G. Berndes, A. Larsson, C. Breitholtz and O. Santos, Advanced biofuel production via gasification - lessons learned from 200 man years of research activity with Chalmers' research gasifier and the

GoBiGas demonstration plant, Energy Science & Engineering 6 (2018) 6-34.

Clathrate Hydrates in Porous Media: Application to Low-carbon Fuels in Clean Energy Transition

Junjie Zheng, Praveen Linga Department of Chemical and Biomolecular Engineering, National University of Singapore, Singapore 117585, Singapore

Abstract

Carbon capture and sequestration (CCS) plays a crucial role in facilitating low-carbon fuel adoption during the clean energy transition. Clathrate hydrates are solid compounds consisting of gas molecules enclathrated in crystalline lattices formed by water molecules. Specifically, CO2 hydrate has become an attractive way for CO2 capture, storage and long term sequestration. For CO2 capture, fixed bed reactor (FBR) configuration using porous media was reported to significantly enhance the kinetics of the hydrate-based CO2 separation process. Porous media are beneficial as they can provide more hydrate nucleation sites, tortuous pathways for fluid migration and sufficient gas water contact area. On the other hand, forming CO2 hydrates in deep marine sediment offers a secure solution for long-term sequestration due to their higher density than seawater, high stability under moderate oceanic depths, and low susceptibility to oceanic flow perturbation. It is also possible to sequestrate CO2 in natural gas hydrate reservoirs via CO2 CH4 swapping and bring more economic benefits by recovering natural gas. This work will highlight the research efforts carried out by our group in the aforementioned aspects and discuss the key roles of porous media in these hydrate processes [1-6]. The major challenges and prospects are also identified and highlighted.

Keywords: Gas Hydrates; CO2 capture; CO2 sequestration; Natural gas hydrates; Porous Media

References

[1] Zheng J, Lee YK, Babu P, Zhang P, Linga P. Impact of fixed bed reactor orientation, liquid saturation, bed volume and temperature on the clathrate hydrate process for pre combustion carbon capture. Journal of Natural Gas Science and Engineering. 2016;35:1499 510.

[2] Zheng J, Zhang B-Y, Wu Q, Linga P. Kinetic Evaluation of Cyclopentane as a Promoter for CO2 Capture via a Clathrate Process Employing Different Contact Modes. ACS Sustainable Chemistry & Engineering. 2018;6(9):11913-21.

[3] Fahed Qureshi M, Zheng J, Khandelwal H, Venkataraman P, Usadi A, Barckholtz TA, et al. Laboratory demonstration of the stability of CO2 hydrates in deep-oceanic sediments. Chemical Engineering Journal. 2022;432:134290. carbon

[4] Zheng J, Chong ZR, Qureshi MF, Linga P. Carbon Dioxide Sequestration via Gas Hydrates: A Potential Pathway toward Decarbonization. 2020;34(9):10529-46. Energy & Fuels.

[5] Liao Y, Zheng J, Wang Z, Sun B, Sun X, Linga P. Modeling and characterizing the thermal and kinetic behavior of methane hydrate dissociation in sandy porous media. Applied Energy. 2022;312:118804.

[6] Liu Z, Zheng J, Wang Z, Gao Y, Sun B, Liao Y, et al. Effect of clay on methane hydrate formation and dissociation in sediment: Implications for energy recovery from clayey sandy hydrate reservoirs. Applied Energy. 2023;341:121064.

CFD investigation of the structural effects of internal gas intake on powder conveying performance in fuel supply systems for aerospace engines

Qingang Xiong[1], Haijun Sun[2], Guanlong Ren[1]
[1]South China University of Technology, Guangzhou, China; [2]Nanchang Hangkong University, Nanchang , China

Abstract
Optimal design of gas intake in powder fuel supply systems is crucial for performance of aerospace engines [1]. There is little research on the impact of intake structure on powder conveying performance [2]. Three novel internal intakes were proposed, which are spherical, cube-shaped, and dome-shaped. After validation, CFD simulations demonstrate that fluctuation of mass flow rate of powders in the dome-shaped intake is reduced by about 73.3% compared with the annular external one, see Fig. 1. Variation trends of phase velocities are similar for the spherical and cube-shaped intakes, while those are similar for the annular external and dome-shaped internal intakes. Fluctuation of area of gas zone for the annular external and spherical internal intakes is larger than that for the cube-shaped and dome-shaped internal intakes. Pressure and relative pressure drop in the fluidization chamber have a stable stage, and fluctuation of relative pressure drop is small when dome-shaped internal intake is used.

Keywords: Powder supply system; Intake structure; Dense gas-solid flow; Two-fluid model; Powder fluidization

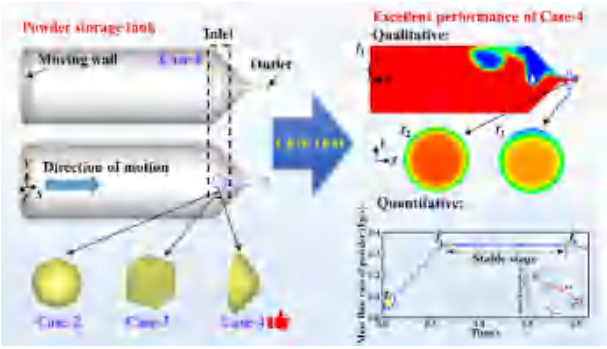


Figure 7-The different powder supply system structures and the presentation of qualitative and quantitative results under optimal structures

References

[1] J. Tang, Y. Yang, Z. Wang, H. Lu, H. Liu, Powder feeding enhancement of powder propellant supply system by using gas-permeable piston, Powder Technology 420 (2023) 118406.
[2] J. Liao, K. Xia, J. Song, S. Luo, D. Xu, Y. Feng, Influence of structural parameters on fluidization effect of typical fluidization unit of metal powder fuel. Advanced Powder Technology 33 (2022) 103790.

Multiscale investigation of fluidized bed reactors for thermochemical conversion of biomass

Xi Gao
1. Department of Chemical Engineering, Guangdong Technion-Israel Institute of Technology, Shantou 515063, China
2. Wolfson Department of Chemical Engineering, Technion-Israel Institute of Technology, Haifa 3200003, Israel

Abstract
The biomass thermochemical conversion fluidized bed reactor is a typical multi-phase, multi-component, multi-scale complex reaction system. This presentation introduces the research progress of our team on advanced experiments and multi-scale modeling of biomass thermochemical conversion reactors. Through high-speed imaging and machine learning, the multi-component fluidization phenomenon in the biomass thermochemical conversion reactor was studied. The non-spherical particle simulation solver SuperDEM was developed to study the fluidization phenomenon of sand and non-spherical biomass particles. Pyrolysis of biomass in pilot pilot-scale fluidized reactor was conducted to investigate the operating conditions of the fluidization behavior and product distributions. A multi-scale model framework was constructed to couple complex reaction kinetics, biomass intra-particle transfer reaction models, and fluidized bed reactor models for the simulation, optimization, and scale-up of biomass thermochemical conversion fluidized bed reactors.
Keywords: biomass; fast pyrolysis; multi-scale; discrete particle simulation; machine learning

Dynamically structured flow patterns in vibrated gas-fluidized beds

Qiang Guo
Institute of Process Engineering, Chinese Academy of Sciences, Beijing, China

Abstract
Gas-solids fluidized beds are widely used in many industrial processes. However, the hydrodynamics of fluidized beds are normally mathematically chaotic and hard to predict, which create significant difficulties in scale-up from laboratory- to pilot- to industrial-scale. In the past few decades, many different ways have been proposed to manipulate the hydrodynamics of fluidized beds to introduce more structures that can simplify the overall scale-up process. Among all of the methods used, we have found that by coupling both gas flow and vertical vibration, a series of structured flow patterns can be formed in the otherwise chaotic fluidized beds. Depending on different conditions, structured gas bubbles, surface waves, and convection cells can be created. These highly ordered flow patterns repeat themselves every two vibration periods. Therefore, they are highly predictable. Further, the characteristic size of these structures remains unchanged when the system width is changed, and using a layered configuration with multiple stages of gas distributors can maintain the ordered structures to a higher particle height. The possibility to maintain these highly-ordered flow patterns with the system width and system height changed opens great opportunities to address key issues in scaling up traditional gas-solids fluidized beds.

Keywords: Fluidized bed, Vibration, Structured flow patterns, Bubble

Introduction

The hydrodynamics of fluidized beds are normally mathematically chaotic and hard to predict, posing a persistent challenge in scale-up and operation. To potentially address this challenge, vibrated gas-fluidized beds operated at certain conditions can produce structured flow patterns. **Figure 1a** shows a regime map for different structured flow patterns that will be discussed in the following based on vibration strength Γ and U/U_{mf}, yet the delineation between regimes can change somewhat with particle layer height and vibration frequency in a complicated manner.

Bubble-free fluidization: At low Γ and U/U_{mf}, the bed can be excited to a fluidization state in which particles move in a densely packed state with no bubbles in the system [1], avoiding issues of decreasing gas-solids contact in conventional fluidized beds.

Structured convection cells: At specific conditions within the bubble-free fluidization state, structured convection cells approximately equal in size and convective velocity to one another can form (**Figure 1b**) [2]. Simulations indicate that the structured convection cells form due to the competition between an effective buoyant force caused by vibration and an effective viscous force caused by inter-particle friction, analogous to the Rayleigh–Bénard instability in conventional fluids.

Structured bubbling: At a resonant frequency of 5 Hz, bubbles of uniform size form and rise without coalescing or splitting in a triangular pattern (**Figure 1c**) [3], avoiding issues with unpredictable bubbling dynamics in conventional fluidized beds. Simulations indicate that the structured bubbling forms due to rapid yet controlled transitions between fluid-like and solid-like behaviour in particles under vibration.

Structured surface waves: In both the bubble-free fluidization and bubbling states, structured surface waves analogous to Faraday waves are formed (**Figure 1d**) [4], with simple waves in pseudo-2D systems and a variety of different forms in 3D systems, including squares, stripes, and hexagons. The wavelength and wave amplitude decreases with increasing vibration

frequency, allowing for control of particle convection behaviour. Due to the drag forces from gas flow, the necessary Γ needed for the structured surface waves decreases with increasing U, including some cases with $\Gamma < 1$.

These structured flow patterns created in vibrated gas-fluidized beds enable a range of opportunities for improving process units. Firstly, these patterns are highly predictable because they repeat themselves every two vibration periods [3,4]. Secondly, scale-up is simplified, since the characteristic size of these patterns do not change with increasing system width [2–4], and these patterns persist to tall bed heights at tens of cm, much higher than those produced by pulsed gas flow [5]. Further, using a layered configuration with multiple stages of distributors can extend the height to which patterns persist (**Figure 1e**) [6]. Thirdly, these patterns structure particle mixing and gas-solids contact, and can control and improve heat and mass transport. For example, at the same U, structured bubbling has been demonstrated to achieve better particle mixing and more uniform particle temperature distribution than free bubbling and packed beds [7].

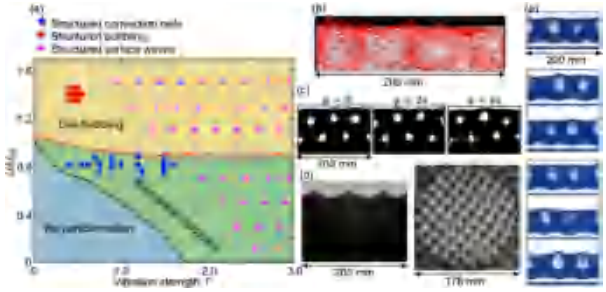


Figure 1. A regime map for structured flow patterns in vibrated gas-fluidized beds.

Methodology

Fig. 2 shows a schematic of the experimental setup for the vibrated gas-fluidized bed. The fluidized bed was placed on an electrodynamical shaker which generated a vertical sinusoidal displacement, $\delta = A\sin(2\pi ft)$to induce vibration. Fully humidified air with the controlled rate enters the fluidized bed through the base of the fluidized bed. Optical images were obtained using a high-speed camera.

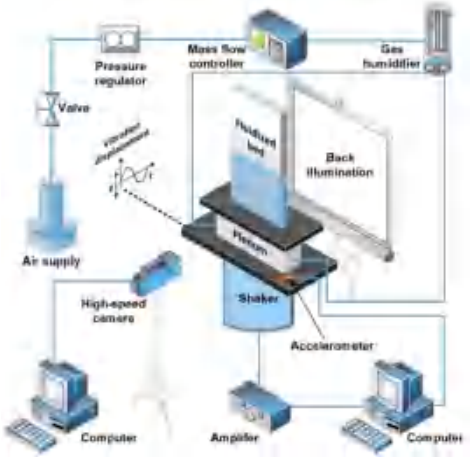


Figure 8 – Experimental setup for vibrated gas-fluidized bed

Conclusions

By coupling both gas flow and vertical vibration, structured flow patterns including structured gas bubbles, surface waves, and convection cells can be formed in the otherwise chaotic fluidized beds. These structured flow patterns are highly predictable and highly ordered, opening the potential to simplify the scale-up and operation of fluidized beds, enabling a range of opportunities for improving process units.

References

[1] C.P. McLaren, T.M. Kovar, A. Penn, C.R. Muller, C.M. Boyce, Gravitational instabilities in binary granular materials, Proceedings of the National Academy of Sciences 116 (2019) 9263–9268.
[2] Q. Guo, Y. Zhang, T.M. Kovar, K. Xi, C.M. Boyce, A Rayleigh–Bénard convection instability analog in vibrated gas-fluidized granular particles, Soft Matter 18 (2022) 3323–3327.
[3] Q. Guo, Y. Zhang, A. Padash, K. Xi, T.M. Kovar, C.M. Boyce, Dynamically structured bubbling in vibrated gas-fluidized granular materials, Proceedings of the National Academy of Sciences 118 (2021) e2108647118.
[4] Q. Guo, W. Da, R. Wu, Y. Zhang, J. Wei, C.M. Boyce, Faraday wave instability analog in vibrated gas-fluidized granular particles, Phys. Rev. E 107 (2023) 034603.
[5] V. Francia, K. Wu, M.-O. Coppens, Dynamically structured fluidization: Oscillating the gas flow and other opportunities to intensify gas-solid fluidized bed operation, Chemical Engineering and Processing - Process Intensification 159 (2021) 108143. https://doi.org/10.1016/j.cep.2020.108143.
[6] Q. Guo, C.M. Boyce, Structured bubbling in layered gas-fluidized beds subject to vibration: A CFD-DEM study, AIChE Journal 68 (2022) e17709.
[7] Q. Guo, S. Chiu, W. Da, C.M. Boyce, Heat transfer within dynamically structured bubbling fluidized beds subject to vibration: A two-fluid modeling study, AIChE Journal 69 (2023) e17970.

A novel circulating fluidized bed process for low-carbon alkane dehydrogenation

Yupeng Du, Hao Cheng, Yanjun Li, Xiaoping Chen, Wanzhong Ren
Yantai University, Yantai, China

Abstract
Chromium contaminates is harmful to environment and human health, its distribution in a CFB setup for low-carbon alkane dehydrogenation is still unknown. For this reason, MP-PIC simulations of the CFB setup are conducted. Cr6+ are found in the whole setup. To reduce its content in the reactor, a novel CFB process with a pre-reduction reactor is proposed and verified.

Keywords: CFB, Chromium contaminates, low-carbon alkane dehydrogenation

Introduction
Dehydrogenation of low-carbon alkanes becomes more and more attractive to produce alkenes with the same carbon number. Commercial dehydrogenation plants employ either fixed beds (e.g. Catofin process) or moving beds (e.g. Oleflex process). However, both of them are facing problems of frequent regeneration of catalysts and/or reaction heat supply because of the endothermic nature of the dehydrogenation reaction and fast deactivation of the catalysts. This has triggered the utilization of the fluidized bed technology for the dehydrogenation process to help alleviate those shortcomings, where chromium-based catalyst is commonly used [1]. Although Cr6+ on catalysts is well-known to be harmful to environment and human health, its distribution in a CFB setup for the low-carbon alkane dehydrogenation process is still unclear.

Methodology
To clarify the distributions of chromium species with various valences (i.e., Cr6+, Cr3+ , and Cr2+) on catalysts, detailed flow dynamics, heat and mass transfers, and chemical reactions in the whole CFB should be performed. As the Multi-Phase Particle-In-Cell (MP-PIC) scheme [2] can offer real possibilities to many physical parameters linked to CFBs and study their effects on the process performance, full-loop MP-PIC simulations of the CFB setup are carried out in this work. The predicted pressure, temperature and product yield distributions are in very good agreements with experimental investigations. Numerical findings also demonstrate that the chromium contaminates on catalysts (i.e., Cr6+) is distributed in the whole CFB setup, while catalysts with Cr3+ and Cr2+ are only distributed in the fluidized bed reactor. It is also found that if a pre-reduction reactor is added into the process, the distribution of Cr6+ in the fluidized bed reactor can be significantly reduced compared to the original process.

Conclusions
Numerical predictions by MP-PIC scheme show very good agreements with experiments. According to the full-loop MP-PIC simulations, catalysts with Cr6+ are found distributing in the whole CFB setup. Therefore, effective measures must be taken to avoid chromium contaminates. To this end, a pre-reduction reactor for CrO3 can be set before the fluidized bed reactor in the CFB process for low-carbon alkane dehydrogenation.

Acknowledgements
This work is financially supported by the National Natural Science Foundation of China (21908186) and the Natural Science Foundation of Shandong Province (ZR2023MB109).

References
[1] Y. Du, H. Cheng, S. Li, X. Chen, Y. Li, W. Ren, C. Yang, Core-shell equivalent reactor network model to bridging CFD and process simulations of a fluidized bed reactor, Chemical Engineering Science 287 (2024) 119772.
[2] Y. Du, X. Chen, S. Li, A.S. Berrouk, W. Ren, C. Yang, Revisiting a large-scale FCC riser reactor with a particle-scale model, Chemical Engineering Science 249 (2022) 117300.

Impact of electrolyte circulation on HTO in alkaline water electrolysis

周钰婕，刘博*，袁方，杨强
（1.华东理工大学，机械与动力工程学院，上海，220000）
(17155169327:, boliu@ecust.edu.cn))

Abstract：
The concentration of hydrogen in oxygen (HTO) is a crucial factor in determining the load limit of alkaline water electrolysis due to the risk of explosion with high HTO levels. In this study, we analyzed the impact of circulating electrolytes, carrying bubbles and dissolved gas, on HTO in a home designed zero-gap alkaline water electrolysis system, operating at atmospheric pressure and constant temperature. Comparing experimental results from mixed and separated cycles, we found that dissolved hydrogen in electrolytes significantly contributes to HTO levels. We then developed a predictive model linking HTO values to the ratio of electrolyte circulation to gas production (QL/Qg), and experimentally demonstrates a linear relationship between HTO and QL/Qg. Additionally, we proposed a new electrolyte circulation control strategy that reduces HTO concentrations by 55% at 15-20% load. These findings could help overcome the load limit of alkaline water electrolysis systems, crucial for their large-scale application.

Keywords：bubble、gas purity、HTO、hydrogen production from alkaline water

Numerical studies on the controlled thermocapillary migration of sessile droplet

Jin-Xin Wang[1,2], Yong-Pan Cheng[1]*, Wei-Cheng Yan[2]*
1. North China Electric Power University, Beijing 102206, China
2. Jiangsu University, Zhenjiang, Jiangsu, 212013, China

Abstract
In this study, a three-dimensional model with level-set method is established to simulate the migration of a sessile droplet under thermocapillary force. The moving contact line is accomplished by extending the point-to-line construction step from the 2D model, incorporating lines to build up interface with a Navier slip boundary condition. After the model is validated, the effects of contact angles, dynamic viscosity ratios, Marangoni numbers, Prandtl numbers, and Ohnesorge numbers on the droplet migration are studied.
Keywords: Droplet migration; Contact angles; Thermocapillary force; Marangoni flow

Introduction

The controlled migration of droplets is of great significance in industrial application and scientific investigation. Besides the external forces, the thermocapillary force may become dominant, which is caused by the non-uniform interfacial tension force due to temperature gradient. Through the previous literature reviews, it is evident that the migration of droplets under thermocapillary force is affected by various factors, including droplet size, temperature gradient and physical properties of droplet and surrounding gas etc [1]. However, previous studies are primarily focused on the parametric studies on droplet migration, and the underlying physical mechanism remains unclear. In this study, a three-dimensional numerical model is built up with implementation of contact angles, the sessile droplets are numerically investigated under a large range of contact angles, dynamic viscosity ratios, temperature gradients and viscosities.

Methodology

Fig. 1 shows the migration of a sessile droplet under the thermocapillary force. The droplet is attached to the centre of a horizontally oriented substrate with a constant temperature gradient. The non-dimensional governing equations for the droplet migration are shown as follows [2]:

$$\nabla \cdot \vec{u} = 0 \tag{1}$$

$$\frac{\partial \vec{u}}{\partial t} + \vec{u} \cdot \nabla \vec{u} = -\frac{1}{\rho^*} \nabla p + \frac{1}{\rho^* \mathrm{Re}} \nabla \cdot \left[\mu^* \left(\nabla \vec{u} + \nabla \vec{u}^T \right) \right] + \frac{1 - Ma \cdot T}{\rho^* \mathrm{Re} \cdot Ca} \kappa \vec{n} \delta(\phi) - \frac{Ma}{\rho^* \mathrm{Re} Ca} \nabla_s T \delta(\phi) \tag{2}$$

$$\frac{\partial T}{\partial t} + \vec{u} \cdot \nabla T = \frac{\mathrm{Oh}}{\rho^* C_p^* \mathrm{Pr}} \nabla \cdot \left(\lambda^* \nabla T \right) \tag{3}$$

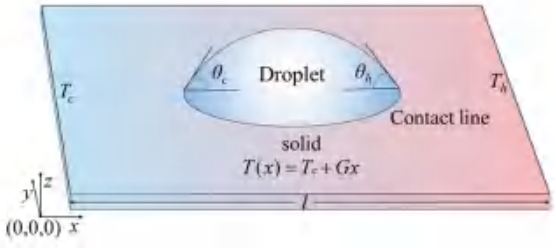


Figure 9 - Schematic diagram of droplet migration on substrate with temperature gradient.

It is challenging to incorporate the moving contact lines in constructing three-dimensional droplet dynamics model. In this study, the Navier slip boundary condition is adopted at the substrate, and the constant contact angle is implemented at the distance of half grid size from the solid boundary and adjusted in the 'reinitialization' step [3].

Conclusions

The results show that at low contact angles the droplet migrates towards the cold region of the substrate, whereas at large contact angles, droplet migrates towards the hot region. The opposite migration directions are due to the variations of the stagnation points and vortex dynamics. The large viscosity ratios between outer gas and inner liquid can decrease the droplet migration speed, and lead the droplet to migrate towards hot region easily. The large Marangoni numbers can increase the droplet migration speed, while the migration direction is fixed. The large Prandtl numbers can weaken the thermocapillary flows, resulting in reduced migration speed at low contact angles while increased migration speed at large contact angles. The large Ohnesorge numbers increase the viscous shear force, thereby reducing the steady droplet migration speed. These findings can provide guidance for controlled migration of sessile droplet.

Acknowledgements

The authors thank the supports from National Natural Science Foundation of China (52276153, 22378171) .

References

[1] Y. Sui, Moving Towards the Cold Region or the Hot Region? Thermocapillary Migration of a Droplet Attached on a Horizontal Substrate. Phys. Fluids. 2014, 26 (9), 092102.

[2] Y. Sui, P. D. M. Spelt, An Efficient Computational Model for Macroscale Simulations of Moving Contact Lines. J. Comput. Phys. 2013, 242, 37-52.

[3] G. Russo, P. Smereka, A Remark on Computing Distance Functions. J. Comput. Phys. 2000, 163 (1), 51-67.

Three-dimensional full-loop simulation of gas-solid flow characteristics in chemical looping combustion system

Xiaoke Ku[1,2,*], Zishuo Wang[1]
[1]Department of Engineering Mechanics, Zhejiang University, Hangzhou, China
[2]State Key Laboratory of Clean Energy Utilization, Zhejiang University, Hangzhou, China

Abstract
Among different carbon capture technologies, chemical looping combustion (CLC) has been recognized as an innovative and promising technique, because of its inherent CO_2 separation characteristics. Meanwhile, biomass is an important renewable energy source due to its abundance and carbon neutrality. The combination of CLC with biomass holds great potential for achieving negative CO_2 emissions, offering various promising applications.
Particle size polydispersity and the structure of fuel reactor (FR) have a considerable influence on the performance of CLC of biomass. In the present work, a three-dimensional multiphase particle-in-cell (MP-PIC) method was established and applied to investigate the gas-solid flow characteristics in the full-loop CLC of biomass system. After model validation, the flow characteristics, solid circulation rate, particle mixing in FR, and biomass leakage at different oxygen carrier (OC) particle size distribution widths were systematically explored under a continuous injection mode. Meanwhile, a new staged FR was also explored, which integrated a bubbling fluidized bed and a spouted bed. The results showed that OC particles significantly stratified within the FR and both loop seals. Small OC particles were primarily distributed in the upper part of the bed, and large particles were mainly distributed in the lower part. Moreover, small biomass particles were more likely to leak. In addition, the spout incoherence also appeared in the two-staged FR during continuous operation, and increasing the initial spouted bed height decreased the dominant frequency of particle blockage. All these observations provide valuable guidance for the design and optimization of the staged FR and the CLC of biomass.

Keywords: Chemical looping combustion; Particle size distribution; Staged fuel reactor; Gas-solid flow characteristics

Fluidization engineering design based on gas-solid structural model

Zheng Zou, Qingshan Zhu, Hongzhong Li
State Key Laboratory of Mesoscience and Engineering, Institute of Process Engineering, Chinese Academy of Sciences, Beijing, PR China

Abstract
Considering the gas-solid interface-structure relationship, heterogeneous transfer-reaction behavior, and multiple reaction kinetics, this paper provides a structural model for the scale-up of fluidized bed reactors.

Keywords: Fluidization, Gas–solid reaction, Structure-based model, Green technology.

Introduction

Gas-solid fluidization technology has been widely applied in many important fields due to its efficient heat-mass transfer performance, but the particles are easy to agglomerate with a wide size distribution, which makes it difficult to develop high-quality product with high efficiency. The key to solving this problem lies in the accurate analysis of the relationship between flow structure and transport reaction for gas-solid phases, coupled with the effective process intensification.

Methodology

The non-uniform fluidized structure determines gas–solid flow and reaction. A structure-based momentum/mass transfer model is constructed based on the hydrodynamic parameters of the dense and dilute phases. Furthermore, coupled with chemical reaction engineering and two-phase flow principle, the structure-based transfer theory extends to: 1) construct a structure-activity relationship model for the wide particle size/aggregative fluidization, predicting the characteristic of non-uniform fluidization accurately; 2) develop a coupling algorithm for the interface structure-transport reaction, analyzing the unsteady conversion mechanism of solids quantitatively; 3) form a CFD-based optimization method for the gas-solid complex reaction network, supporting the development of process industries by using numerical simulation.

Results

Based on the structure-based transfer theory, a number of simulation-based process intensification methods have been applied to a 1,000 t/a pilot scale fluidized direct reduction platform, a fluidized bed reduction of manganese ore with capacity of 200,000 t/a, a directional reduction roasting for the complex iron-manganese ore with capacity of 500,000 t/a, etc.

Conclusions

In the future, the CFD simulation coupled with the structure-based transfer model can be applied to optimize the fluidized bed reactor for the low-carbon engineering application.

References

[1] H. Li, Q. Zhu, Z. Xie, Z. Zou, Fluidized bed structure transfer theory and industrial applications. China Science Publishing&Media Ltd, 2020.

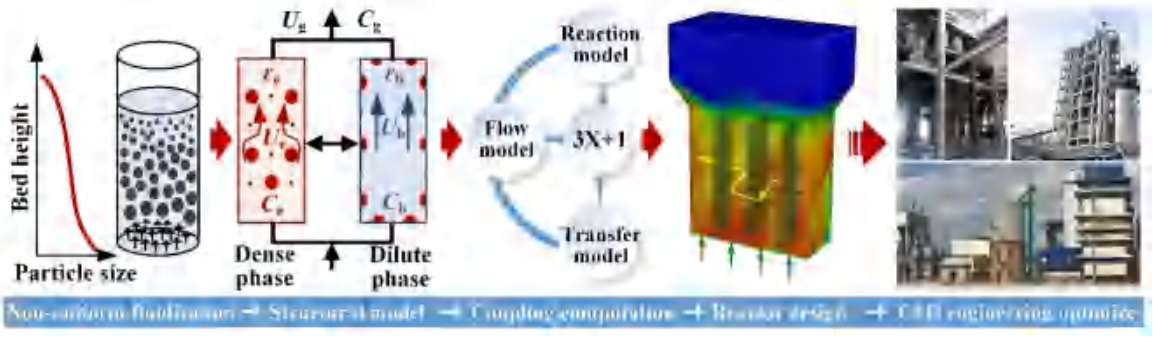


Fig. 1. The methodology of fluidization engineering design based on the structural model.

Experimental and simulation study of flow and mass transfer performance of annular microchannel enhanced by spiral-wound wires

Min An1, Chengxiang Wang1, Wenpeng Li*
Zhengzhou University, Zhengzhou, China

Abstract
The annular microchannels have significant high throughput and low pressure drop advantages. Wires were introduced by wrapping around the inner tube to further improve a liquid liquid reactor performance. The effects of added wires on the turbulence dissipation rate and the specific surface area were analysed by means of VOF simulation studies. An optimized wrapping structure is proposed in terms of pressure drop and mass transfer performance. This study can provide some guidelines for the operation and design of annular microchannels.

Keywords: Annular microchannel, Flow, Mass transfer, VOF

Introduction

The annular microchannel with pore-arrays is a new type of microchannel reactor, in which the discrete phase in the inner tube flows through the microporous to mix with the continuous phase in the annulus[1]. However, 80% of the mass transfer occurs in the former pore-array area, and the performance in the lateral annular space is limited. Therefore, micro wires were introduced in terms of wrapping around the inner tube, and effects of different wrapping style were studied. Methodology Fig.1a is the experimental flow diagram. Kerosene, as the dispersed phase, injects into the annulus from the pores in the inner tube at a high velocity. Deionized water, as the continuous phase, enters the annulus directly at the T-port. Fig.1b is the apparatus scheme with enlargement of pore arrays. Fig.1c depicts different wrapping styles of wires around the inner tube. The Volume of Fluid (VOF) method was used to simulate the flow and mixing behavior of the water and kerosene phases in the annular space. The accompanying mass transfer was not considered for the moment. The simulation results are firstly validated by comparing the measured and simulated total pressure drops of water and kerosene phases.

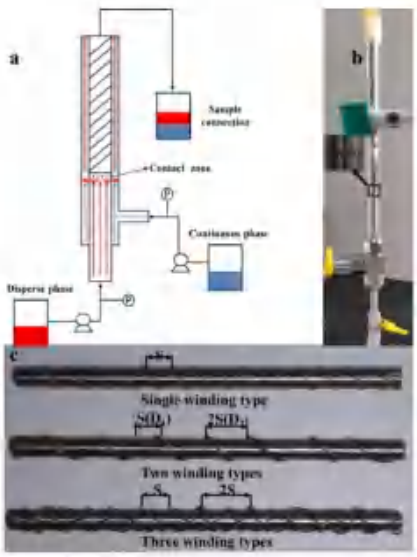


Fig. 1 – Apparatus and flow diagram

The measured total pressure drop increases with growing diameter and number of wires, while it decreases with increasing wrapping batch and diameter difference under two-wires conditions. The additional wires enhance flow resistance and thus increase the pressure drops. Simulation results show that the pressure decreases slightly in the former part and decrease at a higher speed in the later

annular space with wrapping wires along the axial direction.

Both the KLa and E show consistent trends with the pressure drop at different conditions. The influencing mechanism of wrapping wires on the mass transfer performance was analyzed by relevant underlying parameters required by simulations. The turbulence dissipation rate was International Multiphase Flow Technology Forum 2024 Dali, China used to explain the change of mass transfer coefficient, and the specific surface area according to Thomas model [2] were also calculated.

The trends of the simulated specific surface area are consistent with the change of the volumetric mass transfer coefficient, which help to explain the enhancement of mass transfer performance. However, the changes of turbulence dissipation rate are complex.

Conclusions

The performance liquid-liquid in mass a micro-wound transfer wire microchannels has been studied using the water benzoic acid-kerosene system. The effects of single diameter, pitch, wrapping type factors were investigated. The performance index and optimal structure are not the same, but the performance index of WM-1-0.5-30 is far superior to other cases when the flow rate reaches 20 l/h, so it is suggested.

Acknowledgements

The authors sincerely appreciate the financial support of the National Natural 377 Science Foundation of China (grant No.22208320).

References

[1] W. Li, F. Xia, S. Zhao, M. Zhang, W. Li, J. Zhang, Characterization of liquid-liquid mass transfer performance in a novel pore-array intensified tube-in-tube microchannel, AIChE Journal (2019) e16893.

[2] Q. Wu, S. Kim, M. Ishii, S.G. Beus, One-group interfacial area transport in vertical bubbly flow, International Journal of Heat and Mass Transfer 41 (1998) 1103–1112.

Development of Fluidization Technology for Thermochemical Energy Storage Application

Yandaizi Zhou
Wuhan Institute of Technology

Abstract

Due to the inconsistency and intermittence of solar energy, concentrated solar power (CSP) cannot stably transmit energy to the grid. Heat storage can maximize the availability of CSP plants. Especially, thermochemical heat storage (TCHS) based on $CaO/CaCO_3$ or $CaO/Ca(OH)_2$ cycles has broad application prospects due to many advantages, such as high heat storage density, high exothermic temperature, low energy loss, low material price, and good coupling with CSP plants. Fixed beds are usually assumed to be the most suitable reactors for carrying out the cycle steps. However, it can be argued that these reactors have serious limitations for this application that may have prevented the development of the process. In view of these limitations, fluidized bed reactors should be considered as an interesting alternative to $CaO/CaCO_3$ or $CaO/Ca(OH)_2$ energy storage systems due to the high heat/mass transfer coefficients and uniform temperatures within the bed. This work focused on the development and challenges of fluidization technology for TCES-CSP applications, and related modification technology. More specifically, as fine powder fluidization is favored by Ca-Looping energy storage systems, the advantages, challenges and hydrodynamics were presented in this work.

Keywords: Fine powder; Fluidization; Ca-looping; Thermochemical heat storage; Concentrated solar power

Scale-up mechanism of spout fluidized bed by multiple spout channels

Yuanhe Yuea,b, Weiwei Zhaoa,b, Runzhe Duana,b, Zhonghao Raoa,b,*.
a Hebei Engineering Research Center of Advanced Energy Storage Technology and M, School of Energy and Environmental Engineering, Hebei University of Technology, Tianjin, 300401, China
b Hebei Key Laboratory of Thermal Science and Energy Clean Utilization, School of Energy and Environmental Engineering, Hebei University of Technology, Tianjin, 300401, China
Speaker: Weiwei Zhao

Abstract
Scale-up of spout fluidized beds has been a significant concern for decades but has not been solved yet. An important reason for the dilemma is the insistence that symmetrical particle circulation at the reactor level is necessary. This study focuses on achieving scale-up effects of the spouted fluidized bed by allowing multiple deflected spouts to work together. The meso-scale hydrodynamics as well as the underlying mechanism of this new flow pattern is analyzed comprehensively through CFD-DEM approaches. To demonstrate the validity of gas-solid mixing homogeneity, this flow pattern is applied to the vapor deposition coatings process. The results indicate that the uniformity and stability of the reaction process is quite satisfactory. This work provides a new route for the scale-up of spouted beds.

Keywords: Spouted fluidized bed, CFD-DEM, Vapor deposition coatings, Multiphase flow fields.

Introduction

With the further study of spouted fluidized bed reactors, scaling up the reactor has become an important research direction. In addition to various internal and external configurations to promote the stability of single spouting, multiple spout jets have also been studied. For example, Huang and Chyang found that the stability of a bed with multiple spouts was strictly limited to spouting velocity, particle diameter and geometrical configuration [1]. However, these attempts are adding several chambers together with draft plates to keep the independence of each spouting. To overcome this gap, this work introduces the new concept of deflected spout and redesigns the gas-solid mixing pattern.

Methodology

The CFD-DEM approach has been widely applied to study the fluidization process of gas-solid flow because it can capture the discrete solid movement and the fluid phase with satisfying accuracy. In this study, the traditional CFD-DEM approach is adopted and briefly outlined here for completeness. The work is conducted on the open-sourced platform MFIX [3].

Results

With the increase of jet velocity, the distance of the corresponding nozzle vertical jet also increases. In this amplification technology, the gas-solid contact performance is good, and the effect of the vapor deposition coating is also improved.



Figure 1 D=0.14m Snapshot of porosity distribution under different spouting velocities

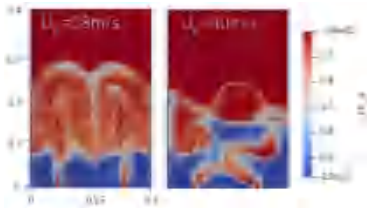


Figure 2 D=0.16m Snapshot of porosity distribution under different spouting velocities

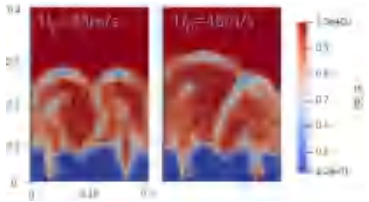


Figure 3 D=0.18m Snapshot of porosity distribution under different spouting velocities

Conclusions

In this work, the hydrodynamics of a two-joint flow pattern was systematically studied using the CFD-DEM approach. The gas-solid mixing performance and the good performance of the reaction process were also revealed. It lays a good foundation for the effect of vapor deposition coating.

Reference

[1] C.-C. Huang, C.-S. Chyang, Multiple Spouts in a Two-dimensional Bed with a Perforated-plate Distributor, J. Chem. Eng. Japan. 26 (1993) 607–614.

[2] Guo L, Wang G, Zhang F, et al. Effect of temperature on the minimum spouting velocity of heavy particles in conical spouted bed used for nuclear fuel coating[J]. Exp. Therm. Fluid Sci, 2023, 144: 110876.

[3] X. Gao, L. Lu, M. Shahnam, et al., Assessment of a detailed biomass pyrolysis kinetic scheme in multiscale simulations of a single-particle pyrolyzer and a pilot-scale entrained flow pyrolyzer, Chem. Eng. J. 418 (2021) 129347.

An Improved Numerical Simulation of Porous Particle Flows Based on A New Drag Correlation Considering the Permeability

Likun Ma[a], Qinghai Huang[a], Zhishan Bai[a,*]
[a]School of Mechanical and Power Engineering, East China University of Science and Technology, Shanghai 200237, China

Abstract
An accurate drag correlation accounting for porous structures is a prerequisite for reliable CFD simulation of industrial processes consisting of porous permeable particles. The traditional CFD simulation generally use drag correlations of the solid sphere to carry out the numerical calculations, which ignores the effect of porous permeable structures within the porous spherical particles and leads to an inaccurate prediction of the fluid flow through porous particles. This work carried out an improved numerical simulation of porous particle flows based on a new drag correlation of porous particles considering the permeability. Compared with the traditional drag correlation of solid sphere, the present numerical simulation agrees better with the experimental results, which shows the new simulation approach can provide a more accurate simulation results for porous particle flows.

Keywords: Drag Correlation; Porous particle; Permeability； Numerical Simulation;

Introduction

Porous particles are commonly used in chemical industries, including porous adsorbent particles in oil/water separation processes, porous catalyst particles in chemical reactors, permeable coal particles in mineral engineering, and so on [1]. An accurate numerical simulation of porous particle flows play an important role in controlling and optimizing these multiphase flow processes. However, the traditional CFD simulation generally use drag correlations of the solid sphere to carry out the numerical calculations, which ignores the effect of porous permeable structures within the porous spherical particles and leads to an inaccurate prediction of the fluid flow through porous particles. Thus, this work carried out an improved numerical simulation of porous particle flows based on a new drag correlation of porous particles considering the permeability, which can promote a more accurate simulation results for industrial processes consisting of porous permeable particles.

Methodology

The numerical simulation was carried out by commercial software MFiX. The new drag correlation used in the simulation is as Figure 1 shown, and a porous particle settling experiment was carried out as a comparison.

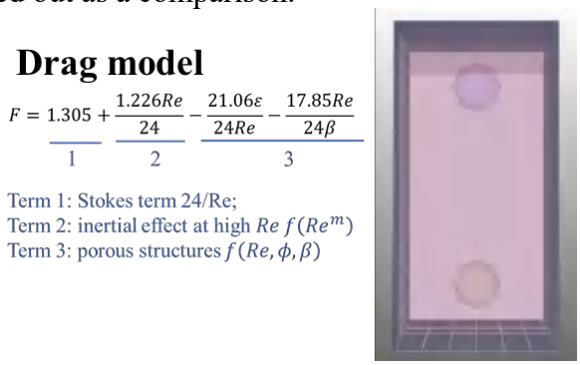


Figure 10 - Numerical model of porous particle flows with a new drag correlation considering the permeability

Conclusions

Compared with the traditional drag correlation of solid sphere, the numerical simulation of porous particle flows based on a new drag correlation of porous particles considering the

permeability agrees better with the experimental results, which shows the new simulation approach can provide a more accurate simulation results for industrial processes consisting of porous permeable particles.

Acknowledgements

This work is part of a research program financially supported by the National Natural Science Foundation of China (No. 22308105), the National Science Fund for Distinguished Young, China (No. 22225804), China Postdoctoral Science Foundation (No. 2023TQ0117).

References

[1] Yu P, Zeng Y, Lee T S, et al. Steady flow around and through a permeable circular cylinder[J]. Computers & Fluids, 2011, 42(1): 1-12.

Kinetic, products formation, and mechanism analysis for the pyrolysis of Ethylene-co-vinyl acetate

Shangming Wang, Yunan Chen, Bin Chen*
State Key Laboratory of Multiphase Flow in Power Engineering, Xi'an Jiaotong University, Xi'an 710049, China
*Corresponding Authors: chenbin@mail.xjtu.edu.cn

A proportionate number of waste PV modules arises because of their limited lifespan. It is estimated that by 2050, there will be approximately 60−78 million tonnes of PV waste. At present, the main methods of recycling end-of-life (EoL) PV modules are physical, chemical and heat treatment approaches. Heat treatment can effectively separate the components of EoL PV modules through temperature control, which is fast and simple, and is currently the most common and promising recycling technology. Ethylene-co-vinyl acetate (EVA) as PV encapsulant is used in both first- and second- generation PV modules, which is the key to recycling and disposal of EoL PV modules. Although there have been studies on EVA pyrolysis recovery, its depolymerization characteristics, kinetic behavior, product formation and other mechanisms under different pyrolysis atmospheres are still unclear.

To systematically explore the pyrolysis kinetics, product distribution and mechanism of EVA, and lay a foundation for the recovery and utilization of PV modules in the future, this study for the first time combined experiments with reactive force field molecular dynamics (ReaxFF-MD) simulations to describe the pyrolysis process of EVA under different atmospheres (nitrogen and air).

Firstly, pyrolysis kinetic parameters of EVA were evaluated by iso-conversional methods (KAS, FWO, and AIC) based on TG analysis. Subsequently, the pyrolysis process and products were studied by TG-IR, and PyGC/MS analysis. Finally, ReaxFF-MD simulations were used to study the microcosmic reaction pathways of EVA at different temperatures (1700-2900 K, interval of 300K) during the pyrolysis process. All simulations were performed in software LAMMPS by using the 2008_field_cho force field. The constructed model consists of 6 EVA chains with polymerization degree of 60, and 100 oxygen molecules are added to the model to correspond to pyrolysis in air atmosphere. After structural and energy optimized relaxation in NPT ensemble, the model will be subjected to formal pyrolysis simulation for 200 ps in NVT ensemble (as shown in Figure 1).

Through the analysis of results, the main conclusions are as follows:

1) The pyrolysis process of EVA goes through two stages under both nitrogen and air atmosphere, and the final weight loss rate exceeds 99%.
2) Although EVA has lower apparent activation energy (E_a) under air atmosphere (as shown in Table 1), its pyrolysis end temperature (about 550 ℃) is higher than that in nitrogen atmosphere (about 500 ℃).
3) The first stage of EVA pyrolysis is deacetylation reaction. In the second stage, the deacetylated carbon atom drives adjacent carbon atom to break bond with parent chain.
4) Oxygen could combine alkyl radicals to form alkyl peroxide, and then peroxy bond breaks to form small molecule products.

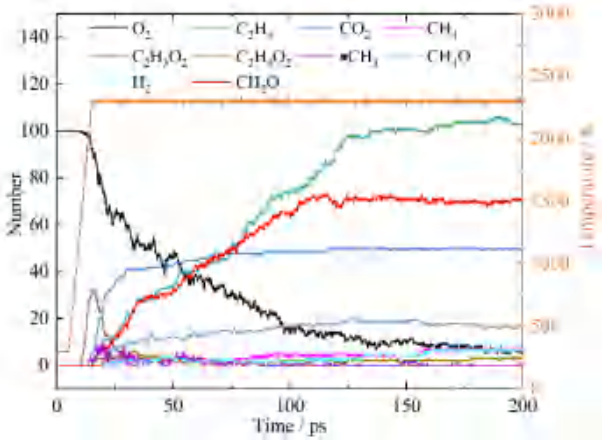


Figure 11 - Products in simulation of EVA

Table 1 - E_a (kJ/mol) of EVA

Methods	**Nitrogen**		**Air**	
	I	II	I	II
KAS	175	260	136	182
FWO	178	264	138	185
AIC	177	273	137	186

Keywords: EVA, Kinetic, ReaxFF-MD, Reaction pathway

Study on the oxidation mechanism of asphaltene in supercritical water by ReaxFF molecular dynamics simulation

Peng Zhang, Xiaoming Luo*, Xinbao Xu
China University of Petroleum(East China), Qingdao 266580, China

Abstract
Asphaltene is a key component limiting degradation in oily sludge. In this paper, the supercritical water oxidation mechanism of asphaltene was investigated using molecular dynamics simulation by ReaxFF. Based on the product distribution and radical reaction theories, the free radical influence mechanism of operating parameters, and the asphaltene degradation pathway were obtained. The results indicate that increasing temperature, oxygen concentration, and water concentration enhance the production of $OH\cdot$, with different effects on $HO_2\cdot$ leading to different outcomes. Higher temperature and oxygen concentration promote the conversion of organic carbon, but high temperatures result in the transformation of CO_2 to CO. Increased water concentration enhances H_2 production. The complete oxidation of N elements during asphaltene degradation requires stricter reaction conditions.

Keywords: Supercritical water oxidation, Radical reaction, Asphaltene, ReaxFF

Introduction

Supercritical water oxidation (SCWO) is an emerging organic waste treatment technology. The strong dissolving power, high diffusivity, and homogeneous reaction of supercritical water were utilized to improve the reaction efficiency significantly, and thus efficient, clean, and harmless disposal of organic matter has been achieved. Oil sludge is a common organic solid waste in oil fields, with the characteristics of large output, high pollution, and difficult treatment. SCWO provides a great application potential in the treatment of oil sludge. Due to the thorough oxidation, simple equipment, skid mounted modules and high Economy, SCWO is more advantageous compared with conventional methods such as pyrolysis and incineration.

As the largest molecule and most complex component of crude oil, asphaltene is the key fraction that limits the complete degradation of oily waste. Rana et al. [1] investigated the gasification process of asphaltene in sub/supercritical water and concluded that the variation in H_2 production is attributed to the changes in the water-gas shift reaction under different reaction conditions. Meanwhile, Li et al. [2] performed a statistical analysis of the products of asphaltene after gasification in supercritical water. However, the complex structure of asphaltene imposes significant limitations on experimental methods, greatly restricting the capabilities and accuracy of detection. Therefore, this study employs a molecular dynamics simulation based on the free radical reaction theory to investigate the reaction mechanism of asphaltene and the micro-level mechanisms of operating parameters such as temperature, oxidant concentration, and water concentration.

Methodology

The reaction model was constructed based on Materials Studio. The structural optimization of asphaltene, water, and oxygen molecules was conducted used Dmol3 and based on GGA and BLYP functions simultaneously. The classical Modified Yen Model was chosen for the asphaltene structure [3], and the asphaltene structure and the constructed Amorphous Cell are shown in the figure 1 below.

The reaction process were conducted by ReaxFF with periodic boundary conditions and the reaction step size was set at 0.25 ps. Initially, the system was heated from 0 K to 300 K at a rate of 30 K/ps, and equilibrated for 10 ps. Subsequently, the system was heated to the simulation temperature at a rate of 100 K/ps and maintained for 3,000,000 steps.

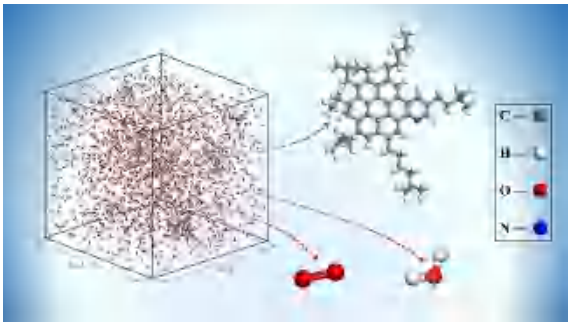


Figure 1 - Reaction system and asphaltene structure

Results and discussion

Table 2 – System components and simulation parameter

Asphaltene	**O_2**	**H_2O**	***T*/K**
5	300	1500	2500~4500
5	300~700	1500	3500
5	300	500~1500	3500

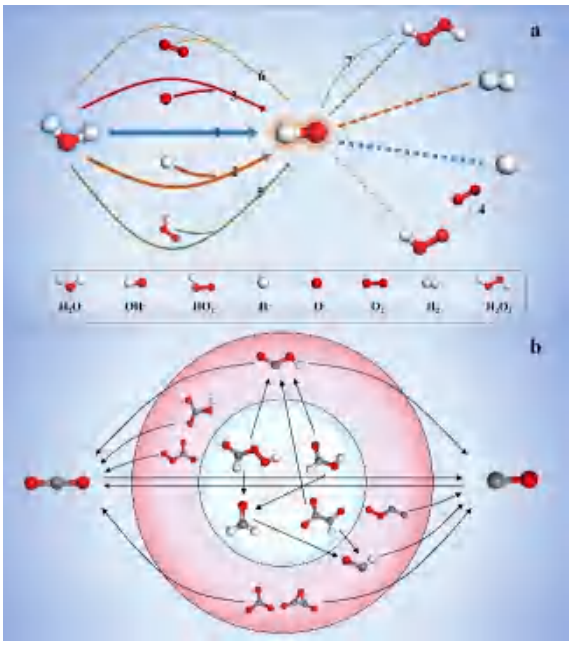


Figure 2 – a Radical reaction network, b CO CO_2 generation pathway

Simulations were conducted to investigate the effects of temperature, oxidant concentration, and water concentration. The molecular quantities and simulation parameters for each component are outlined in Table 1. The analysis of the reaction process focused on the distribution of products, the types and frequencies of radical reactions. The following four aspects were investigated: (1) The changes in total energy, total fragment number, and total species number of the system at different temperatures were Examined. Both the transformation process of asphaltene and the differences in reaction at different temperatures were investigated simultaneously based on the classification of process products; (2) The predominant radical reactions involving OH·, HO_2·, and H· during the reaction process were analysed. Moreover, the impact of operational parameters on the reaction mechanism was explored based on the variations in frequency under different reaction conditions; (3) The distribution of final products under different conditions was analysed, and the pathways for the generation of the three main products, CO, CO_2, and H_2 were proposed. The influence of

operational parameters on the generation pathways was summarized, as shown in Figure 2; (4) Based on the visualization of the reaction process, the open-loop behaviour under the influence of different operational parameters was investigated, and the degradation pathways of asphaltene in terms of the reaction and cracking energies were summarized.

Conclusions

The temperature, oxidant concentration, and water concentration affect the reaction efficiency and product distribution by influencing radical reactions. Increasing the temperature substantially enhances the frequency of radical reactions and suppresses the generation of low-active radicals such as $HO_2\cdot$. Moreover, raising the oxidant concentration significantly enhances the production of $OH\cdot$ while also markedly elevating the production of $HO_2\cdot$, which limits the further improvement of reaction efficiency to some extent. Increasing water concentration promotes the decomposition of H_2O to produce $OH\cdot$, while the production of $HO_2\cdot$ is barely affected. In terms of product distribution, excessive temperature may cause the aggregation of intermediate products and the transformation of CO_2 to CO at the same time. Increased water concentration enhances H_2 production Asphaltene reactions proceed in the sequence of chain hydrogen abstraction, chain carbon stripping, and aromatic ring opening. $OH\cdot$, as the most active radical, promotes the opening process by attracting, substituting, and stretching, deforming, and eventually breaking C-C bonds, making complete oxidation more difficult due to the presence of N elements.

Acknowledgements

The authors acknowledge the financial support provided by the National Natural Science Foundation of China (Grant No. 52074342) and the Taishan Scholar Foundation of Shandong Province (Grant No. tsqn202103041).

References

[1] R. Rana, S. Nanda, A. Maclennan, Y. Hu, J.A. Kozinski, A.K. Dalai, Comparative evaluation for catalytic gasification of petroleum coke and asphaltene in subcritical and supercritical water, J. Energy Chem 31 (2019) 107-118, DOI:10.1016/j.jechem.2018.05.012.

[2] N. Li, X. Zhang, Q. Zhang, L. Chen, L. Ma, X. Xiao, Reactivity and structural changes of asphaltene during the supercritical water upgrading process, Fuel 278-2 (2020), 118331, DOI: 10.1016/j.fuel.2020.118331.

[3] O.C. Mullins, The Modified Yen Model, Energy & Fuels 24 (2010) 2179-2207, DOI:10.1021/ef900975e.

Parallel Session III: Topic3-Fundamentals of dispersed multiphase flow

Study in multiple successive collisions between a flow-driven prolate spheroidal particle and a plane wall

Rongxuan Hu, Yan Cui
Affiliations (Huazhong University of Science and Technology, Wuhan, China)

Abstract
This study explores the numerical solution of dispersed two-phase flows to investigate multiple successive collisions between elastic prolate spheroid particles and a rigid planar wall, and the collisions are modelled accordingly. The authors analyze the influence of various factors such as particle aspect ratio, orientation angle, impact velocity, material properties, size, impact angular velocity and wall friction coefficient by performing finite element simulations (FEM). Four particle aspect ratios (λ = 1.5, 2, 3, and 5) are studied. The results show that multiple collisions are mainly determined by the particle aspect ratio and orientation angle. When λ = 2 to 5, secondary collisions occur. When λ = 5, the particle can collide with the wall three times in a row. The corresponding ranges of the particle orientation angles for secondary and tertiary collisions are provided for different particle aspect ratios. The maximum elastic force acting on the particles at each collision is also analyzed. The proposed model is easily implanted into a Lagrangian particle-tracking algorithm and is verified to be applicable to gas-driven particles.

Keywords: Dispersed two-phase flow, Particle-wall collision, Multiple successive collisions.

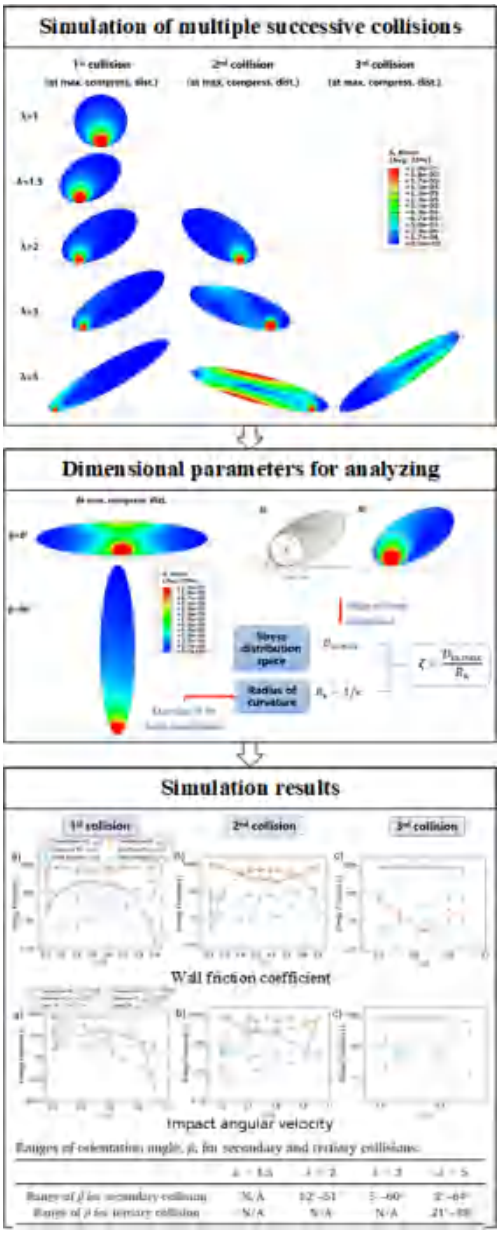


Figure 12 – Method for analyzing of multiple successive collisions between a prolate spheroidal particle and a plane wall

Behavior of suspension cohesive particles in Rayleigh- Bénard turbulence

Han Huang, Shuaiqi Zhao, Rui Zhang, Kunpeng Zhao, Bofeng Bai*
Affiliations (Xi'an Jiaotong University, Xi'an, China)

Abstract
We investigate the dynamic of particles in Rayleigh-Bénard turbulence, based on a two-way coupled LES-DEM method considering Stokes drag, cohesive force and direct contact force. We analyze the temporal evolution of floc size and shape due to aggregation, breakage and deformation. Particles tend to concentrate in the thermal plumes and agglomerate, during the transient flocculation phase. Due to the Kolmogorov scale limiting the floc growth, flocs near the thermal plumes undergo fragmentation and follow the dynamics of Rayleigh-Bénard vortices. During equilibrium, flocs no longer cluster near the thermal plumes, descending at cold plumes and ascending at thermal plumes. We observe flocs more readily achieve an equilibrium state at higher Rayleigh numbers (Ra). Our results elucidate the dynamic behavior of adhering particles in natural convection turbulence, where the circulation of adhering particles enhances the impact of the cold wall.
Keywords: Suspensions, Particle-laden flows, Bénard convection

Introduction

Particle-laden thermal convection flows are widely present in nature such as deep-loop ocean circulation and pollutant particles in the atmosphere[1]. Rayleigh-Bénard convection is a classical phenomenon of thermal convective turbulence. Extensive research has already been conducted on Rayleigh-Bénard turbulence with inertial particles.

Additionally, the flocculation of particles, induced by inter-particle cohesive force, is a widespread occurrence in environmental and industrial processes. In the planetary formation process, collisions and adhesion among dusts are prevalent phenomena. Numerous researchers have considered the aggregation in particle-laden turbulence through high-resolution numerical methods.

In this work, we perform a Large Eddy Simulation to study the interplay between floc aggregation under the influence of Rayleigh Bénard turbulence. A Discrete Element Method (DEM) incorporating inter-particle cohesive forces is utilized to fully resolve the translational and rotational motion of particles. The present investigation aims to explore the aggregation, deformation and fragmentation of particles in the dynamic equilibrium stages interacting with thermal convective turbulence.

Methodology

We consider the two-way coupled motion of suspended cohesive particles in three-dimensional, Rayleigh- Bénard turbulent flow in cavity. Accounting for the compressibility effects induced by variations in fluid properties, the time-dependent equations are defined as

$$\frac{\partial \rho}{\partial t}+\frac{\partial(\rho u_j)}{\partial x_j}=0 \tag{1}$$

$$\frac{\partial}{\partial t}(\rho u_i)+\frac{\partial}{\partial x_j}(\rho u_j u_i)=\frac{\partial p}{\partial x_i}+\frac{\partial}{\partial x_j}\left[\mu(\frac{\partial u_i}{\partial x_j}+\frac{\partial u_j}{\partial x_i})\right]+\rho \boldsymbol{g}+\boldsymbol{F}_p \tag{2}$$

$$\frac{\partial}{\partial t}(\rho C_p T)+\frac{\partial}{\partial x_j}(\rho C_p u_j T)=\frac{\partial}{\partial x_j}(k\frac{\partial T}{\partial x_j}) \tag{3}$$

Where u_i, p, T denotes the velocity vector, pressure and temperature. The subgrid method of large eddy simulation is specifically referenced in BINI M[2]. The source term F_p represents the force exerted by particles on fluids given by

$$\boldsymbol{F}_{p,i}=\sum_{n=1}^{n=N}\boldsymbol{F}_n \boldsymbol{w}_k(\boldsymbol{x}_{p,n}-\boldsymbol{x}_i) \tag{4}$$

In the context of Discrete Element Model. We consider drag force and cohesive force inter-particles. Particle rotation due to collisions was also investigated. Given that the diameters of the particles under consideration significantly exceed 2 μm, the Brownian forces acting between particles can be disregarded (cf. Table 1). Due to ϕ_p exceeds 1×10^{-3}, it is imperative to consider the two-way coupling between particles and the fluid. Due to space limitations, we only give the adhesion forces equations:

$$\boldsymbol{F}_{coh,ij}=\begin{cases}\dfrac{A_H D_p(\zeta_{n,ij}\lambda-\zeta_{n,ij}^2)}{4\zeta_0\lambda^3}\boldsymbol{n} & \zeta_{\min}<\zeta_{n,ij}<\lambda \\ 0 & otherwise\end{cases} \quad (5)$$

Table 3 – Physical parameters in present work: the scale of length, velocity, and time are L_0=200Dp, $U_0=\bar{\alpha}\sqrt{Ra}/L_0$=0.172, and $\tau_0=L_0/U_0$.

Physical parameters				
Particle Diameter	D_p	50 μm		
Particle density	ρ_p	1.2×10^3 kg m^{-3}		
Number of particles	N	20000		
Volume fraction of particles	ϕ_p	1.3×10^{-3}		
Hamaker constant	A_H	8.0916×10^{-21} J		
Temperature difference	Δ	100 K		
Non-dimensional parameters				
Rayleigh number	Ra	5×10^7	Ra	5.0×10^7
Stokes number	St	0.4206		
Reynolds number	Re	5.574×10^3		
Turbulence dissipation rate	$\tilde{\varepsilon}$	1.364		

The key focus of this paper is the dynamics of flocs within Rayleigh-Bénard convection vortices, and the inertial particle diameters must be smaller than the Kolmogorov scale. Therefore, it is necessary to meticulously analyze the correctness and rationality of the relevant fluid parameters. Figure 1 shows the comparison of the Nusselt number (Nu) in this study with the results of other studies, demonstrating good consistency.

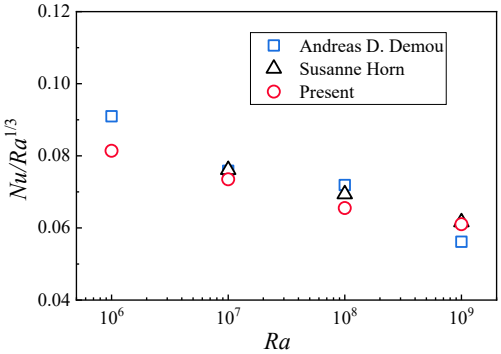


Figure 13 – Compared with Reduce Nusselt Number from other research

Conclusions

Under the non-Boussinesq assumption, the temperature $\langle\theta_m\rangle_{x,y}$ (The average temperature on the xy plane at $\tilde{z}$=0) is no longer a constant zero. Figure 2 illustrates that, under the influence of flocs, $\langle\theta_m\rangle_{x,y}$ is significantly lower compared with single-phase flow field. Figure 3 shows the particles concentrate near the thermal plume and agglomerating. The gradual disappearance of this aggregating effect at the cold wall after the particles reach an equilibrium state.

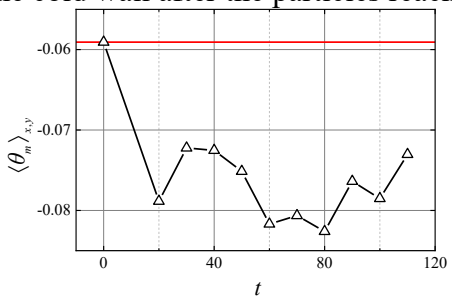


Figure 2 – Compared with Reduce Nusselt Number from other research. The red solid line indicates the temperature of the center plane in single-phase fluid

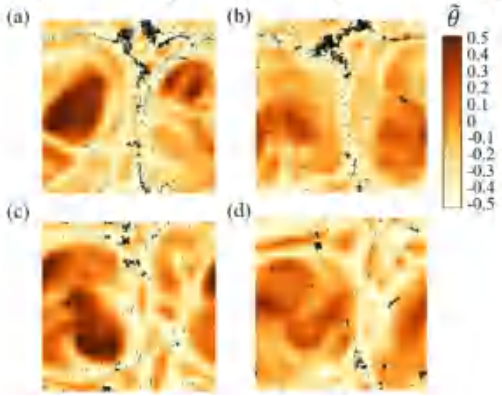


Figure 3 - Time evolution of the scalar field θ and particle distribution near the cold wall at z=0.45. Figures a-d correspond to times t=60, 80, 100, 120, respectively.

Acknowledgements

The author is supported by National Natural Science Foundation(NSFC) of China for Basic Science Center Program for Ordered Energy Conversion (No.52488201). K.Z. gratefully acknowledges support through NSFC grants 52206208.

[1] SEINFELD J H, PANDIS S N. Atmospheric chemistry and physics: from air pollution to climate change [M]. John Wiley & Sons, 2016.
[2] BINI M, JONES W. Large-eddy simulation of particle-laden turbulent flows [J]. Journal of Fluid Mechanics, 2008, 614: 207-52.

Electrospray cooling characteristics and the heat transfer enhancement mechanism

Haojie Xu[1, 2], Junfeng Wang[1], Hyoung-Bum Kim[2]
[1]School of Energy and Power Engineering, Jiangsu University, Zhenjiang, China
[2]School of Mechanical and Aerospace Engineering, Gyeongsang National University, Jinju, South Korea

Abstract
This study reported a systematic experimental investigation on the electrospray cooling process, including the entire cooling performance and key influencing parameters. Meanwhile, the visualization and theoretical analysis of the charged disintegration of coolants and the spreading and evaporation heat transfer of charged droplet were also discussed in detail using the high-speed microscopic amplification method. The purpose is to reveal the heat transfer enhancement mechanism of electrospray and provide some fundamental results and theories for developing of new efficient spray cooling technology.

Keywords: Electrospray, Spray cooling, Charge droplet, Heat transfer enhancement

Introduction
Electrospray cooling is recently a promising heat removal route for electronics due to its powerful cooling capacity, tiny liquid supply, and precise temperature control. Since first reported in 1882 [1], the electrospray technology has attracted increasing research interests. For a typical setup of electrospray, the capillary nozzle is connected to a high-voltage power supply, thus the supplied liquid is going to breakup into numerous ultrafine droplets with electrodynamic (EHD) forces overcoming surface tension. Nowadays, the relevant applications have been successfully employed in ink-jet printing, industrial dust removal, agricultural plant protection, and meso-scale combustion [2].
Previous literatures have confirmed the heat transfer enhancement of electrospray cooling [3-5]. However, the involved multiphase flow characteristics and heat transfer mechanisms are very complicated and still unclear. Specifically, the droplets behaviors of electrospray cooling, such as disintegration, spreading, or evaporation, are quite different from the traditional conditions, which will significantly affect the entire cooling performance.
In this study, the main contribution is to experimentally investigate the impact behaviors and evaporation characteristics of electrospray droplets on hot substrates, as well as the analysis of heat transfer enhancement mechanisms.

Methodology
The experimental setup of present work is shown in shown in Fig. 1. It consists of the spray generation, spray visualization, and heat transfer measurement parts. Deionized water and ethanol are employed as coolant. The liquid was supplied to the metal capillary nozzle by syringe pump with certain flow rates. A high voltage power supply (voltage 0-30 kV, current 0-2 mA) was connected to the nozzle, whereas the hot counter substrate was electrically grounded. The backlit shooting was employed for visualization where a LED cold light was placed opposite a high-speed camera. The resolution was about 1024 × 768 pixels, and the frame rate was fixed as 4000 fps.

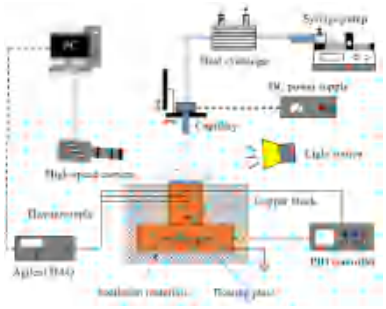


Figure 1-Setup of electrospray cooling



Figure 2-Electrospray mode evolution using ethanol

Fig. 2 shows the effects of electric field intensity on the electrospray morphology of ethanol. The spray would successively experience the so-called dropwise, micro-dripping, cone-jet, and multi-jet modes with the applied voltage increasing to 6.5 kV. From dropwise to multi-jet, the liquid was found to disintegrate more completely and would cover greater area. The visualization results showed that the droplet size decreased significantly to approximately several micrometers for multi-jet mode. In addition, the impingement of spray droplet to the substrate was accelerated with a maximum velocity of about 8 m/s by the electric force.

Fig. 3 shows the spray droplets behavior on an overheated substrate at about 150°C. The Leidenfrost phenomenon was clearly observed for the neutral and weakly charged conditions. However, the droplet rebound would disappear for multi-jet mode, and only very thin liquid film could be found. It is mainly attributed the small droplet size and high impact velocity, which makes the impact become very fast, and few charges will escape to the substrate.

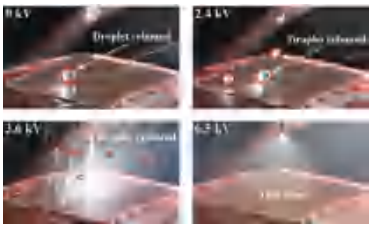


Figure 3-Dynamic behaviors of electrospray ethanol droplets on overheated substrate at 150℃

Droplet impact is the main heat transfer way for spray cooling. Owing to the applied electric field, the droplet impact dynamics of electrospray will differ from traditional spray cooling process. Fig. 4 compares the impact morphology of neural and charged droplets. The results showed that the charged droplet would have a bigger maximum spreading but a smaller maximum recoiling height. In other words, the spreading of impact droplet would be promoted whereas the recoiling would be suppressed for charged droplets. At present, this is primarily attributed to the surface tension weakening effects caused by the surface free charges. In addition, the correlations of the maximum spreading coefficient of charged droplets were established.

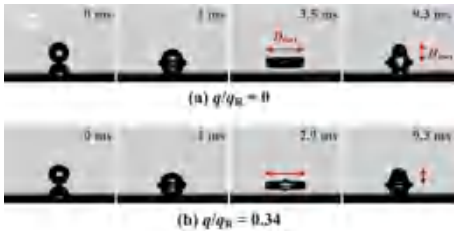


Figure 4- Snapshots of (a) neutral and (b) charged water droplets impact on substrate

Sessile droplet evaporation on hot substrate is crucial to the high heat flux of electrospray cooling in the single-phase region. Fig. 5 compared the life time of sessile droplet on the substrates with different conditions. It showed that both the increase in substrate temperature and electric field intensity would enhance the droplet evaporation of sessile droplets. Theoretically, this enhancement mechanism of non-uniform electric field on droplet evaporation was basically attributed to the combined effects of corona wind blowing, surface tension weakening, and molecular orienting.

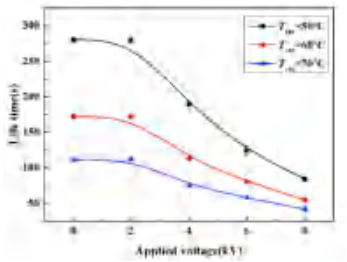


Figure 5- Sessile droplet life time with different substrate temperatures and applied voltages.

Conclusions

In summary, the impact dynamics and heat transfer of electrospray droplets were experimentally investigated in this work. It was expected to a better understanding of the electrospray cooling technique and demonstrate an efficient way for high heat flux dissipation.

Acknowledgements

This work was supported by a National Nature Science Foundation of China (51976084, 52036007).

References

[1] L Rayleigh, On the equilibrium of liquid conducting masses charged with electricity, Phil. Mag., 10 (1882) 184-186.

[2] J Wang, H Xu, Y Huo, Y Wang, M Dong, Progress of electrospray and electrospinning in energy applications, Nanotechnology, 31 (2019) 1-22.

[3] X Feng, J E Bryan, Application of electrohydrodynamic atomization to two-phase impingement heat transfer, J. Heat Transfer, 130 (2008) 750-755.

[4] W Deng, A Gomez, Electrospray cooling for microelectronics, Int. J. Heat Mass Transfer, 54 (2011) 2270-2275.

[5] U Ryu, S Y Lee, Maximum spreading of electrically charged droplets impacting on dielectric substrates, Int. J. Multiphase Flow, 35 (2009) 1-7.

Dynamics of Taylor bubble formation and evolution in a 100μm width microchannel with an acute symmetrical inlet geometry

Xiaozhe Sun
Beijing Jiaotong University, Beijing 100044, China

Abstract
In this study, through the visual experimental method, the formation and flow process of Taylor flow in in a 100μm width microchannel with an acute symmetrical inlet geometry are observed, and the changing rules of important parameters in the process of formation and flow are analyzed. The formation mechanism of Taylor bubble in micron channel is summarized.By analyzing the key factors such as bubble formation frequency, surface velocity and curvature of gas column neck, the typical shape of bubble formation and the changing trend of capillary number and Weber number are fitted.The above results provide a systematic study on the formation of Taylor bubbles in micron microchannels and provide ideas for the development and utilization of micron microchannel reactors.

Keywords: Taylor flow; Bubble formation and evolution; Microchannel; Pattern transitione

Introduction

Microreactor have attracted much attention in many fields because of its large specific surface area, high mass transfer efficiency, good safety performance and low energy consumption. In recent years, microreactor based on two-phase flow has been used in many fields such as chemistry, biology and pharmaceutical engineering. The study of two-phase flow in microchannel plays an important role in the development of microreactor. Among them, Taylor flow pattern has the advantages of high stability, good controllability and wide operation range, so it has become the most suitable flow pattern for microreactor operation. However, the evolution of gas-liquid two-phase flow patterns in microchannels remains to be studied. Especially in the microscale, the formation and mechanism of Taylor flow in the microchannel are not clear.

Methodology

The experimental system is divided into two parts, the working fluid supply part and the bubble test part. The working fluid supply part consists of two sets of microfluidic pumps, microfluidic flow monitors and microfluidic pressure sensors. Among them, the flow monitor and micro-flow pump can correct the action of liquid flow through communication feedback. The bubble test part consists of a microfluidic chip, a high-speed camera and a chip fixture. The main material of the chip device is silicon glass, which is made into the desired channel shape by photolithography and bonding. The cross section of the channel producing bubbles is a rectangle with a length of 47 μm and a width of 100 μm. When the gas channel converges with two symmetrically arranged liquid channels, the whole channel becomes the Taylor flow channel..

The gas phase is nitrogen (99.999%), and the gas source is a compressed gas cylinder. Ethanol aqueous solution was used as liquid phase. The pressure of gas and liquid is controlled by microfluidic pressure pump FLOW-EZ.At the same supply pressure, the gas is introduced into the main channel and the liquid is injected from both sides at an angle of 30°. After changing the new liquid flow rate (Q_L) and pressure (P_L) conditions, consider at least twice the residence time to achieve a stable gas-liquid two-phase flow.

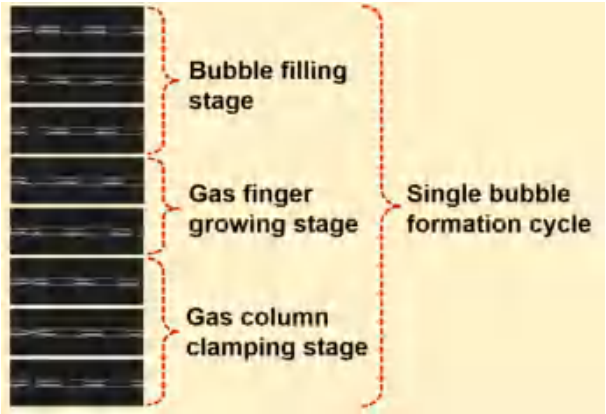


Figure 14 - Flow stage division diagram

Drag coefficient for micron-sized sphere particle in high-speed flow based on symbolic regression

Luxi Xu, Likun Ma, Pengnian Yang, Yifan Duan, Kangchun Zhao, Zhixun Xia, Yunchao Feng
Hypersonic Technology Laboratory (National University of Defense Technology, Changsha 410073, China)

Abstract
The drag force on small particles in high-speed flow is influenced by the combined effects of fluid viscosity, compressibility, and rarefaction. The existing drag coefficient models are still insufficient of accuracy and efficiency for gas-particle flow simulation. This study comprehensively considers these effects and conducts high-fidelity numerical simulations. A new drag coefficient model is generated using Symbolic regression (SR) method. The new drag coefficient possesses clear physical significance, high predictive accuracy, and low computational cost.

Keywords: PR-DNS, DSMC, Symbolic regression, Drag coefficient

Introduction

The interaction of micrometer-scale particles with high-speed flow is a common phenomenon in both industry and nature. To improve the accuracy and efficiency of existing drag models, new drag data using Particle-Resolved Direct Numerical Simulation (PR-DNS) and Direct Simulation Monte-Carlo (DSMC) method are added, then SR is performed on the new dataset to generate new analytical expressions for the drag coefficient. Methodology To consider conditions with no rarefaction, three-dimensional PR-DNS were conducted for a stationary particle in freestream by solving the compressible Navier-Stokes equations. For simulation in the slip regime, Maxwell slip boundary conditions were used. DSMC was used to get the drag force for transition flow. The open-source symbolic regression software PYSR was used to discover analytical relationship between input features and drag coefficient. 4 features were chosen as input:Ma_{p} , Re_{p} , Kn_{p} and drag coefficient $C_{\mathrm{d,in}}$ by Clift and Gauvin [1] for incompressible conditions. Results The new drag coefficient model for $0.3 \leq Ma_{\mathrm{p}} \leq 3.2$ by SR is shown as Figure 1. Table 1 shows that present model has improvements in accuracy at subsonic and transonic conditions, and low Re_{p} compared to the advanced empirical formulas [2]. In addition, the average calculation time for engineering simulation has been reduced by 15%.

- $0.3 \le Ma_p \le 3.2$ (Compressible)
  - $45 \le Re_p \le \min[Re_p, 10000]$

$$C_d = \begin{cases} 1.03 C_{d,in} + 0.35 Ma_p^4 & (0.3 \le Ma_p \le 0.8) \\ \tanh\left[Ma_p^2 \left(C_{d,in} + 0.45\right)\right] + \dfrac{C_{d,in}}{\log_{10} Re_p} & (0.8 < Ma_p \le 1.6) \\ 0.98 - 0.05 * \tanh\left(Ma_p - 2.5\right) + 0.9 \dfrac{C_{d,in}}{\log_{10} Re_p} & (1.6 < Ma_p \le 3.2) \end{cases}$$

  - $Re_p < 45$

$$C_d = C_{d,in} \exp\left\{\tanh\left[0.3 Ma_p \tanh\left(0.36 Ma_p - \log_{10} Re_p\right)\right]^2\right\}$$

Figure 1 – New drag coefficient model.

Table 1 - The relative errors for different models based on all available data.

	Loth [2]	Present
$Ma_p < 0.8$	8.9%	5.3%
$Ma_p = 0.8 \sim 1.2$	9.4%	6.4%
$Ma_p = 1.2 \sim 3.2$	6.4%	6.5%
$Re_p < 45$	7.7%	5.3%
$Re_p > 45$	7.5%	7.3%
All data	7.6%	6.1%

References

[1] R. Clift, W.H. Gauvin, Motion of entrained particles in gas streams, Can J Chem Eng 49 (1971) 439–448.

[2] E. Loth, J. Tyler Daspit et al, Supersonic and Hypersonic Drag Coefficients for a Sphere, AIAA Journal 59 (2021) 3261–3274.

Experimental and numerical investigations on the process of the gas-particle jet in supersonic crossflow

Likun Ma, Luxi Xu, Pengnian Yang, Yifan Duan, Kangchun Zhao, Zhixun Xia, Yunchao Feng
Hypersonic Technology Laboratory (National University of Defense Technology, Changsha 410073, China)

Abstract
The coupling process of gas-solid two-phase jet and supersonic crossflow in solid rocket scramjet is still lack of the accurate experimental and simulation research. To investigate the development and evolution of this process, experiments with plane laser scattering technology, particle image velocimetry technology (PIV) and large-eddy simulations (LES) based on the Eulerian– Lagrangian method have been adopted. Three kinds of macroscopic distribution phenomena of solid particle jet are found in experiments and particles also have a certain modulation effect on the jet flow field. Numerical simulations can well reproduce the characteristic phenomena observed experimentally.

Keywords: Solid rocket scramjet, Supersonic transverse jet, Gas-particle flow

Introduction

The development of solid rocket scramjet has received extensive attention. At present, the numerical simulation research in the coupling process of gas-solid two-phase jet has just started, while the experimental research has still not been publicly reported. To study the development and evolution of this process, experimental research and numerical simulations are conducted.

Methodology

The experiment was conducted on a supersonic gas-solid transverse jet experimental platform [1]. The air heater generated a supersonic inflow of Ma2.6, which interacted with the supersonic jet. The particles are silica with density of 2300 kg/m^3 and particle diameter is normal distribution of 1~100 μm. High speed shadow imaging technology, plane laser scattering technology, and particle image velocimetry technology are used. LES based on the Eulerian–Lagrangian two-way coupled method have been adopted. The specific parameter settings should be consistent with the experiment.

Conclusions

Three kinds of macroscopic distribution phenomena of solid particle jet are found in experiments as shown in Figure 1. In addition, particles also have a certain modulation effect on the jet flow field: increasing the bow shock angle, reducing the Mach disk height, and enhancing the flow field instability in the jet wake region. Numerical simulations can well reproduce the characteristic phenomena observed experimentally, and it is found that the backward dispersion of particles is caused by the downwash airflow on both sides of the jet port, and particles tend to accumulate in regions of low vorticity and high density.

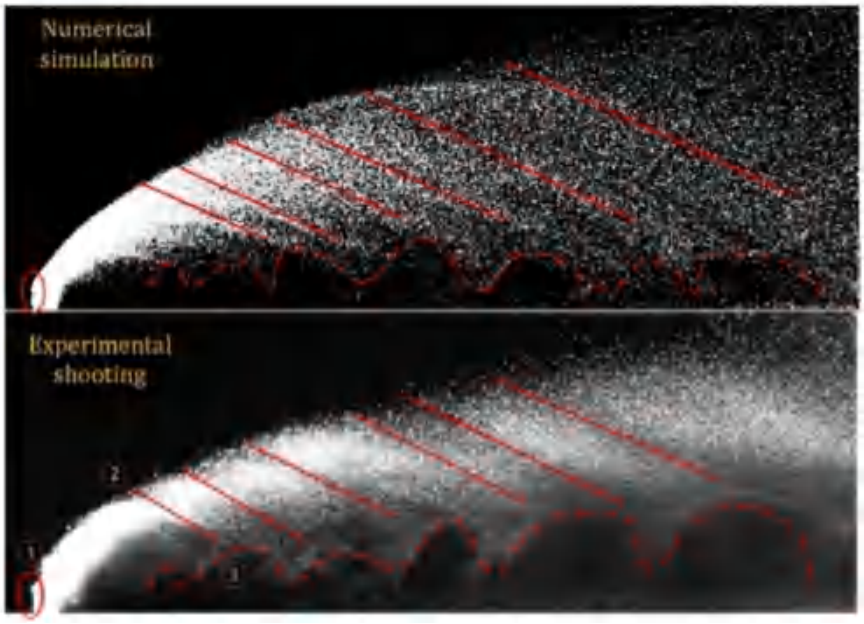


Figure 1 - Comparison of experimental and numerical simulation results on the central plane, ① particle jet fluctuation distribution structure, ② particle jet wire drawing distribution structure and ③ particle jet coherent distribution structure.

References

[1] Y. Duan, P. Yang, Z. Xia et al, Experimental Study of the Formation and Evolution of Gas Jets in Supersonic Combustion Chambers, Applied Sciences 13 (2023) 2202.

Numerical Simulation of Transient Heat Transfer within Rotating drum via Smoothed Particle Hydrodynamics

Liangrui Ding, Qijun Zheng, Zhenbo Tong.
Centre for Simulation and Modelling of Particulate Systems, Southeast University-Monash University Joint Research Institute, Suzhou, Jiangsu, PR China

Abstract
Rotating drums find extensive applications in industrial processes for the purpose of heating or cooling particulate materials, where the flow patterns of particles play a crucial role in influencing both the uniformity and efficiency of the heating process. In this study, the Smoothed Particle Hydrodynamics (SPH) approach is employed to model both the particle flow and the heat transfer between particles within rotary kilns. The results reveal that, while the temperature finally achieves homogeneity given sufficient time, the transient temperature increase exhibits significant non-uniformity, closely linked to the particle flow patterns, resulting in a low-temperature zone at the core. Validation efforts confirm that the SPH can be a dependable approach for predicting the temporal and spatial variations in temperature within the kiln, facilitating the optimization of heat transfer efficiency. Moreover, this study systematically assesses the impacts of rotating speed, filling level, thermal load, thermal conductivity, and internal friction of particles, offering valuable insights for optimizing industrial kilns.

Keywords: SPH, rotating drum, granular flow, granular heat transfer

Introduction

The rotating drum, a prevalent type of thermal processing equipment, employing in industries like cement, metallurgy, and chemical engineering for tasks such as mixing, drying, and conveying of the granular materials. Many researchers have focused on optimizing the heat transfer model of rotating drums, with particular emphasis on two crucial factors: the heat transfer coefficient and the effective heat transfer area. Some prior experimental investigations have elucidated that the heat transfer within the rotating drum is attributed to six mechanisms [1-3], as illustrated in Fig. 1.

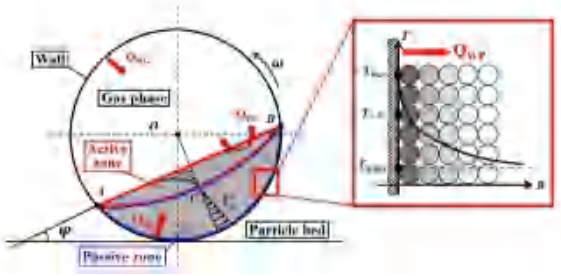


Figure 15 - Cross-sectional schematic of the rotary kiln during the rolling process.

In this study, the temperature range of the system is set between 25°C and 200°C, and the internal medium is set to be air. O'Brien et al. [4] proposed that if $\frac{K_s r\prime}{K_f r} \gg 1$, over 98% of the heat transfer in the system occurs through inter-particle and particle-wall conduction.

$$\frac{K_s r\prime}{K_f r} = \frac{36}{0.0257} = 1400.78 \qquad (1)$$

with the Eq. (1) satisfied, this study primarily focuses on the inter-particle conduction and the particle-wall conduction within the rotary kiln system.

In recent years, various theoretical methods such as FEM [5], CFD [6,7], and SPH [8,9] have been developed to optimize the design and operational parameters of rotating drums. These models consider the bulk of particles as continuum, utilizing governing equations and

constitutive relationships to depict the move-ment and dispersion of particles, without delving into the detailed motion of each particle as in DEM. These continuum modelling approaches are computationally less intensive and can be universally applied. In this study, Smoothed Particle Hydrodynamics (SPH) coupled with thermal analysis is employed to simulate the heat transfer within the recirculating particle bed. Furthermore, this study aims to validate the applicability of the SPH model and elucidate how the flow of particles influences the heat transfer efficiency in the rotating drum, offering valuable insights for industrial applications.

Methodology

SPH is a continuum-based method used in fluid dynamics to simulate fluid motion and deformation by dividing the fluid into "pseudo particles" and performing dynamic calculations on them [10-12]. It has also been widely used to simulate granular systems [13]. In fluid dynamics, three fundamental conservation equations are combined and smoothed by the meshless and adaptive nature of SPH. Recently it is also applied to simulate the particle flow in rotating drum. The kernel approximation uses weighting functions to discretize the governing equations in the following form [14]:

$$\boldsymbol{f(x')} = \sum_{j=1}^{N} \boldsymbol{f(x)\, W(x - x')} \qquad \textbf{(2)}$$

In SPH, the choice of the kernel function is the essential issue. In this research, since the granular material is subject to recirculating flows in rotary kilns, the kernel function and smoothing length could affect the accuracy of the convection modelling. Therefore, several forms of kernel functions are considered in the following simulation.

Additionally, the granular heat transfer model in the drum is generated from the energy equation, the differential equation of heat conduction is defined as:

$$\boldsymbol{\rho \frac{dE}{d\tau} = \frac{\partial q_j}{\partial x_j}} \qquad \textbf{(3)}$$

Quoting the Fourier's Law of the Heat Conduction:

$$\boldsymbol{q_j = -\lambda \frac{\partial T}{\partial x_j}} \qquad \textbf{(4)}$$

Substituting Eq. (3) into Eq. (4) results in:

$$\boldsymbol{\rho \frac{de}{d\tau} = \frac{\partial}{\partial x_j}\left(\lambda \frac{\partial T}{\partial x_j}\right)} \qquad \textbf{(5)}$$

where λ is the thermal conductivity of the particles. The vector form of Eq. (5) is the initial energy conservation equation, which forms the basis of the SPH solution. This simplified model is convenient for SPH calculation and suitable for cases where the particles are well mixed in this study.

In this work, Ls-Dyna in combination with HyperMesh has been used to construct and optimize the quasi-3D model of heat transfer in the rotary kiln. The SPH particles are generated using the "Solid center" method available in the SPH generation keyword, as illustrated in Fig. 2. In order to investigate the influencing factors of heat transfer inside the rotary kiln, the particle density, specific heat, Young's modulus, and Poisson's ratio are assumed to be constants, the detailed numerical values of which are listed in Table 1.

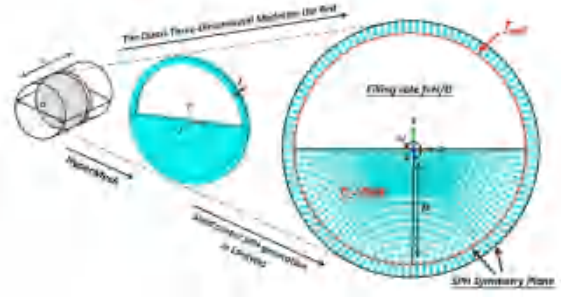


Figure 2 - Illustration of the SPH-based quasi-three-dimensional model of the rotary kiln and its associated geometric parameters.

Table 4 - Drum and material parameters used in the SPH simulations.

Parameters	**Baseline values**	**Variation ranges**
Diameter, D(m)	0.1	-
Thickness, l(m)	0.01	-
Filling level	25%	15%-50%
Rotating speed, ω(rpm)	5	1-20
Wall temperature, T_w(K)	398	323-473
Wall friction, f	0.3	-
Density, ρ(kg/m^3)	3800	-
Young's modulus, G(Pa)	107	-
Poisson's ratio, μ	0.3	-
Thermal conductivity, h(W/mK)	36	15-55
Internal friction angle, φ(degree)	30	15-60

Conclusions

In the rotating drum, the flow pattern of the particles has a significant effect on the efficiency of heat transfer in the whole system. In this work, Smoothed Particle Hydrodynamics (SPH) is used to investigate the internal temperature distribution and heat transfer/diffusion within the particle bed. The key factors affecting the particle flow and heat transfer are investigated. The main conclusions of this work are as follows:

(1) While the temperature within the particle bed eventually achieves homogeneity in rotary kilns over time, the transient temperature increases exhibit strong non-uniformity, particularly influenced by the particle flow pattern. A distinct low-temperature regime is observed at the core of the particle bed due to the recirculating motion of particles, notably pronounced in cases with a high filling level. This underscores the significance of particle flow in the heating process and efficiency, highlighting the need for numerical models like the presented SPH for optimizing heat transfer in rotary kilns.

(2) The SPH, based on the continuum description of flow and heat transfer without delving into microscopic particle details, proves computationally efficient for the large-scale equipment. The validation above demonstrates its reliability in predicting and visualizing the inner temperature distribution within the kiln, contingent upon the selection of appropriate kernel function and smoothing length in SPH.

(3) The increase in thermal conductivity between particles directly accelerates the heat transfer rate at the material property level, consequently enhancing the heat transfer coefficient of the entire system by a substantial 40.37%.

(4) The variation in the internal friction angle indirectly influences the heat transfer coefficient by affecting the flow patterns of the particle bed. The high values detrimentally impact heat transfer efficiency, necessitating appropriate reduction with an effect of 22.91%.

(5) The rotating speed of the kiln has a weak effect on heat transfer efficiency. Up to 5 rpm, increasing the speed improves heat transfer with a fluctuation effect of 8.55%. However, beyond this threshold, further increases in speed do not signific.

Acknowledgements
The authors are grateful to the National Key R&D Project of China (2021YFB1715500) for the financial support of this work.

References

[1] Monaghan, J. J. (1994). Simulating free surface flows with SPH. Journal of computational physics, 110(2), 399-406.
[2] R.W.O. O'Brien, G.K. Batchelor, Thermal or electrical conduction through granular material, Proceedings of the Royal Society of London 355 (1977) 313.
[3] Wes, G. W. J., Drinkenburg, A. A. H., & Stemerding, S. (1976). Heat transfer in a horizontal rotary drum reactor. Powder Technology, 13(2), 185-192.
[4] R.W.O. O'Brien, G.K. Batchelor, Thermal or electrical conduction through granular material, Proceedings of the Royal Society of London 355 (1977) 313.
[5] Yang, L. Y. M., Zheng, Q. J., Bai, L., & Yu, A. B. (2021). Continuum modelling of granular segregation by coupling flow rheology and transport equation. Powder Technology, 378, 371-387.
[6] Rong, WenjieFeng, YuqingSchwarz, PhilWitt, PeterLi, BaokuanSong, TaoZhou, Junwu. (2020). Numerical study of the solid flow behaviour in a rotating drum based on a multiphase cfd model accounting for solid frictional viscosity and wall friction. Powder Technology: An International Journal on the Science and Technology of Wet and Dry Particulate Systems, 361.
[7] Rong, W., Li, B., Feng, Y., Schwarz, P., Witt, P.J., & Qi, F. (2020). Numerical analysis of size-induced particle segregation in rotating drums based on Eulerian continuum approach. Powder Technology, 376, 80-92.
[8] Zhu, C., Peng, C., & Wu, W. (2023). Smoothed particle hydrodynamics modelling of particle-size segregation in granular flows. Journal of Fluid Mechanics, 977, A47. doi:10.1017/jfm.2023.995
[9] Zhu, C. W., Peng, C., & Wu, W. (2022). Lagrangian meshfree particle method (sph) based simulation for granular flow in a rotating drum with regularized μ(i) elastoplastic model. Powder Technology.
[10] R. A. Gingold, J. J. Monaghan, Smoothed particle hydrodynamics: theory and application to non-spherical stars, Monthly Notices of the Royal Astronomical Society, Volume 181, Issue 3, December 1977, Pages 375–389.
[11] Monaghan, & J., J. (1992). Smoothed particle hydrodynamics. Annual Review of Astronomy and Astrophysics, 30(1), 543-574.
[12] Lucy, L. B. (1977). A numerical approach to the testing of the fission hypothesis. The Astrophysical Journal, 8(12), 1013-1024.
[13] Fukagawa, R., Sako, K., Bui, H. H., & Wells, J. C. (2011). Slope stability analysis and discontinuous slope failure simulation by elasto-plastic smoothed particle hydrodynamics (sph). Géotechnique, 61(7), 565-574.
[14] Crespo, A. J. C., Gomez-Gesteira, M., & Dalrymple, R. A. (2008). Modeling dam break behavior over a wet bed by a sph technique. Journal of Waterway Port Coastal & Ocean Engineering, 134(6), 313-320.

Particle Shape-Induced Settling Segregation

Junjie Chen, Yi Liu, Yu Guo
Department of Engineering Mechanics, Zhejiang University, Hangzhou, 310027, China.
Corresponding email: yguo@zju.edu.cn

Abstract
A mixture of cylindrical particles, with different aspect ratios of length to diameter (λ = 0.1, 0.3, 0.5, 0.7, 1), falling in a viscous fluid is numerically investigated using a hybrid approach of Lattice Boltzmann Method (LBM) and Discrete Element Method (DEM) for the Direct Numerical Simulation (DNS). In the particle settling process, significant segregation occurs due to the difference in particle shapes, which leads to different particle settling velocities. The segregation is enhanced by increasing particle shape deference, while it is suppressed by reducing distances between the neighbouring particles (i.e. increasing local solid concentration). It is found that particle Reynolds number ($Re = U_t D_e/\nu$, U_t is the terminal settling velocity, D_e is the particle diameter of an equivalent sphere, and ν is the kinematic viscosity) has an impact on the segregation. The largest extent of segregation is observed at the intermediate Re, attributed to the combined effects of particle settling velocity and hydrodynamic particle-fluid-particle interaction.

Keywords: Sedimentation, Segregation, Particle shape, Coupled DEM-LBM, DNS

Introduction

The introduction describes the development and current situation of non-spherical solid particles in viscous fluid, encompassing various aspects such as the non-spherical particle sedimentation pattern, the behaviour of particle cloud and particle array, and segregation resulting from differences in particle shapes within fluidized beds.

Methodology

The hybrid LBM-DEM method for the particle-resolved DNS simulations of cylindrical particle falling in a viscous fluid is described in [1].

Model setup

As shown in Figure 1, the rectangular container is simulated by a computational domain 300 × 1200 × 600 lattice unit. At time t = 0, the fluid and particles are at rest. Double layers of vertically-arranged particles (2 × 2 × 4) with an given initial attack angle will settle under the gravity.

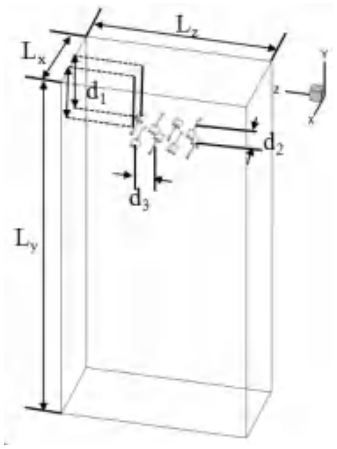


Figure 16 - A numerical model for sedimentation of double layers of particles

Results and discussion

The study examined the impact of packing density, initial attack angle, particle shape, and Reynolds number on segregation. SI is a sedimentation index used to describe the effect of segregation quantitatively. Y* normalized by De indicates the average settlement height of particle which settle faster. The variety of SI based on Y* in double layers of particles with various aspect ratio combinations (AR) is illustrated in Figure 2. Throughout the process, groups with larger differences in particle shapes demonstrated superior segregation effect.

The variety of SI based on Y* in double layers of particles at different Reynolds numbers is shown in Figure 3. Consider the range where Y* is greater than 40, the segregation effect of the disk mixture is the best at the intermediate Re.

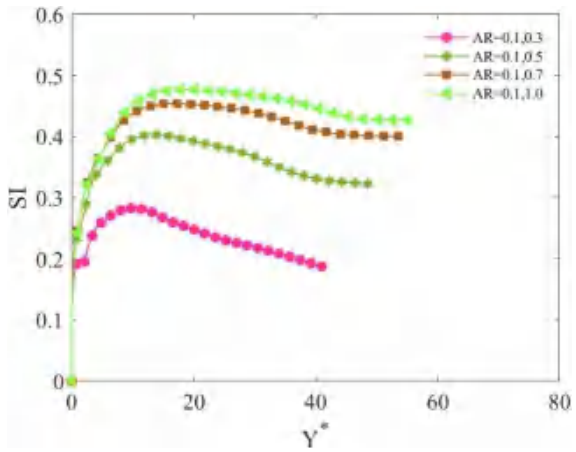


Figure 2 - The variety of SI based on Y* in single layers of particles

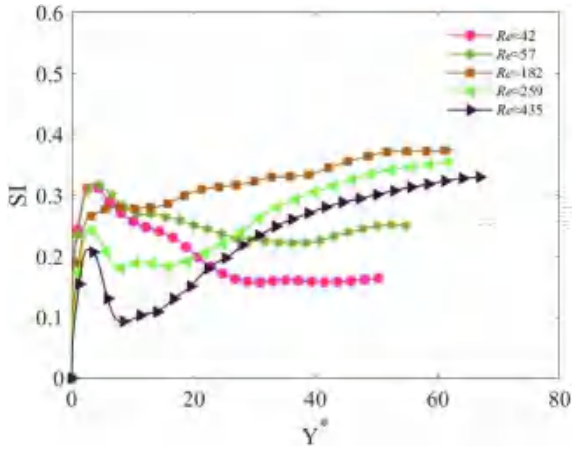


Figure 3 - The variety of SI based on Y* in double layers of particles

Conclusions

By performing numerical simulations, we have examined the settling segregation of regularly arranged particles with different shapes under a range of Reynolds numbers *Re*. When the Re is large, different types of particles form a more stable structure, suppressing the segregation. For the initial attack angles and packing densities considered, the largest degree of segregation occurs with the largest particle shape difference at an intermediate Re.

References

[1] Liu Y, Guo Y, Yang B, Pan D, Xia Z, Yu Z, Wang L-P. Three-dimensional sedimentation patterns of two interacting disks in a viscous fluid. Journal of Fluid Mechanics. 2023, 960, A25.

Effects of complex discrete particles on granular and multiphase flows

Yu Guo
Department of Engineering Mechanics, Zhejiang University, Hangzhou, 320027, China

Abstract
An enormous challenge in complex granular and multiphase flows involving particles is how to quantitatively describe the influences of particle properties on the macroscopic flow behaviours. In response to this challenge, we make an attempt to systematically investigate the effects of large deformation of particles, complex particle shape, and particle size and/or shape polydispersity. In this talk, I will present our recent progress in the following three aspects: the development of numerical methods, the understanding of interactive flow mechanism, and the establishment of rheological models for non-spherical rigid particles and flexible fibrous particles.

Keywords: Complex discrete particles, granular flow, fluid-particle interaction, non-spherical particles

Acknowledgements
The National Natural Science Foundation of China (12372250, 12132015 and 11972321) and Zhejiang Provincial Natural Science Foundation of China (Z24A020005) are acknowledged for the financial supports.

References
[1] Jiang, Y., Guo, Y., Yu, Z., Hua, X., Lin, J., Wassgren, C., & Curtis, J. Discrete element method–computational fluid dynamics analyses of flexible fibre fluidization. Journal of Fluid Mechanics 2021, 910, A8.
[2] Xu D, Wang B, Yu Z, Guo Y. Clustering in Gas-Fluidized Riser Flows of Flexible Fibers. AIChE Journal, 2023, e18024.
[3] Liu Yi; Guo Yu*; Yang Bo; Pan Dingyi; Xia Zhenhua; Yu Zhaosheng; Wang Lian-Ping*. Three-dimensional sedimentation patterns of two interacting disks in a viscous fluid. Journal of Fluid Mechanics. 2023, 960, A25.
[4] Jiahui Hao, Yu Guo*, Zhaosheng Yu, Jennifer S. Curtis. Pressure-controlled secondary flows and mixing in sheared Platonic solid-shaped particles. AIChE Journal 2023, 69(6), e18090.
[5] Jiahui Hao, Yu Guo*. Rheology of sheared polyhedral granular materials in inclined flows. Physics of Fluids 2023, 35, 103310.
[6] Yi Liu, Zhaosheng Yu, Kun Luo, and Yu Guo. Frictional granular flows of rod and disk mixtures with particle shape distributions. Physics of Fluids, 2021, 33: 093303.

Influence of Secondary Flow Induced by Riblets on the Particle Distribution and Transport in Wall Turbulence

Jianda Huang*, Chunxiao Xu*, Lihao Zhao*#
*AML, Department of Engineering Mechanics, Tsinghua University, 100084 Beijing, China
#Corresponding author, e-mail: zhaolihao@mail.tsinghua.edu.cn

Abstract Particle-laden wall-bounded turbulence is widely seen in both natural phenomena and industrial processes, such as the formation of sand ridges due to gravel settling in riverbeds and strip-shaped windbreak forests for sand control. Sand ridges and strip-shaped sand-control forests will induce secondary flows, but how do these formed secondary flows affect the distribution and transport of particles? We conducted a numerical study on the effect of the secondary flows induced by streamwise rectangular riblets in turbulent channel flow on the behavior of particles. Our findings indicate that when the spanwise periodicity of streamwise rectangular riblets remains constant, the intensity of the secondary flow initially decreases and then increases with the increasing riblet width. Meanwhile, the average secondary flow moves closer to the wall. Under the influence of the secondary flow, particles exhibit an uneven spanwise distribution and tend to accumulate at the corners of the riblets. The particle concentration is higher in the upwash regions of the secondary flow, whereas it is lower in the downwash regions. Additionally, increasing the riblet width also leads to a denser distribution of particles in the middle of the channel and enhances the streamwise transport velocity of the particles. When the riblet width exceeds a certain threshold, the streamwise velocity of particles exceeds that of particles over the smooth wall at the same Reynolds number. In summary, as the riblet width increases, the secondary flow moves closer to the wall, facilitating the entrainment of particles near the wall into bulk flow. Consequently, this results in an increase in particle distribution in the channel central region and an enhancement of the streamwise velocity of particles.
Key words: riblets channel flow, particle-laden flow, secondary flow

Research on Initial Stage Behavior of Liquid Film Formation during Bubble Collision using Direct Numerical Simulation

Weidong Yang [1,3-5], Tianshui Li [5], Yali Tang *[2,3], Pan He [5], Luyuan Chang [5], Qingkuan Liu [1,3-5], Niels G. Deen[2,3]

1. State Key Laboratory of Mechanical Behavior and System Safety of Traffic Engineering Structures, Shijiazhuang Tiedao University, Shijiazhuang 050043, China
2. Power and Flow Group, Department of Mechanical engineering, Eindhoven University of Technology, P.O. Box 513, 5600 MB, Eindhoven, The Netherlands
3. Eindhoven Institute for Renewable Energy Systems, Eindhoven University of Technology, P.O. Box 513, 5600 MB, Eindhoven, The Netherlands
4. Innovation Center for Wind Engineering and Wind Energy Technology of Hebei Province, Shijiazhuang 050043, China
5. School of Civil Engineering, Shijiazhuang Tiedao University, Shijiazhuang 050043, China
6.

Abstract: The liquid film behavior is of utmost importance in the bubble coalescence. However, the initial stage of bubble liquid film formation remains undetermined. In this paper, the hydrodynamic behavior of the liquid film is investigated through Direct Numerical Simulation involving a pair of colliding bubbles in the still water. A modified adaptive mesh refinement method is employed to obtain a detailed microscopic evolution of the liquid film during bubble collision, with a minimum mesh size of 20 nm. A detailed study was conducted on the state of the liquid film during its initial formation stage. A scientific criterion for determining the formation of the liquid film is developed by analyzing the variation of bubble interface curvature based on the data obtained from Direct Numerical Simulation. The initial affecting distance between bubbles and initial liquid film thickness were examined, and both were found to increase with an increase in bubble size and contact velocity. What is more, the mathematic models of initial affecting distance between bubbles and initial liquid film thickness in the water system are developed based on theory and DNS data.

Keywords: Liquid film, Direct Numerical Simulation, initial liquid film stage, liquid film thickness.

1. Introduction

Discrete bubbles can be observed in a wide range of natural environments [1] and industrial systems, occurring in applications such as chemical processes [2, 3], bio-chemical systems [4], nuclear reactors [5], mineral extraction [6], and metal fabrication [7, 8]. Dispersed flow is characterized by the presence of numerous small dispersed elements of one phase distributed within a continuous phase of another. Bubble coalescence is a complex dynamic phenomenon, and mechanism of coalescing process has not been fully understood. And the liquid film formed during bubble collision plays very important role for the collision result, (coalescence or bouncing off). However, the initial stage of bubble liquid film formation, which is crucial for understanding liquid film drainage process and constructing mathematical models pertaining to it, remains undetermined due to the extremely microscopic nature of the liquid film drainage process. Therefore, the investigation on the determination of liquid film formation during bubble collision is necessary.

When two bubbles come close to each other, a thin layer of liquid film forms between them due to the influence of surface tension. This liquid film impedes the ongoing approach of the bubbles, gradually diminishing their convergence speed. With the passage of time, the liquid inside the film gradually drains away, resulting in the film becoming progressively thinner. Once the thickness of the film reaches a critical point, it becomes unable to maintain its integrity and ruptures. At the instant of film rupture, the surfaces of the two bubbles come into contact and merge with each other. Gaining a comprehensive understanding of the morphological characteristics during the evolution process of liquid films is crucial for comprehending and effectively controlling the coalescence of bubbles. Over the course of several decades, extensive experimental and theoretical investigations have been carried out to gain insights into the process of thin-film drainage [9-11]. Zawala and Malysa [12] conducted a noteworthy experiment involving the collision of a rising bubble with a water surface, aiming to

examine the characteristics of the liquid film. The study revealed that higher impact velocities resulted in greater bubble deformation, increased liquid film radius, and prolonged contact duration. And the bubble coalescence was observed when the liquid film radius reached a threshold of less than 0.28 mm. Morokuma and Utaka [13] conducted a comprehensive study on the variation of liquid film thickness distribution between adjacent bubbles in water and ethanol. They employed laser extinction measurement apparatus and a twin bubble generation apparatus for their investigation. The results revealed that at low relative velocities, the minimum film thickness was observed at the center of the liquid film. However, as the relative velocity increased, this minimum film thickness shifted from the center towards the periphery of the film. Additionally, it was found that the rupture film thickness decreased with increasing relative velocity, ranging from approximately 0.20-2.50 μm for water and 0.10-1.00 μm for ethanol. Liu et al. [14] conducted a pioneering study, utilizing a developed dynamic force apparatus, to perform simultaneous measurements of the interaction force and spatial thin-film thickness. This investigation focused on the collision between a millimeter-sized bubble and surface micro-bubbles ranging in radii from 30 to 700 μm. The results obtained indicate that the scattering of experimental coalescence time between two rapidly colliding air bubbles is primarily influenced by the nonsymmetric drainage process, rather than the rupture thickness. Moreover, the findings reveal that smaller surface bubbles in the range of 30−100 μm exhibit a higher level of efficiency in attaching to a larger bubble. However, due to limitations in experimental techniques, it is difficult to measure the evolution of the liquid film during the process of bubble collision. However, the majority of these studies concentrate solely on the stable formation of the liquid film, without taking into account the timing or the initial thickness of the liquid film formation.

The investigation of film drainage model is a widely used theoretical approach to understanding bubble coalescence. As commonly acknowledged, the liquid film model determines the coalescence efficiency based on the contact time and the liquid film drainage time, which represents the duration in which the film between the bubbles gradually diminishes until it reaches a critical thickness [15, 16]. Film drainage can be categorized into various regimes based on the rigidity of bubble surfaces (nondeformable [17], deformable [18]) and the mobility of the contact interfaces (immobile [19], partially mobile [20], fully mobile [21-23]). Prince [21] proposed a liquid film drainage model involving several parameters about the liquid film, which is widely applied in the researches of bubbly flow. In this model, the value of initial liquid film thickness is assumed a constant value of 10^{-4} m, which may be different from the actual experiment process. However, few researches focus on the investigation about the initial stage of the liquid film formation, and there is no definitive conclusion regarding the exact thickness of the initial liquid film.

In this paper, the behavior of initial stage of liquid film between a pair of collision bubbles were investigated using Direct Numerical Simulation (DNS) based on the open source code Basilisk which employs the VOF approach. Moreover, the adaptive mesh refinement (AMR) technique embedded in this code, which is further enhanced with a customized refinement method based on Zhang's [24] methodology, makes it possible to properly capture the evolution of the liquid film formed between the two bubbles when they get very close to each other without the immediate coalescence. A scientific criterion for the formation of the initial liquid film was established, followed by a quantitative analysis of the initial thickness of the liquid film.

2. Methods

The VOF model is based on the principle that multiple phases do not interpenetrate. To incorporate each additional phase into the model, a volume fraction variable representing the phase's volume in the computational cell is introduced. In the absence of mass transfer, the continuity equation for the volume fraction of the k_{th} phase can be expressed as follows:

$$\frac{1}{\rho_k}\left[\frac{\partial}{\partial t}\left(\alpha_k\rho_k\right)+\nabla\times\left(\alpha_k\rho_k\boldsymbol{v}_k\right)\right]=0 \tag{1}$$

where ρ_k, α_k and $\boldsymbol{v}_k$ are the density, volume fraction and velocity of the k_{th} phase, respectively. The computation of the volume fraction for the primary phase among the n phases is determined by the following constraint:

$$\sum_{k=1}^{n}\alpha_k = 1 \tag{2}$$

The momentum equation that is applicable to all the phases can be described by:

$$\frac{\partial}{\partial t}(\rho \boldsymbol{v}) + \nabla\cdot(\rho \boldsymbol{v}\boldsymbol{v}) = -\nabla P + \nabla\cdot\left[\mu\left(\nabla \boldsymbol{v} + \nabla \boldsymbol{v}^T\right)\right] + \rho \boldsymbol{g} + \boldsymbol{F} \tag{3}$$

where $\boldsymbol{P}$, $\boldsymbol{g}$, and $\boldsymbol{F}$ are the pressure, gravitational acceleration, and external force, respectively. The physical properties, such as density (ρ) and viscosity (μ), are determined through volume-weighted averages. The volume fraction function is solved using the geometric reconstruction scheme, specifically the piecewise linear interface calculation (PLIC) method. The Continuum Surface Force (CSF) model, developed by Brackbill [26] and represented by Eq. (4), was utilized. In this model, surface tension introduces a source term in the momentum equation.

$$F = \sigma\kappa\delta\left(r - r_{\text{int}}\right)n$$
$$\kappa = \nabla\cdot n \tag{4}$$

where the symbol σ represents the coefficient of surface tension, κ denotes the radius of curvature, δ (r) represents the Dirac delta function, and n signifies the unit normal vector on the interface.

2.2 Adaptive mesh refine

In situations potentially leading to coalescence, one would ideally like to track numerically all steps of the drainage, until non-hydrodynamic effects such as the London–van der Waals force come into play and rupture the film. This typically occurs when the minimum gap between the two interfaces is of the order of 10 nm. Since typically bubbles have diameters in the order of 0.1-10 mm, there is a very large separation of scales. In order to get an affordable computational cost, an efficient mesh refine method is therefore necessary. Fig. 1 illustrates the method used to apply adaptive mesh refinement in this work. We focus on refining the cells of the liquid film and bubble interface. As shown in Fig. 1, if one liquid cell is between two bubble interfaces, it would be considered as a liquid film cell, and will be refined one level, *i.e.* it is split into 2×2 cells. In order to keep the total cell number low, while maintaining stability of the liquid film and the bubble interface close to the liquid film, we keep the grid level of the bubble interface one step smaller than that of liquid film. Simulating down to a minimal grid size of 10 nm as the theory would lead to excessive

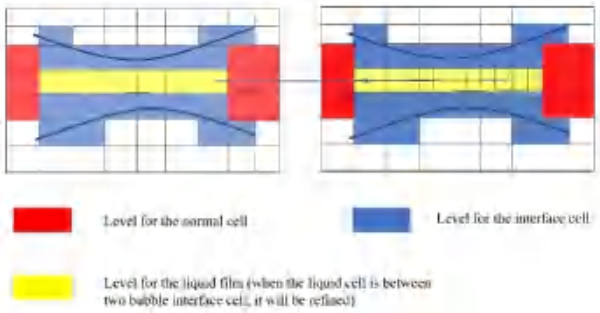


Fig. 1 Illustration of adaptive mesh refine. The black lines indicate the bubble interfaces.

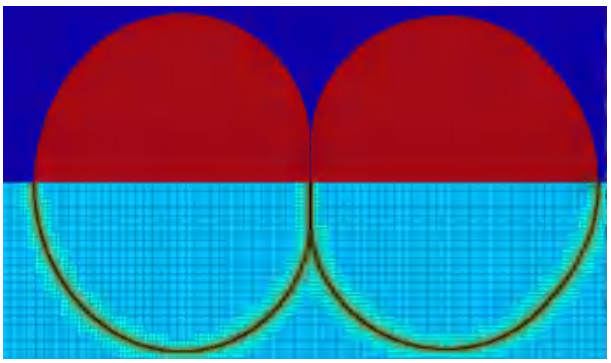


Fig. 2 A typical grid example with different size level

computational costs. Therefore, for two-dimensional simulations, a minimum grid size of liquid film cell with 20 nm is used. For example, for a bubble of d_{eq} = 1.5 mm, a coarse grid of 30 cells across the bubble diameter and using 18 levels of refinement, we obtain a finest grid of x=1.5/30·2^{18}=20 nm. Since our prime interest is in resolving the film dynamics, the grid size of the wake and other regions was set as relatively rough levels. This strategy greatly enhances the computational efficiency while guaranteeing a high numerical accuracy in flow regions where subtle physical phenomena are likely to take place. An example typical computational grid with different grid levels is shown in Fig. 2.

2.3 Numerical details

In this work, the minimal grid size is about 20 nm, and the minimum time step is about 1×10^{-10} s. We consider a collision between a rising bubble and fixed bubble in still water at home temperature (20 °C), which fits with the experiment conducted by Song [27] and Yang [28]. The bubble is free rising under gravity, mirroring the conditions observed in the actual study. The Direct Numerical Simulation was performed based on the open-source code Basilisk. The horizontal width of the tank was set to approximately 20 times the diameter of the bubble, as a result that the effect caused by the finite size of the domain can be considered negligible.

3. Result and discussion

3.1 Validation

Fig. 3 presents a comparison between the experimental results and DNS predictions. In order to validate the accuracy of the DNS predictions, the terminal rising velocity and aspect ratio of a signal bubble are compared across six different sizes using the experimental data. From the figure, it is evident that the DNS predictions closely align

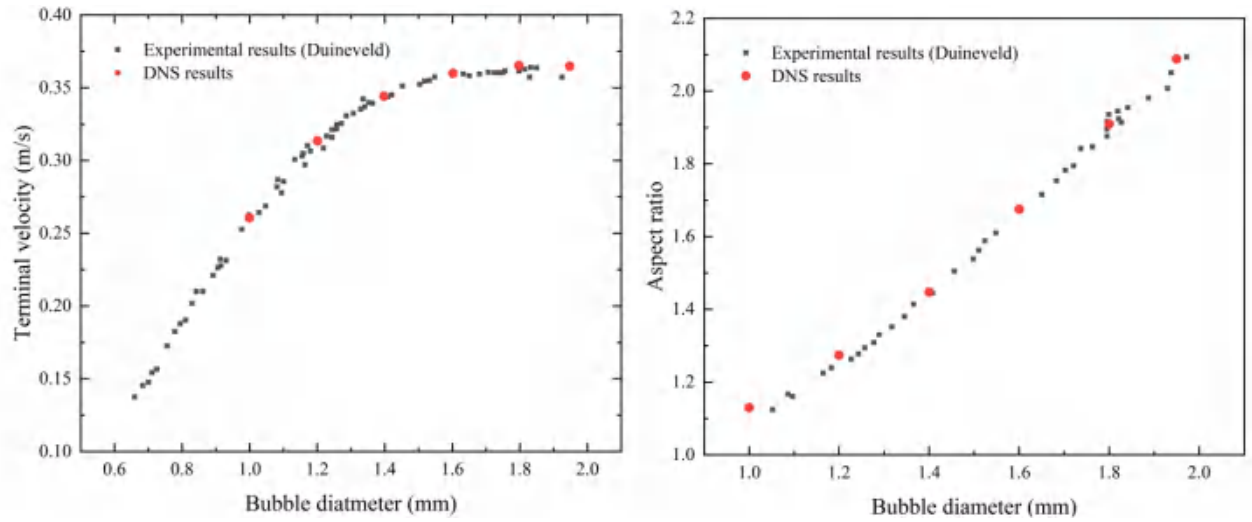


Fig. 3 Comparison about the bubble terminal velocity and aspect ratio between the experimental results and DNS predictions [29]

with the experimental results, indicating a good agreement between the two. The DNS prediction of the liquid film length is compared to the experimental results obtained from the collision between bubbles with an equivalent diameter of 1 mm conducted by Yang [28]. Observing the initial state of liquid film formation during the stage of stable bubble growth presents difficulties due to the limitations of high-speed camera technology and the absence of established criteria for identifying this phenomenon. As a result, it remains challenging to capture accurate observations of the liquid film's initial formation. Based on the figure, it is evident that the comparison reveals a remarkable level of agreement during the stage of stable bubble growth. This indicates a strong correlation between the DNS predictions and the experimental observations, highlighting the consistency between the two sets of data.

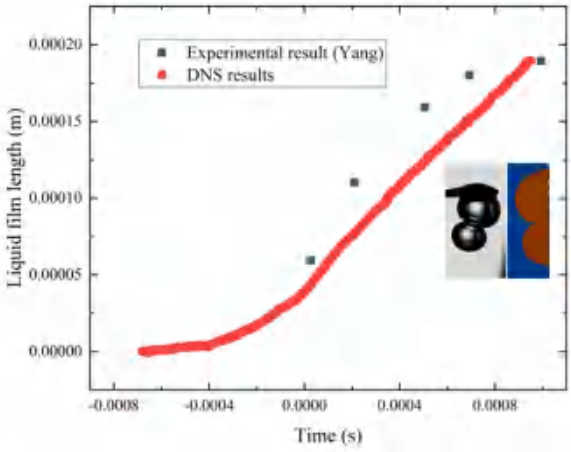


Fig. 4 Comparison about the liquid film length between the experimental results and DNS predictions[28]

3.2 Evolution of the liquid film

The evolution of the liquid film thickness between two bubbles with diameter of 1.5 mm along radius with two different contact velocities is present in Fig. 5. Fig. 5 (a) show the evolution of the liquid film thickness with a small contact velocity of 0.10 m/s, it can be found that the liquid film thickness increases along the radius and the minimal thickness in the center of the interface. As the collision progress going on, two bubble interfaces continuous approach, but the thinning rate of liquid film away from the center in greater than that of the center, and the obvious liquid film disk is formed gradually. Then, the liquid film breaks up near the center, with the result of bubble coalescence. The evolution of the liquid film thickness with a large contact velocity of 0.24 m/s is shown in Fig. 5 (b). At the early stage, the evolution of the liquid film thickness is similar with that of small contact velocity. Before 1.2 ms, there is a section of liquid film with similar thickness, meaning that liquid film flat appears. And the length of liquid film flat in this case is larger than that with small contact velocity. After 1.2 ms, the variation liquid film thickness near the center is very small, but minimal thickness of the liquid film continuous decreases, and the position of the thinnest liquid film gradually moves away from the center with time. From the figure, it can be seen that the thickness of the liquid film at the edge is much lower than the thickness in the middle at 1.8 ms. It means that the dimple between the two interfaces is formed, which has been predicted by the theory and observed in the experiment, which is considered the main reason to prevent the liquid film drainage and bubble coalescence in the case of large contact velocity.

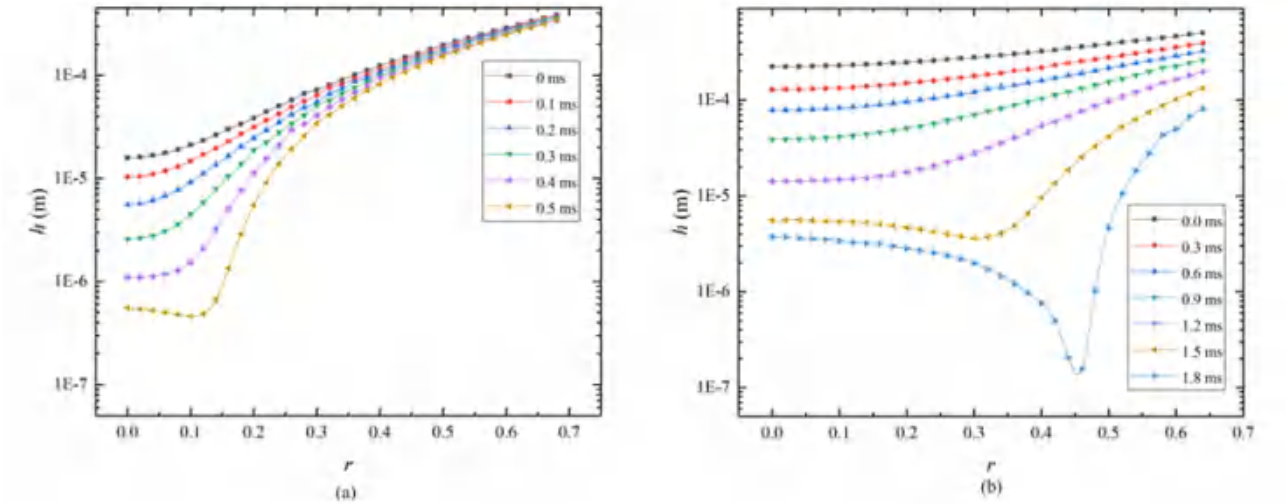


Fig. 5 Evolution of the liquid film thickness of bubbles with diameter of 1.5 mm. (a) 0.10m/s; (b) 0.24 m/s.

From the figure, it can also be observed that the concave of the dimple increases with time, which will be discussed in the following sections.

3.3 Determination of the initial formation of liquid film

For the investigation of the evolution of liquid film, the determination of the condition for the initial formation of liquid film is necessary. At present, there is no clear rule to definite the condition for the initial formation of liquid film. Some liquid film drainage mathematical models [21, 30] set up the initial liquid film thickness to be 10^{-4} m with the assumption that the liquid film disk has been formed. But, for some cases, the bubble interfaces have no obvious deformation i.e. that liquid film disk has not been formed when the gap between bubble interfaces is 10^{-4} m. Some experimental studies [27, 28] about bubble collision assume the initial formation of liquid film with the condition that bubbles are macroscopically close enough. Therefore, it is necessary to determine a more scientific condition for the initial formation of liquid film according to the DNS results. In this work, we definite the condition for the initial formation of liquid film

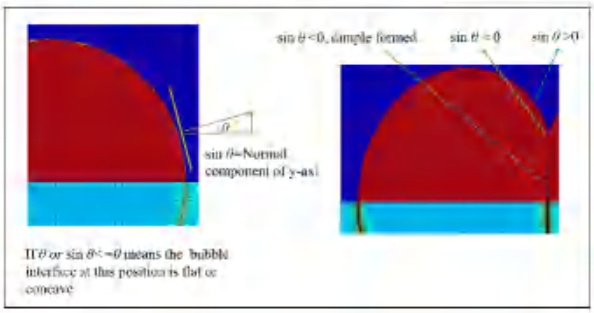


Fig. 6 Illustration of determination for the liquid film morphology

following two basic principles: the gap between two bubble interfaces is close enough; there is significant deformation of the bubble to ensure that the liquid film disk has been formed. For the two-dimensional x-axis symmetry simulation, if the angle θ between the normal vector and the x-direction at one position in the bubble interface is less than or equal to 0 means that the bubble interface at this position is flat or concave, as shown in Fig. 6. If the bubble interface begins to deform due to collision, the point at the low position changes first. So, we first analyze several low position points. The sensitivity of sinθ at the lower position of the bubble interface to the grid size was tested, and the results shows that sinθ at the position near to the x-axis is sensitive to the grid level. The point at the position of 1/30th radius is low enough and is not sensitive to the grid level, so we determine the initial formation of liquid film by the analysis of point at bubble will slowly deform with the time during the rising process due to the drag force. So, it means that two bubbles do not affect each other before t_1. The sharply deceasing of sinθ after t_1 means bubbles start to affect each other at the moment of t_1. From

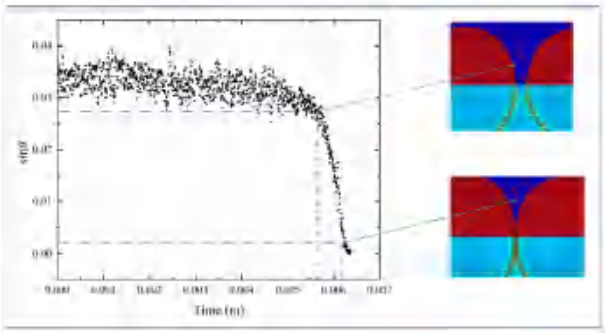


Fig. 7 Variation of sin at position of 1/30th radius with time

the figure, it can be found that the sinθ still much bigger than 0 and there is still an obvious distance between the bubble interface without the formation of liquid film disk at the moment of t_1. Therefore, we can say that t_1 is the moment that the bubbles start to affect with each other but not that of the initial formation of liquid film. We set the moment when sinθ begins to be close to 0 as t_2. which means the liquid film disk formed. So it is reasonable to consider t_2 is the be beginning of the liquid film formation.

From above analysis, it can be found that both initial moments that two bubbles affect each other and the liquid film forms are interesting. Fig. 8 is the variation of minimal distance between bubble interfaces with contact velocity at the moment of t_1 and t_2. It can be found that the distance between bubble interfaces at the moment of t_1 increases with the contact velocity. It is about 0.028 mm with the contact velocity of 0.1 m/s and increases to 0.23 mm as the contact velocity is 0.26 m/s. Because the extend range and velocity value of flow filed in front of the bubble interface driven by the movement of the bubble increases with the bubble rising velocity. It can be also found that the minimal distance between bubble interfaces at the moment of t_2, *i.e.* the initial liquid film thickness, is smaller than that at the moment of t_1, but with the same variation trend with contact velocities. It is 0.0035 mm with the contact velocity of 0.1 m/s, and is 0.048 mm with the contact velocity of 0.26 m/s. It is much smaller than the assumed constant value of 0.1 mm by [21]. The drainage time calculated by film drainage model $t_{\mathrm{dra}} = \sqrt{\frac{d\rho_l}{128}} \ln\left(\frac{\theta_0}{\theta_{\mathrm{bre}}}\right)$ proposed by Prince with various initial liquid film thickness is constant, which is different with the experimental results. But the

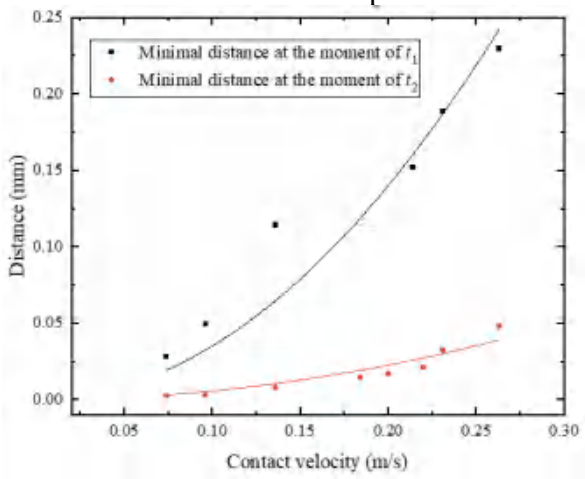


Fig. 8 Variation of minimal distance between bubble interfaces with contact velocity at the moment of t_1 and t_2

drainage time calculated by the initial thickness determined by DNS results increases with initial liquid film thickness, fitting well with the general trend of liquid film drainage time observed by experiment, although it larger than the experimental results with the reason that we have not modified the liquid film diameter in the model.

3.4 Analysis of initial affect liquid film

Fig. 9 presents the comparison of the initial effect distance with various contact velocities between different size bubbles. From the figure, we can find that the all the initial affecting distances of different bubble size increase with the contact velocity. The reason has been mentioned in the preceding paragraph. As shown in Fig. 9, there is a larger initial affecting distance with the larger bubble size. And the difference in the initial effect distance between various bubble size increases with the contact velocity. The DNS results indicate that the moment of t_1 is the time when the flow field boundary caused by bubble motion contacts the fixed bubble interface. The kinetic energy associated with bubble motion is responsible for the extend range flow filed in front of the bubble interface and the deformation of bubbles, and the kinetic energy E associated with bubble motion is calculated as:

$$E = \frac{1}{2} C_{\mathrm{m}} m_{\mathrm{b}} u^2 = \frac{2}{3} \pi C_{\mathrm{m}} \rho r^3 u_{\mathrm{b}}{}^2 \tag{5}$$

where E presents the kinetic energy associated with bubble motion, C_{m} is the added mass

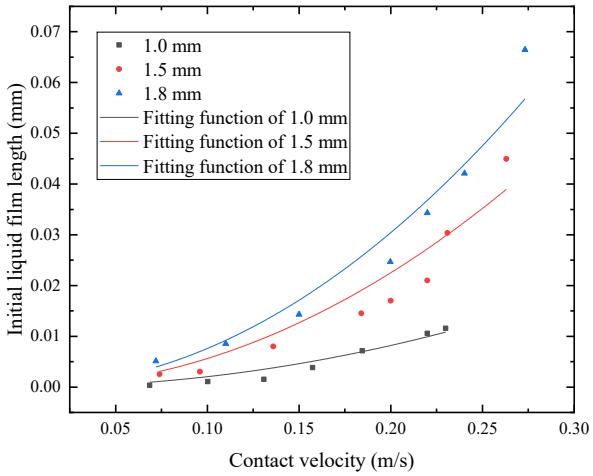


Fig. 9 Comparison of initial liquid film thickness with contact velocity between different size bubbles

coefficient, ρ is the liquid density, r presents the bubble radius, u_b is the velocity of the rising bubble. Therefore, it can be considered that the kinetic energy associated with bubble motion is directly related to the initial effect distance. The kinetic energy equation indicates that the larger bubble size means, the lager kinetic energy at the same velocity, meaning the larger flow filed in front of the bubble interface. This is why there is a larger initial effect distance with the larger bubble size. From the equation, it is reasonable to consider that the initial liquid film thickness is proportional to the square of the contact velocity. So, firstly, it can be assumed that the initial effect distance fit a function of square of the contact velocity as follows:

$$h_1 = A_1 u^2 \tag{6}$$

where h_1 is the initial affecting distance, A_1 is the fitting coefficient, u is the bubble contact velocity. Fig. 9 displays the fitting function of Eq. (6), which fits well with the DNS results. From the fit function, it can be found that A_1 various with the bubble size, which can get the reason from Eq. (5). The kinetic energy equation also reveals that, in the water system, A_1 is positively correlated with cubic power of bubble diameter. So, next, we can assume A_1 calculated as:

$$A_1 = B_1 d^3 \tag{7}$$

where B_1 is the fitting coefficient, d is the bubble diameter.

Fig. 10 presents the curve of the fitting function of A_1 based five bubble sizes, which is good agreement with the DNS results. The value of fitting coefficient B obtained by fitting is 1.03×10^6. Hence, the initial affecting distance in the water system can be calculated as:

$$h_1 = 1.03\times10^6 d^3 u^2 \tag{8}$$

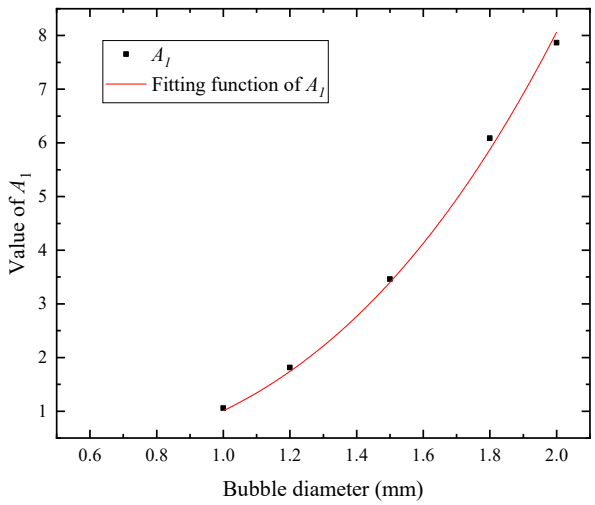


Fig. 10 Fitting function of A_1 with bubble diameter

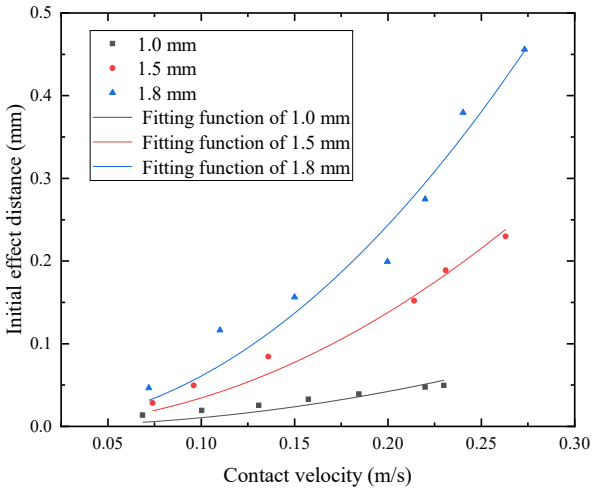


Fig. 11 Comparison of initial liquid film thickness with contact velocity between different size bubbles

3.5 Analysis of initial liquid film thickness

Fig. 11 shows the comparison of initial liquid film thickness with contact time between different bubble sizes. From the figure, it can be found that the various tend of initial liquid film thickness with contact velocity is same with the initial affecting distance. So we also firstly assume that the initial liquid film thickness is positively correlated with square of contact velocity, described as follows:

$$h_2 = A_2 u^2 \tag{9}$$

where h_2 is the initial liquid film thickness, A_2 is the fitting coefficient, u is the bubble contact velocity. The fitting function, present in Fig. 11, shows a good agreement with the DNS results, which indicates the assumption about the contact velocity for the fitting function is also suit for that of the initial liquid film thickness. Same with the initial effect distance, A_2 is assumed to be calculated as:

$$A_2 = B_2 d^3 \tag{10}$$

where B_2 is the fitting coefficient, d is the bubble diameter.

The comparison of DNS results and the fitting function of $A_2 = B_2 d^3$ is present in Fig. 12. It can be seen that there is a significant error for the fitting function that the fitting results are sensitive to the bubble size compared to the DNS results. The initial liquid film thickness is much smaller than the initial affect distance, which means that the initial liquid film thickness is not only affected by the flow field range caused by bubble motion, which is different from the initial affecting distance. During the movement of bubble from moment of t_1 to t_2, two bubbles constantly approach each other, and the bubble liquid film

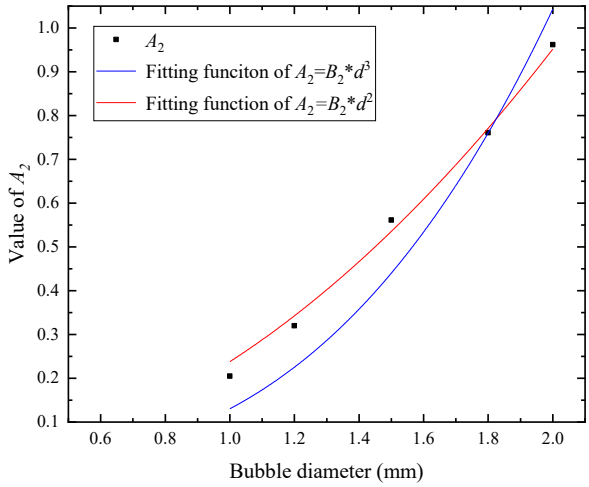


Fig. 12 Fitting function of A_2 with bubble diameter

plane is formed at the moment of t_2 with obvious deformation of the bubble interface, meaning that part of kinetic energy associate with bubble motion transfers into surface potential energy. So the initial liquid film thickness is not only related to the flow field range, but also involves energy conversion. This is why there is a significant error for the fitting function based on the assumption about the kinetic energy. From the comparison of DNS results and the fitting function, it can be found that the fitting results is sensitive to the bubble size, so we refit the results by reducing the power of bubble size. Through refitting, it was found that the fitting function of $A_2 = B_2 d^2$ is in good agreement with the DNS results, as shown in Fig. 12, with the value of fitting coefficient B_2 of 2.38×10^2. So, in the water system, the initial liquid film thickness can be calculated as:

$$h_2 = 2.38\times10^2 d^2 u^2 \tag{11}$$

4. Conclusions

The initial stage behavior of liquid film formation was investigated by conducting Direct Numerical Simulation, which involves studying a pair of colliding bubbles in a quiescent water. A minimum mesh size of 20 nm is realized with the help of the modified adaptive mesh refinement method to accurately capture the authentic evolution process of the liquid film, while ensuring that immediate rupture is avoided. Numerical simulations were performed on multiple sets of varying collision velocities and bubble sizes. A scientific criterion is developed to accurately determine the formation of the liquid film, utilizing data obtained from Direct Numerical Simulation. The initial affect thickness and the initial liquid film thickness were analyzed quantitatively. The following conclusions can be derived:

(1) The DNS results demonstrate that no dimple is formed at low contact velocities, while a dimple appears at high contact velocities, which agree well with theory and the experimental results.

(2) A scientific criterion is developed based on the curvature changes at the interfaces of the bubbles. The initial affecting thickness is larger than the initial liquid film thickness, ranging from an order of magnitude from 10^{-6} m to 10^{-4} m.

(3) Both of the initial affecting thickness and the initial liquid film thickness show an increasing trend with the contact velocity and bubble size. Addition, the predict models for initial affecting thickness and liquid film thickness were developed in the water system, calculated respectively as: $h_1 = 1.03\times10^6 d^3 u^2$ and $h_2 = 2.38\times10^2 d^2 u^2$.

Acknowledgements: This work was financially supported by Funded by Science and Technology Project of Hebei Education Department (Grant No. QN2023093), Innovation research group project of Natural Science Foundation of Hebei Province of China (E2022210078), Central Leading Local Science and Technology Development Fund Project (Grant No. 236Z5410G) and High-end Talents Project of Hebei Province of China (Grant No. [2019] 63).

References

[1] M.K. Tripathi, K.C. Sahu, R. Govindarajan, Dynamics of an initially spherical bubble rising in quiescent liquid, Nature Communications, 6 (2015).

[2] A.R. Sarhan, J. Naser, G. Brooks, Effects of particle size and concentration on bubble coalescence and froth formation in a slurry bubble column, Particuology, 36 (2018) 82-95.

[3] Y. Zhang, W. Ren, P. Li, X. Zhang, X. Lu, Flow regimes and characteristics of dense particulate flows with coarse particles in inclined pipe, Powder Technology, 428 (2023) 118859.

[4] G. Ely, T. Woodman, R. Roberts, E. Jones, T. Wedatilake, P. Sanders, N. Peirce, The impact of living in a bio-secure bubble on mental health: An examination in elite cricket, Psychology of Sport and Exercise, 68 (2023) 102447.

[5] M.V. Tabib, S.A. Roy, J.B. Joshi, CFD simulation of bubble column-An analysis of interphase forces and turbulence models, Chemical Engineering Journal, 139 (2008) 589-614.

[6] A.R. Sarhan, J. Naser, G. Brooks, CFD simulation on influence of suspended solid particles on bubbles' coalescence rate in flotation cell, International Journal of Mineral Processing, 146 (2016) 54-64.

[7] W. Yang, Z. Luo, Y. Gu, Z. Liu, Z. Zou, Simulation of bubbles behavior in steel continuous casting mold using an Euler-Lagrange framework with modified bubble coalescence and breakup models, Powder Technology, 361 (2020) 769-781.
[8] W. Yang, Z. Luo, Z. Zou, C. Zhao, Y. You, Modelling and analysis of bubble entrapment by solidification shell in steel continuous casting considering bubble interaction with a coupled CFD-DBM approach, Powder Technology, 390 (2021) 387-400.
[9] X. Zhang, R. Manica, P. Tchoukov, Q. Liu, Z. Xu, Effect of approach velocity on thin liquid film drainage between an air bubble and a flat solid surface, The Journal of Physical Chemistry C, 121 (2017) 5573-5584.
[10] T.S. Emery, S.G. Kandlikar, Modeling bubble collisions at liquid? Liquid and compound interfaces, Langmuir, 35 (2019) 8294-8307.
[11] S.I. Karakashev, E.D. Manev, Hydrodynamics of thin liquid films: Retrospective and perspectives, Adv Colloid Interface Sci, 222 (2015) 398-412.
[12] J. Zawala, K. Malysa, Influence of the impact velocity and size of the film formed on bubble coalescence time at water surface, Langmuir, 27 (2011) 2250-2257.
[13] T. Morokuma, Y. Utaka, Variation of the liquid film thickness distribution between contacting twin air bubbles during the coalescence process in water and ethanol pools, International Journal of Heat and Mass Transfer, 98 (2016) 96-107.
[14] B. Liu, R. Manica, X. Zhang, A. Bussonniere, Z. Xu, G. Xie, Q. Liu, Dynamic interaction between a millimeter-sized bubble and surface microbubbles in water, Langmuir, 34 (2018) 11667-11675.
[15] Y. Liao, D. Lucas, A literature review on mechanisms and models for the coalescence process of fluid particles, Chemical Engineering Science, 65 (2010) 2851-2864.
[16] S.L. Ross, Measurements and models of the dispersed phase mixing process, University of Michigan1971.
[17] A.K. Chesters, Modelling of coalescence processes in fluid-liquid dispersions: a review of current understanding, Chemical Engineering Research and Design, 69 (1991) 259-270.
[18] C. Coulaloglou, L.L. Tavlarides, Description of interaction processes in agitated liquid-liquid dispersions, Chemical Engineering Science, 32 (1977) 1289-1297.
[19] G. MacKay, S. Mason, The gravity approach and coalescence of fluid drops at liquid interfaces, The Canadian Journal of Chemical Engineering, 41 (1963) 203-212.
[20] C. Tsouris, L. Tavlarides, Breakage and coalescence models for drops in turbulent dispersions, Aiche J, 40 (1994) 395-406.
[21] M.J. Prince, H.W. Blanch, Bubble coalescence and break-up in air-sparged bubble columns, Aiche J, 36 (1990) 1485-1499.
[22] T.O. Oolman, H.W. Blanch, Bubble coalescence in stagnant liquids, Chemical Engineering Communications, 43 (1986) 237-261.
[23] A. Hasseine, A.H. Meniai, M.B. Lehocine, H.J. Bart, Assessment of drop coalescence and breakup for stirred extraction columns, Chemical Engineering & Technology: Industrial Chemistry-Plant Equipment-Process Engineering-Biotechnology, 28 (2005) 552-560.
[24] J. Zhang, M.-J. Ni, J. Magnaudet, Three-dimensional dynamics of a pair of deformable bubbles rising initially in line. Part 1. Moderately inertial regimes, Journal of Fluid Mechanics, 920 (2021).
[25] C.W. Hirt, B.D. Nichols, Volume of fluid (VOF) method for the dynamics of free boundaries, Journal of Computational Physics, 39 (1981) 201-225.
[26] J.U. Brackbill, D.B. Kothe, C. Zemach, A continuum method for modeling surface tension, Journal of Computational Physics, 100 (1992) 335-354.
[27] R. Song, L. Han, L. Zhang, S. Tang, Experiments and modeling of bubbles colliding head-on in water, Aiche J, 67 (2021).
[28] W. Yang, Z. Luo, Q. Lai, Z. Zou, Study on bubble coalescence and bouncing behaviors upon off-center collision in quiescent water, Experimental Thermal and Fluid Science, 104 (2019) 199-208.

[29] P.C. Duineveld, The rise velocity and shape of bubbles in pure water at high Reynolds number, Journal of Fluid Mechanics, 292 (2006) 325-332.
[30] D. Jain, J.A.M. Kuipers, N.G. Deen, Numerical study of coalescence and breakup in a bubble column using a hybrid volume of fluid and discrete bubble model approach, Chemical Engineering Science, 119 (2014) 134-146.
Note: Intention to submit to the journals of *Petroleum Science* and *Particuology.*

Effect of fluid-inertial torque on the orientation of tiny spheroidal particles in turbulent channel flow

Zhiwen Cui, Jingran Qiu, Xinyu Jiang, Lihao Zhao
Tsinghua University, Beijing, China

Abstract

The orientation of tiny spheroidal particles by considering both fluid-inertial torque and Jeffery torque in turbulent channel flow is employed. The findings reveal that the orientation of tiny spheroidal particles is significantly affected by the fluid-inertial torque when the Stokes number (normalized by viscous time scale) is greater than a critical value $Stc \approx 2$, suggesting that the inertial torque is non-trivial for most particle cases considered in earlier studies.

Keywords: Fluid inertial torque, wall turbulence, spheroidal particles

Introduction

The orientation of non-spherical particles in a fluid flow depends on the hydrodynamic torque they experience. However, little is known about the effect of fluid-inertial torque on the dynamics of tiny inertial spheroids in wall turbulence, as only Jeffery torque has been considered in previous studies. In this study, we investigate the orientational dynamics of inertial spheroids in turbulent channel flow by considering fluid-inertial torque.

Methodology

We performed direct numerical simulations of spheroidal particles in a turbulent channel flow by the Eulerian-Lagrangian method. The carrier fluid is computed in the Eulerian frame, and the flow is incompressible and isothermal, and governed by the Navier-Stokes equation and continuity equation. While the particle motions are computed by Lagrangian particle tracking method. In this work, the fluid-inertial torque [1] exerted on the spheroid is

$$\boldsymbol{T_I} = -\rho_F |\boldsymbol{u_s}|^2 \tilde{a}^3 F_\lambda \left(\frac{\boldsymbol{u_s}}{|\boldsymbol{u_s}|} \cdot \boldsymbol{n}\right)\left(\frac{\boldsymbol{u_s}}{|\boldsymbol{u_s}|} \times \boldsymbol{n}\right), \quad (1)$$

Here, λ is the aspect ratio of the spheroid, a is the equatorial radius, $\boldsymbol{u}_s$ is the slip velocity between fluid velocity and particle velocity, and $\boldsymbol{n}$ is the direction of the symmetry axis.

To estimate the relative strengths of the fluid inertial torque and Jeffery torque, a dimensionless parameter $\mathfrak{R}$ is introduced by:

$$\mathfrak{R} = \frac{\langle|\boldsymbol{u}-\boldsymbol{v}|\rangle^2}{\nu\langle|\boldsymbol{\Omega}-\boldsymbol{\omega}|\rangle}, \quad (2)$$

where $\boldsymbol{u}$ is the fluid velocity, $\boldsymbol{\Omega}$ is the angular velocity of the fluid, $\boldsymbol{v}$ is the particle velocity and $\boldsymbol{\omega}$ is the particle angular velocity. As $\mathfrak{R} \gg 1$, the fluid inertial torque dominates while the fluid inertial torque is negligible when $\mathfrak{R} \ll 1$. Figure 1 shows that in the turbulent channel flow the effect of the fluid inertial torque on inertial spheroids cannot be ignored when $St \gg 2$.

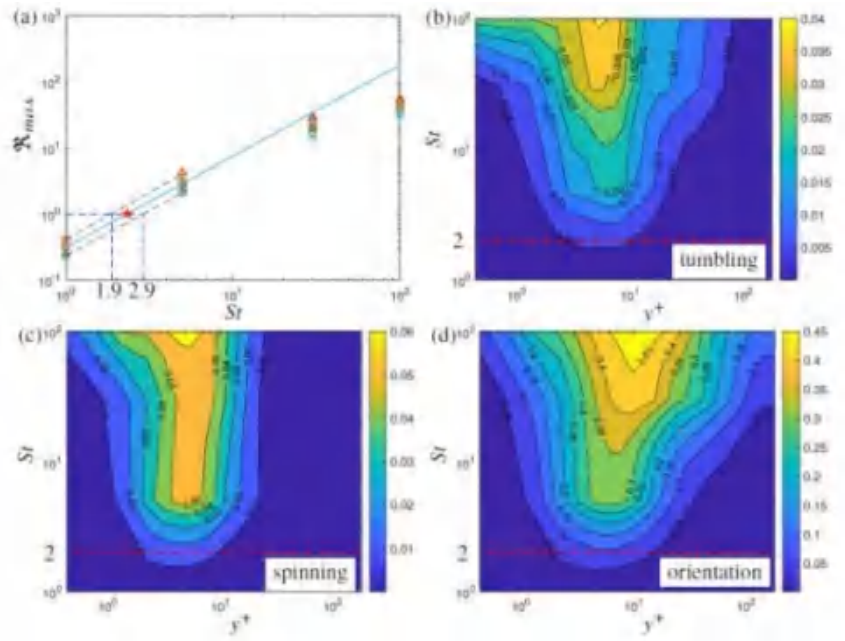


Figure 1 – (a) $\Re$ versus Stokes number. (b-d) Deviations of particle rotations and orientations compared to the results without fluid inertial torque.

Conclusions

In contrast to the earlier findings considering only Jeffery torque, we reveal that the slip-induced fluid inertial torque significantly affects the orientational dynamics of particles over a wide range of Stokes numbers. Notably, the region where the fluid inertial torque is non-negligible is almost throughout the entire channel.

References

[1] V. Dabade, N. K. Marath, G. Subramanian. Effects of inertia and viscoelasticity on sedimenting anisotropic particles. J. Fluid Mech. 778(2015) 133–188.

Particle transport in turbulent square duct flows with a free surface

Yanzhi Wang1 , Wenli Ma1 , Lee F. Mortimer2 , Michael Fairweather2 , Jun Yao3
1 School of Petroleum Engineering and Environmental Engineering, Yan'an University, Yan'an, 716000, China
2 School of Chemical and Process Engineering, University of Leeds, Leeds, LS2 9JT, UK
3 College of Mechanical and Transportation Engineering, China University of Petroleum-Beijing, Beijing 102249, China

Abstract
Direct numerical simulation combined with a one-way coupled Lagrangian particle tracking technique is employed to investigate dilute particle-laden turbulent flows in open square ducts with a free surface. The focus is on examining the influence of the mean cross-stream secondary flow on particle transport near the wall, free surface, and across the duct cross section. Based on the duct half-width and mean friction velocity, a shear Reynolds number of $Re\tau = 300$ is considered, with the corresponding particle Stokes numbers ranging from $St^+ = 0.31$ to 260. The results reveal that particle concentration near the sidewalls is lower than that near the bottom wall, and the minimum particle concentration is observed at the free surface. Along the bottom wall centerline orientated upwards, particle concentration gradually decreases. An exception to this is in the vicinity of the free surface where a slight increase is observed for the heavier particles ($St^+ \geq 25$), and the amplitude of this increase gradually declines as the Stokes number increases. In the streamwise direction near the free surface, heavier particles tend to preferentially concentrate in regions where the instantaneous transverse secondary flow velocity is negative. As the Stokes number increases, the position of the maximum streamwise velocity for heavier particles is closer to the free surface, and the rotation centers of inner and outer secondary particle motions gradually disappear.

Keywords: Particle transport, Secondary flow, Open square duct

Introduction

Particle-laden flows in turbulent open ducts are encountered in various practical applications, with sediment transport and dispersion of floaters on the open free surface of rivers being one of the most prevalent examples. A distinguishing characteristic of these flows is the presence of secondary flows arising from the anisotropy of turbulence [1-3]. The previous studies predominantly focused attention on investigating the interaction between near-wall turbulence and particle behaviour in particleladen open channel flows, where the flow in the spanwise direction is assumed to be homogeneous, thus the effect of secondary flows can be ignored. Accordingly, the focus of this work is to investigate the effects of the secondary flows induced by the interaction of wall turbulence and free-surface turbulence on particle transport in open square duct flows.

Methodology

A schematic diagram of the present particle-laden square duct flow is shown in Fig.1. The flow is assumed to be periodic in the streamwise direction, and no-slip conditions are imposed on the side and bottom walls of the duct. On the top free boundary, the condition of a rigid free-slip wall is applied. Direct numerical simulation based on the spectral-element code Nek5000, developed by Fischer et al. [4] , is adopted to describe the incompressible Newtonian fluid motion. The N-S equations normalized by the integral scales are given as:

$$\nabla \cdot \vec{u}^* = 0. \quad (1)$$

$$\frac{\partial \vec{u}^*}{\partial t^*} + \vec{u}^* \cdot \nabla \vec{u}^* = -\nabla p^* + \frac{1}{Re_b} \nabla \cdot \tau^* + \vec{f}^* \quad (2)$$

where $\vec{f}^*$ is an extra source forcing term along the streamwise direction, which is dynamically adjusted at every timestep to maintain a constant mass flow rate.

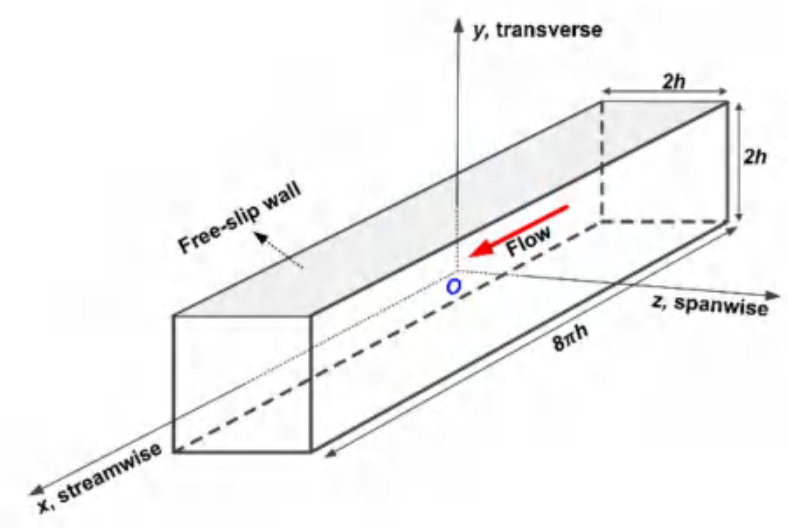


Figure 1. Schematic of the particle-laden turbulent open square duct flow.

Direct numerical simulation of particle deposition in sedimentary pipes

Shengran Ning, Min Liu, Yanlin Zhao, Jun Yao
China University of Petroleum (Beijing), Beijing, China

Abstract
The presence of solid beds modifies the flow field, resulting in secondary motions in the plane of the pipe cross-section, which in turn impact particle transport. In this work, direct numerical simulations combined with one-way coupling techniques and a Lagrangian tracking technique were used to predict the behaviour of particles affected by turbulence in different deposition pipes. The results for flows with beds show that the fluid flow exhibits secondary vortices and an increase in the mean streamwise vorticity caused by corners in the cross-sectional plane of the pipes, with their intensity near the upper curved wall increasing with height of deposited beds. However, the upper vortices remain relative weak compared to those in lower regions of the pipes.
Keywords: Turbulent pipe flows, Deposited beds, Secondary flows, Lagrangian particle tracking

Introduction

Turbulent flows through pipes are ubiquitous in engineering applications such as water supply, ventilation and the transportation of oil and gas. In all these applications, solid materials are frequently carried by the fluid medium to transport them to a desired location. The presence of a particulate phase considerably complicates the pipe's flow dynamics. For example, high concentrations of hydrates in oil pipelines may be deposited at the bottom of a horizontal pipeline due to the gravitational force. This in turn affects extraction efficiency and pipeline life [1-2]. Due to the influence of the secondary flows, the behavior of particles in the pipe will also change. For example, in square duct turbulent flows, the secondary vortices cause particles to move within a single vortex at longer time scales [3]. The influence of the secondary flows on the particle concentration distribution is also very significant. In a square duct flow, for example, the concentration of particles is greatest in the viscous sub-layer at the centre of the walls which is caused by fluid movement from the corners back to the duct centre [4-5]. Therefore, it is of great importance for engineering applications as well as scientific research to investigate the effect of secondary flow on particles in deposition pipes.

Methodology

The flow geometries and coordinate system are shown in Figure 1. The direct numerical simulation code, Nek5000[35], is used to calculate the three flows. The code is based on the spectral element method, and each computational domain is divided into hexahedral elements. Due to its high precision and high efficiency parallelisation character-istics, it is widely used to predict wall-bounded flows.

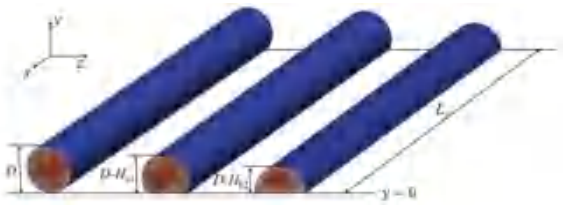


Figure 1 Coordinate system and geometry of pipes with different beds, contours show instantaneous streamwise velocity.

Results and discussion

In proximity to the wall, turbulence invariably demonstrates pronounced anisotropy, where in the magnitudes of fluctuations in various directions are distinctly influenced by the wall. If there is positive fluctuation in the streamwise direction at a local region, due to the fluid's continuity, surrounding fluid will replenish this region within the cross-section.

For three-quarter pipe, which compared with the half pipe, the secondary flow pattern has changed significantly. Therefore, although the fluid similarly flows from the centre to the corner and then returns along the wall to the centre of the pipe, the streamwise vortices near the upper wall become smaller and less intense. In contrast, the intensity of the secondary flow near the bed is not only much larger than that near the upper wall, but is also greater than that near the bed of the half pipe. In addition, at the top of the pipe, away from the corners, induced small vortices are generated that cannot be eliminated by larger averaging timescales.

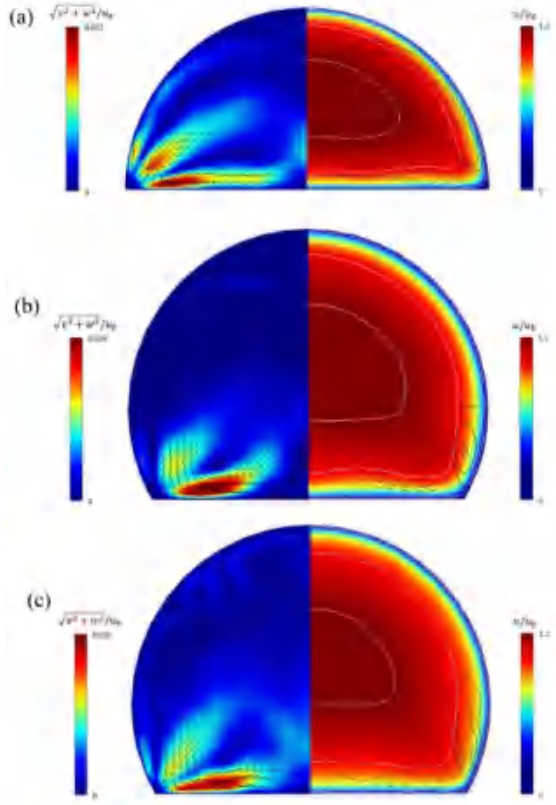


Figure 2 Contours of the magnitude of the mean cross-stream velocity of the fluid flow (ms^{-1}) with superimposed vectors (left), and of the mean streamwise velocity together with isocontours of the cross-flow stream function (right) where dashed lines represent negative values of ψ.

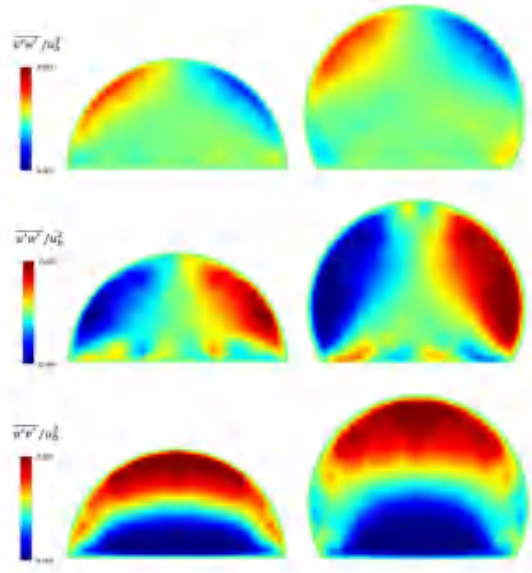


Figure 3 Shear components of the Reynolds stress tensor non-dimensionalised by the square of the bulk velocity for the half-pipe (left) and three-quarter pipe (right).

Conclusions

(1) The pattern of these flows was such that there were two streamwise vortices near each corner in the pipe.
(2) The characteristics of the secondary flows were related to the height of the bed.
(3) The secondary flow intensity near the upper curved wall was always much smaller than that near the pipe floor
(4) It was concluded that the curved boundary inhibits the development of the secondary flow in the upper regions of the pipe, and this effect is related to the flow Reynolds number.

Acknowledgements

This work was supported by the National Natural Science Foundation of China (No. 51876221) and the High-end Foreign Expert Introduction Project (G20190001270; B18054). The authors also gratefully acknowledged the financial support from the China Scholarship Council.

References

[1] J. -A. Wang, Y. Li, J. -F Zhao, B. -H. Shi, J. Gong, Q. -P. Li, Simulation of the effect of hydrate adhesion properties on flow safety in solid fluidization exploitation, Petroleum 9 (2023) 403-411.
[2] G. Zhang, J. Li, H. -W. Yang, G. -H. Liu, Q. Pang, T. Wu, H.-L. Huang, Simulation research on solid fluidization exploitation of deepwater superficial layer natural gas hydrate reservoirs based on double-layer continuous pipe, Journal of Natural Gas Science and Engineering 108 (2022) 104828.
[3] G. Sharma, D. -J. Phares, Turbulent transport of particles in a straight square duct, International journal of multiphase flow 32 (2006) 823-837.
[4] J. Yao, M. Fairweather, Inertial particle resuspension in a turbulent, square duct flow, Physics of Fluids 22 (2010) 3.
[5] J. Yao, M. Fairweather, Particle deposition in turbulent duct flows, Chemical engineering science 84 (2012) 781-800.

Modelling of droplet multiple breakage accounting for entire energy spectrum bottleneck effect and eddy-droplet discrepancy

Shenggao Gong, Ningning Gao
E-mail: gongshenggao0827@163.com
School of Chemical and Environmental Engineering, Hunan Institute of Technology, Hengyyang China

Abstract
This work focuses on the contribution of the two aspects of entire energy spectrum bottleneck effect (BE) and eddy-droplet discrepancy (EDD) to droplet multiple breakage simulation. The droplet breakage mechanism model is closured by more accurate turbulent parameters determined by accounting for the bottleneck effect and a formula is proposed to consider the effect of the eddy-droplet discrepancy. The influences of the two aspects on collision/interaction frequency density, breakage probability, breakage frequency and daughter size distribution (DSD) were analyzed. The proposed model agree well with the measured experimental data from single droplet experiments and drop swarm experiments, and also exhibits a better predictive performance by comparing with other models. To summarize, the improvements of this work are beneficial for consolidating the breakage model physical foundation.

Keywords: Droplet multiple breakage; Entire energy spectrum bottleneck effect; Eddy-droplet discrepancy; Turbulence

Introduction

Immiscible liquid-liquid turbulent dispersion has garnered considerable attention in extraction, emulsification, reaction processes for chemical, petroleum and pharmaceutical industries. The size distribution and holdup of dispersed phase used to characterize the turbulent dispersion performance are determined by the coalescence and breakage behavior of fluid particles. Hence, further learning fluid particle breakage mechanism is meaningful for engineering applications. Research work from experiments[1], direct numerical simulation[2], and theoretical modeling[3, 4] focused on the fluid particle breakage behavior. Over the past decade, entire energy spectrum contribution mechanism of fluid particle breakage (i.e., considering eddies within inertial, dissipation and energy-containing subranges simultaneously) has become a research hotspot in the field, and many theoretical models have been put forward[3,5,6]. However, the BE, which was fully validated by experiments, was failed to be captured by the turbulence parameters required by the modeling of droplet breakage behavior. Ignoring BE hinders acceptable reproduction of longitudinal velocity gradient skewness[7] thereby affecting the prediction accuracy and ability of droplet breakage models. In addition, the range around BE is mistakenly identified as inertial/dissipation range, which may result in incorrect breakage frequencies. Therefore, it is necessary to evaluate the impact of BE on the development of theoretical model for droplet breakage.

The general form of breakage frequency density model could be expressed as the product of collision/interaction frequency density and breakage probability. The existing collision frequency density is determined by the gas kinetic theory and the turbulent eddies are treated as real particles. This treatment defaults actually that the turbulent eddies do not disappear during their movement towards to the droplet. Factually, there is an essentially difference between eddy-droplet collision and particle-particle collision as turbulent eddies are restricted by their lifetime and arriving time. It means that if the time required by turbulent eddies arriving at the collision surface is larger than lifetime, the turbulent eddies has disappeared and cannot collision or encounter with droplet undoubtedly. The effect of arriving time and lifetime of

turbulent eddies on the eddy-droplet collision is called as EDD in this work. Obviously, EDD is not considered in the existing collision frequency model, and is also neglected by most of existing eddy-droplet interaction frequency density model. Ignoring EDD may significantly influence their collision/interaction frequency density. In addition, EDD may have an important effect on breakage probability since it can affect the energy transfer between turbulent eddies and droplets. Hence, considering the influence of EDD may be an important improvement to the turbulent droplet breakage mechanism model.

Methodology

On the basis our previous work[3], this work aims to further develop a low viscosity droplet multiple breakage mechanism model that fully consider the contributions of EDD and BE by using phenomenological method and statistical turbulence theory.

Results and discussion

The effect of BE and EDD on collision frequency $\omega_{collision}(\lambda, d_0)$, interaction frequency $\omega_{interaction}(\lambda, d_0)$, breakage probability $P(f_v, \lambda, d_0)$ and breakage rate $\Omega^*(V_0)$ is presented in Figure 1.

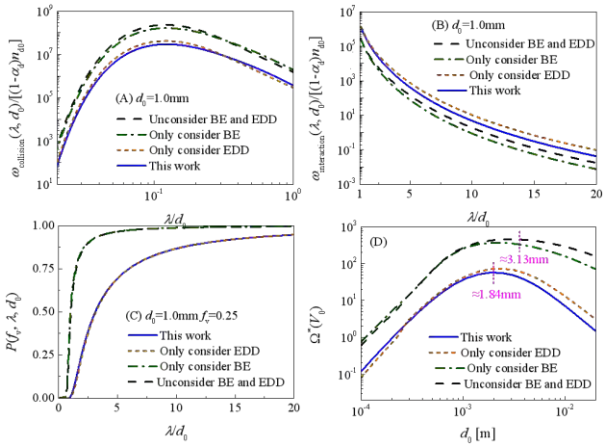


Figure 17 - Influence of BE and EDD on the predictions of $\omega_{collision}(\lambda, d_0)$, $\omega_{interaction}(\lambda, d_0)$, $P(f_v, \lambda, d_0)$ and $\Omega^*(V_0)$

As seen from the figure, BE and EDD have a significant impact on the predictions. In Figure 1A, BE tends to decrease the predictions of $\omega_{collision}(\lambda, d_0)$ and $\omega_{interaction}(\lambda, d_0)$, while the influence of EDD on $\omega_{collision}(\lambda, d_0)$ and $\omega_{interaction}(\lambda, d_0)$ exhibits a complex trend in Figure 1B. That is, EDD seems to be tending to decrease $\omega_{collision}(\lambda, d_0)$, while it conversely tends to increase $\omega_{interaction}(\lambda, d_0)$.

Figure 1C presents the influence of BE and EDD on breakage probability $P(f_v, \lambda, d_0)$ of binary breakage mode. It shows that $P(f_v, \lambda, d_0)$ is weakly affected by BE. While EDD decrease $P(f_v, \lambda, d_0)$ obviously, which enhances the breakage criterion and makes droplet breakage more difficult.

Figure 1D depicts that EDD significantly reduces the quantitative prediction of $\Omega^*(V_0)$ in the whole size range. The impact of BE on $\Omega^*(V_0)$ may be negligible for the condition of 0.2 mm $< d_0 <$ 1.0 mm, while it becomes very prominent for the other size ranges, such as for the range of $d_0 >$ 2.0 mm. In addition, BE and EDD also slightly affect the peak position of $\Omega^*(V_0)$.

Overall,the above analysis demonstrates the necessity of considering the impacts of BE and EDD on the breakage simulation.

The comparison of predicted $\Omega^*(V_0)$ obtained from single droplet experiment[8] is shown in Figures 2A and 2B. Figure 2C presents the comparison of the predicted $\Omega^*(V_0)$ and measured data by droplet swarm breakage experiment from PDDC[9,10], stirred tank[1] and pump-mixer[11].

The experimental data[8] presented a nonmonotonic evolution trend of $\Omega^*(V_0)$ over d_0 for water-petroleum (or toluene) system, while a monotonic increasing trend predicted by the LS model[12]. The nonmonotonic evolution trend is exhibited by CT model[13], but it obviously overestimates the value of $\Omega^*(V_0)$. In a whole, the results of the proposed model not only qualitatively exhibit this nonmonotonic evolution trend, but also quantitatively agree well with the experimental data. However, when BE and EDD are not considered, the model extremely overestimates the breakage frequency.

Zhou et al.[1] measured the relative proportion ($= \Omega_n^*(V_0)/\Omega^*(V_0)$) between different breakage modes (i.e., binary, ternary and quaternary breakage modes). The comparison in Figure 2D indicates that the predicted data is in good agreement with the measurement results.

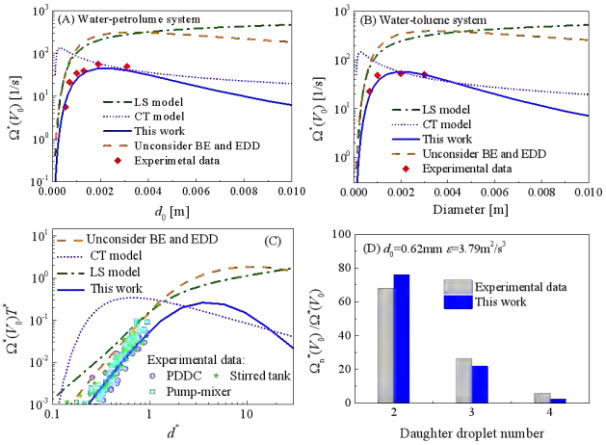


Figure 2 - Comparison of predicted breakage frequencies with measured data

The comparison of predicted diameter-based DSDs of binary, ternary, and quaternary breakage modes with experimental data[14] is shown in Figure 3. The peak of binary breakage predicted by the proposed model appears around at the position of $f_d \approx 0.79$, and the predicted DSD approaches to 0 when f_d tends to 0 or 1, which seems to be consistent with experimental data. For ternary and quaternary breakage modes, the proposed model predicts a relative flat distribution, showing a reasonably coincidence with the experiment measurement trend. In addition, the comparison results illustrate that effect of BE and EDD on diameter-based DSD seems to be negligible in some degree.

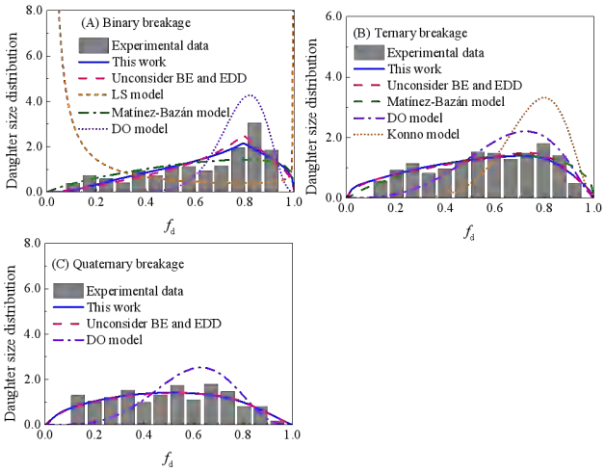


Figure 3 - Comparison of predicted DSDs with measured data

Figure 4 presents the droplet size distribution evolution obtained by coupling the proposed model with PBM. Compared with the predictions of other models, it can be seen that the cumulative volume fraction evolution from the proposed model is very consistent with the

experimental data[17]. Note that, the predicted cumulative volume fractions are obviously overestimated if BE and EDD are not considered (please see Figure 4B). It indicates that BE and EDD may also have a significant influence on PBM simulation and further proving the necessity of model development.

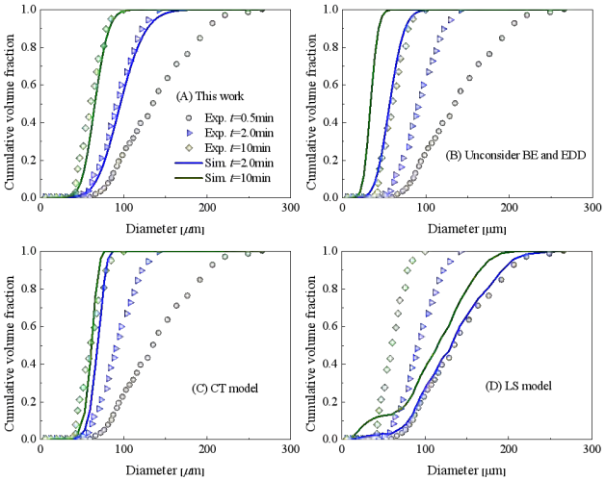


Figure 4 - Comparison of predicted cumulative volume fraction with measured data

Conclusions

This work developed a theoretical model to adequately account for the contribution of BE and EDD to multiple breakage mechanism of low viscosity droplet in turbulent flows. The analysis of the impact of BE and EDD indicated that they have an important influence on the droplet breakage simulation. In addition, the predictions of proposed model accounting for the influence of BE and EDD can agree well with the measured experimental data from different operation conditions and devices. These comparative results and analyses fully proved the necessity and advantage of model improvement.

Acknowledgements

The authors acknowledge the financial support from the National Natural Science Foundation of China (22108068), the Hunan Provincial Natural Science Foundation of China (2023JJ50102), the Scientific Research Fund of Hunan Provincial Education Department (21B0797, 22C0623).

References

[1] H. Zhou, X. Yu, B. Wang, S. Jing, W. Lan, S. Li, Experimental study on drop breakup time and breakup rate with drop swarms in a stirred tank, AIChE J. 67 (2021) e17065.
[2] A. Håkansson, M. Crialesi-Esposito, L. Nilsson, L. Brandt, A criterion for when an emulsion drop undergoing turbulent deformation has reached a critically deformed state. Colloids Surf. A 648 (2022) 129213.
[3] L. Han, S. Gong, Y. Ding, J. Fu, N. Gao, H. Luo, Consideration of low viscous droplet breakage in the framework of the wide energy spectrum and the multiple fragments, AIChE J. 61 (2015) 2147-2168.
[4] H. Zhang , G. Yang , A. Sayyar , T. Wang, An improved bubble breakup model in turbulent flow, Chem. Eng. J. 386 (2020) 121484.
[5]J. Solsvik, H.A. Jakobsen, A review of the statistical turbulence theory required extending the population balance closure models to the entire spectrum of turbulence, AIChE J. 62 (2016) 1795-1820.

[6] M. Karimi, R. Andersson, Dual mechanism model for fluid particle breakup in the entire turbulent spectrum, AIChE J. 65 (2019) e16600.
[7] D.A. Donzis, K.R. Sreenivasan, The bottleneck effect and the Kolmogorov constant in isotropic turbulence, J. Fluid Mech. 657 (2010) 171-188.
[8] S. Maaß, M. Kraume, Determination of breakage rates using single drop experiments, Chem. Eng. Sci. 70 (2012) 146-164.
[9] H. Zhou, S. Jing, Q. Fang, S. Li, Direct measurement of droplet breakage in a pulsed disc and doughnut column, AIChE J. 63 (2017) 4188-4200.
[10] H. Zhou, S. Jing, X. Yu, H. Zhou, W. Lan, S. Li, Study of droplet breakage in a pulsed disc and doughnut column-Part I: Experiments and correlations, Chem. Eng. Sci. 197 (2019) 172-183.
[11] H. Zhou, X. Yu, S. Jing, H. Zhou, W. Lan, S. Li, Measurement of droplet breakage in a pump-mixer, Chem. Eng. Sci. 195 (2019) 23-38.
[12] H.A. Luo, H.F. Svendsen, Theoretical model for drop and bubble breakup in turbulent dispersions, AIChE J. 42 (1996) 1225-1233.
[13] C.A. Coulaloglou, L.L. Tavlarides, Description of interaction processes in agitated liquid-liquid dispersions, Chem. Eng. Sci. 32 (1977) 1289-1297.
[14] A. Zaccone, A. Gäler, S. Maaß, D. Marchisio, M. Kraume, Drop breakage in Liquid-liquid stirred dispersions: modelling of single drop breakage, Chem. Eng. Sci. 62 (2007) 6297-6307.
[15] C. Martínez-Bazán, J.L. Montañés, J.C. Lasheras, On the break-up of an air bubble injected into a fully developed turbulent flow. Part II: size pdf of the resulting daughter bubbles, J. Fluid Mech. 401 (1999) 173-207.
[16] R.B. Diemer, J.H. Olson, A moment methodology for coagulation and breakage problems: Part 3 - generalized daughter distribution functions, Chem. Eng. Sci. 57 (2002) 4187-4198.
[17] M. Konno, M. Aoki, S. Saito, Scale effect on breakup process in liquid-liquid agitated tanks, J. Chem. Eng. Jpn. 16(4) (1982) 312-319.

Sinking behavior of submillimeter microplastic fibers in still water and rising bubbly flow

Fangyang Yuan, Hao Yuan, Chenlong Dai
School of Mechanical Engineering, Jiangnan University, Wuxi 214122, Jiangsu, China

Abstract
Microplastic fibers (MPFs) are a major source of microplastic contaminants of aquatic environments. However, little research has been conducted on the sinking behavior of submillimeter MPFs in water. In this study, we measured the settling of 519 submillimeter MPFs in quiescent water and modelled their settling velocity. We observed different settling patterns and discussed how the length and orientation of MPFs affected their settling velocity and horizontal displacement. We also demonstrated that air flotation was an effective and clean method for separating microplastics from water. Furthermore, we investigated the sinking behavior of microfibers driven by the wake of a single microbubble, both experimentally and numerically. The experimental data agreed well with the simulation results, and the findings provided a theoretical basis for the removal of cylindrical particles with large aspect ratios using microbubbles.

Keywords: Microplastic fiber, Settling velocity, Settling orientation, Drag coefficient, Interaction of microparticles and microbubbles

References
[1] Dai C, Yuan F, et al. Settling velocity of submillimeter microplastic fibers in still water[J]. Science of The Total Environment, 2024, 907: 168054.

Parallel Session IV: Topic 8-Multiphase flow measurement and industrial applications

An Improved Semi-Resolved CFD-DEM Model

Hanqiao Che[1], Haigang Wang[2,3], Kun Li[4], Xinwei Wang[5]
1. School of Mechanical Engineering, Guangxi University, Nanning, Guangxi, 530004, China
2. Institute of Engineering Thermophysics, Chinese Academy of Sciences, Beijing 100190, China
3. University of Chinese Academy of Sciences, Beijing 100049, China
4. Shanxi Key Laboratory of Signal Capturing & Processing, North University of China, Taiyuan China
5. College of New Energy, China University of Petroleum (East China), Qingdao 266580, China

Abstract
Computational Fluid Dynamics coupled with Discrete Element Method (CFD-DEM) can be classified into resolved and unresolved categories. Resolved CFD-DEM employs a no-slip boundary condition with a mesh grid at least ten times smaller than the particle diameter (Knight, 2018). Conversely, unresolved DEM-CFD uses homogenized Navier-Stokes equations, accommodating multiple particles within each mesh grid. However, applying CFD-DEM to systems with large size ratios (> 4) poses challenges, as it would be very computationally expensive if resolved method is used and the empirical drag force correlations would no longer be applicable if unresolved method is used. The semi-resolved CFD-DEM method addresses this by treating coarse and fine particle flows in resolved and unresolved schemes, respectively. In this paper, we will review recent progress in semi-resolved CFD-DEM and showcase a two-grid mapping method.

Keywords: CFD-DEM, Immersed Boundary Method, Polydisperse system

Introduction

Fluid-particle flows, prevalent in diverse industrial sectors, demand a deep understanding of their behavior for advancing downstream processes and formulations. Computational Fluid Dynamics coupled with the Discrete Element Method (CFD-DEM) proves vital in simulating two-phase fluid-particle systems [1]. CFD-DEM is categorized as resolved or unresolved based on the solver's resolution. Resolved CFD-DEM treats particle surfaces with a fine CFD mesh, while unresolved CFD-DEM uses homogenized Navier-Stokes equations and requires a minimum cell size. For bidisperse, bimodal, or gap-graded particle systems with large size ratios, challenges arise with both methods. Semi-resolved CFD-DEM [2, 3], a recent compromise, blends resolved and unresolved schemes for coarse and fine particles, respectively. This approach overcomes limitations of unresolved methods in predicting fluid-particle interaction forces for large size ratios. However, challenges persist in accurately determining the porosity field for finer particles due to mesh size discrepancies.
This work introduces a two-grid semi-resolved CFD-DEM solver, overlaying static and refined meshes. Inspired by two-grid approaches in unresolved CFD-DEM. we will illustrate that this method demonstrates high accuracy and computational efficiency, opening opportunities to use CFD-DEM in modelling biomass gasification reactors and plastic pyrolysis reactors, particularly those with very large particle size ratios.

Methodology

The semi-resolved solver concept involves augmenting the governing equation of the unresolved solver with a source term, similar to the resolved solver, providing resolved functionality. These equations can transform into resolved or unresolved formats, depending on the particle type present in a region, given the physical impossibility of coarse and fine particles coexisting in the same area. The governing equations for the fluid phase in a semi-resolved solver express as follows:

$$\rho_f \frac{\partial \varepsilon_f^{fine}}{\partial t} + \rho_f \nabla \cdot (\varepsilon_f^{fine} \mathbf{u}_f) = 0 \quad \textbf{(1)}$$

$$\rho_f \frac{\partial \varepsilon_f^{fine} \mathbf{u}_f}{\partial t} + \rho_f (\varepsilon_f^{fine} \mathbf{u}_f \cdot \nabla) \mathbf{u}_f \quad \textbf{(2)}$$

$$= -\varepsilon_f^{fine} \nabla p + \varepsilon_f^{fine} \mu \Delta \mathbf{u}_f - \mathbf{S}_{pf}^{fine} + \varepsilon_f^{fine} \rho_f \mathbf{g} - \mathbf{S}_{pf}^{coarse}$$

The fine particle momentum contribution, $\mathbf{S}_{pf}^{coarse}$, is determined by drag forces, expressed as:

$$\mathbf{S}_{pf}^{fine} = G_{pf} \mathbf{u}_f - G_{pf} \mathbf{u}_s^{fine} \quad \textbf{(3)}$$

Here, G_{pf} is a coefficient derived from drag forces on particles, estimated using empirical correlations. The momentum contribution from coarse particles, $\mathbf{S}_{pf}^{coarse}$, is calculated based on existing methods as:

$$\mathbf{S}_{pf}^{coarse} = \frac{\varepsilon_f^{fine}(1-\varepsilon_f^{coarse})(\mathbf{u}_p^{coarse} - \tilde{\mathbf{u}}_f)}{\Delta t_{CFD}} \quad \textbf{(4)}$$

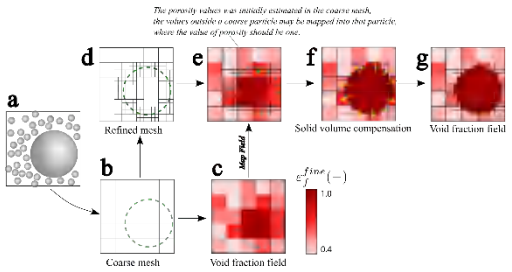


Figure 1 - Two-grid porosity method

Figure 1 shows the flowchart of the two-grid porosity method, such strategy is to refine the mesh close to the coarse particle surface and at the same time allow as little mesh distortion as possible. It does not change the shape of the mesh cells, rather it performs topological refinements. The mesh refinement level (RL) is defined relative to the starting background mesh. Due to the dynamic refinement process, the size of the refined CFD grid may be smaller than the fine particles in the corresponding regions. Therefore, a field mapping procedure has been conducted to transfer the variables from the coarse grid to the fine grid.

Figure 2 illustrates a representative case of a fluidized bed containing bimodal particles with a size ratio of 30. Employing the semi-resolved CFD-DEM approach, distinct regions corresponding to coarse particles are clearly discernible, and the flow field surrounding these coarse particles has been accurately reproduced.

Resolved simulations for bi-modal particle assemblies, for example, typically require 10^6 to 10^7 fluid cells and 12 to 48 hours to reach steady-state flow conditions on 100 to 1000 processing units. In contrast, all the semi-resolved simulations presented in this paper were run using 10^5 to 10^6 fluid cells, requiring 2 to 10 hours to reach steady-state flow conditions on 4 to 12 processing units. The computational cost can be roughly estimated based on the number of CFD cells, as the calculation loads are mainly spent on the CFD solver side.

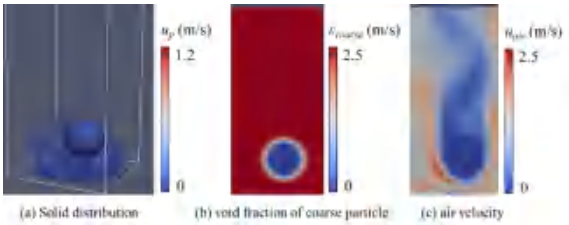


Figure 2 - Semi-resolved CFD-DEM simulation of the gas-solid flow in a fluidized bed with particle size ratio of 30

Conclusions

A two-grid semi-resolved CFD-DEM approach has been proposed, which is suitable for particle-fluid flow scenarios with a high particle size ratio, such as bi-modal particle systems. The semi-resolved CFD-DEM method provides a trade-off between computational efficiency and accuracy, with its range of applicability falling somewhere between resolved and unresolved solvers.

References

[1] Z.Y. Zhou, S.B. Kuang, K.W. Chu, A.B. Yu, Discrete particle simulation of particle–fluid flow: model formulations and their applicability, Journal of Fluid Mechanics 661 (2010) 482-510. https://doi.org/10.1017/S002211201000306X.

[2] T. Tsuji, K. Higashida, Y. Okuyama, T. Tanaka, Fictitious particle method: A numerical model for flows including dense solids with large size difference, AIChE Journal 60(5) (2014) 1606-1620. https://doi.org/10.1002/aic.14355.

[3] Q. Yang, K. Cheng, Y. Wang, M. Ahmad, Improvement of semi-resolved CFD-DEM model for seepage-induced fine-particle migration: Eliminate limitation on mesh refinement, Computers and Geotechnics 110 (2019) 1-18. https://doi.org/https://doi.org/10.1016/j.compgeo.2019.02.002.

Visual experiments and OpenFOAM modelling for gas-liquid bubbling flow and mass transfer process

Luhaibo Zhao
Shanghai Advanced Research Institute, Chinese Academy of Sciences (Shanghai, China)

Abstract
A general two-phase flow and mass transfer OpenFOAM-CFD model for bubbling system was established by the visual experiments, mainly including the image method and the Electrical resistance tomography. The influence of each phase parameter of the Blend interface model was investigated to ensure the accuracy and stability of simulation. The interphase force models (like drag, lift, turbulent) and multi-size bubble models (i.e., the population balance equation and the interfacial area transport equation) were studied and compared with aid of the visual bubble measurements. Furthermore, the multi-size bubbling flow coupled mass transfer model was successfully verified by the experiments.

Keywords: bubbling flow, visual measurement, mass transfer, OpenFOAM-CFD

Introduction

Bubbling reactors are that the gas phase is dispersed into a continuous liquid or slurry phase, and they are widely used in petrochemical, wastewater treatment and multiphase chemical industries (viz. hydrogenation, oxidation, carbonylation etc.) owing to their advantages in simple design and operation[1-2]. Bubble behaviors and gas holdup have significant effects on the performance of bubble columns, as a result that the global and local bubbling-flow characteristics as well as the measuring method need to be studied for the industrial application[3]. Hence, visualization experiments coupling the Electrical resistance tomography and the high-speed photography would be developed to establish the CFD model with the Blend interface model, interphase force models and bubble models based on OpenFOAM.

Methodology

Fig.1 showed that the cylindrical bubble column had an inner diameter of 235 mm and a height of 1 m. The transparent Plexiglas wall thickness was 2 mm for the clear observation of bubble behaviours inside the reactor using a high-speed camera. Air was fed by air compressor through distributor and the flow rate was measured using the calibrated rotameters. The gas distributor was having 160 apertures and the diameter of each aperture was 1 mm. The air volumetric flow rate was varied between from 0-25 m^3/h which corresponded to the range of gas superficial velocity from 0 to 0.16 m/s. In this experiment, the volume of liquid phase was about 18 L and the static height of liquid was approximately 400 mm.

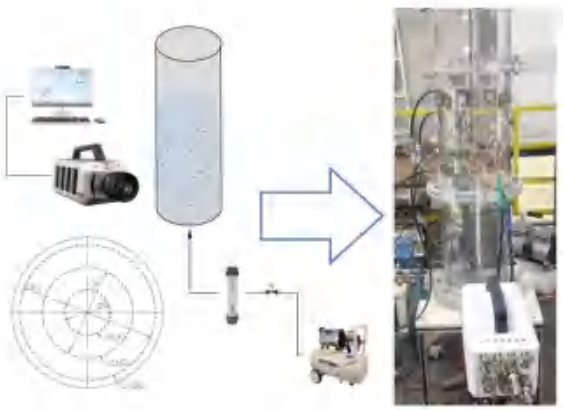


Fig.1 Experimental schematic and device diagram

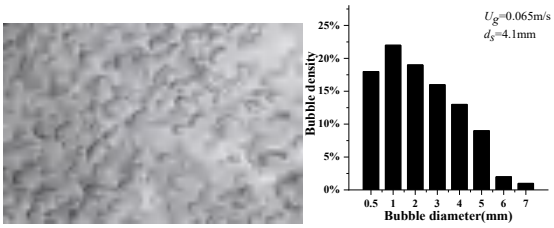


Fig.2 Bubble size measurement

.As shown in Fig. 2, the time averaged bubble size distributions were measured by the visual experiments based on the high-speed CDD capturing and image processing program. Combined with traditional liquid level method and resistance tomography method, the gas holdup parameters of macroscopic gas-liquid two-phase flow are measured, as shown in Fig.3.

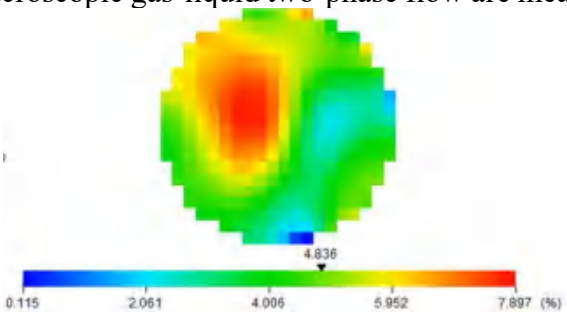


Fig.3 Gas phase distribution by ERT

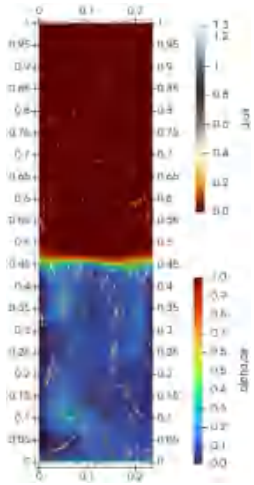


Fig.4 Gas phase distribution by OpenFOAM-CFD

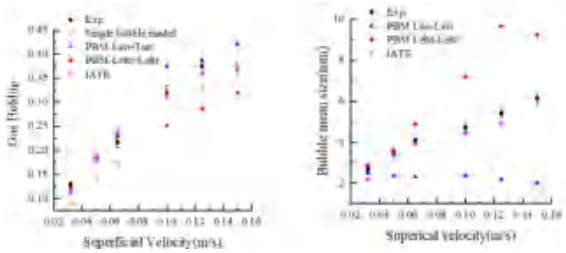


Fig. 5 Effects of different bubble models on gas holdup and bubble mean size

It could be seen from Fig. 5, at the low gas velocity (Ug＜0.1m/s), the whole gas holdup of the Luo-Luo model and the Lehr-Lehr model were similar and closer to the experimental results. At the high gas velocity (Ug≥0.1m/s), the gas holdup of the Luo-Luo model were slightly higher than the experimental results, while those of Lehr-Lehr model were the opposite.

Furthermore, to analyze the average bubble sizes, when the single-size bubble was set, the gas holdup was lower than the experimental data at 0.125m/s, which got the same situation as using the Lehr-Lehr model, which trended to the coalescence process and produced the larger bubble by the reason that the bubbles collision and coalescence frequency were high based on the turbulent vortex induction Fig.6 showed O2 concentration increased with the time and reached a certain concentration for the equilibrium state. The higher the gas inflow rate, the faster the mass transfer efficiency. Furthermore, the mass transfer rates of the IATE model were faster than those of single-bubble model and were closer to the experimental data

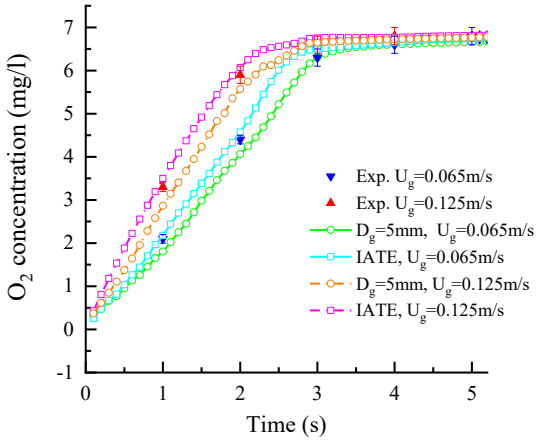


Fig. 6 Dissolved oxygen concentration with mass transfer

Conclusions

In this work, a numerical simulated model for the gas-liquid bubbling flow and mass transfer process was established in OpenFOAM based on the Electrical resistance tomography and the high-speed photograph. The gas holdup and the bubble mean size calculated by the IATE model were more similar to the experimental results. At last, the mass transfer model was added, and the mass transfer rates of the IATE model were faster and more accurate than those of single-bubble model, which demonstrated the validity of the OpenFOAM multi-size bubbles flowing-mass transferring models.

References

[1] Deckwer, W.D. Bubble Column Reactors; John Wiley & Sons Ltd.: Chichester, UK, 1992.
[2] Besagni G., Inzoli, F., Ziegenhein T., Two-Phase Bubble Columns: A Comprehensive Review, ChemEngineering, 2018, 2(2),13
[3] Cheng J., Li Q., Yang C., Zhang Y., Mao Z., CFD-PBE simulation of a bubble column in OpenFOAM, Chinese Journal of Chemical Engineering, 2018, 26, 1773–1784

Research on Mass Flow Measurement Model Based on averaging-velocity tube vortex street flow sensor

Lide Fang[1,2,3,4,*], Qixin Gao[1,2,3,4,] Xinyuan Zhang[1,2,3,4], Zeqi Wang[1,2,3,4]
[1]School of Quality and Technical Supervision, Hebei University, Baoding 071002, China
[2]National &Local Joint Engineering Research Center of Metrology Instrument and System, Hebei University, Baoding, Hebei, 071002, China
[3]Hebei Key Laboratory of Energy Metering and Safety Testing Technology, Baoding, Hebei, 071002, China
[4]Engineering Research Center of Zero-carbon Energy Buildings and Measurement Techniques, Ministry of Education
*Corresponding author, E-mail: fanglide@hbu.edu.cn

Abstract
This study developed an innovative averaging-velocity tube vortex street flow sensor for mass flow measurement in gas-liquid two-phase flows. Utilizing Computational Fluid Dynamics (CFD) simulations, the research numerically modeled the vortex shedding phenomenon and the pressure distribution within the sensor's cavity. Informed by both theoretical and empirical analyses, the optimal dimensions, shape, and pressure tap locations for the sensor were determined. The result is an integrated structural design of the new flow sensor, as well as the construction of a mass flow measurement apparatus that incorporates this sensor. The apparatus employs a high-frequency diffused silicon differential pressure transmitter to capture fluctuations in differential pressure. Analysis of these signals yielded the average differential pressure and vortex shedding frequency, which were then used to establish a mass flow measurement model. This model was rigorously tested and validated through experiments with single-phase water and gas, as well as with gas-liquid two-phase annular mist flows, demonstrating its high precision and accuracy across various flow regimes.

Keywords: Flow sensor, Averaging-velocity tube, Vortex flowmeter, Mass flow measurement

Introduction

Mass flow measurement plays a pivotal role across various industries, including chemical, petroleum, natural gas, pharmaceuticals, food processing, and aerospace. Its accuracy directly impacts process precision, product quality, energy efficiency, and environmental protection. Mass flow measurement techniques can be categorized into two main types: indirect and direct mass flow measurements. Direct mass flow measurement methods enable the direct measurement of fluid mass flow without the need for indirect calculations through other parameters, such as volume flow and density.

There are generally two types of combined mass flow measurement methods. One involves the combination of a standard flowmeter with a densitometer, and the other employs two different types of flowmeters for measurement. Li Tianyi [1] conducted in-depth research on the application of combined vortex flowmeter and V-cone meter instruments in wet steam measurement. Through simulation data, the characteristics of vortex and V-cone in wet steam measurement were thoroughly studied, exploring the influence of dimensionless parameters on measurement performance and their mechanisms, providing theoretical and practical bases for accurate wet steam measurement. Wrasse A D N [2] proposed an innovative two-phase flow measurement method that combines capacitive sensors with Venturi meters, verifying the feasibility of this combined measurement technology in two-phase flow measurement through experiments. Liu Yueyuan [3] introduced a novel averaging-velocity tube vortex street flow sensor that utilizes a dual differential pressure method for measuring both the Pitot tube differential pressure signal and the vortex frequency signal. By integrating differential pressure

measurement and empirical wavelet transform techniques, the accuracy and rangeability of measurements were significantly enhanced.

This study introduces an innovative mass flow measurement apparatus based on a single-channel high-frequency differential pressure transmitter for averaging-velocity tube vortex street flow measurement. This device, employing just one high-frequency differential pressure transmitter, achieves multi-parameter measurement, reducing the cumulative error associated with multi-parameter measurements and better meeting the requirements of practical measurement.

Methodology

Based on the structures and working principles of vortex flowmeters and pitot tubes, the bluff body from the vortex flowmeter is utilized as the body for the pitot tube to generate a differential pressure signal from the dynamic pressure of the flow upstream and the static pressure downstream. Within the pipeline's central axis, a bluff body is positioned, shaped like a trapezoidal column. To measure the average differential pressure and the fluctuating differential pressure signal, two pairs of high-pressure holes are set on the bluff body's approach face according to the equal annular area method. The CFD simulation has been employed to numerically model the vortex shedding phenomenon in the flow field and the pressure distribution within the cavity, with a low-pressure fluctuating pressure port placed at the axis on the backflow surface. A high-frequency diffused silicon differential pressure transmitter is used to obtain the differential pressure fluctuating signal from the high and low-pressure chambers, which allows the analysis of the average differential pressure and vortex shedding frequency, thus establishing a model for measuring mass flow. In this design, the averaging-velocity tube and vortex sensor no longer operate as independent units in parallel but are closely integrated through a carefully designed coupling mechanism, forming a unified flow measurement unit. Moreover, through a single signal acquisition channel, it is possible to simultaneously capture differential pressure fluctuation signals that include both differential pressure and frequency signals. The principle diagram of the mass flow measurement device is shown in Figure 1. The formula for mass flow rate is

$$\boldsymbol{Q = k\frac{\Delta P}{f}} \qquad \textbf{(1)}$$

In the formula, Q represents the mass flow rate, ΔP stands for differential pressure, f is the frequency, and K is the instrument coefficient.

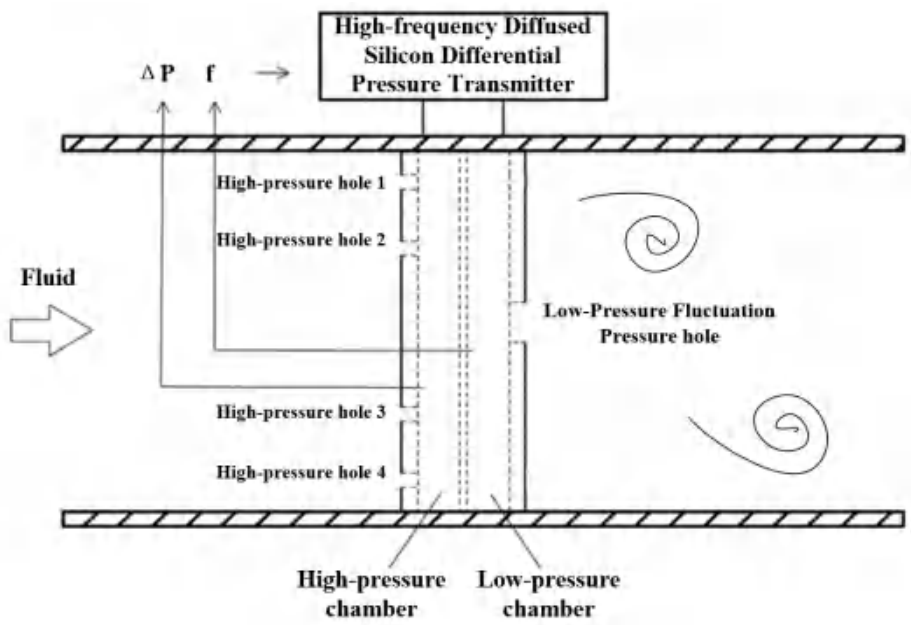


Figure 1 - The principle diagram of the mass flow measurement device

Conclusions

The device underwent experiments with single-phase liquid, single-phase gas, and gas-liquid two-phase annular mist flow. The experimental results are as follows:

Mass flow and phase-specific mass flow parameters were obtained through experimental testing with single-phase flows and gas-liquid two-phase annular mist flows. The relative error range for single-phase water mass flow measurement was -0.738% to 0.771%. The relative error for single-phase gas mass flow measurement was consistently between -1.69% and 1.54%. In gas-liquid two-phase annular mist flows, the relative error range for gas phase mass flow measurement was -6.716% to 6.379%. It was demonstrated that this mass flow measurement device has high measurement accuracy in single-phase flow measurements. Furthermore, a mass flow measurement and mass gas holdup model were established, achieving the measurement of gas phase mass flow in annular mist flows.

Acknowledgements

This work was supported by National Natural Science Foundation of China (Grant number: 61475041), Natural Science Foundation of Hebei Province (Grant number: F2021201031) and Special project for the construction of Beijing Tianjin Hebei collaborative innovation community (Grant number: 20540301D).

References

[**1**] Li Tianyi. Study on Wet Steam Measurement Characteristics Based on Combined Vortex and V-Cone Instruments [D]. Tianjin University.

[2] A.D.N. Wrasse, D. Bertoldi, R.E.M. Morales, et al. Two-phase flow rate measurement using a capacitive sensor and a Venturi meter, 2017 IEEE SENSORS. IEEE, 2017. DOI:10.1109/ICSENS.2017.8234150.

[3] Liu Yueyuan, Liang Yujiao, Zheng Meng, et al. Study on the Measurement Characteristics of a New Averaging-Velocity Tube Vortex Street Flow Sensor [J]. Journal of Electronic Measurement and Instrument, 2022, 36(12): 10-18.

Research on Dynamic Measurement System of Gas Liquid Interface Based on Deep Learning

Lide Fang, Jingchi Zhang
Hebei University, Baoding, China

Abstract

Multiphase flows are widely present in both natural phenomena and industrial processes, playing crucial roles in various fields such as petrochemicals, metallurgical steelmaking, and nuclear power generation. Measuring the gas-liquid interface is fundamental in the study of gas-liquid two-phase flows, aiming to achieve automated detection of the interface for subsequent processing. Current research on real-time measurement of gas-liquid interfaces in two-phase flows lacks sufficient investigation into the real-time nature of the measurement and data preservation and transmission. High-speed imaging, laser-induced fluorescence, particle image velocimetry, and other techniques require expensive equipment and precise design, making them unsuitable for industrial on-site measurements and measurements under harsh conditions. Therefore, achieving low-cost dynamic measurement of gas-liquid interfaces holds significant industrial significance.

This study focuses on online real-time measurement of gas-liquid interface characteristic parameters. Through the combination of object detection and instance segmentation algorithms, the detected gas-liquid interface is segmented, and a tracking algorithm is employed to track the detected gas-liquid interface. Characteristic parameters such as bubble size, velocity, and gas volume fraction in gas-liquid two-phase flows passing through pipelines are statistically analyzed. A user-friendly GUI interface is designed for the system, enabling real-time display of detected gas-liquid interface boundary feature information on the system interface by calling the detection camera. The relative detection error is less than 10%, meeting the requirements of multiphase flow detection in the industrial field.

Keywords: Two-phase flow, Object Detection, Instance segmentation, Tracking algorithm, Dynamic measurement

Introduction

The recognition of gas-liquid interface is a fundamental task in the study of gas-liquid two-phase flows, aiming to achieve automated detection and identification. Traditional image processing algorithms mainly focus on detecting the contour edges of bubbles [1]. However, in industrial environments with dim lighting and low-resolution detection cameras, the features of the gas-liquid interface itself may not be distinct, leading to unclear recognition of the interface contour and the inability to detect a complete boundary contour, with poor generalization and susceptibility to missed detections. In recent years, with the improvement of computer performance, deep learning has been widely applied in image processing.

Cerqueira, RFL presented a convolutional neural network (CNN)-based method for reconstructing the shapes of bubbles in bubble flows using high-speed camera images. Bubble recognition and shape reconstruction employ an anchor-based method with a set of anchors and boxes, where a single anchor is used for different-sized anchor boxes [2]. Cui, YZ developed an image processing method based on Mask R-CNN for bubble detection, segmentation, and shape reconstruction in high gas retention sub-millimeter bubble flows. This method can obtain pixel-level segmentation masks and accurately describe the shapes of overlapping bubbles. Despite the emergence of numerous deep learning-based research methods, none can accurately reconstruct the boundary of the gas-liquid interface [3].

Current research only involves processing captured videos, which cannot achieve real-time detection, thus lacking industrial application value. Developing a system capable of online recognition of the gas-liquid interface would be highly meaningful.

Methodology

This article creates a dataset by using multiple high-speed cameras to capture the interaction phenomenon of gas-liquid two-phase flow at different flow rates. The experimental platform is shown in Figure 1. A dynamic measurement system for gas-liquid interface based on deep learning has been designed. By comparing different object detection algorithms, select the appropriate algorithm for detection. And optimize the algorithm network to improve detection speed and accuracy. On the basis of object detection, add instance segmentation to achieve precise segmentation of gas-liquid interfaces. Add a tracking algorithm to track the flow trajectory of each bubble. Optimizing the network and improving detection speed can meet the needs of real-time detection. Finally, use Qt to design a dynamic measurement system GUI interactive interface. Through the interface, you can select detection sources such as videos and cameras to achieve real-time detection and save detection data. The GUI interaction interface is shown in Figure 2.

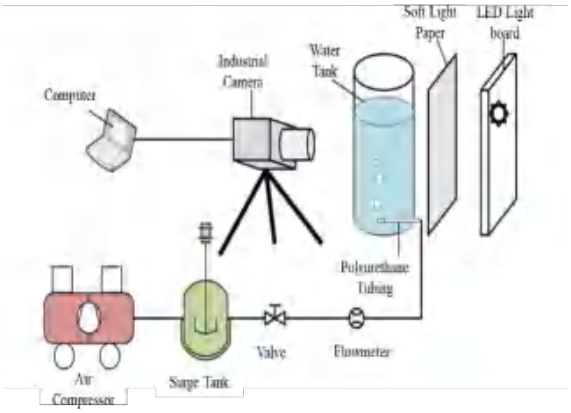


Figure 1 - Schematic diagram of experimental platform



Figure 2 - Dynamic measurement system GUI interface

Conclusions

This paper presents the design and construction of a dynamic measurement system for gas-liquid interface, comprising a measurement platform, deep learning algorithms, and a measurement system GUI (Graphical User Interface). The system enables real-time online detection of the gas-liquid interface and the storage and transmission of parameter data.

Geometric and motion characteristics of bubbles in gas-liquid two-phase flows are analyzed and summarized, and optimization techniques are applied to enhance measurement accuracy. The final system error is less than 10%, meeting the requirements of multiphase flow detection in industrial applications.

Acknowledgements
The authors are grateful for the support by the National Natural Science Foundation of China, China (62173122), Key Project of Natural Science Foundation of Hebei Province (F2021201031) and Beijing-Tianjin-Hebei Collaborative Innovation Community Construction Project (20540301D),Hebei Provincial Postgraduate Demonstration Course Project(KCJSX2021009).

References
[1] Mittal, M. et al. An Efficient Edge Detection Approach to Provide Better Edge Connectivity for Image Analysis, Ieee Access 7(2019).
[2] Cerqueira, R. F. L. & Sinmec, E. E. P. Development of a deep learning-based image processing technique for bubble pattern recognition and shape reconstruction in dense bubbly flows. *Chemical Engineering Science* 230 (2021).
[3] Cui, Y. Z. et al. A deep learning-based image processing method for bubble detection, segmentation, and shape reconstruction in high gas holdup sub-millimeter bubbly flows. Chemical Engineering Journal 449(2022).

Optimizing Electrical Capacitance Tomography Images by ISTA-Net Algorithm Based on Dynamic Simulation of Gas-Oil Two-Phase Flow

Yi Xu[1,2], Zhiyang Ma[1,2] and Haigang Wang[1,2]
1. State Key Laboratory of Coal Conversion, Institute of Engineering Thermophysics, Chinese Academy of Sciences, Beijing, China
2. University of Chinese Academy of Sciences, Beijing, China

Abstract
Due to "soft-field" effect, as well as ill-posed and ill-conditional issues, it poses a great challenge to optimize the quality of electrical capacitance tomography (ECT) image. In this paper, ISTA-Net algorithm, which was initially proposed to solve compressive sensing reconstruction, is modified and extended to the image reconstruction for ECT. In the proposed algorithm, optimization-based Landweber iteration is combined with convolutional neural networks (CNN) to achieve a mathematically interpretable model with learnable parameters. The datasets used for training and test are all generated from dynamic simulation of gas-oil two-phase flow by coupling the flow field with electrostatic field. Test results demonstrate that the modified ISTA-Net algorithm outperforms the traditional image reconstruction method for ECT, especially in image error and gas fraction estimation. The proposed method has been validated by static experimental test.
Keywords: Electrical capacitance tomography, Image reconstruction, Iterative algorithm, Convolutional neural networks

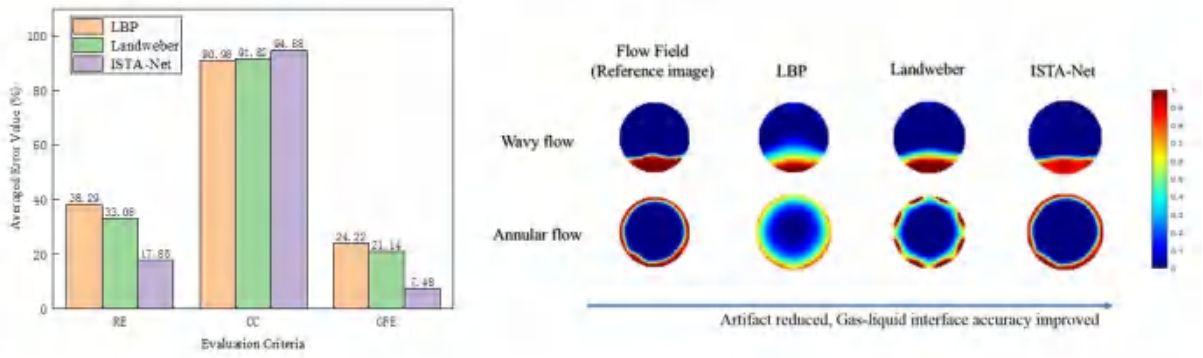


Figure 18 – Image quality comparison between ISTA-Net and tradition algorithms

Erosion of Sediment beds Using Impinging Jets: Application to Nuclear Waste Mixing

Ahmad Mohamadiyeh, Timothy Hunter, Mike Fairweather, Jeff Peakall, Martyn Barnes
University of Leeds, Leeds, United Kingdom

Keywords: Impinging jet, Erosion, Particle properties, Nuclear waste management, Ultrasonic Velocity Profiler (UVP)

Abstract

Impinging jets plays a vital role in nuclear waste mixing. Particles participated in nuclear waste have wide range of properties. Therefore, it is important to understand the effects of particles properties on the erosion by impinging jets. In this study, both cohesion-less and cohesive particles with different properties are tested to understand how they erode by impinging jets using manual measurements, image techniques and Ultrasonic Velocity profiler (UVP)

Introduction

Impinging jets serve as a pivotal mechanism employed across various industrial applications; one of the relevant applications is the nuclear waste management industry. Within the facilities of Sellafield Ltd, impinging jets are used to erode and mix the nuclear waste in the highly active nuclear waste storage tanks (HASTs). It is important to erode the nuclear particles and keep them in suspension inside the tanks to avoid the creation of highly tenacious sediment beds and radioactive hotspots. There are several factors that affect erosion which include the properties of the fluid, the properties of the jet, and the properties of the bed. The effect of bed properties such as bulk yield stress, particle size distribution, and cohesion on erosion is of interest given the wide range of nuclear particles available in the HASTs.

Methodology

Experimentally, the role of bed properties on erosion is investigated. An array of mixed cohesion-less and cohesive beds will be mimicked to investigate the effect of cohesion on jet erosion. The erosion of spherical soda lime glass particles,"Honite, H", with five different particle size distributions (H22, H16, H12, H9, H8) is studied representing cohesion-less particles. The erosion of the cohesion-less particles can be quantified and normalised using the dimensionless Critical Erosion parameter 'Ec' based on properties that can be measured [1]. In addition, the erosion of fine particles such as Barium Sulphate and Calcium carbonate are studied representing cohesive particles.

Erosion experiments are performed on the cohesion-less and cohesive particles to study their erosion and interaction with the impinging jet. The jet is a water jet which is submerged in a cubic tank ($0.125m^3$) filled with water. It impinges on a sediment bed of 3 cm depth. The crater sizes are measured using several techniques. This includes manual measurements such as a scale ruler attached to a stick which is suitable for particles that settle quickly. A camera is placed underneath the tank to measure the radius of clearance using imaging techniques. Additionally, LiDAR was used to obtain a 3D reconstruction of some of the crater profiles. On the other hand, Ultrasonic velocity profilers (UVP) are used to study and track erosion profiles and measure both the static and dynamic erosion of opaque systems with a high load of suspended particles.

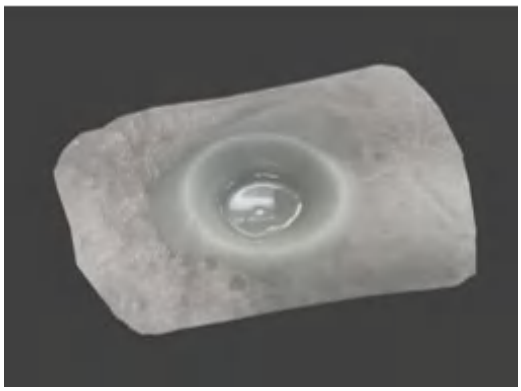


Figure 1: A 3D reconstruction of bed of spherical glass particles ‘H9’

References

[1] Aderibigbe, O.O. and Rajaratnam, N., 1996. Erosion of loose beds by submerged circular impinging vertical turbulent jets. Journal of hydraulic research, 34(1), pp.19-33.

Investigation of Ice Crystal Morphology, Size Distribution and Concentration in Icing Wind Tunnel via HACPI

Boyi Wang, Letian Zhang, Xinyuan Huang, Yingchun Wu*, Xuecheng Wu
State Key Laboratory of Clean Energy Utilization, Zhejiang University, Hangzhou, China

Abstract

Icing is a common natural phenomenon, and ice crystals are prevalent in low-temperature environments, such as high altitudes. When an aircraft flies through areas with ice crystals, cold surfaces like wings may not freeze, but aero-engines or pitot probes can ingest ice crystals. The accretion of ice at the aero-engine inlet and icing on the rear rotating blades can decrease intake efficiency, lead to thrust loss, and even cause stall and surge. Airworthiness authorities worldwide have implemented anti-deicing requirements. Therefore, the simulation of ice crystal icing at high altitudes in the icing wind tunnel holds significant value for the study of icing on the aero-engine, pitot probe and other components of aircraft. Concurrently, the measurement of ice crystals in the icing wind tunnel is an aspect that warrants attention. However, most of the icing wind tunnels are dedicated to the supercooled water droplets icing, and the simulation of ice crystals in icing wind tunnel is still a complex task. In addition, ice crystals exhibit complex morphologies, significant differences exist between natural and artificial ice crystals. Ice crystals generated using various methods also exhibit distinct characteristics. Moreover, the irregular morphology of ice crystals, with sizes ranging from micrometers to millimeters, all of which pose significant challenges to measurements.

This research introduces the Holographic Airborne for Cloud Particle Imager (HACPI) based on in-line holography, capable of measuring particle size distribution, morphology, and concentration. A series of experiments utilizing HACPI have conducted in the icing wind tunnel at AVIC Chengdu CAIC Electronics Co., LTD. The icing wind tunnel (CAIC IWT) is equipped with an ice crystal generation system (ICGS) that operates on a grinding-based method, facilitating foundational research on ice crystal icing. The morphology, size distribution and concentration of the ice crystals are simultaneously measured under airspeeds of Mach 0.55 and Mach 0.62 with HACPI, the results indicate that the morphology of ice crystals generated by the ICGS exhibits randomness. It is observed that with an increase in particle size, the irregularity also increases, and the maximum size of the ice crystals produced can approach 1000 μm. For the analysis of ice crystal particle size distribution, two typical test conditions are selected. The MVD are 202.4 μm and 247.7 μm, and the MMD are 103.7 μm and 166.9 μm, respectively. Comparing the particle size distributions under these two conditions reveals that different particle size distributions can be achieved by adjusting the operating frequency of the grinder. Additionally, the IWC in these test conditions are 4.47 g/m^3 and 6.67 g/m^3, respectively. The fluctuations in IWC and number of particles over time are further analyzed. The result indicates that the concentration of ice crystals might be affected by the operating frequencies of the conveyor belt, grinder, and conveying fan, among other factors. Comprehensive research is required to investigate the interrelationships among these factors. Furthermore, this work demonstrates the significant potential of HACPI based on digital holography in measuring ice crystals in icing wind tunnels.

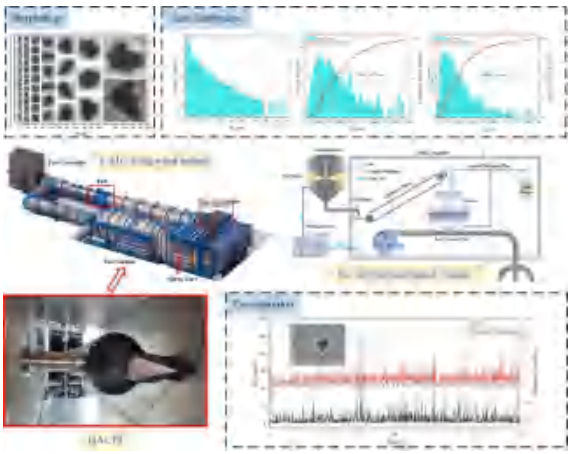


Figure 19 - The experimental setup and results

Online Measurement of Particulate Matter Concentration in Dilute Liquid-Solid Two-Phase Flow

Wenchao Gong[1,2], Rixin Xu[1,2], Wu Zhou[1,2*], Faquan Wang[3], Yu Li[3]
[1]School of Energy and Power Engineering, University of Shanghai for Science and Technology, Shanghai, China.
[2]Shanghai Key Laboratory of Multiphase Flow and Heat Transfer for Power Engineering, Shanghai, China.
[3]Aero Engine Corporation of China, Wuxi, China

Abstract
This paper developed an experimental system for concentration measuring of the solid particulate matter using the light extinction method. The system is calibrated in laboratory with certain particulate pollutants. The system was applied to particle concentration measurement in oil and the results are compared with those from weighing method, with differences less than 10%.

Keywords: Two-Phase Flow, Particle Concentration, Light Extinction Method

Introduction

The solid pollutants consists of Fe_3O_4, Fe_2O_3, dust , lint fibres and salted water with certain constant mass ratios 0.264mg/L, 1.321mg/L, 0.528 mg/L, 0.0264mg/L and 0.01% by volume [1], which is from with fuel oil in a 10 mm pipe. The light extinction measurement system comprises a spectrometer, an optical fibre, a collimating lens, a halogen lamp, and designed tooling for the measurement section. For comparison, samples were weighed when the flow was stable, and experiments were carried out at three different flow rates.

Methodology

The extinction method is used to measure solid pollutants by establishing a linear relationship between the extinction ratio and the mass concentration of particles[2-4], provided that the particle diameter and density are known. The measurement system was first calibrated and the results are shown in Eq.1.

$$ln(\frac{I_0}{I}) = 0.0133C + 0.0523 \quad (1)$$

Where I is the output light intensity, I_0 is the original light intensity, C is the measured concentration.

The application experiment was performed on aviation fuel anti-pollution test bench, as shown in Fig. 1.

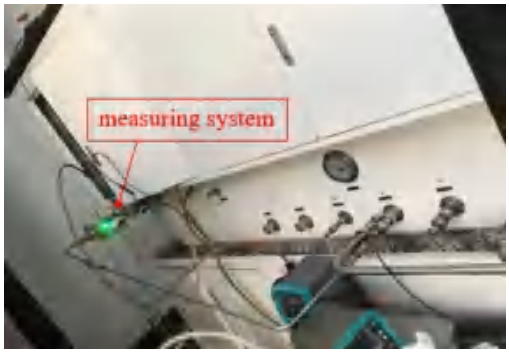


Figure 20 - Application test platform for fuel pollutant concentration

Results

The results of the on-line measurements are shown in Figure 2. The concentration of pollutants initially increases after injection and then stabilises. The flow rates for condition A and E are the same, and so are the flow rates for B and D. Points on the Figure that show sudden changes in concentration indicate ongoing sampling.

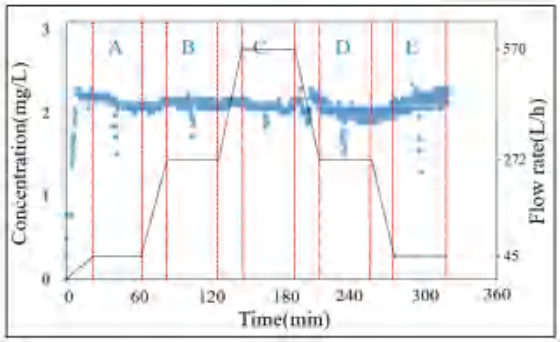


Figure 2 – Pollutants real-time measurement results for Φ10mm workpiece solids

The results of the measured pollutants concentrations at three different flow rates are shown in Table 1.

Table 5 - Table of important data

Flow point/ $L \cdot h^{-1}$	**Weighing method/ $mg \cdot h^{-1}$**	**Extinction method/ $mg \cdot h^{-1}$**	**Differences/ %**
45	2.42	2.21	-8.77
272	2.05	2.16	-5.37
570	2.08	2.12	-1.90

Conclusions

The extinction method can be used to on-line measurement of dilute particulate matter in two-phase flows in pipes, and the results do not differ by more than 10% from the weighing method.

References

[1] GJB 420B-2015, Classification of Solids Contamination in Aviation Working Fluids, Beijing: National Defense Industry Press, 2019.
[2] Allen T, Particle size measurement, Springer, 2013.
[3] MÄTZLER C, MATLAB Functions for Mie Scattering and Absorption, IAP Res Rep 2002–08(July 2002) 1139–1151.
[4] N G Khlebtsov, Determination of size and concentration of gold nanoparticles from extinction spectra, Analytical chemistry, 2008, 80(17): 6620-6625.

Investigation of fluidized bed wetting and drying process by process tomography combined with acoustic sensor

Haigang Wang
1. State Key Laboratory of Coal Conversion, Institute of Engineering Thermophysics, Chinese Academy of Sciences, Beijing 100190, China
2. School of Engineering Science, University of Chinese Academy of Sciences, Beijing 100049, China

To investigate the complex gas-solids flow characteristics in a spout-fluid bed with bafflers for wetting and drying, non-intrusive measurement technique, i.e. electrical capacitance tomography (ECT) combining with pressure and acoustic transmitters are used in this research. The proposed approach can collect acoustic and pressure signals and realize visualization in three flow regions separated by two bafflers synchronously. Based on ECT images and wavelet analysis, two typical flow state transitions in the wetting and drying process can be identified. Key process parameters including the particle-wall collision frequency and the particle-particle collision frequency, are given and analyzed. A key recurrence quantization parameter based on acoustic signal, i.e. Laminarity, is introduced and used to indicate the particle flowability. Laminarity combined with the capacitance signal can be used to indicated the particle moisture content and provide an accurate monitoring of de-fluidization process in the process.

Keywords: Fluidized bed coating, Process tomography, Acoustic sensor

Study on the characteristics of fine particle removal using surfactant-assisted spray

Hailin Gu[1,*], Jiaqi Guo[1], Jinqing Wang[1], Guangxue Zhang[1]
[1]China Jiliang University, Hangzhou, China, 310018, hlgu@cjlu.edu.cn

Abstract
Spraying technology is widely used in the fields of gas purification, and dust control. This study intends to use surfactants to regulate the atomization characteristics to improve spray uniformity and further explore its promotion effect on fine particle removal. An experiment is conducted to analyse the atomization characteristics of three surfactants solutions to figure out the effects of surfactant type and concentration. The results show that compared with deionized water, the addition of surfactants could significantly improve the spray uniformity, the overall droplet size of the spray decreases. The number of droplets of the three types of surfactant solutions peaks when the surfactant solution concentration reached the critical micelle concentration. In addition, the fine particulate removal experiments show that spraying with surfactant solutions can accelerate the removal rate of fine particulate.

Keywords: Spray; Surfactant; Fine particle; Droplet size

Introduction

Fine particulate matter ($PM_{2.5}$) from the combustion of fossil fuels can remain suspended in the air for long periods of time, causing serious environmental and health problems. Among the various dust removal techniques, spray scrubbing is an effective method. Moreover, relevant studies have found that the addition of surfactants can significantly improve the atomization performance of the solution. Therefore, this paper investigates the spraying characteristics of surfactant-containing solutions and explores their effectiveness in removing fine particulate matter.

Methodology

Three different surfactants were used for comparison, namely sodium dodecylbenzene sulfonate, cetyltrimethylammonium bromide, and tween 80. Fine particulate matter is obtained from smoke generated by wood combustion. Spray particle size measurement using phase Doppler velocity particle size analyzer, smoke particles transmittance measurement device for the laser power meter, by receiving the laser light intensity changes to calculate the transmittance, and then reflect the removal efficiency of fine particles.

Results

The results show that compared with deionized water, the addition of surfactants could significantly improve the spray uniformity, the overall droplet size of the spray decreases. The number of droplets of the three types of surfactant solutions peaks when the surfactant solution concentration reached the critical micelle concentration (CMC), which is taken as the optimal atomization concentration. The fine particulate removal effective is accelerated by the spraying with surfactant solutions.

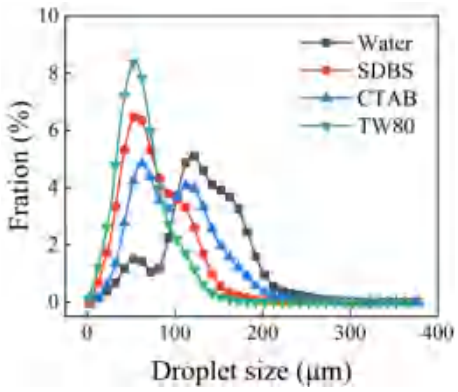


Figure 21 - Particle size distribution of different solution sprays

Conclusions

In this study, an experiment is conducted to analyse the atomization characteristics of three surfactants solutions, and the removal efficiency of fine particle observed to be accelerated by the surfactant-assisted spray.

Study on Measurement of Gas-Liquid Two-Phase Stratified Flow

Lide Fang, Bin Ge, Bangbang Han, Yue Feng, Lunsha Wang
Hebei University, Baoding, China

Abstract
Stratified flow is the basic flow pattern in gas-liquid two-phase flow. A better understanding of flow characteristics of stratified gas-liquid flow is of great significance for the design and operation of pipes and perhaps for the development of accurate flow model. In this study, the experiment is conducted in the standard circulation system of multiphase flow and combined with the Particle Image Velocimetry (PIV) system, the experiment was carried out under different flow conditions, and the distribution characteristics of the two-phase velocity of the cross-section and void fraction are studied. The optical distortion of pipe curvature and optical refraction is corrected by using the method of combining software and hardware. The velocity field of stratified flow at different flow points is calculated, and the velocity distribution law of the corrected stratified flow cross-section at different flow points of the pipe cross-section is studied. The flow characteristics of the cross-section under different condition are obtained, the accurate measurement of which is of great significance to analysis of stratified flow.

Keywords: Two-phase flow; Stratified flow; Particle Image Velocimetry; Void fraction; Cross-section velocity distribution

Introduction

Gas-liquid two-phase flow is widely encountered in many industrial production processes such as oil and gas industry, chemical industry and petroleum industry [1]. The void fraction and velocity field, as the key parameters in the process of gas-liquid flow, reflects the real proportion of liquid phase in the pipeline flow and has a significant impact on the flow pressure drop, phase separation in metering, and heat transfer characteristics in the industrial production process.

PIV is a non-invasive fluid measurement technology that provides qualitative and quantitative measurements of both global and local flow conditions. Ayati et al. [2] used the PIV technique to obtain flow parameters under stratified flow. Vollestad et al. [3] used PIV technology to study the gas phase velocity distribution and the gas phase flow phenomenon in the pipe under gas-liquid stratified flow. PIV technology provides more detailed information about the flow in the pipe.

Methodology

A series of experiments were carried out on a gas-liquid two-phase flow standard circulation facility, which is used for single-phase, two-phase, and multiphase experimental research. The main pipe section of the experiment consists of high transparency acrylic test pipe section (400 mm length, 50 mm inner diameter, and 5 mm wall thickness). The distance between the test section and the ahead/rear straight pipe section at the gas-liquid mixing point is 260D/166D respectively, which can ensure the full flow of fluid in the pipeline, and the fluid in the test section is not disturbed by the local resistance loss of the fluid flowing out of the back straight pipe section. Air and city water are used in the experiments. The liquid phase flow and gas phase flow are measured by liquid flowmeter and gas flowmeter. The experimental device is shown in Figure 1.

An optical correction box is installed outside the experimental test section and deionized water is added into it to reduce the optical distortion of the test section. Rhodamine B fluorescent particles with a particle size of 7 um were added as tracers in the liquid phase. The PIV system is used for measuring the test section. The system adopts a double pulse laser with

wavelength of 532 nm. Based on the principle similar to biological binocular vision, the two CCD cameras (IMPERX-B6640, 6600*4400 pixel) focus on the cross-section illuminated by the laser at the angle of the vertical optical correction box viewable window. The two cameras through synchronous controller connected with the double pulse laser, which adopts internal trigger mode. The liquid phase of stratified flow is shown in Figure 2.

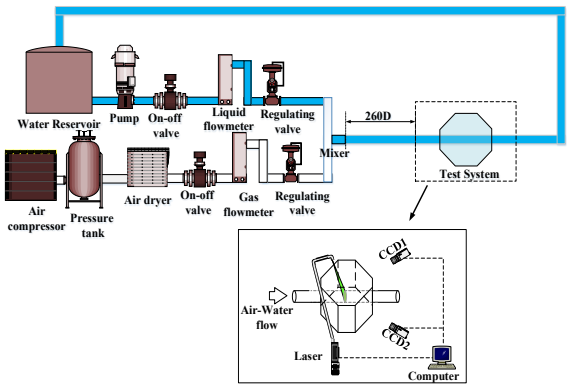


Figure 22 - System diagram of experimental device

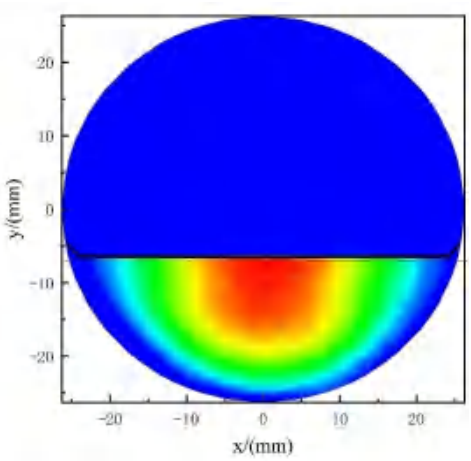


Figure 2 - Stratified flow cross-section

Conclusions

Stratified gas-liquid two-phase is the simplest flow pattern of two-phase flow, which is widely used in industry. The velocity field and void fraction of the two-phase flow can be directly obtained by PIV technology without affecting the internal flow field, and the flow parameters of the two-phase flow can be obtained more accurately.

Acknowledgements

This work is supported by the National Natural Science Foundation of China, China (62173122), Key Project of Natural Science Foundation of Hebei Province (F2021201031) and Beijing-Tianjin-Hebei Collaborative Innovation Community Construction Project (20540301D), Hebei Provincial Postgraduate Demonstration Course Project (KCJSX2021009).

References

[1] Mokhatab. S, Poe. WA, Speight. JG, Handbook of Natural Gas Transmission and Processing, Elsevier Ltd Oxford, 2012.

[2] Ayati. AA, Kolaas. J, Jensen. A, Johnson GW. A PIV investigation of stratified gas-liquid flow in a horizontal pipe. Int J Multiphase Flow, 55(2014) 129–143.
[3] Vollestad. P, Angheluta. L, Jensen. A. Experimental study of secondary flows above rough and flat interfaces in horizontal gas-liquid pipe flow, International Journal of Multiphase Flow, 125(2020) 103235.

Measurement of polydisperse solid-liquid suspensions using positron emission particle tracking

Kun Li1 , Hanqiao Che2 , Yang Liu3 , Chuankun Li1 , Ping Chen1 , Yan Han1
1. Shanxi Key Laboratory of Signal Capturing & Processing, North University of China, Taiyuan, 030051, China
2. School of Mechanical Engineering, Guangxi University, Nanning, Guangxi, 530004, China
3. Wuhan National Laboratory for Optoelectronics, Wuhan, 430074, China

Abstract
The flow dynamics of multi-component solid-liquid suspensions serve as a cornerstone in multiphase process equipment. The uniformity of suspension is defined not only by an approximately uniform solid concentration throughout the entire device but also by a uniform particle size distribution. Detailed experimental measurements of these flows suffered a major challenge because of the absence of non-optical high-spatiotemporal measurement techniques. However, a new protocol for 3D particle motion visualization has been developed since the emergence of positron emission particle tracking (PEPT), which provides non-invasive imaging for the 3D motion of powder, granular and particles. As PEPT is based on detecting γ photons, it has the characteristics of high penetration and anti-electromagnetic interference, meaning particle motions can be tracked inside large, dense, optically opaque systems.

For polydisperse solid-liquid suspensions in a fully-baffled stirred vessel, 20wt% glass particles with five different sizes were suspended in NaCl solution. They were agitated at a just-suspension regime using a down-pumping six-blade 45° pitched-turbine (PBTD). As shown in Fig. 1, PEPT measurements of liquid phase and five solid components were conducted independently using different representative PEPT tracers, providing 3D Lagrangian trajectories (*t, x, y, z*) with high spatial resolution (mm) and temporal resolution (ms). Then, Lagrangian velocities are calculated from the time derivative of PEPT trajectories. Using a predefined mesh system, the Eulerian velocities are derived by averaging Lagrangian velocities of tracer locations within each cell. 3D velocity fields of liquid and solid components are determined independently (Fig. 2), showing a distinctive hydrodynamics difference between different solid particles and liquid phase.
Keywords: Positron emission particle tracking, Particle motion, Multiphase flow measurement, Opaque flows.

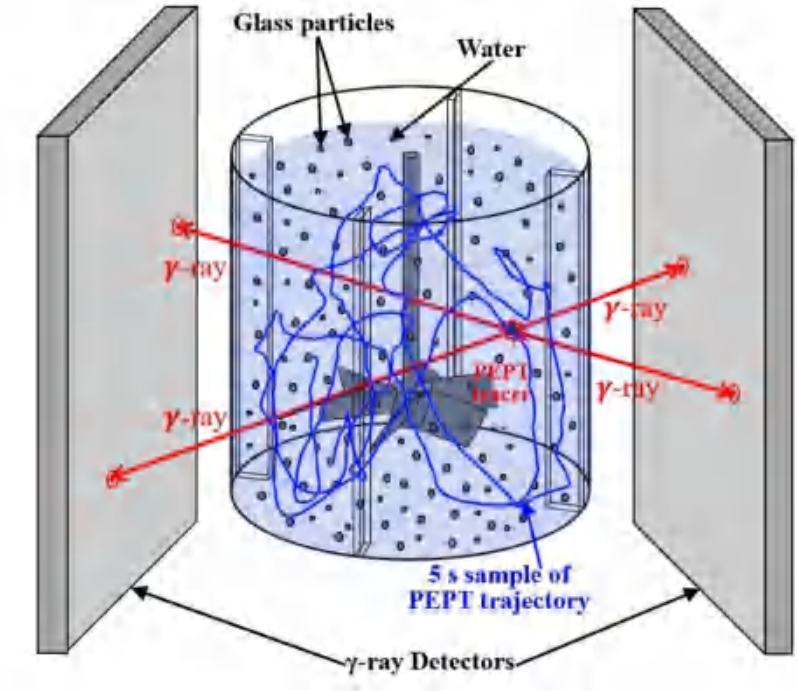


Figure 1 – PEPT experimental setup

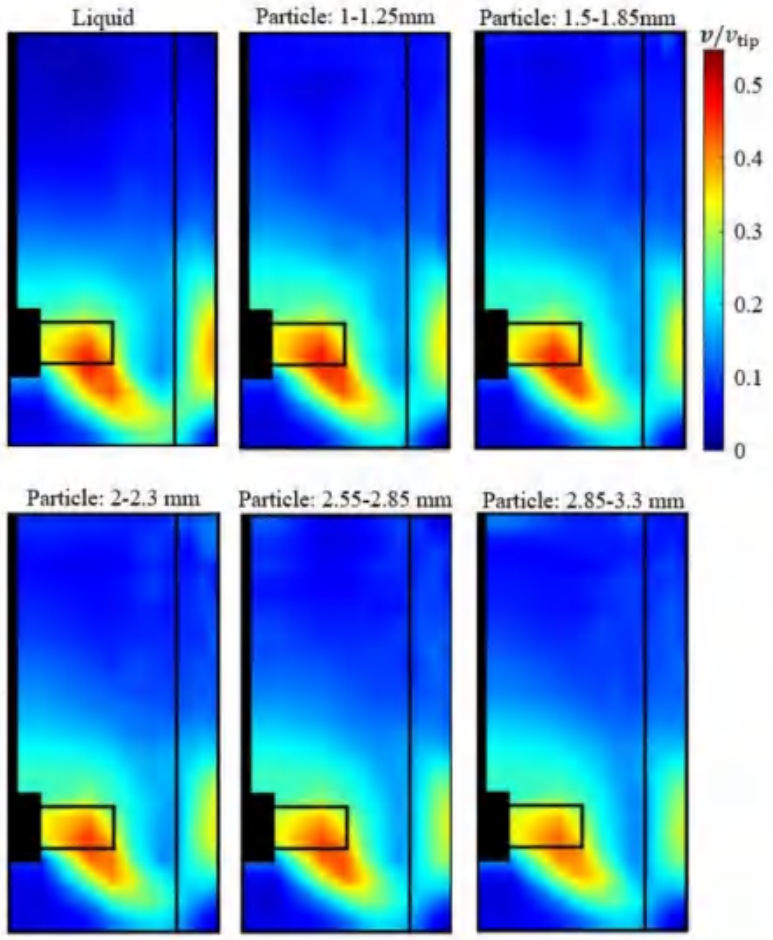


Figure 2 – Velocity fields of liquid phase and solid components.

Removal of fine seaweed from wastewater by means of cylindrical swirl flow and vibration

Hiroaki Tsubone, Daisaku Ishibashi
National Institute of Technology, Ariake College, Omuta, Japan

Abstract
A new separator, which can economically and continuously remove the fine seaweed from the wastewater by means of cylindrical swirl flow and vibration, has been proposed by the authors. In this paper, the characteristics of the removal performance of the seaweed from the wastewater and the effect of mesh size, total volume flow rate and vibration frequency were experimentally clarified.

Keywords: Seaweed, Wastewater, Removal Performance, Swirl Flow, Frequency

Introduction

When commercial dried seaweeds are processed, large amount of wastewater are discharged from an automatic production machine into canals, rivers and seas because no draining standard for the seaweed wastewater has been mandated in Japan. It has caused some environmental problem such as water colour changing, deposition on the bottom of the canals and giving off a bad smell [1]. So, a new separator, which can economically and continuously remove the fine seaweed from the canals by means of cylindrical swirl flow and vibration, has been proposed by the authors.

Experiments

Figure 1 shows the details of the seaweed separator used in this study. As the test fluid, quasi-seaweed waste water, which made of commercial dried seaweed sheets and tap water. The flow of the test fluid became swirl flow in the inner pipe. The swirl flow went into a separation section made of a cylindrical steel mesh and the water of the test fluid flowed through the mesh into an outer pipe by centrifugal force and negative pressure. The majority of the fine seaweed fell down through the inner pipe into a container. In the experiment, removal performance of the seaweed from the quasi-seaweed waste water was evaluated by the volume flow rate fraction.

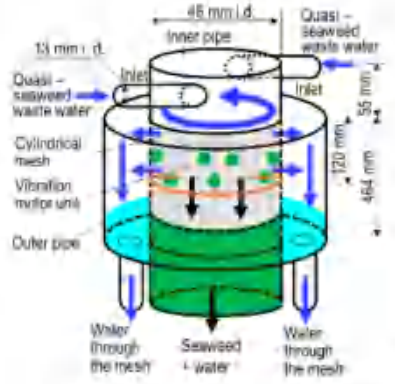


Figure 1 – Details of seaweed separator used in this study

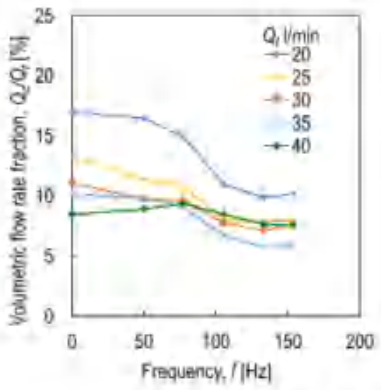


Figure 2 – Relationship between volumetric flow rate fraction and

Results

Figure 2 shows the experimental results of volumetric flow rate fraction. The volumetric flow rate fraction basically decreased with increasing of frequency. In addition, it also increased with decreasing of mesh size. However, these tendencies and/or values were different depending on total volumetric flow rate.

Conclusions

In this study, the characteristics of removal performance for total volumetric flow rate, mesh size and vibration were experimentally investigated and the effects of some parameters were clarified. Particularly, the volumetric flow rate fraction of 6% was achieved at a total volume flow rate of 40 l/min, a frequency of 150 Hz and mesh size of No. 200.

Acknowledgements

We are grateful to support by Harada Memorial Foundation for scientific research.

References

[1] H. Tsubone, M. Shimomura and S. Takesue, Study on Seaweed Removal Efficiency from the Wastewater by Swirl Flow Separator, Proc. of International Conference on Multiphase Flow 2016, Firenze, Italy, May 22nd -27th , 2016.

Coupling Simulation of Holdup and Dielectric Constant Distribution in Electrical Capacitance Tomography

Xiaojie Wang, Lu Ma*,Yi Han
Xi'an jiaotong University, Xi'an, China

Abstract
Electrical capacitive tomography, as an electrical process tomography technology, is widely used in the field of industrial multiphase flow for its many advantages. The key of electrical capacitance tomography is to reconstruct the dielectric constant of the measured region. In this paper, we will explore the relation of permittivity and different multiphase flow holdup by using theoretical derivation and coupling simulation.
Keywords: **Electrical Capacitive Tomography, Multiphase Flow, Coupling Simulation**

Introduction

Electrical capacitance tomography (ECT) is a non-invasive technique, which can reconstruct the permittivity distribution of dialect materials. ECT can provide the measurements of phase volume fraction, and it requires suitable physical models to interpret the link between dielectric constant and concentration.

Methodology

A Principle

The principal diagram of the model is shown in Figure 1[1,2]. This model will explore the relationship between the dielectric constant and concentration in oil and gas two-phase flow.
When the dielectric material is distributed as plates parallel to the electrodes, it called the "series" model.

$$\varepsilon_m = (\varepsilon_1 \times \varepsilon_2)/(\varepsilon_1 \times v + \varepsilon_2 \times (1 - v)) \quad (1)$$

When the dielectric material is distributed as parallel plates normal to the capacitor plates, it called the "parallel" model.

$$\varepsilon_m = \varepsilon_1 \times (1 - v) + \varepsilon_2 \times v \quad (2)$$

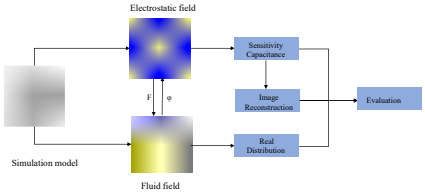


Figure 23 – Principle of coupling simulation

B Coupling Simulation

To explore the relationship between holdup and dielectric constant under different flow patterns, three flow patterns including stratified flow, annular flow and bubbly flow with obvious holdup differences will be studied by model simulation in this paper.
In the simulation procedure, the flowing liquid flows in the pipeline at a fixed speed. The model for two pairs of 8-electrode ECT sensor with three shield layers and cyclic excitation strategy created by COMSOL, as the Figure 2 show, have suitable mesh to guarantee the capacitances and holdup calculated precision.



Figure 2 – Coupling model of ECT

Conclusions

Through model simulation and experiment, the mechanism between holdup and dielectric constants calculated by ECT in different flow patterns can be improved the image reconstruction quality in the case of two-phase flow.

Acknowledgements

Thanks for the Prof. Lu Ma's helpful directions in model building and significant research method.

References

[1] Ye J, Yang W ,Wang C .Investigation of Spatial Resolution of Electrical Capacitance Tomography Based on Coupling Simulation[J]. IEEE Transactions on Instrumentation and Measurement, 2020, PP(99):1-1.

[2] Ye J ,Wang H ,Li Y , et al. Coupling of Fluid Field and Electrostatic Field for Electrical Capacitance Tomography. [J]. IEEE Trans. Instrumentation and Measurement, 2015, 64(12):3334-3353.

Experimental study on the variation of microbubble size in a long vertical pipe

Yuanbiao Hu, Wuguang Chen, Guangyuan Huang, Junlian Yin, Dezhong Wang
Shanghai Jiao Tong University, Shanghai, Shanghai

Abstract
This study conducted experimental research on the size variation of microbubbles in a long vertical pipeline. High-speed cameras were used to capture bubble images. Gaussian high-pass filtering and Hough transform methods were introduced for processing out-of-focus bubbles. The experimental results indicate that with the increase in liquid phase velocity, the trend of microbubble size variation shifts from a decrease to an increase.
Keywords: Microbubble, Image Processing, Bubble Size Distribution

Introduction

There is a relative scarcity of experimental observations on the variation of microbubble size during the flow process. The applicability of the conventional Population Balance Model model for predicting the changes in microbubble size also requires validation with experimental data. Therefore, this paper conducts an experimental study on the size variation of microbubbles in a long vertical pipeline.

Methodology

The experiment employed a rod-shaped sparger of porous media with an average pore size of 0.5 μm. The pipeline had an inner diameter of 50 mm. High-speed cameras were placed at distances of 200mm (L/D=4) and 3500mm (L/D=70) downstream of the bubble generator, respectively. Different gas and liquid superficial velocities (jg:0.00085-0.01697 m/s, jl:1.15-2.93 m/s) were studied.

The captured images contained out-of-focus bubbles, leading to interference in bubble recognition. Therefore, we introduced the Gaussian high-pass filtering algorithm and Hough transform to eliminate interference from the boundaries of out-of-focus bubbles. The image processing workflow is illustrated in Figure 1.

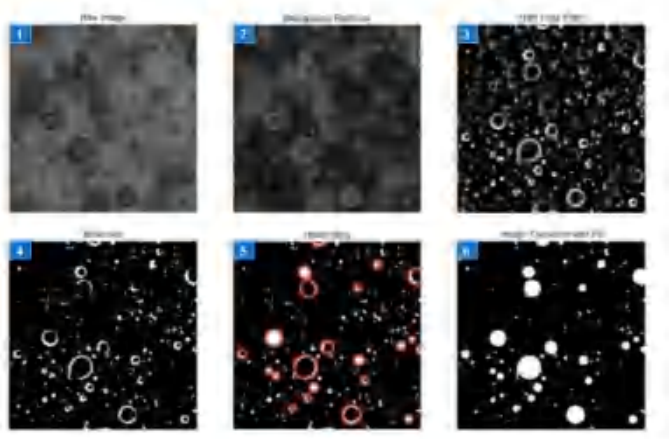


Figure 1 – Workflow of Image Processing

The Sauter mean diameters of bubbles under different operating conditions are statistically obtained and presented in Figure 2. It can be observed that at lower gas void fractions, the bubble size remains relatively constant. However, at higher gas void fractions, the bubble size shows a decreasing trend in conditions with low liquid phase velocity. Conversely, in conditions with high liquid superficial velocity, the bubble size exhibits an increasing trend.

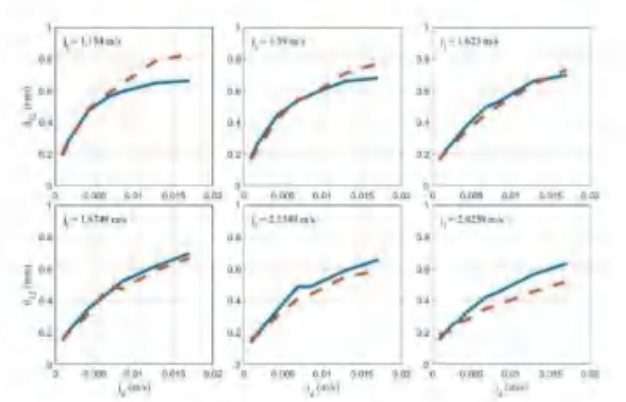


Figure 2 – Sauter Mean Diameter (Red Dashed Line: L/D=4, Blue Solid Line: L/D=70)

Conclusions

This paper conducted a study on the size variation of microbubbles in a long vertical pipeline using high-speed cameras combined with image processing algorithms. The experimental results indicate that with the increase in liquid phase velocity, the trend of microbubble size variation shifts from a decrease to an increase.

A real-time magnetic induction tomography system using differential coils printed by flex circuit boards

Zheng Sun, Lu Ma
Xi'an jiaotong University,Xi'an,China

Abstract
Compared with the traditional imaging mode as one coil excites, one coil receives, it is generally believed that the phase sensitivity to the conductivity would increase by using gradiometer coils[1]. The eight-channel MIT system MIT hardware is based on a dual-channel data acquisition board and a 8-channel FlexRes oscilloscope,the PicoScope 6824E.The PicoScope 6824E also functions as the 10-MHz excitation source.Corresponding to the simulation model, the actual experimental test was carried out, and the corresponding data were obtained .
Keywords: Differential coils,inverse problem, magnetic induction tomography.

Introduction

Magnetic induction tomography (MIT, also known as electromagnetic induction tomography (EMT)) is a technique for imaging the passive electromagnetic properties of an object. In this paper,the differential coils that we use have four joints,including two exciting joints and two receiving joints.

Methodology

I.MEASUREMENT PRINCIPLE

There are two contributions to the signal detected by the sensing coil in MIT. The first is directly induced by the field from the excitation coil (the primary signal, V). The voltages induced by the secondary field in the sensing coils can be expressed by a quasi-static approximation (1):

$$\frac{\Delta V}{V} = \boldsymbol{Q\omega\mu_0[\omega\varepsilon_0(\varepsilon_r - 1) - i\sigma] + R(\mu_r - 1)} \qquad (1)$$

II. SYSTEM DESIGN

According to content mentioned above,we designed 8 flexible coils with 8 turns,the inner and outer diameters of which are 0.0035m and 0.008m,as shown in figure 1.

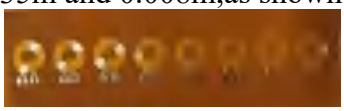


FIGURE 1. The 8-channel gradiometer sensor array

The MIT system(see Fig.2) comprises four subsystems:
(1) the sensor array consisting of 8 gradiometer coils;
(2) the excitation circuits to drive gradiometer coils;
(3) the signal conditioning circuit;
(4) the measurement and channel switching module, including a FPGA board and a host computer.



FIGURE 2. The 8-channel MIT system using differential coils
(a) diagram of one differential coil (b)MIT system controlled by FPGA

III. COMSOL SIMULATIONS

We also construct a comsol model containing the differential coil with 8 turns,excited at 500mA and 10-MHz.

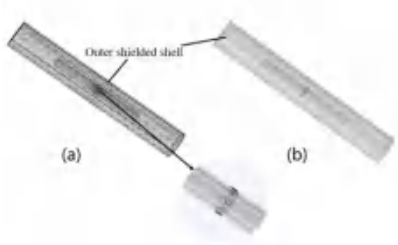


FIGURE 4. The COMSOL model for MIT sensitivity maps calculation. (a) Model mesh diagram (b) Model geometry

Conclusions

With a real-time magnetic induction tomography system,the multiphase flow with conductivity under 10s/m applied at industrial environment could be showed.But there is still a lot of work to do to improve the the resolution of the system.

References

[1] J. Xiang, Y. Dong, M. Zhang and Y. Li, Design of a Magnetic Induction Tomography System by Gradiometer Coils for Conductive Fluid Imaging,*IEEE* Access,vol.7(2019)pp. 56733-56744.

[2]Ma L, Soleimani M. Magnetic induction tomography methods and applications: A review[J]. Measurement Science and Technology, 2017, 28(7): 072001.

Parallel Session V-1: Topic 9- Phase change heat and mass transfer

Breakup Dynamics of Droplets of Complex Fluids

Zhizhao Che
Tianjin University, Tianjin, China

Abstract
Droplet breakup is a fundamental process in fluid atomization and is ubiquitous in numerous applications such as spray combustion, spray coating, spray drying, and pesticide spraying. Understanding and improving the atomization process from the perspective of droplet breakup is an important strategy to optimize the related applications. For fluid atomization in different applications, the fluid properties not only vary dramatically but also have obvious non-Newtonian characteristics, which complicate the atomization processes. These breakup processes are either difficult to control or their breakup mechanisms are unclear. In this talk, I will discuss the breakup process of complex fluid droplets, including the breakup of droplets in high-speed airflow and micro-explosive in high-temperature environments, such as high-viscosity droplets, non-Newtonian fluid droplets, suspension droplets, and emulsion droplets.

Keywords: Droplet, Breakup, Complex Fluid, Atomization

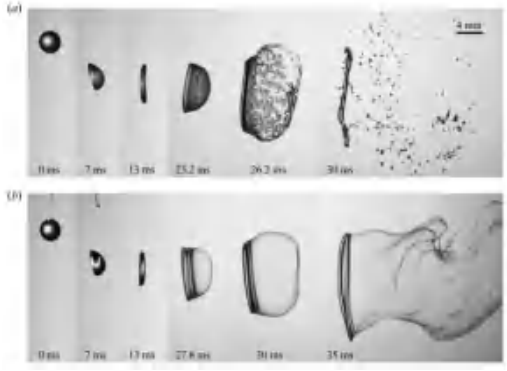


Figure 1. Image sequences of droplet breakup in the bag breakup mode: (a) suspension droplet, (b) silicone oil droplet.

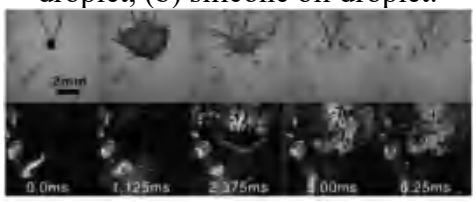


Figure 2. Mist formation during micro-explosion emulsion droplets.

References

[1] Z Xu, T Wang, Z Che. Breakup of particle-laden droplets in airflow. Journal of Fluid Mechanics. 974, A42.
[2] Z Xu, T Wang, Z Che. Droplet breakup in airflow with strong shear effect. Journal of Fluid Mechanics, 941, A54.
[3] Z Xu, Y Zhang, T Wang, Z Che. Deformation and breakup of compound droplets in airflow. Journal of Colloid and Interface Science. 653, 517-527.
[4] Z Xu, T Wang, Z Che. Transitions of breakup regimes for viscous droplets in airflow. Fuel, 339, 127355.
[5] Y Li, Z Xu, X Peng, T Wang, Z Che. Numerical simulation of secondary breakup of shear-thinning droplets. Physics of Fluids, 35, 012103.

[6] Z Xu, T Wang, Z Che. Droplet deformation and breakup in shear flow of air. Physics of Fluids, 32, 052109.
[7] H Zhang, Z Lu, T Wang, Z Che. Micro-explosion of emulsion droplets with nanoparticles at high temperature. International Journal of Heat and Mass Transfer. 219, 124851.
[8] H Zhang, Z Lu, T Wang, Z Che. Mist formation during micro-explosion of emulsion droplets. Fuel, 339, 127350.
[9] S Shen, K Sun, Z Che, T Wang, M Jia, J Cai. Mechanism of micro-explosion of water-in-oil emulsified fuel droplet and its effect on soot generation. Energy, 191, 116488.
[10] S Shen, K Sun, Z Che, T Wang, M Jia. Puffing and micro-explosion of heated droplets for homogeneous ethanol-propanol-hexadecane fuel and micro-emulsified ethanol-biodiesel-hexadecane fuel. Applied Thermal Engineering, 165, 114537.
[11] S Shen, K Sun, Z Che, T Wang, M Jia, J Cai. An experimental investigation of the heating behaviors of droplets of emulsified fuels at high temperature. Applied Thermal Engineering, 161, 114059.

Stall Mechanism of Supercritical Carbon Dioxide Centrifugal Compressor with Vaneless Diffuser

Zhang Lei
North China Electric Power University

Abstract

Supercritical carbon dioxide (s-CO_2) Brayton cycle power generation systems promise highly efficient thermoelectric conversion and hold extensive application prospects in areas such as high-temperature solar-thermal power generation, next-generation nuclear power, waste heat power generation, and advanced ship propulsion systems, and recognized as the most promising next-generation advanced power cycle, the stability of the centrifugal compressor, a key component of the sCO2 Brayton cycle, plays a crucial role in ensuring the overall safety of the system. However, the distinct thermo-physical properties of CO2 near the critical point and the size effects inherent in sCO2 compressors present significant challenges to the operational stability of the compressor.

This presentation will delve into a pivotal scientific question concerning the mechanism of rotating stall induced by real gas effects and size effects in sCO2 centrifugal compressors equipped with vaneless diffuser. The focus will be on elucidating the influencing mechanisms of inter-blade gap leakage flow, local condensation phenomena, three-dimensional distorted boundary layers within the diffuser, and the behavior of supercritical core flow in initiating compressor stall.

Enhanced Condensation Droplet Growth and Shedding Performances under Electrowetting-on-Dielectric (EWOD)

Run YAN1* , Lu LIU1 , Chung-Lung CHEN2
1North China Electric Power University, Baoding, Hebei Province, China
2University of Missouri-Columbia, Columbia, Missouri, USA
*Corresponding Author: yanrun@ncepu.edu.cn

Abstract

A condensation surface coupling with the electrowetting-on-dielectric (EWOD) approach is presented in this study. The EWOD device was designed to be double-layer electrode with the top layer being positive and the bottom layer being grounded. The applied voltage ranged from direct current (DC) to alternating current (AC). By applying an electric field the device, the wettability of the affected areas is altered from hydrophobic to hydrophilic, which promotes droplet nucleation and growth, thereby improving condensation rate. Results revealed that under 20V, 40V, and 60V DC-EWOD, the collected condensate was 138.96%, 171.87%, and 220.43% of the No-EWOD devices, respectively. Different frequency induced different droplet growing performances under EWOD due to two oscillation modes: contact-angle-fully-recover mode and contact-angle-partially-recover mode. The two modes induced distinct droplet coalescence mechanisms and distribution patterns. Compared with low frequency cases, higher frequency all showed higher shedding and condensation rate due to the more vigorous droplet dynamics and lower surface hysteresis. EWOD provided an active and reversible way to interfere with droplet dynamics, and promote droplet growth and coalescence, which demonstrated great potential for future applications in droplet control and condensation enhancement.

Keywords: Electrowetting-on-Dielectric (EWOD), Condensation Droplet Dynamics, Droplet Growth, Droplet Shedding, Condensation Enhancement

Introduction

Condensation serves as an efficient phase change heat transfer technique in various applications, such as aerospace engineering, seawater desalination, electronic industry, building energy conservation, waste heat recovery etc. One strength of this process is that condensation releases its large amount of energy via latent heat by very small temperature differences. Therefore, enhancing condensation heat transfer is one of the crucial research topics for researchers in the field of phase change heat transfer. Many approaches have been promoted to improve condensation rate, such as surfaces with superhydrophobicity and wettability gradient etc. Compared with all these passive approaches, EWOD provided an alternative choice to control surface wettability gradient, with the advantages of active and reversible control. This study discussed on a double-layer electrode EWOD device serving as a condensing surface and tested the droplet dynamics under EWOD. Results revealed an inspiring increment in droplet growth and shedding.

Methodology and Results

The substrate is a 4-inch wafer with a 100 nm silicon nitride (deposited via LPCVD). On top of the silicon nitride layer, 100 nm Au metal was deposited with E-beam. Next, a 150 nm layer of silicon nitride was deposited on the patterned substrate with ICPCVD. Then a 60nm thick Teflon layer was spin coated on the silicon nitride to serve as a hydrophobic condensing surface. The detailed information is depicted in Figure 1.

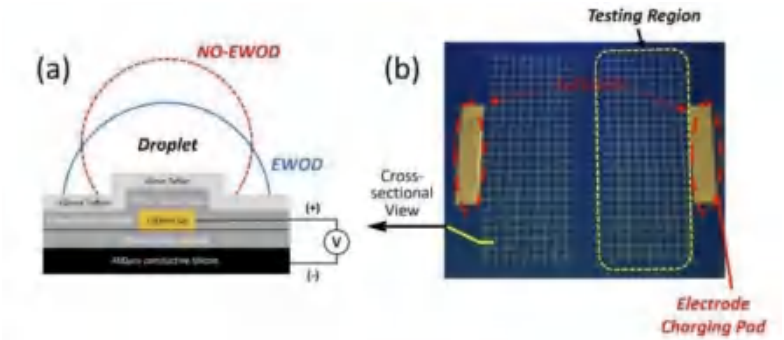


Figure 1 – (a) Schematic diagram of the EWOD sample in this study, drawing not to scale. (b) Top view of the 1mm-by-1mm grid sample. The width of the electrode wire is 50μm.

Then the experiment was conducted under moist air flow and then under steam flow. Side-by-side experiments were carried out to measure the water collection rate.
Results revealed that Results revealed that under 20V, 40V, and 60V DC-EWOD, the collected condensate was 138.96%, 171.87%, and 220.43% of the No-EWOD devices, respectively, under an 8 mins moist air flow testing period. Besides, under the same testing condition, different droplet growth rate and distribution trend was visualized under No-EWOD, DC-EWOD and AC-EWOD cases, as shown in Figure 2a. For the grid wire pattern, the No-EWOD showed a slow droplet growth rate and random distribution; droplets were found to distribute inside the grid under DC-EWOD effect; while the droplets were observed to sit on the intersections or on the wire. This was due to the different growing mode under different frequencies of the applied voltages. In the low-frequency AC and DC cases, droplets oscillated in a contact-angle-fully-recover mode; however, in the high-frequency AC cases, droplets oscillated in a contact-angle-partially-recover mode. But compared with the low-frequency AC cases, the water collection rate was found higher due to the more rigorous droplet dynamics along with lower surface hysteresis. This provides insightful possible solutions for condensation enhancement studies.

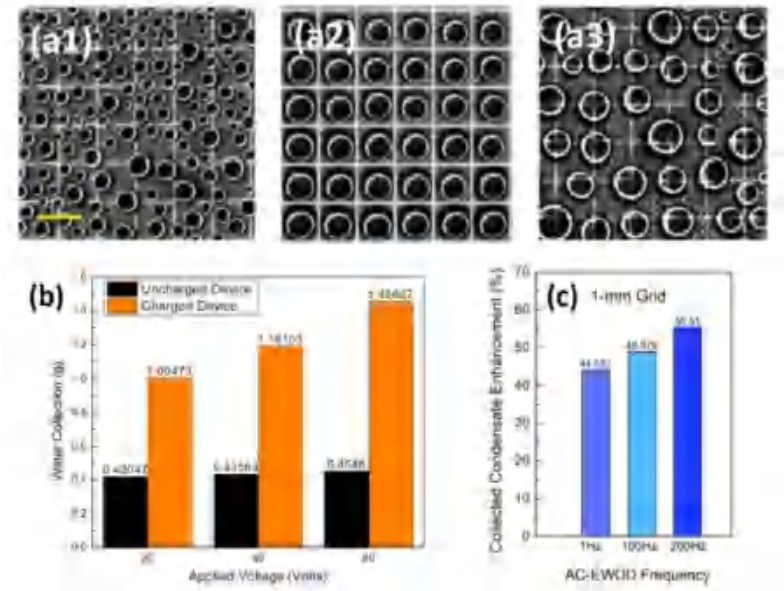


Figure 2 – (a1) Droplet distribution without EWOD, (a2) Droplet distribution under 40V DC-EWOD, (a3) Droplet distribution under 40V AC-EWOD (500Hz). (b) Comparison of EWOD and No-EWOD surfaces on water harvesting. (c) Condensate collection rate comparison under 1Hz, 10Hz and 100Hz AC-EWOD.

Conclusions

This study provided meaningful insights into actively and reversibly interfering droplet dynamics, and purposely controlling (either promote or weaken) condensation rate with the electric field. It indicated the feasibility of further investigating topics of EWOD effect on condensation heat transfer such as new EWOD designs, parametric and optimization studies, theoretical modelling, etc., which also showed great potential for future applications on condensation droplet control, overall condensation enhancement, and energy savings.

Acknowledgements

The organizers would be grateful if you could follow this template in preparing your extended abstract. The authors would like to acknowledge the support from NASA 80NSSC18K1665, the Fundamental Research Funds for the Central Universities, China (2023MS120) and the Natural Science Foundation of Hebei Province, China (Grant No. E2023502054).

Shadowgraphy for the liquid film dynamics in spray cooling under normal and reduced gravity

Xiao Zhao[a], Yin Chen[a, b], Zhuqiang Yang[b], Wangfang Du[a], Kai Li[a], Jianfu Zhao[a, c]
[a] CAS Key Laboratory of Microgravity, Institute of Mechanics, Chinese Academy of Sciences. Beijing, PR China.
[b] Liaoning Key Laboratory of Complex Energy Conversion and Utilisation, School of Energy and Power Engineering, Dalian University of Technology, Dalian 116024, PR China.
[c] School of Engineering Science, University of Chinese Academy of Sciences. Beijing, PR China.
E-mail address for the corresponding authors: xiaozhao@imech.ac.cn (X. Zhao)

Abstract
While liquid film morphologies of spray cooling have been investigated in detail, comparatively little is known about how the liquid films evolve on the surface, owing to the strong interaction and disturbance between atomised droplets and thin films with high turbulence. In this study, the shadowgraphy for liquid film dynamics including the measurement design and the imaging processing method were proposed. The liquid film dynamics and heat transfer characteristics of HFE-7100 spray on a smooth and roughness silicon surface in microgravity were quantitatively captured, including the film morphology, wetted area, equivalent diameter and the velocity under different inlet pressures and heat fluxes.

Keywords: Spray Cooling, Liquid Film Flow, Shadowgraphy

Introduction

Measurement of liquid film dynamics of spray cooling involves complex factors including the shutter speed, aperture, intensity of light source and the surface reflective characteristic. In microgravity, the dominance of tension introduces a new problem that the residual liquid (unused or condensed coolant) would adhere to the inner wall and climb up along it, implying that the optical path would be blocked by the uprising liquid film.

Methodology

A special porous structure made of aluminium alloy was designed to solve this problem. In normal gravity, the residual sprays were collected by the porous structure and flows down to the bottom surface in an organized way. While in microgravity, most of the residual sprays were collected by the porous structure and then further stored inside it, which greatly reduced the liquid at the bottom of the spray chamber and the inner glass wall. Beyond expectation, the strong interaction and disturbance between atomised droplets and thin films (e.g., the rebounded atomized droplets) were greatly suppressed. This observably improved the resolution of visual images and clearer film dynamics were firstly obtained than ever before.

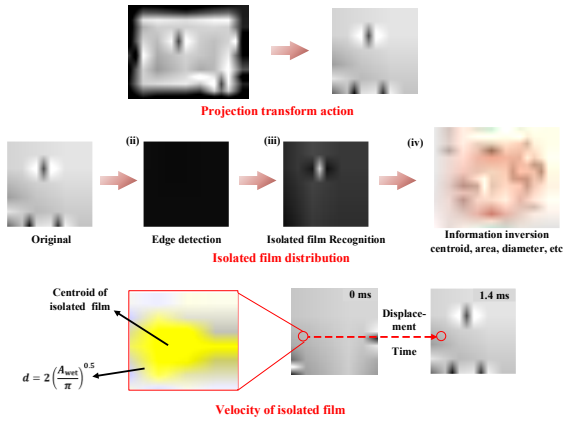


Figure 24 Shadowgraphy for liquid film dynamics

Acknowledgements
This work was supported by the National Natural Science Foundation of China (52106077), the Young Elite Scientists Sponsorship Program by CAST (2022QNRC001).

References
[1] O. Kyriopoulos, Gravity effect on liquid film hydrodynamics and spray cooling, Technische Universität, Darmstadt, 2010.

Experimental investigation of the evaporation characteristics of R1336mzz(Z) droplet at elevated temperature and pressure

Jing Yin, Zhi-Fu Zhou*
State Key Laboratory of Multiphase Flow in Power Engineering, Xi'an Jiaotong University, Xi'an 710049, China
*Corresponding author: zfzhou@mail.xjtu.edu.cn

Abstract
R1336mzz(Z) is a low-global-warming-potential (GWP) refrigerant, which has great application potential in the spray cooling system of electronic equipment. The investigation on the evaporation characteristics of a single cryogen droplet eliminates the uncertainty caused by the collision and fusion of droplets in spray, which could provide the knowledge basis for spray cooling. Therefore, this study experimentally investigates the effect of ambient temperature on the evaporation characteristics of R1336mzz(Z) droplet using the fiber-suspended technique. Two ambient pressures of 0.1 MPa and 2.0 MPa are selected. The ambient temperature ranges from 50 ºC to 250 ºC. It is found that elevated temperature promotes the heating and evaporation of R1336mzz(Z) droplet. Two quasi-steady periods and one turning point are observed on the droplet normalized squared diameter (d^2/d_0^2) curves at 0.1 MPa. This is attributed to the moisture condensation on the surface of an evaporating droplet of R1336mzz(Z). Moreover, a continuous increase in droplet inner temperature (T_d) is observed, and its trend exhibits a three-stage characteristic, including an extremely slow rise, a rapid rise and then another slow rise stages. The first turning point of T_d curve corresponds to the turning point of d^2/d_0^2 curve. However, under the condition of 2.0 MPa, there is no such turning point in the d^2/d_0^2 curve and d^2/d_0^2 decreases smoothly. This is because the condensation temperature of water vapor also increases as the ambient pressure increases. At 2.0 MPa, T_d increases monotonically during the entire evaporation process, and its slope becomes gentle over time.

Keywords: Evaporation characteristics, R1336mzz(Z), Droplet suspension experiment, Spray cooling

Introduction

Spray cooling is considered as one of the most effective cooling technologies in the field of electronic cooling and has attracted widespread attention recently. The mechanism of the spray cooling is quite complicated. However, the essence of spray atomization is to change the continuous liquid into dispersed droplets. Therefore, the research on the evaporation of a single cryogen droplet excludes the uncertainty arising from the collision and fusion of, which is beneficial for investigating the mechanism behind the spray cooling. In the last several decades, the fiber-suspended droplet technique has been widely employed to experimentally investigate the characteristics of isolated droplet evaporation. The recent experimental researches of droplet evaporation focus on the high-boiling point fuel droplets, including alcohol [1], diesel [2], biodiesel [3-6], nano-fuel [7, 8], emulsion fuel [9-12], and so on. Due to the much difficulty in producing individual liquid droplet of low-boiling cryogens, there is currently no available literature discussing the cryogen droplet evaporation characteristics through experiments.

To address the global challenge of climate change, olefin refrigerants with zero ozone depletion potential (ODP) and low global warming potential (GWP) have gained significant attention. Among them, R1336mzz (Z), as a medium saturation-temperature refrigerant, has excellent thermal performance, non-flammable, low-toxic, and environmentally friendly [13-15]. Thus, it has a good application prospect in spray cooling system for thermal control [16]. Motivated in this regard, the droplet evaporation characteristics of R1336mzz(Z) are experimentally investigated by the fiber-suspended droplet technique in this study. An individual R1336mzz(Z)

droplet was suspended at a thermocouple tip with 50 μm diameter, which could obtain the synchronous measurement of droplet temperature and images to analyze the effect of ambient temperature. These results could improve our understanding of the complex spray cooling phenomena.

Experimental apparatus and methods

The experimental apparatus and method are the same as that used in the previous research [17, 18]. Fig. 1 shows the schematic diagram of droplet evaporation experimental apparatus. The experimental apparatus is made up of four main parts: pressure control system, heating control system, droplet generation and transmission system, and data acquisition system. The pressure control system primarily contains a cylindrical pressure vessel, a pressure sensor, a nitrogen cylinder and so on. The heating control system includes a heating furnace, a temperature feedback controller and a temperature sensor. The temperature of the heating furnace can be regulated to a maximum value of 700 °C, with an accuracy of ±0.1 °C. The droplet generation and transmission system mainly consists of a K-type thermocouple wire, a high-pressure syringe pump, an alumina ceramic support, a needle and two sets of stepper motors. The data acquisition system consists of a computer, a NI DAQ system, a LED light source, and a high-speed camera. The high-speed camera (Photron brand Fastcam SA-Z) is matched with a micro-lens (Nikon AF Micro Nikkor 105mm f/2.8D). The frame rate of the high-speed camera is set between 50 and 1000 fps depending on the test conditions, and the resolution is 1024×1024 pixels. The thermocouple tip positioned inside the droplet is used to record the temperature variation of the droplet during evaporation.

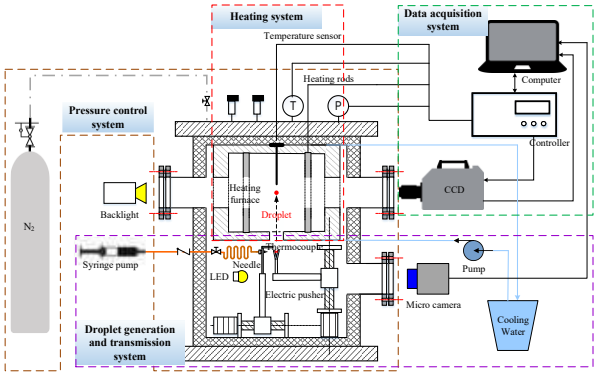


Figure 25 - Schematic diagram of the experimental equipment for single-droplet evaporation

The experiment process consists of the following steps. Initially, the pressure vessel is purged by pressurized dry nitrogen which refreshes the environment of droplet evaporation. The pressure and the inner temperature of the furnace are maintained at the desired level. After that, turn on the high-speed camera. Through the stepper motors, a droplet is produced and suspended at the tip of the thermocouple wire, then is transferred to the final location. Once the droplet reaches the predetermined position, the droplet image and internal temperature are synchronously recorded and saved to the computer. To extract the evolution of droplet diameter during evaporation from the captured images, a flexible image-processing code was executed using MATLAB program. Each group of experiments was repeated at least 5 times under the same environmental conditions to ensure the accuracy and reliability of the results.

Results and discussion

The single droplet evaporation experiments for R1336mzz(Z) are performed at different ambient temperatures under ambient pressure of 0.1 MPa and 2.0 MPa. The ambient

temperature has varied from 50 ºC to 250 ºC in 50 ºC increments. The droplet initial diameters were carefully maintained around 0.7 mm in this work. Since it is too hard to obtain fuel droplets with precisely the same initial size in all experiments, the droplet diameter and evaporation time are normalized by the initial droplet squared diameter to minimize the effect of droplet initial size on the evaporation in the following analysis. Fig. 2 exhibits the variation of droplet normalized squared diameter (d_2/d_0^2) of R1336mzz(Z) with the normalized time (t/d_0^2) at different ambient temperature at 0.1 MPa. As expected, at fixed ambient pressure conditions, elevated ambient temperature promotes R1336mzz(Z) droplet evaporation. This is because the droplet evaporation rate is mainly determined by the binary diffusion coefficient of R1336mzz(Z) vapor and the saturated pressure of vapor at the droplet's surface. And both are positive proportional to ambient temperature, thereby the increasing of ambient temperature significantly enhancing the droplet evaporation.

The evaporation behaviour of R1336mzz(Z) at 0.1 MPa shows a significant deviation from the classical d^2 law. The d_2/d_0^2 curves show some common features, where one turning point and two quasi-steady periods are observed through the entire droplet lifetime. In other words, the evaporation process of R1336mzz(Z) at 0.1 MPa exhibits a two-stage characteristic, namely: rapid evaporation period and slow evaporation period. This is because at first quasi-steady period, only R1336mzz(Z) evaporates, while at second quasi-steady period the evaporation of R1336mzz(Z) is accompanied by the simultaneous surface condensation of water vapor.

Fig. 3 depicts the temporal variation of the droplet temperature (T_d) of R1336mzz(Z) at different ambient temperature under ambient pressure of 0.1 MPa. It can be seen that the droplet is always in the heating process throughout the evaporation process, and the heating rate of R1336mzz(Z) droplet increases at higher temperature. The trend of T_d at 0.1 MPa exhibits a three-stage characteristic. The droplet temperature rises at an extremely slow rate at first, then at rapid rate, and finally slows down again. The first turning point of T_d curve corresponds to the turning point of d^2/d_0^2 curve. This may be explained as follows. The variation of the heat penetrated into droplet interior plays a dominate role on the slope variation of T_d curve. Initially, most of the convective heat transferring from environment to the droplet is used to provide the latent heat of vaporization, resulting in a slightly increase in the droplet temperature. Due to the exothermic of condensation and the decrease latent heat of evaporation, the heat penetrating into the interior of the droplet is enhanced significantly, resulting in a rapid increase in T_d. In the late evaporation process, the continuous reduction in the droplet size and temperature difference between droplet surface and its ambient gas weakens the natural convection effect, which decreases convective heat transfer, and finally decelerates the heating rate of R1336mzz(Z) droplet.

Figs. 4 and 5 depicts the temporal variation of the d_2/d_0^2 and T_d of a single R1336mzz(Z) single droplet at different ambient temperatures under ambient pressure of 2.0 MPa. As can be seen from these figures, the trends of d_2/d_0^2 and T_d are different from the situation at 0.1 MPa. All d_2/d_0^2 at 2.0 MPa decreases smoothly during the entire evaporation process, without the turning point. This can be attributed to the fact that the condensation temperature of water vapor is positive proportional to ambient pressure, consequently, the condensation of water vapor on the droplet surface does not occur when ambient pressure is elevated.

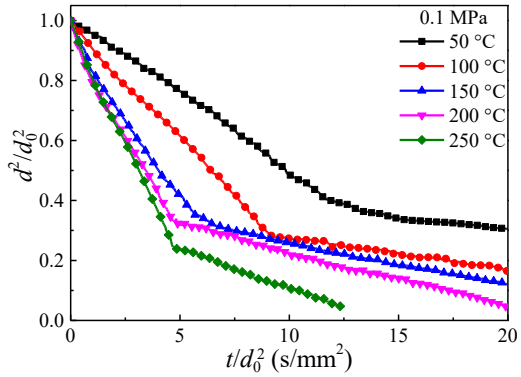


Figure 2 - Temporal variation of droplet normalized squared diameter of R1336mzz(Z) single droplet at different temperature under 0.1 MPa

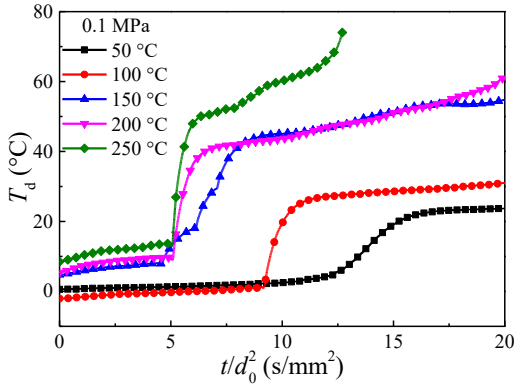


Figure 3 - Temporal variation of droplet inner temperature of R1336mzz(Z) single droplet at different temperature under 0.1 MPa

As indicated in Fig. 5, T_d rises rapidly at the start of evaporation, and its slope becomes gentle gradually over time. Initially, a large difference of temperature exists between the droplet surface and its surrounding gas, indicating the large convective heat transfer, thereby leading to a rapid increase in T_d. With time elapsed, the difference of temperature exists between the droplet surface and ambient gas is narrowed. As a result, convective heat transfer decreases and hence reduces the heating rate of R1336mzz(Z) droplet.

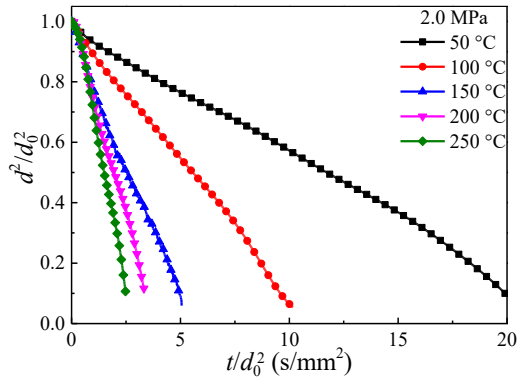


Figure 4 - Temporal variation of droplet normalized squared diameter of R1336mzz(Z) single droplet at different temperature under 2.0 MPa

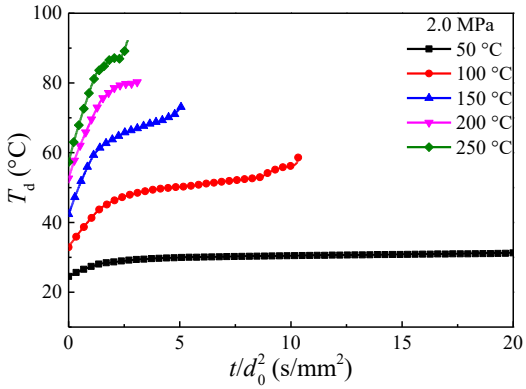


Figure 5 - Temporal variation of droplet inner temperature of R1336mzz(Z) single droplet at different temperature under 2.0 MPa

Conclusions

In this study, the effect of ambient temperature on the evaporation of a single R1336mzz(Z) droplet is investigated by the fiber-suspended technique. The ambient temperature has varied from 50 ºC to 250 ºC in 50 ºC increments. Two ambient pressures of 0.1 MPa and 2.0 MPa are selected. The main results obtained in this study can be summarized as follows.

(1) The tendencies of the droplet normalized squared diameter (d^2/d_0^2) curves are similar at the same ambient pressure. In the course of evaporation of R1336mzz(Z) droplets at an ambient pressure of 0.1 MPa, one turning point and two quasi-steady periods are observed on d^2/d_0^2 curves. And the heating behavior of R1336mzz(Z) droplet exhibits a three-stage characteristic, including an extremely slow rise, a rapid rise and then another slow rise periods. The turning point of d^2/d_0^2 curve corresponds to the first turning point of droplet inner temperature (T_d) curve, which is attributed to the surface condensation of the water vapor on R1336mzz(Z) droplet.

(2) In a case of 2.0 MPa, d_2/d_0^2 decreases smoothly without second quasi-steady period during the entire evaporation process. And T_d increases monotonically, and its slope becomes gentle over time. This is because the condensation temperature of water vapor is positive proportional to ambient pressure. As the ambient pressure increases, the surface condensation is not likely to occur.

(3) Increasing ambient temperature can promote the evaporation and heating of the R1336mzz(Z) droplet. The promotion of droplet evaporation is mainly caused by the increase in the saturated pressure of R1336mzz(Z)vapor at the droplet's surface and the binary diffusion coefficient of vapor. And a higher ambient temperature implies a large driving force of convective heat transfer, resulting in a faster heating rate.

Acknowledgements

This work was supported by the National Natural Science Foundation of China (Grant No. 52176163) and the Ministry of Science and Technology of Shaanxi province of China (Nos. 2024JC-JCQN-58 and 2023GXLH-003), as well as the Fundamental Research Funds for the Central Universities and Cyrus Tang Foundation.

References

[1] B. Yuan, Z. Wang, J. Cao, Y. Huang, Y. Shen, Z. Song, H. Zhao, X. Cheng, Mixture formation characteristics and feasibility of methanol as an alternative fuel for gasoline in port fuel injection engines: Droplet evaporation and spray visualization, Energy Conversion and Management, 283 (2023) 116956.

[2] D. Ju, L. Huang, K. Zhang, M. Ye, Z. Huang, G. Yi, Comparison of evaporation rate constants of a single fuel droplet entering subcritical and supercritical environments, Journal of Molecular Liquids, 347 (2022) 118346.
[3] J. Wang, J. Li, Y. Shen, S. Shi, F. Xiang, Y. Xu, Experimental investigation on evaporation, puffing and vapor jetting of multi-component fuel droplets with high-volatility difference, Applied Thermal Engineering, 239 (2024) 122151.
[4] W. Xue, X.R. Wang, W. Sun, S. Tang, G. Jiang, Experimental study on the evaporation characteristics of Jatropha curcas oil methyl ester (JME)-ethanol blended droplets, Fuel, 333 (2023) 126081.
[5] X.R. Wang, W. Xue, W. Sun, S. Tang, G. Jiang, Investigation of single drop evaporation characteristics of two-component fatty acid methyl esters at high temperature, Fuel, 334 (2023) 126566.
[6] A. Tanner, W. Hallett, Droplet evaporation of alcohol-biodiesel blends, Fuel, 341 (2023) 127647.
[7] D. Mei, Y. Fang, D. Zhang, D. Guo, Z. Chen, Evaporation and micro-explosion performances of nano-fuel droplets, Fuel, 334 (2023) 126623.
[8] E. Marlina, A.F. Alhikami, B. Waluyo, S. Rahima Sahwahita, I.N.G. Wardana, A study of blending carbon nanoparticles made of coconut shell (fullerene C60) in vegetable oils on the droplet evaporation characteristics, Fuel, 346 (2023) 128319.
[9] H. Zhang, Z. Lu, T. Wang, Z. Che, Micro-explosion of emulsion droplets with nanoparticles at high temperature, International Journal of Heat and Mass Transfer, 219 (2024) 124851.
[10] H. Zhang, Z. Lu, T. Wang, Z. Che, Mist formation during micro-explosion of emulsion droplets, Fuel, 339 (2023) 127350.
[11] S. Shen, H. Liu, Y. Liu, X. Liu, H. Hu, Z. Hu, T. Wang, Dynamic details inside water-in-oil (W/O) emulsion droplet and its impact on droplet evaporation and micro-explosion, Fuel, 338 (2023) 127254.
[12] X. Chen, X. Xi, G. Xiao, L. Zhang, Z. Wang, W. Long, Effect of ambient temperature and water content on emulsified heavy fuel oil droplets evaporation: Evaporation enhancement by droplet puffing and micro-explosion, Fuel, 334 (2023) 126614.
[13] Z. Zhang, D. Hu, Q. Li, C. Liu, F. Zhou, Visualization study on atomization characteristics and heat transfer performance of R1336mzz flash spray cooling, Science China Technological Sciences, 64 (2021) 2099-2109.
[14] R.A. Perkins, M.L. Huber, Measurement and Correlation of the Thermal Conductivity of cis-1,1,1,4,4,4-hexafluoro-2-butene, International Journal of Thermophysics, 41 (2020) 103.
[15] P. Giménez-Prades, J. Navarro-Esbrí, C. Arpagaus, A. Fernández-Moreno, A. Mota-Babiloni, Novel molecules as working fluids for refrigeration, heat pump and organic Rankine cycle systems, Renewable and Sustainable Energy Reviews, 167 (2022) 112549.
[16] Z. Zhang, Q. Li, D. Hu, Experimental investigation on heat transfer characteristics of R1336mzz flash spray cooling, Applied Thermal Engineering, 174 (2020) 115277.
[17] J. Yin, S.-Y. Chen, D.-Q. Zhu, S.-Q. Xue, S.-Y. Li, Z.-F. Zhou, B. Liu, Experimental investigation on evaporation characteristics of RP-3 aviation kerosene droplet above the critical temperature under various pressure conditions, Aerospace Science and Technology, 140 (2023) 108463.
[18] J. Yin, Q.-D. Wang, L.-F. Zhang, L.K. Norvihoho, B. Liu, Z.-F. Zhou, Evaporation characteristics of cis-1,1,1,4,4,4-hexafluoro-2-butene (R1336mzz(Z)) droplet in high pressure and temperature environments, Physics of Fluids, 36 (2024) 023335.

Abnormal Gravity Scaling Behaviour and Bubble Dynamics in Low Heat Flux Nucleate Pool Boiling: What Have We Learned from vgBOILING-CSS

Wang-Fang DU [1, 2], Jian-Fu ZHAO [1, 2, *]
1. CAS Key Laboratory of Microgravity, Institute of Mechanics, Chinese Academy of Sciences. Beijing 100190, China
2. School of Engineering Science, University of the Chinese Academy of Sciences. Beijing 100049, China
* E-mail address of the corresponding author: jfzhao@imech.ac.cn

Abstract
Boiling is one of the most effective methods of heat transfer, which is employed widely in component cooling and in various energy conversion systems in normal gravity on the ground, and will be a potential candidate with significant advantages such as compactness, light weight, high efficiency for space applications in microgravity environment. Due to large difference between the densities of the liquid and its vapour, bubble dynamics, flow structures and heat transfer performances of boiling in different gravity conditions exhibit distinct difference. The applicability of common-used correlations, e.g. the Rohsenow correlation for nucleate pool boiling, diminishes quickly to reduced gravity conditions. The fundamental reason is that gravity appeared in those correlations is only a dimensional constant rather than a controllable independent variable. To meet the application requirements of multiple scenarios with different gravity levels in space missions, it is necessary to conduct in-depth research on the influence of gravity on heat transfer and bubble dynamics in boiling phenomenon. With the help of simulated gravity environment provided by the Variable Gravity Science Rack (VGR) in Wentian Lab Module of the China Space Station (CSS), a project vgBOILING-CSS, one of the first batch of two scientific experiment tasks utilizing VGR, was proposed to study heat transfer and bubble dynamics during pool boiling in a wide range of gravity levels from 2g to the background microgravity environment of CSS. The experimental facility of vgBOILING-CSS, including an electronic control box, an experimental box, a connecting cable and a ventilation pipe, was sent to CSS by the cargo spacecraft Tianzhou-5 on November 12, 2022, and was installed by the astronaut crew of Shenzhou-15 on a centrifugal of VGR on December 12, 2022. After successful in-orbit performance testing on December 15, 2022, four stages of space scientific experiments have been conducted in the past period of time. An abnormal gravity scaling behaviour, namely an enhancement rather than deterioration of the heat transfer with the decreasing gravity, has been discovered in the nucleate pool boiling region with low heat flux. The largest diameter of growing isolated bubble attached on the heating surface is found to be inversely proportional to gravity and proportional to the 0.3-power of the superheating. The present lecture will provide a summary on the preliminary findings obtained from the project vgBOILING-CSS.

Keywords: Microgravity pool boiling, Bubble dynamics, Gravity scaling behaviour, vgBOILING-CSS

Acknowledgements
The present research is supported financially by the National Key R&D Program of China under the grant of 2022YFF0503502 and China Manned Space Engineering Program under the grant of YYWT-0601-EXP-18.

Experimental study on flow instability characteristics of supercritical-pressure R134a in a heated tube

Jianguo Yan, Xutao Zhu, Shouchun Liu
State Key Laboratory of Eco-hydraulics in Northwest Arid Region, Xi'an University of Technology, Xi'an, China

Abstract
In this study, the flow instability characteristics of supercritical-pressure R134a were measured in a horizontal heated circular tube. The experimental parameters were as follow: p = 4.1–5.5 MPa, T = 20–300 °C, and q = 0–300 kW/m2 . The effects of mass flux, pressure, and fluid temperature on flow instability were analysed, and the hydrodynamic curves were obtained. The results indicate that the hydrodynamic curve of supercritical-pressure R134a does not possesses a negative-slope region but has a transition region. The transition region becomes weaker with increased pressure or decreased heat flux.
Keywords: Flow Instability; Supercritical Fluids; Supercritical Organic Rankine Cycle

Introduction

Supercritical Organic Rankine Cycle (SORC) technology is an essential means of realizing the efficient utilization of medium and low-temperature heat sources, in which supercritical-pressure fluids, such as R134a, are employed as working fluids. In an S-ORC system, the working fluid is heated to supercritical state. The working fluid in the evaporator channel experiences a trans-critical flow, and its physical properties exhibit severe nonlinear changes near the pseudo-critical point, which may lead to complex heat transfer and flow instability phenomena.

Methodology

Fig. 1 shows the experimental loop. The fluid was heated to the desired temperature in the preheater, and then was heated under a uniform heat flux using an AC power supply. The test section was a horizontal stainless-steel circular tube (inner diameter 2.0 mm, total length 500 mm). The outer wall temperatures were measured with thermocouples at nine sections.

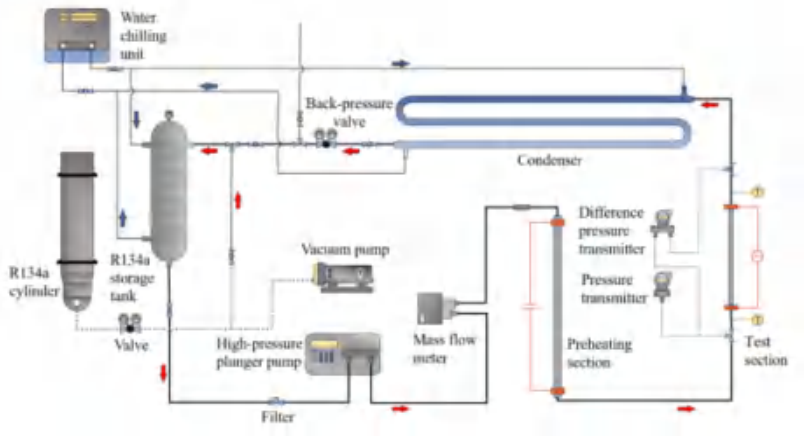


Figure 1 Experimental loop

Results and discussion

As shown in Fig. 2, there is no negative-slope region in the hydrodynamic curve. However, there is an apparent transition region in which the pressure drop varies slowly with mass flux. The onset of the transition region occurs when the bulk temperature is lower than the pseudo-critical temperature, but the wall temperatures are slightly higher than the pseudo-critical temperature. The onset of the transition region shifts in the direction of a high mass flow under a higher heat flux, higher inlet temperature or a lower pressure.

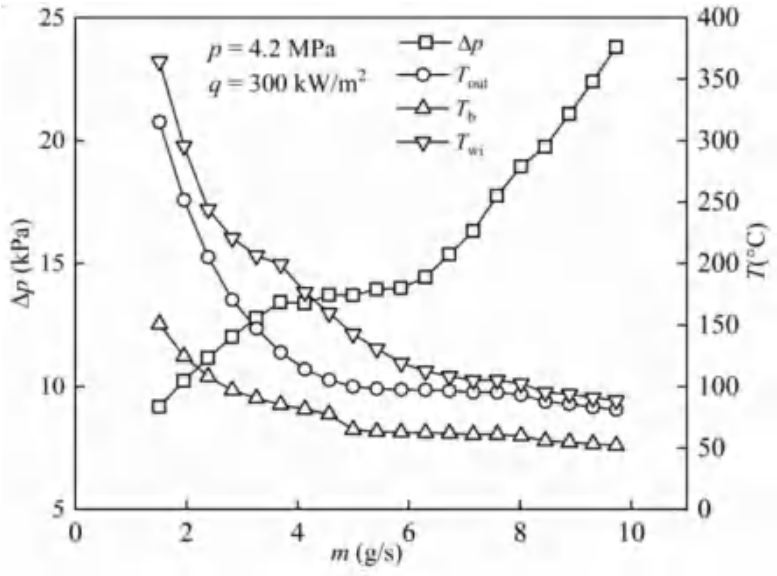


Figure 2 Typical hydrodynamic curve

Conclusions

The hydrodynamic curve of supercritical-pressure R134a does not exhibit a negative-slope region, but a transition region. The transition region becomes more evident with increasing heat flux and disappears with increasing pressure and inlet temperature.

Investigation on flow boiling heat transfer characteristics in parallel microchannels based on temperature sensitive paint

Teng Wang, Haoran Zheng, Yuepeng Ma, Lu Liu
Department of Power Engineering (North China Electric Power University, Baoding, China)

Keywords: Flow boiling, Heat transfer characteristics, Temperature sensitive paint, Parallel channels

Introduction

Microchannel heat sink utilizes fluid boiling in microchannels to absorb a large amount of heat for the purpose of heat dissipation[1]. Researches on microchannel heat exchanger technology have been of great significance in the cooling of high heat flux electronic devices such as chips, lasers, power battery and aero-engine.

Forced convective boiling in channels is a multiscale phenomenon, involving the coupling of heating wall and various two-phase flow patterns. Due to the rapid formation and development of bubbles, the wall temperature and fluid temperature surrounding bubbles undergo rapid changes, necessitating accurate and swift temperature measurements.

This study focuses on flow boiling in parallel microchannels, measuring the two-dimensional temperature distribution on the wall surface employing temperature sensitive paint (TSP) technology[2], and revealing the mechanism of boiling heat transfer in the channel from the perspective of bubble formation.

Methodology

As shown in Fig. 1, heating glass was used to heat the bottom surface of the test section. The TSP was coated on its surface to measure the two-dimensional temperature distribution of the entire surface.



Figure 26 - Test section

The principle of TSP is illustrated in Fig. 2. The TSP comprises probe molecules and adhesives. When stimulated by light of a specific wavelength, the probe molecules produce fluorescence at a distinct wavelength. The fluorescence intensity exhibits temperature dependency, decreasing with increasing temperature.

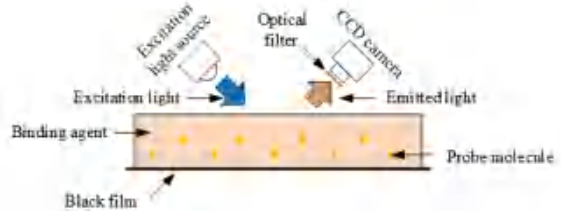


Figure 2 - Principle of TSP

Results

Fig. 3 depicts the typical measurement results from TSP, which displays the temperature distribution at different positions on the heating wall. By combining the temperature distribution with the images of vapor-liquid two-phase flow captured by a high-speed camera, the flow and heat transfer characteristics were analysed from two perspectives.

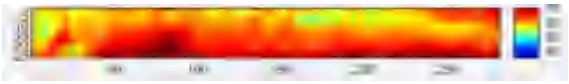


Figure 3 - Typical measurement results

Acknowledgements
The research was supported by the National Natural Science Foundation of China (No. 52306196), and the Fundamental Research Funds for the Central Universities of Ministry of Education (China) (No. 2023MS118).

References

[1] Erp R V, Soleimanzadeh R, Nela L, Kampitsis G, Matioli E. Co-designing electronics with microfluidics for more sustainable cooling [J]. Nature, 2020, 585(7824): 211-216.
[2] Liu L, Zhang K, Liu H, Zhang S, Mi M. Experimental study on the interfacial heat transfer of sessile droplet evaporation using temperature-sensitive paint [J]. Experimental Thermal and Fluid Science, 2021, 128: 110436.

Numericalstudy of flow-boiling heat transfer in a channel partially filled with gradient porous media

Li-Yuan Yang a,b* , Chuang-Yao Zhao a,b*
a School of Building Services Science and Engineering, Xi'an University of Architecture and Technology, Xi'an 710055, P. R. China
b International Joint Laboratory on Low Carbon Built Environment, Ministry of Education of China

Abstract
The escalating issue of heat dissipation in high-density electronic devices hinders industry development[1] . A viable solution involves leveraging porous media, notably gradient porous media (GPM). GPM, exhibiting varied pore structures, enhances fluid heat transfer efficiency[2,3] .
The gradual change in pore structure reduces fluidic resistance[4], ensuring a more uniform distribution of fluid in the medium, minimizing bias flow and deformation. Boasting an ultra-high heat transfer rate, boiling heat transfer facilitates efficient energy transfer over a narrow temperature range. Current research tends to study gradient porosity and phase change separately, highlighting a need for comprehensive investigation into their combined effects.
The design of GPM, integrating the Tanasawa phase change model with the Darcy-Forchheimer model, significantly improves boiling heat transfer by increasing both surface area and boiling cores. Utilizing the open-source Computational Fluid Dynamics (CFD) package OpenFOAM for numerical simulations, our analysis delves into the fluid characteristics within tubes featuring varied fills and gradients. The results are systematically compared with a homogeneous porous media (HPM) control. These findings yield valuable insights for optimizing parameters of gradient porous media (GPM), thereby enhancing the overall efficiency of the system.
Keywords: Gradient porous media(GPM), Heat transfer enhancement, Flow Boiling, CFD.

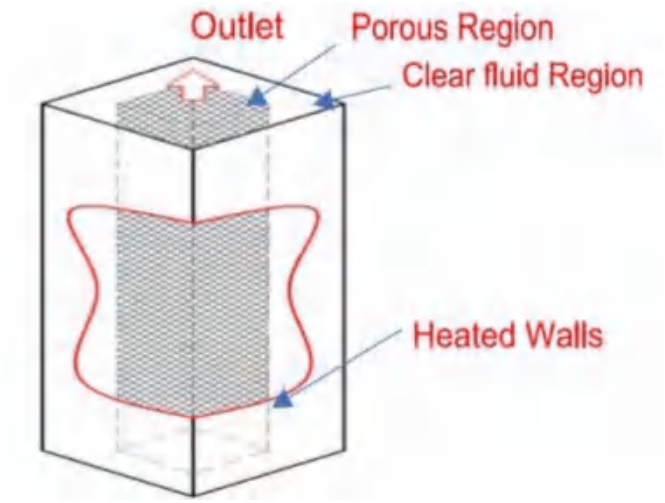


Figure 1 - The physical model of Square channel partially filled by porous medium.

References

[1] Zhen L, Wenjuan M, Xianping Z, Chenglin Y, Xiuy un Z.Remaining Useful Life Estimation of Insulated Gat e Biploar Transistors (IGBTs) Based on a Novel Volterr a k-Nearest Neighbor Optimally Pruned Extreme Learning Machine (VKOPP) Model Using Degradation Data[J]. Sensors.2017,17(11):2524-.
[2] Yang X, Wei P, Wang X, He Y-L.Gradient design of pore parameters on the melting process in a thermal energy storage unit filled with open-cell metal foam[J].Applied Energy.2020,268.

[3] Yang X, Yu J, Guo Z, Jin L, He Y-L.Role of porous metal foam on the heat transfer enhancement for a thermal energy storage tube[J].Applied Energy.2019,239:142-56.
[4] Shi C, Wang M, Yang J, Liu W, Liu Z. Performance analysis and multi-objective optimization for tubes partially filled with gradient porous media[J].Applied Thermal Engineering.2021,188.

Topology Optimization Design of Natural Convection Heat Transfer Fins

ChuanChang Dong[1],GeNing He[2,3],DongHui Li[2,3], ZiWei Zhang[1],JiDong Cong[1],ZhaoMing Meng[1,*]

1 Heilongjiang Provincial Key Laboratory of Nuclear Power System & Equipment, Harbin Engineering University, Harbin 150001, China

2 Nuclear Power Institute of China,Chengdu 610041,China

3 Sichuan Province Key Laboratory of Nuclear Additive Manufacturing,Chengdu 610041,China

Abstract

This study used topology optimization method to design a new fin structure for a natural convection heat exchanger. The optimization in this study utilized a shape-dependent convection model to describe the variation of convective heat transfer coefficient. This model was coupled with the heat diffusion equation to achieve the topology optimization of the natural convection heat exchanger. One advantage of this optimization method is that it doesn't require the use of the Navier-Stokes (N-S) equations, which reduces computational complexity during the optimization process. The topology optimization employed a density-based optimization method and interpolated the thermal conductivity of the distributed material. Under the given shape of the heat source, a novel "tree-like" optimized structure was obtained through shape-dependent natural convection topology optimization method. The new structure extends from the root (at the heat source) and consists of tapered branches of fins that enhance convective heat dissipation. Compared to the traditional plate-fin structure, the new structure not only has a smaller volume but also reduces the convective thermal resistance according to CFD simulations.

Key Words: Natural Convection Heat Transfer · Fin Design ·Topology Optimization

Parallel Session V-2: Topic 10-Multiphase flow applications: electrostatics and bio-medical engineering

Numerical simulation of hemodynamics and spry cooling for the personalized laser dermatosis

Bin CHEN
Xi'an Jiaotong University

Abstract

Meshless methods have great potential for the numerical simulation of multiphase flow due to their Lagrangian nature, among which vortex method and moving particle semi-implicit (MPS) method are promising. In the vortex method, the flow field of the continuous phase is solved by the discretization of vorticity equation, and the bubble/droplet/particle equation is introduced to simulate the motion of discrete phase. In the MPS method, fluids are discretized into different particles, and all the operators in the N-S equations are solved by the interaction of these particles. In this work, these two methods are developed to respectively simulate the cryogen spray cooling to protect epidermis from unwanted thermal damage and laser-induced thrombus formation to destroy malformed subcutaneous blood vessels, thereby achieving parameter optimization and personalized laser dermatosis.

A DEM study on effect of electrostatic interactions on granular flow behaviours during rotating

Jiawei Hu[a,b], Chunlei Pei[c], Cai Liang [a*], Chuan-Yu Wu[b*]
[a] Southeast University, Nanjing, China
[b] University of Surrey, Guildford, United Kingdom
[c] Tianjin University, Tianjin, China
*Corresponding author: Prof. Chuan-Yu Wu, Email: c.y.wu@surrey.ac.uk; Prof. Cai Liang, Email: liangc@seu.edu.cn

Abstract

Frictional electrification between particles and surfaces is prevalent in many powders involved industries, such as food, pharmaceutical and chemical industries [1][2]. Electrostatic charging can cause undesired problems, e.g. agglomeration, dispersion, sticking or adhesion on equipment surface.

The discrete element method (DEM) is widely used to better understand the dynamic behaviour of charged particles by modelling the contact electrification and electrostatic interactions. However, in the previous particle contact electrification model, it was assumed that the charge transfer from one surface to another only takes place once two contacted surfaces separate. If the contact persists, e.g. a particle slides or rolls along a wall, the charge transfer is assumed not occurring and is not considered. These models do not consider frictional charging that does occur in many powders handling processes, and hence they can not predict the behaviour of charged particles precisely.

Aiming to explore the friction-induced electrostatic charging behaviour and the effect of electrostatics on the particle flow, a discrete element method (DEM) is developed for the first time in the current paper, in which a frictional charging model and electrostatic interaction models are implemented. The charge accumulation on both the particles and the surface in a rotational container is then analysed numerically and experimentally to evaluate the developed DEM [3].

Results show that the numerical results are in good agreement with the experimental data, where the average net charge of a single particle gradually increases and achieves an equilibrium state. It is also shown that both the net charge on the particles and the degree of the particle dispersion are a function of the charging time.

Moreover, it is revealed from both experiments and DEM that the friction-induced particle charge enhances particle dispersion and lead to the wall adhesion, as shown in Figure 1.

Keywords: Electrostatic interactions, Frictional electrification, Dispersion, Wall adhesion, Discrete element method

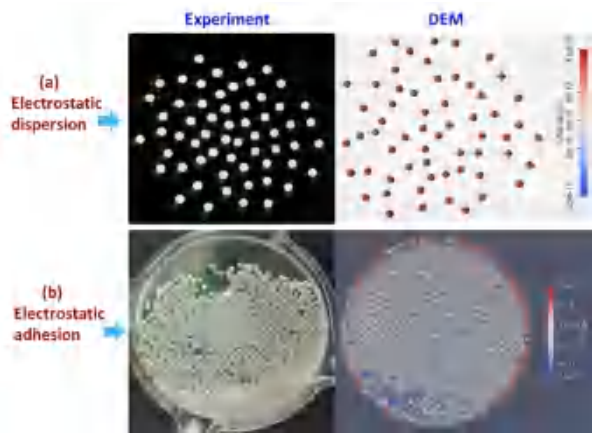


Figure 27 - (a)Dispersion of charged particles from experiment and DEM simulations; (b)Wall adhesion of charged particles from experiment and DEM simulations.

References

[1] Bi HT. Electrostatic phenomena in gas-solids fluidized beds. China Particuology. 2005;3(6):395-399.

[2] Yao J, Zhang Y, Wang CH, Matsusaka S, Masuda H. Electrostatics of the granular flow in a pneumatic conveying system. Ind Eng Chem Res. 2004;43(22):7181-7199

[3] J Hu, C Pei, L Zhang, C Liang, CY Wu. Numerical analysis of frictional charging and electrostatic interaction of particles. AIChE J. 2022;68: 1792-1803.

Experimental investigation of fractional laser's optimization effect for Q-switched laser skin thermotherapy

Xuehao Sang, Dong Li, Bin Chen*
State Key Laboratory of Multiphase Flow in Power Engineering (Xi'an Jiaotong University, Xi'an, 710049, China)
Corresponding E-mail: chenbin@mail.xjtu.edu.cn

Abstract
The hyperpigmented dermatosis is a kind of skin diseases, which can be treated by Q-switched laser thermotherapy. This method lacks in penetration with low clearance rate and serious side effects by laser-induced mechanical vibration. Utilizing fractional ablative laser to create an array of micropores on the skin before laser thermotherapy can enhance the laser penetration and release the cavitation pressure, with lower vibration damage. A novel polyvinyl alcohol (PVA) cryogel skin phantom experiment has been conducted to prove the optimization effect of fractional laser. Threshold energy and density were obtained, above which penetration-enhancing effect is negligible.

Keywords: Hyperpigmented Dermatosis, Vibration Damage, Fractional Laser, Q-switched Laser

Introduction

The hyperpigmented dermatosis is a kind of skin diseases, which affects the health of patients seriously. Based on selective photo-thermolysis, Q-switched laser has been the most widely used treatment strategy in clinic. The pulse duration of the Q-switched laser typically falls within nanosecond to picosecond range, shorter than the thermal relaxation time of the pigments, thus enabling targeted thermal ablation of the pigments and avoiding thermal damage to surrounding tissue. However, the attenuation of laser energy in skin limits the penetrating depth. Increasing laser power density may cause severe cavitation-induced vibration that damages the surrounding tissue. Utilizing fractional ablative laser to create an array of micropores on the skin before Q-switched laser thermotherapy can enhance the laser penetration and release the cavitation pressure, with lower vibration damage.

Methodology

In this study, a novel PVA compound skin phantom mimicking both the mechanical and optical properties of skin based on the freeze-thaw technique was developed, which was made from PVA and pigment granules through layer-by-layer assembly. Vibration sensors were buried under phantom during Q-switched laser irradiation with ultrasonic coupling agent. Fractional laser pre-treatment with different parameters was conducted before Q-switched laser on phantom to study the effect of penetration-enhancing and vibration-decreasing.

Results and Discussion

Phantoms with low fractional laser density and pulse energy shows vibration decreasing or being flat, which verifies the cavitation pressure releasing effect to lower vibration damage. Increasing the density and pulse energy of fractional laser can strengthen the penetration-enhancing effect, with a threshold density and energy of 200 spots/cm^2 and 80 J/pulse, above which the penetration-enhancing effect can be considered negligible.

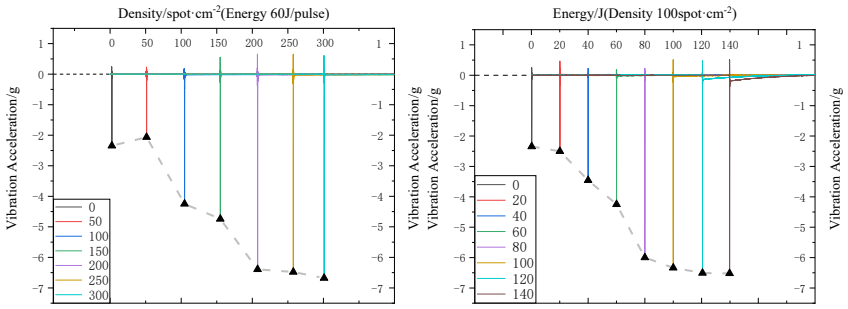


Figure 28 –Variation of phantoms' vibration acceleration with different fractional laser's density and energy during Q-switched laser irradiating

Acknowledgements

This study was supported by the Natural Science Foundation of China (52036007).

Electrostatic discharge properties of charged powders in the silo

Liang Cai
Southeast University

Abstract

Electrostatic discharge as a common electrical hazard in powder handling is under-recognized due to the limitations of detection and characterization methods. This study aims to improve the comprehension of electrostatic discharge mechanisms and energy release law by developing a PIC-MCC model of discharge in powder silo. The validation of this model is carried out by examining discharge patterns and electric fields in an industrial silo. The discharge patterns and evolution laws of different polarity powders are discussed to indicate the discharge disparities observed in the silo. These disparities are further scrutinized in relation to electron density, space charge, electric field, and potential. By changing the charging laws of powders in the silo, the discharge channel sizes and branching characteristics in silos of different polarity powders are summarized, and the total discharge energy is deduced from the space electric field change. Based on the integration method of particle kinetic energy in the discharge channel, we not only predict the instantaneous energy release characteristics of the discharge at different times but also explore the energy accumulation law at different discharge positions.

Efficient Optimization of a Novel Dry Powder Inhaler Design Using Computational Fluid and Particle Dynamics

Binbin Shana , Yan Cuia , Dongmei Cunb
Affiliations (a. Huazhong University of Science and Technology, Wuhan, China; b. Shenyang Pharmac-eutical University, Shenyang, China.)

Abstract
This study explores the application of Computational Fluid and Particle Dynamics (CFPD) to optimize the design of a Dry Powder Inhaler (DPI). The focus is on the effect of the inclination angle of the swirl chamber in the DPI on the retention of carrier particles. CFPD simulations reveal that a small inclination angle promotes constant collisions with the wall, retaining most carrier particles within the chamber. However, a large inclination angle can induce a stronger siphoning effect at the top of the swirl chamber, which should be avoided. Two DPIs, Cyclohaler® and an in-house DPI, were analyzed using CFPD simulations. These simulations were conducted for two inhalation pressure drops (2 and 4 kPa) and two carrier sizes (46 and 83 μm), aiming to determine the optimal inclination angle. The desired outcome is for most carriers to remain in the swirl chamber while most drugs leave the inhaler. For an inclination angle of 5° and a carrier size of 46 μm, more than 50% of drugs escaped while less than 3% of carriers escaped. Experimental studies using a next-generation impactor confirmed the simulation results. These findings highlight the efficacy and precision of CFPD in optimizing DPI design, and provide guidance for preventing carrier lactose particles from leaving DPIs.
Keywords: dry powder inhaler, computational fluid and particle dynamics, swirl chamber, inclined wall, particle-wall collision

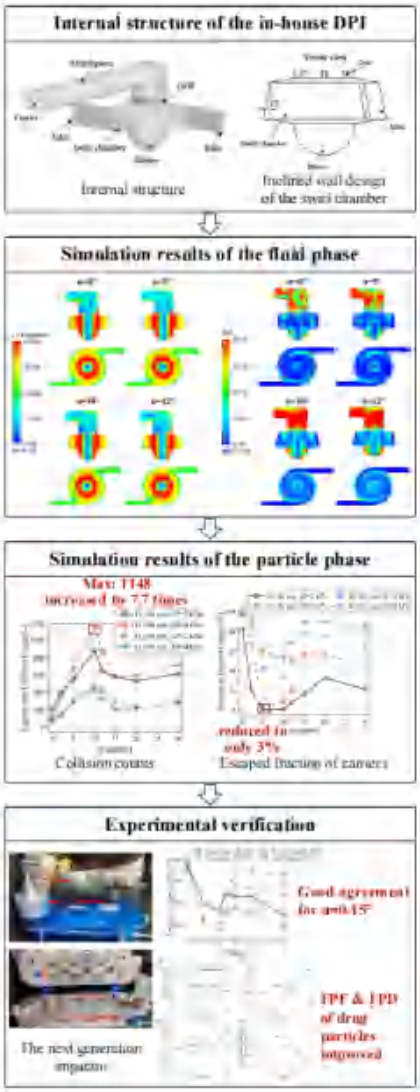


Figure 1 - Employing CFPD for the optimization of the in-house DPI and the experimental verification.

References

[1] B. Shan et al. (2024), Optimizing the inclination angle of the swirl chamber in dry powder inhalers for improved carrier particle retention, submitted to *Aerosol Science and Technology*.
[2] Y. Cui & M. Sommerfeld (2019), The modelling of carrier-wall collision with drug particle detachment for dry powder inhaler applications, *Powder Technology*, 344:741–755.

Experimental investigation on cavitation bubbles produced by laser-induced plasma in water

Chenggang Deng, Jiafeng Wang, Bin Chen*
State Key Laboratory of Multiphase Flow in Power Engineering, Xi'an Jiaotong University, Xi'an, Shaanxi, 710049, China
*Corresponding author: chenbin@mail.xjtu.edu.cn

Abstract

In the realm of biomedical, pulsed lasers are extensively employed for treating a variety of diseases, including cancer, ophthalmic disorders, and dermatological conditions. However, the use of high-energy or focused pulsed lasers can result in optical breakdown in liquids and biological tissues, typically giving rise to phenomena such as plasma formation, cavitation bubbles, and shockwaves. Despite extensive research on laser-induced breakdown, the specific processes and fundamental principles remain not fully understood. Given the significant application value and potential of pulsed laser-induced breakdown, it is imperative to delve into the phenomena and patterns associated with nanosecond laser-induced breakdown in water.

To successfully induce plasma and cavitation bubbles in water through focused pulsed laser and capture their generation process and changes, we constructed an experimental setup illustrated in Figure 1 (a). A single pulsed Nd:YAG laser (1064nm, pulse duration 10ns) was utilized to ablate the water. Plasma images were directly captured by an intensified CCD (ICCD, Andor iStar-SCMOS) to observe plasma evolution and monitor its position. The morphological changes of cavitation bubbles were monitored by a high-speed camera (Fastcam SA-Z, Photron, Japan) with a Nd:YAG laser (532nm) serving as the background light. The imaging system and laser were synchronized through a signal generator for time-delay control. Plasma distribution and cavitation oscillation during laser breakdown are shown in Figure 1 (b) and (c).

Figure 1 (b) illustrates emission images of the plasma captured at different laser energy levels (3.6 mJ, 7.6 mJ, 11 mJ, and 11 mJ). The images reveal that as pulse energy increases, the plasma gradually expands. Plasma intensity experiences a rapid decrease within tens of nanoseconds at the same energy level. Furthermore, the direction of plasma expansion consistently moves near the laser source along the incident direction. Figure 1 (c) displays cavitation bubbles induced in water at a laser energy of 7.6 mJ, captured by a high-speed camera (80000 fps, gate width 5 μs). The time interval for each photocavitation image is 7.5 ms. Clearly, the photocavitation bubble undergoes changes from small to large, oscillates, and moves downward.

In summary, we investigated the temporal and spatial evolution of laser-induced plasma in water. The results indicate that during the passage of the laser pulse, the plasma originates at the focus and then diffused upward along the beam path. With increasing laser energy, the probability, expansion size, and breakdown quantity increase, also leading to multiple breakdown phenomena. Additionally, cavitation bubbles undergo collapse and oscillation, moving along the laser irradiation direction away from the water surface until dissipated, in contrast to the direction of plasma diffusion.

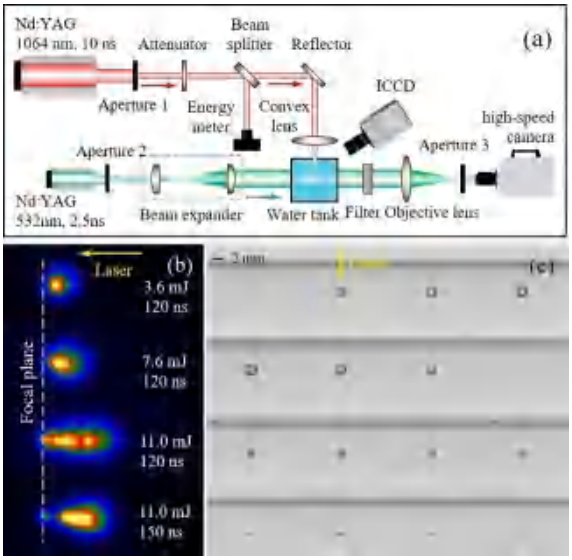


Figure 29 - Experimental setup (a), plasma images (b) and oscillation of cavitation bubble (c).

Keywords: Pulsed laser, Laser-induced plasma, Photocavitation, Bubbles oscillation

Two-phase flashing cryogen spray cooling: a skin pre-cooling technique assisting laser dermatology

Jiameng Tian[1], Mohamed Qenawy[1], Yiqi Chen[1], Bufa Li[1], Junfeng Wang[1*], Dong Li[2*], Bin Chen[2*]

[1] School of Energy and Power Engineering, Jiangsu University, Zhenjiang 212013, China
[2] State Key Laboratory of Multiphase Flow in Power Engineering, Xi'an Jiaotong University, Xi'an, Shaanxi 710049, China
* corresponding author: chenbin@mail.xjtu.edu.cn, wangjunfeng@ujs.edu.cn

Abstract

Cryogen spray cooling (CSC) has become a promising auxiliary-cooling technique for laser dermatology, which recently enhanced by cold air jet (CSC-CAJ). However, the CAJ-to-spray interactions could worsen the CSC performance and associated liquid film behavior. In this study, the transient behavior of liquid film deposition and surface heat transfer of CSC-CAJ was investigated. A high-speed camera was used to capture the film intensity through Mie-scattering technique. Fast-response TFTC thermocouple was used to measure the transient surface temperature. The large eddy simulation (LES) was used to extract the vortical structure, while the discrete-phase model (DPM) and Eulerian wall film (EWF) were coupled for the spray process and the transient film modeling. The results showed that the CAJ significantly enhanced CAJ-to-spray mixing and mitigated the film thickness (i.e., 32% reduction). The CSC-CAJ had asymmetric film coverage due to induced counter-rotating vortex-pairs (CRVP) from the CAJ-to-spray interaction, which laterally clustered the spray. It permitted fast evaporation with dominant CAJ at the spray-periphery while permitting fast evaporation with dominant spray at the spray-core. Consequently, the CSC-CAJ showed 75% temperature increment at the windward side and 15% temperature reduction with 60% convection heat transfer coefficient enhancement at the impingement point. The experimental film intensity and simulated film thickness were linearly correlated and significantly influenced the surface temperature. Meanwhile, the enhanced convective heat transfer coefficient exhibited a cubic correlation with the transient time (t/τ_{CHF}). The combined results affirmed the significance of the CAJ and its impact on the transient film deposition, which potentially helps the community promote advanced cooling technology.

Keywords: Cryogen Spray Cooling, Cold Air Jet, Film Deposition, Two-Phase Flow, LES-EWF

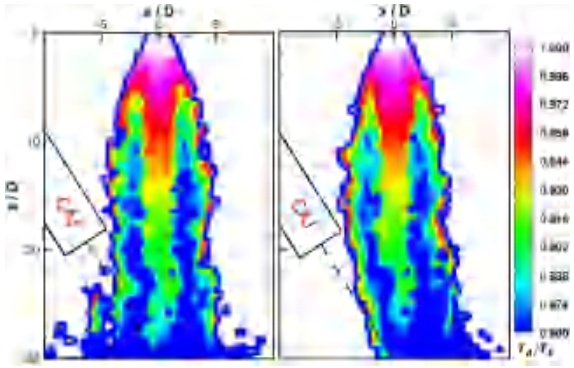


Figure 30 Simulated droplet temperature distribution

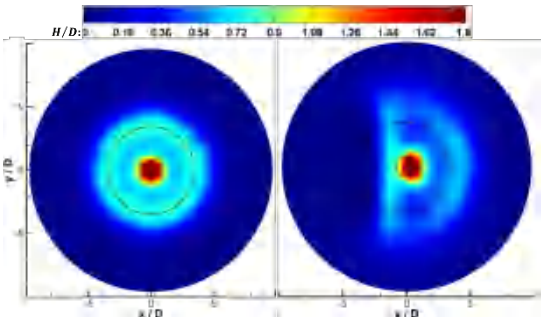


Figure 31 Simulated film thickness distribution

Acknowledgements

The authors gratefully acknowledge the financial support for this study from the National Natural Science Foundation of China (52036007 & 52106201)

Parallel Session VI: Topic11-Multi-scale modeling of multiphase flow

Multiscale kinetic theory for heterogeneous granular and gas-solid flows

Bidan Zhao[a,b], Junwu Wang[a,b]

a. College of Mechanical and Transportation Engineering, China University of Petroleum, Beijing 102249, P. R. China
b. State Key Laboratory of Mesoscience and Engineering, Institute of Process Engineering, Chinese Academy of Sciences, P. O. Box 353, Beijing 100190, P. R. China

Abstract

It has been recognized that the particle phase stress model derived from classical kinetic theory is valid only when sufficient scale resolution is offered to explicitly resolve the heterogeneous structures during numerical simulations, however, industrial applications prefer to use coarse computational grids where the heterogeneous structures are not explicitly resolved but implicitly modeled. Unfortunately, in this case a kinetic theory for heterogeneous granular and gas–solid flows is not available yet. To this end, an attempt was made to tracking this challenge: The single particle velocity distribution function at the nonequilibrium stationary state with heterogeneous structures was firstly derived by combining the idea of doubly stochastic Poisson processes or superstatistics with the concept of compromise in competition in the EMMS (Energy Minimization Multi-Scale) theory, the standard Chapman-Enskog method was then used to develop the constitutive relations of heterogeneous continuum theory. It was found that (i) seven state variables are needed to quantify the heterogeneous structures as compared to three for homogeneous systems; (ii) the constitutive relations not only include the contribution from microscale particle–particle interactions but also those due to the interactions between mesoscale structures; and (iii) the resultant constitutive relations are much more complex than those of homogeneous systems due to the simultaneous consideration of microscale and mesoscale contributions and the appearance of cross-coupling effects, but they correctly contain the constitutive relations of homogeneous systems as a limiting case. Finally, the theory was coupled with an EMMS drag model to offer a preliminary validation and to provide a unified EMMS-based constitutive relations for heterogeneous gas–solid flows.

Modeling of two-phase turbulence and mass transfer in bubble column reactors

Junlian Yin,Yuanbiao Hu, Wuguang Chen, Guangyuan Huang, Dezhong Wang
School of nuclear science and engineering, Shanghai Jiao Tong University, Shanghai, 200240

Abstract：The dynamic behavior of bubbles in two-phase turbulent flow is very important for chemical and petroleum industries. How to predict accurately by numerical simulation mass transfer rate between phases is a prerequisite for the design and analysis of bubble column reactors. however, There are two very key problems that have not been solved in CFD simulations. Bubbles can induce additional turbulence and there is no mature model for two phase turbulence. Another aspect is the sub-model of the mass transfer on the bubble interface cannot accurately predict the mass flux. To solve these problems a two-phase turbulence model based on data assimilation method and two-phase flow laser measurement data is proposed in this paper. The modeling parameters of two-phase flow are adjusted by the data assimilation method. Compared with the experimental data, The modified calculation model can accurately obtain the turbulent kinetic and other parameters under the condition of two-phase flow. The reason for the large uncertainty of mass transfer on bubble interface is that it is difficult to determine the thickness of the concentration boundary layer. To numerical simulate the interfacial mass transfer, an ultra-fine grid is needed to resolve the thin mass boundary layer, while the computational cost is usually unacceptable. In this paper, a sub-grid scale model based on the geometric VOF method has been developed for the hexahedral grid. The sub-grid scale model can reduce the demanding requirement of the mesh resolution and a coarse grid can be used to obtain a good result. By using the method of data assimilation and the improved subgrid model, the numerical calculation accuracy of the bubble-flow mass transfer has been greatly improved.
Keywords: numerical simulation, bubble induced turbulence, mass transfer

Research on influence of periodic magnetic field on photothermal evaporation of ferromagnetic nanofluid droplets

Nongchao Tan[1], Lei Shi[2*] (*Corresponding author: shi.lei@csu.edu.cn)
Department of Nuclear Science and Technology, College of Science, National University of Defense Technology, Changsha, 410073, China
School of Energy Science and Engineering, Central South University, Changsha 410083, China

Abstract
A periodic magnetic field is adopted to explore the variations of the temperature field and velocity field during the evaporation process of ferromagnetic nanofluid droplets. The application of the periodic magnetic field prominently promotes the photothermal evaporation performance of the ferromagnetic droplets, which can be attributed to the deformation of the droplets induced by the periodicity of the magnetic field. The influence of the periodic magnetic field on the variation of multiple physical fields inside and around the heated droplet during its evaporation is revealed, which can provide a theoretical guidance for the application of electric heaters, cooling fluids and heat pipes.

Keywords: Ferromagnetic droplets,
Evaporation performance, Periodic magnetic field

Introduction

The heat transfer is enhanced effectively by introducing the nanofluid particles into the base fluid, which has attracted much attention during the past decades.[1-3] In addition, the magnetic nanofluid droplets achieve a larger convective heat transfer coefficient by applying an external magnetic field.[4,5] However, the applied magnetic field system exhibits the problem of large volume and low energy utilization, which greatly limits the application of magnetic nanofluids in the field of enhanced heat transfer. The existence of periodic magnetic field can effectively solve this problem. Currently, the study of using periodic magnetic field to promote the evaporation of ferromagnetic nanofluids is lacking. To elucidate these concerns of the current research, the evaporation of the ferromagnetic nanofluids on a photothermal substrate is numerically realized in this paper.

Methodology

A droplet evaporation model considering a periodic magnetic field is established. An iron ball with a diameter of 3 mm is added 6.5 mm above a photothermal substrate (carbon felt) as a magnetic field source. The period of the applied magnetic field is 1 s, while the magnetic flux density is 110 mT. Figure 1 demonstrates the residual mass of the ferromagnetic nanofluid droplets with and without a magnetic field. The liquid droplets with a mass of 2 mg remain after 40 minutes of the ferromagnetic nanofluid evaporation without the addition of a magnetic field. After adding a periodic magnetic field, the ferromagnetic nanofluid evaporates in 38 minutes, which indicates that the addition of a periodic magnetic field prominently promotes the evaporation of the magnetic nanofluid droplets. The magnetic particles are inclined to deform under the action of magnetic field force. Additionally, the gas-liquid interface shape is unstable under a periodic magnetic field, which promotes the mass transfer of the droplets.

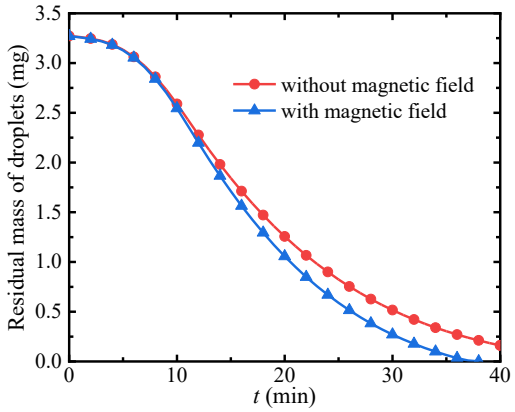


Figure 32 - Residual mass of ferromagnetic nanofluid droplets with and without periodic magnetic field

The temperature field and velocity field of the droplet during the evaporation with and without a periodically changing magnetic field have been compared as well. The droplet applying by a magnetic field evaporates more intensively and consumes more heat for evaporation. Therefore, the temperature of the droplets is lower than that of droplets without a periodic magnetic field. Besides, the internal velocity field is faster than that of the droplets with a magnetic field owing to the higher temperature of the droplets without a magnetic field. Additionally, the photothermal substrate continuously transfers heat upwards during the evaporation process, resulting in an obvious increase of the droplet temperature. The surface area of the droplet gradually shrinks within the evaporation process, while the corresponding evaporation rate gradually decreases as well. As the evaporation capacity of the droplet gradually decreases, the heat absorbed by the surface decreases accordingly, therefore, the droplet temperature continues to rise conversely. This process is illustrated in Figure 2. It can be seen that he average and maximum internal temperature of the droplets with a magnetic field are lower than that of droplets without the influence of a magnetic field.

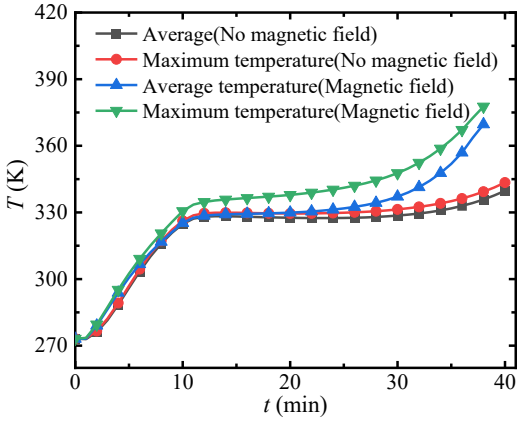


Figure 2 - Average and maximum temperature of ferromagnetic nanofluid droplets with and without magnetic field

Conclusions

The periodic magnetic field potentially promotes the evaporation performance of ferromagnetic nanofluid droplets. the droplet temperature increases in the early stage and then tends to be stable during the evaporation process.

When the droplet evaporation is almost completed and the heat absorbed by evaporation is less than the heat transferred by the photothermal substrate, the temperature of the droplet rises conversely. Although the periodic magnetic field may cause the surface deformation of the

droplet, the internal flow of the droplet remains counterclockwise, and the evaporation process is relatively stable without any droplet breakage.

Acknowledgements
This work is supported by the Natural Science Foundation of China (52206216), the Natural Science Foundation of Hunan Province (2023JJ40744)

References

[1] Hayat T, Nadeem S, Khan A. Aspects of 3D rotating hybrid CNT flow for a convective exponentially stretched surface. Applied Nanoscience, 2020, 10(8): 2897-2906.
[2] John G, Sreeneesh C, Soorej E, et al. Enhancement of cooling rate using nanofluid and hybrid nanofluid in cooling hot titanium plate. Materials Today: Proceedings, 2021, 45(4): 3891-3897.
[3] Shi L, Tao W, Huang C, et al. Magnetic-field tuning of thermal conductivity via bionic nanochain and droplet deformation. International Communications in Heat and Mass Transfer, 2023, 144: 106745.
[4] Zhang T, Zou Q, Li K, et al. Effect of SiO2 nanofluid with different concentrations on the wettability of coal. Fuel, 2022, 321: 124041.
[5] Siddiqui F, Tso C, Fu S, et al. Evaporation and wetting behavior of silver-graphene hybrid nanofluid droplet on its porous residue surface for various mixing ratios. International Journal of Heat and Mass Transfer, 2020, 153: 119618.

Dynamic simulation of the funicular liquid bridge evolution in the separation process among three particles

Dongling Wu, Yinyi Xue, Di Wu, Ping Zhou
Central South University, Changsha, China

Abstract
The distribution of the liquid bridge decides the interaction between individual particles and then the overall system strength. The funicular liquid bridge is the most common one in a medium saturated system. In this study, based on the computational fluid dynamics method, a three-dimensional mathematical model of the liquid phase flow behavior during the dynamic separation of three particles was established. The dynamic evolution characteristics of the bridge profile and the capillary force were analyzed and compared with that of the quasi-static separation process. The results show that the three-particle system has a higher cohesion effect than the two-particle system at a high separation speed.

Keywords: Wet particle, Funicular bridge, Dynamic separation, Capillary force

Introduction

In a medium saturated granular media, the liquid spreads in the form of funicular liquid bridge among three particles. Different from the pendular bridge between two particles, the funicular bridge among three particles can not be described with the toroidal or parabolic profile. Besides, when the bonded particles separate at a high velocity, the liquid bridge also evolves in a way that different from the quasi-statistic separation. Therefore, neither the previous models that used to calculate the pendular liquid bridge force nor those obtained by solving the quasi-statistic separation problem is not applicable to address the dynamic separation issue among three particles.

Methodology

The computational fluid dynamics method was used here to simulate the dynamic separation process of a triple-particle system, in which the particles were bonded with a funicular bridge, as shown in Figure 1. Detailed parameters used in this study are given in Table 1.

Table 6 – Simulation parameter

Parameter	Value
Particle radius R/ mm	5
Liquid volume V* (V/R^3)	0.53
Liquid viscosity /Pa·s	1.003×10^{-3}
Surface tension coefficient /$N\cdot s^{-1}$	7
Separation speed /$m\cdot s^{-1}$	0.073

The VOF and the dynamic meshing methods were used here. Detailed simulation procedures were given in Figure 2.



Fig. 1 Initial geometry of particle and liquid

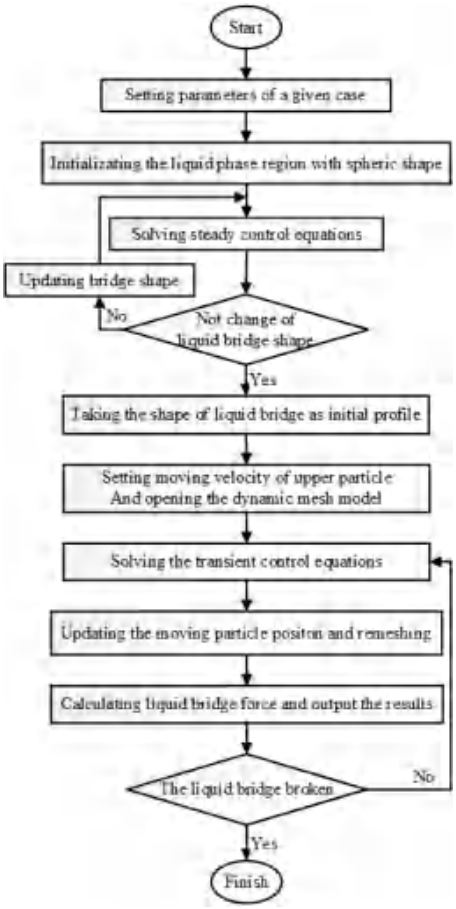


Fig. 2 Procedures of dynamic simulation of liquid bridge

The simulated results were consistent with the experimental data, as shown in Figure 3.

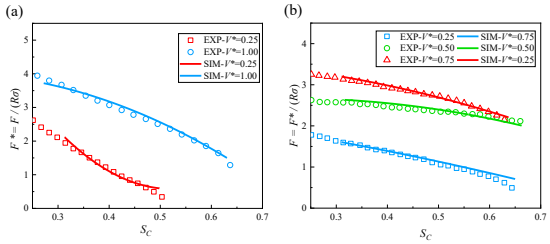


Fig. 3 Comparison of simulation results and experimental data[1]

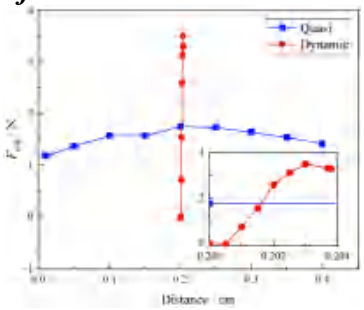
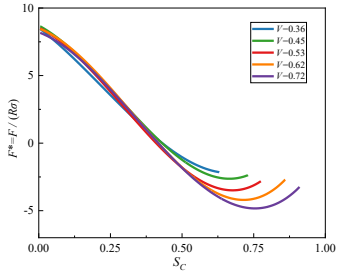


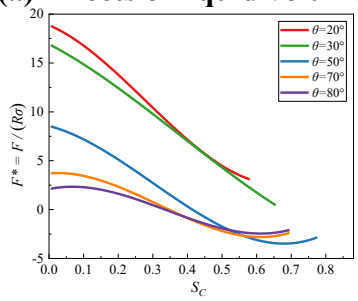
Fig. 4 Comparison of capillary force

Figure 4 shows the obtained capillary force during the dynamic and quasi-static separation process. It's clear that the capillary force during the dynamic separation process is larger than that in the quasi-static condition when the dimensionless separation distance is larger than 0.2. Effects of liquid volume, contact angle and separation speed on the contact force were shown in Figure 5. It shown that the force varies obviously with the separation distance when the dimensionless distance is larger than 0.5. The contact angle affects the force through the whole

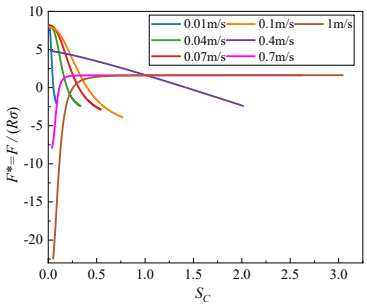
separation process. The particle with small contact angle exhibits large force. As for the separation speed, when the separation speed is smaller than 0.7 m/s, the force decreases as the separation increases, while it increases when the speed is larger than 0.7.



(a) Effects of liquid volume



(b) Effects of contact angle



(c) Effects of separation speed

Conclusions

The dynamic evolution characteristics of the funicular liquid bridge in a three-particle packing unit were obtained through a dynamic numerical simulation based on CFD. It turned out that the force obtained in the quasi-static separation process is different from that in a dynamic condition.

The effects of the liquid volume, contact angle and separation speed on the contact force were investigated. The results show that variations of the force with small and large speed are different. The viscous force dominant the separation process when the speed is larger than 0.7 m/s.

Acknowledgements

This work was supported by the National Natural Science Fund of China (Grant No. 52106217).

References

[1] Lievano D, Velankar S, McCarthy J J. The rupture force of liquid bridges in two and three particle systems. Powder Technology, 2017, 313: 18-26.

Parameter Optimization of Gas-solid Two-phase Flow in a Plasma Melting Furnace

Zhengzong Huang, Hongjie Yan, Liu Liu*
Central South University, School of Energy Science and Engineering, Changsha 410083, China
*Corresponding author, E-mail: l.liu@csu.edu.cn

Abstract
To clarify the impact of the structure and operating parameters of the plasma melting furnace on the blanking process and the melting reaction, parameters optimizations were implemented for the gas-solid two-phase flow in a plasma melting furnace by means of Euler-Lagrange approach, such as the angle and height of the feeding port, the initial velocity of slag particles, and the size of fly ash pelleting. Based on three evaluation indicators, the distribution of slag particles on the bath surface were assessed in detail, aiming to identify the optimal parameter that facilitates the melting reaction and enhances the melting efficiency. The results show that as the angle of the feeding port increases, the mass proportion of slag particles in the effective melting region decreases, their radial distribution peak increases, yet gradually moves away from the center of the bath. Enlarging the height of the feeding port is conducive to increasing the mass proportion of slag particles in the effective melting region and expanding their radial distribution range on the bath surface. Increasing the initial velocity of slag particles results in a decrease in their mass proportion in the effective melting region, while the mass ratio of different slag particles in the same radius domain gradually stabilizes and approaches the incoming ratio, which is beneficial to the melting reaction. With the increase in the size of fly ash pelleting, the mass proportion of fly ash in the effective melting region initially increases and then decreases, whereas SiO_2 is not sensitive. The radial distribution of slag particles on the bath surface is relatively stable. Only in the area away from the center of the bath the mass ratio of different slag particles varies considerably from the incoming ratio, which is not conducive to the melting reaction.

Keywords: Plasma Melting Furnace, Parameter Optimization, Gas-solid Two-phase Flow, CFD, Evaluation Indicator

Research on characteristics of the external and internal flow coupling of supercavitating vehicle

Huang Ziguang, Xiang Min
National University of Defense Technology，Chang Sha，China

Abstract
The tail gas jet of supercavitating vehicle involves a complicated flow mechanism and interaction with the head ventilation cavitation. Therefore, it is of great significance to study the coupling characteristics of the internal and external flow fields for the control of supercavitation vehicle. By changing the strength of the tail gas jet and combing with different initial supercavitation characteristics, we can observe the cavitation morphology under different experimental conditions and study the influence of internal and external flow coupling. In this paper, the method of numerical simulation is adopted, and the Mixture multi-phase flow model is coupled with the Schnerr-Sauer cavitation model to simulate and calculate the coupling characteristics of the internal and external flow of supercavitating vehicle at high speed in water. The analysis of the calculation results shows that under the condition of ventilated supercavitation, the gas of tail jet mixes with the gas in the supercavitation, causing different degrees of pressure oscillations which significantly increases the unsteady characteristic of the wake flow field. The total temperature of the tail gas jet has little influence on the size of the cavitation and the resistance of the body while the increase of the total pressure of the tail gas jet causes growth in the size of the cavitation and the resistance of the body, which suppress the head ventilation cavitation and intensifies the instability of it. Understanding the specific influence of the coupling characteristics of the internal and external flow fields on supercavitation can provide theoretical support for the research of controlling supercavitating vehicle.

Keywords: **Supercavitation; Gas jet; Ventilated supercavitation; Internal and external flow coupling**

Numerical Simulation

We conducted the experiment by numerical simulation, the emulation model is shown in Figure 33:



Figure 33 the emulation model （mm）

The mesh used for numerical simulation is shown in Figure 34:

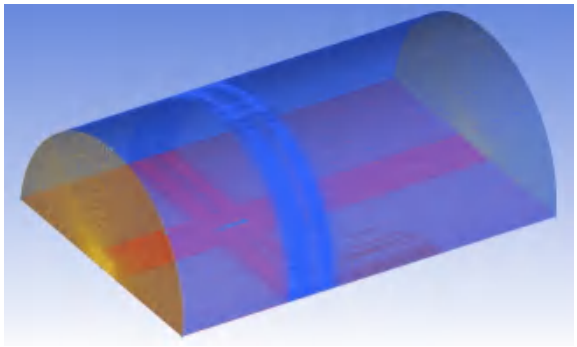


Figure 34 – the mesh used for simulation

The experimental facility used for comparison validation is shown in Figure 3:



Figure 3 – the experimental facility

Particle-resolved CFD modeling of the transfer performance in gas-solid fixed beds

Mukhtiar Ahmeda, b, Yang Yanga , Xiaoxing Liua, b, *
a State Key Laboratory of Multiphase Complex Systems, Institute of Process Engineering, Chinese Academy of Sciences, Beijing 100190, China
b University of Chinese Academy of Sciences, Beijing 100190, China

Abstract
Particle-resolved CFD simulations are a powerful tool to analyze the intricate hydrodynamic and transfer behavior occurring at the level of individual particles within a fixed bed. In this study we employ a combination of sequential Rigid Body Dynamics (RBD) method and Computational Fluid Dynamics (CFD) simulations to investigate the local flow structures and transfer phenomena within random packings composed of spheres, cylinders, and trilobes. By conducting these simulations and analyses, the we seek to advance the understanding of particle-fluid interactions in fixed beds and provide valuable insights for optimizing processes involving fixed bed reactors.

Keywords: Particle-resolved CFD, Fixed bed, particle shape, Hydrodynamics, transfer coefficients

Introduction

In recent years, advanced computational techniques have revolutionized our ability to understand and optimize the behavior of fixed bed reactors at the particle level [1,4]. One such technique is particle-resolved simulation, which enables the detailed modeling of individual particles within the packed bed. By employing this method researchers can gain valuable insights into the flow patterns, transfer mechanisms, and the impact of particle shape on reactor performance [2,3] . Furthermore, we seek to understand how variations in bed size, characterized by parameters such as bed length and diameter, affect the overall performance of fixed bed reactors. Through this research, we contribute to advancing the understanding of flow and heat/mass transfer phenomena in fixed bed reactors, paving the way for improved reactor design to enhanced process performance in chemical, petrochemical, and other industrial sectors [1-4] .

Mathematical Model

Continuity equation

$$\frac{\partial \rho}{\partial t} + \nabla \cdot (\rho \boldsymbol{u}) = 0$$

Momentum equation

$$\frac{\partial}{\partial t}(\rho \boldsymbol{u}) + \nabla \cdot (\rho \boldsymbol{u}\boldsymbol{u}) = -\nabla p + \nabla \cdot (\tau) + \rho \boldsymbol{g} + \boldsymbol{S}$$

Energy equation for fluid

$$\frac{\partial}{\partial t}(\rho E_f) + \nabla \cdot (u_f(\rho E_f + p)) = \nabla \cdot (k_f \nabla T + (\tau \cdot u_f)) + S_h$$

Energy equation for solid

$$\frac{\partial}{\partial t}(\rho S_e) = \nabla \cdot (k_s \nabla T) + S_h$$

Heat transfer coefficient

$$Nu = \frac{h d_p}{k_f}, \quad where\ h = \frac{Q_{wall}}{\Delta T}$$

$$\Delta T = (\Delta T_B - \Delta T_A)/ln\left(\frac{\Delta T_B}{\Delta T_A}\right)$$

Mass transfer coefficient

$$Sh = -\frac{Pe}{AL} ln\left(1 - \frac{P_{out}}{P_{sat}}\right)$$

$$k = \frac{Sh \times D_{A,f}}{d}$$

Geometrical Model

Table 1 Structural parameters for the catalyst particles with different shapes

	Sphere	Cylinder	Trilobe
d	1.5 mm	1.5 mm	1.5 mm
l	-	1.5 mm	1.5 mm
d_{eq}	1.5 mm	1.67 mm	1.660 mm

The RBD approach utilized in this work to simulate the packing behavior of particles with 3 different particle shapes including sphere, cylinder, and trilobe within a confined cylindrical tube. In this particular work, the focus is on investigating the behavior of fixed beds using above three distinct shapes. Each of these shapes has unique characteristics that affect how they pack within the bed. For instance, spheres tend to form close-packed arrangements, while cylinders may exhibit more ordered stacking patterns., trilobes introduce additional complexities (the geometrical scheme can be seen in fig.1) due to their specific geometries, which can influence factors such as flow dynamics, and transfer coefficients within the fixed bed [4] .

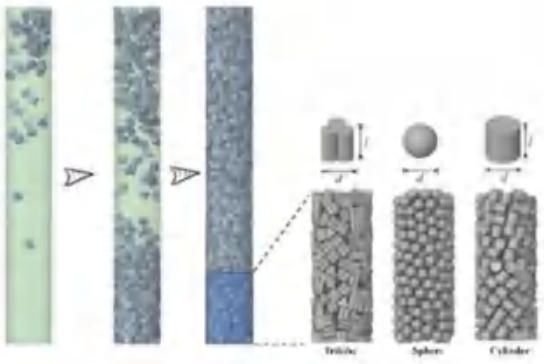


Fig. 1 Representative snapshots of structures of spheres, cylinders and trilobe with N = 5.3.

In the Ansys mesh setup, we employ a refined grid strategy starting with a fundamental grid size of d/30. It incorporates a boundary layer comprising 5 layers, expanding with a growth rate of 1.2. The initial layer is especially fine, with a grid size of d/1000, contributing to an overall grid count of approximately 10 million.. To ensure smooth contact regions, each shape is slightly shrunk by 1% around its center (fig.2. a and b). Verification of grid independence of PRCFD- simulation results have been onducted, can be seen in fig.2c [4] .

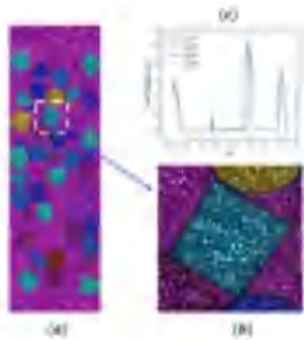


Fig. 2 (a) CFD grid, (b)mesh, and (c) verification of mesh independence of the grid

The velocity profiles for particles of varying shapes for spherical particles, the flow tends to be more uniform and streamlined, allowing for predictable velocity gradients throughout the bed, which are illustrated in fig.3 (a and b). Cylinder and trilobe introduce complex flow patterns due to their irregular geometries. This study meticulously quantifies Heat transfer efficiency across different particle shapes and bed sizes. Spherical and cylindrical particles facilitate a more efficient heat distribution. Trilobe particles present a challenge for heat transfer due to irregular surface area, which can be seen in fig.3 (c and d) [2].

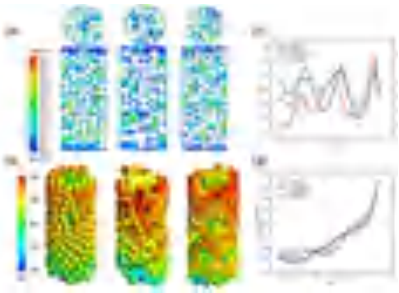


Fig.3 (a and b) velocity and (c and d) temperature distribution of particles in the bed

The mass transfer efficiency is intricately linked to the flow characteristics and structural attributes of the particle bed.

Fig.4(a-c), indicating the concentration and the impact of particle shape on mass fraction distribution is significant.

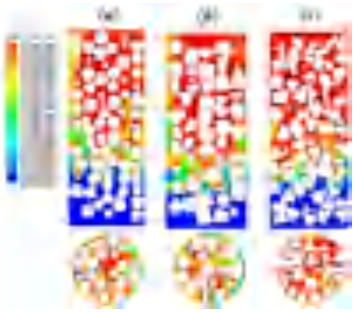


Fig. 4 (a-c) Mass fraction or concentration distribution of the beds

Fig.5 (a-d) demonstrate the precision of the method introduced in this study for calculating mass and heat transfer coefficients in fixed bed reactors. The Sherwood and Nusselt numbers derived from this method align closely with those obtained from experiments across various velocities [2,3].

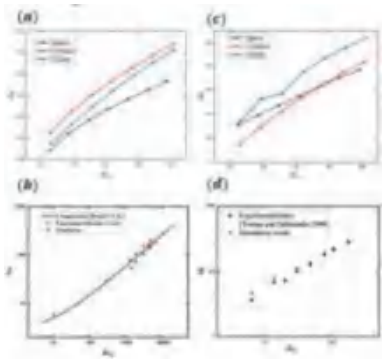


Fig.5 (a and b) calculated Nusselt and Sherwood number and (c) calculated Nusselt numbers with experimental ones and (d) calculated Sherwood numbers with experimental ones

Conclusions

Particle-resolved simulations offer crucial insights into flow and transfer behaviors in fixed bed reactors, highlighting how particle shape and bed size affect these processes. Validating these simulations with Nusselt and Sherwood numbers ensures their accuracy and reliability, aiding in model refinement and the design of more efficient reactor systems. This ongoing improvement allows to enhance reactor performance, optimize designs, and facilitate industrial scaling.

Acknowledgements

Mukhtiar Ahmed acknowledge funding from the National Key Research and Development Program of China (Grant No. 2022YFB4101703), the Innovation Academy for Green Manufacture at the Chinese Academy of Sciences (IAGM- 2019-A13), and the State Key Laboratory of Multiphase Complex Systems (MPCS-2021-A-14).

References

[1] B. Niu, M. Ahmed, T. Wen, G. Xu, X. Liu; Particle- resolved CFD modeling of the flow and heat transfer characteristics of the fluid in a fixed bed, Powder Technology 421 (2023) 118445.

[2] E.M. Moghaddam, E.A. Foumeny, A.I. Stankiewicz, J.T. Padding, Heat transfer from wall to dense packing structures of spheres, cylinders andRaschig rings, Chem. Eng. J. 407 (2021) 127994.

[3] E.M. Moghaddam, E.A. Foumeny, A.I. Stankiewicz, J.T. Padding, Fixed bed reactors of non-spherical pellets: Importance of heterogeneities and inadequacy of azimuthal averaging, AIChE Journal 69 (2023) 1-14.

[4] E.M. Moghaddam, E.A. Foumeny, A.I. Stankiewicz, J.T. Padding, Multiscale modelling of wall-to-bed heat transfer in fixed beds with non-spherical pellets: From particle-resolved CFD to pseudohomogenous models, Chem. Eng. J. 236 (2021) 116532.

Multiscale discrete–continuum simulation of granular flow

Shuai Zhang, Wei Ge*
State Key Laboratory of Mesoscience and Engineering, Institute of Process Engineering, Chinese Academy of Sciences, Beijing, 10049, China

Abstract
With various discrete or continuum-based methods facing different aspects of the complexity of granular materials, their multi-scale coupling may lead to more effective and efficient methods. In this work, a novel spatial-temporal multiscale method is proposed with spatially overlapped continuum and discrete systems running alternately at different time steps to accelerate the simulation. The feasibility and accuracy of this method are demonstrated by comparing to typical traditional methods for silo discharge.

Keywords: Continuum-discrete method; Discrete element method (DEM); Granular flow; Moving-particle semi-implicit (MPS)

Introduction

Taking advantages of both continuum and discrete methods and alleviating their drawbacks, two kinds of hybrid methods, concurrent methods and hierarchical methods, have been proposed recently to accelerate the simulation of granular flow[1]. However, almost all methods speed up the simulation by reducing the particles tracked, leading to the loss of particle-level information. In this study, a spatial-temporal multiscale method is proposed to accelerate the simulation of granular flow. The two methods are spatially overlapped and temporally alternative, running at different time steps to achieve much higher overall performance than pure discrete or continuum methods [1].

Methodology

As shown in Figure 1, the spatial-temporal multiscale hybrid method consists of two spatially overlapped and temporally alternative systems where granular material was described by MPS in the continuum system and by DEM in the discrete system. As shown in Figure 2, the two systems exchange information through mapping with linkage and weight function, and the momentum coupling method assuming a virtual coupling force enforces their consistency. The large time step enabled by the semi-implicit scheme in the continuum system (Typically Δt_{MPS}>10~100 Δt_{DEM}) and the particle-level characteristic and information reserved in the discrete system are integrated to achieve both high efficiency and resolution.

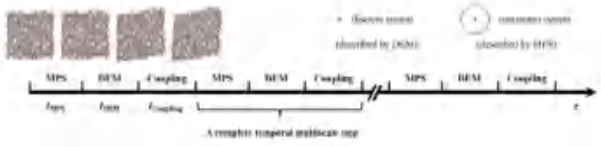


Figure 35 - Schematic diagram of the evolution for the hybrid method

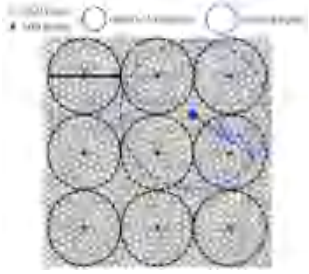


Figure 2 - The spatial distributions of the continuum and discrete systems

Conclusions

In the spatial-temporal multiscale method, the MPS was used for the continuum system as a predictor to estimate the potential position of each particle, and the 'coarse-grained' MPS particles governed by semi-implicitly solved N-S equations evolve at large time step to accelerate the computation. The DEM was employed for the discrete system to correct the predicted position and provide more accurate particle-level information. The feasibility and accuracy of this method are demonstrated in the case of silo discharge where a comparable flow field and 12× speedup compared to DEM were reached.

References

[1] S. Zhang, W. Ge, C.J. Liu, Spatial–temporal multiscale discrete–continuum simulation of granular flow. Physics of Fluids, 35(2023) 053319.

Soft coarse-grained particle model for particle-fluid systems

Wei Ge*, Shuai Zhang, Yanhao Ye, Ji Xu
State Key Laboratory of Mesoscience and Engineering, Institute of Process Engineering, Chinese Academy of Sciences, Beijing, 10049, China

Abstract
The coarse-grained discrete particle method (CG-DPM) made it possible to simulate industrial-scale particle-fluid systems. However, a systematic approach to determine the CG particles' (CGPs) properties and develop their interaction models is still lacking. In this study, a soft-shell CG model was developed by analyzing the collision between two predefined particle groups. Its capability was demonstrated in the simulation of a 3.5 Mt/a industrial-scale maximizing iso-paraffins (MIP) reactor-regenerator loop.

Keywords: Coarse-grain (CG); Discrete particle method (DPM); Fluidized bed; Multiscale simulation

Introduction

CG-DPM has been demonstrated effective to bridge lab-scale simulation with industrial application. However, due to the complexity of granular interactions, strict similarity is hardly achievable, which restricts the applicable range and the CG ratio k ($k = d_{\mathrm{CGP}}/d_{\mathrm{r}}$, with d_{CGP} and d_{r} being the diameter of CGPs and real particles). The EMMS-DPM presented in our early work introduces the internal porosity and soft shells to CGPs and treats the interactions between two CGPs as gradual engagement of two swarms of member particles. However, the interactions between the soft shells are neglected. In this study, the total collisional forces between two approaching groups of physical particles are measured to establish the CG model containing the soft-shell interactions [1,2].

Methodology

Identical real particles are generated randomly inside two virtual spheres representing the contours of the two equal-sized CGPs which move towards each other for a head-on collision. Once the members are in contact, their collisions are processed in the discrete element method (DEM), which produces an effective contact force $\mathbf{F}_{\mathrm{x}}$ between two CGPs. Then $\mathbf{F}_{\mathrm{x}}$ can be correlated as a function of the CGP and real particle parameters, denoted as $\mathbf{F}_x(k, \varphi, e_{\mathrm{r}})$, where φ is the internal solid fraction of CGPs and e_{r} is the restitution coefficient of real particles. A fitting coefficient λ is introduced to develop a general form of the CGP model $\mathbf{F}_{\mathrm{c,shell}} = \lambda\mathbf{F}_{\mathrm{x}}$, with its value determined by matching the statistical properties of the CG and real systems. In this work, the model parameters λ and γ (ratio of granular temperature between CG and real systems) are determined by ensuring the equivalence of granular pressure and granular temperature dissipation rate.

Conclusion

As shown in Figure 1, the soft-shell CG-DPM is verified in the simulation of an industrial-scale MIP reactor-generator loop with a CG ratio of up to 800, making it one of the most complex discrete simulations reported to date. The solid fraction showed good agreement with the factory data, indicating that the model is capable of correctly predicting the particle-fluid dynamic in the industrial fluidized bed.

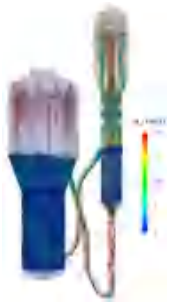


Figure 36 - Snapshot of the particle in the loop

References

[1] Y.H. Ye, J. Xu, W. Ge, Soft coarse-grained particle model for particle-fluid systems. Particuology, 84(2024), 178-193.
[2] Y.H. Ye, S. Zhang, J. Xu, et al, 3D coarse-grained DPM simulation of the MIP reaction-regeneration loop. Particuology, 89(2024), 57-66..

Numerical study on the flow field about steam condensation in the suppression pool by multi-hole spargers

Weixiong Chen *, Zhenghang Luo, Jingyu Li, , Quanbin Zhao, Daotong Chong, Junjie Yan
State Key Laboratory of Multiphase Flow in Power Engineering,
Xi'an Jiaotong University, Xi'an 710049, PR China

Abstract

Direct contact condensation (DCC) between subcooled water and superheated steam is a common event encountered in many two-phase systems. Considering the computational efficiency, long transient simulation studies are not suitable due to the complexity of DCC. A multi-scale modeling approach is introduced for long-time simulations of steam condensation into the suppression pool from spargers. The thermal stratification and mixing phenomena are well captured in the simulation.

Keywords: Direct Contact Condensation, Multi-scale Modelling, Numerical simulation, Pressure Suppression Pool

Introduction

The pressure suppression pool (PSP) is a key component in the safety systems in BWRs. The release of high-temperature steam into the PSP results in significant thermal stratification, and the water may boil and cause a rapid rise in containment pressure. Therefore, the prediction of temperature distribution in the PSP becomes crucially important.

The effective heat source and effective momentum source (EHS/EMS) models have been proposed to simulate the pool flow behavior and widely developed [1]. Moreover, the direct modeling of DCC is carried out in this study assisting to model the EMS region.

Methodology

In this study, a multi-scale modeling method is adopted to accurately simulate the DCC phenomena and thermal stratification happening during the pressure relief. Only the water space of PSP is considered in this study: the water space has a volume of 355 m^3 and a height of 4.1 m. When an overpressure accident occurs, high-temperature steam will be injected into the PSP through two pressure relief pipelines. In the jet scale, the direct modeling of steam injection from single/multi orifices is carried out to determine the characteristics of steam plumes. From these results, the steam penetration length is identified to be 62 mm and the EMS region is modeled in the pool scale. In the pool scale, the effective heat source and effective momentum source (EHS/EMS) models are used for simulating the thermal stratification and mixing. The temperature field is plotted as Figure 1 shows. The heat accumulates on one side of the PSP and temperature continues to rise. Clear stratification can be observed.

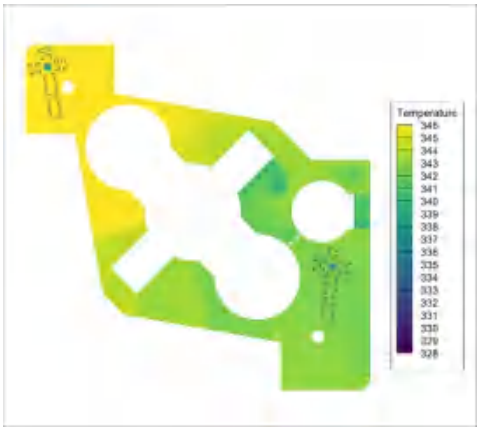


Figure 37 – Contour of temperature distribution in PSP at t=360 s

Conclusions

A numerical simulation of long-term transient steam injection into PSP is conducted. The multi-scale modelling approach is established: the direct modeling at jet scale; the EHS/EMS model at pool scale.

Acknowledgements

This work was supported by National Natural Science Foundation of China (No. U2241257, No.51876166).

References

[1] H.S. Kang, C.H. Song, CFD analysis for thermal mixing in a subcooled water tank under a high steam mass flux discharge condition, Nucl. Eng. Des., 238 (3) (2008) 492-501.

Simulation of gas-solid two-phase flows with two-fluid model and data-driven closures

Yunhua Zhao, Jiahao Xu, Haoyang Cao
Zhejiang University of Technology, Hangzhou, China

Abstract
Efficiently simulating gas-solid flow in fluidized bed remains still challenging due to it intricate multi-scale structures. In this study, two-fluid model (TFM) simulation of a specific fluidized bed is separated into two steps. The first step entails local fine grid simulations to establish data-driven closures, and the second step is whole-domain simulations using coarse grid. It is shown that this two-step approach improves the prediction accuracy when using coarse grid, while significantly reduces the computing cost regarding whole-domain fine grid simulations.

Keywords: Two-fluid Model, Two-step Approach, Gas-solid Flow, ANN Model

Introduction

The TFM has great potential for the simulation study of industrial fluidized beds, because it is not directly limited by the number of particles. Usually, industrial apparatuses are of large dimensions, and the corresponding TFM simulations might be feasible only if coarse mesh grids are used. Following the idea of the Filtered TFM, numerical simulation of a specific fluidized bed is separated into two steps to enhance the prediction performance with data-driven method.

Methodology

For the first step, local domain simulations with various solid holdups were carried out to resolve the spatial and temporal heterogeneity of gas-solids flows. The Gidaspow drag model and the kinetic theory (KT) of granular flow model were employed for all the simulations. Then the gas velocity, solid velocity and concentration were averaged over the filtered-scale. At the same time, the superficial drag force, solid viscosity and pressure within the filtered-scale region were calculated. After that, artificial neural network (ANN) models were trained for predicting the drag, solid viscosity and pressure.
For the second step, the ANN models were incorporated into the global domain simulations.

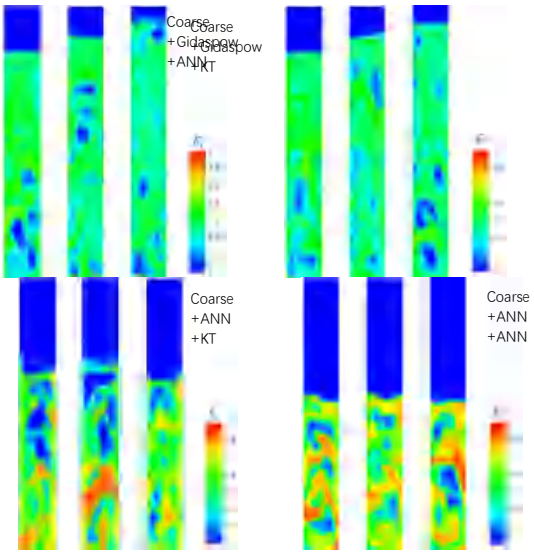


Figure 38 – Snapshots of solid distribution

Table 7 – Comparison of Computing cost

Simulation setups			Computing time	Storage space
Grid	Drag	Solid		
Coarse	Gidaspow	KT	96 s	113 Mb
Coarse	ANN	KT	100 s	113 Mb
Coarse	Gidaspow	ANN	57 s	113 Mb
Coarse	ANN	ANN	67 s	113 Mb
Fine	Gidaspow	KT	13 h 50 m 28 s	2.39 Gb

Conclusions

The TFM with ANN models improves the gas-solid flow prediction, with the drag model exhibiting a more crucial effect than the solid constitutive model. Furthermore, the two-step separated approach significantly reduces the computing cost during global domain simulation.

Acknowledgements

The authors gratefully acknowledge financial support from the National Natural Science Foundation of China under Grant No. 51976194.

Nucleation and Growth of Au Nanocrystals during Aerosol Synthesis

Yi Wang, Kai H. Luo, Sotiris E. Pratsinis
Tsinghua University, Beijing, China

Keywords: Nucleation, Aerosol synthesis, Flame reactor, Au nanoparticle, Molecular dynamics

Introduction

Gold nanoparticles have versatile applications in catalysis, sensing, medicine, nanolithography, and ion detection [1]. Even though they are commercially manufactured by wet-phase processes, gas-phase (flame, plasma, laser, etc.) processes are becoming attractive for their simplicity and proven scalability [2]. Flame aerosol processes in particular have been proven most advantageous for manufacturing commercial nanoparticles with high purity and well-controlled size and morphology [1]. The crystallinity of Au nanoparticles can influence their performance in electronic devices. Moreover, the Raman-scattering, absorption, fluorescence as well as two-photon emission properties depend on Au crystallinity and grain size, while the nanoparticle shape depends also on crystalline structure.

Due to the high flow rate and short nanoparticle residence time in flame reactors, the Au crystallinity dynamics (nucleation and growth) are hard to study experimentally, especially for sub-10 nm sizes. At such conditions, molecular dynamics (MD) simulations provide valuable insight of the major physicochemical processes (surface vs. bulk particle composition, sintering rate etc.) affecting aerosol dynamics and their quantitative description [3].

Results

During flame synthesis, particles are formed under high temperature, steep cooling rates and short residence times. The flame temperature has been proved profound effects on the crystallinity, size, and morphology. The crystallization onset mechanism as well as the crystal growth variables under isothermal conditions are our main foci.

Here, the onset of Au crystal formation is closely monitored after rigorous method validation [1]. A metastable region during Au solidification is revealed. Sub-critical, critical and super-critical cluster formation and growth are elucidated.

The self-defined crystal atoms keeping ratio is used to quantify the change in the nanoparticle crystal structure. This is observed to increase from 10 to 80 % during the crystallization onset of a 10 nm Au at 800 K (Fig. 1, $t \leq 0.8$ ns). Meanwhile, the average crystal size grows from 0 to 3.2 nm continuously. The 3D & cross-section snapshots of the Au particle show crystal growth by accretion and cluster merging. Moreover, reorganization of the lattice after nucleation and the final crystal sizes reveal the influence of the crystallization temperature.

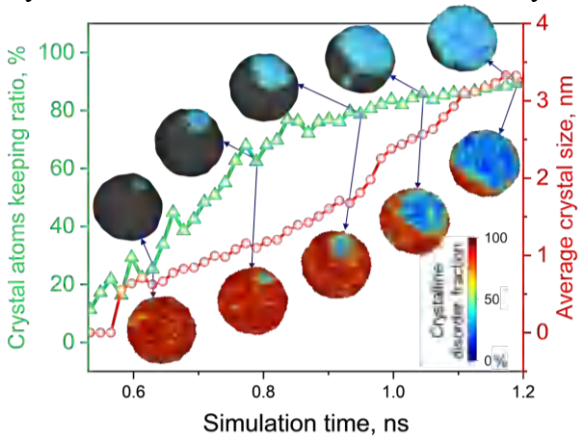


Figure 1. Crystal atoms keeping ratio and crystal size of a 10 nm Au particle @ 800 K with its 3D-snapshots (upper sequence) and their cross-sections (lower sequence) colored according to crystalline disorder.

Conclusions

Crystallization near the supercooled solidifying temperature results in the largest Au crystals. The onset of crystallization is accompanied by a sharp drop of the potential energy and the amorphous fraction during which the subcritical nuclei transform to super-critical crystals. Crystallization usually starts near the surface of the nanoparticle as a result of the lower kinetic energy barrier of the surface atoms. The dynamics of phase transition and crystal growth are elucidated from XRD patterns and are compared to direct tracing of crystal sizes.

[1] E. Goudeli, S. E. Pratsinis, (2016). AIChE J. 62: 589-9.
[2] G.A. Kelesidis, S.E. Pratsinis (2021). Chem Eng J. 421:129884.
[3] V. G. Mavrantzas, S. E. Pratsinis, (2019). Curr. Opin. Chem. Eng. 23: 174-83.

Complex non-Newtonian droplet generation and flow pattern evolution in geometrical confined microfluidic cross-junctions

Lian Duan, Wenjun Yuan*, Nanjing Hao
School of Chemical Engineering and Technology, Xi'an Jiaotong University, Xi'an, China

Abstract
Droplets with complex rheology are pivotal in various engineering domains. Nevertheless, their formation mechanisms remain underexplored. This work employs finite-volume direct numerical simulations to study viscoelastic and yield stress droplet formation in cross-junction microchannels. The volume of fluid approach, combined with cell-based adaptive mesh refinement, is utilized for interface tracking. To accurately depict the rheological properties of the fluids, the exponential Phan-Thien-Tanner model is employed for viscoelastic fluids, while the Herschel-Bulkley model is utilized to characterize yield stress fluids. Simulations align well with experimental data. Three typical flow patterns of dripping, jetting, and threading are obtained in viscoelastic droplets, influenced by elasticity (Weissenberg number *Wi*) and viscosity (capillary number *Ca*). Elastic effects are pronounced in dripping, notably diminishing axial tensile stress. Variations in polymer macromolecules' stretched states at constant *Wi* but varying *Ca* impact the extension length and droplet pinch-off timing. For yield stress droplets, flow pattern and droplet size are regulated by geometric constraints within microchannels while enhancing droplet generation efficiency. This study culminates in semi-empirical models for predicting the size and generation frequency of both droplet types.

Keywords: Direct numerical simulations, Viscoelasticity, Yield stress, Droplets, Geometric constraints.

Introduction

In recent years, microreactor technology has made significant strides, with applications for precise droplet manipulation in chemical, materials, and biomedical industries. Investigating microreactors' hydrodynamics enhances droplet behaviour understanding, microreactor usage, and microchemical technology progression. However, there is still a limited selection of complex fluids available for manipulation [1, 2].

This study explores polymeric and yield stress droplet hydrodynamics in cross-junction microchannels using 3D simulations. The simulation results are first compared with the experimental results in the literature to verify the numerical models. Then, the flow patterns of different viscoelastic fluids are obtained to study the droplet formation mechanism. Meanwhile, the influence of geometric constraints of microchannel on flow patterns, droplet size, and frequency is assessed. Ultimately, semi-empirical models to predict droplet size and frequency for both droplet types are proposed.

Methodology

Assuming an incompressible and isothermal flow, the governing equations for the velocity field are initially discussed as follows:

$$\nabla \cdot \boldsymbol{u} = 0, \tag{1}$$

$$\rho[\frac{\partial \boldsymbol{u}}{\partial t} + \boldsymbol{u} \cdot \nabla \boldsymbol{u}] = -\nabla p + \nabla \boldsymbol{\tau} + \gamma \delta \kappa \boldsymbol{n}. \tag{2}$$

The viscoelastic PTT model developed by Phan-Thien and Tanner [3] was used to account for the effects of extensional viscosity. The constitutive equation is shown in equation (3):

$$f(\mathrm{tr}(\boldsymbol{\tau}))\boldsymbol{\tau} + \lambda \overset{\triangledown}{\boldsymbol{\tau}} = 2\eta_{\mathrm{P}} \boldsymbol{D}, \tag{3}$$

where λ, $\overset{\triangledown}{\tau}$, and η_{P} are the relaxation time of the polymer, Gordon–Schowalter derivative, and viscosity of polymers, respectively.

The Herschel–Bulkley model could explain the motion of yield stress fluids [4], where the viscosity is described by:

$$\eta = \begin{cases} \eta_0 & \tau < \tau_0, \\ \frac{1}{|\dot{\gamma}|}\left(\tau_0 + k\left(|\dot{\gamma}|^n - (\tau_0/\eta_0)^n\right)\right) & \tau \geqslant \tau_0. \end{cases} \quad (4)$$

Below yield stress τ_0, fluids display solid-like behaviour with set viscosity η_0. Exceeding τ_0, viscosity follows a power-law model defined by consistency k and behaviour index n.

Results and Discussion

In Fig. 1, as for the viscoelastic droplet formation, at lower *Ca*, *Wi* has little effect on the flow patterns, which are all dripping flow. When *Ca* is increased, the higher viscous forces allow the emergence of jetting and threading flow patterns. Interestingly, at higher *Ca*, the increase in *Wi* results in a transition of the flow pattern. In Fig. 2, it is evident that tr($\boldsymbol{\Theta}$) for the dripping flow > tr($\boldsymbol{\Theta}$) for the jetting flow > tr($\boldsymbol{\Theta}$) for the threading flow, which is caused by slower diffusion of the polymer chains at high viscosities.

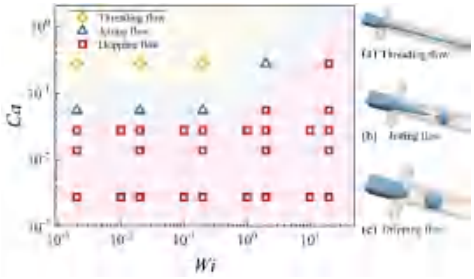


Figure 1 - Flow patterns transition with different Wi and Ca.

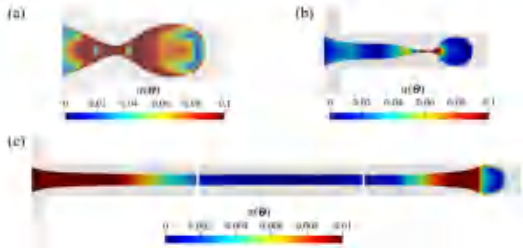


Figure 2 - The distributions of the trace of the natural logarithm of the conformation tensor Θ: (a) dripping flow, (b) jetting flow, and (c) threading flow.

Furthermore, we employed a semi-empirical correlation equation considering the Weissenberg number *Wi*, the dispersed phase capillary number Ca_d, and the superficial velocity ratios to predict the droplet size and generation frequency. By fitting the data to the operating conditions, the droplet dimensionless volume and generation frequency are predicted as shown in the following equations:

$$\frac{V}{w_d^3} = 0.57 Wi^{0.04} Ca_d^{-0.13} \left(\frac{U_c}{U_d}\right)^{-0.33} \quad (R^2 = 0.98), \quad (5)$$

$$f = \frac{Q_d}{V} = \frac{U_d}{0.57 w_d Wi^{0.04} Ca_d^{-0.13} \left(\frac{U_c}{U_d}\right)^{-0.33}}. \quad (6)$$

Figure 3 demonstrates the flow transition of the yield stress droplet generation for different channel contraction lengths *l** and contraction widths *w**. It can be seen that the increase in the *w** and *l** of the channel constriction facilitates the conversion of jetting flow into a quasijetting or dripping flow, which is conducive to the generation of stable droplets.

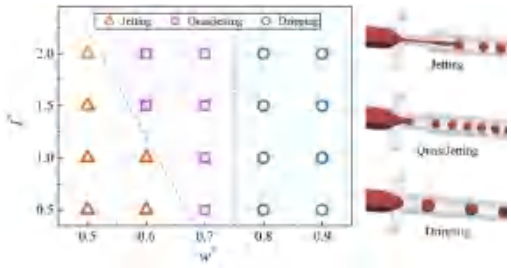


Figure 3 - Flow patterns transition with different l* and w*.

Conclusions

This study elucidates the formation mechanisms of viscoelastic and yield stress droplets in microchannels. Three typical flow patterns of dripping, jetting, and threading were obtained, under different *Wi* and *Ca*. Elastic effects are pronounced in dripping flow, notably diminishing axial tensile stress. In addition, yield stress droplet behaviour is significantly influenced by microchannel geometry contraction. The research concludes with semi-empirical models for predicting droplet size and frequency, contributing valuable insights to the field of complex fluid manipulation.

Acknowledgements

We gratefully acknowledge the supports of the National Natural Science Foundation of China (No. 52306203), QCY Innovative and Entrepreneurial Talent Programme of Shaanxi Province (No. QCYRCXM-2022-134) and the Young Talent Support Plan of Xi'an Jiaotong University - XJTU (No. 71211222010703).

References

[1] X. Xiang, Z. Wang, Y. Dong, C. Zhu, T. Feng, Y. Ma, T. Fu, Droplet formation of yield stress fluids in asymmetric parallelized microchannels, Chem. Eng. Sci. 285 (2024) 119561.

[2] Q. Shang, H. Wang, X. Xiang, C. Zhu, Y. Ma, T. Fu, Formation of droplets of yield stress non-Newtonian fluids at T-junctions within parallelized microchannels, Chem. Eng. Sci. 274 (2023) 118696.

[3] N. Phan-Thien, R.I. Tanner, A new constitutive equation derived from network theory, J. Non-Newtonian Fluid Mech. 2 (1977) 353-365.

[4] Z. Ren, X. Zhao, H. Liu, Numerical study of the landslide tsunami in the South China Sea using Herschel-Bulkley rheological theory, Phys. Fluids 31 (2019) 056601.

Study on Regulation of Drying Process of Non-spherical Wet Particles

Hanyu Jin, Yaochen Zhu, Yuhua Lai, Shuai Wang *（shuaiwang@hit.edu.cn）
School of Energy Science and Engineering, Harbin Institute of Technology, Harbin, China

Abstract
The mass and heat transfer behavior and drying regulation method of ellipsoid wet particles in fluidized bed dryer are studied by computational fluid dynamics - discrete element method (CFD-DEM). The results show that the agglomeration of particles can be effectively broken and the drying rate of wet ellipsoid particles can be increased by pulsating flow.
Keywords: Wet Particle, Non-spherical Particle, Fluidization, Drying Regulation

Introduction

In this work, CFD-DEM simulation is implemented to investigate the mass/heat transfer behavior of ellipsoid wet particles in a fluidized bed dryer. In our recent study, a wet particle liquid bridge model has been established. Based on this, the drying regulation method of ellipsoidal wet particles will be further explored.

Methodology

The governing equations of the continuous and discrete phases and the liquid bridge force model is adoped following the previous work[1]. The energy transport equation is shown as follows:

$$\frac{\partial(\varepsilon_{\mathrm{f}}\rho_{\mathrm{f}}C_{p,\mathrm{f}}T_{\mathrm{f}})}{\partial t}+\nabla\cdot(\varepsilon_{\mathrm{f}}\rho_{\mathrm{f}}\boldsymbol{u}_{\mathrm{f}}C_{p,\mathrm{f}}T_{\mathrm{f}})=\nabla\cdot(\varepsilon_{\mathrm{f}}\kappa_{\mathrm{f}}^{eff}\nabla T_{\mathrm{f}})+Q_{\mathrm{pf}} \quad (1)$$

$$m_{p,i}C_{p,i}\frac{dT_{\mathrm{p},i}}{dt}=Q_{\mathrm{pf},i}+Q_{\mathrm{eva},i}+Q_{\mathrm{pp},i} \quad (2)$$

$$Q_{\mathrm{plp}}=\frac{\pi r^2\Delta T}{h/k_{\mathrm{f}}} \quad (3)$$

$$Q_{\mathrm{pp},ij}=\frac{4\kappa_{\mathrm{p},i}\kappa_{\mathrm{p},j}}{\kappa_{\mathrm{p},i}+\kappa_{\mathrm{p},j}}(T_{\mathrm{p},j}-T_{\mathrm{p},i})\left[\frac{3F_{\mathrm{n}}r_{ij}}{4E_{ij}}\right]^{0.33} \quad (4)$$

Results and Discussion

A two-dimensional spouted bed in the previous work is chosen. The drying regulation method of wet particles is evaluated. Figure 1 shows the drying characteristics of wet particles under the pulsating flow. The results show that the pulsating flow can break the agglomeration of particles. The drying rate of wet elliptic particles can be effectively improved by the pulsating flow.

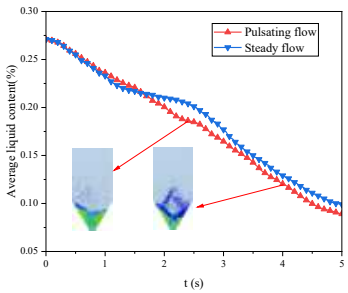


Figure 1 - The change of particle average liquid content with time under pulsating flow and steady flow

Conclusions

A heat and mass transfer model considering the change of liquid bridge volume and liquid content is used to study the regulation method of wet particle drying process. The results show that the introduction of pulsating flow can effectively break the agglomeration between ellipsoidal wet particles, strengthen the heat and mass transfer in the fluidized bed, and increase the drying rate of wet particles. Therefore, the drying process of wet particles can be accelerated by pulsating flow.

Acknowledgements
This research is conducted with financial support from the National Natural Science Foundation of China (52076060)

References

[1] S. Wang, Q. Wu, Y. He. Estimation of the fluidization behavior of nonspherical wet particles with liquid transfer. Ind. Eng. Chem. Res. 2022, 61, 10254−10263

Parallel Session VII: Topic 2-II- Multiphase flow： innovations and low-carbon engineering applications

Multi-Fidelity Optimization of Geological CO_2 Sequestration with Brine Extraction using Coarse Grid Network Model

Billal Aslam, Bicheng Yan*
Physical Science and Engineering (PSE) Division, King Abdullah University of Science and Technology (KAUST), Thuwal, 23955-6900, Saudi Arabia
*Corresponding author. Email address:bicheng.yan@kaust.edu.sa(B. Yan)

Abstract
This study presents the Coarse Grid Network Model (CGNet) as an efficient approach for simulating and optimizing CO2 sequestration with brine extraction in deep saline aquifers. CGNet is configured by aggressively coarsening the reservoir model and employing an auto-differentiable simulator based on finite volume method (FVM) to perform model training based on high-fidelity simulation outputs. Trained CGNet is used for multi-fidelity optimization of the well control with two different control parameter initialization schemes. Proposed optimization methods are tested using Johansen GCS Model with results showing up to 3.2 times
speedup compared to high fidelity optimization.

Keywords: Reduced order modelling, Reservoir simulation, Geological Carbon Storage (GCS), Multifidelity Optimization.

Introduction
Injecting CO2 into deep saline aquifers for geological storage may cause pressure build-up, which can risk storage integrity. This study addresses the optimization of well control for injection and brine extraction to manage pressure build-up. Multi-fidelity optimization with efficient surrogate model known as Coarse Grid Network Model (CGNet) is proposed.

Methodology
CG-Net can be seen as a graph-based analogy from the FVM model [1]. We consider only the compressible flow of two phases, water and super-critical CO2 (gas), with gravity effects during the injection operation.

$$\frac{1}{\Delta t}[(\Phi S_\alpha \rho_\alpha)^{n+1} - (\Phi S_\alpha \rho_\alpha)^n] + \mathbf{div}(\rho_\alpha v_\alpha)^{n+1} = q_\alpha^{n+1}, \alpha \in \{w, g\} \quad (1)$$

$$v_\alpha = -\mathbf{upw}(\lambda_\alpha)\mathbf{T}(\mathbf{grad}(p) - \mathbf{gavg}(\rho_\alpha)\mathbf{grad}(z)) \quad (2)$$

$$q_\alpha = \lambda_\alpha^{wc}\mathbf{WI}(p^{wc} - p) \quad (3)$$

We solve the mass conservation equation (Eq. 1) along with the flow equation (Eq. 2), using FVM discretization and two-point flux approximation (TPFA) for transmissibility calculation. Peaceman well model(Eq. 3) is used to represent the well inflow performance from the well block. Using Johansen formation public dataset [2], the CGNet configured from the fine scale model is illustrated in **Figure 1**. We use a 30 year duration of injection to represent the operational phase of typical GCS project.

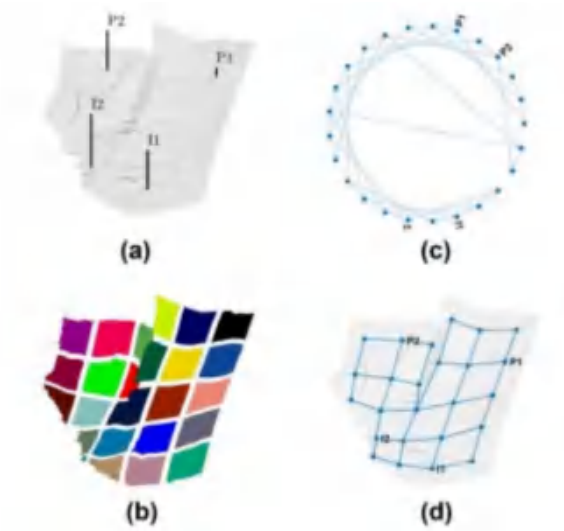


Figure 1. An example of a CG-Net model using the Johansen formation with two injectors and two producers: (a) Fine-scale mesh, (b) coarse- grid partition, (c) connectivity of the network graph shown with a circular layout, and (d) reservoir/well nodes and edges shown in physical space

To train the CGNet based on the output of the high-fidelity simulation, we minimize the misfits between the production well rates, injection well bottomhole pressure and upscaled saturation states by tuning the transmissibility (T), node pore volumes (Φ), relative permeability end-points and well indices (WI) using Levenberg-Marquardt algorithm [3]. **Figure 2** shows the verification of CGNet in predicting the upscaled saturation states at the end of the training period.

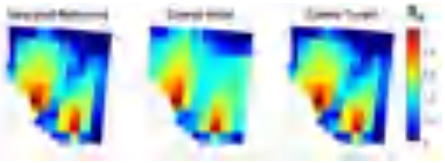


Figure 2. Upscaled Saturation Maps Comparison for the testing data

The trained CGNet is then used for well-control optimization (rate management) by maximizing the NPV of the storage operation under operational constraint (BHP limit in injector). **Figure 3** shows the NPV evolution during the optimization iteration.

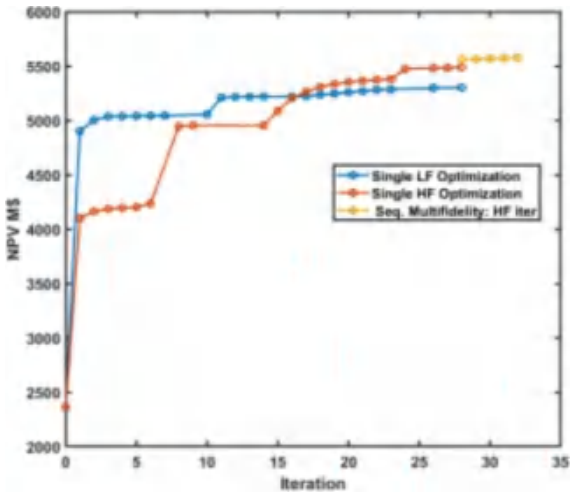


Figure 3. Objective function (NPV) evolution during optimization iteration. LF - low fidelity; HF - high fidelity.

We observed that the Multifidelity optimization using CGNet achieve similar NPV value compared to direct high-fidelity optimization. This indicates that the trained CGNet is able to lead the optimizer into the optimal solution space. **Table 1** compares the NPV at the end of optimization along with the CPU time. In total, we achieve around 3.2 times speedup. This is attributed to the faster simulation runs from the low fidelity model (CGNet) and less iteration in the high fidelity optimization stage.

Table 1 - Table of NPV and CPU time for each Optimization Scheme

Scheme	Low Fidelity Runs	High Fidelity Runs	CPU time (sec)	NPV (M$) @ref
Single LF Optimization (CG)	28	-	522.84	5,563.6
Single HF Optimization (Fine)	-	28	4245.15	5,489.3
Seq. Multifidelity	28	5	1352.18	5,576.1

Conclusions

Using the Norwegian Johansen GCS model for numerical experiment, CGNet demonstrated significant improvements in efficiency and accuracy. Speedup of up to seven times compared to high-fidelity simulations is achieved at the optimal coarsening level with less than 0.1% error. In optimizing well controls, CGNet was 3.2 times faster than direct high- fidelity optimization while achieving comparable results. CGNet thus offers a valuable tool for rapid and accurate simulation and optimization of geological CO2 sequestration processes.

Acknowledgements

We acknowledge the Research Funding from King Abdullah University of Science and Technology (KAUST), Saudi Arabia for the generous support and grants in this work, including BAS/1/1423-01-01 and FCC/1/4491- 39-01. We also thank Knut-Andreas Lie and Stein Krogstad from SINTEF for the useful suggestions to develop this work.

References

[1] K.-A. Lie and S. Krogstad, “Comparison of two different types of reduced graph-based reservoir models: Interwell networks (GPSNet) versus aggregated coarse-grid networks

(CGNet)," *Geoenergy Science and Engineering*, vol. 221, p. 111266, Feb. 2023, doi: 10.1016/j.petrol.2022.111266.
[2] G. T. Eigestad, H. K. Dahle, B. Hellevang, F. Riis, W. T. Johansen, and E. Øian, "Geological modeling and simulation of CO2 injection in the Johansen formation," *Comput Geosci*, vol. 13,no. 4,pp. 435–450, Dec. 2009, doi: 10.1007/s10596-009-9153- y.
[3] B. Aslam, B. Yan, Z. Tariq, S. Krogstad, and K.-A. Lie, "Rapid Simulation and Optimization of Geological CO2 Sequestration Using Coarse Grid Network Model," presented at the SPE/IATMI Asia Pacific Oil & Gas Conference and Exhibition 2023, OnePetro, 2023.

Solid-solid stress model for the gas-fluidization of binary mixtures based on Inertial number

Guodong Liu, Junnan Zhao, Xinyao Guo
Harbin Institute of Technology, Harbin, China

Abstract
Diverse flow regimes often coexist in gas-solid two-phase flows. Particles of different sizes and densities exhibit complex flow behaviours and thus forming different flow regimes. A cross-flow-regime constitutive model of solid phase including the cross-flow-regime solid stress model (CFR-SM) and cross-flow-regime solid-solid drag model (CFR-DM), is developed. The model provided accurate predictions from a bubbling fluidized bed with particle density and size differences and could physically explain the viscosity variations through all the flow regimes.

Keywords: Bubbling Fluidized bed, Two Fluid Model, Solid-Solid Stress, Density Segregation, Size Segregation

Introduction

Diverse flow regimes often coexist in gas-solid two-phase flows, resulting in a cross-flow-regime phenomenon where particles exhibit a variety of behaviours such as kinetic, collision and friction. Existing numerical models, within the framework of two-fluid model (TFM), can describe the motion and force of particles in a single flow regime to a certain extent, but fail to accurately capture the complex and various interactions among particles when multiple flow regimes coexist. Therefore, it is necessary to account for the flow characteristics and interaction mechanisms among particles in different flow regimes and develop a cross-flow-regime constitutive model for the solid phase.

Methodology

Based on the theory of continuous media, for a non-sticky particle material, the frictional shear stress tensor resulting from continuous contact between particles is expressed as a function of frictional viscosity of the particles:

$$\mu_{f,m}=\frac{\eta(I_{mix})p_{s,m}}{2\|\boldsymbol{D}_{s,m}\|} \quad (1)$$

The calculation of the mixture-averaged inertial number (I_{mix}) is based on the total particle pressure of all the particle phases, as well as the average particle diameter ($d_{s,ave}$), average density ($\rho_{s,ave}$), and average strain rate deviation ($\boldsymbol{D}_{s,ave}$) of each phase:

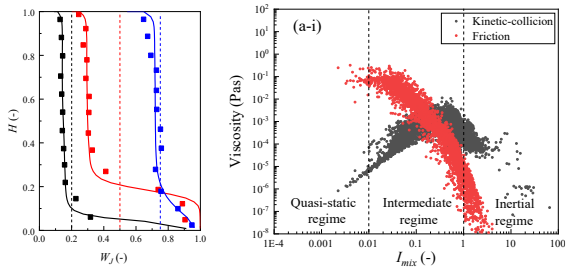
$$I_{mix}=\frac{2\|\boldsymbol{D}_{s,ave}\|d_{s,ave}}{\sqrt{p_s/\rho_{s,ave}}} \quad (2)$$

By considering that only the inertial part contributes to the viscous energy production rate, the pseudo-thermal energy balance of the m_{th} phase is established. The simulations were performed to validate the experimental setups for density segregation of Joseph et al. [1] and for size segregation of Girimonte et al. [2].

Table 8 - Table of important data

Parameters	***Joseph et al. Density segregation***	***Girimonte et al. Size segregation***
W_J:W_F	***20:80***	***30:70***
u_g	***5.94 cm/s***	***8.13 cm/s***
H_{ini}	***23.1 cm***	***17.0 cm***

Compared with the results of density segregation experiments by Joseph et al.[1] and size segregation experiments by Girimonte et al.[2], the present model predicts reasonable results for both density segregation and size segregation. Consequently, the CFR-SM model shows a significant improvement in capturing the stress transition between dilute two-phase flows.



(a) comparison with Exp. (b)Viscosity distribution

Figure 39 – Comparison of simulated results with experiments of Joseph et al. and viscosity distributions at different flow regimes

Conclusions

We have developed a stress model to describe the transitions from inertial regime to quasi-static regime. The model shows accurate prediction of bi-dispersed particles fluidization for size segregation and density segregation, as well as a significant improvement in capturing the stress transition between dilute two-phase flows.

References

[1] G.G. Joseph, J. Leboreiro, C.M. Hrenya, A.R. Stevens, Experimental segregation profiles in bubbling gas-fluidized beds, AICHE J. 53 (2007) 2804-2813.
[2] R. Girimonte, B. Formisani, V. Vivacqua, The concentration profile of two–solid beds after slow defluidization: model and experiment, Chem. Eng. J. 359 (2019) 1006-1012.

Novel design of baffled Micro-fluidized beds and its hydrodynamic behavior investigations: experiment and numerical simulation

Lei Yanga,[d*], Zhuojun Jiang[b,d], Chao Yang [c,d]
a State Key Laboratory of Biochemical Engineering, Key Laboratory of Biopharmaceutical Preparation and Delivery, Institute of Process Engineering, Chinese Academy of Sciences, Beijing 100190, China bCAS Key Laboratory of Green Process and Engineering, Institute of Process Engineering, Chinese Academy of Sciences, Beijing 100190, China
cState Key Laboratory of Petroleum Molecular & Process Engineering, Key Laboratory of Green Process and Engineering, Institute of Process Engineering, Chinese Academy of Sciences, Beijing 100190, China
d School of Chemical Engineering, University of Chinese Academy of Sciences, Beijing 100408, China*
Corresponding author*yanglei@ipe.ac.cn (Lei Yang)

Abstract
This study presents a novel design of baffled Micro-fluidized beds (MFBs) and offers valuable insights into the effects of baffles on hydrodynamic behaviors. Various amount of cylindrical baffles, located at different positions within the MFBs, were constructed using 3D printing techniques. By means of fluidization experiments and Two-Fluid Mode (TFM) simulations, impacts of baffle position and number on the fluidization behaviors of Geldart Group B particles was evaluated. Both experimental and numerical simulation results show that introduction of baffles remarkably suppresses the formation of slugs and expands the bubbling regime. Significantly, in comparison with the baffles placed at the bottom of the bed, the baffles placed in the middle of the bed demonstrates a more pronounced effect in disrupting fully developed slugs. An increased number of baffles enhances the efficiency of bubble-breaking effect. Besides, our numerical simulations further imply that baffles placed at lower part of the bed are more effective in the inhibition of global solid back-mixing. The outcomes of this study shed new light on the design and optimization of baffled MFBs.
Keywords: Micro-fluidized bed, Baffles, Hydrodynamics, Two-Fluid Model, Solid back-mixing.

Introduction

Micro-fluidized beds (MFBs) with a bed diameter of only a few centimeters or even millimeters, was first proposed by Poticetal. [1].

Compared with traditional fluidized beds (TFBs), MFBs possess an exceptional surface area-to-volume ratio, enabling them to achieve ultra-fast heat dissipation. Thisadvantageous feature makes MFBs superior in a wide range of exothermic reactions, including biomass pyrolysis, methanation, etc. [2-5]. In MFBs, bubbles could evolve into slugs, leading to insufficient gas-solid contact and hindering the conversion and selectivity of chemical reactions [6-7].

In this study, free baffled and three baffled MFBs were manufactured. The baffles were designed as cylinder-shaped tubes and were placed at the bottom, middle, and combined positions, respectively. We investigated the influence of baffle placement and number on the hydrodynamic behaviors of Group B particles (glass beads). To gain more insights into local hydrodynamics, we also performed TFM (computed using Ansys Fluent 2023R1 software) simulations of fluidization behavior in the same structured MFBs.

Methodology

Experimental procedures

The setup comprises of a gas supply device, fluidized beds, signal acquisition and processingdevices (see figure 1). Compressed and dried air was employed as the fluidizing gas, with its flow rate being regulated using a set ofrotameters. In order to investigate the hydrodynamics, we measured and analyzed the global pressure fluctuations within the beds, and then processed utilizing statistical analysis and a Fast Fourier Transform (FFT).

Simulation methods

In this study, we performed TFM simulations using the commercial CFD software Ansys Fluent 2023R1. The gas flows into the computational domain at the bottom via a prescribed inlet cell and a pressure outlet boundary is prescribed at the top of the bed. No-slipboundary condition was applied between gas and wall while partial slip boundary condition was used for particles and wall. The maximum simulation time was limited to14 s to ensure stable simulation results.

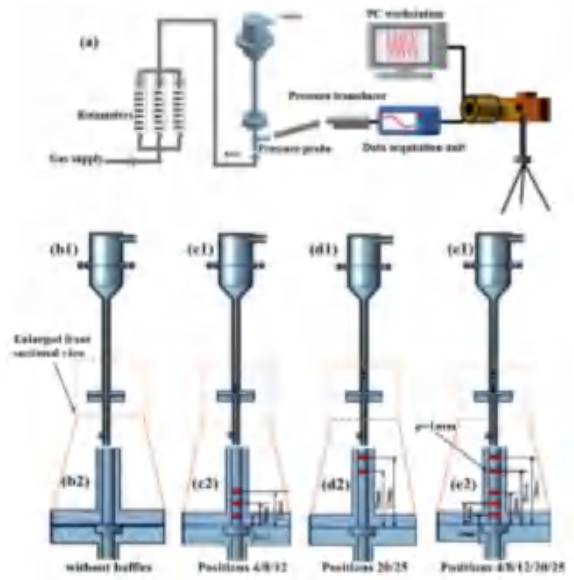


Figure 1. Schematic view of the experimental set-up **(a)**, cross-sectional front view of baffledMFBs (**b1**, **c1**, **d1**, and **e1**), enlarged view cross-sectional front view of baffled MFBs (**b2**, **c2**, **d2**, and **e2**).(without baffles, Positions4/8/12, Positions 20/25, and Positions 4/8/12/20/25).

Conclusions

In this study, through a combination of experimental investigations and TFM simulations, we analyzed the hydrodynamic behaviors of MFBs, focusing on the influence of baffle position and number. The main conclusions can be summarized as follows:

(1) The incorporation of baffles proves to be highly effective in disrupting slug formation within MFBs.

(2) As *Ug* increases, it becomes evident that placing the baffles in the middle section of MFBs yields a more pronounced disruption of slugging, compared to their placement at the bottom of the bed.

(3) The utilization of baffles extends the range of the bubble regime and delays the bubble movements within the bed.

Acknowledgements

Zhuojun Jiang would like to thank China Scholarship Council for his PhD stipend. The authors thank The National Key Research and Development Program of China (2022YFB3504003), CAS Project for Young Scientists in Basic Research (YSBR-038) for the financial support.

References

[1] B. Potic, S.R.A. Kersten, M. Ye, M.A. van der Hoef, J.A.M. Kuipers, W.P.M. van Swaaij, Fluidization with hot compressed water in micro-reactors, Chemical Engineering Science 60(22) (2005) 5982-5990.
[2] F. Wang, X. Zeng, Y. Wang, J. Yu, G. Xu, Characterization of coal char gasification with steam in a micro-fluidized bed reaction analyzer, Fuel Processing Technology 141(2016) 2-8.
[3] Y. Li, H. Wang, W. Li, Z. Li, N. Cai, CO2 Gasification of a Lignite Char in Microfluidized Bed Thermogravimetric Analysis for Chemical Looping Combustion and Chemical Looping with Oxygen Uncoupling, Energy & Fuels 33(1) (2019) 449-459.
[4] Y. Shen, X. Li, Z. Yao, X. Cui, C.-H. Wang, CO2 gasification of woody biomass: Experimental study from a lab-scale reactor to a small-scale autothermal gasifier, Energy 170(2019) 497-506.
[5] Y. Zhang, M. Zhao,R. Linghu,C. Wang, S. Zhang, Comparative kinetics of coal and oil shale pyrolysis in a micro fluidized bed reaction analyzer, Carbon Resources Conversion 2(3)
(2019) 217-224.
[6] H. Li, X. Lu, M. Kwauk, Particulatization of gas-solids fluidization, Powder Technology 137(1) (2003) 54-62.
[7] Y. Pottimurthy, D. Wang, C. Park, S. Patil, A. Tong, L.-S. Fan, Three-dimensional dynamic characterization of square-nosed slugging phenomena in a fluidized bed, Particuology 67 (2022) 35-46.

Enhanced hydrogen production in novel reactor based on porous micro-structure flowing

Senqing Fan, Jingyun Liu, Zeyi Xiao
School of Chemical Engineering, Sichuan University, Chengdu, Sichuan 610065, China

Abstract : Porous media (porous foam/membrane) with porous micro-strucure have unique advantages in promoting fluid flow and transfer, since the interconnected pore structure of porous foam/membrane can enhance the momentum exchange of fluid flowing through the porous micro-strucure. The mass transfer can be confined in the micro-scale pores and the distance of the transfer can be significantly shortened during reactant is flowing through t the porous micro-strucure, leading to the increase of the rate of the mass transfer and reaction rate. Immobilization of the catalyst microparticles in the pores of a porous foam/membrane as an inner component of a hydrogen production reactor can significantly increase the hydrogen productivity, the selectivity of the hydrogen and reduce the size of the reactor. For the alkaline water electrolysis, the adhesion between hydrogen and the electrode was significantly reduced and the bubble size decreased from 41.76 μN to 23.17 μN after the Co-based catalytic microparticles were immobilized in porous foam Ni to form a self-supporting electrode. In order to further remove the bubbles generated on the surface of the electrodes, the flow-through operation was applied with electrolyte force flowing through the pores of the electrodes. The results show that the hydrogen overpotential can be reduced by 100 mV and the oxygen overpotential can be reduced by 57 mV at a current density of 300 mA cm^{-2}. After the electrodes were assembled into an electrolyzer with porous micro-structure flowing integrated with electrolytic water splitting, the energy consumption for hydrogen production was only 4.4 kW Nm^{-3} at 6 M KOH, 338 K, 1 atm, and 200 mA cm^{-2}. The energy consumption can be further reduced if the oxidation of alcohols (ethanol, n-propanol, benzyl alcohol) with lower overpotential is happened on the anode. In addition, the alcohol oxidation reaction is confined within the porous micro-structure, and the reaction rate, the selectivity of organic acids, and the Faraday current efficiency are all significantly improved. For the hydrogen production in the proton exchange membrane (PEM) electrolyzer with porous micro-structure flowing, a current density of 2.48 A cm^{-2} can be achieved under the condition of 2 V cell voltage and 80°C, which is much better than that conventional rib-channel structure. For hydrogen production from methanol reforming, Cu/Zn/Al catalyst microparticles were immobilized in the pore of porous membrane, which avoided the internal diffusion effect caused by the granulation of catalyst microparticles, and enhanced the contact between the reacting fluid and the catalyst. Under the flow-through operation, the hydrogen productivity can reach 5-10 Nm^3 kg^{-1} h^{-1}, and the gas hourly space velocity can reach 20000-40000 h^{-1}, both of which are several times higher than those of conventional fixed-bed reactors. Besides, the equipment volume of the reactor was significantly reduced compared with that of a conventional fixed bed, which shows a promising potential for application in the area of distributed/moveable hydrogen production. In the future, we will focus on the key scientific and technological issues such as the porous micro-structure and interfacial effect of catalyst microparticles, the coupling mechanism between flow transfer and reaction in porous micro-structure, and the scaling-up design and optimization of the equipment, so as to accelerate the development and application of the hydrogen production based on this new structure.

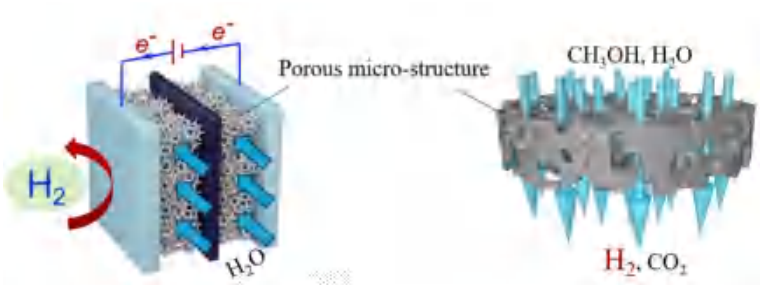


Figure 1- Principle of hydrogen production in novel reactor based on porous micro-structure flowing

Keywords: Hydrogen production; Reactor; Porous micro-structure; Flowing through

A coarse-grained MP-PIC model for bubbling fluidization simulation

Fei Li, Xing Zhao, Wei Wang
State Key Laboratory of Mesoscience and Engineering, Institute of Process Engineering, Chinese Academy of Sciences, Beijing, 100190, China
School of Chemical Engineering, University of Chinese Academy of Sciences, Beijing, 100049, China

Abstract
A scaling law is developed based on a similarity analysis, and then it is used to scale the multi-phase particle-in-cell (MP-PIC) method, and validated in the simulation of two bubbling fluidized beds. The simulation result shows this scaled MP-PIC can reduce the errors of solids volume fraction and velocity distributions over a wide range of coarse-graining ratios. In future, we expect that a scaling law with consideration of the heterogeneity inside a parcel or numerical particle will further improve the performance of coarse-grained modeling in simulation of fluidized beds.

Keywords: Coarse-graining, Scaling, MP-PIC, Simulation

Introduction

Coarse-grained model makes it possible to simulate large-scale industrial reactors with limited computational resources [1]. But using of numerical particle in coarse-grained model implies a tradeoff between the efficiency and accuracy. Usually, we hope to reproduce with high fidelity the flow field of a fluidized bed with larger coarse-grained particle. The most concerned behavior here refers to the time-resolved fields of the gas velocity, particle velocity and solid volume fraction. To achieve this goal, the key issue of a coarse-grained model is to determine its scaling law, which relates the force parameters of the coarse-grained system with those of original particles.

Methodology

A coarse-grained model is developed based on a similarity analysis of coarse-grained particle motion equation[2]. The scaling laws of gravity, gas pressure gradient force, interparticle contact force and drag force are derived as

$$m_{\mathrm{CG}}\boldsymbol{g} = k^3 m_{\mathrm{p}}\boldsymbol{g} \quad \textbf{(1)}$$

$$\boldsymbol{F}_{\mathrm{gp,CG}} = k^3 \boldsymbol{F}_{\mathrm{gp,O}} \quad \textbf{(2)}$$

$$\boldsymbol{F}_{\mathrm{c,CG}} = k^2 \boldsymbol{F}_{\mathrm{c,O}} \quad \textbf{(3)}$$

$$\boldsymbol{F}_{\mathrm{d,CG}} = k^3 \boldsymbol{F}_{\mathrm{d,O}} \quad \textbf{(4)}$$

These scaling laws are applied in the MP-PIC method, and validated in the simulations of bubbling fluidization beds [3] with different coarse-graining ratio. As a comparison, simulations of the same cases with the original MP-PIC are also performed.

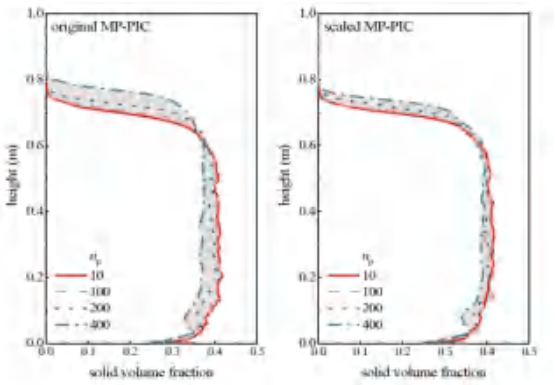


Figure 1- Axial distributions of solid volume fraction predicted with different coarse-graining ratio.

Fig. 1 compares the axial distributions of solid volume fraction predicted with the scaled MP-PIC and the original MP-PIC under different coarse-graining ratio. It shows that the bed expansion height changes obviously with coarse-graining ratio when using original MP-PIC, while the bed expansion height changes a little when using scaled MP-PIC.

Conclusions

- The inter-particle contact force of a numerical particle follows a scaling of k^2.
- The drag force of a numerical particle follows a scaling of k^3.
- The scaled MP-PIC method reduces the errors of solids volume fraction and particle velocity distribution in simulation of bubbling fluidized beds.

Acknowledgements

This work was financially supported by the National Natural Science Foundation of China (Nos. 22161142006, 51876212) and the State Key Laboratory of Mesoscience and Engineering, Institute of Process Engineering, Chinese Academy of Sciences (Nos. MESO-23-D03, MESO-23-A02).

References

[1] M. Sakai & S. Koshizuka, Large-scale discrete element modeling in pneumatic conveying, Chem. Eng. Sci. 64 (2009) 533-539.

[2] C. Bierwisch, T. Kraft, H. Riedel, M. Moseler, Three-dimensional discrete element models for the granular statics and dynamics of powders in cavity filling, J. Mech. Phys. Solids 57 (2009) 10-31.

[3] T. McKeen & T. Pugsley, Simulation and experimental validation of a freely bubbling bed of FCC catalyst, Powder Technol. 129 (2003) 139-152.

Fast pyrolysis of large biomass particles in a diameter transformed fluidized bed reactor

Hanbin Zhong[1], Keyu Chen[1], Qingang Xiong[2]
1. Xi'an Shiyou University, Xi'an, China;
2. South China University of Technology, Guangzhou, China

Abstract
Bubbling fluidized bed is an important reactor for biomass fast pyrolysis, and small biomass particles are required to ensure the efficient entrainment of bio-char. However, the energy consumption of biomass milling significantly increases with the decrease of particle size. Therefore, a new diameter transformed fluidized bed reactor was developed for the fast pyrolysis of large biomass particles. The multi-fluid model was used to simulate the flow and reaction characteristics of different types of fluidized bed reactors. The results indicate that this diameter transformed fluidized bed reactor ensures the efficient entrainment of bio-char while keeps the sand particles in the reactor, which provides an efficient route for the low-carbon conversion of biomass resources.

Keywords: Diameter transformed fluidized bed, Biomass, Fast pyrolysis, CFD, Multi-fluid model

Introduction

Renewable biomass resources emerge as a pivotal energy solution to combat the rapid depletion of conventional fossil fuels, where their exceptional attributes not only contribute to reduction of greenhouse gas emissions but also promote energy security. Fast pyrolysis is a promising approach to effectively utilize biomass, where abundant raw biomass is mainly converted into liquid bio-oil for use of transportation and fine chemicals. Bubbling fluidized beds, due to their high performance of mass and heat transfer, have become one of the dominant reactors for biomass fast pyrolysis. However, small biomass particles are required to ensure the efficient entrainment of bio-char, while the energy consumption of biomass milling significantly increases with the decrease of particle size. Therefore, it is urgently to develop new fluidized bed reactor which is able to handling larger biomass particles.

Since the experiments on fluidized bed reactor are time-consuming and need high financial cost because of the complex gas-solid hydrodynamics and reaction process. Therefore, with the fast development of theoretical models and computational ability, the computational fluid dynamics (CFD) has increasingly become an indispensable tool to design and optimize the fluidized bed reactor for biomass fast pyrolysis

Methodology and Results

Three types of bubbling fluidized bed reactor were designed and used as the modelling system. Multi-fluid model considering the effects of particle shrinkage and intra-particle heat conduction was used to simulate the biomass fast pyrolysis process in these reactors. The distributions of phase, temperature, and species were studied, and the products yields were discussed. The results demonstrate that the new diameter transformed fluidized bed reactor with expanding section in the middle and reducing section at the top is able to ensure the efficient entrainment of bio-char while keeps the sand particles in the reactor. In addition, the high product yield of bio-oil is maintained for biomass particles of up to 3 mm.

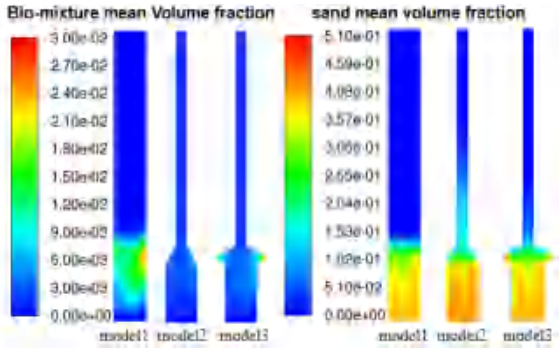


Figure 40 – Time-averaged volume fractions of biomass and sand particles

References

[1] H. Zhong, Q. Xiong, Y. Zhu, S. Liang, J. Zhang, B. Niu, X. Zhang, CFD modeling of the effects of particle shrinkage and intra-particle heat conduction on biomass fast pyrolysis, Renew. Energy 141 (2019) 236-245.

A reactor concept for water-gas shift with in-situ CO2-mineralization

Qi Chang, Wei Ge
State Key Laboratory of Mesoscience and Engineering, Institute of Process Engineering, Chinese Academy of Sciences, Beijing, 10049, China

Abstract
Packed fluidized beds make it possible to integrate the production of H2 through the water-gas shift reaction (WGSR) and the mineral carbonation (MC) of CO2 in a single reactor. However, simple stoichiometries belie the complex multiphase flow and its effect on the reactions. No published work has quantified the kinetic compatibility between WGSR and MC. In this study, a grain-scale model for MC sorbent in water steam is incorporated into a one-dimensional multiphase reactor model to investigate the amount of CO2 mineralized. When the powder size of MC sorbent is 50 μm, almost 50% of CO2 could be sequestrated for integrated WGSR-MC in a 750 MW integrated gasification combined cycles (IGCC) plant.

Keywords: Hydrogen production; Water-gas shift; Carbon mineralization; Calcium silicate; Packed fluidized bed

Introduction

Hydrogen is an essential raw material and clean energy source. It is mainly produced from fossil fuels due to the high cost of renewable resources. To increase the purity of hydrogen in syngas produced from fossil fuels, the water-gas shift reaction (WGSR) is used. Unfortunately, this reaction co-generates CO2. To permanently sequester CO2, in-situ mineral carbonation (MC) for WGSR can be used. This process utilizes abundant industry silicate residues (such as fly ash and slag) as a calcium source for carbonation. It also stabilizes these wastes and helps produce low-CO2 cement. The high pressure, humidity, and temperature of WGSR accelerate MC, making it a promising way to integrate reactions in a one-step reactor [1]. An environment in which gas-carrying MC sorbent powders pass through packed WGSR catalyst pellets can be achieved using packed fluidized beds. Before building a realistic reactor, modeling and simulation are used to assess this integration.

Methodology

The hydraulic parameters are determined by balancing the drag of gas on powder, the dry collision force of packing on powder, and the friction force of packing on gas [2]. In the steady-state reactor model, the sources of MC and WGSR are calculated using a proposed grain-scale MC model based on [3] and a generalized Thiele modulus model. The latter reflects the impact of intra-pellet mass transfer on the WGSR source.

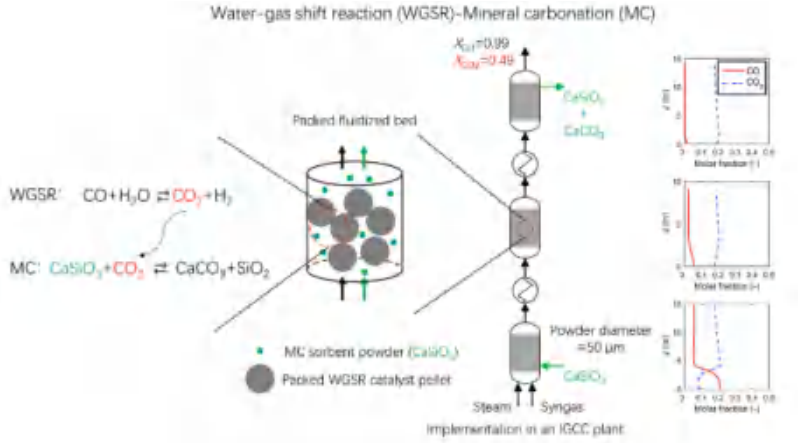


Figure 1 - Integrated WGSR-MC reactor and its implementation in a 750 MW IGCC plant

Conclusion

For the WGSR-MC in a 750 MW integrated gasification combined cycle (IGCC) plant, the CO2 conversion rate achieved using 50 μm MC sorbent powder is 49%. However, this rate is

expected to increase as the MC sorbent powder size decreases. Based on this information, it is possible to assess the reactor concept's capacity.

References

[1] G. Gadikota, Multiphase carbon mineralization for the reactive separation of CO2 and directed synthesis of H2, Nature Reviews Chemistry 4 (2020) 78-89.
[2] X. Song, Z. Wang, Y. Jin, Z. Tanaka, Gas-solids circulating fluidization in a packed bed, Powder Technology 83 (1995) 127-31.
[3] H. Wang, Z. Li, N. Cai, Multiscale model for steam enhancement effect on the carbonation of CaO particle, Chemical Engineering Journal 394 (2020) 124892.

CFD-DEM simulation of particle mixing and cycling characteristics in liquid-containing gas-solid fluidized bed reactor and spatial-temporal scales analysis

Junyuan Luan[1], Delong Feng[1], Luchang Han[1], Yefeng Zhou[1,*]
1 Xiangtan University, Xiangtan, China(zhouyf@xtu.edu.cn)

Abstract
Due to the existence of the liquid phase, the liquid-containing gas-solid fluidized bed reactor has higher interphase contact efficiency and heat and mass transfer efficiency than the traditional gas-solid fluidized bed reactor. In this paper, the effect of liquid addition to the convection bed reactor on the mixing and cycling characteristics of particles is studied from temporal and spatial scales with the help of CFD-DEM numerical simulation method. Taking surface tension, viscosity and liquid content as the key research parameters, the Lacey index was selected as the quantitative characterization of the mixing degree of particles, and the particle circulation flux was used to characterize the particle circulation.

Keywords: Liquid-containing gas-solid fluidized bed reactor, CFD-DEM, Mixing and circulation, Temporal and spatial scales

Introduction

The particles circulate in the reactor to achieve mutual contact and mixing, which reduces the inhomogeneity in the reactor and provides an important guarantee for its heat and mass transfer, chemical reaction and other processes[1,2]. However, the excess liquid in the bed will aggravate the agglomeration of particles in the reactor, and then inhibit the mixing and circulation of particles, and the influence on the hydrodynamics in the bed cannot be ignored[3].

Previous studies have focused more on the effects of changes in liquid content on particle mixing and cycling processes[4,5]. In fact, changes in surface tension and viscosity can also significantly alter the fluidization characteristics of the particles[6,7]. Therefore, this paper comprehensively explores the horizontal and vertical mixing and cycling characteristics of particles under the influence of multiple liquid parameters such as liquid content, surface tension and viscosity from the two scales of time and space.

Methodology

Using the Lacey index and the axial flux of particles as the characterization parameters of particle mixing and cycling characteristics, the effects of liquid addition on the horizontal and vertical mixing characteristics and cycling characteristics of particles were comprehensively explored from temporal and spatial scales, and the effects of liquid action on the horizontal and vertical mixing processes of particles were systematically compared.

On the temporal scale, firstly, the differences in the mixing and cycling behaviors of dry and wet particles were compared, the surface tension, viscosity and liquid content were taken as the key research parameters, focusing on the influence of liquid action on the horizontal and vertical mixing process and circulation process of particles at different times. The circulating flux of particles was used to characterize the circulating capacity of particles, and the circulating fluxes of particles at different heights were comprehensively analyzed on the spatial scale.

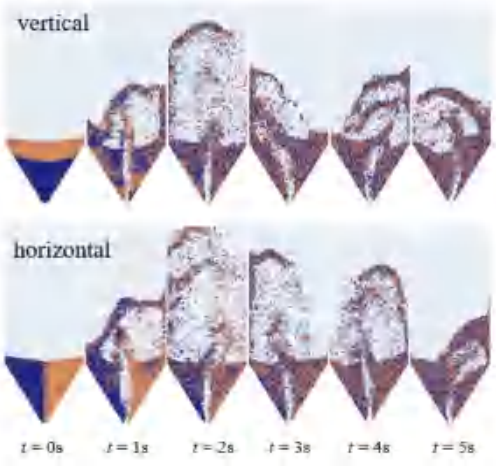


Figure 41 - Distribution of the vertical and horizontal mixing state of particles under different fluidization moments (V^* = 1%, μ = 10 mpa*s, Bo = 1).

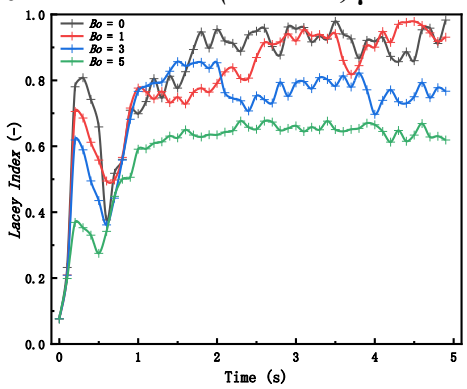


Figure 2 - Lacey Index distribution of vertical mixing under different surface tensions (V^* = 1%).

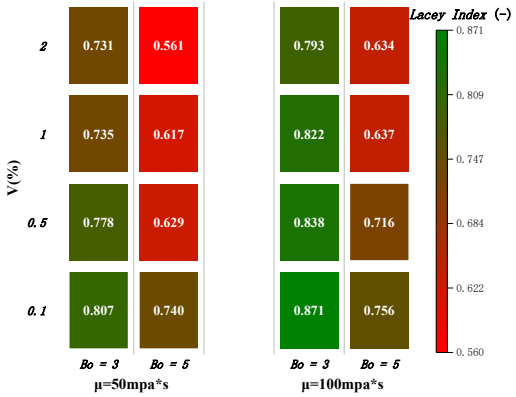


Figure 3 - Time-averaged Lacey Index distribution of horizontal mixing under different surface tensions and liquid contents (μ = 50, 100 mpa*s).

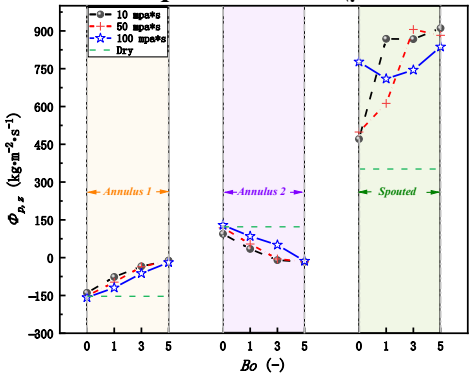


Figure 4 - Distribution of particle flux under different surface tensions and viscosities (V^* = 1%, μ = 10 mpa*s, h = 55mm).

Conclusions

In this paper, the Lacey index and particle flux are used as the parameters to characterize the degree of particle mixing and cycling capacity, and the differences in the influence of liquid action on the horizontal and vertical mixing process of particles are compared and analyzed and the main conclusions are as follows:

The increase of surface tension leads to a decrease in the degree of horizontal and vertical mixing of particles. At high surface tension (Bo = 3, 5) and high viscosity (μ = 50, 100 mpa*s), the increase in viscosity and liquid content leads to an increase and decrease in the horizontal and vertical mixing of particles, respectively.

Acknowledgements

The work was supported by the National Natural Science Foundation of China (22078278), Hunan Innovative Talent Project (2022RC1111), Hunan Provincial Education Bureau Foundation (22A0131), Natural Science Foundation of Hunan Province (2021JJ30653), and Hunan Province Higher Education Key Laboratory of Green Catalysis and Industrial Reaction Process Intensification.

References

[1] Boyce C M. Gas-solid fluidization with liquid bridging: A review from a modeling perspective[J]. Powder Technology, 2018, 336: 12-29.

[2] Sarafan K, Molaei Dehkordi A. Experimental Investigation and CFD–DEM Simulation of Solids Mixing in Tapered Fluidized Beds[J]. Industrial & Engineering Chemistry Research, 2023, 62(51): 22115-22130.

[3] Boyce C M, Ozel A, Kolehmainen J, et al. Analysis of the effect of small amounts of liquid on gas-solid fluidization using CFD-DEM simulations[J]. AIChE Journal, 2017, 63(12): 5290-5302.

[4] He Y, Peng W, Wang T, et al. DEM Study of Wet Cohesive Particles in the Presence of Liquid Bridges in a Gas Fluidized Bed[J]. Mathematical Problems in Engineering, 2014, 2014: 1-14.

[5] Tang T. DEM numerical investigation of wet particle flow behaviors in multiple-spout fluidized beds[J]. Chemical Engineering Science, 2017, 172: 79-99.

[6] Song C, Liu D, Ma J, et al. CFD-DEM simulation of flow pattern and particle velocity in a fluidized bed with wet particles[J]. Powder Technology, 2017, 314: 346-354.

[7] Feng D, Li H, Han L, et al. CFD-DEM Coupling Simulation and Cross-Scale Correlation Analysis of a Liquid-Containing Gas–Solid Spouted Fluidized Bed Reactor[J]. Industrial & Engineering Chemistry Research, 2023, 62(37): 15240-15254.

Euler-Lagrange simulations of large-scale reactive particle-laden flows

Yali Tang, Chih-Chia Huang, Xin Liu, Niels Deen
Power and Flow group, Department of Mechanical Engineering, Eindhoven University of Technology, the Netherlands

Abstract
Particle-laden flows are ubiquitous in nature and industries. Often in industrial applications, chemical reactions are also involved. Computer simulation plays an integral role in research and industrial development to obtain a detailed insight into such complex multiphase physics. Particle-unresolved Euler-Lagrange (E-L) simulation has becoming more and more popular for modelling such flows at large scales (even at industrial scale) due to its compromising between accuracy and computational efficiency.
Our research has been dedicated in developing E-L model reduction methods that enable simulations of particle-laden reactive flows at life sizes. One important example is a coarse-graining method that solves so-called parcels representing groups of original particles, reducing the total number of simulated particles in discrete element model. In this talk, I will showcase two simulation examples using our developed coarse grid model. One is modelling of raceway formation in a real blast furnace at a steelmaking company TataSteel. The other is modelling of direct reduction of iron oxide fines in fluidized beds using hydrogen.

Keywords: particle-laden flows, coarse graining, CFD-DEM, sintering, blast furnace

Introduction

To date, blast furnaces (BF) have been the most crucial ironmaking process. More than 70% of the iron consumed worldwide is produced via BF. In modern blast furnaces, pulverized coal is injected with hot blast air. The introduction of pulverized coal can effectively reduce expensive coke consumption, adjust furnace stability, provide heat, and reduce carbon footprint. The momentum thrust brought by this high-speed air pushes coke particles away and creates a void region, called "raceway", nearby the injection zone. The combustion performance of pulverized coal in gas-coke-coal flows in this raceway is thus crucial for the efficiency of iron production. Direct measurement of such performance is almost impossible due to the harsh conditions in the injection zone, i.e. high temperature and high pressure. This project resorts to numerical modeling and tries to unveil the complex underlying physics in the raceway.

Methodology

A model that uses Computational Fluid Dynamics (CFD) coupled with the Discrete Element Method (DEM) is developed as it is able to capture all the mentioned physics. CFD is a versatile method as it can simulate from compressible to incompressible flows with added features like combustion and turbulence. DEM treats particles as soft spheres and can resolve individual particles' motion, collision, rotation, and friction. The combination of CFD and DEM incorporates forces, like drag force, to couple the gas and solid phases.
We further develop this CFD-DEM framework with two computational-reduction models: 1) reducing the number of simulated particles via a coarse-graining (CG) method that resolves so-called parcels representing groups of original particles, 2) reducing combustion modeling using the Flamelet Generated Manifold (FGM) method that makes use of a looking-up table of the reaction information from a pre-built database. Further model development includes a cohesive model that calculate the inter-particle solid bridge force for description of particle sintering behaviour, as well as a Unreacted Shrinking Core model for solid surface reactions using TGA-based reaction kinetics.

Results

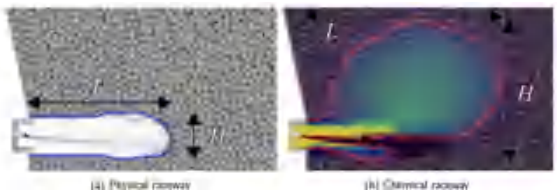


Figure 1. Illustration of the physical and chemical raceway definition. (a) Physical raceway: the boundary of the physical raceway is outlined in blue. (b) Chemical raceway: the boundary of the chemical raceway is outlined in red. Coke particles are made transparent. The color map depicts the concentration of O_2 and the boundary is where the O_2 concentration falls below 5%.

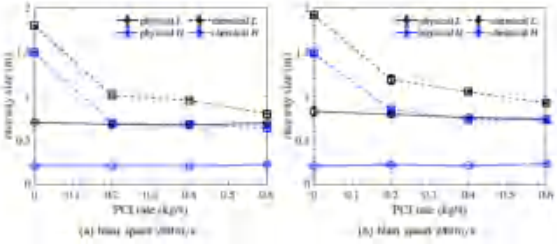


Figure 2. Physical and chemical raceway size as a function of PCI rate. Only raceway length and height are shown for clarity. (a) blast speed 200 m/s. (b) blast speed 240 m/s.

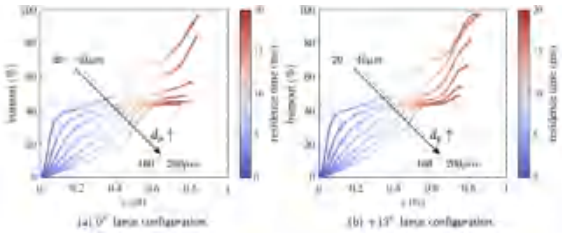


Figure 3. Burnout in different particle size groups. Each line displays information averaged within the corresponding particle size group. The gray dashed line indicated burnout contribution from the devolatilization.

Acknowledgements
This work was carried out on the Dutch national e-infrastructure with the support of SURF Cooperative and under project number T18021 in the framework of the Research Program of the Materials innovation institute (M2i) (www.m2i.nl) supported by the Dutch government. Financial support by Tata Steel Nederland is gratefully acknowledged.

References

[1] Huang, C. C., van Oijen, J. A., Deen, N. G., & Tang, Y. (2022). Incorporation of flamelets generated manifold method in coarse-grained Euler-Lagrange simulations of pulverized coal combustion. *Chemical Engineering Science*, *260*, 117838.
[2] Huang, C. C., van Oijen, J. A., Deen, N. G., & Tang, Y. (2023). A particle-size dependent smoothing scheme for polydisperse Euler-Lagrange simulations. *Chemical Engineering Science*, *277*, 118765.
[3] Huang, C. C., Born, S., Klaassen, M., van Oijen, J. A., Deen, N. G., & Tang, Y. (2024). Comprehensive Numerical Modeling of Raceways in Blast Furnaces. *Chemical Engineering Science*, 119857.

Hydrogen production from methanol by liquid phase discharge

Wei Zhang[1,2], Junfeng Wang[1,3], Tianyi Wu[1], Junjie Zhang[1], Bin Li[1]
[1]Jiangsu University, Zhenjiang, China
[2]Aarhus University, Aarhus, Denmark
[3]Chongqing University, Chongqing, China

Abstract
The decomposition of hydrocarbons or alcohols by non-thermal plasma discharge has potential for rapid hydrogen production. Hydrogen production using liquid raw materials is more secure and economical for transportation. In this study, liquid plasma discharge was used to induce methanol decomposition and analyzed factors affecting the decomposition reaction as well as the evolution of the plasma bubble. A liquid plasma discharge reactor was designed for visualization. Liquid-phase discharge and methanol decomposition processes were imaged in detail using a high-speed camera. At the plasma-liquid interface of a bubble substrate, energy is concentrated and methanol is decomposed into gaseous products. The bubbles detach from the tip of the plasma bubble substrate and the decomposition reaction is continuous and stable. Two typical plasma discharge modes were obtained by adjusting the electrode spacing: gliding arc discharge (GAD) and glow discharge (GD). The voltage and current curves of GD approximate the sinusoidal waveform of the alternation current power supply, and the range of discharge power is 130.4–460.2 W. However, GAD has feature of the bipolar pulses with a high transient peak current (420.6–690.9 mA) that causes discharge power of GAD excitation is 30.7–110.3 W. Primary analyzes indicate that the energy consumption of GAD is less than that of the GD due to the difference in discharge characteristics. An optimized energy consumption of 1.63 kWh/Nm3H2 was achieved for hydrogen production. The maximum hydrogen proportion of the gaseous product is 63.21%, which corresponds to a carbon monoxide proportion of 26.38% as the main byproduct. The effects of the discharge power, electrode distance, and electrode diameter on methanol decomposition were analyzed.

Keywords: Non-thermal plasma, Hydrogen production, Liquid plasma discharge reactor, Plasma mode

Introduction

Recently, non-thermal plasma (NTP) decomposition of hydrocarbons and alcohols for hydrogen production has attracted attention due to its high production rate and moderate reaction conditions [1]. NTP for hydrogen production is typically excited by an electric field (direct current, alternating current, pulsed) or microwave. Typical NTP discharge patterns include dielectric barrier discharge (DBD), gliding arc discharge (GAD), microwave discharge, and glow discharge (GD) [2]. NTP excited in the gas phase has been shown by previous studies to enhance the reforming reaction. Wang et al. [3] used a knife-shape GAD plasma reactor for SMR to produce hydrogen. The research results show that the dominant products are H2 and CO, and the H2/CO ratio of the system is mainly affected by steam to carbon molar ratio and input power. The compact structure of a NTP reactor is suitable for vehicle-mounted hydrogen production or distributed hydrogen refuelling stations. The basic mechanism for most of these applications is the conversion of electrical energy to generate an energetic discharge region with sufficient energy transfer to particular reactants [4]. The plasma discharge region contains a variety of charged (electrons, ions, and radicals) and neutral particles. Based on the synergistic effect of these reactive species, advanced oxidation or decomposition reactions can be induced under ambient conditions without catalysts [5].

Methodology

Fig. 1 shows a schematic of the liquid phase discharge system used for hydrogen production. Methanol (Aladdin, 99.5%) decomposition was carried out in a plasma reactor made of quartz with a total capacity of 360 mL. The plasma reactor was operated at atmospheric pressure and in the temperature range 35-38 ℃ to keep the decomposition reaction stable and inhibit methanol evaporation. The micro-diaphragm pumps were used to circulate methanol from the reactor to the thermostatic water bath. The liquid temperature was controlled by adjusting the circulation flow rate when the temperature fluctuation in the reactor exceeded the threshold.
The liquid level was maintained to submerge the electrode pair. The high-voltage (HV) electrode was a nickel wire that was completely covered by dielectric tubing, with a stainless-steel ring (inner diameter of 6 mm and outer diameter of 9 mm) placed coaxially above it as the ground electrode. The electrode distance was adjusted from 0 to 30 mm. The dielectric tube, made of alumina ceramic with an inner diameter of 1 mm and outer diameter of 3 mm, confines the discharge region to the tip of the inner electrode. This representative electrode configuration for igniting plasma has been reported previously.

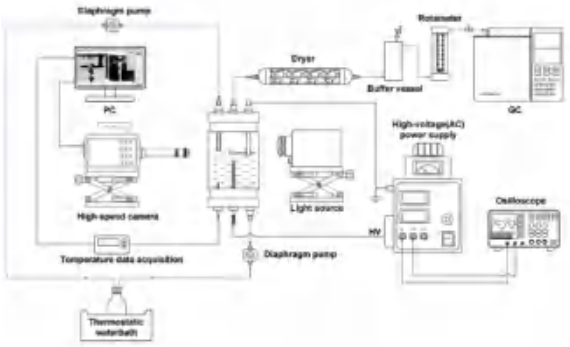


Figure 42 - Schematic diagram of the liquid phase discharge system for methanol decomposition and visualization research.

Conclusions

Hydrogen production via methanol decomposition was investigated in a liquid phase discharge reactor. Visualization analysis based on the growth characteristics of the plasma bubble demonstrates that the decomposition of liquid methanol into a hydrogen-rich gaseous mixture occurs at the plasma-liquid interface. In addition, the effects of the discharge power, electrode spacing, and electrode diameter on the hydrogen production performance were experimentally determined. Increasing the electrode diameter decreases the electric field strength of the discharge region, resulting in a lower gas flow rate in both plasma modes. Two typical NTP modes were visually observed using a high-speed camera, that is, GAD and GD. The voltage and current waveforms indicate that GAD has an instantaneous peak current at the point of arc ignition, which is analogous to features of pulsed discharges. The gliding arc enhances the methanol decomposition and leads to a range of the discharge power for a stable GAD of 30.7-110.3 W, which is far below that of GD (130.4-460.2 W). The hydrogen flow rate increases with the discharge power and heat loss accounts for a substantial part of the energy injection. At a discharge power of 40.96 W, the lowest energy composition for GAD was 1.63 $kWh/Nm^3 \cdot H_2$. GAD is more suitable for constructing an on-board hydrogen production system than GD.

Acknowledgements

This work was financially supported by National Natural Science Foundation of China (No. 52206201), and Jiangsu Funding Program for Excellent Postdoctoral Talent (No. 2022ZB663).

References

[1] H. Rahmati, A. Ghorbanzadeh, Parallel electrodes gliding plasma: Working principles and application in dry reforming of methane, Energy. 230 (2021) 120753.
[2] Z. Yan, Li C, Lin W. Hydrogen generation by glow discharge plasma electrolysis of methanol solutions. International Journal of Hydrogen Energy. 2009;34(1):48-55.
[3] B. Wang, Y. Cheng, C. Wang, J. Zou, Steam reforming of methane in a gliding arc discharge reactor to produce hydrogen and its chemical kinetics study, Chemical Engineering Science, 253 (2022), 117560.
[4] A. Fridman, A. Chirokov, A. Gutsol, Non-thermal atmospheric pressure discharges, Journal of Physics D: Applied Physics, 38 (2005), R1-R24.
[5] B. Eliasson, U. Kogelschatz, Nonequilibrium volume plasma chemical processing, IEEE Transactions on Plasma Science, 19 (1991), 1063-1077.

Methodology of measuring parameters for particles based on their settled state

Quanhong Zhu*, Yalong Cao, Qiang Zhang
College of Chemical Engineering, Qingdao University of Science and Technology, Qingdao, China

Abstract

Gas-solid heterogeneous reactions are frequently encountered in the chemical industry. To reduce the internal diffusion step and promote the overall reaction rate, the solid phase is generally broken up or prepared into small particles or fine powders. Most gas-solid reactions turn into ones between gas and solid particles. Physical properties of particles (rather than a single particles) are of great significance to designing/operating the storage and handing devices, such as hoppers, storage bins, fixed bed and fluidized bed reactors. It has been a fundamental subject in the many fields to accurately measure these properties.

However, the traditional measurement of many parameters for particles suffers severely from poor reproducibility, further causing the outcomes to be seldom comparable. A typical example is the measurement of minimum fluidization velocity (U_{mf}) based on the bed pressure drop curve that is measured during the step-wise increase of gas flow from zero to fluidization. It remains a huge challenge to compare the U_{mf} reported by different scholars. Many other parameters with the same problem include the loosely-packed density, sphericity, angle of repose, and segregation index.

The measurement of these parameters generally involves two independent steps: preparation of the desired/defined packed state for the particles and specific measurement from as-prepared packed state. From our perspective, the poor reproducibility results from the first step: The desired/defined packed state of particles cannot be prepared with good reproducibility simply *via* the traditional methods. In other words, distinct packed states are probably prepared by different scholars for the subsequent measurement.

To solve this problem, we proposed to measuring the aforementioned parameters for particles based on their settled state: The desired packed state of particles was acquired in the fluidized bed *via* decreasing gas flow gradually from full fluidization to zero. The settling process could be comprehensively quantified by the decrease rate (α) of gas flow. It was found that provided α was controlled to be the same and smaller than a certain value, the obtained settled state as well as the subsequent measurement was quite reproducible. Among the various settled states complying with common sense and definitions of these parameters, sound rules were established to unify the choice from different scholars and further make their outcomes become fairly comparable. Eventually, the universal methodology of measuring parameters for particles based on their settled state was established.

Last but not least, the poor reproducibility of preparing the packed state of particles results eventually from that the particles can inherently and readily take on different packed states. Supposing the particles could have only one unique packed state, the obtained packed state would be always the same and hardly depend on the preparing history. However, it remains unclear why a group of particles can have diverse packed states. From another perspective, the phenomenon that particles could have different packed states means that the packed particles could be polymorphic in state. This is similar to the amorphous matter such as glass and agar. The so-called internal friction was believed to responsible for such polymorphism. Additionally, many packed states of particles were demonstrated to be in metastable equilibrium.

Numerical and experimental investigation of a fluidized bed intensified with volatiles distributors for biomass chemical looping combustion

Hao Luo[a,*], Xiaobao Wang[a], Xiaoyun Li[b], Lan Yi[a], Anders Lyngfelt [b], Tobias Mattisson[b], Xiaoqin Wu[a], Qingang Xiong[c,*]

[a]*School of Chemistry and Chemical Engineering, Hubei Key Laboratory of Coal Conversion and New Carbon Materials, Wuhan University of Science and Technology, Wuhan, 430081, China*

[b]*Division of Energy Technology, Department of Space, Earth and Environment, Chalmers University of Technology, 412 96 Gothenburg, Sweden*

[c]*State Key Laboratory of Pulp and Paper Engineering, South China University of Technology, Guangzhou, 510640, China*

Email: haoluo@wust.edu.cn (***Hao Luo***), qingangxiong@scut.edu.cn (***Qingang Xiong***)

Abstract:

The full combustible gas conversion in the fuel reactor of chemical looping combustion of biomass is critical for the inherent CO_2 capture advantage and negative CO_2 emission goal. However, due to the fast devolatilization process and limited injection ports of biomass, a local plume of volatiles would be formed and has limited contact with the oxygen carriers or reactive bed materials in the fluidized bed reactor. A concept called volatiles distributor (VD) has recently been proposed and investigated in a cold-flow fluidized bed, which shows excellent performance in achieving an even distribution of volatiles over the cross section[1]. To deeply understand VD's impact on hydrodynamics behaviors, pioneering three-dimensional full-loop CFD simulations were conducted using an Eulerian multiphase granular model. Three drag models, i.e., Gidaspow[2], Filtered[3], and two-step EMMS/bubbling[4], were evaluated against experimental data. While all models perform well in bubbling fluidization, the two-step EMMS/bubbling model excels in turbulent fluidization. The validated EMMS/bubbling model was further used to evaluate and optimize the configuration of VD, the CFD simulations of both original designs, i.e. Modes 1A, 1B, 2A, and 2B, and new designs, i.e. Modes 1C, 1D, 2C, and 2D, reveal that the performance of the VD can be improved by reducing the open area of the distribution holes of the VD near the injection port and increasing it further away from the injection port. Among all investigated VDs, Mode 2D shows the overall best performance in achieving even distribution and avoiding leakage of simulated volatiles.

Keywords: Drag model, Biomass chemical looping combustion; Fluidized bed; Volatiles distributor; Intensification;

References

[1] X. Li, A. Lyngfelt, C. Linderholm, B. Leckner, T. Mattisson, Performance of a volatiles distributor equipped with internal baffles under different fluidization regimes, Powder Technology 409 (2022) 117807.

[2] D. Gidaspow, Multiphase Flow and Fluidization, 1994.

[3] A. Sarkar, F.E. Milioli, S. Ozarkar, T. Li, X. Sun, S. Sundaresan, Filtered sub-grid constitutive models for fluidized gas-particle flows constructed from 3-D simulations, Chemical Engineering Science 152 (2016) 443-456.

[4] H. Luo, B. Lu, J. Zhang, H. Wu, W. Wang, A grid-independent EMMS/bubbling drag model for bubbling and turbulent fluidization, Chemical Engineering Journal 326 (2017) 47-57.

Improving ethylene selectivity in MTO process by regulating the arrangement of coke in SAPO-34 molecular sieve crystals

Guida Li[1,2], Jinling Zhang[2], Mao Ye[1,2*], Zhongmin Liu[2]
1 Department of Chemical Physics, University of Science and Technology of China, Hefei 230026, China;
2 National Engineering Research Center of Lower-Carbon Catalysis Technology, Dalian Institute of Chemical Physics, Chinese Academy of Sciences, Dalian 116023, China
*Corresponding author: maoye@dicp.ac.cn

Abstract
As one of the important coke regulation methods, partial regeneration commonly used in the MTO processes can restore the activity of catalysts and provide the most operational window to maintain high selectivity for light olefins. Here, we demonstrate a strategy of regulating the arrangement of coke species in SAPO-34 zeolites via low-temperature air regeneration. The maximum ethylene selectivity of SAPO-34 catalyst regenerated at 743 *K* can increase by up to 5.5 % compared with high temperature situations, which comes from extension of the reaction zone brought about by optimizing spatial distribution of residual coke.

Keywords: Methanol-to-Olefin, Air Regeneration, Coke Spatial Distribution, Process Intensification.

Introduction
The SAPO-34 catalyst used in methanol-to- olefins (MTO) industry exhibits high selectivity for light olefins due to the cage structure with small-pore openings, while also rapidly deactivating resulting from accumulation of coke inside the cage. The previous studies have shown that coke not only affects catalyst activity but is also closely bound up the selectivity of light olefins, making the regulation of coke in cages extremely important [1]. According to the dual-cycle mechanism, the species of the active hydrocarbon pool confined within zeolite cage are conducive to production of light olefins. And these can be converted from other inactive components by partial regeneration, or incomplete regeneration which refers to not completely removing coke for shortening the time to enter the aromatic cycle. For instance, Zhou et al. developed a steam regeneration approach to directionally transform deactivating

coke species to active naphthalenic species that not only impetus ethylene formation in MTO conversion, but also yields valuable synthesis gas [2]. In this work, we found that the distribution of coke within the deactivated catalyst can be regulated for improving ethylene selectivity by reducing the air regeneration temperature, also analyzed the discrepancies with high temperature conditions through microfluidized bed reactor experiments, *in situ* infrared spectroscopy, gas chromatography- mass spectrometry (GC-MS) and structured illumination microscopy (SIM).

Methodology
The commercial shaped catalyst is loaded into a microfluidized bed reactor for MTO reaction (atmospheric pressure, *WHSV* = 2 *g*MeOH *g*CAT-1 *h*-1, 748 *K*), and the effluent products are analyzed by online gas chromatograph equipped with capillary column and FID detector. When the methanol conversion is lower than 80 %, it is considered that catalyst is deactivated, and then it is raised to 743 and 873 *K*under N2 purge, and then switched to air with *WHSV* of 1 *g*ai*g*CAT-1 *h*-1 for regeneration for different times. GC-MS is used to identify the retained species liberated by HF dissolution-solvent extraction method in deactivated samples. The recovery of acid sites of deactivated catalysts during the regeneration is obtained through in-situ infrared (IR) spectroscopy at 3590 and 3610 *cm*-1. The spatiotemporal distribution of the soluble coke species located in zeolite crystals is obtained by SIM.

Results and Discussion

The MTO reaction performance represented as the maximum ethylene selectivity is compared firstly at the same residual coke content after different regeneration times at 743 *K* and 873 *K* (Figure 1). Compared tohigh- temperature regeneration at 873 *K*, the SAPO-34
catalyst regenerated at 743 *K* can increase ethylene selectivity by up to5.5%, but the difference gradually decreases to zero as the amount of residual carbon decreases.

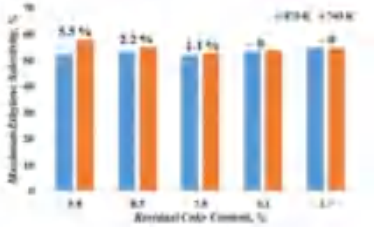


Figure 1 The maximum ethylene selectivity of the reactivated catalyst at the same residual coke content after different regeneration times at 743 K and 873 K

The investigation reveals that the samples regenerated at low temperature have a larger specific surface area, thus providing more sufficient reaction space. Low temperature reduces the oxidation ability of oxygen molecules, causing soluble carbon in the deactivated crystals to be quickly cleared (Figure 2a), while the remaining insoluble species that are difficult to clean continues to occupy the active sites (Figure 2 b).

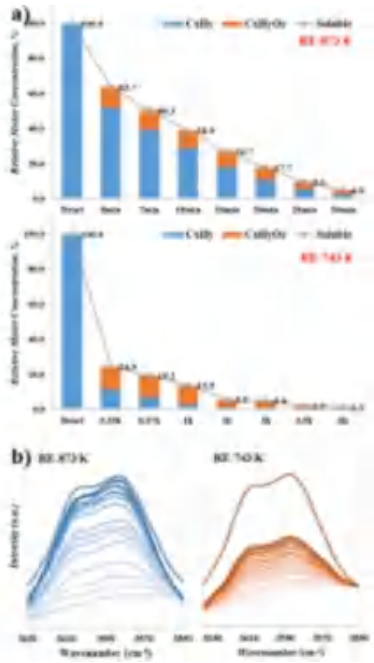


Figure 2 a) the changes in soluble carbon content of different regenerated samples at 873 K and 743 K, b) in-suit IR spectra of the deactivated samples treated by air at 873 K and 743 K.

To recap briefly, lowering regeneration temperature changes the decoking mode, thereby altering the spatial arrangement of remaining coke. As shown in Figure 3, the decoking manner of low-temperature regeneration tends to be a uniform model, while the high-temperature situation is more in line with the shrinking model. Consequently, the increase in ethylene selectivity originates from the expansion of the available confined space caused by the change in decoking mode under low-temperature regeneration conditions.

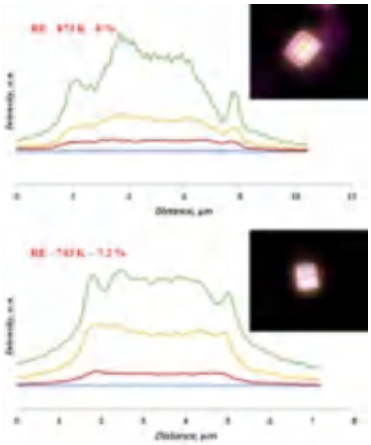


Figure 3 The spatiotemporal distribution of carbonaceous species (blue: benzenic, green: naphthalenic, yellow: phenanthrenic, red: pyrenic carbocations) obtained from the SIM images of regenerated materials at 873 K and 743 K.

Conclusions

In this study, the enhancement in ethylene production can be achieved after air regeneration at low temperature resulting from the better distribution of coke within the deactivated catalyst. The weak oxidation ability of oxygen at low temperatures first removes the more evenly distributed soluble carbon, resulting in a larger nanoconfinement space. This strategy of increasing ethene yield has higher economic efficiency and can be used as a process intensification method for MTO industry.

References

[1] M. Ye, H. Li, Y. Zhao, T. Zhang, Z. Liu, Advances in Chem. Eng. 47 (2015) 279-335

[2] J. Zhou,M. Gao,J. Zhang,W. Liu, T. Zhang, H. Li, Z. Xu, M. Ye, Z. Liu, Nat. Commun. 12 (2021) 17-28

Numerical simulation of particle erosion coupled with flue gas desulphurization in the spouted bed

Biao Sun, Feng Wu*, Wenbin Li (School of Chemical Engineering, Northwest University, Xi'an, China)
*Corresponding author:
Email: wufeng@nwu.edu.cn
Tel: +86-15309202861; Fax: +86-029-88302632

Abstract： The addition of an axial swirl vane (ASV) and multi-jet distributor plate to a conventional spouted bed (CSB) to form an integrated multi-jet swirling spouted bed (IMSSB) combined with internally reinforced components optimized its desulphurization efficiency and exacerbated the erosion of particles on the bed and the internal components. Erosion experiments have obtained the characterization of particle erosion on internal components and verified the relevant numerical models. Coupled study of the particle erosion and the desulphurization reaction in the flue gas desulphurization process of the IMSSB was carried out based on the CPFD numerical simulation. The results show that: the internal reinforcement components effectively enhance the mass and heat transfer between the gas and particle phases in the bed; In the cold mold condition, the inlet speed and the filling height of the filling particles will aggravate the erosion of the particles on the bed wall surface and the internal reinforcement components, the desulfurization efficiency of IMSSB is increased by 16.6 % compared with that of the CSB; in terms of wall erosion, the maximum particle erosion rate in IMSSB is about four times that of CSB; the erosion of particles on the axial swirl vane mainly occurs in the middle and lower vane, and the severity of erosion increases in the vane from the centre to the edges; particle erosion is most severe in the fountain area.

Key words: Integrated multi-jet swirling spouted bed, Particle erosion, Desulfurization efficiency, Swirl blade

Three-dimensional Numerical Investigation of Flow Past a Porous Spherical particle

Qinghai Huanga , Hang Yanga , Likun Maa,*, Zhishan Baia,*
aSchool of Mechanical and Power Engineering, East China University of Science and Technology, Shanghai200237, China

Abstract
This study utilizes FLUENT, a standard CFD software, to conduct numerical simulations of three-dimensional flow through porous spheres, investigating Darcy numbers ranging from 0 to 4.9 × 10-5 and Reynolds numbers from 0.01 to 1400. By approximating particle porosity with agglomerates of small spherical particles, the simulation provides a more precise portrayal of porosity's influence on the flow field compared to two-dimensional models. This work can provide the internal flow field results which are difficult to capture in the experiment, and the flow field variation results in the large permeability range can provide theoretical guidance for the industrial multiphase flow process with porous particle flow. Furthermore, the study emphasizes the practical significance of understanding the interplay between Darcy and Reynolds numbers in determining drag coefficients. The findings not only shed light on the intricate mechanisms governing fluid-particle interactions but also provides valuable guidance for the optimization of chemical process with porous particles.

Keywords: Porous sphere; Permeability； Flow field; Drag coefficient

Introduction

Understanding the interaction between porous particles and fluids is essential for accurate simulation of various industrial and natural processes. The traditional permeability model, which describes porosity on a macro scale, is often unable to accurately predict the flow of fluid through porous particles because of the complex geometry of the pore structure. [1] This work precisely controls porosity, pore structure and permeability by assembling small spherical particles to form a porous structure, thus promoting a more accurate three-dimensional simulation.

Methodology

The geometric model of porous particles is established by commercial software EDEM and Creo. After the point contact is treated by cutting method, the simulation calculation and analysis are carried out by CFD software.

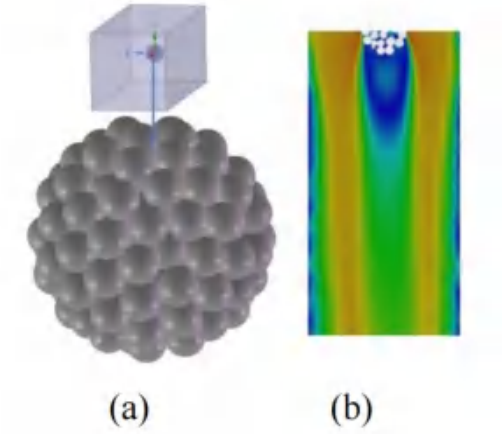


Figure 1 - (a)Geometric model of porous particles, (b) Vector field for flow past a porous sphere

Conclusions

A three-dimensional numerical simulation of flow past a porous spherical particle revealed that both the Darcy number and Reynolds number significantly affect the vector field distributions.

The study showed that drag coefficient variations within the examined Darcy number range correlate with internal flow fields of porous spheres, indicating circulating and back flow at intermediate Darcy numbers. Moreover, pressure fields varied with Darcy number, reflecting penetration flow effects through the particle.

Acknowledgements

This work is part of a research program financially supported by the National Natural Science Foundation of China (No. 22308105), the National Science Fund for Distinguished Young, China (No. 22225804), China Postdoctoral Science Foundation (No. 2023TQ0117).

References

[1] Yu P, Zeng Y, Lee T S, et al. Steady flow around and through a permeable circular cylinder[J]. Computers & Fluids, 2011, 42(1): 1-12.

Parallel Session VIII: Topic 4: Multiphase flows in heat exchangers

Thermal performance investigation of soil heat storage wall in solar greenhouse in severe cold regions

Shuang Xu, Zehui Chang※, Yanan Peng, Wenfu Xu
College of Energy and Power Engineering, Inner Mongolia University of Technology, Hohhot, China

Abstract

Low air temperature in solar greenhouse in winter lead to crop freezing damage and complete crop failure. In this work，A soil heat storage wall to heat crop canopy temperature zone in greenhouse is proposed. The soil heat storage wall starts to store heat with the heat being transferred to the interior through heat conduction when receiving sun irradiation, and begins to release heat by convection heat transfer when air temperature decreasing. The heat transfer process of soil heat storage wall is studied by establishing a heat transfer model of porous media. Results indicate that heat transfer in the soil heat storage wall is mainly one-dimensional along the thickness of the wall driven by temperature difference. In the severe cold regions, the function of soil heat storage wall is heating preservation as well as heating storage and release. When the ambient temperature is about -7°C at night, the indoor air temperature of greenhouse can be kept above 8°C. In a typical sunny day, the heat absorption of the soil storage wall is 1.90 MJ/m2 during the daytime, and the heat release to the crop canopy temperature zone in greenhouse is 0.04 MJ/m2 . This study can provide a reference for solving the winter planting in solar greenhouse in severe cold regions.

Keywords: heat storage, greenhouse, solar energy, porous medium, thermal performance

Introduction

The solar greenhouse realizes the anti-season production of crops and is widely used to grow vegetables in the winter [1]. However, low temperature at night still occurs in solar greenhouses without any auxiliary heating in winter, which seriously affects the normal growth of crops [2]. Using solar energy to supply energy for solar greenhouses can solve this problem [3]. Solar energy utilization technologies using in greenhouse include photovoltaic [4], solar thermal collectors and phase change material and so on [5] . However, the above methods still have a series of problems such as high price, poor effect and high risk. In this study, a novel soil heat storage wall is proposed, which has low construction cost, easy to obtain materials, and long service life.

Methodology

The greenhouse includes north wall, north roof, south roof, other enclosure structure, thermal insulation quilt and soil heat storage wall. The soil heat storage wall in this study is located in the south of the north wall of the greenhouse, which is made of soil brick with the surface being sprayed with black coating. Theoretical model of heat transfer in porous media was established to study the heat transfer process of soil heat storage wall. The experimental test site was located in Ulanhot, Inner Mongolia, which is belongs to the severe cold area. In order to monitor the temperature of the soil heat storage wall, the temperature at different points in the wall were collected.

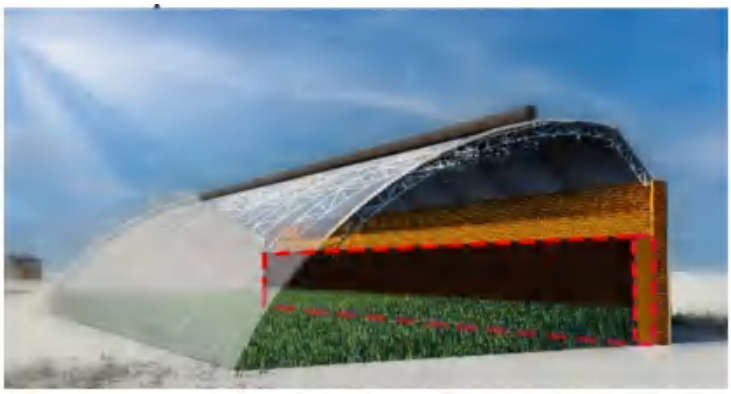


Figure 1. Schematic diagram of solar greenhouse

Conclusions

A method using soil heat storage wall to improve the solar greenhouse temperature was proposed. The conclusions of this study are as follows: (1) The heat transfer in soil heat storage wall is mainly one-dimensional along the thickness direction driven by temperature difference. (2) The indoor air temperature can be kept above 8°C in the greenhouse with soil heat storage wall, while the ambient temperature is about -7°C at night. (3) The heat absorption and released by the soil heat storage wall is 1.90 MJ/m2 and 0.04 MJ/m2 .

Acknowledgements

We gratefully acknowledge the financial support for this research provided by the National Natural Science Foundation of China (No. 51966012) Projects, Central Government Guiding Local Science and Technology Development Funds (No. 2022SZY0085), Innovative Research Team in Universities of Inner Mongolia Autonomous Region (NMGIRT2404).

Thermal Performance of a helical channel printed circuit plate heat exchanger

ZeHua YUN, QiuXia Yang, Chen GAO, KeWei Song
Lanzhou Jiaotong University, Lanzhou, China

Abstract
Printed circuit plate heat exchanger (PCHE) has the advantages of small size, high heat transfer efficiency, and the ability to adapt to high temperature and high pressure and other extreme working conditions, so it is widely used in industry. In this paper, the helical channel is applied to PCHE, and the enhancement of heat transfer performance by changing the parameters of the helical channel is investigated. When the pitch is smaller, the scouring of the boundary layer is more intense and more favorable for heat transfer. In the *Re* range of 100~900, the *PEC* is improved by 61%~161% compared to the straight channel when the *p*=5 mm.

Keywords: Printed circuit plate heat exchanger, Helical Channel, Thermal Performance

Introduction

PCHE is widely used as a kind of high-efficiency heat exchanger, which has the advantages of small size, high temperature and high pressure resistance, high compactness, and high thermal efficiency [1]. The helical channel enhance heat transfer by destroying the thermal boundary layer in the flow. The helical channel also has a relatively small increase in friction [2]. Therefore, the application of helical channel in PCHE can improve the overall heat transfer performance. Fig. 1 below shows the intercepted computational cell model with dimensions of 200 mm × 2.8 mm × 2.92 mm.

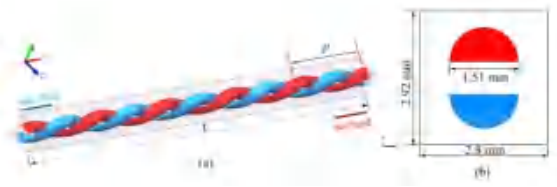


Figure 43 - Schematic diagram of the helical channel model: (a) overall structure; (b) inlet cross-section.

Methodology

The numerical solutions are obtained using the commercial CFD code FLUENT. All equations are solved using a second-order windward scheme. The semi-implicit method pressure coupled equations (SIMPLE) is used to couple velocity to pressure.

Conclusions

Fig. 2(a) and (b) shows the variation of *Nu* and *PEC* with *Re* for different pitches, it is observed that *Nu* and *PEC* gradually increase as the pitch decreases. When *p* = 5 mm, *Nu* increased by 86% to 274% compared to the straight channel. The *PEC* is largest for *p*=5 mm and reaches 2.61 at *Re*=830.

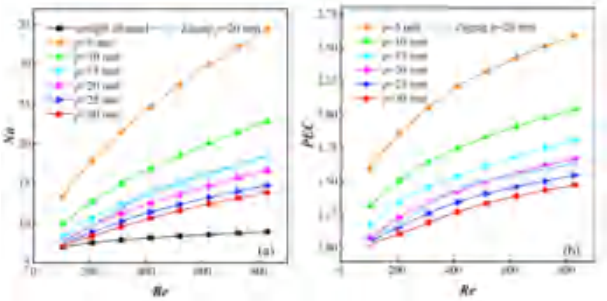


Figure 2 - Nu and PEC at different pitches.

Acknowledgements
Supported by National Natural Science Foundation of China (52266003), Research Programs in Lanzhou Jiaotong University (ZDYF2302 and 2022JC11), and the Innovation Star project of outstanding graduate students of Gansu Province (2023CXZX-566, 2023CXZX-519).

References
[1] F. Xin, T. Ma, Y.T Chen, Q.W. W, Study on chemical spray etching of stainless steel for printed circuit heat exchanger channels, Nuclear Engineering and Design, 341 (2019) 91-99.
[2] A. Aldor, Y. Moguen, K.E. Omari, C. Habchi, P. Cocquet, Y.L. Guer, Heat transfer enhancement by chaotic advection in a novel sine-helical channel geometry, International Journal of Heat and Mass Transfer, 193 (2022) 122870.

Thermal performance of a novel battery thermal management system combining phase change material and air-cooled technologies

Rong He, QiuXia Yang, KeWei Song
Lanzhou Jiaotong University, Lanzhou, China

Abstract

In order to improve the heat transfer on the surface of the battery's leeward side and the temperature uniformity of the battery pack in the traditional air-cooled battery thermal management system(BTMS), this paper proposes a novel hybrid BTMS coupled with phase change and air-cooled heat dissipation. BTMS 1 adopts a semi-ellipsoidal arrangement of phase change materials(PCMs). The air-cooled channel is formed between the two adjacent battery cells. It is compared with the air-cooled BTMS (BTMS 2) and the BTMS with PCM uniformly wrapped around the cells (BTMS 3). The numerical results show that the semi-elliptical PCM in BTMS 1 improves the heat transfer effect in the flow dead zone by latent heat absorption, improving the heat transfer performance of BTMS 1. The maximum temperature (T_{max}) of BTMS 1 was 314.79 K and the temperature difference (ΔT) of the battery pack was kept within the safe operating temperature range of 5 K at the inlet velocity is 2 m/s.

Keywords: Phase change material, Air-cooled, Battery thermal management system

Introduction

Power batteries typically play an essential role in electric vehicles and significantly influence their performance.Studies have shown that the optimal operating temperature range of batteries is 20~50℃ [1]. Therefore, an efficient BTMS is needed to keep the temperature within the safe temperature range, thus ensuring the optimal performance and the safe of the electric vehicles [2]. In this paper, the novel hybrid BTMS numerical calculation models for different structures are shown in Figure 1.

Methodology

In this paper, the battery is considered as a heat source with uniform volume ratio.The PCM does not consider convective term and gravity. The boundary conditions of the computational domain are velocity inlet and pressure outlet.

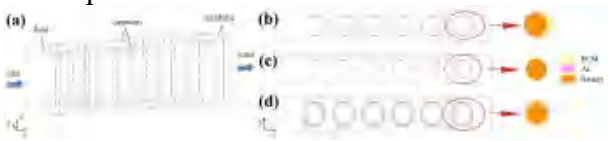


Figure 44 - Physical model, (a) BTMS calculation model, (b) BTMS 1, (c) BTMS 2,(d) BTMS 3.

Conclusions

The T_{max}, ΔT and f are shown in Figure 2. The T_{max} and ΔT of BTMS 1 are 314.79 K and 4.32 K, respectively.Compared with BTMS 2 and BTMS 3, the T_{max} was reduced by 1.2%~2.8%, the ΔT was reduced by 2.9%~50.1%. While both the T_{max} and ΔT decreased, the f of BTMS 1 was 41% lower than that of BTMS 3. The effectiveness of BTMS 1 is fully verified.

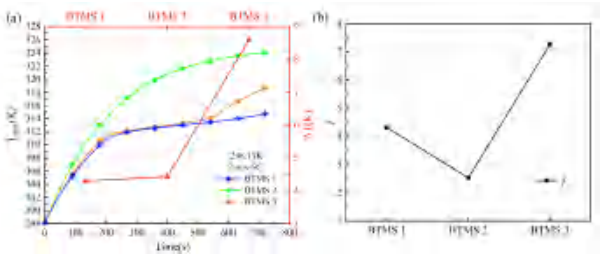


Figure 2 - Variations of T_{max} , ΔT and f at different BTMS.

Acknowledgements

This work was supported by the National Natural Science Foundation of China (52266003), Research Programs in Lanzhou Jiaotong University (ZDYF2302 and 2022JC11), and the "Innovation Star" project of outstanding graduate students of Gansu Province (2023CXZX-566, 2023CXZX-519).

References

[1] Y. H. Li, Z. L. Chen, Y. Feng, M. N. Liu, C. Z. Kang, K. J. Yang, J. Yuan, C. H. Qiu, H. Shi, Y. L. Jiang, A novel petal-type battery thermal management system with dual phase change materials, International Journal of Heat and Mass Transfer, 207 (2023) 123989.

[2] R. C. Sahin, S. Gocmen, E. Cetkin, Thermal management system for air-cooled battery packs with flow-disturbing structures, Journal of Power Sources, 551 (2022) 232214.

Machine learning prediction for thermal-hydraulic parameters of propane condensation flow in a PCHE straight channel

Qian Li[1,2],Xiangyu Fu[1,2], Rongmin Zhang[1,2], Liu Yang[1,2], Weihua Cai[1,2,*]
1. Laboratory of Thermo-Fluid Science and Nuclear Engineering, Northeast Electric Power University, Jilin, China
2. School of Energy and Power Engineering, Northeast Electric Power University, Jilin, China
Weihua Cai: caiwh@neepu.edu.cn

Abstract
In the LNG regasification process, the printed circuit heat exchangers(PCHE) is an ideal choice for vaporizer, with propane as the intermediate working medium in the hot side of PCHE. In this work, numerical simulations of propane condensation flow and heat transfer at different operating parameters was carried out in a semi-circular straight channel of PCHE. The micro-segment analysis method was used to present the local heat transfer coefficient and pressure drop in the channel. The results indicate that the propane condensation process can be divided into three stages: the "constant temperature condensation stage" in the droplet condensation state, the "variable temperature condensation stage" in the film condensation state, and the "subcooled stage" in the liquid phase state. Different operating parameters can affect the start and end position of each stage, as well as the parameter values in the same state. An artificial neural network method was used to predict the local heat transfer coefficient and pressure drop, with the predicting error of less than 5% and 10% respectively. This study provides a machine learning method to accurately predict the flow and heat transfer parameters for propane condensation flow in PCHE channel and valuable for future design of LNG vaporizer.

Keywords： printed circuit heat exchanger, propane condensation, micro-segment analysis, artificial neural network, machine learning

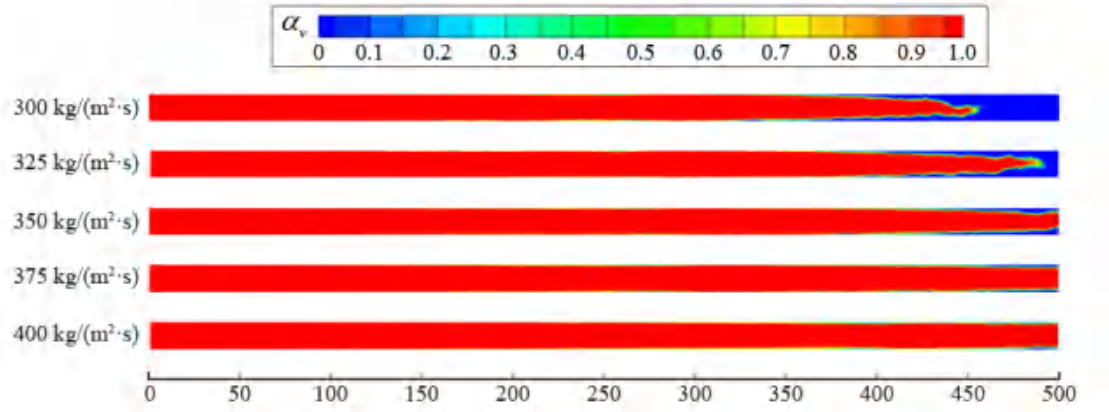


Fig. 1. Liquid and vapor phase distribution along the channel at different mass flow rate

The experimental study on frictional pressure drop characteristics of two-phase fluids flow across the spiral tube bundles

Wenke Zheng[a,b*], Yaolong Wang[a,b], Jiwei Guo[a,b], Zhongyun Tian[a,b], Fenggang Wang[a,b], Yiqiang Jiang[a,b], Cheng Sun[a,b]
a School of Architecture and Design, Harbin Institute of Technology, Harbin, China
b Key Laboratory of Cold Region Urban and Rural Human Settlement Environment Science and Technology, Ministry of Industry and Information Technology, Harbin, China

Abstract
The frictional pressure drop characteristics of two-phase fluids flow across the spiral tube bundles are not fully understood yet. Therefore, we constructed the experimental platform to investigate the effects of total mass flow rates and vapor quality on the frictional pressure drop characteristics. Results indicate that the frictional pressure drop increases with vapor quality and total mass flow rate. When vapor quality rises from 0.19 to 0.27, the frictional pressure drop gradient increases from 21.18 $Pa \cdot m^{-1}$ to 84.58 $Pa \cdot m^{-1}$. When total mass flow rate increases from 921 $kg \cdot h^{-1}$ to 1327 $kg \cdot h^{-1}$, the frictional pressure drop gradient rises from 11.15 $Pa \cdot m^{-1}$ to 47.52 $Pa \cdot m^{-1}$. Because the increasing vapor quality and total mass flow rate enhance the gas-shear effect, which will lead to an increase in the frictional pressure drop. Therefore, the frictional pressure drop increases with vapor quality and total mass flow rate.
Keywords: Two-phase fluids; Operational parameters; Frictional pressure drop

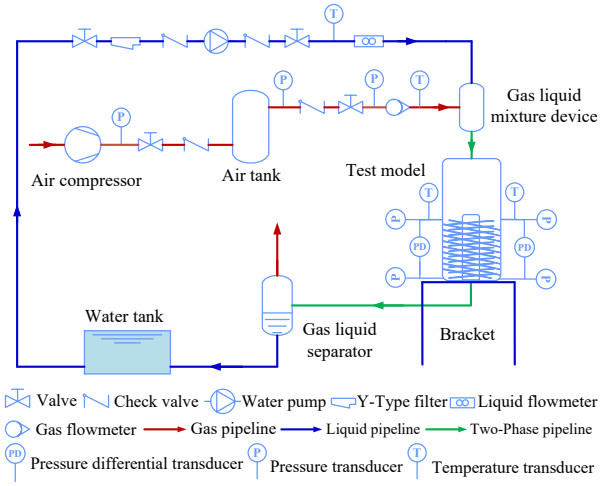


Figure 45 Schematic diagram of the experimental platform

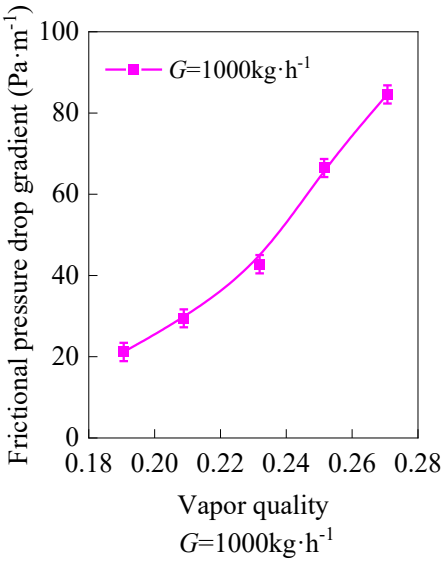


Figure 46 The frictional pressure drop versus vapor quality

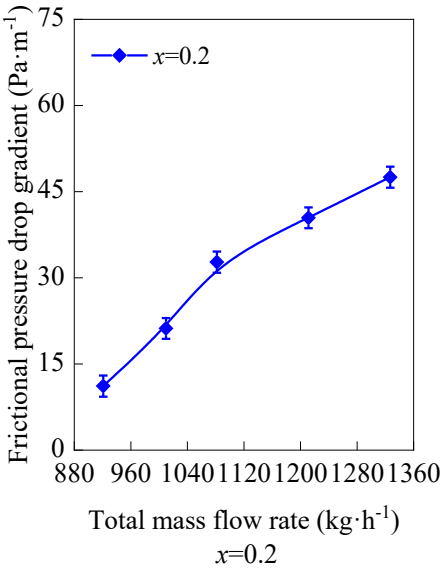


Figure 47 The frictional pressure drop versus total mass flow rate

Molecular dynamics study on the heat transfer properties of organic fluid based on deep learning potential

Dan-Dan Su, Xiao-Bin Li*, Hong-Na Zhang, Feng-Chen Li
School of Mechanical Engineering, State Key Laboratory of Engines, Tianjin University, Tianjin 300350, China

Abstract
Since the prevalence of electronic devices, heat dissipation efficiency of heat exchangers has been a subject of constant attention. Organic fluid is the promising candidate for transferring heat in heat dissipation system owing to the excellent physical properties (high thermal stability, wide working range, high heat conductivity). In the study, a deep learning potential model of organic fluids is established. Based on the deep learning potential model, the molecular dynamics calculation on heat transfer properties of organic fluids is performed. The results of traditional molecular dynamics calculations are compared with that of molecular dynamics based on deep learning potential. Radius distribution function (RDF), temperature distribution, and heat flux are analysed. The results show that there are great difference in the temperature difference, radial distribution function, and heat flux for the deep potential molecular dynamics simulation (DPMD) and the traditional molecular dynamics simulation (TMD). The peak of the RDF in TMD is distributed in the range of distance 2.6-3.6 Å. However, in DPMD, the peak of RDF is distributed in the range of distance t from 0.8 to 1.6 Å. Compared to TMD, the calculation accuracy of the heat flux is improved by 8.46% when a deep potential model is used. This study lays a theoretical foundation for the study of heat transfer of organic fluid efficiency in heat exchangers.

Keywords: Molecular dynamics, Heat transfer properties, Organic fluid, Deep learning potential

Introduction

Since the prevalence of electronic devices, heat dissipation has been a subject of constant attention. With the rapid development of science and technology, the size of electronic devices has gradually become smaller, even reaching the nanoscale, which leads to a rapid increase of thermal load, with a heat flow density of more than 10MW/m2. Hence, improving heat dissipation efficiency is of great importance.

Organic fluid is the promising candidate for transferring heat in heat dissipation system owing to the excellent physical properties (high thermal stability, wide working range, high heat conductivity). The study of the heat transfer properties of organic fluid has always attracted the great attention to scholars. The research methods for investigating the heat transfer properties of organic fluid primarily includes three types: experimental measurement, theoretical prediction and molecular dynamics calculation. In terms of experiment, Gong's team conducted more comprehensive experimental measurements on thermophysical properties in heat transfer, mainly including viscosity [1, 2], specific heat capacity [3, 4], and critical physical property parameters[5-7].

Theoretical predictions are also commonly used to obtain the thermophysical properties of organic fluid in heat transfer. The more commonly used theoretical prediction model is the Helmholtz energy equation of state with high accuracy and great universality. In addition, some scholars [8-10] have also proposed predictive models for specific fluid or specific physical properties.

In addition to the above two methods, molecular dynamics (MD) is a common method used to study the heat transfer properties of organic fluid in recent years. The most critical factor affecting the accuracy of MD calculations is the choice of force fields, which describe the inter-

and intra-molecular interactions for molecules. Currently, commonly used force fields include empirical force fields and ab initio-based force fields. As is well known, ab initio-based force field has higher precision, because that it calculates the energy and force of atom using quantum chemical methods and considers the movement of electrons. However, due to the limitations in computing costs and resources, the simulation time is short and the simulation system is small for calculation using ab initio-based force field. It is not practical to employ ab initio force field for the calculations of the thermophysical properties of organic fluid in larger-scale systems. Over the past decades, A series of studies on the MD calculation of the heat transfer properties have been reported[11-13], where the empirical force field is used to calculate the inter- and intra-molecular interactions for molecules.

However, the accuracy of describing molecular interactions and properties with above force filed is limited due to the limitation of the force field function. To address the above problems, in recent years, scholars [14, 15] have proposed the application of machine learning to the development of force fields, which can simultaneously achieve the same high computational efficiency as classical molecular dynamics and the same high computational accuracy as ab initio molecular dynamics (AIMD). For the heat transfer properties, there are many MD calculations using deep learning potentials[16-18]. However, all of these studies were on heat transfer property calculations of molten salts. No deep potential molecular dynamic simulations on the heat transfer properties of organic fluid have been found. In order to solve the above problems, in this study, a deep learning potential model of organic fluids is established. Based on the deep learning potential model, the molecular dynamics calculation on heat transfer properties of organic fluids is performed.

Methodology

In this study, R134a is used as organic fluids. The initial structure of R134a fluid was built using the Material Studio software package. The molecular number of R134a is 25. Based on the above structure, Vienna Ab Initio Simulation Package (VASP) software was used to perform the AIMD simulation. The NVT was used for systerm, the temperature was fixed at the temperature corresponding to the initial structure, respectively. The time step size was set to 1 fs, and the number of steps was 2000, to calculate the energy and force of the molecules at different temperatures. Calculated results were used as the database for deep potential training.

Deep potential training is performed by the software deepMD-kit. The first eighty percent of the data at each temperature was used as the training set and the second twenty percent of the data at each temperature was used as the validation set. Based on the above actions, the deep learning potential model of organic fluids is obtained.

Using the deep learning potential model, the molecular dynamics calculation on heat transfer properties of organic fluids is performed. The physical model of simulation system is shown in Fig. 1. The model dimension in x, y and z directions are3.15 nm, 3.15 nm and 8.8 nm respectively. The simulation model is arranged with periodic boundary conditions in all directions.

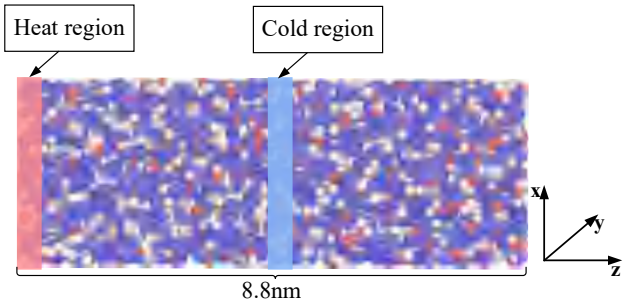


Figure 48 physical model for simulation.

Simulation process can be divided into three stages. The first is relaxation process: the canonical ensemble (NVT) is adopted to fix the temperature of system at a target value (270K), and the relaxation time is 1ns. The second is non-equilibrium molecular dynamics (NEMD) process: the heat source and cold source are added, as shown in Figure 1. The last is the data collection process. All the simulations are performed via the large-scale atomic / molecular massively parallel simulator (LAMMPS)[19]. The motion of atoms is calculated by the Velocity-Verlet [20] algorithm with a time step of 1fs.

Results and discussion

Figure 2 represents the comparison of the deep potential energy model prediction results with the DFT calculation results. it can be seen from fig.2 that the energy predicted using the deep potential model is very close to that calculated by DFT. This proves that the prediction accuracy of the deep potential model is high.

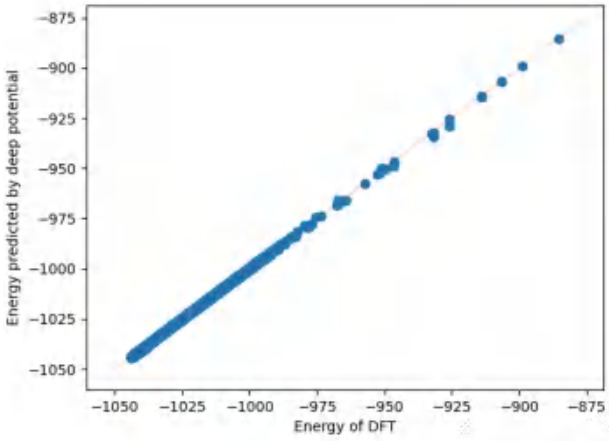


Figure** 2 **validation results of deep potential energy model.

Figure 3 shows the variation of temperature at the equilibrium stage under different simulation methods. It can be seen from Fig. 3 that the temperature of the system during the equilibrium stage stabilises at the initial temperature, i.e. 270 K, in both the deep potential molecular dynamics simulation (DPMD) and the traditional molecular dynamics simulation (TMD). This indicates that the system has reached equilibrium in the simulation.

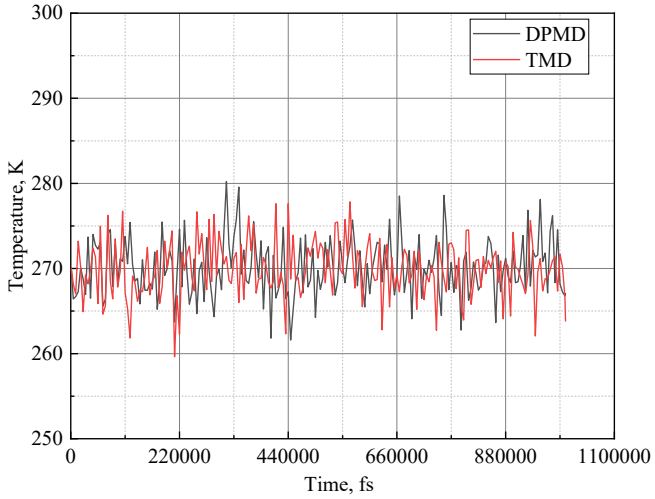


Figure* 3 *the temperature of systerm at the first stage of simulation.

Figure 4 represents the pressure variation of the system during equilibrium for different simulations. From the figure, it can be seen that the pressure gradually fluctuates around a constant value during the equilibrium process, which again indicates that the system has reached equilibrium. However, there are differences between the pressure value calculated by DPMD and the pressure value calculated by TMD. This is mainly due to the difference in potential energy calculation in the two molecular dynamics calculations.

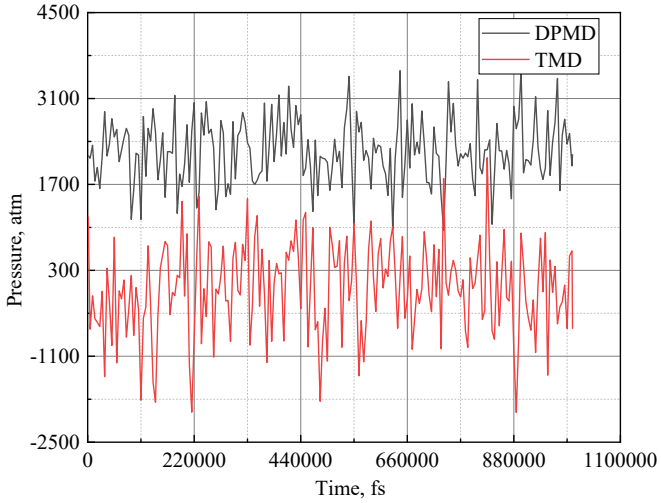


Figure* 4 *the pressure of systerm at the first stage of simulation.

Figure 5 shows the temperature changes in the heat source region and the cold source region after the addition of a stabilised heat and cold source to the system. As shown in Fig.5, for TMD, the temperature in the heat region rises and then stabilises at a constant value, and the temperature of the cold region falls sharply and then stabilises at a constant value. In other words, there is a fixed temperature gradient between the cold region and the heat region. For DPMD, temperature changes in the heat region and the cold region are not obvious compared to TMD, but there are also slight increases and decreases in heat and cold region. When the system reaches equilibrium, for DPMD and TMD, the stable temperature difference between the cold region and heat region is 7.35 K and 232.37 K, respectively. The reason for this difference is also due to the different methods of energy calculation.

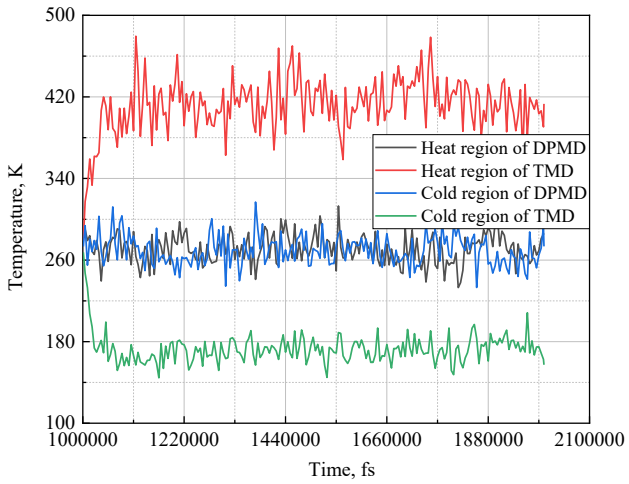


Figure** 5 **the temperature of heat region and cold region at the second stage of simulation.

Figure 6 represents the radial distribution function (RDF) at different moments in the DPMD. As shown in Fig.6, it can be seen that the values of RDF are almost the same at different moments, thus indicating the validity of the data collection. As the distance increases, the RDF first rises and then gradually stabilises at a constant value. The peak distribution of the RDF is in the range of distances from 0.8 to 1.6 Å. At the same time, the RDF in DPMD have two peaks.

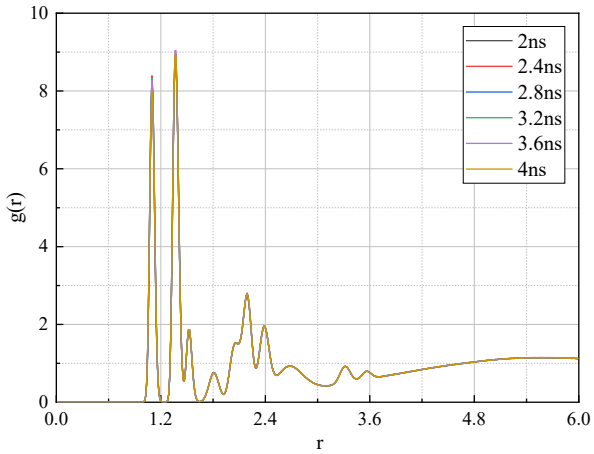


Figure** 6 **the radial distribution function at the last stage of DPMD.

Figure 7 represents the variation of RDF for TMD over the cutoff radius distance. As can be seen from the figure, the RDF first rises and then shows small fluctuations and finally stabilises at a constant value. The peak of the RDF is distributed in the range of distance 2.6-3.6 Å.

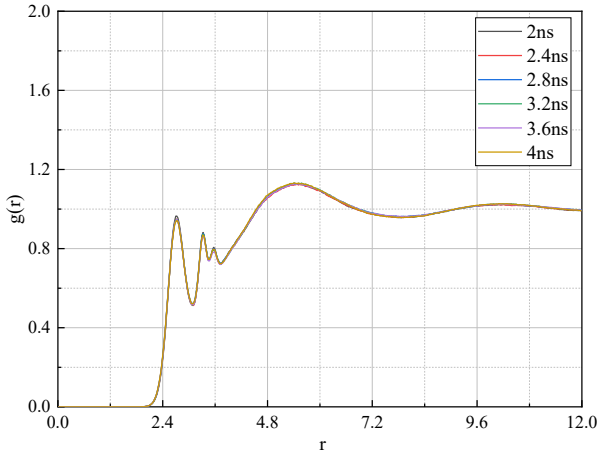


Figure* 7 *the radial distribution function at the last stage of TMD.

From Fig. 6 and Fig.7, it can be noticed that the RDF varies in different moments in the same way. Fig. 8 represents the comparison of the variation of RDF in different simulation cases at 4ns. As can be seen from the figure, when the distance is greater than 2.6 Å, the values of the RDF for the two simulation cases are essentially the same. When the value of the distance is less than 2.6 Å, there is a large difference in the change of RDF between DPMD and TMD. For DPMD, RDF is constantly fluctuating. For TMD, RDF gradually increases. This is the reason for the difference in energy calculations between the two simulation, and the reason for the difference in calculations of all parameters.

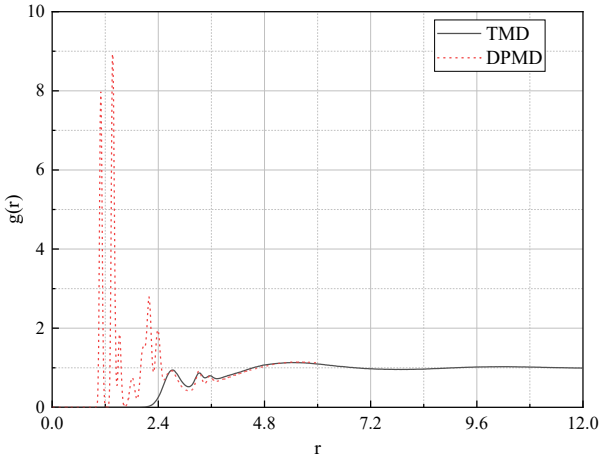


Figure* 8 *the radial distribution function under different simulation.

Figure 9 represents the variation of the heat flux of system under different simulation cases. As can be seen from the figure, the heat flux fluctuates around a constant value as the simulation progresses in both DPMD and TMD. However, the fluctuations are larger in DPMD compared to TMD. For DPMD, the average value of heat flux is 5.83×10^9 W/m^2. For DPMD, the average value of heat flux is 5.23×10^9 W/m^2. However, in the second stage of simulation , the heat flux of 7.08×10^9 W/m^2 is added in the systerm. Compared to TMD, the calculation accuracy of the heat flux is improved by 8.46% when a deep potential model is used.

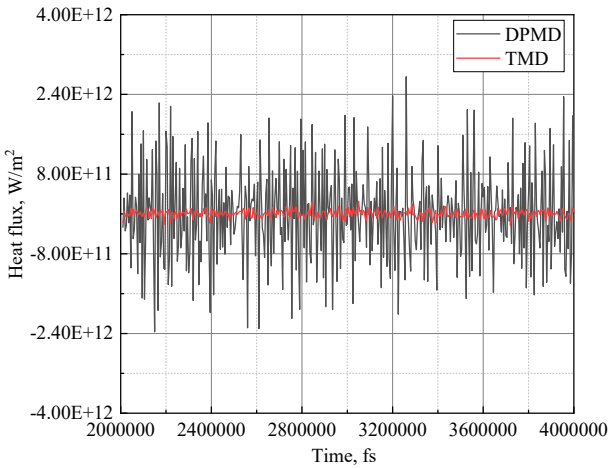


Figure* 9 *the change of heat flux under different simulation.

Conclusions

In the study, a deep learning potential model of organic fluids is established. Based on the deep learning potential model, the molecular dynamics calculation on heat transfer properties of organic fluids is performed. The results of traditional molecular dynamics calculations are compared with that of molecular dynamics based on deep learning potential. The key conclusions are as follows.

(1) When the same cold and heat sources are added to the system, the temperature difference between the cold region and heat region in TMD is greater than that in DPMD.

(2) When the distance is greater than 2.6 Å, the values of the RDF for the two simulation cases are essentially the same. When the value of the distance is less than 2.6 Å, there is a large difference in the change of RDF between DPMD and TMD.

(3) When the heat flux of 7.08×109 W/m2 is added in the systerm, for DPMD and TMD, the average calculation value of heat flux is 5.83×10^9 W/m^2 and 5.23×10^9 W/m^2, respectively. The calculation accuracy of the heat flux is improved by 8.46% when a deep potential model is used.

References

[1] S. Sun, B. Sheng, Y. Wang, Y. Zhao, X. Dong, M. Gong, Viscosity measurements of liquid ethene + ethane binary mixtures at temperatures from 173.150 K to 243.150 K and pressures up to 5.5 MPa, The Journal of Chemical Thermodynamics, 181 (2023).

[2] S. Sun, Z. Yang, B. Sheng, Y. Wang, Y. Zhao, X. Dong, M. Gong, The viscosity of liquid ethene: Measurement and molecular dynamic simulation, The Journal of Chemical Thermodynamics, 178 (2023).

[3] B. Sheng, L. Ding, X. Dong, Y. Zhao, H. Guo, M. Gong, Measurements of isobaric specific heat capacity (c) for pure trans-1,3,3,3-tetrafluoropropene and (trans-1,3,3,3-Tetrafluoropropene + 1,1,1,2-tetrafluoroethane) binary mixtures at temperatures from (231.84 to 338.68) K and pressures up to 8.2 MPa, The Journal of Chemical Thermodynamics, 172 (2022).

[4] B. Sheng, X. Dong, M. Gong, Y. Zhao, Density and isochoric heat capacity of {x trans-1,3,3,3-Tetrafluoropropene + (1-x) Propane} at temperatures from (285.45 to 349.71) K and pressures up to 10.384 MPa, International Journal of Refrigeration, 150 (2023) 349-356.

[5] B. Tang, X. Yao, X. Dong, B. Sheng, Y. Zhao, J. Shen, M. Gong, Experimental investigation of saturated vapor pressure and critical parameter for R1234ze(Z) (cis-1,3,3,3-tetrafluoropropene) and R1336mzz(Z) (cis-1,1,1,4,4,4-hexafluoro-2-butene), The Journal of Chemical Thermodynamics, 189 (2024).

[6] X. Yao, J. Shen, H. Kang, B. Tang, Z. Li, J. Li, X. Dong, M. Gong, Measurement of critical properties for the binary mixture of R744 (carbon dioxide) + R1234ze(E) (trans-1,3,3,3-tetrafluoropropene), International Journal of Refrigeration, 152 (2023) 369-375.
[7] X. Yao, J. Shen, H. Kang, Z. Li, X. Dong, M. Gong, Measurement of critical parameters for the binary mixture of R744 (carbon dioxide) + R1234yf (2,3,3,3-tetrafluoropro-1-ene), The Journal of Chemical Thermodynamics, 178 (2023).
[8] B. Sheng, Y. Zhao, X. Dong, H. Lu, W. Dai, H. Guo, M. Gong, A new prediction equation of compressed liquid isochoric heat capacity for pure fluids and mixtures, Journal of Molecular Liquids, 343 (2021).
[9] X. Zhao, X. Wang, Y. Zhao, X. Dong, Y. Wang, M. Gong, Prediction of the Thermal Conductivity for Liquid Hydrocarbons and Halogenated Hydrocarbons, Industrial & Engineering Chemistry Research, 62 (2023) 2968-2977.
[10] M.E. Mondejar, J. Frutiger, S. Cignitti, J. Abildskov, G. Sin, J.M. Woodley, F. Haglind, Uncertainty in the prediction of the thermophysical behavior of new halogenated working fluids, Fluid Phase Equilibria, 485 (2019) 220-233.
[11] M.S. Alam, J.H. Jeong, Calculation of the thermodynamic properties of R448A and R449A in a saturation temperature range of 233.15 K to 343.15 K using molecular dynamics simulations, International Communications in Heat and Mass Transfer, 116 (2020).
[12] M.S. Alam, J.H. Jeong, Thermodynamic properties and critical parameters of HFO-1123 and its binary blends with HFC-32 and HFC-134a using molecular simulations, International Journal of Refrigeration, 104 (2019) 311-320.
[13] G. Raabe, Molecular modeling of fluoropropene refrigerants, J Phys Chem B, 116 (2012) 5744-5751.
[14] A.P. Thompson, L.P. Swiler, C.R. Trott, S.M. Foiles, G.J. Tucker, Spectral neighbor analysis method for automated generation of quantum-accurate interatomic potentials, Journal of Computational Physics, 285 (2015) 316-330.
[15] S.A.T. Chmiela, Alexandre %A Sauceda, Huziel E. %A Poltavsky, Igor %A Schütt, Kristof T. %A Müller, Klaus-Robert, Machine learning of accurate energy-conserving molecular force fields, Science Advances, 3 (2017).
[16] M. Bu, T. Feng, G. Lu, Prediction on local structure and properties of LiCl-KCl-AlCl3 ternary molten salt with deep learning potential, Journal of Molecular Liquids, 375 (2023).
[17] Y. Xie, M. Bu, Y. Zhang, G. Lu, Effect of composition and temperature on microstructure and thermophysical properties of LiCl-CaCl2 molten salt based on machine learning potentials, Journal of Molecular Liquids, 383 (2023).
[18] D. Guo, J. Zhao, W. Liang, G. Lu, Molecular dynamics simulation of molten strontium chloride based on deep potential, Journal of Molecular Liquids, 348 (2022).
[19] S. Plimpton, Fast parallel algorithms for short-range molecular dynamics, Journal of Computational Physics, 117 (1995) 1-19.
[20] W.C. Swope, H.C. Andersen, P.H. Berens, K.R. Wilson, A computer simulation method for the calculation of equilibrium constants for the formation of physical clusters of molecules: Application to small water clusters, The Journal of Chemical Physics, 76 (1982) 637-649.

Numerical study on propane condensation in airfoil-enhanced PCHE for S-LNG vaporization

Zhen Tian*, Xiangjie Chen
Shanghai Maritime University, Shanghai, China
ztian@shmtu.edu.cn
+86 18818213836

Abstract

The Printed Circuit Heat Exchanger (PCHE) has been adopted as LNG vaporizer because of its compactness and high-pressure resistance. As for the Fuel Gas Supply System (FGSS), the LNG is supplied at the pressure of 32 MPa for the main engine with the vaporization process from -162°C to about 20°C. The ethylene glycol is generally utilized hot fluid in the PCHE. However, the icing block in the mini channel limited the application of PCHE. To avoid the icing problem, the propane with lower boiling temperature is selected as the hot fluid for LNG vaporization in PCHE.

In this study, the studied unit consists of a cold channel and a hot channel. The hydraulic diameter of the channel is 1 mm, and the length of the unit is 20π mm. The effects of LNG mass flow rate (0.4~1.2 kg/h) on the heat transfer coefficients and pressure drops are investigated. In particular, the thermohydraulic performances of the sinusoidal channel and sinusoidal channel with airfoil enhancement are compared.

The temperature field, velocity field, VOF results are analysed. The results demonstrates that the propane *Nu* varies between 201.05-119.6 for the sinusoidal channel, and the *Nu* changes between 185.01-103.29 for the airfoil-enhanced PCHE. The friction factor *f* increases from 0.196-0.054 to 0.239-0.078 because of the installation of the airfoil.

Numerical model and experimental verifications on turbulent CO_2 flow in supercritical and trans-critical regions inside a long thin circulation loop

Rufan Song[1,2], Dong Yang[1,3], Quanyu Gong[1,3], Yongchang Feng[1], Deqing Mei[2], Igor Pioro[4], Lin Chen[1,3,*]

1. Institute of Engineering Thermophysics, Chinese Academy of Sciences, Beijing 100190, China
2. Jiangsu University, Zhenjiang 212013, China
3. University of Chinese Academy of Sciences, Beijing 100049, China
4. Ontario Tech University, Oshawa ONL1G0C5, Canada
* Corresponding author (Prof. Lin Chen): chenlin2018@iet.cn

Abstract

Precise prediction of convective heat transfer characteristics of CO_2 under supercritical pressure conditions is essential for the secure design of heat exchangers with supercritical and trans-critical CO_2 energy systems. In this study, experimental and numerical studies have been carried out to analyse the supercritical CO_2 vertical loop heat transfer flow. Multiple turbulent model verifications and validations have been made against experimental results. Supercritical and trans-critical flow behaviours have also been discussed in detail in this study.

The experimental section has a total length of 3.5 m. The experimental part is subjected to heating via a uniform and constant heat flow. A range of inlet temperatures from 15 to 40°C, inlet pressures from 7.6 to 9 MPa, mass flow rates from 200 to 1200 kg/m^{2}s, and heat flow densities from 0 to 240 kW/m^2 have been tested. the effects of various parameters including inlet temperature, inlet pressure, mass flow rate, and heat flow density on heat transfer were examined. The results indicate that increasing the mass flow rate effectively enhances supercritical CO_2 heat transfer performance and mitigates heat transfer deterioration.

The heat transfer process of CO_2 vertical loop can be simplified into a 2D axisymmetric model. The number of mesh selected in this paper is 3.0×10^5, and the relative deviation with the experiments is 0.087%. The mesh size of the first node in the boundary layer is 1 μm with a growth ratio of 1.1 to ensure y+ ≈ 1.

The numerical results have been validated against the experimental data. The SST *k-ω* model with modified parameters agree well with the experimental data and are recommended for the current test parameter ranges.



Figure 49 – Experimental system (IET-CAS)

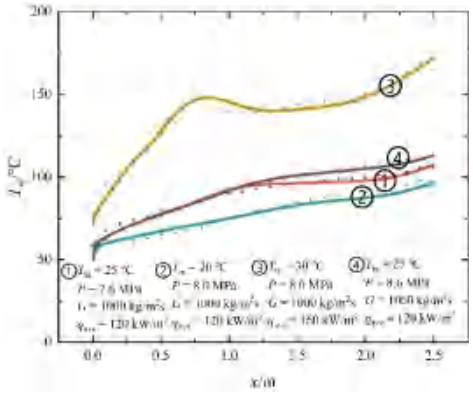


Figure 2 - Comparison plots between numerical results and experimental data

Keywords: Supercritical carbon dioxide; Heat exchange; Experiment; Turbulent model

References

[1] L. Chen, *Handbook of Research on Advancements in Supercritical Fluids Applications for Sustainable Energy Systems*, IGI Global, USA (2021).
[2] D. Yang, L. Chen, J. Chen, Y. Feng. *Int. J. Energ. Res.*, 2022; 46:16375–16393.

Numerical Simulation on Direct Contact Condensation Heat Transfer characteristics in Steam-Water Film

Chai Yinghua[1,2], Lin Yuansheng[1,2*], Xiao Qi[1,2], Huang Chonghai[1,2], Ke Hanbing[1,2], Li Bangming[1,2]

1. Science and Technology on Thermal Energy and Power Laboratory, Wuhan, Hubei, 430205, China;
2. Wuhan Second Ship Design and Research Institute, Wuhan, Hubei, 430205, China;

Abstract

The mixed type condenser, utilizing a water film, which formed by the supercooled water jet to directly contact with the steam. With the advantages of high heat transfer coefficient、compactness、reliability and low heat transfer temperature difference, it is considered to be an optimal choice for ships and offshore platforms. The direct contact condensation of steam and water film is the key process of mixed type condenser, which has the characteristics of large velocity and density between the two phases, accompanied by the strong turbulence and interphase heat transfer. There are many influences in this process, no mature experience database or prediction model can provide guidance for the design and optimize of mixed type condenser. In this paper, a heat and mass transfer model based on VOF model and Lee model is established.

This paper analyzes the influences of steam and water mass flow rates, ranging in 0.002 kg/s-0.01 kg/s and 0.3 kg/s-0.83 kg/s respectively. The impact of three different flow: cross flow, parallel flow and countercurrent flow on flow field have been discussed. The results reveal that in both cross flow and parallel flow, as the mass flowrates of steam increase, the condensation heat transfer coefficients also increase. In the situation of contercurrent flow, heat exchange becomes more intense, which leads a blurry interface between the vapor and liquid phase.

Keywords: Water Film, VOF, Direct contact Condensation, Heat Transfer Coefficient

Introduction

The mixed type condenser, adopting the water film to directly contact with the steam, the heat transfer coefficient of mixed type condenser (0.1-10MW/m^2•K) is much greater than wall-type condenser. Due to its advantages in high heat transfer coefficient, no moving parts, compactness and low temperature difference, which can achieve the maximum heat transfer limit[1-3]. It considered to be an ideal choice and widely used in the fields of electric power and nuclear energy.

Methodology

This study adopts the VOF (Volume of Fluid) method and condensation model (Lee model) to perform a 3D CFD simulations for steam-water film direct contact condensation. Due to the full-scale 3D steam-water film direct contact condensation simulation in the mixed type condenser is too large, this paper chooses a 10cm×10cm×11mm region of mixed type condenser containing water film and vapor space as study object,which as shown in Fig. 1.

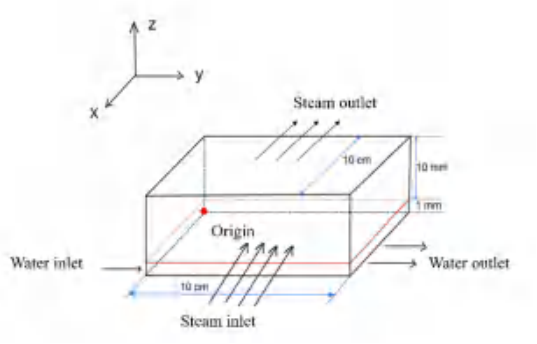


Figure 50 - Geometry structure of computational configuration

The condensation heat transfer coefficient h can be calculated using the following equations.

$$Q_1 = \Delta m \times h_{fg} \quad \textbf{(1)}$$

$$Q_2 = C_p \times \Delta m \times (T_{sat} - \overline{T}) \quad \textbf{(2)}$$

$$h = \frac{Q_1 + Q_2}{S_{surface} \cdot \Delta T} \quad \textbf{(3)}$$

Where Δm represents the condensation amount of steam; $\overline{T}$ represents the outlet average temperature of the water film; $S_{surface}$ represents the heat transfer area; ΔT represents the temperature difference.

Results Analysis

Fig.2 shows that the condensation heat transfer coefficient increases with the steam mass flowrates in both cross flow and parallel flow. Increasing the steam flowrate results in a higher water film interfacial velocity, which enhances the convective heat transfer capacity between the steam and water film, leading to a great amount of heat transfer quantity.

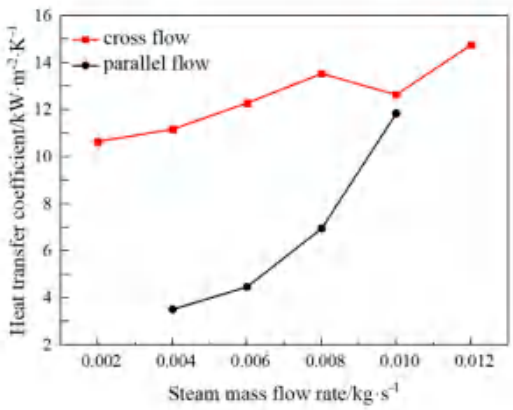


Figure 51 - Comparison of heat transfer coefficient between cross and parallel flows

Fig.3 and Fig.4 show the liquid film thickness at different flow paraments. Both in cross flow and parallel flow, the liquid film thickness increase along the water flow direction. Because of the condensation of steam, the water gradually gathered in the surface of water film, which leads an increase of the liquid film thickness.

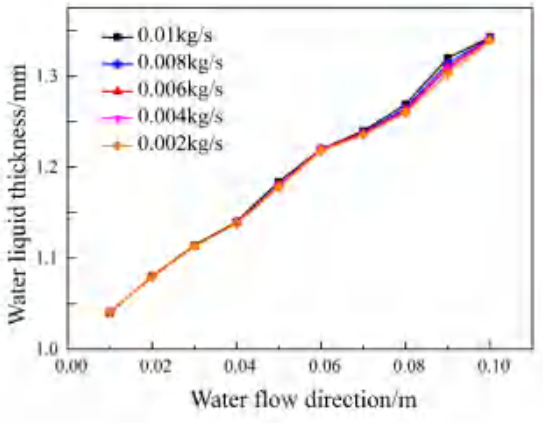


Figure 52 - Liquid film thickness of cross flow for different flow rates

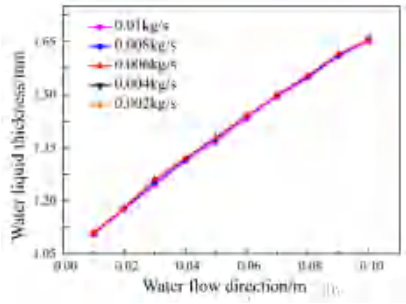


Figure 53 - Liquid film thickness of parallel flow for different flow rates

As shown in Fig.5, in the case of countercurrent flow, the water suffers an impact from the counterflowing steam. This leads the steam-water film interface blurry, and the water exhibits a conical shape at the downstream end. Due to the countercurrent flow of two-phase fluids, heat exchange becomes more intense, and there is a significant turbulence at interface. The distribution of the subcooled water and steam phase is uneven. The water film may be destroyed in the countercurrent flow conditions.

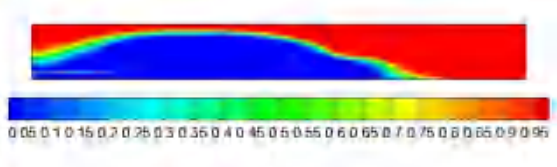


Figure 54- Steam volume fraction at yoz section（x=0.035）

Conclusions

1) The heat transfer coefficient increases with the steam mass flow rate in both cross flow and parallel flow. Cross flow has a better effect on condensation heat transfer process.

2) The liquid film thickness increase along the water flow directions.

3) The water film may be destroyed in the countercurrent flow conditions.

References

[1] Fu J.X. Theoretical and experimental study on jet type condenser used in peak cooling of air cooling unit[D]. North China Electric Power University，2019.
[2] Liu Z.H. The study on the cold-end of heller type air-cooling unit [D]. Tianjin University，2003.
[3] H. R. Jacobs. Direct-contact condensation heat transfer[M]. Springer. 1988.

Identification of Flow Patterns in an Opaque Condenser Tube by Distributed Fiber Bragg Gratings

HaoQi Wang [a], ShiZhe Wen [a] ,ZhenHui He [a] *
Center for Space Technology, School of Physics and Astronomy, Sun Yat-sen University, Zhuhai, 519082, China
Zhu Hai, 519000, China
* Corresponding Author: stshzh@mail.sysu.edu.cn

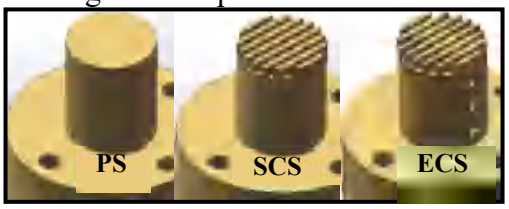
Abstract:
The flow pattern of vapor-liquid two-phase flow in tubes is the basis of the study of two-phase flows. At present, there are many methods on the identification of flow pattern, except for direct observation of that in a double-tube heat exchanger; and most of the methods can not combine with the study of heat transfer performance, resulting in uncertainty and research cost increases. In this paper, a method based on distributed fiber Bragg gratings(DFBGs) is used to measure the fluid temperature distribution in a tube, which can identify the flow pattern, and study the heat transfer performance at the same time. The flow patterns of condensing R134a is identified in a double-tube heat exchangers, which were captured and verified by a high-speed camera before flowing vertically up into the double-tube heat exchanger. The flow pattern transitions for several mass flow rates (40-160kg/m2*s) are observed and discussed, especially, for the characteristics of temperature from oscillation for slug flow, to fluctuation for churn flow(ΔT_s≈0.5K), and annular flow with even lower magnitude($\Delta T_c \approx 0.2K$). The length of each flow pattern during condensation can be quantitatively analyzed from the temperature characteristics, which is important for the design of condenser length. Furthermore, the liquid phase and vapor phase velocity can be quantitatively obtained from the characteristics of the slug flow pattern in low mass flow rate, and the parameters such as slip ratio and void fraction can be obtained. The void fraction is more comparable to that by the Zuber-Findlay model than to others.

keywords*: Flow patterns; Identification; Temperature characteristics; Distributed fiber Bragg gratings*

Effects of heat flux, pressure, and surfactant concentration on pool boiling of water using expanding-channeled surface

Yifei Hu [a], Sihui Hong [a] , Zhijie Gao [a]
Center for Space Technology, School of Physics and Astronomy, Sun Yat-sen University, Zhuhai, 519082, China
Zhu Hai, 519000, China
* Corresponding Author:hongsh23@mail.sysu.edu.cn

Abstract
Comparative tests were experimentally conducted to observe the effect of heat flux(10-180 W/cm^2), saturated pressure(8.8-38.5kPa), surfactant concentration(Tween20：0.1-0.5ml/L) on pool boiling enhancement. Deionized water was used as working fluid, and expanding-channeled surface was compared with plain surface. With visualization method, the dynamic behaviors of bubbles were analyzed， the effect of which on the temperature oscillations were verified. The experimental results manifested the heat transfer coefficients of the surfaces with expanding microchannels can be enhanced under all working conditions. The additional force accelerates the detachment of bubbles along the channels, and the timely wetting of the liquid is the main reason for the enhancement.



Keywords: Pool boiling; Surfactant solution; Sub-atmospheric pressure; Bubble dynamics

Introduction

Compared with the traditional cooling technology, two-phase submerged cooling due to high heat transfer efficiency is getting more and more attention. Due to high latent heat, environmental protection and economical benefits, water has gradually replaced fluorine-containing liquid as the main working medium. However, the issue to utilize water for electronic cooling need to solve the problem of high boiling point. Low-pressure state can effectively reduce the starting temperature of the two-phase phase transition. Yet, compared to the state of atmospheric pressure, under low-pressure, intermittent boiling occurred owing to the increased surface tension and cause large fluctuation of surface temperature, which is not expected to occur in the heat dissipation of electronic components. Effectively improve the heat transfer coefficient and critical heat flux in low-pressure environment is one of the main objectives of the present work. We proposed to use the gradual expansion of microchannel to assist the detachment of bubble, as well as the supply of liquid to the heated surface. Besides, surfactants were added to produce more tiny bubbles to intensify the perturbation of the superheated liquid layer in the low-pressure process, in order to achieve the purpose of improving the heat transfer coefficient, and to further delay the occurrence of the film state boiling.

Table 1 the list of operating conditions

Parameters	**Values**
Pressure (kPa)	8.8 13 18 26 38.5
***q* (W/cm^2)**	10~180 (10 W/cm^2 per step)

Concentration (ml/L)	0.1	0.2	0.3	0.4	0.5

Figure 55 various surfaces

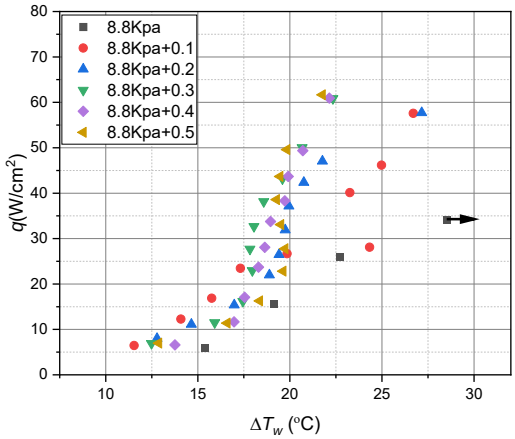


Figure 2 Boiling profiles of PS the different concentrations of TWeen20 at low pressure

Research on the Influence of Ocean Conditions on the Film-Forming Characteristics of Jet Ejector Condensers

Chu Weiyu, Meng Zhaoming, Xiao Qi
Harbin Engineering University,Wuhan Second Ship Design and Research Institute

Abstract：In order to provide selection guidance for the design of jet ejectors, this study focused on the film-forming characteristics of jet ejector nozzles. A visualization experimental platform for nozzle film formation under cold conditions was designed and constructed. Through techniques such as high-speed photography and image processing, experimental investigations were conducted on the film-forming phenomenon of jet ejector nozzles under marine conditions. The study explored the effects of factors such as tilt angle, oscillation amplitude, and oscillation period on nozzle film formation. Additionally, it analyzed the differences in film-forming characteristics and variations in film area between marine and stationary land conditions, aiming to provide reference for nozzle selection under marine conditions.
Keywords: Ocean conditions; Jet ejector condenser; Liquid film; Film-forming characteristics.

Experimental investigations on water film flow inside the jet-type condenser

Chai Yinghua1,2 ,Xiao Qi1,2* , Liu Shaoyou2 , Liu Ziping1,2, Huang Chonghai1,2, Meng Zhaoming3

1. Science and Technology on Thermal Energy and Power Laboratory, Wuhan, Hubei, 430205, P.R. China;
2. Wuhan Second Ship Design and Research Institute, Wuhan, Hubei, 430205, P.R. China;
3. College of Nuclear Science and Technology, Harbin Engineering University, Harbin, Heilongjiang, P.R. China

Abstract

The jet-type condenser, adopting the steam-water film direct contact condensation, is identified as an ideal choice for marine steam power systems due to its advantages in high heat transfer coefficient, near-zero heat transfer terminal difference, compactness and reliability. Revealing the mechanisms of heat and mass transfer and interface evolution turns to be the basis of quantitative design and precise regulation of the jet-type condenser, and vapour-water film surface area is the key parameter for heat and mass transfer calculations. The water film inside the jet-type condenser is a typical multiscale structure, double-side unsteady free surface, which propose a great challenge for the numerical and experimental investigations. In this paper, a thickness measuring method for water film is proposed and an experimental system is constructed for water film surface area and thickness investigations. Then the influences of water mass flow flux, jet angle, jet diameter, jet-baffle distance on the water film are investigated. The rim, wave, perforation and turbulent disintegrations of water film are observed. The surface area increases at low water mass flow rate, then decreases due to the water film breakage caused by the initial disturbance. Increasing the jet angle, a maximum water film area could be achieved due to the compromise of disturbance and flow expansion. As the water viscosity decreases with the temperature, the water film surface area would decrease with the water temperature, and the effects of water temperature turns to be significant for the low water mass flow rate.

Keywords:jet-type condenser, water film, interfacial area, film disintegration

Introduction

The jet-type condenser condensates the steam through water liquid film ejecting into the condensation region. The heat transfer coefficient of the jet-type condenser (0.1- 10MW/m2 • K) is much higher than that of normal condenser (＞10kW/m2•K). And it also exhibits the advantages such as near-zero heat transfer terminal difference, compactness and reliability [1-3], which is identified as an ideal choice for marine steam power systems. The water film surface area and thickness are key parameters for the condensation process, while there are few investigations on water film flow inside the limited space. In this paper, a cold state experimental system was constructed for water film flow inside jet-type condenser, and a thickness measuring method for water film is proposed.

Methodology

As shown in Figs 1-2, the experimental system contains water film generation system, water supply system, observation and data acquisition system and high-speed camera.

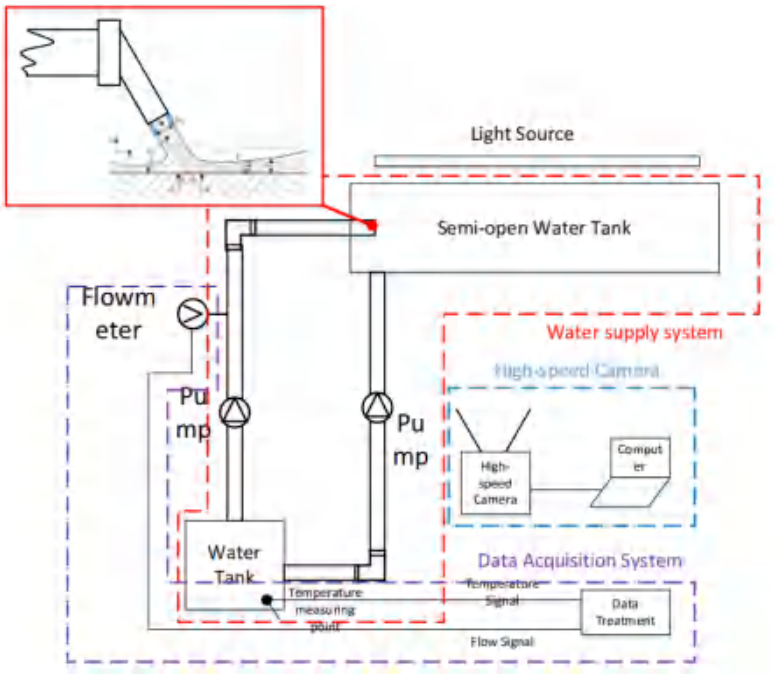


Figure 1 – Schematic of the experimental system

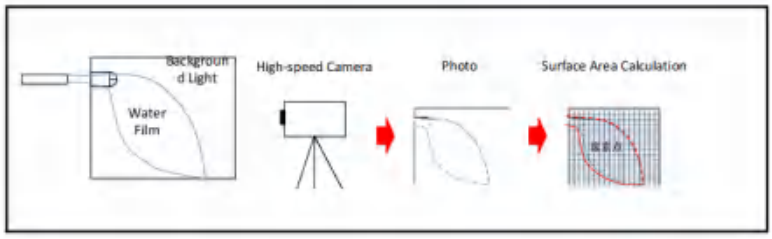


Figure 2 – Schematic of surface area calculation

Results Analysis

All the four water film disintegrations [4] have been observed in our experiments (Fig 3). The rim disintegration is caused by the compromise of surface tension and aerodynamic force at the edge of water film. The rim disintegration would increase water mass flow rate. The wave disintegration is mainly caused by the disturbance, and the perturbation would develop with the time and space. Further increasing the water mass flow rate, the turbulent disintegration appears.

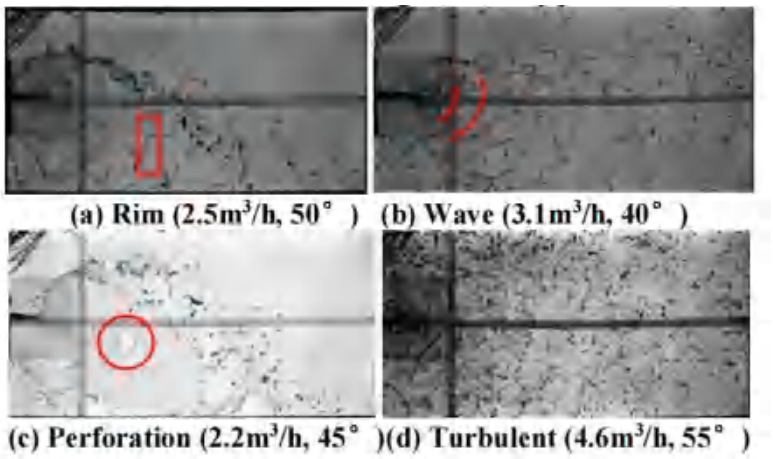


Figure 3 – Four typical water film disintegrations observed in experiments

Increasing the water mass flow rate, the water film interfacial area would firstly increase and then decrease. A maximum interfacial area could be achieved. The water film shape would remain and its length and width both increase at low water mass flow rate (<0.4m3 /h in our

experiments). Increasing the water mass flow rate, wave disintegration appears at the edge of the water film, and the water-vapour interfacial area decreases. When the water mass flow rate exceeds 0.7m3 /h, the turbulent disintegration appears and the interfacial area further decreases.

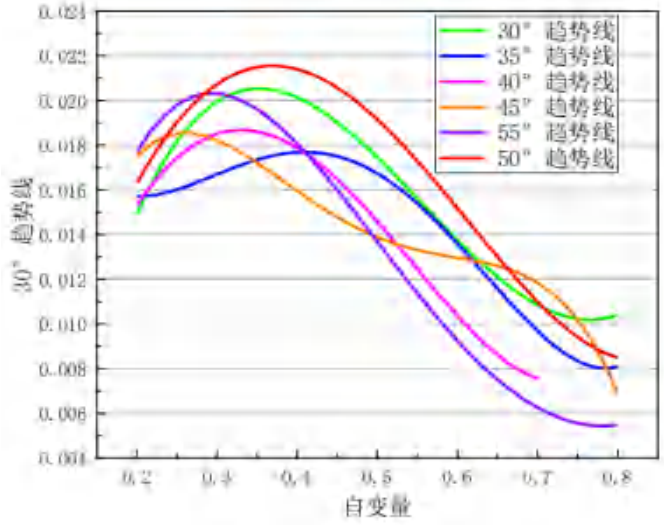


Figure 4 – Effects of water mass flow rate on water film surface area (jet diameter 5mm)

As shown in Fig 5, the interfacial area increases firstly with the jet angle and then decreases. Increasing the jet angle makes the normal velocity at the baffles higher, which increase the interfacial area. While the perturbation would also be induced increasing the jet angle, which decreases the interfacial area. As a compromise between the normal velocity and perturbation, the interfacial area reaches the maximum around 50°. It should be noted that the maximum point varies with the water mass flow rate and the jet diameter.

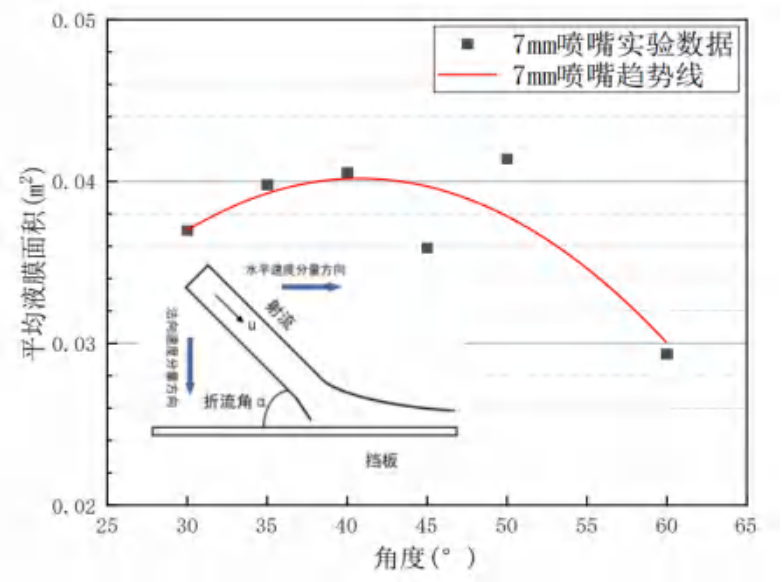


Figure 5 – Effects of jet angle on water film surface area (jet diameter 7mm)

Conclusions

1) A cold test experimental system was constructed, and four water film disintegrations have been observed; 2) The water film interfacial area would firstly increase and then decrease with the mass flow rate, jet angle and jet diameter; 3) The water film thickness would increase with the mass flow rate, and not sensitive to the jet angle.

Acknowledgements

The authors wish to thank the financial supports from the National Natural Science Foundation of China (12302334)

References

[1] S. Sideman, D. Moalem-Maron. Direct contact condensation. Advances in Heat Transfer [M]. Elsevier, 1982.

[2] H. R. Jacobs. Direct-contact condensation heat transfer [M]. Springer, 1988.

[3] E. A. Demekhin, E. N. Kalaidin, A. S. Selin. Three-dimensional localized coherent structures of surface turbulence. III. Experiment and model validation [J]. Physics of Fluids, 2010, 22: 114103.

[4] R. P. Fraser, N. Dombrowski, J. H. Routley. The mechanisms of disintegration of liquid sheets in cross-current air streams [J]. Applied Scientific Research, Section A, 1963, 12: 143-150.

Parallel Session IX: Topic 5: Measurement methods and techniques in multiphase flow

External Field Intensified Particle Preparation and Machine Learning Assisted Flow Pattern Recognition

Tao Dong[1], Jin-Xin Wang[1,2], Yong-Pan Cheng[2], Wei-Cheng Yan[1]*
1. Jiangsu University, Zhenjiang, Jiangsu, 212013, China
2. North China Electric Power University, Beijing 102206, China

Abstract
In this presentation, external-field (electric, microwave, ultrasound etc.) intensified particle preparation techniques will be introduced first. Subsequently, machine learning (ML) assisted methods for recognizing complex flow patterns will be presented by taking electrohydrodynamic (EHD) atomization as the key example of electric-field intensified process. The artificial neural network (ANN) and support vector machine (SVM) models are trained based on the collected data to give excellent performance in prediction of EHD spraying patterns. With the testing set data, the accuracy of the EHD spraying patterns recognition is 99.611% for ANN model, and the result is 99.867% for SVM model. Furthermore, 30,000 images were obtained to train a convolutional neural network (CNN) model for recognizing EHD spraying patterns, which exhibited a remarkable accuracy of 99.80%. Finally, a database consisting of 11,650 experimental data points was constructed to train a deep neural network (DNN) model, aiming to reduce the number of experiments.

Introduction
Effective recognition and prediction of flow patterns are extremely important for high quality micro/nanoparticles preparation, chip coating, droplet-reactor design, and high precision printing etc. Electrohydrodynamic (EHD) atomization, also named as EHD spraying, is an atomization technique for conducting liquids which can be used in many areas including chemical engineering, material science, biomedicine et al [1-2]. Due to great significance for achieving cone-jet mode, it is necessary to give the range of controlling parameters that can give rise to cone-jet pattern for different fluids and products directly. However, for various specific applications, the requirement for the diameter of the atomized droplets is different. Given that EHD spraying process could be affected easily by so many parameters, it is almost impossible to achieve the goal by trial and error of experiment measurements.

Methodology
The EHD spraying patterns are firstly divided into three categories, namely, dripping, stable cone-jet and unstable cone-jet. A database consisting of 86140 EHD spraying patterns data are used to build the recognition models. The artificial neural network (ANN) and support vector machine (SVM) models are trained based on the collected data to give excellent performance in prediction of EHD spraying patterns. Then, six distinct spray patterns, namely dripping, spindle, cone-jet, rotational jet, atomization, and skew jet-atomization, were classified through experiments. Subsequently, 30,000 images were obtained to train a convolutional neural network (CNN) model for recognizing EHD spraying patterns. Dimensionless groups were established and the generalized spraying pattern maps were drawn. Finally, a database consisting of 11,650 experimental data points was constructed to train a deep neural network (DNN) model. The DNN model was employed to predict the spraying patterns, by which a rapid but comprehensive analysis of the impact of different conditions was achieved.

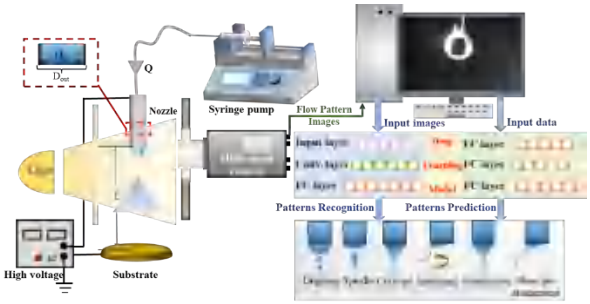


Figure 56 - Schematic illustration of experimental EHD spraying system with pattern recognition process.

Conclusions

After training, the SVM model achieving the highest accuracy of 99.867% for EHD spraying pattern recognition. The ANN model can precisely predict the droplet diameter with a high R^2 of 0.9998 and a low MAE of 0.007. The predicted results by ANN model are consistent with the CFD simulation results and experimental measurements. Some examples were provided through predicting EHD spraying pattern maps and droplet diameter in terms of various key parameters. which could guide the design, optimization and operating of the EHDA system. With the developed pattern recognition and prediction models (CNN and DNN models) in hand, the rapid and comprehensive analysis of the impact of massive parameters can be achieved, which avoids the large computational burden, low efficiency and limited applicability of the existing models built based on the conservation of mass, momentum and charge.

Acknowledgements

The authors thank the supports from National Natural Science Foundation of China (22378171,52276153) .

References

[1] S.H. Park, L. Lei, D. Dsouza, E.T. Dimartini, M. Atzampou, E.O. Lallow, J. Shan, J. D. Zahn, D. J. Shreiber, H. Lin, J. N. Maslow, J.P. Singer, Efficient electrospray deposition of surfaces smaller than the spray plume. Nat. Commun. 2023, 14 (1), 4896.

[2] J. X. Wang, T. Dong, Y. P. Cheng, W. C. Yan, Machine Learning Assisted Spraying Pattern Recognition for Electrohydrodynamic Atomization System. Ind. Eng. Chem. Res. 2022, 61(24), 8495–8503.

Effects of submicron particle layers on microparticle impact dynamics

Yuxing Wang [a], Yueming Wang [a,*], Minmin Zhou [a], Lunbo Duan[a,*]
[a]Key Laboratory of Energy Thermal Conversion and Control, Southeast University, Nanjing 210096, China

Abstract
Particle-wall collision deposition is a classic physical process. In the domain of energy utilization, the issue of ash deposition on heat exchanger surfaces during the combustion of high-alkali coals, such as Zhundong coal, is a significant challenge. This deposition decreases the efficiency of heat transfer and affects the stable operation of the boiler. Prior researchers has indicated that large particles are not easily deposited directly onto smooth wall surfaces. However, thermophoresis and condensation can promote the deposition of fine particulate matter on the smooth surfaces of heat exchanger tubes, creating a glue-like effect that enhances the adhesion probability of large particles upon impact. Some researchers have utilized simulation methods to examine the collision behaviour of microparticles when in contact with a granular layer. Nonetheless, the scarcity of relevant standard experimental data complicates the accurate determination of some essential parameters required for modelling particle collisions.
This study explores the collision process between particles and a submicron particle layer through both experimental and simulation research. We prepare long-range ordered submicron particle layers via particle self-assembly to mimic the initial fine-grained ash layer formed under actual working conditions. The changes in the motion state of single microparticles before and after collision with the particle layer are recorded using a high-speed camera. This approach allows for the observation of the macroscopic influence of the particle layer on the incident particles impacting the target surface. Based on the data obtained from these experiments, the discrete element method (DEM) is employed to simulate the contact of particles with the granular layer and to further analyse the nature of the granular layer's effect. The results suggest that the presence of the particle layer significantly reduces the normal recovery coefficient of single-particle collisions compared to when particles contact a smooth wall surface. This reduction is attributed to the rapid multiple impacts of particles within the particle layer on the incident particles. Additionally, the particle size of the constituent particles and the physical parameters of the granular layer can alter the effect exerted by the granular layer. Moreover, due to the substantial difference in particle sizes between the incident particles and the particles in the particle layer, the particle layer does not influence the angular change of the incident particles before and after the collision.
This study introduces a novel experimental approach to examine the influence of particle layers on particle impacts against smooth wall surfaces. More systematic experiments will be conducted in the future to provide empirically relevant formulas for the recovery coefficients of incident particles under granular layer coverage to aid in the understanding of collisional deposition of particles on granular layers.

Keywords: Ash deposition, Micro-particles, Submicron particle layer, Coefficient of restitution, Discrete element method

The dynamic characteristics of impulse waves generated by landslides containing erratic boulders

Chuanqi Shia* , Jiajun Jiaob , Yunhui Sunb , Yi Ana
a Key Laboratory for Mechanics in Fluid Solid Coupling Systems, Institute of mechanics, Chinese Academy of Sciences, Beijing, 100190, China
bDepartment of Mechanics, School of Aerospace Engineering, Beijing Institute of Technology, Beijing 100081, China
Email： * shichuanqi@imech.ac.cn

Abstract
Landslide-generated impulse waves (LGIWs) present natural disaster scenarios that involve fluid-solid coupling problems. In nature, landslides often consist of a mixture of soil and rocks, exhibiting deformation and movement characteristics distinct from those of homogeneous soil. The deposition of erratic boulders post-landslide movement is a fascinating and extensively studied phenomenon in geology, offering valuable insights into geological events. In this study, a self-sustaining intelligent particle capable of measuring three-dimensional acceleration and angular velocity is developed using IMU (Inertial Measurement Unit) technology (***Figure 1***) to characterize erratic boulders. Subsequently, we investigate the impact of erratic boulder positions and landslide mass (***Figure 2***) on leading wave amplitude and boulder movement, establishing criteria for identifying the final deposition states of the boulder. Additionally, we analyze the conversion rate of potential energy to kinetic energy during the downhill movement of the boulder. Our findings reveal that the proportion of rotational kinetic energy is minimal, exhibiting a high level of randomness in its variation pattern.

Keywords: Landslide generated impulse waves, Inertial measurement unit, Soil-rock mixture landslides, Erratic boulder

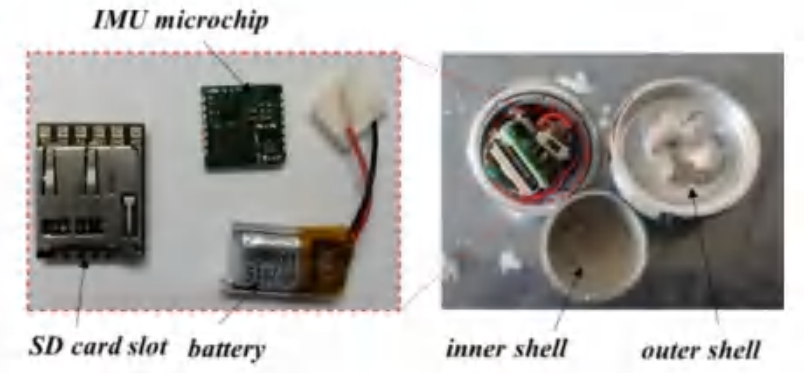


Figure 1 – IMU intelligent particle

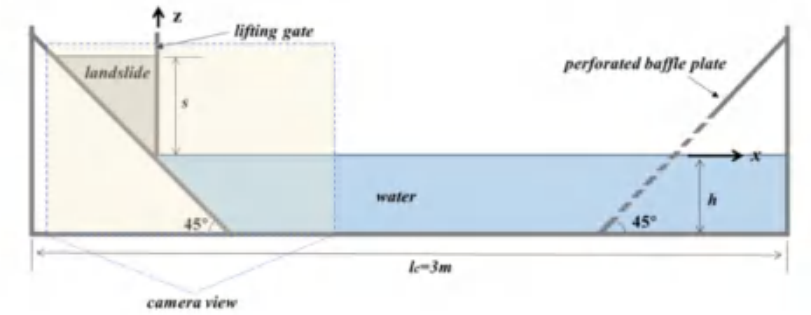


Figure 2 –Schematic diagrams showing a water tank for LGIWs experiments

Acknowledgements
This work is financially supported by National Natural Science Foundation of China (No. 12202460, 12032005).

Mixing of Highly Viscous Fluids: Flow Visualization and Intensification

Hailong Liu, Yurong Wu, Junfeng Wang and Jingang Lu
School of Energy and Power Engineering, Jiangsu University, Zhenjiang, 212013, China

Abstract
Agitation technology is widely used in various fields such as chemical industry, food processing and wastewater treatment. In the laminar mixing mode, the closed annular flow field (IMR) inside the mixing tank leads to restricted fluid exchange inside and outside the region and reduces the mixing efficiency. In this paper, a scheme to enhance laminar flow stirring by applying an external electric field along with variable speed stirring is proposed. The scheme is based on planar laser-induced fluorescence (PLIF) technology, which realizes the visualization of the planar structure of the liquid-phase mixing flow field and facilitates the observation of the flow field changes and the mixing effect. The experimental results show that in the first half of the cycle, due to the presence of an electric field, the free charge drives the fluid to move in the direction of the electric field, resulting in a shift of the impeller mixing region (IMR) position. In the second half of the variable-speed cycle, periodic wave-like patterns, known as the Kelvin-Helmholtz phenomenon, form at the edges of the IMR structure at certain times. The periodic instability changes caused by the mixing blades and the external electric field work together to gradually destroy the IMR structure completely, and ultimately realize efficient mixing. Compared to conventional mixing, the mixing efficiency is increased by 37% (compared to 60%). Compared with single-field mixing under the same electric field conditions, the mixing effect is further enhanced due to the unstable rotation of the mixing blades, and the mixing efficiency is increased from 79.4% to 97.1%. At the same time, with the increase in rotational speed, the liquid flow is accelerated and the mixing time is reduced from 50 minutes to 35 minutes.

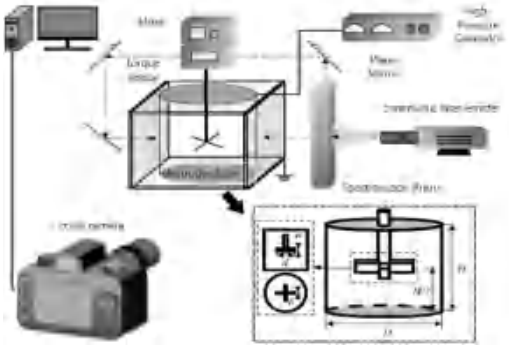
Keywords: Laminar Mixing, Laser-Induced Fluorescence, Kelvin-Helmholtz Instability, Flow Field Control

Introduction

Stirring technology is a prevalent unit operation within the industrial sector, widely used in fields including the chemical industry, food processing, and wastewater treatment [1-9], as demonstrated in Figure 1. Various complex fluids in advanced materials synthesis, biogenetic engineering, and semiconductor manufacturing processes require homogenised mixing through stirring techniques [10-13]. The stirring process promotes uniformity of the medium in the mixing vessel, thereby increasing heat and mass transfer reactions, which is imperative for improving industrial production efficiency.

Understanding the structure of the internal flow field in stirred tanks is critical for achieving effective laminar mixing. Flow field visualization and measurement techniques have provided powerful experimental tools for studying the flow field structure within stirred tanks. Researchers in the past [8] employed dyeing techniques to observe fluid flow within stirred tanks and found evidence of isolated flow fields. High et al. [9-10] conducted extensive research on mixing processes within stirred tanks using acid-base indicator techniques. They discovered that modifying the relative displacement of combinatory impellers and periodically varying impeller speeds could prevent incomplete mixing during the stirring process. These experimental techniques allowed for a comprehensible and logical observation of the flow field structure. Their applicability was limited due to specific requirements for the chemical properties of the mixing medium and challenges in conducting quantitative analysis of the flow field.

Recently, Particle Image Velocimetry (PIV) technology has emerged as a potent tool for quantitative measurement and analysis of flow field structures. Parvizi et al. [11] utilized PIV technology to observe and analyse the flow field within stirred tanks quantitatively, conducting comparative studies on how variations in impeller geometry parameters impact mixing efficiency. Although PIV technology can offer instantaneous data on speed distribution in the flow field, it is intricate to operate and presents notable obstacles in precisely measuring three-dimensional flow fields.



Planar Laser-Induced Fluorescence (PLIF) utilizes the fluorescence emission of luminescent groups in specific substances when they absorb photons of certain frequencies to provide measurement of flow fields without contact. This method offers numerous benefits for flow visualization measurements [12]. Liu et al. [13] employed PLIF technology to examine the laminar mixing efficiency in diverse circumstances, including those with internal baffles and eccentric stirring modes. They discovered that the implementation of invasive geometric baffles or eccentric stirring modes could disrupt isolated flow fields successfully and improve mixing efficiency.

Within the current body of research, there are two primary approaches for enhancing mixing efficiency: modifying the agitator's geometry or the internal structure of the mixing vessel, and altering the mixing impellers. Nevertheless, these methods consume substantial energy and require extensive alterations to the original equipment, making them operationally intricate. Therefore, there is a demand to investigate gentle, energy-saving, and effective laminar mixing techniques.

This study employs Planar Laser-Induced Fluorescence (PLIF) technology to visualize the flow field structure in a stirred tank. It examines the optimization of laminar mixing by means of variable-speed control under low electric field intensity conditions. The research offers both experimental techniques and theoretical guidance for the design of efficient laminar mixing devices with minimal external electric field intensity, and thus addresses the aforementioned challenges.

Methodology

Figure 1 illustrates both the schematic and physical representations of the visual experimental platform for enhancing laminar mixing through an external electric field. In this study, a cylindrical flat-bottom stirred tank with an inner diameter (D) of 100 mm and a height (H) of 100 mm was employed, constructed from organic glass material. The stirring impeller utilized a four-blade straight paddle-wheel design with a diameter (d) of 50 mm, a height (w) of 10 mm, and a thickness (b) of 5 mm. The upper end of the stirring impeller was connected to a high-precision stirrer (G300, DLAB Corporation) and a dynamic torque measurement instrument (DYN-200, Ocean Sensor Systems Engineering Ltd.). The stirring medium employed was glycerol (propane-1, 2, 3-triol, provided by Wuxi Yatai United Chemical Co., Ltd.), and its relevant physical properties are detailed in Figure 3.2.

Figure 1: Schematic and Physical Representation of the Experimental Setup

A CMOS camera (AF MICRO NIKKOR 200 mm 1:4D lens) was positioned on the side of the stirred tank to capture real-time images of the flow field. In the experiments involving the external electric field, two circular copper electrodes with radii matching the stirred tank's dimensions were placed on the upper and lower sides of the stirred tank. The upper electrode was connected to a high-voltage generator (DW-N303, Dongwen High Voltage), while the lower electrode was grounded. Control over the external electric field intensity was achieved by adjusting the power of the high-voltage generator. The experiments were conducted at standard atmospheric pressure in an environment devoid of visible light, with the temperature maintained at 23 °C. To prevent static electricity buildup, all measuring instruments and components were insulated or grounded.

The study utilised Laser-Induced Fluorescence (LIF) technology to observe and measure the stirred tank's flow field in real-time. LIF technology offers several benefits, including high precision, rapid response, high spatiotemporal resolution and easy equipment set-up, making it a popular choice for the analysis of fluid mixing behaviours. By utilizing the Stokes shift phenomenon, laser and fluorescence signals can be separated via filters, guaranteeing accurate measurement results [17]. When the laser intensity remains constant, the fluorescence intensity caught by the camera shows a linear correlation with the concentration of tracer dye in the fluid. By utilizing this association, various levels of tracer dyes can dissolve in two fluid streams and unveil the attributes of mass transfer mechanisms via alterations in fluorescence intensity within the combination area [18-21].

Results

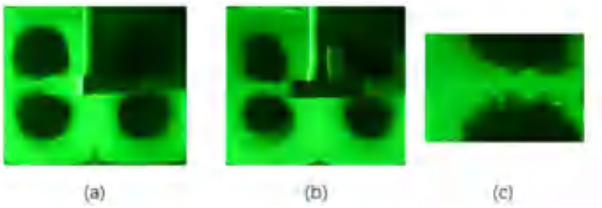


Figure 2: Experimental Results of Variable-Speed Scheme with K-H instabity.

Figure 2 illustrates the variations in the unmixed region during the stirring process under the variable-speed scheme. Upon commencement of stirring, the fluid undergoes radial flow under the periodic rotation of the impeller. As radial flow progresses, the fluid collides with the walls of the stirred tank, leading to upward and downward movement on either side. After completing a full circular motion, the fluid returns to the impeller region, forming a stable IMR structure (as shown in Figure a). As the variable-speed stirring cycle begins, the flow field structure undergoes significant changes in response to the sudden increase or decrease in velocity. In the first half of the variable-speed cycle, with the rapid increase in impeller speed, the fluid around the impeller region accelerates its outward radial movement, and the jet boundary further expands outward. The jet width increases and tends to stabilize. The originally clear IMR boundary starts to become disordered, with a noticeable increase in boundary rotation speed. In the second half of the variable-speed cycle, as the impeller speed suddenly decreases, the jet boundary gradually contracts. At the boundary's end, high-velocity fluid slowly extends inward towards the IMR boundary. The jet width starts to decrease and slowly stabilize, and the IMR boundary begins to exhibit oscillations. The boundary rotation speed gradually becomes smoother, and the IMR region becomes relatively smaller compared to before the variable-speed (as shown in Figure b). Especially at the interface between the jet region and the IMR boundary, the fluid exhibits a wave-like motion with long and sparse waves near the jet region's proximal end and short and dense waves at the distal end, forming an unstable light-dark

interface, representing Kelvin-Helmholtz instability (as shown in Figure c). This is because, in the latter half of the variable-speed cycle, the decrease in impeller speed leads to a corresponding reduction in the momentum of the jet region's fluid. However, due to the inertia of the fluid, the fluid at the IMR boundary within the jet region continues to move at a relatively high speed, creating a velocity gradient. This, combined with the difference in the proportion of mixed substances between the mixing and unmixed regions and a certain concentration difference, results in the formation of a K-H instability structure.

Conclusions

In this study, transient observations of the flow field structure under laminar mixing conditions were conducted using PLIF (Planar Laser-Induced Fluorescence) technology. Under the scheme of coupling an external electric field with variable-speed stirring, the mixing efficiency exhibits a stepwise increase within each variable-speed cycle, followed by a gradual enhancement. This behavior is attributed to the combined effects of Kelvin-Helmholtz instability and electro hydrodynamic effects, resulting in the complete disruption of the IMR (Isolated Mixing Region) structure, ultimately achieving high-efficiency mixing.

Acknowledgements

This work was supported by National Natural Science Foundation of China (No. 51876086).

References

[1]Dusting J, Sheridan J, Hourigan K. A fluid dynamics approach to bioreactor design for cell and tissue culture [J]. Biotechnology and bioengineering, 2006, 94(6): 1196-208.

[2]Bulnes-Abundis D, Carrillo-Cocom L M, Aráiz-Hernández D, et al. A simple eccentric stirred tank mini-bioreactor: Mixing characterization and mammalian cell culture experiments [J]. Biotechnology and bioengineering, 2013, 110(4): 1106-18.

[3]Lamberto D, Alvarez M, Muzzio F. Computational analysis of regular and chaotic mixing in a stirred tank reactor [J]. Chemical Engineering Science, 2001, 56(16): 4887-99.

[4]Cybulski O, Dygas M, Mikulak-Klucznik B, et al. Concentric liquid reactors for chemical synthesis and separation [J]. Nature, 2020, 586(7827): 57-63.

[5]Sun J-K, Sobolev Y I, Zhang W, et al. Enhancing crystal growth using polyelectrolyte solutions and shear flow [J]. Nature, 2020, 579(7797): 73-9.

[6]Hwang W, Jun H, Kwon T. Experiments on chaotic mixing in a screw channel flow [J]. AIChE journal, 2002, 48(8): 1621-30.

[7]Dong Z, Macmillan D W. Metallaphotoredox-enabled deoxygenative arylation of alcohols [J]. Nature, 2021: 1-10.

[8]Sahota S, Shah G, Ghosh P, et al. Review of trends in biogas upgradation technologies and future perspectives [J]. Bioresource Technology Reports, 2018, 1: 79-88.

[9] Zhao, Shufang, Wang Wentan, Hu Yinyu, et al. Preparation of Nano Curcumin Particles via Liquid-Liquid Mixing Precipitation Method in Stirred Tank Reactor [J]. Journal of Chemical Engineering. 2013, 64(3): 841-8.

[10]Jung S Y, Ahn K H, Kang T G, et al. Chaotic mixing in a barrier-embedded partitioned pipe mixer [J]. AIChE Journal, 2018, 64(2): 717-29.

[11]Ottino J M. Mixing in the process industries Edited By N. Harnby, MF Edwards, and AW Nienow, 1992, Butterworth-Hinemann, Oxford, 414 pp [Z]. Wiley Online Library. 1993

[12] Wang, Peng, Bai Minli, Lü Jizhu, et al. Turbulent Flow Characteristics in Nanofluid Circular Pipes [J]. Journal of Chemical Engineering. 2014, (S1): 17-26.

[13] Liu Hailong, Cao Yu, Ding Xuechong, et al. Liquid Phase Laminar Flow Fluorescence Visualization and High-Efficiency Mixing Techniques in Stirred Tanks [J]. Journal of Chemical Engineering, 2018, 69(12): 5042-8.

[14]Kourmatzis A, Shrimpton J. Electrohydrodynamic inter-electrode flow and liquid jet characteristics in charge injection atomizers [J]. Experiments in fluids, 2014, 55(3): 1-13.

[15]Castellanos A. Basic concepts and equations in electrohydrodynamics [J]. Courses and Lectures-International Centre for Mechanical Sciences, 1998, 1(380): 1-82.
[16]Paul E L, Atiemo-Obeng V A, Kresta S M. Handbook of industrial mixing: science and practice [M]. John Wiley & Sons, 2003.
[17]Arbeloa I L, Rohatgi-Mukherjee K. Solvent effect on photophysics of the molecular forms of rhodamine B. Solvation models and spectroscopic parameters [J]. Chemical Physics Letters, 1986, 128(5-6): 474-9.
[18] Fan Jiechuan. Modern Flow Visualization Techniques [M]. Modern Flow Visualization Techniques, 2002.
[19]Arcoumanis C, Mcguirk J, Palma J. On the use of fluorescent dyes for concentration measurements in water flows [J]. Experiments in Fluids, 1990, 10(2-3): 177-80.
[20]Larsen L, Crimaldi J. The effect of photobleaching on PLIF [J]. Experiments in fluids, 2006, 41: 803-12.
[21]Walker D. A fluorescence technique for measurement of concentration in mixing liquids [J]. Journal of Physics E: Scientific Instruments, 1987, 20(2): 217.

Secondary Droplets Measurement during A Single Droplet Impacting on Heated Surfaces

WANG Qian[1*], ZHUANG DanLing[1], Luo Kaihong[2]
1. Shanghai Jiao Tong University, Shanghai 200240;
2. Tsinghua University, Beijing, 100084

Abstract
Spray cooling features with high heat flux and good temperature control ability, which has been widely used in industrial environments such as electronic devices and nuclear power plants. In this study, the transient process of droplet-wall collision under film and transition boiling conditions has been investigated experimentally via the high-speed shadowgraph imaging and state-of-the-art image processing techniques. Based on intensive test conditions, the impact morphology, number, size, trajectory, ejecting angle and velocity of secondary droplets are presented and analyzed comprehensively.
Keywords: Shadowgraph imaging; Droplet splashing; Secondary droplets; Particle tracking

Introduction
For a droplet impinging on the solid wall, as the temperature of the wall rises, the droplet will go through natural convection, nuclear boiling, transition boiling and film boiling in turn [1]. The occurrence of secondary atomization has a great influence on the spray cooling efficiency. In this study, the dynamic droplet splashing phenomena in transition and film boiling conditions are systematically studied by the high-speed shadowgraph imaging technology.

Methodology
As shown in Fig.1, the droplet impacts on a heated surface, while the images are taken using a high speed shadowgraph system. The Weber number changes from 15.4 to 104.2, while the wall temperature varies from 307.6℃ to 511.8℃.
As shown in Fig.2, with the same Weber number, the size and number of secondary droplets first increase slowly with the increase of temperature, then decrease sharply near the dynamic Leidenfrost temperature. A four-frame optimal estimation particle tracking algorithm is applied to get the particle trajectories. As shown in Fig.3, the secondary droplets are ejected from the impact centre. The velocity shows variances under different test conditions.

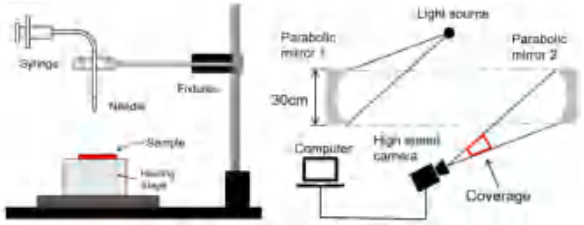
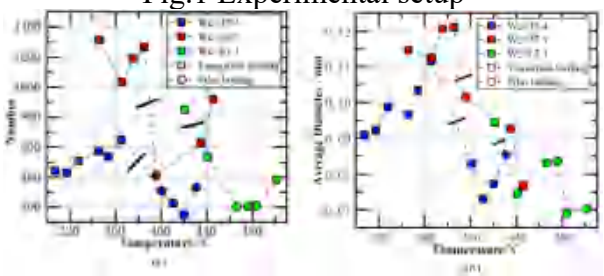


Fig.1 Experimental setup


Fig.2The number and size of secondary particles at different wall temperatures

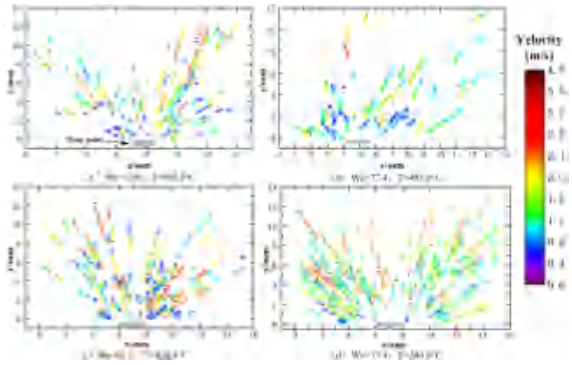


Fig.3 Trajectories of secondary droplets

Conclusions

The experimental results have shown great variances under film and transient boiling conditions, which are essential for the development of efficient spray cooling devices and simulation calculation verification.

References

[1] Zhang N, Yang W J. Evaporation and explosion of liquid drops on a heated surface. Experiments in Fluids, 1983, 1(2): 101-111.

Refractive Index Matching and Inertial Measurement Unit Particle Tracking Techniques for Application in Particle-Liquid Mixture Flow

Jiajun Jiao*, Yunhui Sun, Yi An, Xiaoliang Wang, and Qingquan Liu
Beijing Institute of Technology, Beijing, China
* Corresponding author: jjj18811480824@163.com

Abstract
Dense particle-liquid mixture flows are ubiquitous in various industrial and natural settings. Investigating the motion of particles is of significant importance for an enhanced understanding and description of particle rheology. Numerous scientists have employed techniques such as Particle Tracking Velocimetry (PTV) and Particle Image Velocimetry (PIV) to track particles and obtain information on their motion. However, there remains a scarcity of research on the observation of internal particle motion with negligible side-wall effects and on the direct measurement of collision forces associated with particle movement. In this study, utilizing a refractive index matching (RIM) approach, we examined the dense flow of particulate-liquid mixtures down an inclined channel with roughened frictional boundaries, yielding detailed insights into internal particle flow behavior including velocity, shear rate, particle temperature, and solid concentration. Furthermore, this paper developed an inertial measurement unit (IMU) particle capable of measuring collision forces in particle-liquid mixture flows, and precise values of collision forces between these IMU particles and the channel walls were measured.

Keywords: Ractive index matching, Internal particle flow, Inertial measurement unit particle, Collision force

Introduction

Optical measurement techniques such as Particle Image Velocimetry (PIV) and Laser Doppler Velocimetry (LDV) are typically employed for tracking the motion of particles in particle-liquid mixture flows[1]. This article focuses on the introduction of an internal particle motion tracking method in particle-liquid mixture flows based on Refractive Index Matching (RIM) technology[2], as well as a direct measurement method for particle collision forces in particle-liquid mixture flows utilizing Inertial Measurement Unit (IMU) particle technology.

Methodology

We employed high-borosilicate glass beads as the particle phase and a dimethyl sulfoxide (DMSO) aqueous solution for the liquid phase, achieving refractive index matching between the liquid and the particles. Fluorescent dye was added to the liquid to facilitate contrast in laser illumination, where the solid particles appear dark, while the liquid phase is brightly illuminated, as depicted in Figure 1. The quasi-steady liquid–particle mixture flow down an inclined channel is studied experimentally using the refractive index matching method, which gives the internal flow structures including the velocity, solid concentration, shear rate, and granular temperature.



Figure 57 - Representative imagery of dense particle-liquid mixture flow in an inclined flume using refractive index matching technology, and the effectiveness of particle motion identification.

We engineered an inertial measurement unit (IMU) particle designed for measuring collision forces of particles within particle-liquid mixture flows, as shown in Figure 2. This IMU particle maintains the same density and coefficient of restitution as an aluminum sphere of equivalent diameter. Utilizing this IMU particle, we have measured the detailed collision forces experienced by particles upon impact with the wall surface.



Figure 2 - Schematic representation of the inertial measurement unit (IMU) particle

Conclusions

Refractive index matching technology enables the tracking of internal particle motion within particle-liquid mixture flows, thereby facilitating the acquisition of particle motion information on the observation plane. Furthermore, the use of Inertial Measurement Unit (IMU) particles allows for data collection on particle collision forces and collision frequencies within the mixture flow. These two experimental methodologies provide robust support for researching dense particle-liquid multiphase flows.

Acknowledgements

The authors are grateful for financial support from the National Natural Sciences Foundation of China (Grant No. 12032005, 12172057).

References

[1] Armanini, A., Capart, H., Fraccarollo, L., & Larcher, M. (2005). Rheological stratification in experimental free-surface flows of granular–liquid mixtures. Journal of Fluid Mechanics, 532, 269-319.

[2] Sun, Y., Jiao, J., An, Y., Wang, X., & Liu, Q. (2023). Experimental study on internal flow structure and dynamics of dense liquid-particle flow down inclined channel. Experiments in Fluids, 64(9), 150.

Image quality evaluation of EIT sensors on dynamic multiphase flows with coupling field simulation

Qiu Junzhe, Wang Shengnan*, Kong Ming
China Jiliang University, Zhejiang Hangzhou 310018, China

Abstract
In this study, we explore the impact of electrode number on the performance of Electrical Impedance Tomography (EIT) for dynamic multiphase flow imaging, employing a three-dimensional Fluid-Electrodynamic field Coupling Model (3D-FECM). Four distinct EIT sensors with 8, 16, 24, and 32 electrodes were designed to instantaneously capture the complex dynamics of water-gas flows and their associated electrical measurements. We utilized the Structure Similarity Index Measurement (SSIM) and Peak Signal-to-Noise Ratio (PSNR) to assess the Tikhonov Regularization (TREG) and Landeweber Iterative (LI) reconstructed images.

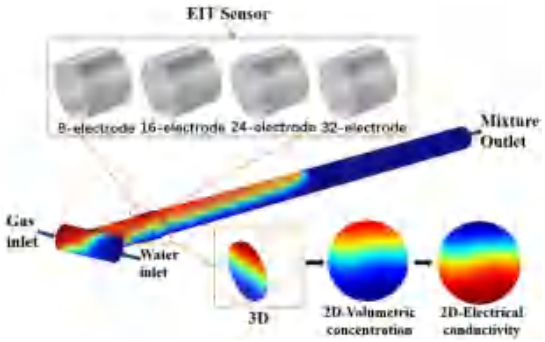


Figure 1 - Geometric structure of the 3D-FECM model

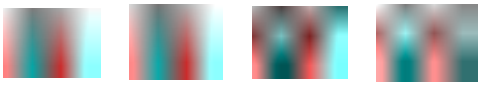
Keywords: multiphase flow, electrical impedance tomography, electrode number, three-dimensional Fluid-Electrodynamic field Coupling Model

Introduction

Electrical Impedance Tomography (EIT) stands out as a cutting-edge technique for visualization and detection, known for its non-invasive, real-time, and cost-effectiveness [1]. However, its application in qualitative multiphase flow imaging is limited by the spatial resolution challenges stemming from the ill-posed and nonlinear nature of its inverse problem. A promising solution to enhance EIT's performance is increasing the electrode number, which boosts the measurement data and mitigates the ill-posed issue. In this research, we utilize the 3D Fluid-Electrodynamic field Coupling Model (3D-FECM) to explore how varying electrode numbers on EIT sensors affect dynamic multiphase flow imaging.

Methodology

We adopt the 3D-FECM to simulate dynamic water-gas flow, and four EIT sensors with 8, 16, 24 and 32 electrodes are designed to measure the water-gas flow (see Fig. 1). TREG and the LI are used to reconstruct EIT images, and SSIM and PSNR are used to quantify the imaging performance of these EIT sensors on dynamic flow patterns (see Fig. 2).

Ground Truth	8electrodes		16electrodes	
	TREG	LI	TREG	LI
				
SSIM	0.7446	0.714	0.864	0.832

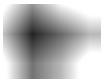
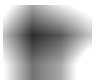
PSNR	59.072	57.587	64.471	61.239
					
SSIM	0.769	0.719	0.797	0.805
PSNR	63.774	61.744	62.821	62.930
Ground Truth	**24electrodes**		**32electrodes**	
	TREG	**LI**	**TREG**	**LI**
					
SSIM	0.840	0.834	0.845	0.802
PSNR	62.318	63.094	61.608	59.505
					
SSIM	0.705	0.753	0.704	0.703
PSNR	60.806	63.172	59.887	60.377

Figure 2 - Quantitative evaluation results

Conclusions

In this study, EIT sensor with 16 electrodes generally provides the most accurate image reconstructions, while the 8-electrode configuration tends to exhibit the lower precision overall.

References

[1] Sheng-Nan Wang, Francesco Giorgio-Serchi, Yun-Jie Yang; A virtual platform of electrical tomography for multiphase flow imaging. Physics of Fluids, 2022, 34 (10): 107104.

A learning-based volumetric reconstruction method for light field PIV

Xiaoyu Zhu, Mengxi Fu, Chuanlong Xu*
School of Energy and Environment, Southeast University, Nanjing 210096, China

Abstract
This study presents a learning-based volumetric reconstruction method for 3D particle reconstruction in light field PIV. A tailored deep learning model incorporating a modified CNN architecture is employed to predict the particle distributions from the LF images. Synthetic and experimental tests indicate that the proposed method outperforms the traditional tomographic reconstruction algorithms in terms of reconstruction quality, mitigation of elongation effect and computational efficiency.

Keywords: Flow measurement, Light field PIV, Deep learning networks

Introduction

Light field PIV (LF-PIV) is a promising single-camera volumetric velocimetry technique for space-constraint applications. However, due to the finite viewing angle of the single lens, significant elongation effect is demonstrated in particle reconstruction result of LF-PIV [1], which degrades the velocity estimation accuracy. Moreover, the iterative process of tomographic reconstruction always consumes long time and demands a large computer storage space.

Methodology

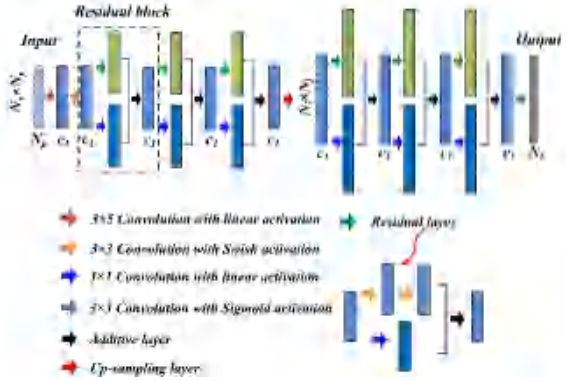


Figure 58 - Architecture of LF-PR-net

This study proposes learning-based framework for accurate and fast 3D particle reconstruction in LF-PIV. The architecture of the tailored deep neural network (LF-PR-net) is shown in Fig. 1. Two convolutional layers followed by three residual blocks are employed to encode the spatial information of input into features, and an up-sampling layer is utilized to scale up the feature maps. The processed feature maps are then decoded by the residual blocks, culminating in the generation of output particle volumes.

Results

Figure 2 illustrates the reconstruction quality index (Q) by LF-PR-net and conventional MART and PR-MART algorithms. It can be seen that Q index for LF-PR-net exceeds 0.75 at varying seeding concentrations (C), approximately doubling that of MART. This suggests that the reconstruction elongation effect presented in MART results has been significantly mitigated. Besides, LF-PR-net requires merely 1.2s for reconstructing each LF image, while that for MART and PR-MART is 0.38h and 0.28h, respectively.

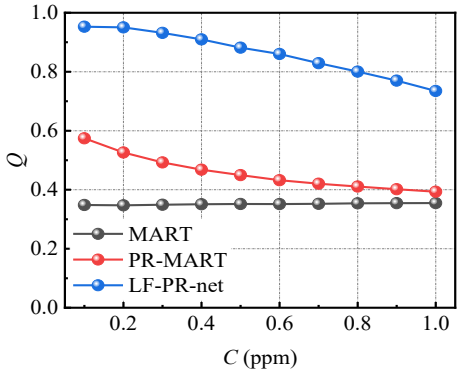


Figure 2 – Reconstruction Q index of LF-PR-net, MART and PR-MART

Conclusions

The LF-PR-net demonstrates superior performance than the state-of-the-art MART and PR-MART algorithms regarding mitigation of reconstruction elongation and higher reconstruction efficiency. It can be integrated in the single-camera LF-PIV for enhancing accuracy of 3D flow measurement.

References

[1] Mei D, Ding J, Shi S, et al. High resolution volumetric dual-camera light-field PIV[J]. Experiments in Fluids, 2019, 60: 132.

Application of Stacking Ensemble Learning in the Measurement of Suspended Sediment Particle Size Distribution

Changquan Yuan[1],Zhanhong Shi[2],Dailiang Xie[1*],Ya Xu[1],Zhenwei Huang[1],Tiejun Liu[1]
(1.China Jiliang University, Hangzhou, China,310018, dlxie@cjlu.edu.cn;
2.Inspecting and Testing Centre for Hydrological & Geotechnical Instrument's quality，MWR,Nanjing,China)

Abstract
We developed an IGWO-Stacking ensemble model to simplify the traditionally complex task of inverting suspended particulate matter size distribution. This model combines Extreme Random Trees, Decision Trees, and XGBoost as base learners, with the Random Forest algorithm serving as the meta-learner. Particulate samples were prepared by sieving them into predefined size distributions, and ultrasonic attenuation experiments were conducted to create the dataset. Feature selection employed the Boruta algorithm, and hyperparameters were optimized using the improved Grey Wolf Optimization algorithm. An inversion performance comparison between the Random Forest algorithm and the proposed model was conducted. The results indicate that the proposed model consistently exhibits higher accuracy, with a consistently lower relative root mean square error in the inversion of particle size distribution on the test set compared to the Random Forest algorithm. This approach proves effective for the inversion of suspended sediment particle size distribution.

Keywords: Suspended Sediment;Particle Size Distribution;Stacking Ensemble Learning;Improved Grey Wolf Optimization Algorithm

Introduction

Suspended sediment is a typical liquid-solid two-phase flow, and the particle size and distribution of its particles are of significant importance for studying river sediment composition and water-sediment environmental management [1].The use of traditional methods for particle size distribution inversion can lead to significant errors in practice [2]. In our study, within the Stacking ensemble framework, we constructed an inversion model for particle size distribution. We optimized the model hyperparameters using an improved Grey Wolf Optimization algorithm and validated the effectiveness of the model through comparisons with other algorithms.

Experiment and Data Processing

The experimental setup is illustrated in Figure 1. By extracting 53 distinctive features to characterize the ultrasonic attenuation signal, we utilized the Boruta algorithm for feature selection,successfully reducing the dimensionality to 7 key features.

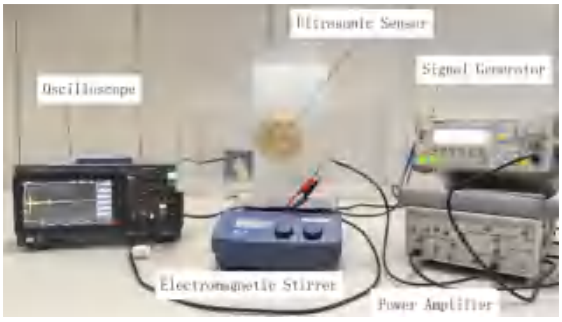


Figure 59 - The experimental setup

Improved Grey Wolf Optimizer

Shortcomings in the initialization and parameter adjustment of GWO may result in insufficient exploration and getting trapped in local optima.We enhance the Grey Wolf Optimizer algorithm through strategies including the random initialization of multiple wolf packs within a predefined search space, dynamically adjusting the balance between exploration and exploitation during iterations, and regularly exchanging the best solutions among packs. Figure 2 depicts the Improved Grey Wolf Optimizer.

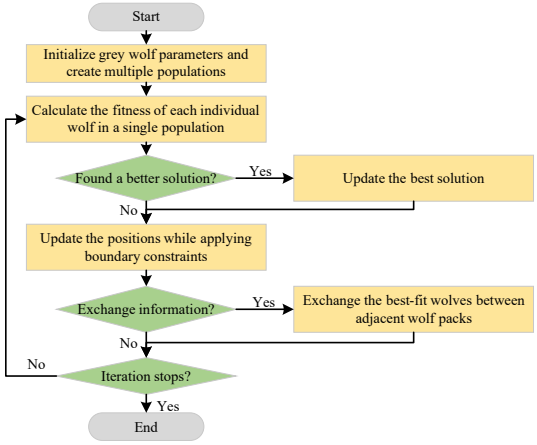


Figure 2 - The Improved Grey Wolf Optimizer

Algorithm Overall Procedure

We proposed an improved Stacking ensemble learning inversion model based on the IGWO algorithm (IGWO-Stacking), as illustrated in Figure 3.

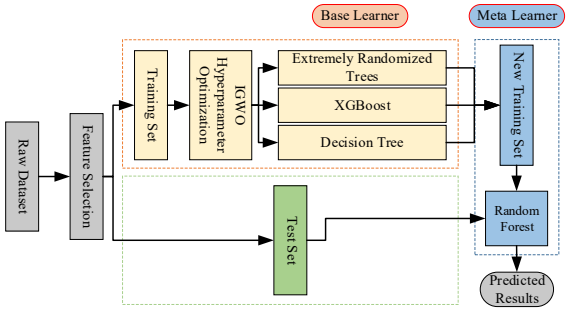


Figure 3 - Algorithm Overall Procedure

Inversion Results and Analysis

We tested and compared the Random Forest (RF) algorithm and the IGWO-Stacking model on RR, Beta, and random distributions. Evaluation was based on Relative Root Mean Square Error (RRMSE), presented in Table 1. It indicates that the IGWO-Stacking model has demonstrated excellent performance in the inversion of different distributions.

Table 9 - Performance Comparison of RF Algorithm and IGWO-Stacking Model

Model	**RRMSE/%**		
	RR	**Beta**	**Random**
RF Algorithm	**8.811**	**0.548**	**0.467**
IGWO-Stacking model	**4.166**	**0.167**	**0.070**

We tested the model with sieve experiments using bimodal RR distribution samples. Figure 4 demonstrates favorable inversion results.

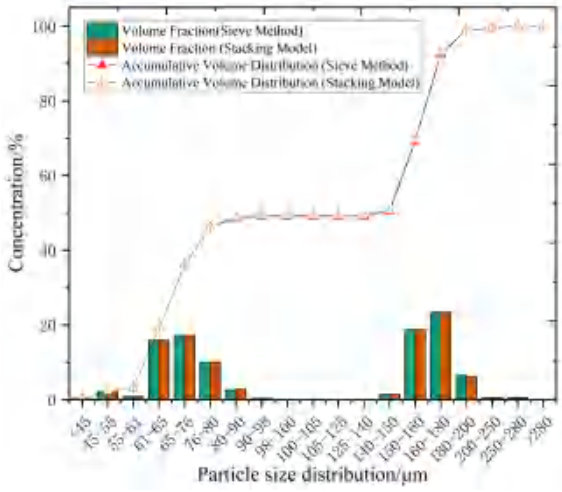


Figure 4 - Inversion Results for Bimodal RR Distribution

Conclusions

The IGWO-Stacking ensemble learning model exhibits commendable performance in inverting particle size distributions.It provides an effective approach for the inversion of suspended sediment particle size distributiont.

Acknowledgements

We would like to acknowledge the support provided by the National Key Research and Development Project#2022YFC3204504.

References

[1] H.Yanfang,L.Baoyaun, Y.Yang, et al. Particle size distribution characteristics of erosion and sediment in five typical soils in China.Journal of Soil and Water Conservation 32 (2018) 150-159.

[2] F.R Crucinio, A. Doucet, A.M Johansen. A particle method for solving Fredholm equations of the first kind. Journal of the American Statistical Association(2021)1–11.

Two-phase stereo-PIV techniques for gas-liquid two-phase flow

Wuguang Chena Guangyuan Huanga Junlian Yina* Dezhong Wanga
a School of Mechanical and Engineering, Shanghai Jiao Tong University, China
* Corresponding author, Email: jlyin@sjtu.edu.cn

Abstract

This study introduces two-phase stereo-PIV techniques for simultaneous measurement of 3C velocity and bubbles. Methods based on optical and image phase discrimination were proposed, with corresponding image processing and velocity reconstruction methods. Validation tests confirmed accuracy. Applications to pipe and swirl flows demonstrated technique efficacy. Results from bubbly pipe flow and bubble column indicated successful acquisition of 3D velocity and bubbles. Comparatively, the IPD method is recommended for 2D measurement due to its simplicity and high resolution.

Keywords: turbulent bubbly flows; two-phase stereo-PIV; phase discrimination;

Introduction

The objective of the present study is to develop the two-phase stereo-PIV measurement techniques and verify the accuracy, which is expected to help promote further studies in turbulent bubbly flows. To ensure affordable cost and camera placement difficulty, we require not to increase the number of cameras for single-phase stereo-PIV. According to the different phase discrimination methods, optical phase discrimination-based and image phase discrimination-based two-phase stereo-PIV techniques were developed in the present study. In addition, multi-validation tests were conducted to give a quantitative representation of the accuracy of the new measurement methods. The comparison between these two techniques in the application of turbulent bubbly flow was also illustrated.

Methodology

Based on the difference in the methods taken for phase discrimination, optical phase discrimination-based and image phase discrimination-based two-phase stereo-PIV techniques were proposed, as shown in Figure 1. Both two-phase stereo-PIV techniques consist of an LED array, a laser, a mirror, a test section and viewing box, fluorescence seeding particles, two CCD cameras, and several customized optical filters, while two image doublers were only used in the optical phase discrimination based two-phase stereo-PIV technique. Both techniques are equipped with a mirror to minimize the blocking effect of bubbles on the laser light and a viewing box to minimize the refractive index effect during the measurement. It should be noted that there are three light sources with different wavelengths in both techniques: the background light of 640nm wavelength, the laser light of 532nm wavelength, and the fluorescence light of 585 wavelengths.

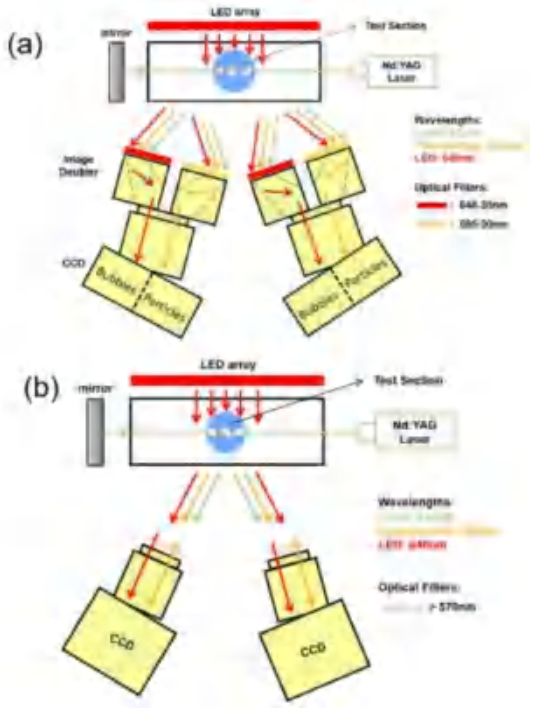


Figure 1 – two-phase stereo-PIV methods

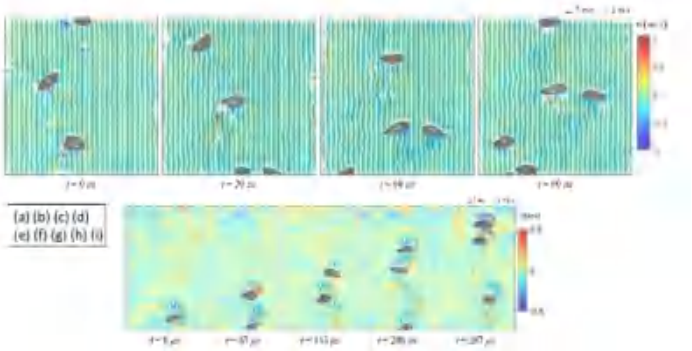


Figure 2 –results of two-phase stereo-PIV methods

Conclusions

The proposed two-phase stereo-PIV techniques, based on image and optical phase discrimination, were introduced with detailed principles and processing methods. Three validation tests confirmed accuracy. Both IPD and OPD methods successfully obtained bubble and 3C velocities.

An experimental investigation on characteristics of liquid film thickness of gas-liquid Taylor flow in rectangular microchannel

Dengwei FU, Sihui Hong
Sun Yat-Sen University, Zhuhai, China

Abstract

Liquid film thickness is one of the most important parameters for understanding two-phase flow in micro-scales. In the present work, experiments were conducted to investigate the variation of liquid film thickness in square tubes with hydraulic diameter Dh = 0.3, 0.5, 0.7, 1.0 mm, and rectangular tubes with a depth of 0.5mm and widths of 0.3, 0.5, 0.7, 1.0 mm. The experiments revealed that at low capillary numbers, surface tension determines the lower limit of the liquid film thickness in either square or rectangular microchannels. At medium capillary numbers, viscous force becomes prominent, and increase the thickness of the liquid film. At high capillary numbers, inertia forces determine the upper limit of the liquid film thickness. The non-uniform distribution of the liquid film thickness in rectangular channels intensifies with the increase in the aspect ratio of channel width to depth.

Keywords: Liquid film thickness, Gas-liquid two-phase flow, Square microchannel, Rectangular microchannel, Precision measurement

Introduction

Liquid film thickness is one of the key parameters in studying the mechanisms of heat and mass transfer and performance improvement in microchannel flow boiling. It plays a crucial role in calculating two-phase flow pressure drop, heat transfer coefficients, void fraction, and other important factors. The formation mechanism of gas-liquid Taylor flow in rectangular microchannels is complex, and the dynamic characteristics of liquid film are still unclear. Compared with uniform distribution of liquid film in a circular tube, the circumferential distribution of liquid film in rectangular microchannels is uneven due to the corner of the cross section. Surface tension, viscous forces, and inertia forces are important factors influencing liquid film thickness. In this paper, as shown in Figure 1, through the method of laser focus ranging and synchronized visualization experiments under adiabatic two-phase flow conditions, the impact of different hydraulic diameters on the variation of liquid film thickness at the central position inside small rectangular channels was investigated. Figure 2 shows the relationship between dimensionless liquid film thickness and capillary number in square tubes with different hydraulic diameters. At low capillary numbers (Ca < 0.01), the dimensionless liquid film thickness δ/D for different microchannels appears similar. When 0.01 < Ca < 0.02 the dimensionless liquid film thicknesses δ/D in microchannels with Dh = 0.7 mm and 1.0 mm increase sharply whereas the increments of δ/D in microchannels with Dh = 0.3 mm and 0.5 mm are relatively gentle. Further increasing Ca, the increase in δ/D in microchannels with Dh = 0.3 mm also become significant.

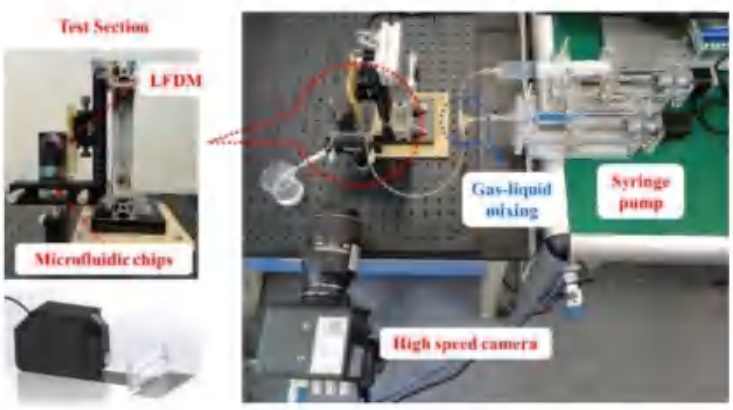


Figure 1 - Picture of the air-water two-phase flow test loop used in the present work

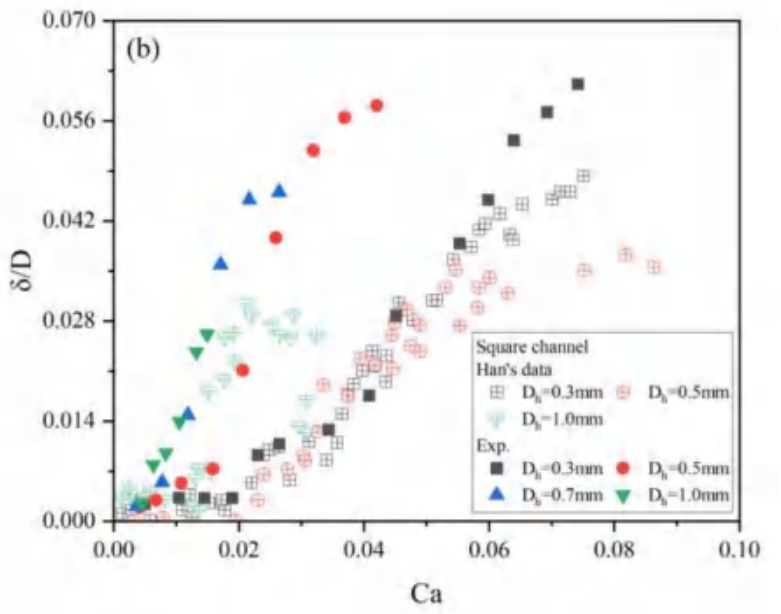


Figure 2 - Dimensionless liquid film thickness against Capillary number

Study on the liquid-solid two-phase flow phenomenon and stress distribution characteristics in a batch slag-discharge lock hopper

Feihu Shen, Guiling Xu, Chengzhi Chen, Ping Lu
School of Energy & Mechanical Engineering, Nanjing Normal University, Nanjing 210042, China

Abstract
In order to study the stability of liquid- solid two-phase flow, flow pattern transformation and stress distribution characteristics during the slag-discharge process in the batch slag-discharge system, a slag- discharge lock hopper discharge test platform made of plexiglass was established. The effects of lock hopper structure (lock hopper half cone angle, flushing water adding position), operating parameters (flushing water volume flow rate, initial height of material in the lock hopper), and material characteristic (material particle size) on the liquid-solid two-phase flow and stress distribution characteristics in the slag-discharge lock hopper were studied. The Janssen and Jenike theory were used to analyse the wall stress variation in the lock hopper during the slag discharging process, and to calculate the distribution and evolution of the velocity field inside the lock hopper. Results show that during the material discharging process, the flow patterns inside the lock hopper could be divided into the increasing flow rate stage and the stable flow rate stage. The stable flow ratestage is mainly funnel flow, and the normal stress on the wall surface of the cone-cylinder junction for the lock hopper is the largest. The material discharge rate and the wall normal stress inside the lock hopper both increases with the increase of flushing water volume flow rate. The initial height of the material in the lock hopper has little effect on material discharge rate.

Keywords: slag-discharge lock hopper, liquid-solid two-phase flow characteristics, stress distribution, arching mechanism

Introduction

Coal gasification is widely used in major industrial fields such as energy, chemical industry and metallurgy. The slag-discharge system is an important part of the gasification device. Its operation is related to the safe and stable operation of the entire gasification device and is an important part of ensuring the normal operation of the gasifier [1]. In the gasification reaction, not only the required product syngas is generated, but also a large amount of solid slag is produced. If it is not discharged in time, it will accumulate, occupy the effective volume of the washing and cooling room, be brought into the back systemby black water, and block the pipeline, equipment and so on. When it accumulates to a certain extent, it will block the black water outlet, and it can be imagined that the water cycle will not be able to proceed, and finally the gasifier will not be able to operate [2]. The slag-discharge lock hopper mainly collects anddischarges the gasification slag of the gasifier. Due to the periodic work of the slag-discharge system, the lock hopper is subjected to alternating loads, which can easily cause fatigue damage to the lock hopper. Therefore, it is very important to analyse the stress distribution in the slag-discharge lock hopper [3].

Methodology

Jenike found through experiments that in the initial stage of discharge, there was a large degree of overpressure at the connection between the silo and the hopper. The circular silo was divided into two parts: vertical silo and inclined hopper. The relationship between the ratio of the maximum wall side stress to the material weight and the height-to-diameter ratio of the silo and the relationship between the silo diameter and the height-to-diameter ratio were established in the form of charts, and the static and dynamic stress formulas of the silo were obtained. For the cylinder section, a variable lateral pressure coefficient kh was used to reflect the dynamic

stress state and the static stress state. The expression of the generalized stress σn of the bucket section is:

$$\sigma_{ti} = \gamma k_h \left\{ \frac{h_0 - z}{n-1} + \left[h_1 - \frac{h_0}{n-1} \right] \left[\frac{h_0 - z}{h_0} \right]^n \right\} \quad (1)$$

$$n = (m+1)\left[k_h \left(1 + \frac{\mu}{\tan\theta} \right) \right] - 1 \quad (2)$$

$$h_1 = \frac{R}{\mu_w k_h} \left(1 - e^{-\frac{\mu_w k_h h_0}{R}} \right) \quad (3)$$

The objectives of this paper were as follows:

(1) The liquid-solid two-phase flow and discharge characteristics in the process of slag-discharge in the lock hopper were studied. The liquid-solid two-phase flow characteristics in the slag-discharge lock hopper and its mechanism of action on the material flow pattern and discharge stability in the process of slag-discharge in the lock hopper were revealed.

(2) The liquid-solid two-phase flow pattern in the discharge process of slag lock hopper is investigated, and the typical flow pattern and its transformation law in the discharge process of slag lock hopper are obtained.

(3) The phenomenon of material arching in the process of slag-discharge lock hopper is studied, and the variation law of wall stress at the junction and outlet of the cylinder cone is obtained. The internal relationship between the arching phenomenon in the slag-discharge lock hopper and its stress distribution characteristics is discussed, and the mechanism of material arching in the process of slag-discharge lock hopper is revealed.

The discharge test device of slag-discharge lock hopper is shown in Fig. 1. The lock hopper is made of organic glass with a wall thickness of 5 mm. The upper part is a cylinder with a height of 600 mm and an outer diameter of 210 mm. The lower part is a cone with a height of 208 mm and a half cone angle of 20°. The bottom end is the discharge outlet of the device, and the outlet diameter is 30 mm. The discharge is controlled by a ball valve. The normal stress of the wall surface is collected during the material discharging process, and the flow of the material in the device is not affected.

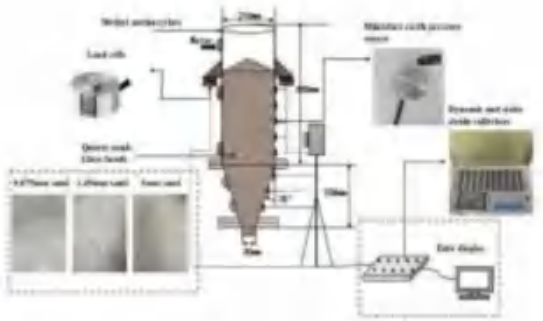


Figure 1 - Schematic diagram of lock hopper discharging test device

Conclusions

The whole material discharging process consists of two parts, namely the increasing flow rate stage and the stable flow rate stage. According to the flow pattern transformation during the material discharging process, the material sparse area appears at the bottom of the cone in the lock hopper during the increasing flow rate stage, and the material discharging mass flow rate is large. The average particle size of the material is inversely proportional to the material discharge rate. The normal stress on the wall surface of the cone-cylinder junction is the largest. The greater the flushing water flow rate, the more obvious the turbulence in the lock hopper, corresponding to the greater the discharge mass flow rate, as well as the greater the wall normal

stress. The initial height of the material in the lock hopper has little effect on the material discharge rate.

Acknowledgements
This work was funded by the National Natural Science Foundation of China (51506100).

References

[1] Wang X T, Guo H T, Gasification slag- discharge system pipe vibration cause analysis and transformation [J]. China Petroleum and Chemical Standards and Quality. 2013, 33(14): 236.
[2] Bao W N, Zhu Y R, Xu J G. Slag plugging phenomenon and treatment method of gasifier lock hopper system [J]. Chemical technology and development. 2009, 38 (9): 59- 61.
[3] Fu L. Stress Analysis of Slag-discharge System Pipeline in Coal Chemical Project [J]. Chemical Management. 2020, (22): 172-174.

Experimental and simulation studies based on an improved drag model

Lei Wang, Jinyi Li, Hongwei Li, Changhe Du, Wenpeng Hong
School of Energy and Power Engineering (Northeast Electric Power University, Jilin, China)

Abstract
Whether the fluidized bed can accurately describe the drag force suffered by particles in the fluidization process is the key to the numerical solution method. In this paper, to address the problem of particles affected by the drag force in the fluidization process, the experimental device for particle fluidization is firstly constructed. Then, an improved drag model is proposed in the numerical simulation method, coupled with the Eulerian two-fluid model to study the flow characteristics inside the bubbling fluidized bed. Finally, the transient fluidization diagrams, pressures, and axial velocities obtained in the experiments are used to compare with the simulation results. The results show that the simulation results of the improved drag model match the experimental results in terms of bubble equivalent diameter. Compared with the Gidaspow model, the improved drag model gives better results for the bed pressure drop, and the prediction of time-averaged axial velocity of particles is significantly improved.

Keywords: Fluidized bed, Fluidization experimental device, Drag force, Eulerian two-fluid model.

Introduction

In a fluidized bed, the motion behavior of bubbles makes the flow structure in the fluidized bed non-uniform. The non-uniformity of bubble generation and distribution also causes changes in bed pressure drop, changes in bubble behavior characteristics, and changes in bed expansion rate. The Eulerian two-fluid method plays an important role in gas-solid fluidization systems. The drag calculation method has a significant impact on the accuracy of the two-fluid model. A modified drag model is applied to simulate the non-uniformity caused by bubbles. The results are compared with the experimental results and Gidaspow drag model results.

Methodology

The fluidized bed experimental setup is shown in Figure 1. It mainly includes gas supply device, fluidized bed body, pressure measurement device, high-speed camera, doppler velocimeter, and computer.

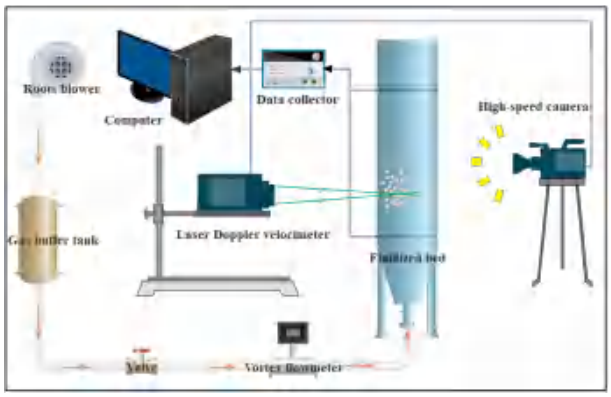


Figure 60 - Experimental system diagram

A typical subscale drag model, Mckeen drag model is introduced for simulation.
Modification of the drag model:

$$k_{gs} = \varphi k_{gs-Ergun} + (\psi - \varphi) k_{gs-Mckeen} + (1-\psi) k_{gs-Wen\&Yu} \qquad \textbf{(2)}$$

Results and discussion

The corrected drag model has less error with the experimental results.

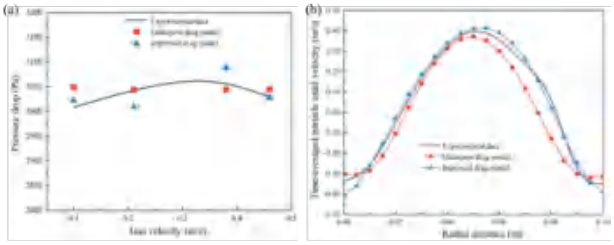


Figure 2 - Comparison of simulation and experimental results, (a) pressure drop (b) velocity

Conclusions

Compared with the Gidaspow model, the improved drag model gives better results for the bed pressure drop, and the prediction of time-averaged axial velocity of particles is significantly improved.

Acknowledgements

The authors gratefully acknowledge financial support from National Natural Science Foundation of China (No. 12102089 and No. 52376097).

Parallel Session X: Topic 6-Multiphase flow in oil ang gas development and conversion

Multi-scale flow and transport dynamics in porous media

Senyou An
Shenzhen University, Shenzhen, China

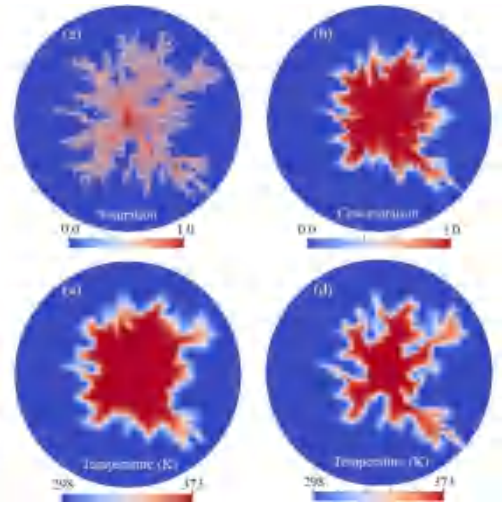
Abstract
Fluid flow and solute/heat transport in porous materials are ubiquitous in nature, as well as in many scientific problems and engineering applications, which touch almost every aspect of our daily lives. This talk will focus on understanding and enhancing the predictive capabilities for processes, such as multi-phase flow, fluid-solid interaction, reactive transport, and non-Newtonian fluid flow in porous media, which are directly linked to many subsurface processes (e.g., enhanced oil recovery, geological CO2 storage, and contaminant hydrogeology). In this talk, both computational and experimental approaches will be involved, and the aforementioned processes will be discussed. Particularly, I will highlight our efforts to understand complex phenomena in porous media by developing advanced algorithms.

Keywords: Flow in porous media, Transport phenomena, CO2 sequestration, Subsurface energy

Introduction

Accurately characterizing subsurface multiphase flow in permeable rocks is critical for analyzing a wide range of natural and engineering phenomena, such as environmental contaminant remediation, subsurface energy resource development, and carbon geosequestration for climate change mitigation. Difficulties in modeling the physical processes governing fluid flow can lead to inaccurate field-scale flow simulations. This issue is prominent at CO2 storage sites, where scientific pilot and industrial demonstration projects have demonstrated unexpectedly rapid CO2 migration in directions that are difficult to forecast and history match using conventional workflows. Heterogeneity in the multiphase flow properties, relative permeability and capillary pressure, has been identified as a cause of the unexpected flow phenomena observed at field sites (An et al, WRR, 2023).

Some results



Snapshots of instabilities in two-phase flow and transport simulated using in-house developed pore-network modelling enhanced by the graphics processing unit, The network in all four cases had a radius of 50 mm and thickness of 0.2 mm, comprising about one million pore bodies and four million pore throats, with an average pore radius of 0.0257 mm and variance of 2.12×10^{-4} mm. (a) Saturation distribution: viscous fingering during two-phase flow, the viscosity of invading and receding phases were 1 mPa·s and 50 mPa·s respectively. The interfacial tension was 50 mN/m, The flow rate at the inlet boundary (from the centre) was 1 mm^3/s. (b) Concentration distribution: instability in solute transport in a shear-thinning fluid visualised at the breakthrough time for the injection rate of 0.1 mm^3/s. (c) Temperature distribution: instability in heat transfer in water as a Newtonian fluid for the injection rate of 0.1 mm^3/s. (d) Temperature distribution: instability in heat transfer in crude oil as a non-Newtonian fluid with temperature and local shear-dependent rheology for the injection rate of 0.1 mm^3/s. fluid for the injection rate of 0.1 mm^3/s. (d) Temperature distribution: instability in heat transfer in crude oil as a non-Newtonian fluid with temperature and local shear dependent rheology for the injection rate of 0.1 mm^3/s.

Estimation of CO_2-Oil Minimum Miscibility Pressure based on Integrated Machine Learning approach

Guoqing Zhao[1], Youwei He[1], Yong Tang[1], Jiazheng Qin[1]
[1]State Key Laboratory of Oil and Gas Reservoir Geology and Exploitation, Southwest Petroleum University, Chengdu, Sichuan 610500, China

Abstract
CO2 Enhanced oil recovery (EOR) and Storage in oil reservoirs has become a preferred way to efficiently utilize CO2 and increase the CO2 storage. CO2-oil minimum miscible pressure (MMP) is a significant factor for CO2 EOR performance. How to accurately and efficient estimate the CO2-oil MMP is still challenging due to the high cost and heavy time burden for experiment tests. This work proposes an integrated Machine Learning approach to forecast the MMP between CO2 and Oil phase by introducing improved Grey Wolf optimization (i-GWO) into the Support Vector Machine-Random forest (SVM-RF) algorithm. The data sets are firstly optimized to reduce the robustness of data sets. The MMP is estimated by SVM and RF methods. The average of the calculated MMPs is considered as the final MMP when the MAE of the MMP obtained by the SVM and RF is lower than 0.1. Then, GWO and IGWO algorithms are involved to improve the MMP prediction accuracy. Finally, the estimated MMPs are compared among four methods. Results show that the accuracy is improved by 37% and 40% using SVM-RF-GWO and SVM-RF-IGWO. The calculated MAPE are 0.16, 0.10, and 0.09, and the accuracy is improved by 37.8% and 41.3% by introducing GWO and IGWO. The SVM-RF-GWO and SVM-RF-IGWO enhances the accuracy by 54.16% and 57.12% based on R2. The developed model can efficiently estimate the CO2-oil MMP. This work is helpful for operation and optimization for CO2 EOR-Storage projects.

Keywords: Carbon capture, utilization and storage; Minimum miscibility pressure; Support vector machine; Random forest; Improved grey wolf optimization

Evolution characteristics of CO_2 plume and trapping under heterogeneous capillary pressure and geochemical reactions during injection and post-injection

Guodong Cui [a*], Zhe Hu [a], Fulong Ning [a], Rui Wang [b], Xi Chen [a], Zhenyu Liu [a], Yinghua Lian [a]
a Faculty of Engineering, China University of Geosciences, Wuhan 430074, China; b Petroleum Exploration and Development Research Institute, SINOPEC, Beijing 100083, China

Abstract
To safely store CO_2, it is necessary to accurately predict the behaviors and trapping evolution of CO_2 in saline aquifers. In this paper, based on the Gaussian stochastic geological modeling method, after combining the gas-liquid two-phase seepage equation and the Arrhenius equation, we established a comprehensive CO_2 reaction flow model in heterogeneous saline aquifers. Based on the model, the CO_2 plume and trapping evolution under the capillary pressure heterogeneity and geochemical reactions were analyzed in detail. The results showed that capillary pressure heterogeneity can impede CO_2 upward migration, increasing lateral spread. The geochemical reactions mildly affect CO_2 migration and reservoir properties within 100 years. However, the effect of geochemical reactions on CO_2 migration, trapping, and reservoir physical properties is small and can be ignored. Higher capillary pressure and heterogeneity slow the vertical migration of CO_2, reducing residual, dissolution, and mineral trapping fractions, but improving local capillary trapping fraction. Horizontal correlation of capillary pressure reduces vertical migration, increasing residual trapping but decreasing dissolution trapping. With the increase of reservoir temperature and the ration of vertical/horizontal permeability, the vertical migration rate is accelerated, and CO_2 is more likely to bypass the local capillary barrier under the action of buoyancy, which reduces the transverse sweep volume. However, this condition benefits CO_2 dissolution and mineral reactions, resulting in a decrease in local capillary trapping fraction. For long-term safety, saline aquifers with high temperature, isotropy, and horizontal correlation are recommended. For short-term storage and local trapping, those with high capillary pressure and heterogeneity may be preferable.
Keywords: Saline aquifer; Heterogeneous capillary pressure; Geochemical reactions; CO_2 plume; Local capillary trapping

Introduction

CO_2 geological storage is a promising method to reduce carbon emissions, crucial for stabilizing atmospheric CO_2 levels and mitigating the greenhouse effect. Deep saline aquifers are particularly promising for CO_2 storage due to their widespread distribution and ample storage capacity.

Previous research in saline aquifers has focused on understanding CO_2 storage and migration patterns under either heterogeneous capillary pressure or the influence of geochemical reactions on porosity and permeability changes. However, there's a lack of exploration into how heterogeneous capillary pressure and geochemical reactions together affect CO_2 storage and migration in saline aquifers. This research gap calls for a more comprehensive understanding of the process.

Methodology

The paper adopts the Gaussian probability method to generate different heterogeneity fields of porosity, permeability, and capillary pressure and combines two-phase seepage to establish a CO_2 reaction and flow model. Based on the model, a numerical simulation of CO_2 storage and migration under the heterogeneous capillary pressure and geochemical reactions in the saline aquifer is carried out. In this paper, we extend our previous work to quantitatively analyze the CO_2 migration morphology and the spatial and temporal evolution of trapping forms with/without heterogeneous capillary pressure and geochemical reaction. Then we analyze the changes of CO_2 storage and migration under different sensitivity parameters.

Considering the actual CO_2 storage in the saline aquifer, the area centered on the vertical injection well is selected as the research object. In order to improve the storage efficiency, we adopt the method of "low injection, make rise" to shoot holes in the bottom of the model (Fig. 1), so that CO_2 can fully contact and react with water and minerals [错误!未找到引用源。]. The study dimensions of the saline aquifer are 720 m × 120 m, with grid blocks of 1.8 m by 1.2 m length, thus involving 40,000 grid blocks. The saline aquifer is assumed to be located 1600 m below the surface with the pressure of 16 MPa and the temperature of 50 °C without temperature change. The salinity is 100,000 ppm, and the rest of the parameters are shown in Table 1.

Table 10 - Basic parameters of the geological model

Parameters	Value	Parameters	Value
Model size/m^2	720×120	The mean porosity	0.26
Grid block size/m^2	1.8×1.2	The mean permeability/mD	200
Grid block quantity	40000	The Vertical mean permeability/mD	70
Top reservoir depth/m	1600	Capillary entrance pressure /kPa	8.12
Top reservoir depth /MPa	16	CO_2 injection rate /（m^3/year）	534
Reservoir temperature /℃	50	CO_2 injection time/year	5
Saltwater salinity /ppm	100000	Simulation time/year	100

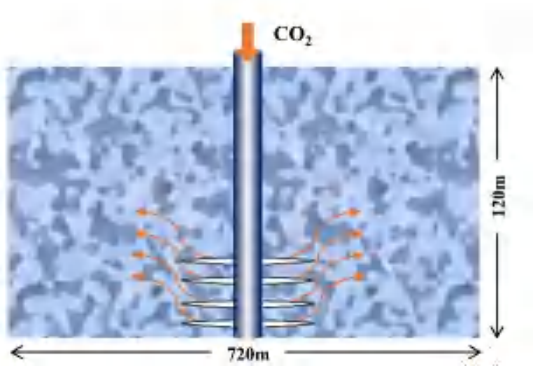


Figure 61 - Schematic diagram of CO_2 storage in saline aquifers

Conclusions

(1) The presence of heterogeneous capillary pressure reduces the rate of vertical CO_2 migration but expands the lateral sweep zone of gaseous CO_2. The geochemical reactions have little effect on gaseous CO_2 migration, but the geochemical reactions affect dissolved CO_2 migration,

resulting in a more homogeneous distribution and a larger ripple area. These reactions are insufficient to significantly change the physical properties of the reservoir and consequently do not have a substantial impact on CO_2 migration with 100 years.
(2) Higher capillary pressure magnitude and heterogeneity slow vertical migration of CO_2. The capillary pressure with a lateral correlation length severely restricts the vertical migration of CO_2, significantly expanding the lateral sweep zone. Higher reservoir temperature, injection rate, and k_v/k_h make CO_2 more likely to migrate across the local capillary barrier, accelerating vertical migration of CO_2. What's more, increased reservoir temperature accelerates the geochemical reaction rate and exacerbates porosity and permeability changes.
(3) Increased capillary pressure magnitude and heterogeneity increase local capillary trapping fraction. Capillary pressure with lateral correlation length increases local capillary, dissolution, and mineral trapping, enhancing the security of storage. More gaseous CO_2 is converted to dissolution by increasing density convection with increasing reservoir temperature, injection rate, and k_v/k_h. Therefore, for long-term safety, high reservoir temperature, and k_v/k_h are more favorable to storage CO_2. If local capillary trapping and short-term storage are considered, those with high capillary pressure and heterogeneity may be preferable.

References

[1] Saadatpoor E, Bryant S L, Sepehrnoori K. Effect of capillary heterogeneity on buoyant plumes: A new local trapping mechanism[J]. Energy Procedia, 2009, 1(1): 3299-3306.
[2] Trevisan L, Krishnamurthy P G, Meckel T A. Impact of 3D capillary heterogeneity and bedform architecture at the sub-meter scale on CO_2 saturation for buoyant flow in clastic aquifers[J]. International Journal of Greenhouse Gas Control, 2017, 56: 237-249.
[3] Cui G, Hu Z, Wang Y, et al. Migration characteristics and local capillary trapping mechanism after the CO_2 leakage out of saline aquifers[J]. Fuel, 2024, 356: 129347.
[4] Ren B, Sun Y, Bryant S. Maximizing local capillary trapping during CO_2 injection[J]. Energy Procedia, 2014, 63: 5562-5576.

Experimental study of monitoring fluid migration in CO_2 reservoir by fiber optic strain sensing

Jintao Xu, Menglan Shi, Chunlai Li, Boran jia, Lanlan Jiang*, Mingjun Yang, Yongchen Song

Key Laboratory of Ocean Energy Utilization and Energy Conservation of Ministry of Education, Dalian University of Technology, Dalian 116024, China

Abstract

To ensure the safety of carbon dioxide geological storage, effective monitoring of pore pressure, reservoir deformation, and fluid plume migration is essential. An innovative monitoring method based on a Distributed Fiber Optic Sensing System (DFOSS) is employed to real-time monitor the strain response distribution induced by fluid injection. Three experiments monitoring the distribution of reservoir strain field under different injection rates are designed. The results demonstrated that the DFOSS accurately captured the reservoir expansion deformation induced by fluid injection. The maximum expansion strain in the high injection rate experiment group (114.75με) is significantly higher than that in the low injection rate group (68.9με). The time for the wetted phase interface to break through the sensing position was accurately captured in the three experimental cases, which were 12.94, 3.85 and 1.71 min, respectively, coinciding with the injection rate trend. The obtained data and conclusions are meaningful for further enhancing the application capability of DFOSS in reservoir monitoring for CCS (Carbon Capture and Storage) projects.

Keywords: Fluid Migration; Carbon Capture and Storage; Fiber Optic Sensing; Strain Response;

Introduction

Climate change is one of the greatest challenges facing the world today, yet ensuring energy accessibility to maintain people's quality of life and economic development is equally important. Currently, fossil fuels account for approximately 80% of global primary energy demand, with the CO_2 they produce being the main cause of global warming, and the energy sector remains one of the major sources of CO_2 emissions [1]. Due to differences in the transition ability of different energy sectors, renewable energy cannot completely replace fossil fuels on a large scale. Therefore, alternative technologies that can replace current production techniques have not yet reached the required scale, and existing technologies will continue to be used in short to medium term [2]. In this context, Carbon Capture and Storage (CCS) technology is almost the only solution to meet current needs, which can buy necessary time for the development of alternative energy sources. The emergence and progress of CCS technology have added confidence and hope for carbon neutrality in the energy system.

As an integral part of CCS, CO_2 geological storage technology is gradually being recognized as the optimal choice for permanent storage due to its abundant reserves and wide distribution [3]. Throughout the entire process from CO_2 injection to stable storage, both the reservoir and artificial facilities (such as injection wells, monitoring wells, samplers, etc.) are constantly disturbed by fluid flow and phase change. In particular, fluid injection leads to increased reservoir pressure, which may induce geological deformation or cap rupture, creating or reactivating fractures. These CO_2 leakage risks have led to widespread concern and discussion on the integrity of underground reservoirs and related seismic activities [4]. In order to alleviate public concerns and ensure storage safety, monitoring technologies for CO_2 geological storage have emerged, which are crucial for reducing the risks of CO_2 storage and understanding various aspects such as reservoir response and CO_2 migration [5]. Currently, there are various monitoring technologies developed for the above-mentioned issues, but there are still challenges in current monitoring tasks. These technologies often find it difficult to directly track the diffusion process of CO_2 in underground reservoirs. Performing in-situ permanent

real-time monitoring in large-scale geotechnical engineering projects is also difficult [6]. Moreover, accurately monitoring the behavior of injected CO_2 has always been a challenge, whether in deep locations and large storage sites or laboratories. The complexity and invisibility of underground storage environments make accurate observation and measurement more difficult. In addition, the heterogeneity of underground environments and the complexity of porous media increase the complexity of monitoring [7]. Distributed Fiber Optic Sensing System (DFOSS) based on strain response may be an ideal choice for such monitoring projects. It can real-time monitor the geological mechanical properties, fluid state, and migration underground, providing researchers with more direct data and effectively ensuring geological safety. Currently, there are also some related attempts to apply fiber optic sensing technology to monitoring in CCS projects, and the results showed that distributed fiber optic sensing technology has great potential for monitoring reservoir deformation states and tracking CO_2 plumes in key areas [8].

In this study, to real-time detect the strain response distribution caused by fluid injection, the DFOSS system was used to measure the strain response of rocks during fluid displacement. Three sets of experimental cases were designed to study the distribution of reservoir strain fields under different injection rates. The strain history of rocks during dynamic displacement processes was analyzed to accurately capture real-time information on two-phase motion. These fundamental findings may help further understand whether deformations caused by fluid injection can be used to monitor and characterize the migration process of multiphase fluids within reservoirs.

Methodology

2.1. Experimental Materials

A simplified schematic diagram of the core displacement system is shown in Figure 1. The core holder in the system can accommodate rock samples with a maximum length of 70 mm and a diameter of 25.4 mm, capable of pressures up to 15 MPa. Cylindrical rock samples are placed in the core holder, with the upper and lower ends of the core connected to the inlet and outlet, respectively. Two high-precision injection pumps (Model 500X, Teledyne Isco Inc.) are connected to the inlet of the core holder to inject two-phase fluids. Two pressure sensors (GE DRUCK) are connected to the inlet and outlet of the holder to measure pressure. The full-scale accuracy of the pressure sensors is 0.4% (±100 kPa), with a measurement range of 25 MPa. The confining pressure is controlled by an injection pump (Model 500X, Teledyne Isco Inc.). The outlet is connected to a backpressure regulator (model K93 series, Xiongchuan) to control the effluent pore pressure, maintaining a constant pressure inside the sample with an accuracy of 0.5%. The Optical Distributed Sensing Interrogator (ODiSI-6100, Luna Innovations Inc.) measures the reflected waveform signals of the measurement channels, then outputs and saves the strain response values in real-time on the controller. Injection pressure is also recorded and controlled using ADAM equipment and the MCGS software package on another computer.

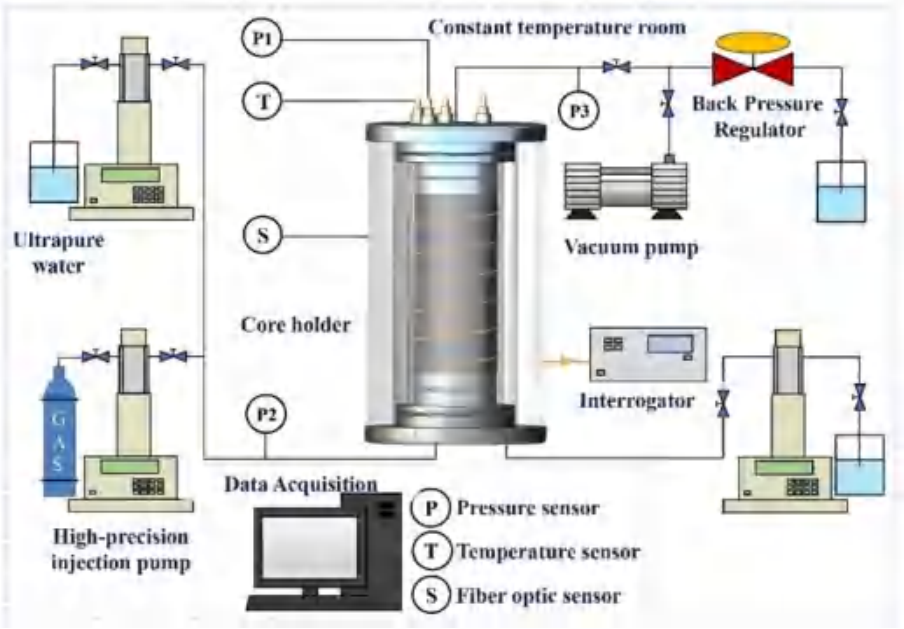


Figure 1 Core Flooding Fiber Monitoring Experiment Diagram

N_2 with a purity of 99.9% was selected as the experimental gas to avoid significant dissolution between wetting/non-wetting phases during the displacement process. Ultra-pure water with a resistivity of 18.5 MΩ·cm was used to prepare the base solution for all experiments and was prepared by a deionizer (Aquapo 2S, Chongqing Changrong, China).

Natural low-permeability Berea sandstone (Northern Ohio, USA) was used. Berea sandstone and core samples are widely used in testing, simulation, and other experiments in fields such as petroleum, exploration, and chemistry due to their good homogeneity and stability. The core sample is 57.7 mm long and has a diameter of 25.2 mm, with axial parallel bedding structures. To measure rock deformation, a single-mode quartz fiber was spirally wound around the core sample, and the fiber sensor itself and the contacting part of the core were coated with two-component epoxy resin. Before the epoxy resin completely solidified, the fiber was constantly subjected to a pre-tension force of about 2 N to ensure sufficient conformity with the sample surface and avoid fracture during sample deformation. After curing for 24 hours, single-component silicone rubber was uniformly applied to the column surface of the core to isolate the pore and confining pressure media while leading out the fiber optic sensor.

2.2. Experimental Procedure

The encapsulated sample is installed into the core holder, and the fiber optic is carefully threaded through the high-pressure optical feedthrough and fusion spliced with the prepared fiber pigtail. The quality of the fiber optic signal is checked to meet the transmission requirements. Using the contact positioning function, six sensor units are manually selected as observation feature points on the fiber, and the spatial coordinates of these feature points relative to the sample are recorded. Then, the confining liquid is injected into the space between the sample and the core holder's confining shell, and the air inside is purged as thoroughly as possible. The sample is finely encapsulated to ensure good sealing between the fiber optic sensor lead-out portion and the pore fluid and confining fluid.

Before the experiment, the components of the pipeline are checked for leaks. A vacuum pump is connected to the core holder for at least 24 hours to evacuate all pipelines and rock samples. The confining medium is injected into the confining chamber, and controlled by an injection pump. Then, ultrapure water and N_2 are injected from the bottom of the core holder to fully saturate the sample. The pore fluid is pressurized by a high-pressure pump to the selected pressure, stabilized for 24 hours to fully saturate the core, and establish adsorption equilibrium,

while simultaneously increasing the confining pressure to ensure it is greater than the pore pressure.

Displacement experiments are designed at three injection rates to investigate the effects of different flow rates on strain response. Since fiber optic sensors are sensitive to both temperature and stress, to prevent temperature changes from affecting strain measurements, all equipment is placed in a closed room maintained at 25°C by a large constant temperature device. Results from a temperature sensor placed at the center show that the ambient temperature varied within ±0.3°C during the experiment period, which can be considered negligible for the experimental results.

Results and Discussion

3.1. Strain field history analysis of Gas/Water displacement

As the wetting front of the two-phase fluid moves into the sensing area, it causes a wide range of spectral changes reflected in the strain response, resulting in strain responses at the selected observation points. Figure 2 presents the time-varying heatmap of the strain field distribution during the displacement process. The vertical axis in the image represents the number of the distributed sensor sensing units, and at the selected time, the image in the vertical direction shows the strain field distribution of the sensing area at that moment. For an individual sensing unit, the horizontal axis can display the strain history of that sensing unit throughout the entire period.

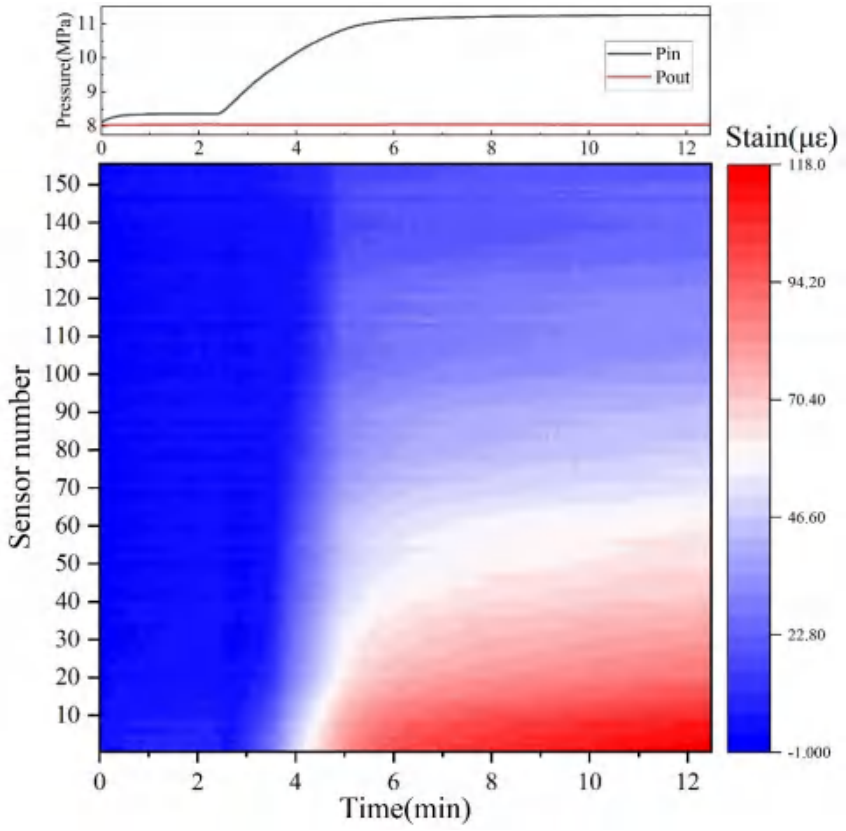


Figure 2 Time-varying hot map of strain field distribution in the displacement process

As shown in Figure 2, the history of the entire strain field exhibits good consistency with the variation of inlet and outlet pressures. Following the commencement of injection, the interval with the highest strain response consistently remains on the inlet side of the core and gradually attenuates along the direction of fluid displacement. The inlet pressure continues to rise as the fluid enters, and the strain response also increases, reaching approximately 120 microstrains at 12 minutes. This increase in strain is controlled by the increase in pore pressure induced by the poroelastic effect.

3.2. Influence of Injection Velocity on Strain Response

Figure 3 illustrates the time-varying curves of strain responses at surface feature points of the core under different injection velocities. As shown in Figure 3d, the observation points are evenly distributed in the same direction on the surface of the core, which is very suitable for interface resolution during the advancement of the wetting phase interface. From Figure 3, it can be observed that after fluid injection, the selected six observation points produce strain responses sequentially. The maximum rock expansion strain of the high injection velocity experimental group (114.75 με) is significantly higher than that of the low injection velocity experimental group (68.9 με). When the wetting front of the two phases moves into the sensing area, the spectrum undergoes a wide range of changes, manifested as a rapid increase in strain values. Information about the front position can be obtained through the rapid change in strain values at the sensing points. The distributed fiber optic technique could be used in fluid flow monitoring to accurately characterize the position and moving velocity of the two-phase front. When the wetting front moved into the sensing region, six selected observation points successively generated strain responses. Taking the response time of strain generation at point a as time = 0, the time of strain generation at point f in the three cases is 12.94, 3.85 and 1.71 min, respectively. High-precision optical sensing offers the possibility to accurately analyze the history of the strain field distribution in the core displacement process, as well as the relationship between the sensing units and the location of the wetting front. This capability is essential for capturing detailed information on the displacement front interface.

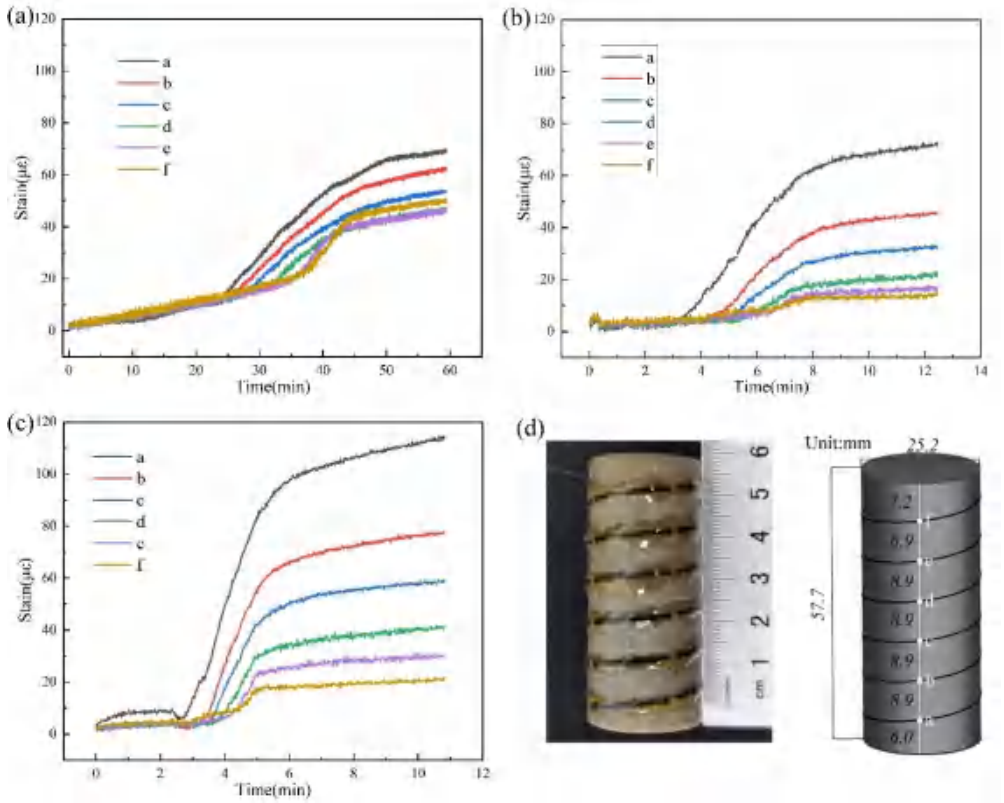


Figure 3 Strain response curve of core surface feature points with time (a)0.1ml/min (b) 0.1ml/min (c) 0.1ml/min (d) sensor feature points

Conclusions

In this study, a high-resolution distributed fiber optic strain measurement system was used to monitor the distribution of strain responses induced by fluid injection during CO_2 storage. The distributed fiber optic sensors were spiral-mounted on the surface of rock core samples, resulting in an approximate circumferential strain at that point and forming a strain field at the core scale. The analysis of experimental results leads to the following conclusions:

1. The distributed fiber optic strain sensing system accurately captures the reservoir expansion deformation induced by fluid injection and rock strain is consistent with pressure changes. The highest strain response range always occurs on the inlet side of the core and gradually attenuates along the gradient of fluid flow direction.
2. The maximum rock expansion strain of the high injection velocity experimental group (114.75 με) is significantly higher than that of the low injection velocity experimental group (68.9 με).
3. After fluid injection, the selected six observation points produced strain responses sequentially, and information about the front position was accurately obtained by the rapid change of the strain value at the induction point, which is consistent with the trend of the fluid injection rate.

The distributed fiber optic system demonstrates great potential in detecting rock deformation induced by fluid injection. This study contributes to the application of near-field monitoring technology from laboratory scale to CCS sequestration sites.

Acknowledgements

This study has been supported by the National Key Research and Development Program of China for Young Scientists (Grant No. 2023YFB4104100), National Natural Science Foundation of China (Grant 52176057), National Key Research and Development Program of China (Grant No. 2023YFB4104201), Excellent Youth Foundation of Liaoning Province (Grant 2022YQ-12), Shenzhen Science and Technology Program (No. JCYJ20220818095605012). Meanwhile, it was also supported by the Young Changjiang Scholars programme of China.

References

[1] J.D. Colgan, International Energy Agency, GPPi Policy Paper No. 6 (2009).

[2] C.-F. Schleussner, J. Rogelj, M. Schaeffer, T. Lissner, R. Licker, E.M. Fischer, R. Knutti, A. Levermann, K. Frieler, W. Hare, Science and policy characteristics of the Paris Agreement temperature goal, Nature Climate Change, 6 (2016) 827-835.

[3] M. Arens, M. Åhman, V. Vogl, Which countries are prepared to green their coal-based steel industry with electricity?-Reviewing climate and energy policy as well as the implementation of renewable electricity, Renewable and Sustainable Energy Reviews, 143 (2021) 110938.

[4] M.D. Aminu, S.A. Nabavi, C.A. Rochelle, V. Manovic, A review of developments in carbon dioxide storage, Applied Energy, 208 (2017) 1389-1419.

[5] J. Rutqvist, C.-F. Tsang, Coupled hydromechanical effects of CO_2 injection, Developments in Water Science, 52 (2005) 649-679.

[6] T.D. Rathnaweera, P. Ranjith, M.S.A. Perera, S. Yang, Determination of effective stress parameters for effective CO_2 permeability in deep saline aquifers: An experimental study, Journal of Natural Gas Science and Engineering, 24 (2015) 64-79.

[7] R. Arts, O. Eiken, A. Chadwick, P. Zweigel, L. Van der Meer, B.J.E. Zinszner, Monitoring of CO_2 injected at Sleipner using time-lapse seismic data, Energy, 29 (2004) 1383-1392.

[8] D. Vasco, A. Rucci, A. Ferretti, F. Novali, R. Bissell, P. Ringrose, A. Mathieson, I. Wright, Satellite-based measurements of surface deformation reveal fluid flow associated with the geological storage of carbon dioxide, Geophysical Research Letters, 37 (2010).

Study on the influence of heterogeneity of porous media on CO_2 immiscible displacement in pore scale

Minfeng Li, Shuyang Liu*, Hangyu Li
School of Petroleum Engineering, China University of Petroleum (East China), Qingdao 266580, China;
* Corresponding Email address: shuyang_liu@126.com (S. Liu).

Abstract
Enhanced oil recovery with CO2 (CO2-EOR) is a green and promising technology that can improve crude oil recovery rates while reducing carbon emissions. The micro-pore structure of porous reservoirs has a significant impact on the effectiveness of CO2-EOR, making research in this area of great importance. In this study, a numerical simulation of CO2 immiscible displacement in the micro-scale two-phase flow within porous media was conducted based on the coupling of the N-S equations and phase-field method. From the perspective of the impact of heterogeneity in porous media, the study investigated the influence of heterogeneity of porous media on the shape and stability of the CO2-oil displacement front, type and spatial distribution of residual oil under different capillary numbers. The results indicate that under neutral wetting conditions ($\theta=\pi/2$) and low capillary numbers (logCa=-6.253), the heterogeneity in porous media enhances the curvature of the interface, leading to increased instability of the displacement front. As heterogeneity increases, the influence of capillary number on the displacement front, various types of residual oil, spatial distribution, and breakthrough time in the model become less significant. In models with weak heterogeneity ($\sigma=0.004$), the ultimate oil recovery at breakthrough generally increases with the increase in capillary number. In models with strong heterogeneity ($\sigma=0.008$ and $\sigma=0.012$), the presence of preferential pathways causes the ultimate oil recovery at breakthrough to decrease with the increase in capillary number.
Keywords: CO2 immiscible displacement, pore scale, heterogeneity, capillary number

Pore-scale study of mineral dissolution-precipitation during saline aquifer storage

YE Hang, LIU Qi*, MICHELLE Tiong
National Key Laboratory of Petroleum Resources and Engineering, Unconventional Petroleum Research Institute, China University of Petroleum-Beijing, Beijing 102249, China

Introduction

Saline aquifer CO_2 geological storage, as a pivotal component of Carbon Capture, Utilization, and Storage (CCUS) technology, is considered as an effective means to achieve carbon neutrality goals. However, uncertainties persist regarding the characteristics of CO_2-rock-H_2O interactions under reservoir pore conditions, as well as the kinetic mechanisms of mineralization reactions. Additionally, geochemical reactions may lead to solid particle transport and deposition, potentially causing pore throat occlusion. Pore-scale study of mineral dissolution/precipitation is of significant importance for elucidating the physical-chemical mechanisms occurring at the fluid-solid interface and understanding the coupled dynamics of geochemical reactions and fluid transport.

Methodology

Pore-scale mineral dissolution-precipitation experiments were conducted using a microfluidic device, capable of reaching pressures up to 15 MPa and temperatures up to 80℃ to meet diverse CO_2 phase requirements. The microfluidic chip model was loaded into a specially designed high-pressure chamber with a visual unit, enabling dynamic visualization through an inverted microscope system that included a fluorescence module. SEM-BSE and EDS were employed to characterize the elemental distribution and mineral composition of each sample before and after the reactions. Throughout the dissolution-precipitation experiments, quasi-2D surface changes in cracks were determined based on microscopic images.

Results and Discussion

The results indicated that mineral dissolution alters the pore structure by enlarging pore throats and reducing the specific surface area, leading to changes in relative permeability. This positive feedback loop may enhance the permeability and expose fresh surfaces to the fluid phase, thereby promoting mineralization reactions. Time-resolved images of the rock revealed the spatiotemporal dynamics of dissolution, including real-time two-phase flow effects, highlighting variations at crack interfaces within different compositional ranges. The microfluidic results indicated that the exposure of non-active particles, fracture morphology, and rock strength loss strongly depended on the relative volume and distribution of active particles. Additionally, the growth of secondary minerals or nanoalteration layers was observed, which can impede transport near the fluid-solid interface in multi-mineral rocks, thereby constraining the overall reactivity of the carbonate matrix.

Conclusions

Utilizing a microfluidic experimental platform based on real rock samples, we observed in real-time the mineral dissolution and crystallization processes within porous media at the pore scale. The results indicated that the interactions between rocks and CO_2 fluid were intricate, dynamic, and contingent on the properties and morphology of the rock. This study provides a dynamic characterization approach for geochemical reactions, further enhancing our understanding of mechanisms in saline aquifer sequestration.

Keywords: dissolution; microfluidics; pore-scale; saline aquifer storage; CCUS

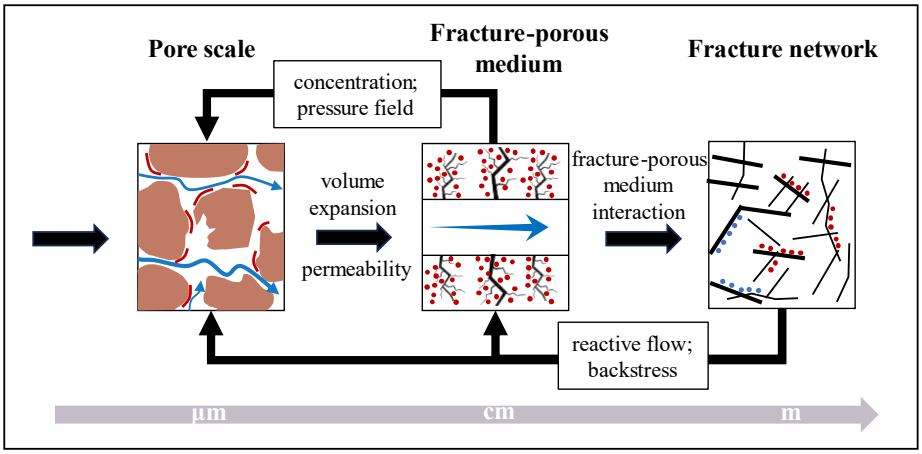


Fig 1 Interactions and multi-scale processes in mineral carbon storage

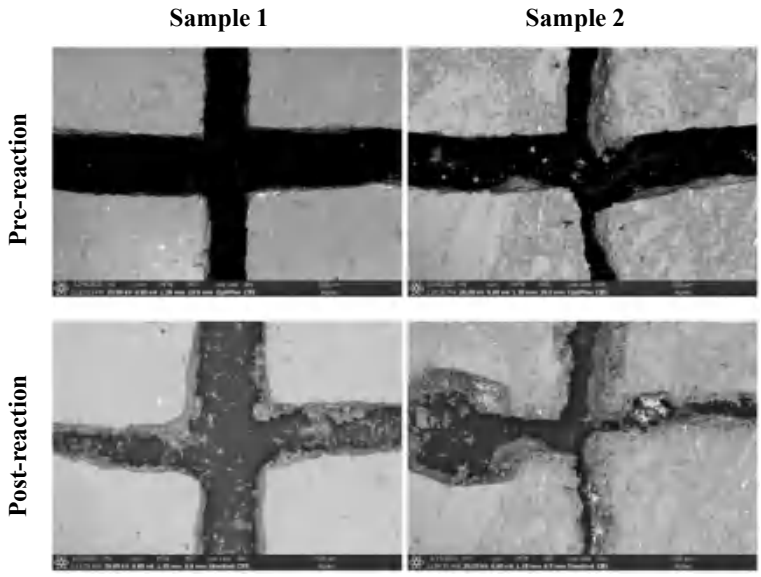


Fig 2 SEM-BES images before and after reaction

A Study on the Structural Characteristics and Transport Properties of Porous Media based on Fractal Geometry and Deep Learning

Peng Xu, Lida Zhang, Zhili Cai, Zhuo Gong, Shuxia Qiu
China Jiliang University, Hangzhou, China

Abstract
The structural characteristics and transport properties of porous media take decisive role in a variety of industry processes including oil and gas flow in reservoirs, carbon dioxide capture and storage, heat and mass transfer in cooling and drying, ionic migration in electrode, adsorption and separation etc. With the development of deep learning method, it has been proposed and applied to improve the digital image resolution and predict transport properties of porous media. In this paper, a new super resolution generative adversarial network is developed to enhance the resolution of CT images of porous media. And a graph neural network is then trained based on results from the lattice Boltzmann simulation in order to predict the permeability of porous media.

Keywords: Porous Media; Super Resolution; Generative Adversarial Network; Graph Neural Network; Fractal Geometry; Permeability

Introduction

The characterization of microstructures and prediction of properties of porous media are significant in the fields of energy, environment and chemical industry. Although the development of digital image technology has realized the direct visualization and quantification of pore structures, the accuracy is generally limited by the experimental methods and equipment resolution. And the numerical methods to study the transport process through porous media also confront a few challenges such as consumption of computing resources, reliance on empirical data, nonlinear and multiphasic coupling etc. The artificial intelligence bring a new window for fine characterization and reconstruction, and fast and accurate prediction of transport properties of porous media [1,2].

Methodology

A new super resolution generative adversarial network (SRGAN) is developed to reconstruct the texture structure in CT images of porous media and enhance image resolution. HRNet is sued as the generator, and the feature layers of different dimensions are extended to the same dimension after parallel calculation to generate super-resolution images. Both the porosity and pore fractal dimension are introduced to evaluate the reconstructed porous media images. With processed CT images and lattice Boltzmann method, the single phase fluid flow through porous media are simulated. And then, a graph neural network (GNN) is trained to predict the effective permeability of porous media. The training and testing sets in SRGAN contain 9,600 and 1,200 2D images of carbonate, sandstone and fractured coal, respectively. While 1000 processed images and permeability are used in GNN.

Conclusions

The experimental results show that the proposed SRGAN can effectively deblur low-resolution images of μ-CT images, recover the texture details, and exhibit a certain level of generalization ability. The effective permeability of porous media can be fast predicted by GNN, and the accuracy of which is higher than that of CNN. The present method indicates great potential in multi-scale and complex porous media.

Acknowledgements

This work was jointly supported by the National Natural Science Foundation of China through grant number 52376079 and Zhejiang Provincial Natural Science Foundation of China through grant number LZ24E060002.

References

[1] H. Zhang, et al. Fast and accurate reconstruction of large-scale 3D porous media using deep learning. Journal of Petroleum Science and Engineering 217 (2022) 110937.
[2] K.M. Graczyk, M. Maciej Predicting porosity, permeability, and tortuosity of porous media from images by deep learning. Scientific Reports 10 (2020) 21488.

Dynamic behavior of the oil-air interface in a hard disk drive' spindle under centrifugal force or axial shock

Qing Liu[a*], Ming Feng[a], Shuochong Hao[a], Ruihuan Ge[b]
[a]School of Mechanical Engineering, University of Science and Technology Beijing, Beijing 100083, China. [*]Email: qingliu@ustb.edu.cn
[b]Department of Chemical and Biological Engineering, The University of Sheffield, Sheffield S10 2TN, UK

Abstract
In this paper, the oil leakages of fluid dynamic bearings (FDBs) spindles with a surface tension sealing structure in a hard disk drive under axial shocks are analyzed. The two-phase flow of air and oil in FDBs is simulated by applying the finite volume method, volume of fluid, and dynamic mesh technique to analyse the anti-shock capacity during and after axial shock. The results are of great importance for optimal design of the sealing structure in hard disk drive FDB spindles.

Keywords: Two-phase flow, Oil leakage,
Surface tension, Non-contact sealing, Fluid dynamic bearings

Introduction

Fluid dynamic bearings (FDBs) have been mostly utilized in the hard disk drives' (HDD) spindle motors for the better dynamic and tribological characteristics than conventional bearings [1-2]. The sealing technology is one of the critical issues concerning stable operations [3]. The surface tension seal (STS) has been widely adopted in FDBs in light of its reliable, economical and compact characteristics. Concerning the requirements of high reliability, long lifespan, and high-density memory storage in HDDs that are often applied to computer servers, the oil leakage of the FDBs in the HDDs caused by external shock is an important issue in industry [4].

Methodology

Fig. 1 demonstrates the schematic of a HDD FDB spindle motor with the axial STS configuration. The FDB spindles have two radial and one axial hydrodynamic bearings. Sealing failure mainly claims for the FDBs' wear and lifespan deterioration. The STS failure is defined by the air-oil interface breakup in the sealing clearance in case that a shock and/or centrifugal force exceed their limits. Here, the shock acceleration which results in the interface breakup and oil leakage are figured out by the computational fluid dynamic analysis.

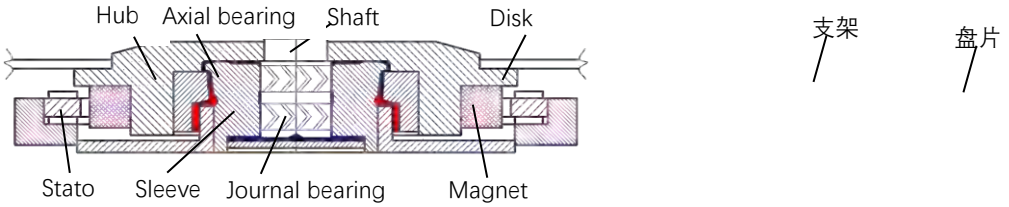


Fig 1. Schematic of axial surface tension seal in HDDs (Blue:oil, Red:air)

张力密封结构

A shocking course can be modeled as a half sinusoidal wave acceleration with a certain initial drop velocity applied to the spindles, which can be expressed as:

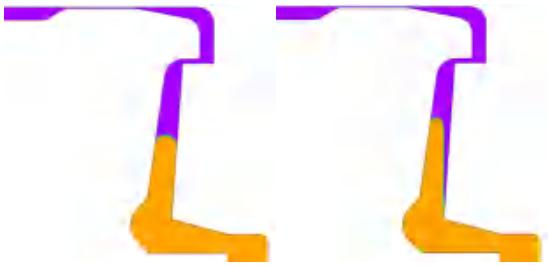
$$\sum F_Z = -m(xg)\sin \omega t \quad (1)$$

where x is shock magnitude to gravity.

Table 11 - Properties of fluid lubricant (20°C)

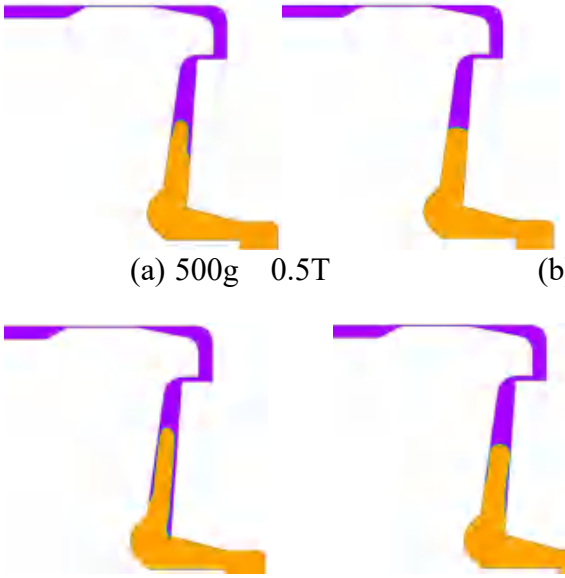
Parameter	Value
Oil density	860 kg/m^3
Oil viscosity	0.034 Pa·s
Air density	1.3 kg/m^3
Surface tension coefficient of oil and air	0.04 N·m
Static contact angle of wall	10°

Figure 2 shows the shape changes of the oil-air interface of the sealing structure under no impact conditions of 5400 r/min and 18000 r/min. It can be seen that as the centrifugal force rises, the deformation length of the tension sealing interface increases along the wall.



(a) 6000 r/min (b) 18000 r/min

Fig 2. Changes in oil-air interface of axial sealing structure under centrifugal force



(a) 500g 0.5T (b) 500g 2T

(c)1500g 0.5T (d) 1500g 2T

Fig 3. Changes in oil-air interface shape of the sealing structure under 500G and 1500G impacts (5400r/min)

Figure 3(a-b) show the oil-air interface change process of the sealing structure under 500G impact at a rated speed of 5400r/min, and the final sealing interface returns to its original shape without any leakage. Figure 3(c-d) show the oil-air interface change process of the sealing

structure under 1500G impact at the rotating speed of 5400r/min. The final sealing interface cannot recover its shape before the impact, and the sealing interface ruptures, resulting in oil leakage.

Conclusions

This paper analyses the effect of the centrifugal force and the axial shock on the oil-air interface of the surface tension sealing structures. The results can support for the design of surface tension sealing structures in hard disk drive' spindles.

Acknowledgements

The authors are grateful for the support of Fundamental Research Funds for the Central Universities (Grant No. FRF-TP-22-034A1).

References

[1] W.C. Blount . Fluid dynamic bearing spindle motors: Their future in hard disk drives. White Paper published by Hitachi Global Storage Technologies, San Jose, CA; 2007.

[2] Bouchard G, Lau L, Talke FE. An investigation of non-repeatable spindle runout. IEEE Trans Magn 1987;23(5):3687-9.

[3] Feng M, Li C, Characteristics of Axial and Radial Surface Tension Sealing Structures for HDD FDB Spindles. IEEE Transactions on Magnetics, 2013; 49(6): 2521-5.

[4] C Kang, Y Jung, J Lee, M Lee, B Kim, G Jang, Dynamic behavior of air-oil interface in fluid dynamic bearings with a double sealing structure in a 2.5'' hard disk drive due to non-operating axial shock, Tribology International, 2016; 98: 306-16.

Study on Characteristics of Hydrate-based CO_2 Sequestration in Marine Sediments

Weixin Pang[1, 2], Shouwei Zhou[1, 3], Qingping Li[1, 2], Yang Ge[1, 2], Huiyun Wen[1, 2], Mingqiang Chen[1, 2, 3], Xiaohan Zhang[1, 2, 3]
[1]State Key Laboratory of Offshore Natural Gas Hydrate, Beijing, China
[2]Research Institute of China National Offshore Oil Cooperation, Beijing, China
[3]Huairou Laboratory, Beijing, China

Abstract
Hydrate-based CO_2 sequestration in marine sediments possesses the advantages of good stability, widespread distribution of storage sites, and immense potential. From the perspective of field operations, this study investigated the impact of key factors such as injected CO_2 forms (liquid, supercritical state, emulsions), well patterns, and CO_2 injection layers on characteristics of CO_2 transport and hydrate formation in marine sediments during hydrate-based CO_2 sequestration. The findings provide valuable guidance for hydrate-based CO_2 sequestration in marine sediments in field scale.

Key words：CO_2 hydrate, Solidification, Injected CO_2 forms, Permeability, CO_2 injection layers

Introduction

Hydrate-based CO_2 sequestration in marine sediments is a novel form for CO_2 geological storage, which holds great stability and potential [1-3]. In this work, the effect of CO_2 injection forms and multiphase flow characteristics on CO_2 hydrate formation regularity in marine sediments was firstly studied. Afterward, the impact of CO_2 injection well patterns on CO_2 sweep efficiency and sequestration effectiveness was analyzed. Furthermore, the effectiveness of hydrate-based CO_2 sequestration at different CO_2 injection layers was evaluated. This study provides novel insights and valuable guidance for the on-site implementation of hydrate-based CO_2 sequestration in marine sediments.

Methodology

This study respectively employed the 3D experimental apparatus with varying scales to investigate the influence of key factors including CO_2 injection forms, well patterns, and injection layers on CO_2 transport properties and the effectiveness of hydrate-based CO_2 sequestration.

The experiments of hydrate-based CO_2 sequestration with different CO_2 injection forms indicated that the injected CO_2 exhibits different transport behavior in the sediment. CO_2 noticeably moves upward with the injection form of liquid and supercritical stated due to low density, whereas CO_2 emulsions demonstrate superior flow properties and seep efficiency. Under the experimental condition in this study,

the injected CO_2 forms are respectively arranged as emulsions, liquid and supercritical state according to hydrate-based sequestration effectiveness from good to poor. However, the injection pressure of CO_2 emulsions is high and prone to resulting in blockage in the area with large CO_2 hydrate saturation. In addition, the cost of preparation and injection of CO_2 emulsions is relatively high. As a result, liquid CO_2 form is more proposed when injecting CO_2 in the layer which is suitable for CO_2 hydrate formation. When injecting CO_2 into the layer underneath the CO_2 hydrate stability zone, the injected CO_2 forms of liquid, supercritical state and emulsions can all be taken into consideration in terms of the actual temperature and pressure of the target zone.

The experimental apparatus with the volume of 1.8 L and 1695 L were respectively employed to investigate the impact of injection well patterns on CO_2 sequestration effectiveness. The

results showed that there were more advantages in the effectiveness of CO_2 injection and hydrate-based sequestration with horizontal wells than vertical ones. The area of CO_2 dispersion is larger, and CO_2 hydrate formation is more uniform. The leakage risk of CO_2 is reduced, and pressure propagation in the sediment is also improved. Through opening side holes in the horizontal wells, the risk of CO_2 injection blockage can be reduced, further enhancing CO_2 sequestration potential. Meanwhile, CO_2 hydrate conversion rate is almost the same in the experiments with different scales, with no amplification effect observed.

The results of the injection layer effect on hydrate-based CO_2 sequestration illustrated that the storage efficiency of CO_2 is better in underlying layers compared to overlying ones. The optimal CO_2 sequestration effectiveness can be achieved by first synthesizing a tight sealing cap layer through hydrate before CO_2 injection.

Additionally, it is found that CO_2 injection rate and reservoir characteristics also significantly influence CO_2 hydrate formation and the sequestration effectiveness.

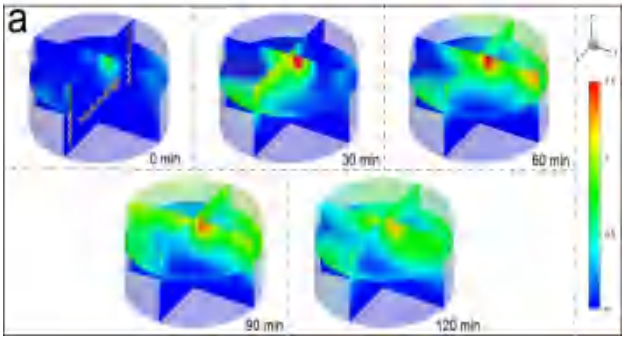


Figure 62 - Liquid CO_2 flow and hydrate formation characteristics in the sediments

Conclusions

The findings suggest that different CO_2 injection forms possess a certain influence on CO_2 hydrate formation and sequestration effectiveness in marine sediments while the detailed selection should be made based on the actual conditions of the target sequestration area. CO_2 hydrate nucleation is fast in the experiments, but there exists a "comfort zone" within the sediments suitable for CO_2 hydrate growth. Excessive or insufficient driving force for hydrate formation both result in a decrease in the density. The flow characteristics and sweep efficiency of CO_2 ultimately determine the effectiveness of hydrate-based CO_2 sequestration in marine sediments.

Acknowledgements

The work is financially supported by Research on Hydrate-based CO2 Sequestration Technology in the marine sediments (KJGG-2022-12-CCUS-0302).

References

[1] Almenningen S, Gauteplass J, Fotland P, Aastveit G, Barth T, Ersland G, Visualization of hydrate formation during CO_2 storage in water-saturated sandstone, International Journal of Greenhouse Gas Control,79(2018) 272-8.

[2] Tohidi B, Yang J, Salehabadi M, Anderson R, Chapoy A, CO_2 Hydrates Could Provide Secondary Safety Factor in Subsurface Sequestration of CO_2, Environmental Science & Technology, 44(2010) 1509-14.

[3] Gauteplass J, Almenningen S, Ersland G, Barth T, Yang J, Chapoy A, Multiscale investigation of CO_2 hydrate self-sealing potential for carbon geo-sequestration, Chemical Engineering Journal, 381(2020) 122646.

An improved model for heavy oil-water eccentric core annular flow in a horizontal pipe

Jie Sun[1,2], Yufan Yang[1], Shuyun Cui[1], Yu Zhu[1], Yuxin Zheng[1], Gaojun Shi[1]
1. School of Oil & Natural Gas Engineering, Southwest Petroleum University, Chengdu 610500, China
2. Oil & Gas Fire Protection Key Laboratory of Sichuan Province, Chengdu 611731, China

Abstract
Eccentric core-annular flow (ECAF) is encountered in water-lubricated transport of heavy oil in horizontal pipes. The core eccentricity results from the tendency of the phases to stratify due to a buoyant force that results from their different densities, whereby a shape of a circular core may not be maintained. To model such a flow configuration, an improved three-zone model is proposed based on the Two-Fluid approach. The model's performance was examined by comparing its predictions with a large data set of pressure gradient and water holdup values obtained under different experimental conditions. It is shown that the proposed model enables better agreement with the data available in the literature. Thus, the proposed approach appears to be a useful framework for modeling heavy oil-water eccentric core-annular flows. It can also be applied for other types of Newtonian/non-Newtonian or non-Newtonian/non-Newtonian liquid-liquid core flows encountered in industrial applications.

Keywords: Heavy oil, Eccentric core-annular flow, Pressure gradient, Two-fluid model

Introduction

With the depletion of conventional oil resources, unconventional heavy crude oil will be a strategic replacement resource for global oil development in the 21st century. The reserves of unconventional heavy crude, which are about six times that of conventional oil [1-2], will play an important role in the global energy market in the next few decades. The core-annular flow method for viscous oil transportation, where water flows in the annulus serves as a lubricant, has been considered one of the most economical, efficient and promising technologies. The present study aims to establish a new mechanistic model for predicting CAF characteristics in oil-water horizontal flow based on a three-zone configuration of ECAF and is likely to be more consistent with practical heavy oil-water CAF characteristics. The modeling efforts and comparative analyses suggest that the new modeling framework can provide a practical tool for reliable pressure gradient and water holdup predictions in realistic viscous oil-water ECAFs, as encountered in viscous oil production and transportation.

ECAF model

On the basis of the liquid-liquid concentric core-annular flow model developed by Brauner [3], we propose a more realistic model for predicting the pressure gradient of eccentric CAF with a non-circular shape of core phase as mentioned above. As shown in Figure 1, the dimensionless height of the lower water interface is $\tilde{h} = h/D$. Most of the water flows in a thick layer (of thickness $\tilde{h}_w = 1 - \tilde{h}$) at the bottom of the pipe (for oil lighter than water), while a thin water layer (of thickness $\tilde{\delta}'$, assumed constant) is maintained along the remaining pipe periphery and lubricates the oil flow. Accordingly, the cross-sectional area of the annular water phase is divided into two parts (A_{wh}, $A_{w\delta}$). Given the values of the film thickness $\tilde{\delta}'$ and the oil average velocity, $U_{o'}$, the average water velocity, $U_{w\delta}$, the corresponding wall shear stress, $\tau_{w\delta}$, and the interfacial shear stress, $\tau_{i\delta}$, in the film region can be assumed to be the same as those obtained in concentric core flow for the same input parameters (i.e., U_o, $\tilde{\delta}$). Note,

however, that the corresponding superficial velocities and the core flow cross-section area that are obtained in this case ($U_{os'}$, $U_{ws'}$, $A_{o'}$) are different from the superficial velocities and oil flow cross-section area in the considered concentric CAF configuration, (U_{os}, U_{ws}, A_o). The subscripts *o'* and *w'* refer to the oil and water phases in the ECAF configuration.

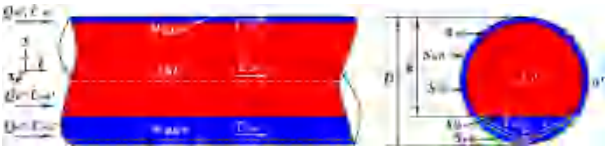


Figure 63-Schematic description of eccentric core annular flow configuration (note that $A_{w'} = A_{wh} + A_{w\delta}$ ***)***

Assuming a fully developed flow, the integral form of the momentum equations for the oil core and annular water phase are:

$$-A_{o'}\left(\frac{dp}{dz}\right) - \tau_{i\delta}S_{i\delta} - \tau_{ih}S_{ih} = 0 \qquad \text{oil} \qquad (1)$$

$$-A_{w'}\left(\frac{dp}{dz}\right) - \tau_{w\delta}S_{w\delta} - \tau_{wh}S_{wh} + \tau_{i\delta}S_{i\delta} + \tau_{ih}S_{ih} = 0 \qquad \text{water} \qquad (2)$$

where A, τ and S are the cross-sectional area, the shear stress and the wetted perimeter. *ih* and *iδ* refer to the two segments of the interface between the two phases, while *wh* and *wδ* refer to the pipe surface segments that are wetted by the annular lower layer and film region, respectively. $\tau_{w\delta}$, τ_{wh} are the wall shear stresses (i.e., opposite to the flow direction of the water phase), and $\tau_{i\delta}$, τ_{ih} represent the shear stresses exerted by the water phase on the oil core.

Results and discussion

Figure 2 shows the experimental data of Sotgia et al. [4] obtained in a 26 mm pipe and predicted values of the dimensionless pressure gradients, ϕ_{tp}^2 as a function of the Lockhart-Martinelli parameter χ^2 in eccentric CAFs. It is shown that when an ECAF configuration is considered, the predicted dimensionless pressure gradients (scaled with reference to single phase oil flow) are in the range of $0.01 < \phi_{tp}^2 < 0.07$, and are in good agreement with the measured values (relative errors in the range -9.43−2.83%.

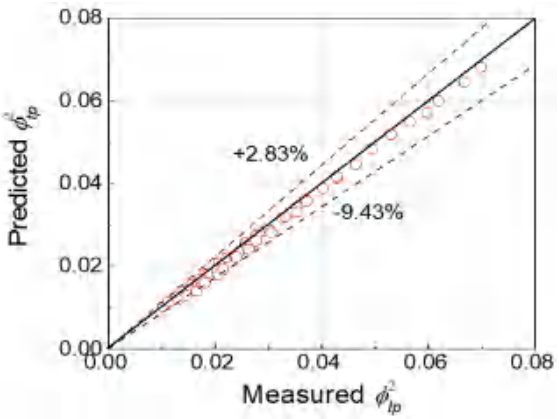


Figure 2-Comparison of the experimental and predicted dimensionless pressure gradients.

Figure 3 shows a comparison of the water holdups predicted by the present model with experimental data obtained under various operational conditions by Strazza et al. [5]. In general, good agreement is shown between the predicted water holdups and the corresponding data. The deviation between the data and the predictions of the present ECAF model is less than ±20%, where the model tends to underestimate the water holdup to some extent. It implies that the velocity of the water bottom layer is somewhat over predicted. This, in turn, should be attributed to some underestimation of the wall shear experienced by the turbulent bottom layer

(since the predictions are quite insensitive to the interfacial friction factor). Such underestimation may result from the assumption of a plane interface between the bottom layer and the oil-core (compared to the concave interface), and/or a higher wall friction factor than that introduced by the Blasius correlation.

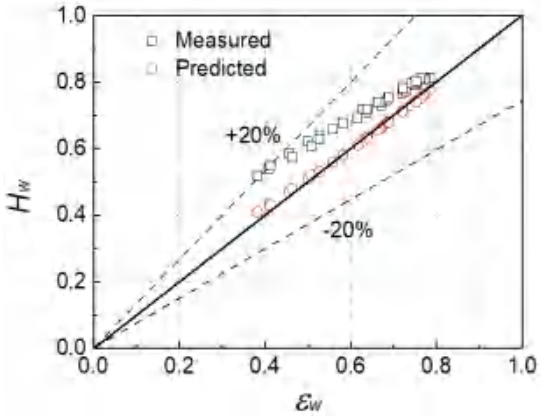


Figure 3-Comparison of predicted water holdups by the ECAF model with the experimental data from Strazza et al., μ_o =0.9 Pa·s, ρ_o=886 kg/m^3.

Conclusions

An improved three-zone mechanistic model for viscous oil-water core annular flow (CAF) in horizontal pipes was developed to account for the impact of oil core eccentricity and its non-circular shape. The model enables predicting essential flow characteristics of oil-water core flows, including pressure gradient, water holdup etc., over a wide range of operational conditions. The ECAF model relative prediction errors of the pressure gradients are basically within ±10%, while the predicted water holdups are also in reasonable agreement with the available data. The proposed ECAF model offers the flexibility of treating cases where the properties of the lubricating phase are different in these two regions. It can also provide a basis for the establishment of models for predicting the flow characteristics of other types of Newtonian/non-Newtonian or non-Newtonian/non-Newtonian two-phase flow encountered in actual applications.

Acknowledgements

This work is supported by the National Natural Science Foundation of China (Grant No. 52106208) and Natural Science Foundation of Sichuan Province (2023NSFSC0924).

References

[1] J. Liggio, S. Li, K. Hayden, et al., Oil sands operations as a large source of secondary organic aerosols, Nature 534(2016) 91-94.

[2] L. Hao, L. Cheng, S. Huang, et al., Evolution characteristics of SAGD steam chamber and its impacts on heavy oil production and heat consumption, International Journal of Heat Mass Transfer 121(2018) 579-596.

[3] N. Brauner. Liquid-liquid two-phase flow systems, in: Modelling and Experimentation in Two-Phase Flow. Springer (2003) 221-279.

[4] G. Sotgia, P. Tartarini, E. Stalio. Experimental analysis of flow regimes and pressure drop reduction in oil-water mixtures, International Journal of Multiphase Flow 34(2008) 1161-1174.

[5] D. Strazza, M. Demori, V. Ferrari, et al., Capacitance sensor for hold-up measurement in high-viscous-oil/conductive-water core-annular flows. Flow Measurement and Instrumentation 22(2011) 360-369.

Investigation into pore-scale multiphase reactive heat and mass transfer mechanisms during methane hydrate dissociation

Junyu Yang, Kai H. Luo
Department of Mechanical Engineering, University College London, Torrington Place, London WC1E 7JE, United Kingdom

Abstract

Methane hydrate is a promising source of alternative energy. An in-depth understanding of the hydrate dissociation mechanism is crucial for the efficient extraction. Methane hydrate dissociation is a typical multi-scale multiphysical process involving gas-water multiphase flow, interfacial mass transport of methane molecules, conjugate heat transfer between phases and heterogeneous dissociation reactions. These mechanisms are fully coupled within the complex sediment pore structure, determining the hydrate dissociation phenomenon, as shown in Figure 1. To gain a comprehensive understanding of the decomposition processes of hydrates within sediment reservoirs, it is necessary to look into the pore space and understand the synergistic competition mechanism between multiple physical processes in the multiphase system. In the present work, a comprehensive set of pore-scale numerical studies of hydrate dissociation mechanisms is presented. Pore-scale lattice Boltzmann (LB) models are proposed to simulate the multiphysical process during methane hydrate dissociation. The simulations employ the actual pore structure of hydrate sediments, as revealed by micro-CT imaging. These simulations are validated against experimental data from xenon hydrate dissociation, demonstrating the accuracy of the proposed LB models in capturing the evolution of hydrate pore habits. Additionally, the research explores methane hydrate dissociation under varying conditions of sediment water saturation, fluid flow rates, and thermal environments. Both heat and mass transfer constraints are found to significantly impact methane hydrate dissociation rates, with bubble movement further affecting the process. Dissociation patterns are categorized into uniform, non-uniform, and wormholing types. The study reveals that fluid flow impacts hydrate dissociation rates more diversely in three-dimensional real structures than in two-dimensional idealized models, due to variations in hydrate pore habits and flow properties. Upscaling investigations provide insights into permeability and kinetic models for the representative elementary volume (REV)-scale production forecasting. Notably, the three-dimensional upscaling results exhibit significant differences from previous two-dimensional findings, reflecting the variation in hydrate pore habits and dissociation mechanisms. This work sets a new benchmark for pore-scale numerical simulation studies on hydrate dissociation, offering theoretical guidance for efficient hydrate extraction.

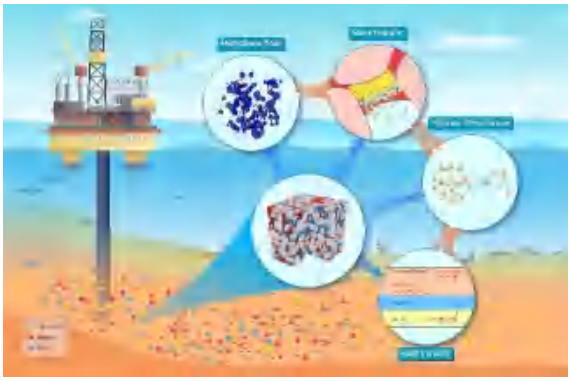


Figure 64 – Schematic of multiphysics processes during methane hydrate dissociation.

Keywords: Methane hydrate dissociation, Multiphase flow, Heat and mass transfer, Micro-CT image, Lattice Boltzmann method

Wettability effect on the two-phase flow-induced vibration in response to a micro-scale ⊥- shaped pipe

Zhicheng YUAN
Affiliations (Tongji University, Shanghai, China)

Abstract
Immersion lithography is a key technology for manufacturing advanced integrated circuits (IC). However, serious two-phase fluid-induced vibration can be brought about because of the gas-liquid extraction introduced by the dynamic sealing strategy. This work aims to the influence of surface wettability on the two-phase flow pattern and flow-induced vibrations (FIV). Simulations are conducted by using the open-source package OpenFOAM. To track the liquid-air interface, the volume of fluid (VoF) method based interFoam solver is selected, and its shipped dynamic contact angle model is modified to obtain better accuracy when considering the wettability of pipe's inner-surface. Then, the validated solver is extended to investigate the effect of wettability on flow pattern and FIV. The findings will provide effective technical support for the control of two-phase vibration in immersion lithography.
Keywords: Immersion lithography, Two-phase Flow-induced Vibration, interFoam solver

Acknowledgements
This research was supported by the Fundamental Research Funds for the Central Universities (10002150058).

Influence of the operation pressure on gas-liquid two-phase severe slugging flow in a pipeline-riser system

Yingjie Chang[1,2], Qiang Xu[2], Yubo Wang[3], Liejin Guo[2]

[1.]Shaanxi Key Laboratory of New Transportation Energy and Automotive Energy Saving, Chang'an University, Xi'an 710064, China;

[2.]State Key Laboratory of Multiphase Flow in Power Engineering, Xi'an Jiaotong University, Xi'an 710049, China;

[3.]School of Thermal Engineering, Shandong Jianzhu University, Jinan 250101, China.

Abstract

The pipeline-riser system in offshore oil and gas fields is crucial equipment to ensure safe flow within the pipes for economic development and marine ecological preservation. There are numerous studies on gas-liquid two-phase flow in pipeline-riser system under normal pressure, but only few studies on high pressure conditions. Compared to atmospheric conditions, increased pressure leads to greater gas density, which in turn affects the distribution characteristics of gas and liquid within the pipes. This paper conducted experiments on gas-liquid two-phase flow in a pipeline-riser system ranging from atmospheric pressure (1 bar) to 50 bar, with a horizontal pipe length of 314 m, a downward inclined pipe length of 25 m with -5°, and a vertical pipe height of 21.5 m. Sensors were installed at various positions along the pipeline (horizontal, downward inclined, and vertical sections) to measure differential pressures and liquid holdup at these locations. Flow regime maps were plotted for atmospheric pressure, 10 bar, and 50 bar, with the horizontal and vertical axes representing the gas and liquid superficial velocities. The results indicate that increasing pressure reduces the varieties of flow regimes (shown in Figure 65), leading to a gradual stabilization of flow types; and it decreases the occurrence region of severe slugging flow, as shown in Figure 66. The primary component affecting the frequency of severe slugging cycles is the cumulative liquid velocity within the riser. It was observed that the impact of superficial liquid velocity on the frequency of severe slug flow is stronger than that of superficial gas velocity. A comparison of severe slugging frequency variations under two mixing velocity methods (volume-equivalent and mass-equivalent) revealed that a more pronounced relationship between severe slugging frequency and mixing velocity by the volume-equivalent method. Furthermore, a new empirical relationship for severe slugging frequency is proposed, which is in good agreement with the experimental results.

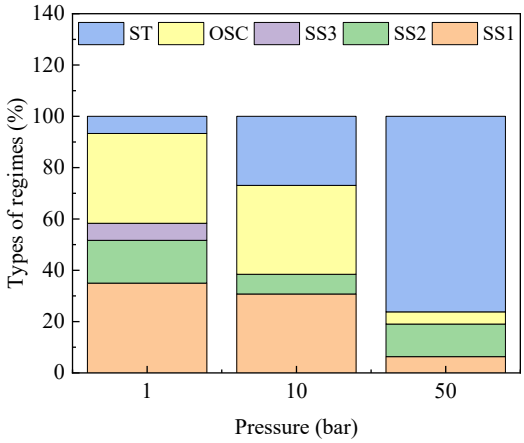


Figure 65 Varieties of the regime types with the increasing pressures

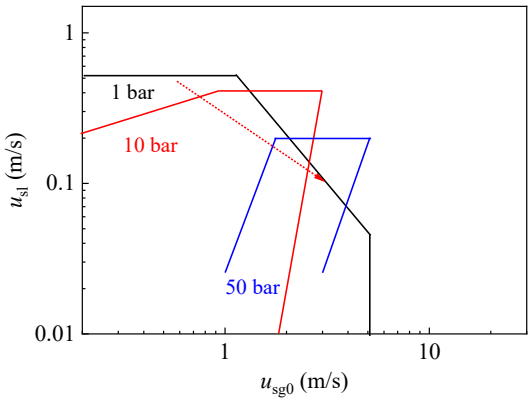


Figure 66 Comparison of severe slugging transition boundaries with increasing pressures

Keywords: Pressure; Severe slugging; Flow regime; Frequency; Pipeline-riser

SuperDEM-CFD modeling of fluidization of spherical and cylindrical particles binary mixtures and experiment validation

Jianjian Dai [1,2], Xi Gao [1,2,3*]

1. Department of Chemical Engineering, Guangdong Technion-Israel Institute of Technology, Shantou 515063, China
2. Wolfson Department of Chemical Engineering, Technion-Israel Institute of Technology, Haifa 3200003, Israel
3. Guangdong Provincial Key Laboratory of Materials and Technologies for Energy Conversion, Guangdong Technion-Israel Institute of Technology, Shantou 515063, China
*Email: xi.gao@gtiit.edu.cn

Abstract

Understanding the fluidization behavior of binary mixtures containing spherical and non-spherical particles is essential for better designing and optimizing pyrolysis fluidized bed reactors. This study experimentally investigated the fluidization behaviors of spherical, cylindrical plastic particles and their binary mixtures. A machine learning-aided image processing method was developed to segment different particles from the background for the analysis of particle dynamics. Fluidization experiments on glass sand-plastic cylinder binary mixtures with different volume fractions were also conducted, and fluidization behaviors, height distribution, and bubble properties were investigated. The SuperDEM-CFD method in the open-source MFiX was extended to simulate the fluidization behaviors of binary mixtures and validated by comparing simulation results with experimental data. It was found that the developed Di Felice & HS hybrid drag model could better predict pressure drops than previous drag models. The predicted fluidization and mixing behaviors, particle height, and orientation distribution by the improved SuperDEM-CFD method agreed well with the experiments. The proposed model could predict both fluidizations of monodispersed non-spherical particles and binary mixtures with density and shape segregation. Large-scale simulations of binary mixture particles were realized by coupling coarse-grained DEM with SuperDEM. This study provides experimental and theoretical foundations for further developing the binary fluidized bed reactor's heat and mass transfer models at the reactor scale.

Keywords: Non-spherical, Binary mixture, Fluidization, SuperDEM-CFD

Parallel Session XI: Topic 7- Multiphase flows in thermal management and thermal energy storage

Effects of particle's surface properties and aggregation modes on heterogeneous condensational growth of droplets on particle surfaces

Qian Lijuan
China Jiliang University

Abstract

Heterogeneous condensation of water vapor on particles to form droplets is widely used in the fields of atmospheric cloud physics and industrial particulate abatement. Particle's surface properties and aggregation modes play a fundamental role in water vapor condensation, but a microscopic insight is lacked. Therefore, the Environmental Scanning Electron Microscope (ESEM) is adopted to directly visualize vapor condensation on particles with different surface properties and aggregation modes at a microscopic scale. Firstly heterogeneous condensation of water vapor on the hydrophilic and hydrophobic particles is obtained by the ESEM. The results show that when water vapor condenses on the hydrophilic particles, a spherical cap-shaped embryo first appears and subsequently develops into a spherical droplet to finally wrap the single particle. While on the hydrophobic particles, a spherical cap-shaped embryo will first appear and continue to grow into a spherical droplet to finally detach from the particle. Then the line tension is investigated to explain the condensation mechanism. On the hydrophilic particles, when the droplet has crossed the equatorial line of the particle, the positive line tension promotes the spreading movement of the droplet over the particle to form a wrapped spherical droplet. While on the hydrophobic particle, the negative line tension suppresses the spreading movement of the droplet over the particle to form a detached spherical droplet. Finally, the impact of particle's aggregation modes on water vapor competition is also visualized by the ESEM. The results show that when the vapor supersaturation is constant, water vapor only nucleates on the two-close and three-circled particles while particles nucleation on the single particle is never observed. This is due to the strong water vapor competition at the particle's junction, where the embryos will collide and coalesce to form an embryo larger than the critical size to activate particles nucleation.

Effect of large material compliance on water skipping physics of deformable spheres

Yang Liu
Hebei University of Technology

Abstract

Water skipping has attracted significant focus in fluid dynamics, with robust research on rigid spheres but scant exploration into elastomeric sphere dynamics. At low impact Froude numbers, the effect of large material compliance on water skipping physics of deformable spheres are investigated. At low impact Froude numbers, the effect of large material compliance on water skipping physics of deformable spheres are investigated. The result shows that the deformability of elastic spheres enhances the ability to skip on the water surface compared to the rigid sphere. This improved skipping is attributed to the internal responses induced by deformation and an increased wetted area. The dynamics such as elastic wave propagation and motion characteristics of these spheres during skipping are influenced by their density and shear modulus. Elastic spheres demonstrate asymmetrical cavity formations and consistent deformation patterns during water skipping. Additionally, an optimal impact duration crucial for optimizing skipping efficiency of elastic spheres is determined, characterized by an inverted parabolic relationship.

Explorations of scaled-up spout fluidized beds in heat exchange of thermochemical particles

Yuanhe Yue[a,b], Weiwei Zhao[a,b], Chenzhen Liu[a,b], Zhonghao Rao[a,b]

[a] Hebei Engineering Research Center of Advanced Energy Storage Technology and Equipment, School of Energy and Environmental Engineering, Hebei University of Technology, Tianjin, 300401, China

[b] Hebei Key Laboratory of Thermal Science and Energy Clean Utilization, School of Energy and Environmental Engineering, Hebei University of Technology, Tianjin, 300401, China

Abstract:

Bubbling fluidization is commonly used for heat exchange in thermochemical solar storage applications due to its strong heat and mass transfer performance. However, the unstable particle accumulation in the bubbling fluidization will unavoidably cause particle sintering and agglomeration leading to poor cyclability, due to dense collisions with low intensity between particles. In this work, we explore the heat transfer performance of a new configuration, a two-joint spout-fluidized bed, with special attention to particle sintering aspects. This study first focuses on the scale-up of spouted beds by adopting spout deflection rather than traditional vertical spouting by the CFD-DEM approach. The basic unit setting of cooperated two-spout was discovered. After that, the system was adopted to the thermochemical Fe3O4-FeO system. It was demonstrated that this flow pattern has better heat transfer performance and reaction homogeneity. Moreover, the preliminary results show that the particle sintering was greatly alleviated under this system. This could be because the deflected spout provides much horizontal particle transport and needs fundamental study. This work provides some insights into the reactor design of heat exchangers for thermochemical heat storage particles in solar thermal power generation.

Keywords: Spouted fluidized bed, CFD-DEM, Thermochemical particle, Multiphase flow fields.

Design and simulation of transpiration cooling combined with Solid-Solid PCM at leading edge of hypersonic vehicles

Xinlan GAO , Xinzhu MOU*
Nanjing University of Aeronautics and Astronautics, Nanjing, China, 211106
Email:xinzhumou@nuaa.edu.cn

Abstract
This paper aims at the thermal barrier phenomenon caused by high heat flux and shock wave interference on the leading edge of hypersonic vehicles. A kind of cooling device with solid-solid phase change material (S-S PCM) as porous support for transpiration cooling is designed for thermal protection of leading edge. Results shows that the maximum temperature of S-S PCM is 14.8K lower than non-PCM when the Mach number is 6 and the mass flow of coolant is 0.1kg/s. A tree-branch structure of rear wall is also designed to improve cooling efficiency by topology optimization.

Keywords: Transpiration Cooling, Solid-Solid PCM, Topology Optimization, Hypersonic Vehicles

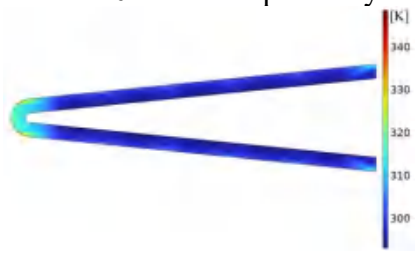
Introduction

So far, there are two main types of thermal protection methods for hypersonic vehicles: passive cooling and active cooling[1]. Passive cooling is achieved by means of heat sink, ablative heat protection and high temperature resistant material heat insulation[2]. Although it is simple in structure, it has defects such as redundancy in design and destruction of aerodynamic shape[3]. Active cooling is improved on the basis of passive cooling, mainly arranged in the key high temperature parts[4], which takes away most of the heat flow in combination with the transportation of the coolant. Generally divided into convective cooling, film cooling and transpiration cooling[5].

In addition, the development of solid-solid phase change materials (S-S PCM) also brings a new idea for hypersonic vehicle thermal protection[6]. S-S PCM is made of alloy material and has stable shape, high latent heat, high mechanical strength, and adjustable phase change temperature[7-9]. It is used as excellent heat storage material in energy, construction and other fields. In this paper, we describe in detail an aircraft leading edge model cooled by a combination of transpiration cooling and S-S PCM. The fluid flow and temperature field distribution are obtained by numerical study. Results show the new structure has better cooling effect and can cope with heat flow impact under high Mach number flight.

Methodology

In order to minimize the leading edge average temperature of hypersonic vehicles,
The topology optimization was adopted to design the structure [10]. The leading edge radius was set as 3mm, the thickness as 3.6mm, and the length as 76mm. The material was set as Nickel base alloy. Set 5 cold ends on the upper and lower inner walls, and the heat flux at the leading edge and outer wall were 2×10^6 and 1×10^6 W/m^2 respectively.



(a)



(b)

Figure 1 – (a)Temperature cloud image after topology optimization and (b)Heat transfer topology optimization results

As shown in Figure 1, the optimized structure with "tree branch" shape has better cooling efficiency on the leading edge side. Thus, we built a 2D geometry model, as shown in Figure 2, segmented the structured grid by ICEM, and encrypted it near the shock wave and boundary layer. ANSYS fluent was used to solved the flow and temperature fileds.

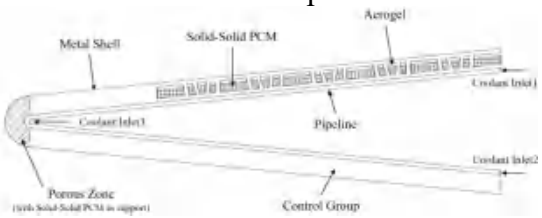


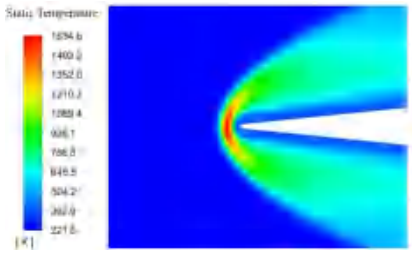
Figure 2 - Schematic design of the leading edge model

We adopted S-A turbulence model and Air-N_2 species transport model. Incoming flow was set as the pressure-far-field inlet, Ma=6, gauge pressure as 2511Pa, temperature as 221.65K, mass flow at the front coolant inlet as 0.1kg/s, temperature as 500K. The outlet is set as pressure outlet. The parameters of S-S PCM we used are shown in Table 1.

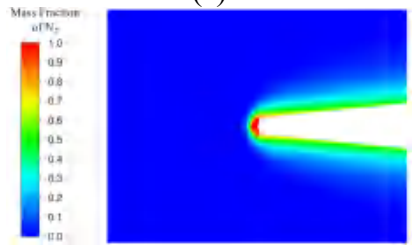
Table 12 - Parameter of Solid-Solid PCM

Density [kg/m^3]	**8420**
Themal Conductivity [W/(m K)]	**20.615**
Specific Heat [J/(kg K)]	**460**
Initiation Temperature [K]	**510**
Phase Change Temperature [K]	**520**
Latent Heat[kJ/kg]	**35.4**

We can see from the Figure 3(a) that the temperature distribution and shock wave impact in high speed flow. As shown in Figure (b), the coolant N_2 is concentrated on the front side where the temperature is higher, and a small amount is evenly distributed on the back side.



(a)



(b)

Figure 3 – (a) Temperature cloud image under Ma=6 and (b) Mass fraction of N_2 under Ma=6

The temperature distribution in porous support is shown in Figure 4. It shows the temperature of S-S PCM ranges from 435.3K to 722.9K, while the temperature of non-PCM is from 428K to 737.7K. It proves that S-S PCM absorbs heat from hot areas, which is useful to lower leading edge's temperature and keep temperatures more even across parts.

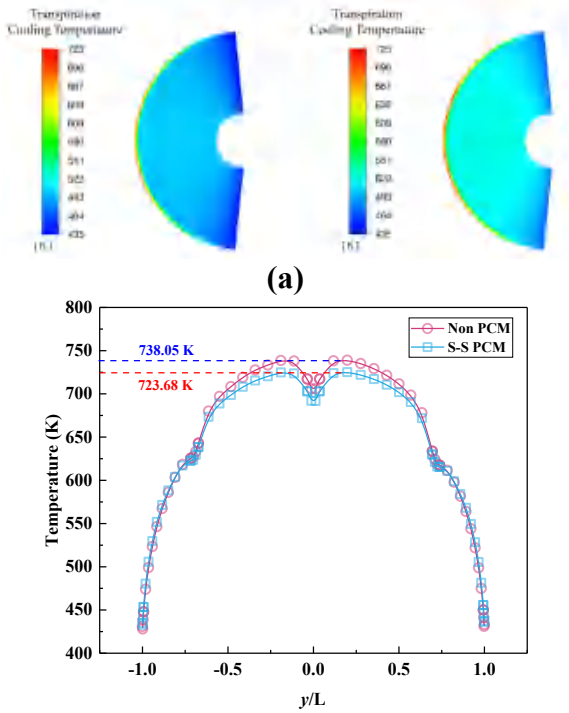


Figure 4 – (a) Temperature distribution of S-S PCM (left) and non-PCM (right) and (b) Temperature along leading edge surface

The S-S PCM thermal protection in the rear area is shown in the Figure 5. Here, Five cases were investigated by setting Ma=8 and the rear coolant inlet velocity is 4, 4.25, 4.5, 4.75, 5m/s, respectively.

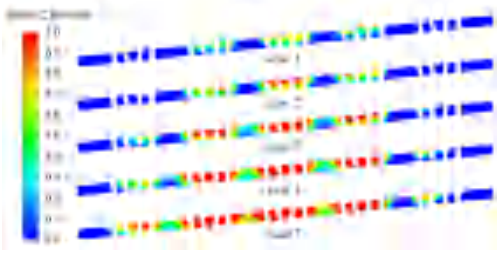


Figure 5 - Phase change fraction of S-S PCM

With the application of S-S PCM and "tree-branch" shape structure, the temperature of rear side can be stabilized between the beginning temperature and the end temperature of the phase transition. It is an important feature for improving aircraft's thermal stability and mitigating thermal shock.

Conclusions

In this paper, we have proposed a combined cooling method using transpiration cooling and S-S PCM for the leading edge of hypersonic aircraft. Topology optimization was used to design the structure of the rear wall. Results showed that S-S PCM performs a better cooling effect both in porous zone and rear wall. In the future, we will design more types of S-S PCM with different

phase change temperature and higher latent heat to increase the cooling efficiency and thermal stability of hypersonic aircrafts.

References

[1] H.Y. Huang，L.J. Su，C.S. Lei, et al. Reusable thermal protective materials: application and research progress. Acta Aeronautica et Astronautica Sinica, 2020, 41(12), 023716(in Chinese).

[2] Y.S. Liu, L.Y. Cao, Y.H. Z, et al. Research progress on ultra-high temperature composites for thermal protection of hypersonic vehicles. Composites Science and Engineering, 10 (2022) 107-118(in Chinese).

[3] J.F. Chen, Internal and External Aerodynamic Optimization Design for Hypersonic Axisymmetric Vehicle, National University of Defense Technology, 2020.

[4] J. Gou, Y. Chang, Z. Yan, B. Chen, C. Gong. The design of thermal management system for hypersonic launch vehicles based on active cooling networks. Applied thermal engineering. 159 (2019) 113938.

[5] Langener T, von Wolfersdorf J, Selzer M, Hald H. Experimental investigations of transpiration cooling applied to C/C material. International journal of thermal sciences. 54 (2012) 70-81.

[6] S. Zhang, D.L. Feng, L. Shi, et al. A review of phase change heat transfer in shape-stabilized phase change materials (ss-PCMs) based on porous supports for thermal energy storage, Renewable and Sustainable Energy Reviews, 135 (2021) 110127.

[7] S.W. Li, L.H. He, H.L. Lu, et al. Ultrahigh-performance solid-solid phase change material for efficient, high-temperature thermal energy storage,Acta Materialia, 249 (2023) 118852.

[8] G.J. Liu, S.W. Li, C. Song, et al. High-entropy Ti-Zr-Hf-Ni-Cu alloys as solid-solid phase change materials for high-temperature thermal energy storage, Intermetallics, 166 (2024) 108177.

[9] C.Y. Cao, R.X. Wang, X.D. Xing, et al. Performance improvement of integrated thermal protection system using shaped-stabilized composite phase change material, Applied Thermal Engineering, 164 (2020) 114529.

[10] G. Hao , J. Jin , C. Zhong. Topology Optimization and Material Selection of Cooling Fin Structure in Submarine Data Center. Journal of Physics: Conference Series. 2247 (2022) 12007.

Fluid Flow and Heat Transfer in Microchannels with Porous Bio-Inspired Fish Scale Structures

Jinqiu Yu, Zhonghao Rao*
Hebei University of Technology, Tianjin, China

Abstract
Bionic microchannels designed to simulate fish scales are finely investigated through numerical simulations to examine how variations in microchannel geometry, surface porosity, spatial structure, coolant flow rate, and heat source heat flow intensity directly affect the system's ability to dissipate heat. Detailed analyses reveal the extent to which each parameter affects the thermal resistance and hydraulic performance, with special attention paid to the balance between maximizing the heat transfer rate and minimizing the pressure drop across the microchannel network. This study provides a new perspective on optimizing microchannel coolers aimed at improving the efficiency of electronics cooling in high power density compact devices.
Keywords: Bionic microchannels, Heat transfer, Porous Structures

Introduction

Please use this template and following the guideline in preparation of your extended abstract. All abstracts must be submitted electronically in one of the following formats: *.doc, *.docx, *.odt or *.pdf.

Methodology

Prepare your abstract using A4 page size of 21cm × 29.7 cm. Set top and bottom margins to 2.0 cm, left margin to 2.54cm and right margin to 1.5cm. Use a two-column layout with spacing of 10 mm between columns, and justified format for each column. Indent paragraphs by 5 mm. Use single line spacing. Try to use SI units and leave a space between number and units. Do not insert page numbers. Use 16 point **bold**, capital letters for the title in Times New Roman, 10-point Times New Roman (**BOLD**) characters for author names and affiliations and 11-point Times New Roman characters for the body text.

The title of the extended abstract should be placed at the top of the page with a single column. The title should be flushed left. There should be a spacing of one line between the title and the names of the authors. The name(s) and affiliation(s) of author(s) should be flushed left. The name(s) should be in bold and the presenting author should be underlined. Only the affiliation of corresponding author includes the postal and email addresses.

All paragraphs should be fully justified. There should be no empty lines between paragraphs in the same section. Leave an empty line between the last paragraph of this section and the heading of the subsequent section. Each section needs a heading. All headings should be flushed to the left. Use 14-point Times New Roman (**BOLD**) characters and the first letter of headings should be in uppercase.

All tables should be horizontally centred across the column, with their headings centrally placed above the table. Leave one empty line above and below the table.

Table 13 - Table of important data

	X	**Y**
A	1	4
B	2	5
C	3	6
D	7	8

All figures should be horizontally centred with their captions below the figure and centrally justified. There is no restriction on the type of font in figures. However, the size of the characters

must be legible (not smaller than size ~9). Drawings, graphs and charts should be embedded in the document as images. Leave one empty line above and below the figure.

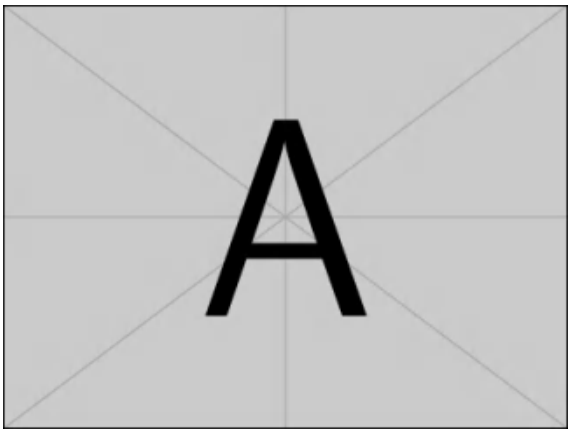


Figure 67 - An example figure

Equations should be flushed left and numbered according to the following example:

$$k = Ae^{\frac{-E_A}{RT}} \qquad (1)$$

Poster Submissions

An abstract is required for each poster submission. Posters should be created in portrait orientation for A0 pages. Posters larger than this may not fit on the provided poster boards and may be excluded from the poster sessions.

Conclusions

This is the template for the two-page extended abstract.

Acknowledgements

The organizers would be grateful if you could follow this template in preparing your extended abstract.

References

References should be cited consecutively in square brackets [1]. The sentence punctuation follows the bracket [2]. Use the preferred referencing style as given in the following reference examples.

[1] Y. Guo, K.D. Kafui, C.-Y. Wu, C. Thornton, J.P.K. Seville, A coupled DEM/CFD analysis of the effect of air on powder flow during die filling, AIChE Journal 55 (2009) 49-62.
[2] K.L. Johnson, Contact Mechanics, Cambridge University Press, 1985.

Numerical investigation on the supercritical startup of cryogenic loop heat pipe for space application

FaLong He[a,c], WangFang Du[a,c], JianFu Zhao[a,c,*], JianYin Miao[b], HongXing Zhang[b], Chang Liu[b], Sixue Liu[b]

[a] CAS Key Laboratory of Microgravity, Institute of Mechanics, Chinese Academy of Sciences. Beijing, PR China.

[b] Beijing Key Laboratory of Space Thermal Control Technology. Beijing, PR China.

[c] School of Engineering Science, University of Chinese Academy of Sciences. Beijing, PR China.

*E-mail address for the corresponding authors: jfzhao@imech.ac.cn (J.F. Zhao)

Abstract

To better understand the thermodynamic characteristic and improve the design of cryogenic loop heat pipe (CLHP) for space application. A transient thermodynamics simulation model of CLHP is established. Basing on the validated model, the effects of heat sink temperature and charged pressure on a Neon charged CLHP (Ne-CLHP) supercritical startup is numerically investigated.

Keywords: Cryogenic Loop Heat Pipe, Transient Model, Supercritical Startup

Introduction

The increasing requirements of space-based infrared detection technology to space exploration depth stimulate the development of CLHP. Recently, the SJ-20 satellite has successfully demonstrated in orbit the heat transfer technology based on CLHP. In this study, the previously developed transient thermodynamic model for CLHP [1] is extended to the simulation of supercritical startup characteristics for the satellite SJ-20 carried CLHP.

Methodology

To verify the applicability of the model, it was validated against ground test data [2] from the Ne-CLHP aboard the SJ-20 satellite. The simulation results accurately depicted the supercritical startup characteristics of Ne-CLHP, thereby confirming the reliability of the model. The startup range of the carried Ne-CLHP simulation results, as shown in Figure 1, illustrate the comparison between the supercritical startup range envelopes for two types Ne-CLHP. It was observed that an optimal filling pressure still exists, which enables the system to achieve the widest range of heat sink temperatures necessary for supercritical startup. However, it was also noted that as the system volume decreases, the range for supercritical startup charged pressure range narrows.

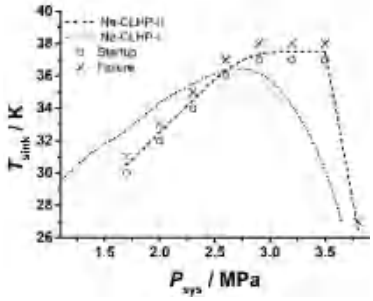


Figure 1 The startup state of Ne-CLHP

Conclusions

The validated model was employed to simulate the impact of charged pressure and heat sink temperature on the supercritical startup of the CLHP onboard SJ-20. For different configurations Ne-CLHP, the existence of an optimal charged pressure for supercritical startup was confirmed.

Acknowledgements
This work was supported by the National Natural Science Foundation of China (No. 11972040)

References
[1] J. He, Y.D. Guo, J.Y. Miao, et al. Pre-flight thermal performance test of a 35 K cryogenic integrated system. International Journal of Refrigeration, 2019, 98.
[2] He F.L., Du W.F., Zhao J.F. et al. Numerical simulation on the effects of component layout orientation on a neon-charged cryogenic loop heat pipe. Microgravity Science Technology, 2020, 32, 179-188.

Polymeric Flocculation of Multiphase Nuclear Waste Suspensions

Jacob R L Rumney, Dr Nicholas Warren, Prof Jeffrey Peakall, Dr David Harbottle, Dr Alexander Lockwood, Dr Timothy Hunter
University of Leeds, Leeds, United Kingdom

Abstract

The primary aim of this study was to optimise polymeric flocculation as a novel dewatering method for multiphase nuclear waste suspensions. Synthesis and characterisation of multiple non-ionic polyacrylamide (nPAM) samples along with characterising flocs formed with mineral-based nuclear waste simulants allowed optimised flocculation performance to be determined at solids concentrations encountered at legacy nuclear facilities. Flocculation of calcite (Sturcal-L®) suspensions using synthesised nPAM performed better than its commercial alternative (FLOPAM FA920SEP®), achieving 116% faster zonal settling with 6% less supernatant turbidity at half the dose. Such results give nuclear sites such as Sellafield Ltd confidence in adopting innovative techniques to accelerate decommissioning and increase solids concentrations in disposed nuclear waste.

Keywords: Polymerisation, Flocculation, Agglomeration, Sedimentation, Shear Mixing

Introduction

Nuclear sludge retrievals have exacerbated the persistence of suspended colloids which may aid transportation of radionuclides, compromising the long-term safe operation of nuclear facilities [1]. Polymeric flocculation has been touted as an improved settling method for various radwaste sludges, where using high molecular weight polymers is proven to be effective in many wastewater applications [2] [3] [4]. To understand the settling characteristics of polydisperse flocs formed in multiphase mixing and agglomeration systems, this work investigates the performance of a series of nPAM to determine the impact of molecular weight on flocculation of nuclear waste.

Methodology

Polymer samples PAM#1 and PAM#2 were synthesised via free radical polymerisation [5]. PAM-R-01 and PAM-R-02 were synthesised via aqueous RAFT polymerisation [6]. Molecular weights were determined via viscometry for Free Radical polymers and proton NMR for RAFT polymers. Hindered settling rates of flocculated calcite samples were determined by measuring interfacial height over time in a volumetric flask. Supernatant turbidity was made taking a 10 ml aliquot for analysis with a Eutech TN-100 meter. Floc size and shear strength was measured *in-situ* with a ParticleTracker G400 FBRM probe.

Results

Floc sizes were increased upon polymer dosage and remained large when lowering the shear rate, seen in Figure 1 below. At high shear rates their size reduced drastically, only slightly recovering when lowering shear again to 250 rpm, showing no thixotropic behaviour as observed for magnesium hydroxide nuclear wastes [7] [8] [9].

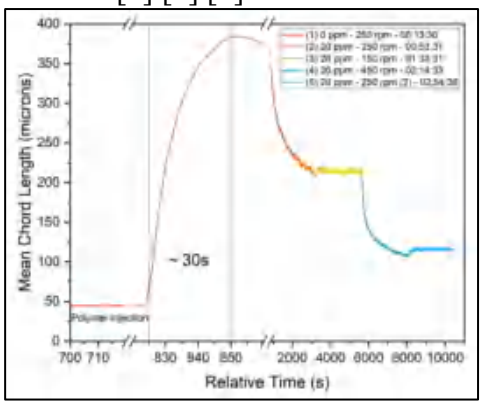


Figure 68 – Shear response of flocs (20 ppm)

Conclusions

nPAM effectively flocculated the waste simulant material by improving the zonal settling rates and supernatant turbidity significantly. Floc sizes showed strong shear-dependence, likely due to nPAM forming large, open flocs as it adsorbs via relatively weak hydrogen bonds.

Acknowledgements

I'd like to extend my gratitude to my supervisors at University of Leeds for their support and guidance, UKRI and GREEN CDT (EP/S022295/1) for their funding, Sellafield Ltd for their sponsorship, and IMFTF24 for the opportunity to showcase my research on a global platform.

References

[1] Kaminski, M.D. Dimitrijevic, N.M. Mertz, C.J. Goldberg, M.M. Colloids from the aqueous corrosion of uranium nuclear fuel, Journal of Nuclear Materials 347 (2005) 77-87.

[2] Yang P, Li D, Zhang W, Wang N, Yang Z, Wang D, Ma T. Flocculation-dewatering behavior of waste activated sludge particles under chemical conditioning with inorganic polymer flocculant: Effects of typical sludge properties. Chemosphere 218 (2019) 930-40.

[3] Lockwood, A.P.G. Rumney, J.R.L. Barnes, M.G. Dodds, J.M. Peakall, J. Hunter, T.N. Approximation of hindered zonal settling rates for flocculated inorganic/organic composite suspensions in inertial flow conditions, Journal of Water Process Engineering 51 (2023) p103459.

[4] Lockwood, A.P.G. Peakall, J. Warren, N.J. Randall, G. Barnes, M. Harbottle, D. Hunter, T.N. Structure and sedimentation characterisation of sheared Mg(OH)2 suspensions flocculated with anionic polymers, Chemical Engineering Science 231 (2021) p116274.

[5] Alnuaimi, G.H. Synthesis and Solution Characterization of Water-Soluble Polyacrylamide and Its Applications in Oil Industries, Theses 384 (2005) 39-48.

[6] Liang, J. Shan, Gr. Pan, Pj. Aqueous RAFT polymerization of acrylamide: A convenient method for polyacrylamide with narrow molecular weight distribution, Chin J Polym Sci. 35 (2017) 123–129.

[7] Moghimipour, E. Handali, S. Salimi, A. Masoum, M. The Effect of Electrolyte Concentration and Polymer Content on the Rheological Behavior of Magnesium Hydroxide Suspension, British Journal of Medicine and Medical Research 3.4 (2013) 1979-1987.

[8] Johnson, M. Fairweather, M. Harbottle, D. Hunter, T. N. Peakall, J. Biggs, S. Yield stress dependency on the evolution of bubble populations generated in consolidated soft sediments, AIChE Journal 63(9) (2017) 3728-3742.

[9] Chang C, Smith PA. Rheological characterization of nuclear waste slurries, Part Sci Technol. 14 (1996) 165–180.

Numerical investigation on center-dispersed microchannel liquid-cooling plates for battery thermal management

Weiming Luo, Youfu Lv*

Abstract

The battery thermal management system is critical to the operating safety of power batteries. To alleviate the temperature gradient effect caused by the high local temperature of the battery, a center-dispersed square spiral ring (SSR) and a center-dispersed tree-fork (TF) shaped mini-channel liquid cooling plate are designed for battery thermal management. Firstly, the effects of the number of SSR channel laps, channel width, channel bend radius and inlet mass flow rate on the temperature characteristics of the battery and coolant pressure drop are investigated. Then, the effects of inlet and outlet arrangement way, main channel width, bifurcation channel factors, and inlet mass flow rate on the temperature performance of TF liquid cooling panels were investigated. When the inlet mass flow rate is increased to exceed 0.8 $g \cdot s^{-1}$, the maximum temperature and temperature distribution characteristics are also shows a weak optimized. The battery maximum temperature on SSR cooling panels with 5mm wide branch channels is lower, and better uniformity of battery temperature distribution is achieved. However, in comparison, the TF liquid cooling plate had a lower battery maximum temperature, a lower maximum temperature difference, and a lower pressure drop. When the inlet mass flow rate is 0.16, the battery maximum temperature of TF is 38.57°C less than that of SSR by 0.18°C during discharging at 2C, and the pressure drop of TF is 25.7 Pa, which is 15 times lower than that of SSR. All these results and evidence provide an option for the development of two types of novel mini-channel liquid cooling plates for battery thermal management.

Keywords: lithium-ion batteries, battery thermal management, mini-channel liquid cooling plate, bifurcation channel.

Pore-Scale Numerical Modelling of Multiphase Flow in Chemical Flooding of Oil Reservoir

Su Junwei; Hu Yingxue
Department of Earth Environment Science, Xi'an Jiaotong University, Xi’an Shaanxi

Abstract: Chemical flooding is an important method for improving oil recovery in oil fields after water flooding. Chemical flooding typically involves multiple phases (oil, water, polymer, particles, etc.) or species (salt, surfactant, alkali). There are complex interactions and flow behaviors. A deep understanding of interactions and flow behaviors is of great significance for further improving reservoir recovery and chemical agent evaluation. From the mechanism of improving oil recovery through chemical flooding, chemical agents can be divided into four types: adjusting bulk viscosity (polymer), adjusting phase interface interaction (surfactant), enhancing interphase mass transfer (emulsifier), and changing flow path (viscoelastic particle flooding). There are significant differences in the process and model of different types of chemical agents. This article first elaborates on the details of chemical flooding modeling for four types of chemical agents from two aspects: phase tracking and flow behavior prediction. Then, the solution algorithm and coupling strategy of the model are provided. Finally, the developed pore scale universal chemical flooding numerical simulation platform and its application are introduced. This study can provide a new tool for improving reservoir recovery and evaluating chemical agents in chemical flooding.

Keywords: Pore-Scale; Chemical Flooding; Enhancing Oil Recovery

Solid particles as solar receiver and thermal energy storage media: flow behaviour and heat transfer characteristics

Sheng Chen[a,*], Wenchao Fang[a], Jianhong Fu[a], Shuiqing Li[b], Xiaoze Du[c]
a. Huazhong University of Science and Technology, Wuhan 430074, China
b. Tsinghua University, Beijing 100084, China
c. North China Electric Power University, Beijing 102206, China

Abstract
Understanding the flow and heat transfer characteristics of dense particle flows is essential for the efficient operation of high-temperature particle-based solar thermal and thermal energy storage systems. This work presents a comprehensive investigation using the discrete element method and Monte Carlo ray tracing to elucidate the intricate relationship between particle shape, packing structure, and radiative transfer characteristics at the particle scale. This study reveals the matching mechanism between heat flux and flow patterns in fluidized beds subjected to concentrated radiation input. Furthermore, the influence of particle diffusion in confined spaces on heat transfer is explored and the transition from flow to clogging in complex structures is investigated. A clogging diagram is proposed, considering the influence of pore size and particle friction coefficient. Finally, the heat transfer performance of particle heat exchangers in concentrated solar power (CSP) systems is studied using a continuum model, establishing a universal correlation between the heat transfer coefficient and particle flow characteristics. This research contributes to the fundamental understanding and optimization of particle-based thermal energy storage systems.

Keywords: Monte Carlo ray tracing; Discrete element method; Concentrating solar power; thermal energy storage

Introduction

Solar thermal and thermal energy storage systems utilizing solid particle technology have emerged as highly promising approaches for efficient solar energy conversion. These systems adopt low-cost solid particles as the medium for heat collection and storage, enabling reliable operation at temperatures >1000°C. However, the discrete nature of particles introduces complexities in predicting flow behaviour and heat transfer: the influence of particle shape and packing structure on inter-particle radiation energy transfer remains unclear; there is a lack of comprehensive understanding relationship between the energy transfer pathways and flow patterns of fluidized particles under concentrated radiation; the impact of particle diffusion on the heat transfer coefficient within heat exchangers lacks clarity; and the problem of clogging in confined structures remains unresolved. This study aims to delve into these fundamental issues and provide insights for the advancement of solid particle technology in solar thermal and thermal energy storage systems.

Methodology

In this work, the discrete element method is utilized in the modelling of dense particle flows, which tracks the motion, forces, and temperature variations of individual particles. Monte Carlo ray tracing method is employed to calculate the radiative transfer between particles and the absorption of external radiation by the bed. The heat transfer characteristics of a particle heat exchanger are examined using a continuum modelling approach.

Conclusions

Positioning, the shielding effect, and indirect radiation are identified as crucial factors that impact radiation heat transfer between particles. The increase in gas velocity leads to a higher frequency of particles entering and leaving the heat-collecting zone, thereby significantly reducing the occurrence of overheating. The impact of particle diffusion on heat transfer in confined spaces is clarified. A clogging diagram is proposed, considering the influence of pore

size and friction coefficient. At last, a universal correlation between the local heat transfer coefficient and the particle flow properties is proposed for a particle heat exchanger.

Acknowledgments

We acknowledge support from the National Natural Science Foundation of China (52376144, 52130607)

Research on Steam Mass Flow Measurement Based on a Novel Vortex Flowmeter with Annubar Tube

Danlei Zhao[a,b,c,d] , Lide Fang[a,b,c,d†]

a College of Quality and Technical Supervision, Hebei University, Baoding, 071002, China

b National &Local Joint Engineering Research Center of Metrology Instrument and System, Hebei University, Baoding, Hebei, 071002, China

c Hebei Key Laboratory of Energy Metering and Safety Testing Technology, Baoding, Hebei, 071002, China

d Baoding Industrial Metrology Engineering Technology Research Center, Baoding, Hebei, 071002, China

†Corresponding Author Email: fanglide@hbu.edu.cn

Abstract

In recent years, with the increasing global concern for environmental issues, people have realized the importance of energy production and conservation. Steam generation and utilization have gained more attention as a result. Steam, being the most commonly used heat carrier in various industries, plays a significant role in industrial production. Steam measurement has been increasingly valued in various industries, and its flow measurement accuracy has a crucial impact on production efficiency and product quality. However, the current methods have some problems in practical applications, such as low accuracy and poor stability, thus requiring the exploration of new measurement methods.

This paper proposes a novel intelligent integrated flowmeter using annubar tube and vortex flowmeter with advantages from two different structures, enabling precise measurement of steam mass flow. Firstly, this study establishes the measurement models of the new flowmeter in single-phase and steam through theoretical analysis. Then, in terms of instrument design, the hardware structure, signal analysis system, and upper computer system of the instrument are designed to facilitate remote measurement in high-temperature and high-pressure environments. In the laboratory, experiments are conducted to measure the flow rates of single-phase water, gas, and two-phase flow. The experimental data is processed and analyzed, followed by model validation and result discussions. Based on these findings, steam measurement is conducted on the superheated steam device at the national steam flow measurement station, with experimental test pressures ranging from 0.3 to 0.5 MPa and temperatures ranging from 136 to 152 ℃. The experimental results show that the measurement error of the flowmeter is less than ±1.0%, and the repeatability is also below 0.08%. Compared to the original combined measurement apparatus, the new vortex flowmeter with annubar tube demonstrates good applicability and stability in practical engineering applications, meeting the demand for accurate steam flow measurement in industrial production. It has promising prospects for promotion and application.

Keywords: steam flow measurement, vortex flowmeter, annubar flowmeter， measurement accuracy

Numerical study on surface coating of phase change materials based on coaxial technology

Guangtong Zhang, Zhonghao Rao*
Hebei University of Technology, Tianjin, China

Abstract
The phase change capsules with core-shell structure can be prepared by coaxial double-needle technique. In order to further understand the coating process of phase change capsules and optimize the preparation process parameters, a coaxial double-needle model was established in this paper, and numerical simulation method was used to reveal the influence law of the shell material viscosity, core wall material flow rate and the ratio of inner and outer diameters on the paraffin surface coating.

Keywords: Phase Change Capsule, Coaxial Double-needle, Surface Coating

Introduction

Please use this template and following the guideline in preparation of your extended abstract. All abstracts must be submitted electronically in one of the following formats: *.doc, *.docx, *.odt or *.pdf.

Methodology

Prepare your abstract using A4 page size of 21cm × 29.7 cm. Set top and bottom margins to 2.0 cm, left margin to 2.54cm and right margin to 1.5cm. Use a two-column layout with spacing of 10 mm between columns, and justified format for each column. Indent paragraphs by 5 mm. Use single line spacing. Try to use SI units and leave a space between number and units. Do not insert page numbers. Use 16 point **bold**, capital letters for the title in Times New Roman, 10-point Times New Roman (**BOLD**) characters for author names and affiliations and 11-point Times New Roman characters for the body text.

The title of the extended abstract should be placed at the top of the page with a single column. The title should be flushed left. There should be a spacing of one line between the title and the names of the authors. The name(s) and affiliation(s) of author(s) should be flushed left. The name(s) should be in bold and the presenting author should be underlined. Only the affiliation of corresponding author includes the postal and email addresses.

All paragraphs should be fully justified. There should be no empty lines between paragraphs in the same section. Leave an empty line between the last paragraph of this section and the heading of the subsequent section. Each section needs a heading. All headings should be flushed to the left. Use 14-point Times New Roman (**BOLD**) characters and the first letter of headings should be in uppercase.

All tables should be horizontally centred across the column, with their headings centrally placed above the table. Leave one empty line above and below the table.

Table 14 - Table of important data

	X	**Y**
A	1	4
B	2	5
C	3	6
D	7	8

All figures should be horizontally centred with their captions below the figure and centrally justified. There is no restriction on the type of font in figures. However, the size of the characters must be legible (not smaller than size ~9). Drawings, graphs and charts should be embedded in the document as images. Leave one empty line above and below the figure.

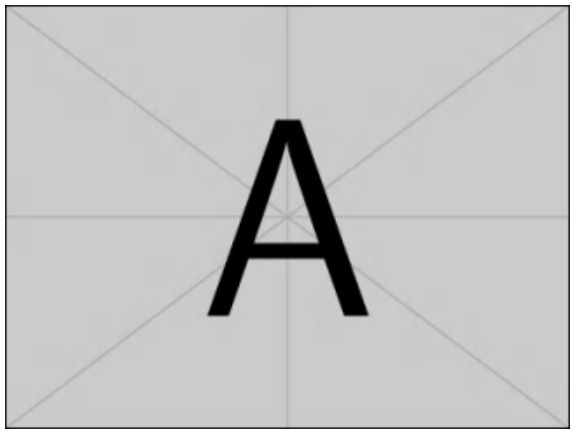


Figure 69 - An example figure

Equations should be flushed left and numbered according to the following example:

$$k = Ae^{\frac{-E_A}{RT}} \qquad (1)$$

Poster Submissions

An abstract is required for each poster submission. Posters should be created in portrait orientation for A0 pages. Posters larger than this may not fit on the provided poster boards and may be excluded from the poster sessions.

Conclusions

This is the template for the two-page extended abstract.

Acknowledgements

The organizers would be grateful if you could follow this template in preparing your extended abstract.

References

References should be cited consecutively in square brackets [1]. The sentence punctuation follows the bracket [2]. Use the preferred referencing style as given in the following reference examples.

[1] Y. Guo, K.D. Kafui, C.-Y. Wu, C. Thornton, J.P.K. Seville, A coupled DEM/CFD analysis of the effect of air on powder flow during die filling, AIChE Journal 55 (2009) 49-62.
[2] K.L. Johnson, Contact Mechanics, Cambridge University Press, 1985.

Parallel Session XII: Topic12-Multiphase flow: Complex granular flows: new progress in numerical simulations and rheological models

A modified kinetic theory for the grain phase in dense liquid-particle mixture flow

Xiaoliang Wang, Yuxin Tian, Qingquan Liu, Yunhui Sun
Beijing Institute of Technology, No.5 South Zhongguancun Road, Beijing, China

Abstract
An experimental flume was constructed to study the internal motion of dense liquid-particle mixture flows, with techniques including transparent borosilicate glass beads, refractive index matching, and PTV. A series of chute experiments were carried to obtain the internal microscopic flow fields, with which we developed a modified kinetic theory for the granular phase. By implementing the modified kinetic theory in OpenFOAM, a Euler solver was developed for two-phase dense granular flow. Through the simulation of a typical chute two-phase dense granular flow, the modified kinetic theory was validated.
Keywords: Liquid-Particle Flows, Kinetic Theory, Dense Granular Flow

Introduction
Dense liquid-particle mixture flows are a widely observed complex flow in nnatural environments, such as landslides, sheet flows, and debris flows. The flow of dense liquid- particle mixtures is an open scientific problem as listed in Science in 2005. Therefore, it is important to study the behaviour of dense liquid- particle two-phase flows.
In the study of dense liquid-particle two- phase flows, the most critical issue is the constitutive equation for the granular phase. Unlike the constitutive equations for fluids, the behaviour of granular matter is closely related to the flow state of the mixture. Collisions and frictional effects during particle motion play a crucial role in modifying the flow state. In recent years, scholars have made continuous progress in understanding the stress description of granular phases, but there is still a lack of a unified theory [1]. We carried out a series of inclined channel flow experiments for liquid- particle mixtures, with which a modified kinetic theory for the grain phase is developed. We then implemented this new kinetic theory in the platform of OpenFOAM to develop a two-phase Euler solver for two phase granular flows.

Methodology
An experimental setup as shown in Fig.1 used transparent borosilicate glass beads, refraction index matching method, fluorescence tracing technology, and PTV. Detail is found in Sun et al. [2] Through this technique of synchronous observation of the internal particle and liquid phase motions in liquid-solid two- phase flow, information such as velocity, shear rate, particle fluctuation, and volume fraction is obtained.

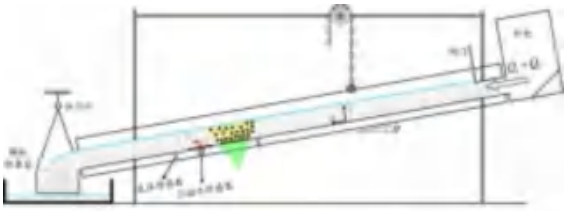


Figure 1 - Inclined channel flow experimental device

Based on the momentum equation of the particle-liquid mixture, with the introduction of steady-state assumption and hydrostatic pressure assumption, expressions for the effective normal stress and effective shear stress of the particle phase are derived as in Eqs.(1-2).

$$\sigma'(z) = (\rho_s - \rho_f) g \cos\theta \int_z^H c_s \mathrm{d}z + p_0 + G_{uns} \cos\theta \qquad (1)$$

$$\tau(z) = \int_z^H \left(\rho g \sin\theta - \partial u / \partial t\right) \mathrm{d}z + G_{uns} \sin\theta \qquad (2)$$

All the other kinematic variables such as shear rate, granular temperature, et al., are extracted through graph analysis. Then, a modified kinetic theory is developed for the closure of granular phase for a wide range of states, where a good collapse for the experimental results is found as shown in Fig. 2. Under weak shear, the granular rheology exhibits a friction mechanism, while under strong shear, it exhibits a collision mechanism. Additionally, it can also be observed that frictional stresses exist over a wide range of volume fractions, which differs from the traditional understanding that frictional stresses disappear below a critical volume fraction.

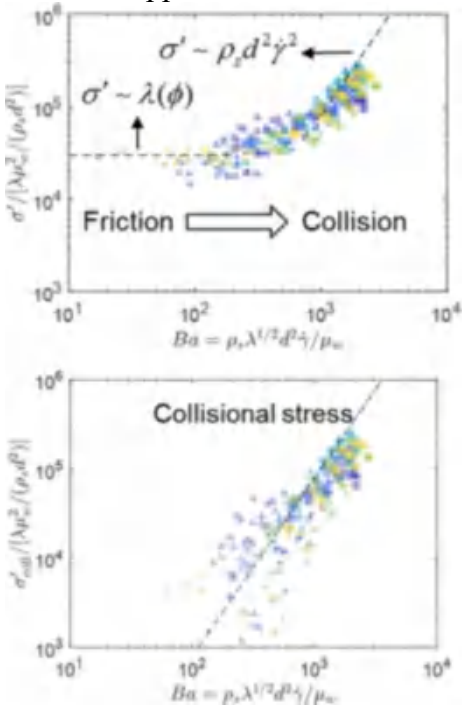


Figure 2 - Frictional-collisional model for the solid phase stress.

The modified kinetic theory is implemented in OpenFOAM to develop a Euler solver for dense two-phase granular flow. Then, a typical chute two-phase dense granular flow is simulated, with results shown in Fig. 3. It is found that the profiles of solid fractions, velocity, shear rate and granular fluctuation, agree well with the experimental results carried out in our lab. Therefore, we believed that the modified kinetic theory for the grain phase can basically describe the motion of liquid-particle two-phase flow.

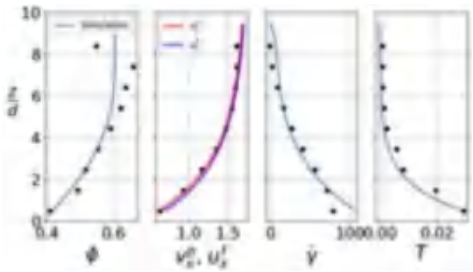


Figure 3 - Comparison of the simulated (solid lines) and experimental (points) results concerning the volume fraction, velocity, shear rate and granular fluctuation from left to right.

Conclusions

(1) An experimental flume was constructed to investigate the motion of dense liquid-particle mixture flow. By utilizing refractive index matching experimental techniques in conjunction with PTV flow field measurement methods, an experimental approach enabling simultaneous observation of particle and liquid motion was achieved.

(2) A modified kinetic theory for the grain phase was developed, and the preliminary validation was conducted in conjunction with a two-phase flow model.

References

[1] R. Maurin, J. Chauchat, P. Frey, Dense granular flow rheology in turbulent bedload transport, Journal of Fluid Mechanics 804 (2016) 490-512.

[2] Y. Sun, J. Jiao, Y. An, X. Wang, & Q. Liu, Experimental study on internal flow structure and dynamics of dense liquid-particle flow down inclined channel. Experiments in Fluids, 64(2023), 150.

Boundary Conditions Alter Inhomogeneity and Stress Fluctuations in Shear-Thickening Suspensions

Song-Chuan Zhao
Xi'an Jiaotong University, Xi an, China

Abstract

Discontinuous shear thickening (DST) in dense suspensions is accompanied by significant fluctuations in shear and normal stress at a fixed shear rate. In this work, normal stress fluctuations are shown to have a one-to-one relationship with the formation and diffusion of local high-density regions. We also observed that a decrease in boundary stiffness significantly alters the formation scale and spatiotemporal distribution of these fluctuations, from transient and short-lived to more sustained and enduring patterns, potentially extending the lifetime of corresponding density inhomogeneities.

Keywords: shear-thickening, non-Brownian suspension

Introduction

During the last decade, the shear thickening in non-Brownian suspensions has been demonstrated to result from a transition from a frictionless flow state to a frictional flow state. A noticeable feature accompanying DST is the significant temporal fluctuations in stress. Recent advances in experiments and simulations suggest that the uniform state of a system undergoing DST is unstable. This study presents temporal measurements of normal forces in DST suspensions under different boundary constraints accompanied by simultaneous inhomogeneity observation.

Methodology

The dense suspension consists of cornstarch particles dispersed in a density-matching solvent with a volume fraction of 43%. The suspension is confined between two parallel plates. The bottom plate moves along an orbit in the horizontal plane (Fig.1a), and the top shear plate is fixed. To investigate the influence of boundary conditions, we use the bare acrylic plate (rigid) and additional layers optionally: a silicone oil layer (viscosity 100cSt) and soft and hard PDMS films. The heterogeneous states are measured through backlight attenuation, and the normal force on the top shear plate is recorded simultaneously.

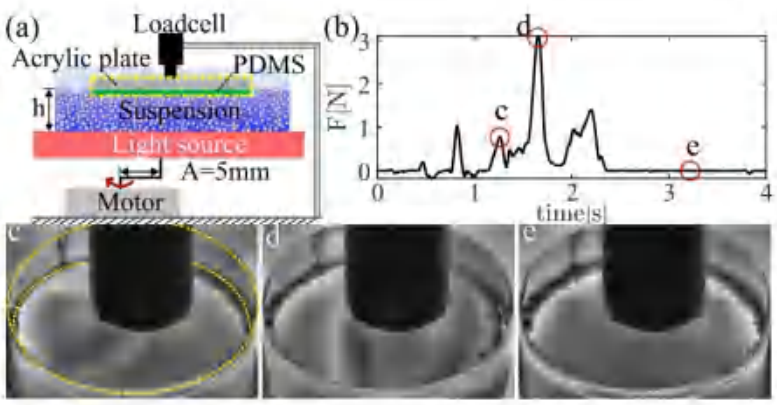


Figure 1 – (a) A schematic of the experimental setup (b) Normal force time-series diagram F(t) with the hard PDMS layer at shear rate of 24.3 s-1 . (c-e) Snapshots at the moments marked in (b).

Conclusions

The time series of the normal force, *F(t)*, is analyzed for various shear rates. The time average, standard deviation, and autocorrelation time of the time series all rise dramatically at a common critical shear rate, marking the onset of DST. Beyond the onset, non-zero values in *F(t)* are accompanied by the appearance of heterogeneities (Fig.1b-c). Boundary types significantly alter the details of *F(t)*. The complexity of *F(t)* is quantified by statistical analysis. Our findings call for revisions of the mean-field rheology constitutive relation. Moreover, the consideration of

boundary stiffness is essential for experimental techniques like Boundary Stress Measurement [1], where measurement precision and the physics of interest may present a trade-off.

References

[1] V. Rathee, and D. L. Blair, and J. S. Urbach, Localized transient jamming in discontinuous shear thickening, PNAS 64 (2017) 8740

CFD-DEM modeling and investigation of the heat transfer behaviors in a fluidized bed containing rod-like particles

Huaqing Ma[a,b], Yuhao Hu[a], Lianyong Zhou[a], Kaiwei Chu[b], Yongzhi Zhao[a,*]
[a] Zhejiang University, Hangzhou, China
[b] Shandong University, Jinan, China

Abstract
As the primary form of biomass, rod-like particles can be widely encountered in industrial applications, and its utilization often involves the heat transfer. Therefore, understanding the heat transfer characteristics of rod-like particles should be of great practical significance for developing new processes or optimizing existing ones. However, previous studies mainly focused on the heat transfer of spherical particles, and the relevant research for rod-like particles is currently scarce. In response to this situation, this study employes a Computational Fluid Dynamics - Discrete Element Method (CFD-DEM) model to numerically simulate the heat transfer behavior of rod-like particles in a fluidized bed, in which the rod-like particles are described by the super-ellipsoid model. Considering the lack of suitable heat transfer models for rod-like particles, a convective heat transfer model for a single rod-like particle is first established through a direct numerical simulation study based on lattice Boltzmann method. Subsequently, this convective model is modified to be applicable to multi-particle systems by a series of experiments for the heat transfer of rod-like particles in a lab-scale fluidized bed. Finally, the CFD-DEM numerical simulations of the heat transfer behavior of rod-like particles with different aspect ratios in a fluidized bed are carried out. According to simulation results, a rather in-depth investigation for the heat transfer characteristics of rod-like particles is conducted (*e.g.*, the influence of particle aspect ratio and the interaction mechanism between the particle flow and the heat transfer).

Keywords: Rod-like particles; Heat transfer; Fluidization; CFD-DEM; Non-spherical particles

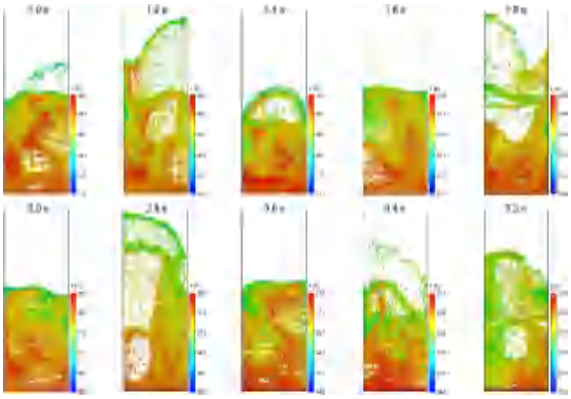


Figure 70 – Heat transfer behaviors of rod-like particles in a fluidized bed

Study on the effects and mechanisms of vibration insert to the discharging process in silos

Jie Gao[1], Guangyang Hong[2], Qijun Zheng[3*]

1. Southeast University - Monash University Joint Graduate School (Southeast University, Suzhou, China)
2. Key Laboratory of Structural Dynamics of Liaoning Province, College of Sciences, (Northeastern University, Shenyang, China)
3. Southeast University - Monash University Joint Graduate School (Southeast University, Suzhou, China)

Abstract

Although researchers have recognized that the installation of insert can improve the discharge rate of silos, the requirements for the position and parameters of insert are stringent, and the improvement effect is often not ideal. This study applies vibration to the insert to improve the discharge process. The discrete element method (DEM) is employed to investigate the impact of vibration frequency and amplitude on the increase rate (the ratio of discharge rate after vibration to discharge rate without vibration) in three-dimensional granular flow in silos with different parameters such as silo orifice diameter, insert height, size, and shape. The results show that the discharging rate under different operating conditions is improved when vibration is applied to the insert. While the relationship between the improvement rate and the amplitude is non-monotonic when the height of the insert is low. The discharge rate is significantly increased in scenarios with larger insert size and smaller orifice diameter, while the shape has a minor impact on the discharge rate. It is observed that the vibration of insert increases the horizontal velocity component, then disrupts force chains near the insert, suppressing arch formation, and consequently enhances the discharge rate.

Keywords: Silo, Granular flow, Discharge rate, Discrete element method, Vibration of insert

Particle kinetics with sintering force under high temperature

Fu Jingwen, Liu Wenwei, Huang Yun
State Key Laboratory of Mesoscience and Engineering, Institute of Process Engineering, Chinese Academy of Sciences, Beijing 100190, China
School of Chemical Engineering, University of Chinese Academy of Sciences, Beijing 100049, China

Abstract
The force involved in particle sintering is essential for understanding and optimizing the manufacturing of particulate materials. In this work, the sintering force is measured and the sintering model is extended. A discrete element method (DEM) simulation is conducted to further investigate the particle agglomeration due to sintering force under high temperature.

Keywords: Sintering, Solid bridge, DEM

Introduction

Sintering is a key process in material science, metallurgy and chemical engineering [1], which refers to the bonding and the merging of particles under high temperature. Several models have been proposed to describe the sintering force [2,3]. However, few of them focus on shear stress of sintered particles. Meanwhile, force prediction relies on parameters obtained from experiment [4]. In this work, the normal and tangential stresses between two sintered particles are experimentally measured. A numerical simulation with extended sintering force model is performed based on the experiment data.

Results and discussion

A comparison of the interparticle forces, including the elastic force, the van der Waals force and the sintering force is shown in Fig. 1, where the parameters are the same with Kuwagi's work [3]. Particle diameter is 0.02m and particle relative velocity is 0.0005m/s. τc is the characteristic collision time estimated via the Hertz contact model. The sintering force strongly depends on the particle contact time. Within the characteristic collision time, the value of sintering force is close to the van der Waals force, but is insignificant compared with the elastic force. However, the sintering force increases evidently with increase of contact time.

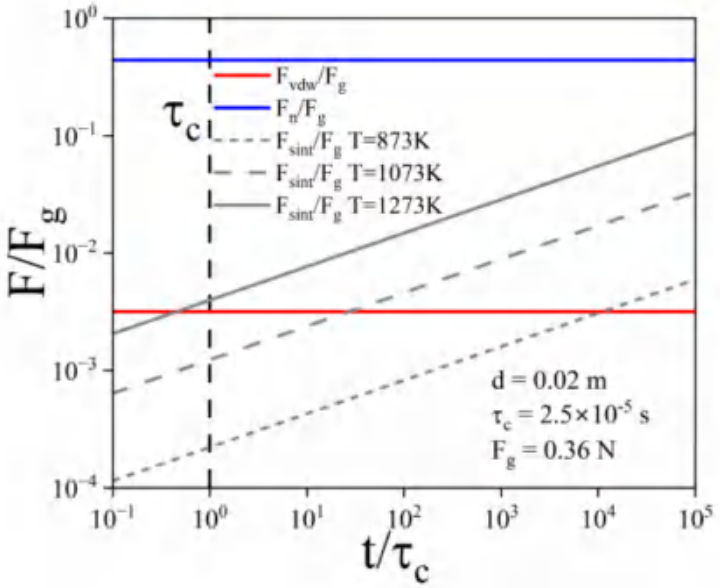


Figure 1 – Comparison of interparticle forces as a function of time

Conclusions

In this work, the normal and tangential sintering force between two particles are measured. Subsequently, the sintering model is extended based on the experimental data. Eventually, a DEM simulation considering the sintering force is conducted. Our results provide a fundamental

insight into the mechanism of defluidization due to particle agglomeration under high temperature condition, which may bring further perspective on fluidized bed control.

References

[1] Yi M, Wang W, Xue M, et al. Modeling and simulation of sintering process across scales, Archives of Computational Methods in Engineering 30.5 (2023): 3325-3358.

[2] Mikami T, Kamiya H, Horio M. The mechanism of defluidization of iron particles in a fluidized bed, Powder technology 89.3 (1996): 231-238.

[3] Kuwagi K, Mikami T, Horio M. Numerical simulation of metallic solid bridging particles in a fluidized bed at high temperature, Powder Technology 109.1-3 (2000): 27-40.

[4] Luan C, You C. A novel experimental investigation into sintered neck tensile strength of ash at high temperatures, Powder Technology 269 (2015): 379-384.

Unjamming and yielding of intruder-deformation-driven dense granular materials

Guangyang Hong, Qijun Zheng, Aibing Yu, Jian Li
Key Laboratory of Structural Dynamics of Liaoning Province, College of Sciences, Northeastern University, Shenyang 110819, China

Abstract

Dense driven granular materials have garnered significant interest due to their complex rheological phenomena such as dynamical heterogeneities and frequency dependence. However, the unjamming/yielding transition induced by intruder deformation, which is critical for applications in living matter interactions with sand and foundation-soil, remains poorly understood compared to boundary- or friction-driven granular systems. To address this knowledge gap, we first study the relaxation dynamics of granular medium driven by oscillatory intruder deformation, and the evidence of an abrupt unjamming/yielding transition in frequency domain is provided. The evaluation was performed by combining the bulk rheology manifested as the temporal evolution of beam deformation, dynamical and mesostructural heterogeneities. We find that the transition is characterized by the emergence of vortices, which cause shear bands accompanied by superdiffusion, transforming spatial correlations from exponential to power-law decay. This study demonstrates the potential for controlling and predicting elastic and flow properties in the intruder-deformation-driven flow and provides future theoretical or numerical modeling of active mesorheology through comparisons with complex fluids and boundary-driven scenarios.

Keywords: Granular materials, Intruder deformation, Unjamming, Yielding

The restitution coefficient and critical sticking velocity of small particles: simulation and experiment

Shumiao Zhao, Zhu Fang, Zhikai You, Yiyang Zhang*
Tsinghua University, Beijing, China

Abstract

The collision between small adhesive particles and flat substrate is a fundamental phenomenon occurring in various natural and industrial processes, such as fine particle deposition, aerosol filtration, abrasive blasting process, and powder transportation etc. [1-5]. The essential parameter within the process of particle collision are the restitution coefficient and the sticking velocity which plays an important role in particle deposition. Due to the complex coupling relationship between elastic deformation, surface adhesion, and viscoelastic damping, obtaining a universal correlation for the restitution coefficient remains challenging.

In our study [6], we used the finite element method (FEM) to numerically investigate the wall collision of small adhesive particles, which has been modelled as Maxwell standard linear solid. Initially, we established the relationship between the restitution coefficient and relaxation time in pure viscoelastic collisions. Moreover, the FEM model naturally captures the coupling between the surface adhesion and viscoelastic damping, and thus is capable to predict the proper restitution coefficient by directly using the surface energy of bulk materials, without any adjustment or fitting. By simulating a large number of wall collision cases in a wide range of impact parameters, we present new universal correlations for the restitution coefficient and critical sticking velocity, which agree well with the classic experimental data in a wide range of the incident velocity, particle size and particle/substrate material properties.

$$v_c = 404.07 \frac{\gamma^{1.125} \tau^{0.242}}{\rho^{0.621} E^{0.504} R^{1.366}}$$

In this equation, relaxation time τ is regarded as material property which cannot be directly obtained. Thus, we present an experimental investigation on the wall collision of particles. The wall collision process of particles is recorded using a high-speed camera together with a microscope. By processing the experimental images, we can obtain the curve of the restitution coefficient changing with the incident velocity, and then combine it with the previously obtained unified correlation to obtain the relaxation time of the material, providing conditions for calculating the critical sticking velocity. The result of this work can be easily incorporated into Eulerian – Lagrangian simulations for quantitatively describing the sticking/rebound behaviors of laden aerosol particles.

Key words: Particle-wall collision, Restitution coefficient, Critical sticking velocity, Relaxation time

References

[1] Cai, Y., Tay, K., Zheng, Z., et al Modeling of ash formation and deposition processes in coal and biomass fired boilers: A comprehensive review[J]. Applied Energy, 230(2018) 1447-1544.

[2] Chen, S., Liu, W., & Li, S. Effect of long-range electrostatic repulsion on pore clogging during microfiltration. Physical Review E, 94 (2016) 063108.

[3] Kleinhans, U., Wieland, C., Frandsen, F. J., & Spliethoff, H. Ash formation and deposition in coal and biomass fired combustion systems: Progress and challenges in the field of ash particle sticking and rebound behavior. Progress in Energy and Combustion Science, 68 (2018) 65–168.

[4] Liu, W., & Wu, C. Y. Lateral migration of a neutrally buoyant particle in Couette flow with thermal convection. International Journal of Multiphase Flow, 138(2021) 103612.

[5] Ruan, X., Chen, S., & Li, S. Effect of long-range Coulomb repulsion on adhesive particle agglomeration in homogeneous isotropic turbulence. Journal of Fluid Mechanisms, 915 (2021) A131.

[6] Fang, Z., Zhang, Y., Wu, X., et al New explicit correlations for the critical sticking velocity and restitution coefficient of small adhesive particles: A finite element study and validation[J]. Journal of Aerosol Science, 160 (2022) 105918

Intermittent Jamming of Cohesive Particle Flow in FT4 Rheometer

Wenguang Nan[1, 2],Wenbin Xuan[1]*

1. School of Mechanical and Power Engineering, Nanjing Tech University, Nanjing 211816, China

2. Faculty of Engineering and Physical Sciences, University of Leeds, Leeds LS2 9JT, UK

**Contact Email: nanwg@njtech.edu.cn*

Abstract

Dense granular flows are widely found in nature and industrial engineering, such as landslide, food processing, and additive manufacturing. Understanding of the rheological behaviour of fully three-dimensional and non-uniform granular flow through constrictions is of great interest. We simulated the granular flow in an impeller-based rheometer using Discrete Element Method (DEM), where a twisted blade rotates and moves downward and upward in the particle bed, and we focus on the dynamics of particles around the constriction between the blade and its surrounding vessel wall. The results show that mechanical jamming in the impeller-based powder rheometer is transient, and it could occur and disappear frequently. The jamming is limited in a narrow region and short duration. Jamming is more serious in the test mode with soft and lifting flow pattern, and it is sensitive to particle stiffness, where larger stiffness is more prone to the occurrence of jamming. The flow energy used in the rheometer could not represent the flowability of bulk particles anymore if jamming occurs. The scaling law used to speed up the DEM simulation by reducing particle stiffness may fail for the granular flow passing through the clearance. Jammed particles are almost all located in the gap between the blade tip and vessel wall. The jamming structure may only be able to resist the load from the blade in its rotational direction, as shown in Figure 1. The particle surface maybe damaged by the blade tip during the survival time of jamming. The dynamics of jammed particles are determined by the combined effects of stationary wall and blade shearing. The jamming of particles in the impeller-based powder rheometer is in low frequency with value less than 50 Hz, and its duration is usually less than 0.04 s, as shown in Figure 2.

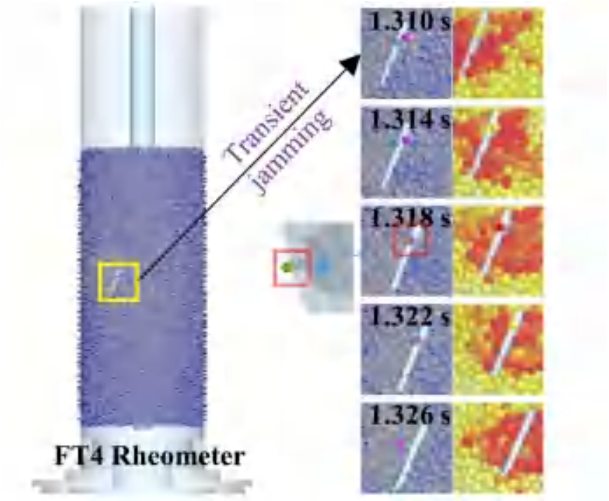


Figure 71 - Snapshot of evolution of the jamming event in downward test，where both force chain (jammed particle is colored by purple) and velocity of particles are included.

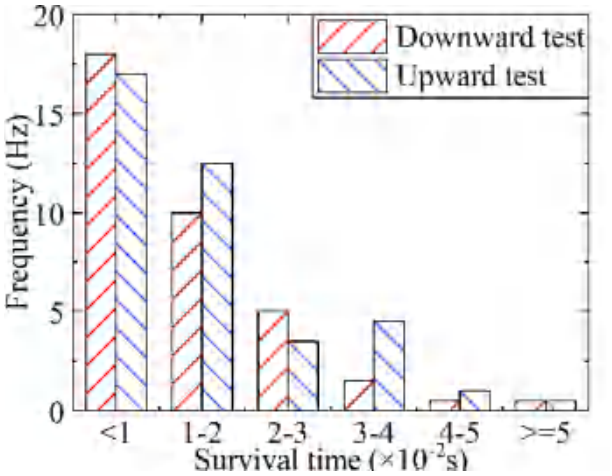


Figure 2 - Variation of the frequency with the survival time for the jamming events in case A.

Keywords: Granular flow; Jamming; Rheology; Rheometer; Discrete element method.

Length-scale-based rheology for dense granular suspensions

Teng Man[1], Zhuan Ge[1,2], Zaohui Zhang[1,2], Sergio A. Galindo-Torres[1], Kimberly M. Hill[3]
1. Westlake University, Hangzhou, China
2. Zhejiang University, Hangzhou, China
3. University of Minnesota, Minneapolis, United States

Abstract
In this study [1], we present a length-scale-based rheological model for dense sheared granular suspensions as they transition from inertial- to viscous-dominated regimes. Different from dimensionless numbers previously derived from time-scale ratios [2,3], we derive a length-scale ratio using straightforward physics-based considerations for a particle subjected to pressure and drag forces. In doing so, we demonstrate that an appropriately chosen length-scale ratio intrinsically provides a consistent relationship between the normal stress and the system proximity to its "jammed" or solid-like state, even as a system transitions between inertial and viscous states, captured by a variable Stokes number. The theoretically derived dimensionless number is then verified by experimental data extracted from previous studies, as well as by our own simulation results drawn from the discrete element simulations.

Keywords: Rheology, Dense suspensions, Length-scale, Discrete element method

References
[1] Z. Ge, T. Man, H. E. Huppert, K. M. Hill, S. A. Galindo-Torres, Unifying length-scale-based rheology of dense suspensions, Physical Review Fluids 9 (2024) L012302.
[2] P. Jop, Y. Forterre, O. Pouliquen, A constitutive law for dense granular flows, Nature 441 (2006) 727-730.
[3] F. Tapia, M. Ichihara, O. Pouliquen, E. Guazzelli, Viscous to inertial transition in dense granular suspension, Physical Review Letters 129 (2022) 078001.

A new numerical method for dynamic resuspension of particles

Zhikai You, Shumiao Zhao, Zhu Fang, Yiyang Zhang*
Tsinghua University, Beijing, China

Abstract

Particle resuspension is a common phenomenon in nature and industries, such as the resuspension of radioactive dust in nuclear reactors (including fission reactors and fusion reactors) [1-2], dust removal from the surface of spacecraft solar panels on Mars [3,4]. As a long-term process, the resuspension rate usually scales inversely with duration t, which has been verified both theoretically and experimentally [5]. The challenges in the simulation of resuspension of particulate matter lie in the resolution of turbulence near the wall and in the implementation of the resuspension rate as a function of time. In the simulation of the Euler-Lagrange method, a common approach is the torque balance model [6], where remobilization of particles occurs when the aerodynamic torque to which they are subjected is greater than their critical adhesion torque. Due to the small scale of the particles (typically smaller than the viscous sublayer), the near-wall turbulence need to be fully resolved. Meanwhile, the time dependence of resuspension rate can not be represented because in the simulation code, particle resuspension occurs in very short timescales, usually smaller than the Kolmgorov timescale.

In this work, a new simulation approach for the prediction of particle resuspension is proposed, which enables the simulation of particle dynamic resuspension at a much smaller computational cost. This method is based on the physical mechanism of particle resuspension, i.e., stochastic oscillatory motion, and requires only the resolution of the mean velocity and turbulent kinetic energy k or Reynolds stress near the wall to implement the dynamic simulation of particle resuspension. In the simulation code, whether the particles are resuspended or not is treated as a random event, the probability of which depends on the local flow field statistics, the physical properties of the particles, and the run time. We couple the resuspension model to the fluid computation and consider the difference between the Lagrangian time step and the resuspension time step. Resuspension of micron spheres is simulated and the effects of particle size, surface energy and flow conditions on resuspension are discussed. The evolution of the suspension rate versus time is verified and is in good agreement with classical experiments as shown in Fig.1. The potential and limitations of the code application are also evaluated.

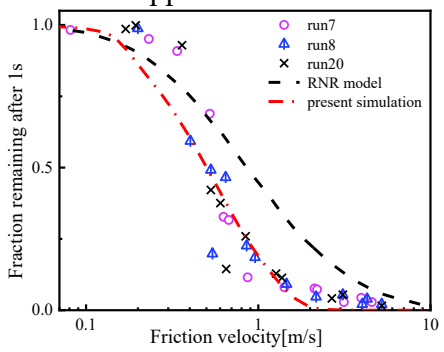


Fig 1 Comparison of experimental results with simulation predictions for the 20 μm alumina spheres.

Key words: Particle resuspension, Dynamic simulation, RANS

References

[1] P. W. Humrickhouse, HTGR dust safety issues and needs for research and development, (2011).

[2] S. Ratynskaia, A. Bortolon, et al., Dust and powder in fusion plasmas: Recent developments in theory, modeling, and experiments. Reviews of Modern Plasma Physics 6.1 (2022) 20.

[3] G. Bermudez, P. Voarino, and O. Raccurt. Environments, needs and opportunities for future space photovoltaic power generation: A review. Applied Energy, 290 (2021) 116757.

[4] C. I. Calle, et al., Active dust control and mitigation technology for lunar and Martian exploration. Acta Astronautica, 69.11-12 (2011) 1082-1088.
[5] D. Hall, and J. Reed. The time dependence of the resuspension of particles. Journal of aerosol science, 7 (1989) 839-842.
[6] C. Henry, and J. P. Minier, Progress in particle resuspension from rough surfaces by turbulent flows. Progress in Energy and Combustion Science, 45 (2014) 1-53.

Machine Learning Based Surrogate Models for Efficient Particulate Flow Simulation

Xizhong Chen
Department of Chemical Engineering, School of Chemistry and Chemical Engineering, Shanghai Jiao Tong University, Shanghai 200240, PR China

Abstract
Particulate flow plays a pivotal role across a wide array of industrial processes and natural phenomena, posing a significant challenge for swift and precise simulation. Conventional simulation techniques, notably those employing the Discrete Element Method (DEM), are known for their high computational demands, often at the expense of balancing accuracy with efficiency. The advent of artificial intelligence heralds a transformative shift, igniting a surge in interest towards harnessing machine learning for the simulation of particulate flows. In this study, we explore the application of cutting-edge machine learning methods such as Graph Neural Networks (GNNs) to learn the interactions between particles and develop corresponding reduced-order models for the efficient simulation of particulate flows.

Keywords: Machine Learning, Discrete Element Method, Granular Flows

Introduction
Particulate flow simulation is critical for optimizing a multitude of industrial processes and understanding various natural phenomena. Despite its importance, accurately simulating particulate flows remains a formidable challenge due to the complex interactions between particles. Traditional methods like the Discrete Element Method (DEM) offer detailed insights but at the expense of high computational demands, often necessitating a compromise between precision and efficiency. In recent years, the burgeoning field of artificial intelligence has presented novel alternatives to conventional simulation approaches. Machine learning, in particular, has shown promise in transcending the limitations of traditional methods, offering a blend of accuracy and computational efficiency. Among the various machine learning paradigms, Graph Neural Networks (GNNs) stand out for their ability to model complex systems through the interactions between entities, making them exceptionally suited for particulate flow simulations.

Methodology
GNNs are a class of deep learning models designed to capture the dependency of graphs through message passing between the nodes of graphs. In the context of particulate flow simulation, each particle can be considered a node, with edges representing the interactions between particles. This structure allows GNNs to effectively learn the underlying dynamics of particulate systems. Here, GNNs are used as surrogate models for inverse design of granular flows and particulate systems.

Conclusions
The developed approach reduces computational demands and also maintains a high level of accuracy in predicting particulate flow characteristics. The application of machine learning methodologies in the context of liquid-solid stirred tanks and gas-solid fluidized beds were further explored, showcasing the versatility and potential of machine learning-based surrogate models in capturing the complex dynamics of particulate systems.

Acknowledgements
The financial support from National Natural Science Foundation of *China Excellent Young Scientists Fund Program (Overseas)* and*National Natural Science Foundation of China (grant no. 22308212)* are acknowledged.

References
[1] Sanchez-Gonzalez A, Godwin J, Pfaff T, et al. Learning to simulate complex physics with graph networks[C]. International conference on machine learning. PMLR, 2020: 8459-8468.

[2] Jiang Y, Byrne E, Glassey J, et al. Reduced-order modeling of solid-liquid mixing in a stirred tank using data-driven singular value decomposition[J]. Chemical Engineering Research and Design, 2023.

Interface-resolved simulations of particles in active nematics

Zhenyu Ouyang
(Laboratory of Impact and Safety Engineering (Ningbo University), Ministry of Education, Ningbo 315201, China)

Abstract

An accurate coarse-grained simulation of an active fluid is invaluable as a tool to understand its hydrodynamic behaviors. The study on the dynamics of particles immersed in an active fluid also requires accurate resolution of the fluid–particle interaction. In this paper, we propose a robust direct forcing fictitious domain method to study the dynamics of suspended particles in an active fluid modeled by "active nematics." This method serves as both a coarse-grained approach and an accurate model of fluid–particle interaction. We first validate the method by computing the kinetic energy spectrum for the bulk active nematics and find that it accurately reproduces the scaling laws reported theoretically and experimentally. By utilizing these interface-resolved simulations, we illustrate that the model's activity parameter cannot be simply considered as the concentration of bacterial suspensions. Moreover, we find that the diffusion coefficient DT of an individual disk is relevant to the length scale lc of the active nematics, following a power-law scaling DT~lc 1.5. Regarding collective dynamics, we discover a self-organized length scale of approximately 7.5 times the disk's diameter in the active nematics. Additionally, the disks modify the kinetic energy spectrum of the active nematics at both the self-organized length scale and the individual disk's diameter scale, respectively.

Keywords: Active fluids, Particle suspension

Acknowledgements

The authors would like to thank the National Natural Science Foundation of China (Grant Nos. 12302333;12132015)

A combined DEM and Positron Emission Particle Tracking (PEPT) study on continuous blending

Jiawei Hu[a], Bernardus Joseph Nitert[b], Chao Zheng[a], Nicolin Govender[a], Chuan-Yu Wu[a]*
[a] University of Surrey, Guildford, United Kingdom
[b] Johnson & Johnson Innovative Medicine NV, Beerse, Belgium

*Corresponding author: Prof. Chuan-Yu Wu, Email: c.y.wu@surrey.ac.uk

Abstract

Continuous powder blending plays a pivotal role in the realm of continuous manufacturing industries. The Positron Emission Particle Tracking (PEPT) technique and the Discrete Element Method (DEM) are widely utilised to investigate the intricate behaviours of powder flow within continuous blenders.

In this study, the Discrete Element Method (DEM) and Positron Emission Particle Tracking (PEPT) techniques were employed for the first time in a comparative analysis of powder flow behaviours in continuous blenders, focusing on residence time distribution (RTD), velocity magnitude distribution, radial movement, and dispersion coefficients across various blade configurations. As shown in Figure 1, the full-scale of continuous blender is modelled by the GPU-based Blaze-DEM code, which is developed by Govender et al. [1]. During experiments, the continuous blender was positioned between two PEPT cameras. Once the radioactive tracer passes through the PEPT camera zone, the back-to-back gamma rays from the radioactive tracer would be detected and its position can be determined [2].

Results reveal nearly identical RTDs and average radial dispersion coefficients between DEM and PEPT. Both methods yield consistent trends in average velocity magnitude distributions and similar asymmetrical patterns in radial velocity distributions across the blender's cross-section. Notably, a decrease in mixing elements leads to reduced mean residence times and increased average axial dispersion coefficients, as observed through both DEM simulations and PEPT measurements.

In conclusion, DEM simulations predict powder flow behaviours comparable to the PEPT measurements across various aspects.

Keywords: Discrete element method, Positron Emission Particle Tracking, Continuous blending, Full scale simulation，Mixing

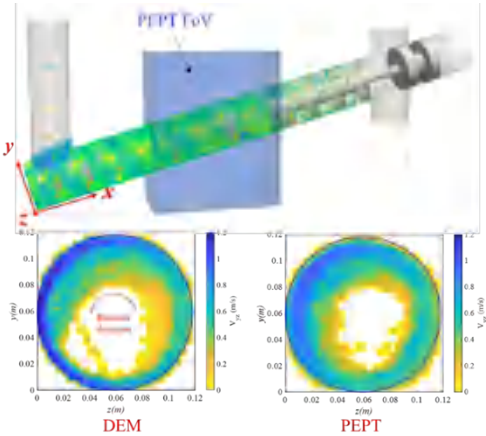


Figure 72 - Schematic diagram of relative position of PEPT cameras and the continuous blender, and asymmetrical patterns in radial velocity distributions across the blender's cross-section observed from both DEM and PEPT.

References

[1] N. Govender, R. Rajamani, D.N. Wilke, C.Y. Wu, J. Khinast, B.J. Glasser, Effect of particle shape in grinding mills using a GPU based DEM code, Miner. Eng. 129 (2018) 71–84.
[2] A.L. Nicuşan, C.R.K. Windows-Yule, Positron emission particle tracking using machine learning, Rev. Sci. Instrum. 91 (2020).

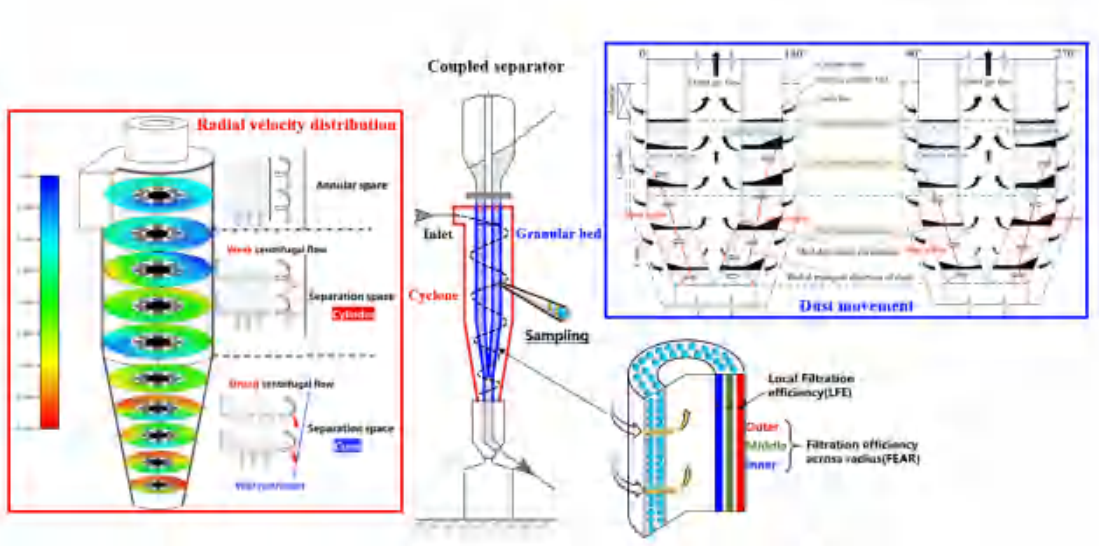
Poster Session

Filtration performance of a granular bed filter in a coupled separator

Ming Chang, Yiping Fan, Chunxi Lu
State Key Laboratory of Heavy Oil Processing, College of Chemical Engineering and Environment, China University of Petroleum, Beijing, 102249, China

ABSTRACT: In this study, the filtration performance of the built-in granular bed in a cyclone-granular bed coupled separator is investigated. Cyclone is used to recover catalyst particles from the regenerated flue gas in the Fluid catalytic cracking by centrifugal force. While the granular bed captures fine dust particles smaller than 10 μm. Catalyst loss problem can be addressed by coupling different separation mechanisms in the coupled separator. To clarify the separation process, the necessity to elucidate the filtration performance is shown. The investigation has been performed for the velocity distribution, the bed dust deposition, and the filtration efficiency in the coupled separator under varying operating parameters. Experimental results indicate that the radial velocity component is a main influencing factor on the granular bed filtration efficiency. The outer-layer bed collector particles exhibit superior dust collection capabilities. Based on the intrusive dust sampling, a diagram is presented to clearly illustrate the primary mechanisms that govern dust movement in the bed. Furthermore, two parameters named by the local filtration efficiency (LFE) and the filtration efficiency across radius (FEAR) are proposed for analyzing the granular bed filter performance. The LFE exhibits a declining trend as the inlet air velocity increases. The dust size distribution analysis highlights the capacity of the bed to capture fine dust particles (<5 μm) which tended to accumulate at the inner layer. The FEAR, ranging from 91% to 97%, offers a comprehensive assessment of the coupled separator performance and structural optimization.

Keywords: Filtration performance; Coupled separator; Local filtration efficiency; Filtration efficiency across radius; Dust movement



Performance evaluation of a wet air oxidation reactor with external circulation for high-chemical oxygen demand wastewater treatment

Feng Zhang, Xiemin Liu
Nanjing University, Nanjing 210023, China

Abstract
The presence of high-concentration organic contaminants in wastewater poses considerable risks to the health of both humans and ecosystems. Although wet air oxidation (WAO) is an attractive treatment option, it requires the consumption of freshwater resources for dilution. Herein, we effectively addressed the constraints of traditional WAO reactors by introducing an external circulation loop. We further proposed an energy optimization model and an improved CFD model to optimize the parameters of the external circulation reactor. The results show COD removal efficiency increased by 21.6%, while energy consumption decreased by 34.8%. Using the optimized parameters, we modified an industrial-scale external circulation wastewater treatment system, achieving long-term stable operation over a wide range of wastewater COD.

Keywords: Wet air oxidation, External circulation, Energy consumption, Computational fluid dynamics

Introduction

Wet air oxidation (WAO) is regarded as one of the most efficient treatment for hazardous and non-biodegradable wastewater with high concentrated pollutants[1]. However, the COD of wastewater for the traditional WAO or catalytic WAO processes has to be limited below 50000 mg/L to avoid excessive temperature rise from the bottom to the top of the reactor or polymerization of high-concentration organic matter under high-temperature conditions[2]. Consequently, the highly concentrated wastewater has to be diluted to reach the meet requirements of the water intake for WAO. This inevitably increases the equipment size and operating costs, also wastes resources.

To address this, the paper proposes a feasible solution, which involves drawing high-temperature and high-pressure oxidized liquid from the upper part of the WAO reactor and circulating it to the reactor bottom to preheat and dilute the highly concentrated raw wastewater. The proper circulation flow rate and the right location of the circulation inlet for the design of external circulation should be determined**.**

Therefore, a suitable CFD simulation method for optimizing the external circulation WAO reactor was established. The fluid dynamics and reaction kinetics were coupled and simulated for the WAO reactor with an external circulation to assess the effect of structural and operational parameters. The energy consumption was also calculated to identify the proper parameters, which can induce the lowest energy consumption and the most COD removal. Finally, based on the optimized parameters, a set of industrial-scale external circulation WAO reactors were modified, and the improved model was validated.

Methodology

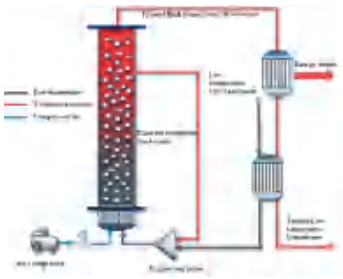


Figure 73 - The industrial project for external circulation WAO reactor

The detailed reactor configuration and process flow diagram for the industrial-scale plant are shown in ***Figure 1***. The circulated wastewater is drawn from the reactor at a height of 5-20 m and mixed with preheated raw wastewater before entering the reactor bottom.

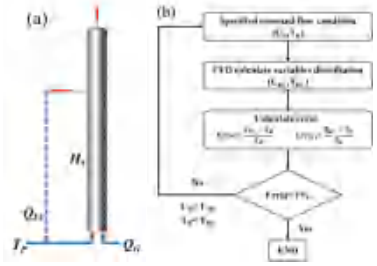


Figure 74 - Numerical settings

The Eulerian-Eulerian two-fluid method is used for three-dimensional numerical simulation. The external circulation is simplified as a side stream outlet, and solved through an iterative method as shown in ***Figure 2***.

Results and discussion

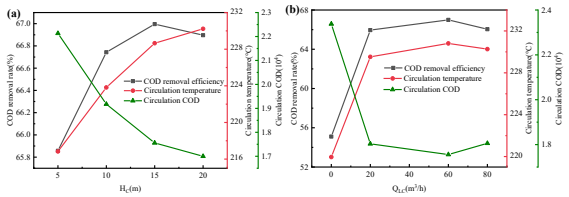


Figure 75 - Effect of parameters on COD removal efficiency

The higher H_C means longer reaction time and thus lower COD and higher temperature of circulation flow, which benefit the COD reduction. However, when H_C is too high, COD removal efficiency slightly drops, due to the decrease in the residence time of raw wastewater. The highest COD removal efficiency (67.0%) is achieved for H_C of 15 m (***Figure 3a***). A Q_{LC} of 60 m^3/h attains the highest COD removal efficiency, as shown in ***Figure 3b***.

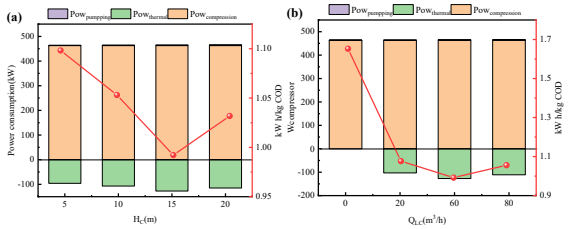


Figure 76 - Effect of parameters on energy consumption

Due to the significant COD removal ability, H_C of 15 m achieves the lowest energy consumption per COD removal (0.99 kWh/kg COD), about 65.2% of the energy consumption of WAO without circulation. Q_{LC} of 60 m^3/h presents the lowest energy consumption per COD removal (***Figure 4***).



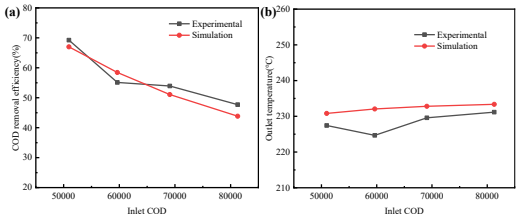


Figure 77 - Industrial performance

Based on the simulation results, an industrial external circulation WAO reactor was constructed. The predicted COD removal efficiency matches well with the factory data. The outlet temperature is slightly overestimated, but the maximum relative error is less than 10% (***Figure 5***).

Conclusions

For the effective treatment of industrial wastewater with high COD, an industrial-scale WAO reactor with external circulation was designed and simulated with the CFD method.

(1) the WAO reactor with external circulation saves 34.8% of energy consumption and COD removal efficiency is increased by 21.6%.

(2) The predicted COD removal efficiency and outlet temperature by the CFD model match well with the industrial data, confirming the simulation and optimization method proposed in this paper.

Acknowledgements

The authors are grateful for the financial support of the National Natural Science Foundation of China (No. 22278202).

References

[1] E. Gout, F. Toure Lo, M. Monnot, Coupling membrane processes with wet air oxidation for the remediation of industrial effluents, Chemical Engineering Journal 472 (2023) 144937.

[2] S.T. Kolaczkowski, P. Plucinski, F.J. Beltran, Wet air oxidation: a review of process technologies and aspects in reactor design, Chemical Engineering Journal 73(2) (1999) 143-160.

Optimization of process parameters in an entrained flow gasifier

Ping Li[1,2], Cai Chen[2], Yixin Zhang[1], Fanhui Guo[1], Jianjun Wu[1*]

1. School of Chemical Engineering and Technology, China University of Mining and Technology, Xuzhou 221116, China

2. State Key Laboratory of High-efficiency Utilization of Coal and Green Chemical Engineering, College of Chemistry and Chemical Engineering, Ningxia University, Yinchuan 750021, China

Abstract

Entrained-flow gasifier has been widely applied in coal gasification due to its advantages of high coal conversation rate, wide adaptability of coal types and large operation flexibility. The process parameters are the main influencing factors for the long-term stable operation of the entrained-flow gasifier. The CFD simulation was employed to study pulverized coal gasification which contained multiphase flow and complex reactions in this paper. The process parameters of the pulverized coal entrained-flow gasification process were optimized based on orthogonal experiment design method and the temperature and flow fields distribution in the gasifier were investigated by improving the nozzle model. Two-competing rates model, unreacted-core shrinking model, Discrete Phase Model and Eddy Dissipation Concept (EDC) model were used for coal devolatilization, heterogeneous and homogenous reactions process. The optimized process parameters were obtained by both range analysis and variance analysis of the orthogonal test data. The results showed the m(C)/m(O) is primary factor among three factors that be investigated factors. When the operation pressure is 4MPa, m(C)/m(O) is 1.4 and m(H_2O)/m(O) is 0.1/0.9, the temperature in the outlet is 1680 K and the syngas species H_2 and CO achieve 93.22%. The new gasifier model with a detailed nozzle model was established that is close to the actual injection situation. The gasification process was simulated under the optimal parameters obtained from orthogonal experiments. The results revealed that the pyrolysis zone in the detailed nozzle model is smaller, while the flame region extends further along the axial direction compared to the simplified model. In terms of radial distribution, an uneven temperature profile is exhibited with a smaller temperature gradient in the detailed model. The flame area increases and the maximum temperature at the flame location is 100K lower than in the simplified model. The maximum velocity in the detailed nozzle model is predominantly located at the nozzle inlet, which is 45 m/s higher than that of the simplified model. The recirculation zone within the detailed model is also more pronounced. However, the difference in velocities between the two models inside the furnace is little. Regarding the distribution of components, the detailed nozzle model presents a fairly consistent pattern with the simplified model. At the outlet, the mole fractions of H_2 and CO in the detailed model are recorded as 92.88%, which is consistent with the simulation results under the simplified model. But the temperature and flow fields distribution are more reasonable.

Keywords: Multiphase flow, Flow field, Parameters optimization, CFD simulation, Entrained-flow gasification

Temperature Regulation of Polyethylene Composite Materials

Chenjia(Zhejiang University,Hangzhou)
Rencongjing(310058,seasonrcj@zju.edu.cn)

Abstract
Personal Thermal Management (PTM) plays a significant role in maintaining individual health, conserving energy consumption, and mitigating the greenhouse effect. Thermal radiation, as the most universal heat transfer route for the human body, has proven to be an effective method for managing radiative heat that surpasses traditional ways of heating or cooling. In this paper, based on the principle of radiative control, the structure-performance relationship of polyethylene with asymmetric structures and thermal conductivity is studied. By in-situ addition of nanoscale copper, carbon, and other coatings, the relationship between material structure and temperature regulation is understood, thereby achieving good thermal insulation effects in low-temperature environments, and effective passive cooling in high-temperature environments.

Keywords: PTM, PE, Radiative Control, Metal Coating

Introduction

Personal Thermal Management (PTM) is crucial for achieving sustainable development. It is not only related to individual comfort and health[1], but also affects the effective use of energy and environmental sustainability. Clothing, as the interface between the human body and the environment, plays a key role in heat exchange. PTM is based on advanced textiles, which regulate human body temperature and the microenvironment. Traditional thermal management methods are no longer suitable for the needs of modern society. In high-temperature environments, the structure of polyethylene and carbon layers allows the fabric to dissipate heat towards the skin, while in low-temperature environments, the structure is adjusted to dissipate heat towards the environment, achieving a warming effect. This design enables the fabric to automatically regulate heat conduction according to the environment, achieving both cooling and warming functions[2].

Methodology

Select PE plain woven fabric (100D, 65 g/m², thickness 0.145 mm). First, fully immerse the fabric in anhydrous ethanol, ultrasonically clean for 1 hour, then ultrasonically clean in deionized water for 1 hour, and finally dry at 60 °C to remove stains from the fabric.

Preparation of low-emissivity copper layer: The copper paste is commercial copper paste purchased from a supplier. The copper paste is coated on the pre-treated PE fabric using an infrared drying flat coating machine, with a copper layer thickness of 20 μm.

Preparation of high-emissivity carbon layer: The carbon paste is made by dispersing carbon black and polyacrylonitrile (molecular weight 150,000) (carbon black: polyacrylonitrile = 1:1) in an appropriate amount of N,N'-dimethylformamide, stirred for at least 12 hours. The prepared carbon paste is coated on the pre-treated PE fabric using an infrared drying flat coating machine, with a carbon coating thickness of 20 μm.

After coating with the carbon and copper layers, the PE fabric is combined face-to-face, with the thickness of the PE layer on the carbon side being twice that of the copper side, to create thickness asymmetry.

Results

Table 1 - In the insulation mode, the artificial skin test temperature

Ambient Temperature(℃)	Body Temperatur(℃)	Skin Temperature Over The Carbon Layer(℃)
15.5	32.5	33.5
19.4	32.2	33.3
21.7	32.5	33.2
22.5	33.9	34.2

Table 2 - In the cooling mode, the artificial skin test temperature

Ambient Temperature(℃)	Body Temperature(℃)	Skin Temperature Over The Carbon Layer(℃)
24.5	33.9	33.1
30.0	34.0	33.0
32.2	35.0	33.6
38.4	34.9	33.5

Conclusion

Compared to PE covering, the PE coated fabric in the insulation mode (with the low-emissivity layer facing outward) can increase the skin temperature by 0.3-1.1 ℃, indicating that the coated fabric can provide insulation effect at low temperatures; compared to PE covering, the PE coated fabric in the cooling mode (with the high-emissivity layer facing outward) can decrease the skin temperature by 0.8-1.4 ℃, indicating that the coated fabric can provide a cooling effect at high temperatures.

References

[1] Hu, R., et al., Emerging Materials and Strategies for Personal Thermal Management. Advanced Energy Materials, 2020. 10(17).

[2] Hsu, P.C., et al., A dual-mode textile for human body radiative heating and cooling. Science Advances, 2017. 3(11).

Explosion-driven fragmentation of particle shells

Chuanshan Zhang [a], Chun Feng [b], Kun Xue [a*]

[a] *State Key Laboratory of Explosion Science and Technology, Beijing Institute of Technology, Beijing 100081, Beijing, China*

[b] *Key Laboratory for Mechanics in Fluid Solid Coupling Systems, Chinese Academy of Science, Beijing 100190, Beijing, China*

Abstract:

The study investigates the breakage characteristics of brittle particles subjected to central explosive detonation, considering blast wave propagation, stress transmission, and Weibull distribution of breakage strength. Experimental analysis, varying granular media to explosive mass ratio (M/C), reveals its pivotal role in particle crushing. Due to experimental limitations, numerical methods (FEM-DEM) in 2D and 3D settings are employed. Finite Element Method (FEM) models explosive detonation and product expansion, while Discrete Element Method (DEM) simulates particle dynamics. Non-equilibrium internal stress due to blast wave pulse nature challenges Weibull distribution applicability. A model incorporating induced stress within blast wave propagation time, non-uniform stress propagation, and modified Weibull distribution explains broken particle volume variation with scaled distance, corroborated by simulation results.

Keywords: explosion-driven; coupling algorithm; breakage; fragmentation; particle shells

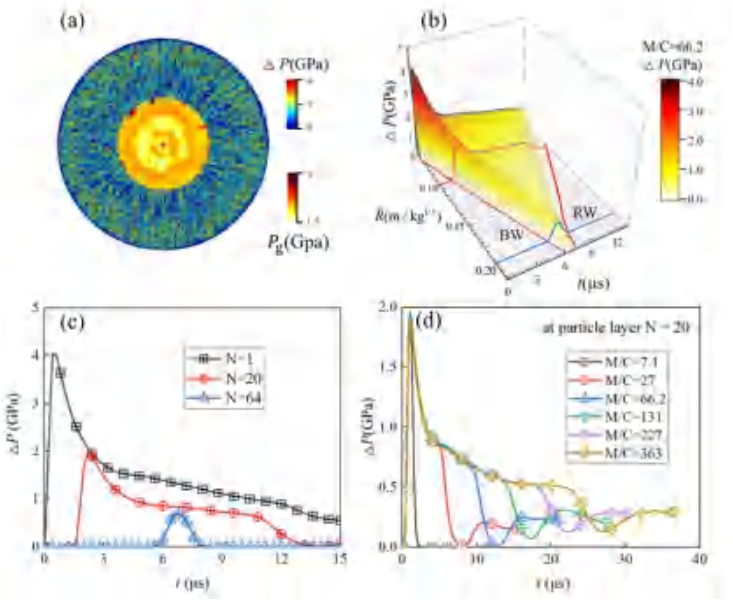


Fig. (a) Numerical computation model pressure rendering results diagram, (b) Spatiotemporal evolution diagram of particle stress along the radial direction, (c) Pressure-time curve diagram of different particle layer,(d) Pressure-time curve diagram at different equivalent ratios for the same particle layer position

Spontaneous transfer of droplets across a microfluidic liquid-liquid interface

Haozhe Yi, Taotao Fu, Daofan Ma, Chunying Zhu, Youguang Ma
Tianjin University, Tianjin, China

Abstract
In this experiment, we observe a novel flow pattern of droplet transfer induced by interfacial tension. By deeply analysing the mechanism, an accurate prediction equation for determining the critical condition of droplet transfer is proposed to precisely forecast the flow pattern. Simultaneously, the occurrence of liquid film entrainment is observed, resulting in the formation of an oil-in-water-in-water system under appropriate conditions.

Keywords: Microchannel, Microfluidic, Droplet, Interface.

Introduction

The interphase transfer can change the surrounding environment of droplets, offering extensive prospects for applications in various fields. However, limited research has been conducted on the mechanism, and no accurate equation for predicting flow patterns has been proposed. In this experiment, the contact mode between the droplet and the interface is different from the traditional methods, and the driving force is distributed along the axial direction. By utilizing this flow pattern, droplets transfer from the oil phase to the water phase, resulting in the formation of an aqueous two-phase system. By coupling the mechanism with the flow parameters, the prediction equation of the critical condition of droplet transfer is proposed, and the flow pattern is accurately predicted. Additionally, a special flow pattern of oil-in-water-in-water (O/W/W) system is observed. This study expands the potential for the application of droplet transfer.

Methodology

A high-speed camera was used to observe the flow process of the three-phase system in the microfluidic device shown in Fig. 1. The three-phase system was composed of 24wt% trisodium citrate solution, 24wt% polyethylene glycol solution and ionic liquid [BMIM]- [PF6].

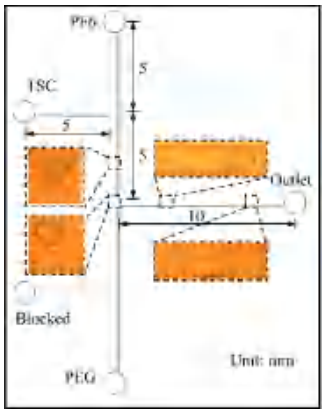


Figure 78 - The structure diagram of the microchannel.

Conclusions

Three flow patterns are distinguished based on the transfer rate: complete transfer, partial transfer and non-transfer. Then, the prediction equation of liquid film drainage time is proposed as: $T_{dr} = 11.76L_{TSC}^{*-0.96}Ca^{-0.3}Q_{PEG}^{0.6}W^3/Q_{total}^{1.6} + 1.29(W^3/Q_{PEG})^{0.74}$. By comparing the residence time of the droplet in the main channel with the liquid film draining time, the flow pattern can be accurately predicted and the flow pattern diagram is drawn. In the complete transfer pattern, both a W/W system and an O/W/W system are observed. The modified capillary number Ca^* is proposed as a criterion for determining the feasibility of forming the O/W/W system.

Acknowledgements
This work is supported by the National Natural Science Foundation of China (No. 22308246, 21978197), China Postdoctoral Science Foundation (No. 2023M732587), and the Key Project of State Key Laboratory of Chemical Engineering (No. SKL-ChE-23Z03).

The response of droplet traffic to a perturbation of flow resistance at the arms of a micro-T-junction

Kui He, Liangzhen Zhang, Si-Min Huang
(Guangdong Provincial Key Laboratory of Distributed Energy Systems, Dongguan University of Technology, Dongguan, 523808, China)

Abstract
The response of water-oil droplet flow to a perturbation of flow resistance added at the arms of a bypassed micro-T-junction are studied. Once an additional flow resistance is introduced at the arms of the T-junction, the flow self-adapts to the perturbation and droplets show complex dynamics at the junction, including splitting, merging and reshaping. During the self-adaptive process, the instantaneous splitting ratios of the dispersed flow show positive correlations with that of continuous flow. The correlation coefficient reduces as the increase of the amplitude of the perturbation. The ensemble splitting ratios of them, however, are independent. It shows a rather simple law that the ensemble splitting ratios of oil anchor at around a constant value while the corresponding parameter of water varies from 0 to 1. It illustrates that the droplet flow splitting at a T-junction resembles a resilient system, the stiffness of which depends on the capillary number of the flow. The energy loss of the system induced by a perturbation of flow resistance is self-reduced by just redistributing of droplets into the two arms.

Keywords: droplet flow; collective behaviour; resilient system

Introduction

In droplet microreactors, parallelizing of the microchannels is a straightforward way to scale up the output of them, which are frequently encountered in various droplet microfluidics[1-5]. The branching channels are frequently used to distribute the flow from the main channel to the branching channel. The typical unit model is a branching T-junction, which has an inlet, a straight arm and a side arm. As droplet flow comes cross a T-junction, two basic questions are interesting. The first one is focused on the conditions a droplet can be split into two daughter ones. Numerous research has been devoted to study the typical instantaneous splitting modes of a droplet at micro-T-junctions[6-8]. Basically, a droplet split at two modes, including blocking splitting and non-blocking splitting. The transitional conditions for blocking/non-blocking splitting/non-splitting are functions of Ca number of continuous flow and the length of droplets.

The second question is the ensemble splitting features of the flow, i.e., how droplet traffic as whole is distributed into the two arms of a T-junction. This research is devoted to the traffic problem of droplet flow at a bypassed T-junction. Study of the bulk (collective) splitting features of droplet flow is meaningful in terms of at least two aspects. The splitting manipulation of droplets at T-junctions is continuous but not always periodic process. In a dense droplet flow, complex mutual interaction between them happens at the splitting place. For this situation, the bulk splitting features are preferred to know. Furthermore, the response of droplet flow immediately after the introduction of a flow perturbation is interesting but still unknown. It reflects the robustness of the splitting droplet flow as they are exposed to a perturbation. In this study, a new method is raised to study these features. A 3-D model based on volume of fluid method (VOF) is developed to obtain detailed instantaneous flow parameters. A series of artificial additional flow resistance is introduced at one of the arms of a bypassed T-junction, in which the splitting of droplet flow is in a steady state. The additional flow resistance perturbs and pushes the flow away from a steady state. The response of droplet traffic to the perturbation is recorded and studied carefully to understand the differences in flow path priority of droplets and oil, respectively.

Methodology

A 3D VOF model is developed to investigate the splitting dynamics of droplets at the junction part. The models with different detailed modifications have been proven reliable in studying the generation of droplets and splitting of droplets at T-junctions[9-13]. The width and depth of the channels are 0.5 mm and 0.1 mm, respectively. Two T-junctions are constructed. The length of the two arms of the T-junction is 4 mm. The distance between two T-junctions are 7 mm. The details of the model are introduced in a previous paper[12]. Once the steady state (referred as base case hereafter) is reached, different constant atmospheric pressure was introduced at the outlets of the splitting T-junction. This treatment is equivalent to introduce an additional pressure drop at one of the outlet arms. It suddenly changes the flow rate ratio at the two arms of the splitting T-junction. The magnitude of the flow resistance perturbations was varied from -40% to 40% of time-averaged inlet pressure ($\hat{P}_{\mathrm{in,std}}$) of the base flow. The details of base cases are listed in Table 1. The ensemble splitting ratios of dispersed water (SR_{w}) and silicone oil (SR_{o}) taken off at the side outlet, are defined as following for latter discussion.

$$SR_{\mathrm{w}} = \frac{m_{\mathrm{wside}}}{m_{\mathrm{wt}}} \quad (1)$$

$$SR_{\mathrm{o}} = \frac{m_{\mathrm{oside}}}{m_{\mathrm{ot}}} \quad (2)$$

where m_{wside}, m_{oside} are mass of water and silicone oil taken off from the side arm of the splitting T-junction. The m_{wt} and m_{ot} refers to the total mass of water and oil flowing into the splitting T-junction, respectively. The capillary number of the flow is defined as following.

$$Ca = \mu_{\mathrm{c}} U_{\mathrm{c}} / \sigma \quad (3)$$

$$Re = \rho U_{\mathrm{c}} D_h / \mu_{\mathrm{c}} \quad (4)$$

where μ_{c} and U_{c} are the viscosity and superficial velocity of the continuous fluid. σ is the interfacial tension between two fluids. ρ is the density of oil. D_h is the hydraulic diameter of the channel. In this study, pure water and silicone oil are selected as the continuous and dispersed fluids, respectively.

Table 15 – details of base cases

Group	Ca	Re	ΔP_{ad}
G1	0.007	0.32	(-40%~40%)$\hat{P}_{\mathrm{in,std}}$
G2	0.01	0.46	(-40%~40%)$\hat{P}_{\mathrm{in,std}}$
G3	0.015	0.65	(-40%~40%)$\hat{P}_{\mathrm{in,std}}$
G4	0.02	0.92	(-40%~40%)$\hat{P}_{\mathrm{in,std}}$
G5	0.028	1.32	(-40%~40%)$\hat{P}_{\mathrm{in,std}}$
G6	0.034	1.6	(-40%~40%)$\hat{P}_{\mathrm{in,std}}$

Results and discussions

The numerical result agrees well with those obtained from experiment, where the error bar represents ±8% of the value (Fig. 1). Overall, the ensemble averaged splitting ratios of oil are independent of the splitting ratios of water. The distribution features are summarized as following. The data points on the ordinate denote that all the droplets flow into the side arm. It is marked as region one (R1) on the figure. The base flow is shown at this region, where no additional flow resistance is introduced. As the flow resistance at the straight arm is further increased, the SR_{o} increases but SR_{w} remains at 1. The SR_{o} reaches 1 only if the straight arm is closed. Similarly,

the data points on the abscissa denote that all the droplets flow into the straight arm. It is marked as R3 on the figure. There is a decreasing SR_o but a constant SR_w (=0) as the flow resistance at the side arm increases. At $0.1 < SR_w < 0.9$, it is marked as R2. It is interesting to see that the SR_o just slightly increases from 0.49 to 0.5 at $Ca = 0.007$, as the SR_w increases from 0.1 to 0.9. Correspondently, at $Ca = 0.034$, the SR_o slightly increases from 0.35 to 0.41. The SR_o anchors at a region of 0.42±0.08, despite of the large variation of SR_w and Ca number of the flow.

Fig.2 (a) and (b) shows the response of droplet flow exposed to the flow perturbation of two amplitudes. The Ca number of the flow is 0.034. The size of the droplets and space between them is reduced and merging of droplets happens. Before the addition of a perturbation, the volume of each droplet at the side arm is about 12.4 nl. The volume of a mother droplet at the inlet of the splitting T-junction is about 6.2 nl (Ca=0.034). After the continuous flow slows down at the junction, two droplets merge as one (a diploid). It is shown in Fig. 3, where the droplets are contoured by flow velocity and flooded by strain rate. The volume of a merged droplet is just two multiples of 6.2 nl. The volume of oil bridges has no such multiple correlation due to the continuous feature. Fig. 2(a) illustrates that the response of water and oil to the perturbation is different. The size of the oil bridge increases immediately after the addition of the perturbation but the volume of first two droplets is not changed. To the third one, the volume of the droplet becomes 24.7 nl, which is about four times of the volume of the inlet droplets. By comparison, the volume of oil bridges immediately reduces and then increases to a constant value. The size of oil bridges doesn't change after t=0.32s. The flow recovers its periodic features. The delayed response of droplets could be explained by the variation of strain rate after the perturbation (Fig. 3). It is interesting to note that the strain rate is larger at the beginning of the perturbation but it reduces as time goes. It is apparently shown in the flow of Ca=0.034 and ΔP_{ad}=30%$P_{in,sd}$. It illustrates that the additional flow resistance is transformed directly to the continuous flow but it retardedly affects droplets through the varying shear strain.

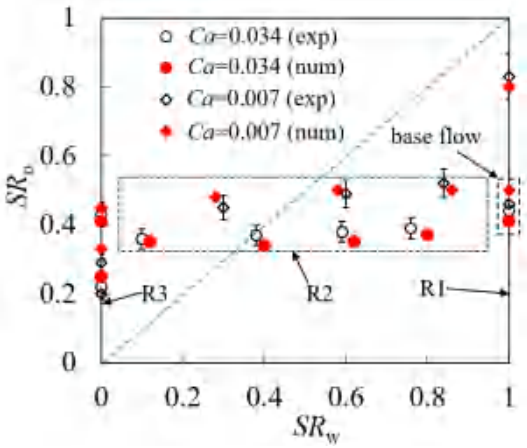


Figure 79 - Comparison of ensemble averaged phase splitting ratios obtained from simulations and experiment

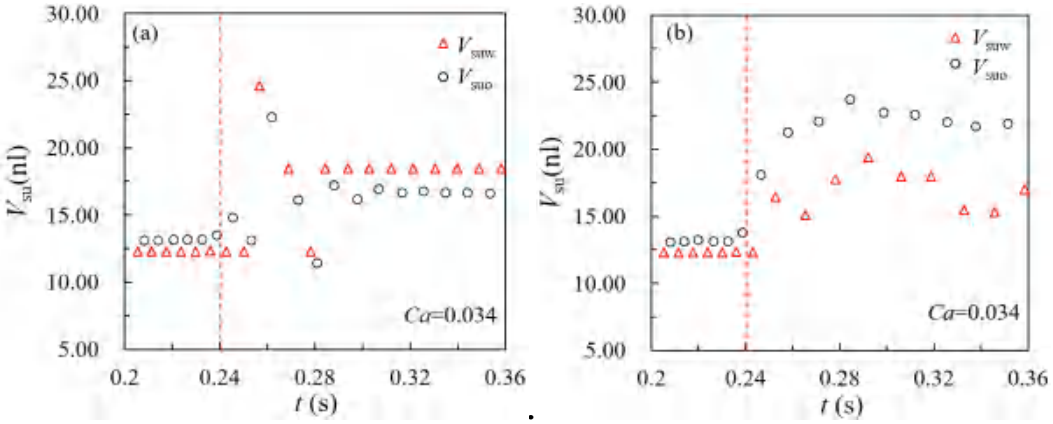


Figure 2 -The volume of droplets and neighbour oil bridges at the flow of high Ca numbers before and during the relaxation of the flow, (a)$\Delta P_{ad} = 10\%\widehat{P}_{in,std}$; (b)$\Delta P_{ad} = 30\%\widehat{P}_{in,std}$.

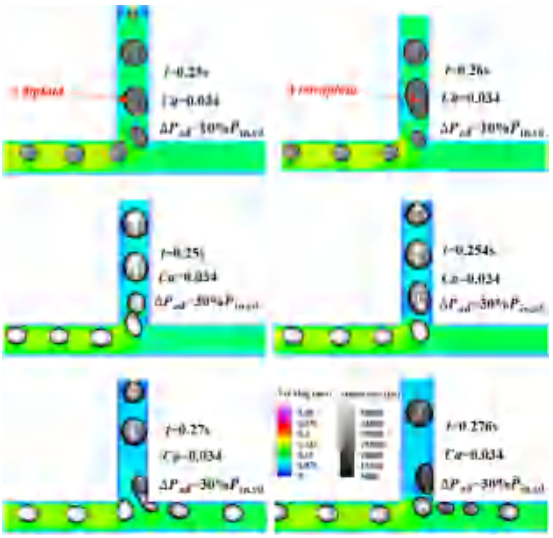


Figure 3-The splitting, reshaping and merging of the droplets at various cases. The droplets are flooded by the strain rate and plotted together with the contour of velocity magnitude. The zero time (t=0) starts at the beginning of the perturbation.

Fig. 4 shows the instantaneous pressure at the inlet of the splitting T-junction. It is seen that as flow resistance perturbation is introduced the side arm of the T-junction, the unit-averaged inlet pressure increases (indicated by the dashed curves with arrow) and it reduces after a certain period. With the perturbation of flow resistance of different amplitudes, it shows similar trends. It is indicated that the inlet pressure is reduced through redistributing of droplets into the two arms of the T-junction. In order to clearly demonstrate this concept, a counterpart simulation of single oil flow is conducted. The inlet velocity is the same to the corresponding droplet flow. It is clearly shown in Fig. 4 that the inlet pressure increases instantly and remains a constant value afterwards for the single oil flow. The relaxation time of the single-phase flow is too short to be observed due to the laminar features of the flow. Comparatively, in a two-phase system, the droplet flow has much longer relaxation time. The unit-averaged inlet pressure indicated by dashed curve with arrow is apparently reduced by redistributing of the droplets and oil into the two arms.

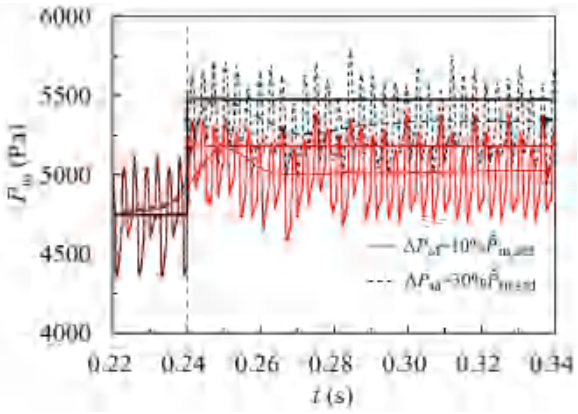


Figure 4-The instantaneous pressure of droplet flow and counterpart single oil flow at the inlet of the splitting T-junction. The Ca of the steady state flow is 0.034. The solid line is the corresponding simulation results of single-oil flow. The dashed curves with arrow are the unit-averaged value of instantaneous inlet pressure.

Conclusions

In this paper, the self-adaptive process of water-oil droplet flow subjected to a perturbation of flow resistance at the side arm of a hydrophobic branching micro-T-junction are systematically studied via VOF method. The rules of droplet traffic adjusting itself to the change of flow resistance are summarized: The response (splitting) of water flow and oil flow to the perturbation is different. The splitting (response) behavior depends on the amplitude of the perturbation and the Ca number of the flow. With a small perturbation of pressure drops (2%$\hat{P}_{\mathrm{in,std}}$~10% $\hat{P}_{\mathrm{in,std}}$), the droplet traffic with various Ca numbers shows "side arm priority" and periodic features are regained after a relaxation process. A sufficient large flow resistance (6% $\hat{P}_{\mathrm{in,std}}$~20% $\hat{P}_{\mathrm{in,std}}$) added at the side arm turns the droplets redistributing into the straight arm and the splitting of flow becomes non-periodic. Beyond a critical ΔP_{ad}, all droplets flow into the straight arm. The value of $\Delta P_{\mathrm{ad,cr}}$ linearly correlates with the Ca numbers of the continuous flow. During the adaptive process, the instantaneous splitting ratios positively correlate with that of water, accompanying with complex topological variation of droplets. However, the ensemble averaged splitting ratios of them show no dependence.

It clearly demonstrates that the droplet flow splitting at a T-junction resemble a resilient system, compared to a single-phase flow. As a perturbation is introduced, the instantaneous splitting ratios of the continuous flow (oil) change temporally but the ensemble averaged data anchors at a constant value. In a stiff single-phase system, there is no such relaxation process. The "spring-like" splitting features of droplet flow reflect a universal rule, i.e., the energy loss of a perturbated droplet flow can be automatically reduced through redistributing droplets into the two arms of a T-junction.

Acknowledgements

The project is supported by: (1) Guangdong Basic and Applied Basic Research Foundation (No. 2023A1515030105); (2) National Natural Science Foundation of China (NSFC, No. 52090061); (3) Guangdong Provincial University Innovation Team Project, No. 2023KCXTD038

References

[1] A.R. Abate, and D.A. Weitz, Faster multiple emulsification with drop splitting, Lab Chip 11 (2011) 1911-1915.

[2] F. Ahmadi, K. Samlali, P.Q.N. Vo, and Steve C.C. Shih, An integrated droplet-digital microfluidic system for on-demand droplet creation, mixing, incubation, Lab Chip 19 (2019) 524-535.

[3] M. Jiang, H. Zhu, N. Zhou, C. Liu, C.-Y. Jiang, Y. Wang, and S.-J. Liu, Droplet microfluidics-based high-throughput bacterial cultivation for validation of taxon pairs in microbial co-occurrence networks, Scientific Reports 12 (2022) 18145.
[4] T.S. Kaminski, and P. Garstecki, Controlled droplet microfluidic systems for multistep chemical and biological assays, Chem. Soc. Rev. 46 (2017) 6210-6226.
[5] Y. Zhang, and H. Jiang, A review on continuous-flow microfluidic PCR in droplets: Advances, challenges and future, Anal. Chim. Acta 914 (2016) 7-16.
[6] D.R. Link, S.L. Anna, D.A. Weitz, and H.A. Stone, Geometrically mediated breakup of drops in microfluidic devices, Rev. Lett. 92 (2004) 054503.
[7] M.-C. Jullien, M.-J. Tsang Mui Ching, C. Cohen, L. Menetrier, and P. Tabeling, Droplet breakup in microfluidic T-junctions at small capillary numbers, Phys. Fluids 21 (2009) 072001.
[8] S. Protière, M.Z. Bazant, D.A. Weitz, and H.A. Stone, Droplet breakup in flow past an obstacle: A capillary instability due to permeability variations, Europhys. Letters 92 (2010) 54002.
[9] M. Nekouei, and S.A. Vanapalli, Volume-of-fluid simulations in microfluidic T-junction devices: Influence of viscosity ratio on drop, Phys. Fluid 29 (2017) 032007.
[10] S.G. Sontti, and A. Atta, CFD analysis of microfluidic droplet formation in non-Newtonian liquid, Chem. Eng. J. 330 (2017) 245-261.
[11] D.A. Hoang, L.M. Portela, C.R. Kleijn, M.T. Kreutzer, and V. van Steijn, Dynamics of droplet breakup in a T-junction, J. Fluid Mech. 717 (2013) R4.
[12] K. He, Z. Zhang, L. Zhang, W. Yuan, and S.M. Huang, Effects of geometrical confinement on the generation of droplets at microfluidics T-junctions with rectangle channels, Microfluid. Nanofluid. 27(67) (2023) 1-13.
[13] N.X. Ho, and T.V. Vu, Numerical simulation of the deformation and breakup of a two-core compound droplet in an axisymmetric T-junction channel, Int. J. Heat Fluid Flow 86 (2020) 108702.

Explosion-driven expansion instability study of granular media

Lin Min 1 , Xue Kun 1* , Shi Xiaoliang 1

State Key Laboratory of Explosion Science and Safety Protection, Explosion Protection and Emergency Disposal Technology Engineering Research Center of the Ministry of Education, Beijing Institute of Technology, Beijing 100081, China

Abstract

When a particle system expands and moves under the explosive load, a non-uniform particle jet structure, i.e., explosion-driven particle expansion instability, will be formed in its interior and at the interface between gas and solid phases. Explosion-driven particle expansion instability is closely related to a large number of natural phenomena and engineering applications, such as supernova explosions, volcanic eruptions and laser-driven inertial confinement fusion. To address this kind of instability, researchers have achieved a large number of valuable results through theoretical, experimental, and numerical studies, but the formation conditions, evolution laws, and physical mechanisms behind the instability are still unclear. Therefore, in this paper, a quasi-two-dimensional explosion-driven evanescent surge tube system is established independently, and two interfacial perturbation modes are used to study the coupling evolution process between the central explosion flow field and the particle ring, and the method of coupling compressible computational fluid dynamics and coarsened discrete elements in the Eulerian-Lagrangean framework (CMP-PIC) is used to simulate and study the driving mechanism of the particle expansion under the explosive shock load, the destabilization criterion and other issues, and reveal the driving mechanism of particle expansion under the explosive shock load and the instability criterion and so on. problems, and revealed the physical mechanism of the particle system destabilization under the explosion impact load.

Driven by the blast load, the interior of the particle ring without prefabricated perturbation (Figure. 1) gradually develops filamentary folds, intra-particle ring stratification, and radial jet structures during the expansion process. The structural evolution of the granular ring under different equivalence ratios varies due to the non-uniformity of the pressure gradient distribution inside the granular ring. At the same time, due to the non-uniformity of the pressure gradient distribution, under the condition of large equivalence ratio (M/C=1986), the particle ring per unit mass has insufficient energy, expands slowly, and is unable to get out of the central flow field, and is strongly affected by the negative pressure, and the inner interface undergoes a complicated movement and then appears obvious inward contraction. Under the condition of small equivalence ratio (M/C=810), due to the uniform distribution of pressure gradient inside the ring, the interface inside the ring moves quasi-linearly and then decelerates slowly. Different equivalence ratio conditions outside the ring outside the surface of the quasi-linear expansion followed by slow deceleration of the movement.

The explosion load on the ring produces an initial transverse particle flow, and the particles collide with each other and move outward until the outer surface of the ring, and then the sparse wave starts to drive the expansion of the outer surface, and the particles appear to move from the two sides of the ring surface to the center of the depression of the ring velocity, the outer surface of the particle ring is inverted, and the amplitude of the perturbation decelerates to 0 and then grows linearly (Figure. 2). The non-uniformity of the pressure annular distribution and the annular flow of particles are the fundamental reasons for the morphological evolution of the outer surface after destabilization. Thereafter, the effect of localized particle flow drives the continuous growth of the perturbation amplitude. The evolution of the preformed perturbed particle ring at the external surface explosive loading produces "spike" and "bubble" structures similar to the RM instability, but unlike the growth pattern of the perturbation amplitude in the RM instability, the perturbation amplitude exhibits linear- accelerated growth after the expansion motion of the particle interface, which indicates a fundamentally different pattern. This indicates a fundamentally different evolutionary mechanism.

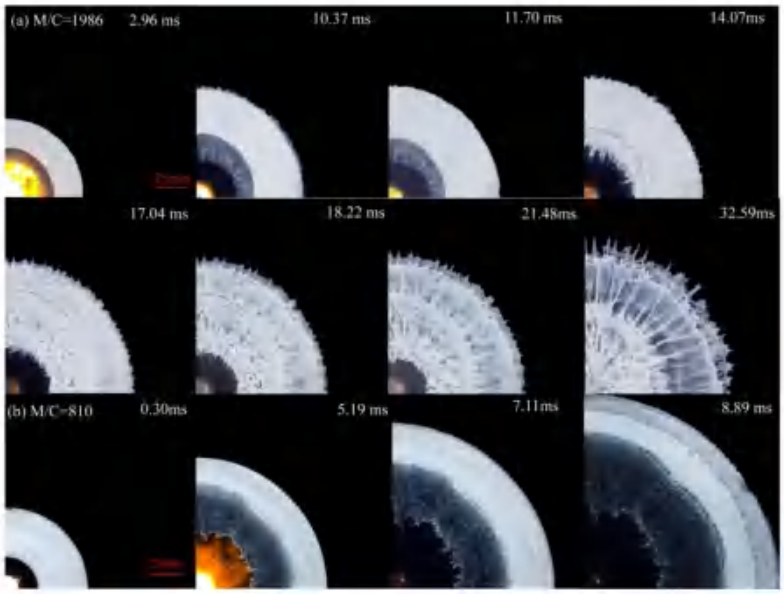


Figure 1 -Time evolution images of particle ring dispersion without predetermined disturbances under two typical cases

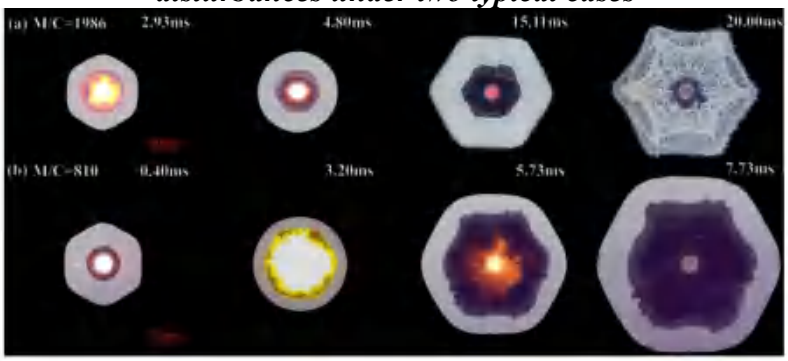


Figure 2 -Time evolution images of particle ring dispersion with predetermined external disturbances under two typical cases

Keywords: Multiphase flow instability, Granular media, Explosive loading; Fluid-solid coupling effects

Research on the Distribution of Residual Oil during the Ultra-High Water-Cut stage of Bottom Water Reservoir and the Enhancing Oil Recovery Methods

Liu Rongjiang, Li Hangyu ,Liu Junrong,Liu Shuyang*
Affiliations (China University of Petroleum (East China), Qingdao, China)
* Corresponding E-mail: Shuyang_liu@126.com

Abstract

The bottom-water oil reservoirs exhibit characteristics of rapid water breakthrough, fast decline in production, and low oil recovery during the ultra-high water-cut stage, At this stage, significant changes occur in the distribution of oil and water within the reservoir. The focus of exploitation has shifted from large, contiguous bodies of residual oil to small, dispersed areas that locally contain higher concentrationsof residual oil. Consequently, it is crucial to understand the distribution of residual oil and develop appropriate exploitation measures for enhancing oil recovery.

This study uses actual reservoir parameters to established a geological model and employs numerical simulation methods to investigate the distribution of residual oil in bottom water reservoirs during the ultra-high water-cut period, and thus propose methods to enhance oil recovery. The research analyzed the impact of bottom water sweep efficiency, energy of edge water, presence of barrier beds, and the degree of well network completion on the distribution of residual oil. It is found that residual oil is mainly concentrated in the following areas: the upper part of the reservoir unswept by bottom water, the periphery of water cones formed after water breakthrough, the "roof oil" area formed by barrier beds, and the inter-well area with low well network control.

For developing the remaining oil in bottom water reservoirs during the ultra-high water-cut period, this research conducted the optimizations of the design and production parameters of horizontal wells. The research found an optimal length for the horizontal section of wells, accounting for approximately 46% of the reservoir ize, which provides good control over the well network while preventing well interference. Furthermore, it is observed that positioning horizontal wells closer to the bottom of barrier beds can effectively enhance oil recovery in the "roof oil" area. Additionally, increasing the liquid production rate can enhance oil displacement efficiency in the swept areas during the ultra-high water-cut period. For areas severely affected by water invasion, implementing water shut-off measures further improves oil recovery in these regions.

Keywords: Bottom-water Reservoirs, Ultra-High Water-Cut Period, Distribution of Residual Oil, Enhanced Oil Recovery

A Review on the flow modification technology of multiphase flow systems using electric fields

Haihong CHEN, Haiyuan YAO, Qingping LI…
(CNOOC Research Institute Ltd., Beijing**Abstract**

One of the flow safety challenges faced by deepwater oil and gas development is how to improve the low-temperature fluidity of the multiphase system of oil gas water in deepwater subsea pipelines. Electric field modification technology is an emerging flow modification technology, which can reduce the viscosity and yield stress of waxy crude oil under the action of a high-voltage electric field. This article elaborates on the research progress of electric field modification technology from three aspects: electric field modification experimental equipment, electric field modification effect, and electric field modification mechanism. According to the different flow states of the experimental medium, the electric field modification experimental device can be divided into static experimental device and dynamic experimental device. However, currently, the electric field modification dynamic experimental device can only be used for experimental research on waxy crude oil and cannot be directly applied to multiphase systems. In terms of electric field modification effect, electric field can not only reduce the viscosity of crude oil, but also weaken the structural strength of crude oil. However, the effect of electric field modification on multiphase flow systems is not yet clear. In terms of electric field modification mechanism, traditional negative electrorheological effect mechanisms such as electrophoresis mechanism, particle polarization electrospinning mechanism, and interaction mechanism between polarized particles cannot explain the phenomenon that "the modification effect of crude oil still exists after the electric field is removed". Therefore, researchers have proposed mechanisms for particle aggregation and chain formation, wax crystal particle aggregation and enlargement, and wax crystal particle interface polarization, but these mechanisms still have significant controversy. At the end of the article, the development direction of low-temperature flow modification technology for deep-water multiphase mixed transportation systems is pointed out.

Keywords: Multiphase flow, Electric fields, Flow modification, Oil and gas transportation

Study on the behavior characteristics of the oil leakage from submarine pipeline

Haoyu Liu, Yanlin Zhao, Jun Yao
China University of Petroleum (Beijing), Beijing, China

Abstract
Based on the actual situation of the sea area, a computational fluid dynamics (CFD) model considering water flow is proposed in this paper. The finite volume method is used to combine the k-ε turbulence model, and the numerical model is verified by small-scale repeated experiments. Numerical simulations of underwater oil diffusion from the seafloor to the sea surface are carried out under the action of water flow. The influence of oil spill velocity, seawater velocity, pipe leakage aperture and oil density on underwater oil diffusion is analyzed. This study can provide reference for the safety application of offshore oil spill accidents.

Keywords: Submarine pipeline; Underwater oil spill; Turbulence; Diffusion rule; Numerical simulation

Introduction

Due to the prolonged exposure to marine environments, underwater pipelines are prone to punctures and leaks. [1] Studying the dispersion patterns of oil spills from underwater pipelines can help predict the extent and impact of oil spreading, providing scientific evidence for emergency response and environmental protection. [2] This study utilizes a two-dimensional flow model to simulate the release and dispersion of underwater oil, considering the significantly wider spreading range in the direction of water flow compared to other directions.

Methodology

The Volume of Fluid (VOF) multiphase flow approach is applied to track free surfaces, simulating oil dispersion in seawater, with geometric reconstruction methods used to monitor the interface between two continuous phases, as shown in Eq. (2). [3]

$$\frac{\partial F_q}{\partial t} + \vec{v}\nabla_{F_q} = 0 \quad (1)$$

The dispersion of oil in seawater adheres to the conservation of mass, momentum, and energy. Under the influence of ocean currents, oil disperses within a complex, turbulent, and time-dependent hydrodynamic field. Oil and water are considered incompressible fluids. The RANS equations and Realizable k-ε turbulence model are employed to describe the multiphase flow and predict the dispersion range of oil post-leakage.

Results and discussion

To validate the numerical model's accuracy, a quantitative comparison with experimental data is conducted. Areas where the leaked oil volume fraction exceeds a 0.05 threshold are defined as the oil film diffusion zone. [4] The oil dispersion trajectories in seawater are compared with the experimental values from Fan's study, as illustrated in Fig. 1. [5] The good agreement between the numerical model's results and the experimental data demonstrates the accuracy of the computational approach presented in this paper.

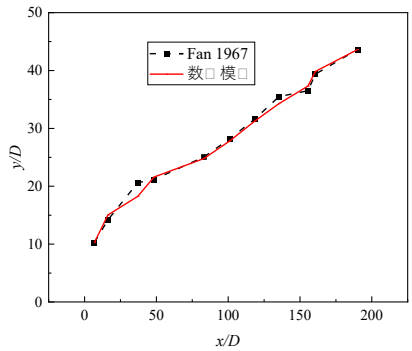


Figure 80 Comparison of experimental data with numerical simulation values (F_{r0}=20, R_0=4)

Different influencing factors on oil dispersion in seawater were altered, and simulations under various conditions were analyzed. The diffusion distance of oil plumes at different leakage rates is shown in Fig. 2. Initially, the dispersion of oil plumes is irregular and primarily influenced by the leakage rate, not allowing sufficient time for dispersion. However, as time progresses, the plume stabilizes and is influenced by hydrodynamic effects, leading to increased dispersion distances with higher leakage rates. Fig. 3 illustrates the dispersion under different seawater currents after an oil leak at 10 m/s for 60 seconds. Ocean currents primarily affect the horizontal spread of underwater oil plumes; their impact on the plume increases with current speed. It is observed that as the seawater velocity increases, the inclination angle of the oil plume with the seabed decreases. With sufficiently high flow rates, underwater plumes may descend to the seabed, posing additional challenges for oil containment and recovery.

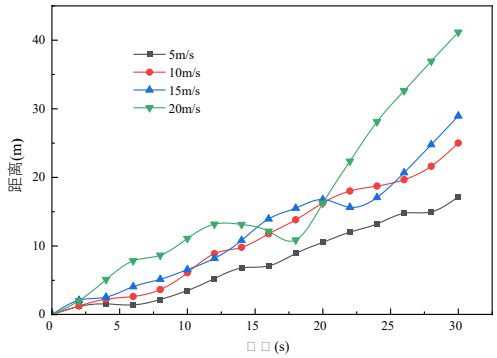


Figure 2 Dispersion distance of crude oil plume under different oil spill velocities

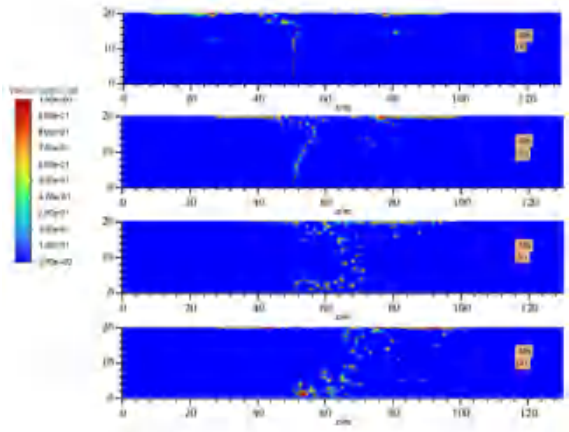


Figure 3 Underwater crude oil release and dispersion with release rate of 10m/s at 60s under different current velocities: (a) uc = 0m/s, (b) uc = 0.1m/s, (c) uc = 0.3m/s, (d) uc = 0.5m/s

Conclusions

The following results can be obtained from this two-dimensional finite element simulation study.

(1) Varying the oil discharge rate: As the oil discharge rate increases, the time it takes for the oil to reach the sea surface decreases, and the rise height of the oil column at the same moment increases. Initially, the dispersion distance of the oil plume is irregular, but as time progresses, the diffusion distance enlarges with the increasing leakage rate.
(2) Altering seawater current speed: An increase in seawater current speed causes the oil to drift further in the direction of the water flow, with both the lateral drift distance and the spread of the oil spill on the sea surface expanding as the current speed increases.
(3) Modifying oil density: The lower the oil density, the higher it rises at a given moment and the shorter the time it takes to reach the sea surface. Over an extended period, the dispersion distance of the oil plume in seawater decreases as the oil density increases.
(4) Adjusting pipeline leak aperture: Larger leak apertures result in greater initial jet momentum, producing higher injection heights within the same timeframe.

References

[1] T. Dalton, J. Di, Extent and frequency of vessel oil spills in US marine protected areas, Marine Pollution Bulletin 60 (2010) 1939-1945.
[2] H. Zhu, J. You, H. Zhao, Underwater spreading and surface drifting of oil spilled from a subsea pipeline under the combined action of wave and current, Applied Ocean Research 64 (2017) 217–235.
[3] B. REN, X. LI, Y. WANG, An irregular wave maker of active absorption with VOF method, China Ocean Engineering 22 (2008) 94-105.
[4] H. Zhu, P. Lin, Q. Pan, A CFD (computational fluid dynamic) simulation for oil leakage from damaged subsea pipeline, Energy 64 (2014) 887–899.
[5] F. Loh-Nien, Turbulent buoyant jets into stratified or flowing ambient fluids, economia aziendale online web (1967).

Experimental study on static immersion cooling of large-scale lithium-ion battery

Weixiong Wu, Shaohong Zeng
(Jinan University, Zhuhai, China, weixiongwu@jnu.edu.cn)

Abstract

This study established an experimental platform for static immersion cooling (SIC) of large-scale lithium-ion battery. The research focuses on the battery temperature characteristics of SIC. The experimental results indicate that the maximum temperature and temperature difference of the battery increase with higher discharge rates when using natural air convection (NAC), reaching 67.71 ℃ and 8.5 ℃ at 5 C. However, when using the SIC of mineral oil at 5 liquid height, the maximum temperature decreases to 53.68 ℃, while the temperature difference increases to 8.81 ℃. As the height of the mineral oil liquid increases, the maximum temperature decreases, and the temperature difference follows a parabolic pattern with an initial increase and subsequent decrease. It is worth noting that the temperature uniformity is significantly improved when the battery is inverted. Additionally, the temperature difference is kept below 5°C for longer periods of time. The movement of the battery high-temperature area is due to liquid natural convection. Optimal cooling capacity can be achieved by fully immersing the battery in liquid after it has been inverted. Furthermore, fluoride fluid with lower viscosity exhibits better thermal performance than mineral oil and silicon oil. This study provides new insights into immersion cooling technology for lithium-ion battery.

Keywords: Lithium-ion battery, Static immersion cooling, Immersion liquid height, Immersion cooling fluid

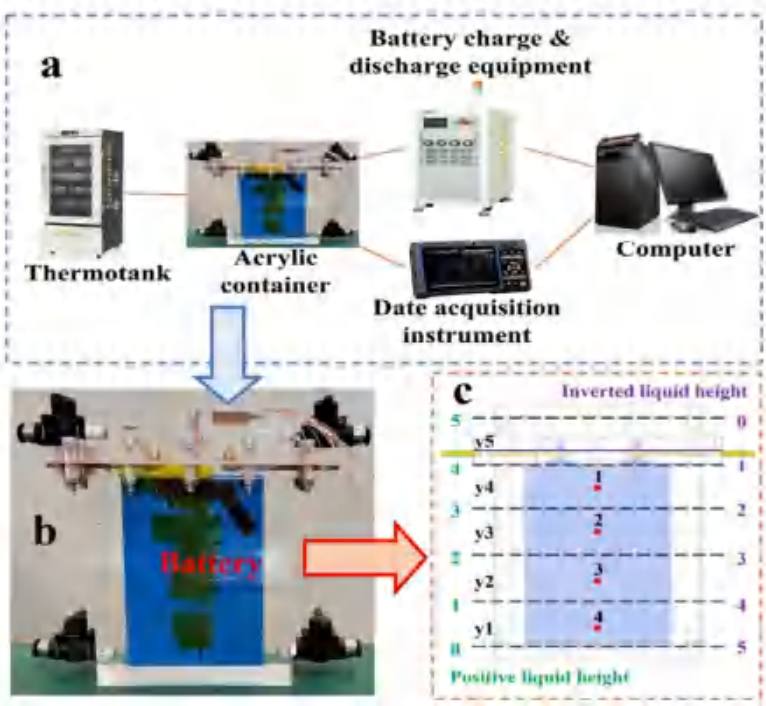


Figure 1 – (a) Experimental platform for static immersion cooling of lithium-ion battery, (b) acrylic container, (c) temperature measurement point and liquid height

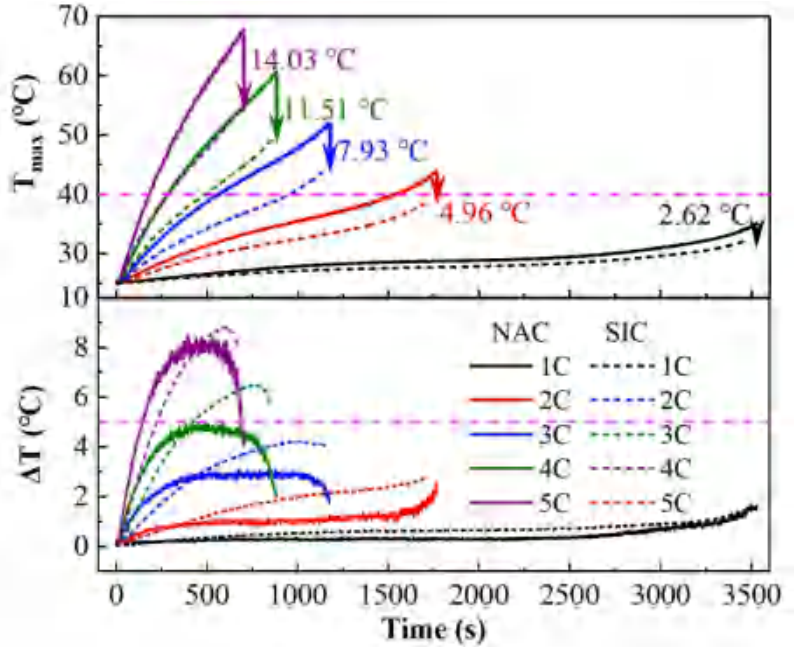


Figure 2 – Comparison of SIC and NAC at different discharge rates with 5 immersion height.

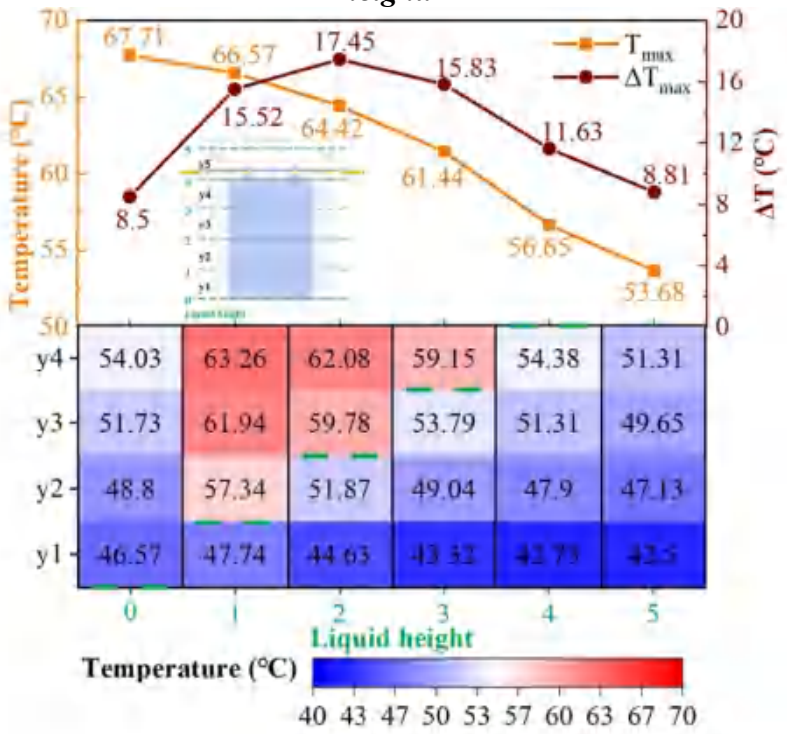


Figure 3 – Battery temperature characteristics and maximum temperature difference thermograms at different liquid heights

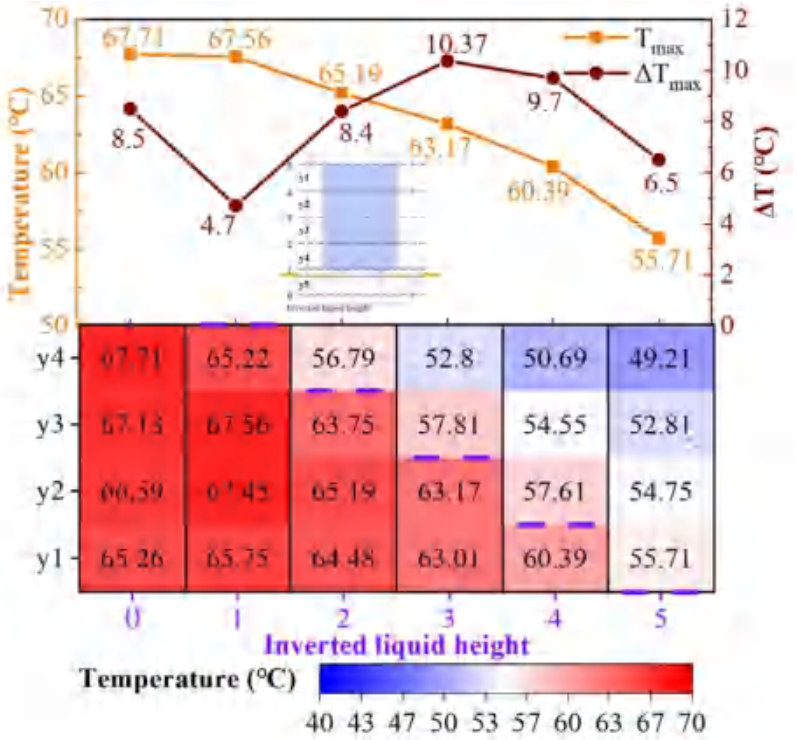


Figure 4 –Battery temperature characteristics and maximum temperature thermograms at different liquid heights when the battery is inverted

Optimization of the battery thermal management system with phase change materials, aerogel and cold plates

Lingfeng Yu, Qin Huang, Shuangfeng Wang, Kai Chen*
Key Laboratory of Enhanced Heat Transfer and Energy Conservation of the Ministry of Education, School of Chemistry and Chemical Engineering (South China University of Technology, Guangzhou, China)**Abstract**
The cooling system with phase change materials (PCMs) and cold plates (CPs) is effective of thermal management of battery packs. In this study, aerogel as the typical lightweight flame retardant materials (FRMs) is adopted to replace the un-melted PCMs to reduce the weight of the system. An optimization strategy for the distribution of PCMs/FRMs in the coupled BTMS is proposed to improve the cooling performance with the system's volume fixed. After the optimization, the maximum temperature (T_{max}) and temperature difference (ΔT) inside the battery pack are reduced by 1.1 K and 55% respectively, with the weight of the filling materials among battery cells decreasing by 23%.

Keywords: Battery thermal management, PCMs, Aerogel, Cold plates, System optimization

Introduction

The increase in energy crisis and environmental pollution have led to the thriving development of electric vehicles (EVs). The appropriate operating temperature of the lithium-ion battery is between 25°C and 50°C, and the appropriate temperature difference is less than 5 °C [1]. The system with PCMs and CPs is effective of battery thermal management. However, part of the PCMs inside the existing systems contribute less to the cooling performance due to unreasonable distribution. To solve this problem, an effective strategy is developed to optimize the PCMs distribution.

Methodology

The FRMs (aerogel) are introduced to partially replace the un-melted PCMs in the coupled system, and an efficient strategy is proposed to adjust the distribution of PCMs and FRMs to effectively improve the cooling performance and reduce the weight of the system simultaneously. After the optimization, again, the un-melted PCMs are replaced by the aerogel. The performance of the designed system is evaluated using numerical simulation method, and is compared with that of the traditional one.

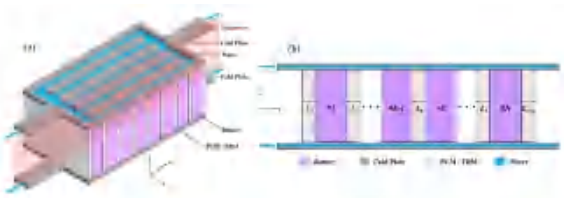


Fig. 1 Scheme of the BTMS with PCMs/FRMs and CPs: (a) Three-dimensional system; (b) Symmetry.

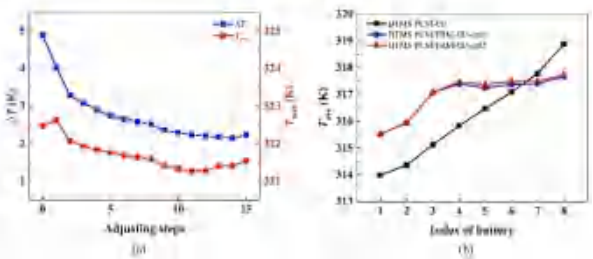


Fig. 2 Optimization result: (a) T_{max} and ΔT with adjusting step (b) T_{ave} of different BTMSs

Conclusions

The results indicate that the developed strategy takes only 14 adjusting steps to achieve the optimal material distribution, and the system's performance is improved effectively. T_{max} and ΔT decrease by 1.1 K and 55%, respectively. Moreover, the un-melted PCMs are replaced with lighter FRMs, and the weight of the filling materials among battery cells is reduced by 23%, with the system's cooling performance unaffected.

Acknowledgements

This research is supported by National Natural Science Foundation of China (Grant No. 52276063).

References

[1] He L, Tang X, Luo Q, Liao Y, Luo X, Liu J, Ma L, Dong D, Gan Y, Li Y. Structure optimization of a heat pipe-cooling battery thermal management system based on fuzzy grey relational analysis. Int J Heat Mass Transf 2022;182:121924.

Imaging Hydrogen Bubble Distribution and Flow through Granular Material with X-Ray Computed Tomography

Gamuchirai Ashley Sibanda, Michael Fairweather, Jeffrey Peakall, David Harbottle, Martyn Barnes, Alice Macente and Timothy Hunter University of Leeds, Leeds, United Kingdom
Sellafield LtD, United Kingdom

Abstract

Hydrogen gas is released from nuclear waste from radiolysis and corrosion of metallic wastes. Gas behaviour in granular material in waste silos or ion exchange material is not well understood for the mobilization and long-term storage planning. This project simulated hydrogen bubble growth in these systems by generating hydrogen from magnesium corrosion in columns of silica glass beads of varying sizes. The bubble sizes, shapes distributions and flow over time are imaged using X-Ray Computed Tomography (xCT) at low and high resolutions.

Keywords: Granular, Hydrogen, XCT

Methodology

A sample of hydrogen bubbles in 203 µm silica glass beads was imaged using micro-CT and reconstructed at pixel size of 53 µm and at a lower resolution with reconstruction pixel size of 200 µm. The hydrogen was produced from corrosion of magnesium powder in water with sodium chloride added to disrupt the protective magnesium hydroxide layer. Post-processing was done using Fiji ImageJ, Dragonfly and Avizo.

Results

There was coalescence of bubbles at the edges of the sample imaged at high resolution from the wall effects. This effect is reduced with the larger sample as shown in Figure 1. Object counting at 200 µm gives the volume/surface area ratio distribution in Figure 2 which shows that most of the bubbles are small with some larger coalesced pores (red objects) which aid gas release. The CT images gave an estimation of 17.06 % gas hold-up and this was supported by experimental data which gave a gas retention percentage of 17.11% after 6 hours.

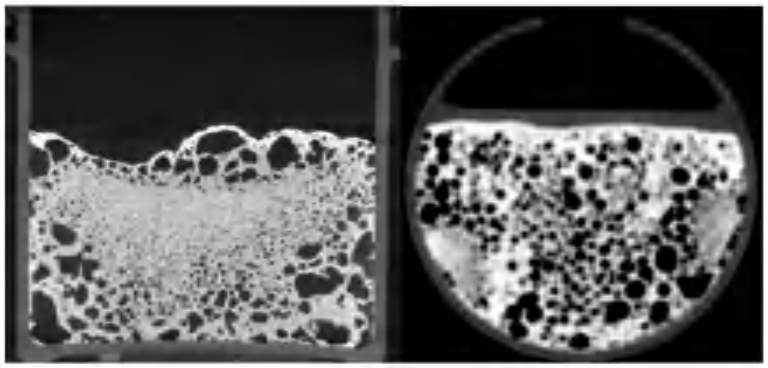


Figure 1 - xCT images of hydrogen bubbles in silica glass beads with reconstruction at 53 µm (left) and 200 µm (right).

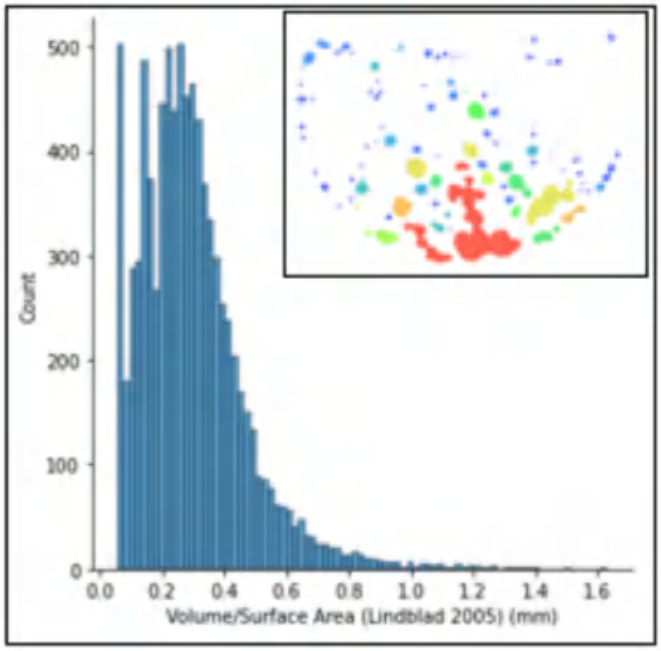


Figure 2 - Volume/Surface Area bubble distribution

Conclusions

High resolution imaging requires smaller samples which results in dominant wall effects. A central region of interest can be extracted to exclude these edge bubbles and study the meso-bubbles. Imaging at a lower resolution allows for quantification of larger pores that act as a transport media reducing gas retention.

References

[1] J. Lindblad, Surface area estimation of digitized 3D objects using weighted local configurations, Image and Vision Computing 23, 2, (2005) 111-122.

Hydrodynamics and mass transfer in a planar bubbly cyclone

Siyi Li, Xiao Xu*
School of Mechanical and Power Engineering, East China University of Science and Technology, Shanghai, China

Abstract
In modern industrial production and various fields of science and technology, the study of the motion law of polydispersed phase mixed fluid in centrifugal force field is not enough.To address the drawbacks of previous technologies, a unique planar bubbly cyclone (PBC) for continuous gas–liquid mass transfer is designed. This PBC meets the requirements of gas stripping, including a lower gas-to-liquid volumetric flow rate. A complex situation is formed by the combination of multiple flow fields, such as swirl flow field, jet flow field and impact flow field under the constraints of the guide vanes and the cylinder wall. The population balance model accurately predicts the bubble diameter (1 to 6 mm), while the Kawase correlation gives excellent results and is in good agreement with the experimental data (±0.001 m/s). Overall, the PBC provides an alternative approach to gas stripping, exhibiting low consumption, long-term capabilities, and good reliability.

Keywords: Multiphase flow, Planar bubbly cyclone, Interphase mass transfer, Process intensification

Experimental

The experimental process (see Fig. 1) involved the injection of nitrogen (the inert gas) from a nitrogen cylinder at the gas inlet and the injection of tap water at the liquid inlet using a pump. The dissolved oxygen concentration is 8×10^{-6}mg/L measured by a DO porbe which was also confirmed by previous work at temperature of 293K. The gas and liquid flows were controlled by gas and liquid mass flowmeters, respectively. The liquid volume flow was set at 3×10^{-4} m^3/s, while the gas volume flow ranged from 3.75×10^{-5} to 2.82×10^{-4} m^3/s. The liquid
flow rate was measured using a Coriolis mass flow meter (Yinuo Ltd., China), with a <0.5% error. The pressurized air flow rate was measured and controlled using a gas mass flow meter and a controller (Kongxin Ltd., China), with a <0.5% error. The liquid used for this purpose was tap water with a density, viscosity, surface tension, and temperature of 998 kg/m^3, 0.9 mPa·s, 0.072 N/m, and 293±1 K, respectively. Because the fresh tap water was injected and none of liquid perform circulation, the temperature is kept constant.

Introduction

Cyclone separator, as a compact separator, is commonly used in degassing process. In the field of chemical industry, cyclone separators are mainly used for the removal of methane from crude oil, hydrogen removal from hydrogenated oil, and hydrogen sulfide removal from wastewater. Due to the lack of sufficient information on the two-phase flow phenomenon and the associated mass transfer rate, the analysis of liquid degassing with cyclone separators is often more complicated than with other degassing methods. In order to be able to develop improved degassing methods, the process of bubble separation and dissolved gas separation in the cyclone should be better understood. The plate bubble cyclone separator provides an alternative method of gas stripping, which is of great significance in this field.

Simulations

The Euler–Euler approach was considered in this simulation because it allows the solution of each phase to be obtained[30, 31]. The continuity and momentum equations are expressed as follows:

$$\frac{\partial(\alpha_q \rho_q)}{\partial t} + \nabla \cdot \left(\alpha_q \rho_q \mathbf{u}_q\right) = 0 \qquad (1)$$

$$\frac{\partial(\alpha_q \rho_q \mathbf{u}_q)}{\partial t} + \nabla(\alpha_q \rho_q \mathbf{u}_q \mathbf{u}_q) = -\alpha_q \nabla p + \nabla \cdot [\alpha_q(\tau_{ij,q} + \tau_{ij,q}^{Re})] + \mathbf{F}_{i,q} + \alpha_q \rho_q \mathbf{g} \quad (2)$$

In the above equations, q represents the gas or liquid. α_q, ρ_q, and u_q represent the volume fraction, density, and velocity of phase q, respectively. p and g denote the pressure and gravitational acceleration, respectively. In addition, τ and τ^{Re} are the laminar and turbulent stress tensors, respectively. $F_{i,q}$ represents the interfacial forces, consisting of the drag, virtual mass, lift, wall lubricant, and turbulent dispersion forces[32]. For gas–liquid flows under the Euler–Euler approach, the drag and virtual mass force are significant interfacial forces:

$$\mathbf{F}_{i,g} = -\mathbf{F}_{i,l} = \mathbf{F}_{D,l} + \mathbf{F}_{V,l} \quad (3)$$

where g and l represent the gas and the liquid, respectively. The interfacial force between the gas and the liquid due to drag is defined as:

$$\mathbf{F}_{D,l} = \frac{3}{4}\alpha_g \rho_l \frac{C_D}{d_b}|\mathbf{u}_l - \mathbf{u}_g|(\mathbf{u}_l - \mathbf{u}_g) \quad (4)$$

where α_g represents the gas volume fraction and d_b is the diameter of the bubble. According to Schiller and Naumann[33], the drag coefficient C_D is correlated to the Reynolds number as follows:

$$C_D = \begin{cases} 24(1 + 0.15Re^{0.687})/Re & Re \le 1000 \\ 0.44 & Re > 1000 \end{cases} \quad (5)$$

where Re denotes the relative Reynolds number. The relative Reynolds numbers for the gas and liquid phases can then be obtained using the following expression:

$$Re = \frac{\rho_l |\mathbf{u}_l - \mathbf{u}_g| d_b}{\mu_l} \quad (6)$$

It can be seen that the high-velocity liquid flow is located near the edge of the guide vanes, resulting in a swirling flow and the backflow of liquid (liquid volume flow = 3×10^{-4} m^3/s, gas volume flow = 1.5×10^{-4} m^3/s). The cross-sections with height values of 0.001, 0.005, 0.01, 0.015, and 0.019 m from the bottom of the cyclone were selected. For cross-sections with a height of ≤0.01 m, the injected liquid swirls in a counterclockwise manner under the action of the guide vanes, while in the cross-sections with a height of >0.01 m, clockwise swirling is observed. This reversed swirling flow of liquid in the PBC can be explained by the characteristics of the three-dimensional (3D) streamlines. More specifically, according to the 3D streamlines shown in Fig. 2, the backflow of a liquid can be achieved under the actions of the injected liquid velocity and the cylinder wall constraints. It can therefore be inferred that the bubbles travelling in a quasi-helical trajectory originate from both the swirling centrifugal acceleration and the centripetal liquid backflow.

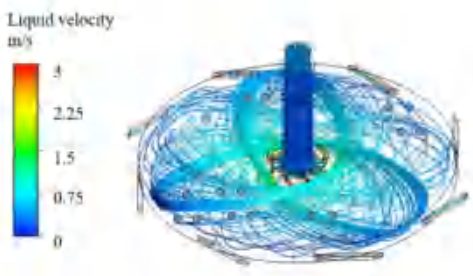


Fig. 2 CFD simulation results showing the 3D streamlines in the fluid domain.

Conclusions

Due to its absence of moving components and the presence of a millimeter-scale fluid channel size, the planar bubbly cyclone (PBC) is an extremely promising gas–liquid mass transfer device that meet the requirements of long-term usage and a good reliability. Under the action of guide vanes, the liquid injected into the inlet in the central region adopted a swirling flow moving from the center to the sidewall, whilst the gas bubbles moved from the wall towards the center. As a

result, a cluster of bubbles formed, which presented an increased interfacial area. The PBC demonstrated a gas plug flow and a well-mixed liquid flow similar to those of a rotor–stator spinning disc reactor.
Overall, the developed PBC provides an alternative approach for gas stripping, and could lead to process intensification. This study provides the first step in the scale-up of a PBC. Future work will focus on the investigation of additional operational parameters to extend the application scenario of the PBC. For example, the swirling flow in the central region of the PBC shall exhibit a negative pressure which can achieve gas self – suction and it will be easy to series connection.

Acknowledgements
The authors wish to express their sincere gratitude to the National Natural Science Foundation of China (52025103), and the Chenguang Program supported by Shanghai Education Development Foundation and Shanghai Municipal Education Commission (20CG39).

References

[1] P. Moschou, M.H.J.M. de Croon, J. van der Schaaf, J.C. Schouten, Nitrogen stripping of isopropyl-alcohol and toluene in a falling film micro reactor: Chemical Engineering Science 76 (2012) 216-223. 10.1016/j.ces.2012.03.048.
[2] V.N. Maleta, O. Bedryk, A. Shevchenko, A.A. Kiss, Pilot-scale experimental studies on ethanol purification by cyclic stripping, AIChE Journal 65(9) (2019).
[3] K.E. Deaton, L.R.L.d. León, S. Pascual, M.A. Deshusses, Critical assessment of gassing-in methods to determine mass transfer coefficient in miniature and microbioreactors with gas-liquid flow, Biochemical Engineering Journal 187 (2022) 108655.

A structural optimization method for conductivity array liquid film sensor

Chao Wang, Yanfeng Zhu, Hongjun Sun, Yishan Huang
(Tianjin University, Tianjin, China)

Abstract
Conductive array liquid film sensor is an important method for liquid film measurement. This paper optimized the structure of the sensor. The influence of conductivity is eliminated by the method of double-electrode ratio. The method of cross use of far and near electrodes improves the measurement range.

Keywords: Liquid Film, Conductivity Array Sensor, Conductivity

Introduction

Conductivity array liquid film sensors can obtain global liquid film information and have attracted attention [1]. The current flowing between the electrodes will reach saturation at a certain liquid film thickness. This limits the sensor measurement range. The variation of conductivity will also cause uncertainty in the measurement accuracy of electrical sensors [2]. A conductivity array liquid film sensor is designed to increase the measurement range and eliminate the influence of conductivity.

Methodology

This article is optimized based on the sensor structure of Damsohn et al. [1], as shown in Figure 1. There are two transmitter electrodes, two receiver electrodes and two ground electrodes in the periodic boundary unit. The ground electrode is kept at zero potential. Other electrodes of the same type will be excited or measured simultaneously. Therefore, there are 4 combinations of a periodic boundary unit. They are Near Distance Electrode (ND), Mid Distance Electrode 1 (MD1), Mid Distance Electrode 2 (MD2) and Far Distance Electrode (FD).

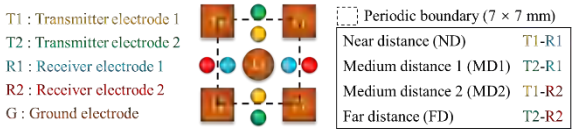


Figure 1 - Sensor periodic boundary structure

By performing ratio processing on the signals obtained from different measuring electrodes and considering the differences in IV amplification circuits, the measured voltage values (MVV) of the same receiving electrode are ratio processed. That is, the ratio of MD1-MVV and ND-MVV is done, and the ratio of FD-MVV and MD2-MVV is done. The result is shown in Figure 2. It was found that under different conductivities, the liquid film sensors after ratio processing almost completely overlap.

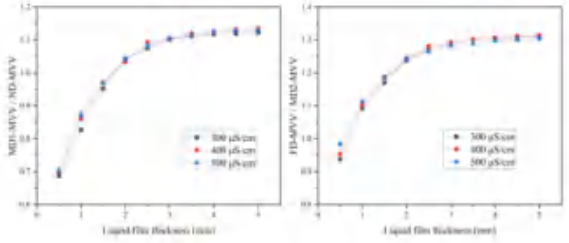


Figure 2 - Ratios for each electrode combination

Conclusions

A new conductivity array liquid film sensor was designed. Experiments found that the influence of conductivity can be eliminated through the double-electrode ratio method. It was

found that the ratio of MD1-MVV and ND-MVV reached saturation at a thinner liquid film thickness than the ratio of FD-MVV and MD2-MVV. And the ratio results of MD1-MVV and ND-MVV have better linearity under thin liquid film thickness. It is proved that the measurement range can be improved by cross-using far and near electrodes.

References

[1] M. Damsohn, H.M. Prasser, High-speed liquid film sensor for two-phase flows with high spatial resolution based on electrical conductance, Flow Measurement and Instrumentation, 20 (2009) 1-14.

[2] D. Wang, N. Jin, L. Zhai, Y. Ren, Measurement of Liquid Film Thickness Using Distributed Conductance Sensor in Multiphase Slug Flow, IEEE Transactions on Industrial Electronics, 67 (2020) 8841-8850.

Droplet shape acquisition by its light scattering pattern assisted with deep learning

Qingwei DUAN[1], Qinyao LI[1], Xiang'e HAN[1], Kuan Fang REN[1,2]
[1]School of Physics, Xidian University, Xi'an 710071, China
[2]CORIA-UMR 6614, Normandie Université, CNRS, Saint-Etienne du Rouvray 76801, France

Abstract
To identify the 3D shape of a nonspherical droplet has been a challenging problem in the study of multiphase flow. The traditional method to predict the 3D shape of a non-spherical droplet requires synchronous photography from multiple angles, which is difficult to operate and incurs high costs. In this study, we propose a method to acquire the 3D shape of a nonspherical droplet by its light scattering pattern assisted with deep learning.
Keywords: Nonspherical Droplet, 3D Shape, Light scattering pattern, Deep Learning
Introduction
Nonspherical droplets are common in multiphase flow and a precise characterization of their parameters such as shape, size, and temperature is of significant importance [1]. It has been found that the light scattering pattern of a liquid droplet is highly sensitive to the shape of the droplet. With the progress of light scattering models, it is now possible to simulate the light scattering patterns from large nonspherical droplets [1, 2], making it feasible to establish the one-to-one correspondence between a nonspherical droplet and the light scattering pattern. As a first step, here we show how an ellipsoidal droplet can be predicted from its light scattering pattern.
Methodology
Firstly, the scattering patterns of ellipsoidal liquid droplets are simulated with the 3D vectorial complex ray model (VCRM3D) [3]. For different shape parameters (a, b and c, i.e., the three semi-axes of ellipsoidal droplets), the database containing the scattering pattern for each parameter is then established. Figure 1 shows one part of the database. The refractive index of the droplets is 1.333, and the wavelength of light is 638.8 nm. Then a convolutional neural network is trained with the database. The training result is shown in Figure 2. The mean absolute error (MAE) for predicting the shape parameters (a, b, c) is about 10 μm after 30 epochs of training.

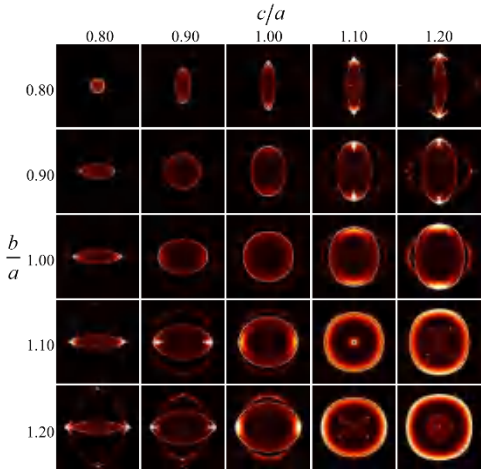


Figure 81 –Light scattering patterns of tri-axial ellipsoidal droplets simulated with VCRM3D.

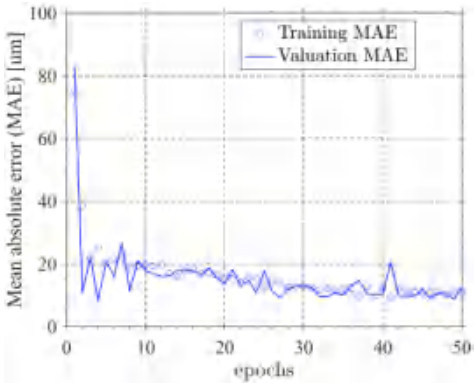


Figure 2 –Mean absolute error (MAE) versus training epochs.

Acknowledgements
National Natural Science Foundation of China (62205262)

References

[1] M. Agrawal et al., Physics of Fluids 32, 112105 (2020).
[2] K.F. Ren et al., Optics Letters, 36, 370-372 (2011)
[3] Q. Duan et al., Optics Express, 31, 34980-35002 (2023).

A new ultrasonic attenuation model based on gas-liquid two-phase flow

Mi Wang[ab*], Jiegui Liu[ab], Yuxin Bai[ab], Dandan Zheng[c], Lide Fang[ab*]
[a] College of Quality and Technical Supervision, Hebei University, Baoding, 071000, China
[b] National and Local Joint Engineering Research Center for Measuring Instruments and Systems, Baoding, 071000, China
[c] School of Electrical and Information Engineering, Tianjin University, Tianjin, 300072, China
* Corresponding author.
E-mail address: wangmi@hbu.edu.cn (Mi Wang), fanglide@hbu.edu.cn (Lide Fang)

Abstract

Gas-liquid two-phase flow is common in the process of natural gas exploitation and transportation, and has great research value. In order to measure droplet size and holdup in gas, ultrasonic attenuation method was used in the study, and an ultrasonic attenuation model adapted to the full wavelength range was proposed to provide a basis for inversion. The reliability and accuracy of ultrasonic attenuation method are tested by comparing it with optical image method.

Keywords: Ultrasonic attenuation, Gas-liquid

Introduction

In a two-phase flow, due to the viscosity and heat transfer effect, the ultrasonic wave will attenuate during the propagation process. These two effects are mainly caused by the anisotropy of the two media. It is shown that ultrasonic attenuation is closely related to the size and distribution of particles in an appropriate range. Therefore, people often measure the size and distribution of particles by measuring the attenuation of ultrasonic wave, and this measurement method and related equipment have been widely used.

Methodology

In order to obtain the particle size information according to the measured ultrasonic attenuation, it is necessary to study the most suitable theoretical attenuation model. The McClements model is more ideal in the area of small particles. The BLBL model is for long wavelength, large size particles. For the applicability of the model to large and small size particles, the McClements model and the BLBL model can be merged, and the result of the merger is shown below.

$$\begin{aligned}\boldsymbol{\alpha_T} &= \boldsymbol{\alpha_{MC}} + \boldsymbol{\alpha_{BL}} \\ &= -\frac{3}{2}\frac{\varphi}{k_c^2 r^3} Re(A_0 + A_1) + \frac{3\varphi}{8r} K_{ext}\end{aligned} \quad (1)$$

The above formula is called MCBL model. and it not only considers the viscosity attenuation and thermal attenuation between the droplet and air, but also considers the scattering attenuation, which is suitable for the whole wavelength region. The theoretical model is verified by finite element simulation.

In order to verify the accuracy of the method, the results are compared with those of the optical image method. Therefore, r_u and r_i are the drop radius measured by the image method and by the ultrasonic attenuation method respectively. e_i is the relative error of the radius.

Table 1 - Comparison of the results of ultrasonic attenuation method and optical image method for measuring droplet radius

Device	$r_u(um)$	$r_i(um)$	e_i(%)
Humidifier	**4.0841**	**3.5604**	**14.71**

	4.2565	**3.7665**	**13.01**
Atomizer	**255.8445**	**270.2248**	**-5.32**
	242.6885	**280.6642**	**-13.53**

Conclusions

The MCBL model and hybrid particle swarm inversion algorithm are proposed and verified by simulation. Compared with the results of the image method, the accuracy of the ultrasonic attenuation method is proved to be accurate and applicable.

Experimental and modeling study on liquid film thickness of horizontal gas-liquid annular flow using ultrasonic method

Mi Wang[ab*], Yuxin Bai[ab], Jiegui Liu[ab], Dandan Zheng[c], Lide Fang[ab*]
[a] College of Quality and Technical Supervision, Hebei University, Baoding, 071000, China
[b] National and Local Joint Engineering Research Center for Measuring Instruments and Systems, Baoding, 071000, China
[c] School of Electrical and Information Engineering, Tianjin University, Tianjin, 300072, China
* Corresponding author.
E-mail address: wangmi@hbu.edu.cn (Mi Wang), fanglide@hbu.edu.cn (Lide Fang).

Abstract
In this paper, the ultrasonic echo resonance main frequency (UERMF) method and the ultrasonic reference signal elimination (URSE) method are compared by numerical simulation method. The experimental data is processed using the URSE method to analyze the characteristics of the liquid film under different operating conditions. A new liquid film thickness correlation suitable for different system pressures and pipe diameters is proposed. The improved correlation has the applicability and extrapolation for different system pressure and pipe diameter conditions.

Keywords: Liquid film thickness, Ultrasonic method, Horizontal gas-liquid annular flow, Numerical simulation, Prediction correlation

Introduction

The measurement range and application of the URSE method in horizontal gas-liquid two-phase flow is studied in this paper. And based on the obtained experimental data, it is carried into the correlation for prediction. Although scholars have done a lot of work, the correlation of liquid film thickness under different pressures and different pipe diameters were rarely studied by scholars.

The pressure, pipe diameter and entrainment are improved based on the existing liquid film thickness correlation in this paper, so that the new correlation can better realize the prediction of liquid film thickness.

Methodology

The URSE method is based on the calculation of propagation time through cross-correlation algorithm, and then the thickness of liquid film is calculated.

In order to obtain the fitting coefficients in Eq. (1), the nonlinear least squares algorithm Levenberg-Marquardt iterative algorithm (LM algorithm) is used to fit the wave velocity prediction correlation.

$$h^* = 0.0207 \times \left(\frac{D}{D_{ref}}\right)^{0.6734} \left(\frac{\mathrm{Re}_{lf}^{1.8417}}{\mathrm{Re}_{g}^{1.4343}}\right) \left(\frac{u_g}{u_l}\right)^{1.4062} \left(\frac{p}{p_{ref}}\right)^{1.2631} \quad \textbf{(1)}$$

The new correlation is compared with the existing liquid film thickness data, and the comparison results are shown in Figure 1.

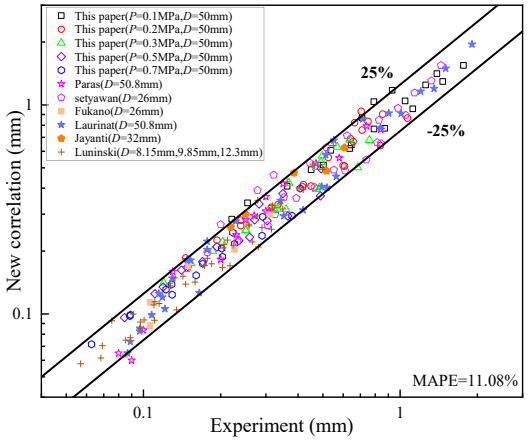


Figure 1 - Applicability of the new model

Conclusions

Based on the URSE method, this article proposes a prediction model for the thickness of two-phase annular flow liquid film. The model significantly improves the prediction performance under pressure conditions. The extrapolation and applicability of the new liquid film thickness correlation are verified.

Acknowledgements

This work is supported by the Advanced Talents Incubation Program of Hebei University (No. 521100222043) and the National Natural Science Foundation of China (No. 62071321, 62173122).

Friction nanogenerator based on solid-liquid contact initiation principle

Jiaying Li, Xianda Qiu, Taiyu He, Rui Xue, Chaofan Li, Jianxiong Luo, Weixuan Huang, Yanlin Zhao, Jun Yao
China University of Petroleum (Beijing), Beijing, China

Abstract
Nanogenerators, as a novel energy technology, are capable of converting fugitive and disordered energy in the environment into electrical energy, becoming a promising solution to the current situation of relying on traditional fossil energy sources. In this study, a nanogenerator based on the principle of solid-liquid contact initiation was designed using polytetrafluoroethylene sheets. It is found that the nanogenerator can effectively light up dozens of LED lights using both deionized water and tap water. Among them, the effect of utilizing deionized water is better than the former. This study provides some reference for further research on friction nanogenerators.

Keywords: Triboelectric nanogenerators (TENGs), Solid-liquid interface, Charge separation, Charge transfer mechanism

Introduction

Water is the world's largest energy carrier, and if it is utilized effectively, it can meet global energy supply requirements. Modern hydroelectric power generation technology mainly utilizes intensive low entropy water energy, however, most of the water energy in nature is distributed water energy in the form of high entropy. However, this energy is easily accessible yet difficult to harvest. Harvesting clean energy from water has become a promising approach to address the challenges of sustainable development. Nanogenerators (TENG), with their unique advantages of low cost, low-frequency drive, and high output, are a promising method for capturing energy from water droplets. Nanogenerators can convert the kinetic energy of water droplets into electrical energy without causing any pollution or significant impact on the environment, offering unrivaled advantages in clean energy harvesting.

Converting the various forms of energy found in nature into efficient and manageable electrical energy is a key development in the advancement of the energy industry. Advances in innovative water energy harvesting technologies portend great potential for application. Since water droplets are ubiquitous in nature, the energy released by their movement has the potential to be a never-ending source of energy. The movement of water droplets represents a constant source of clean energy [1-2]. Researchers are developing water droplet-based energy harvesting systems such as water/solid friction nanogenerators (TENG) [3-4] and droplet electric generators (DEG) [5-6], which promise to be a new source of clean energy. The fact that the kinetic energy of water droplets can be converted into electrical energy without pollution while having a negligible impact on the environment highlights their unique advantages for clean energy harvesting.

Methodology

In this study, a friction nanogenerator based on solid-liquid contact electrification was prepared using PTFE sheet, copper tape and metallic platinum wire as shown in Fig. 1, in which the negative electrode is copper tape with platinum wire, the positive electrode is copper tape and the carrier is PTFE sheet.

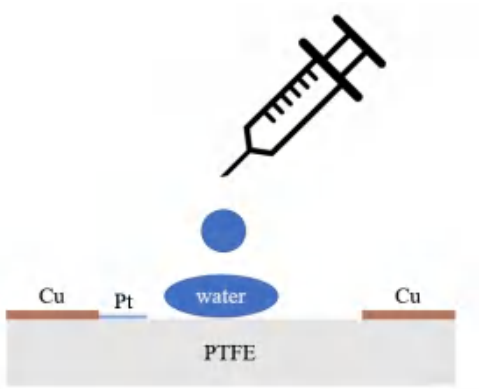


Figure 1 Schematic diagram of nanogenerator

Results and discussion

The experiment revealed that by applying deionized water droplets to the friction-based nanogenerator developed in this study, it was possible to efficiently illuminate dozens of LED lights. Moreover, the faster the water droplets flowed, the more sustained the brightness of the LEDs was. The height from which the droplets fell did not significantly affect the brightness of the LEDs.

The experiment also showed that tap water could be used to light up the LEDs, although under the same conditions, the brightness achieved with tap water was found to be dimmer compared to that with deionized water.

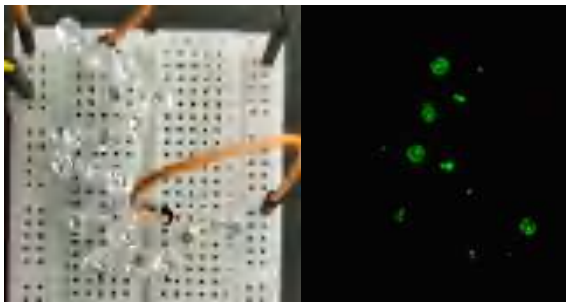


Figure 2 Light up LED light experiment diagram, LED light board diagram(left), light up LED light after diagram(right).

Conclusions

(1) The LED lights are best lit using deionized water.

(2) Increasing the flow rate of the water droplets can significantly enhance the brightness of the LED lights.

(3) Tap water also has the ability to light LEDs.

Acknowledgements

This work was supported by the National Natural Science Foundation of China (No. 51876221) and the High-end Foreign Expert Introduction Project (G20190001270; B18054). The authors also gratefully acknowledged the financial support from the China Scholarship Council.

References

[1] Z. L. Wang, Catch Wave Power in Floating Nets [J], Nature 542 (2017) 159-160.

[2] Z. H. Zhang, X. M. Li, J. Yin, Y. Xu, W. W. Fei, M. M. Xue, Q. Wang, J. X. Zhou, W. L. Guo, Emerging Hydrovoltaic Technology [J], Nature Nanotechnology 13 (2018) 1109-1119.

[3] Z. H. Lin, G. Cheng, S. Lee, K. C. Pradel, Z. L. Wang, Harvesting Water Drop Energy by a Sequential Contact-Electrification and Electrostatic-Induction Process [J], Advanced Materials 26 (2014) 4690-4696.

[4] Z. H. Lin, G. Cheng, L. Lin, S. Lee, Z. L. Wang, Water-Solid Surface Contact Electrification and Its Use for Harvesting Liquid-Wave Energy [J], Angew Chem Int Ed, 52 (2013) 12545-12549.
[5] H. Wu, N. Mendel, S. Van Der Ham, L. Shui, G. Zhou, F. Mugele, Charge Trapping-Based Electricity Generator: An Ultrarobust and High Efficiency Nanogenerator for Energy Harvesting from Water Droplets [J], Advanced Materials, 32 (2020) 2001699.
[6] W. Xu, H. Zheng, Y. Liu, X. Zhou, C. Zhang, Y. Song, X. Deng, M. Leung, Z. Yang, R. X. Xu, Z. L. Wang, X. C. Zeng, Z. Wang, A Droplet-Based Electricity Generator with High Instantaneous Power Density [J]. Nature, 578 (2020) 392-396.

Simulation study of synthetic jets for enhanced jet breakup in liquid-liquid systems

Jiateng Duan, Kunpeng Xue, Dianqiang Xu, Kaixuan Feng, Yu Liu*
Dalian University of Technology, Dalian, Liaoning, China
Ningbo Institute of Dalian University of Technology, Ningbo, Zhejiang, China

Abstract
The phenomenon of liquid-liquid jets is prevalent in the petroleum, chemical, and aerospace industries. In this study, numerical simulation is employed to delve into the evolving pattern of a synthetic jet within a liquid-liquid system. The findings demonstrate that both the periodic fluctuations of jet velocity and the nozzle configuration featuring side openings can significantly enhance the jet breakup. This research will likely contribute valuable insights towards the innovative advancement of practical engineering applications.

Keywords: Liquid-Liquid System, Synthetic Jet, Helmholtz Frequency, Atomizer Structure, Jet Breakup Enhancement

Particle movement mode effect on electrostatics

Jun Yao, Haoyu Liu, Yanlin Zhao, Qichao Fang
China University of Petroleum (Beijing), Beijing, China

Abstract
In this work, particle electrostatics was studied by experiment methods. A single particle was tested for charge generation through moving along a metal inclined plate. It is found that particle movement mode does an important role in determining electrostatics generation. The sequence of particle movement mode to generate electrostatic charge from high to low is sliding, sliding-rolling and rolling. Particle sphericity determines the mode of particle movement along the inclined plate. The electrostatics generated decreases with increasing sphericity. Such trend becomes less from sliding to rolling and decreases with increasing the plate inclination. In addition, a granular pneumatic conveying system was set up to measure the electrostatics generated by multiple particles, where particle movement mode is found to make an obvious effect on electrostatic charge generation. Due to particle–wall contact area being large, sliding particles can generate more electrostatic charge than rolling particles do. It is found that electrostatics increases with particle size, particle loading and pipe length.

Keywords: Particle, Electrostatic charge, Movement mode, Experiment

Introduction

During the processing of particles including producing, transporting, storing and so on, particle–wall contact causes electrostatic charge generation. Charges accumulated become more and more until reach the equilibrium stage [1–3]. As the electrostatics becomes so strong that penetrates air to form electric brushes, electrostatics discharge and even cause explosions or fires. In order to prevent the harm of electrostatics, this work aims to study the effect of particle movement mode on electrostatics generation including single particle and multiple particles. For the single particle, the electrostatics was generated by its movement along an inclined plate. The effects of particle sphericity and inclined angle of the plate on charge generation were considered. Particle movement mode was studied by several related factors including plate length, particle placement and particle size. For the multiple particles, a pneumatic conveying system was set up and the electrostatics was generated due to particle–wall contact. Flow velocity, particle size, particle loading mass, pipe length and relative humidity were considered for their effects on electrostatics generation.

Methodology

Generally, the initial shape of polypropylene particles is ellipsoidal and the particle used in this experiment, where relevant physical parameters are shown in Table 1.

Table 16 – Material property parameters

Material	**density /g.cm^{-3}**	**Poisson's ratio**	**Work function/eV**
SUS3 04	7.93	0.3	4.64
PP	0.89	0.25	5.43



Figure 1 - Single particle charging setup and measurement: (1) high-speed camera; (2) stand; (3) 304 stainless steel inclined plate; (4) computer; (5) electrometer; (6) Faradaycage.

To study the movement behavior of a particle effect on electrostatics generation, a single-particle electrostatic experiment device was set up as shown in Fig. 1. A particle is set at the top of the inclined plate that is made of 304 stainless steel. Due to gravity effect, the particle slides along the plate and fall into the Faraday cage set at the bottom of the plate. In this experiment, instruments used include high-speed camera (FASTCAM Mini AX100), digital galvanometer (ADVANTEST R8252), computer and Faraday cage, where all are grounded. In this work, particle movement is variable but all others are well controlled including humidity (20%) and temperature (25°C). Particle surface roughness is the same and each particle was polished by 2000 grid sandpaper. Particles were weighed by an electronic weighing balance with the accuracy of 10^{-6}g. After each experiment, particles were subjected to electrical discharge treatment.

Results and discussion

The sphericity of particles is an important factor that affects the electrostatic charge generation. Under the condition of 20%–22% relative humidity, a polypropylene particle is set at the top of the inclined steel plate (with inclination angle 40°) as shown in Fig. 1, and slides down 20 cm before falling into the Faraday cage set at the plate bottom, where particle motion is taken by a high-speed camera. As a result, the electrostatic charge generated is measured and charge-to-mass ratio is calculated as shown in Fig. 2. It can be seen that after sliding along the 304 stainless steel plate, the polypropylene particle obtains negative charges and the charge-to-mass ratio decreases with increasing sphericity. As particle sphericity is 0.37, there is a large reduction of the charge-to-mass ratio found in Fig. 2, which may be explained by particle behavior captured by the high-speed camera as shown in Fig. 3.

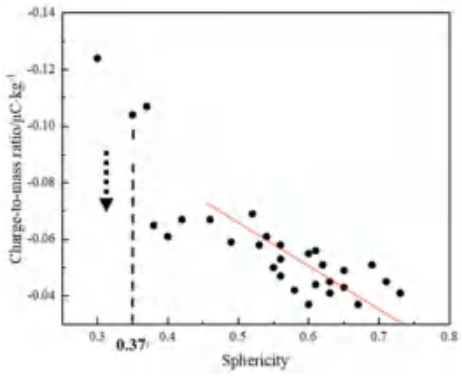


Figure 2 - Charge-to-mass ratio of particles with different sphericity



Figure 3 - The model of particle movement along the inclined plate (a), (b) sliding; (c) sliding and rolling; (d) rolling

Conclusions

In this work, it is found that particle movement mode does an important role in determining electrostatic charge generation. The sequence of particle movement mode to generate electrostatic charge from high to low is sliding, sliding-rolling and rolling. Generally, a particle set at the vertical placement can produce more electrostatics than that does at the horizontal placement. The conclusions obtained can be further analyzed by particle sphericity and plate inclined angle.

(1) Particle sphericity determines the mode of particle movement along the inclined plate. For a particle with low sphericity, its movement mode is determined by the friction and supporting force and tends to be sliding. For a particle with high sphericity, its movement mode is rolling.

(2) The electrostatics generated decreases with increasing the inclined angle of the plate, which causes particles more rolling and less sliding. The effect of inclined angle of the plate on the electrostatic charge generation is more significant for a particle with low sphericity than that for a particle with high sphericity.

(3) The electrostatics increases with particle size, and its growth rate increases with particle size as well. However, the charge-mass ratio (particle charge density) decreases with particle size increasing. Particle charge density decreases with increasing the flow speed.

References

[1] J. Yao, Y. Zhang, C.H. Wang, Y.C. Liang, On the electrostatic equilibrium of granular flow in pneumatic conveying systems, AIChE J. 52 (2006) 3775–3793.

[2] Y.L. Zhao, F. Zhou, J. Yao, Z.L. Ji, Electrostatic charging of single granules by repeated sliding along inclined metal plates, J. Electrostat. 87 (2017) 140–149.

[3] J. Yao, F. Zhou, Y.L. Zhao, Charge generation and electrostatic equilibrium for single granules during sliding, Particuology 29 (2016) 126–134.

Numerical simulation of fuel droplet breakup and dispersion cross-scale behavior

Xin Dajun[1]， Xue Kun[1]
1. Beijing Institute of Technology ,Haidian District, Beijing, China;

Abstract
The breakup and dispersion behavior of liquid fuel droplets driven by the central explosive flow field is studied on a multi-scale in order to meet the engineering requirement of explosive dispersion control technology in the development of cloud explosive weapons. Based on the discrete element method, a cross-scale droplet breakup and dispersion calculation method is developed to ensure the reasonable description of key physical processes while taking into account the calculation scale, efficiency and accuracy of engineering problems. The accuracy of the numerical method is verified by comparing the numerical simulation method with the experiment of droplet atomization and dispersion in shock tube. The research method established in this paper lays a foundation for the development of explosive distributed precision control technology and the controllable optimization design technology of cloud explosive charge warhead.

Keywords: Secondary breakup; Shock tube; Discrete element method; Multiphase flow;

Numerical Simulation of Cut Tobacco Flow in a Fluidized Bed

Duoduo Huang[a], Guangxi Tan[a], Hui Li[a], Le Wang[a], Wenkui Zhu[a*]
a Zhengzhou Tobacco Research Institute of CNTC, Zhengzhou, Henan 450001, China
* E-mail: wkzhu79@163.com(Wenkui Zhu)

Abstract
To verify the correctness and accuracy of the two-phase flow model and its implementation, the flow process of different types and sizes of cut tobacco in a laboratory two-dimensional fluidized bed was simulated. Models of square, rectangular, and circular cut tobacco particles were constructed, and parallel computing using domain decomposition was employed to simulate the fluidization process in a laboratory two-dimensional fluidized bed, providing material for the verification of the correctness of the two-phase flow model and program.

Key words: Cut tobacco, Two-phase flow model, Numerical simulation

Introduction

Tobacco processing widely involves gas-solid two-phase flow processing stages. Although the processing tasks in these processes are different, their basic principles are the same. They involve the transport movement and mass and heat transfer between solid phase tobacco particles and the fluid phase, achieving different processing objectives such as component separation, quantitative conveyance, and dehydration and drying of tobacco materials. In recent years, with the rapid development of high-performance computing technology, process virtual simulation technology, which combines computational fluid dynamics, discrete simulation, and large-scaleparallelcomputing, has been increasingly applied to the analysis and optimization of gas-solid flow fields in equipment. This study focuses on the simulation of gas-solid two-phase flow processes in tobacco, and a simulation of a laboratory two-dimensional fluidized bed device was conducted.

Methodology

Parallel computing employs a domain decomposition method, dividing the space along the height direction (Y direction) into four equal-sized regions. Each region corresponds to a parallel computing process in the program, and in hardware, it corresponds to a CPU computing core and a GPU computing card. To realistically represent the shape, distribution, and movement of cut tobacco, this example is based on the dimensions of flake tobacco from the experiment. Square (see Table 1 and Figure 1), rectangular (see Table 2 and Figure 2), and circular (see Table 3 and Figure 3) cut tobacco particle models were constructed accordingly.

Table 1 Construction Information of the Square Flake Particle Model

Particle chain number	1	2	3	4
Thickness (mm)	0.2	0.2	0.2	0.2
Area (mm^2)	20.0	30.0	50.0	80.0
Side length	22	27	35	44
Number of particles per chain	484	729	1225	1936
Particle chain mass (g)	0.0022	0.0034	0.0056	0.0089

Distribution ratio (%)	40	35	20	5

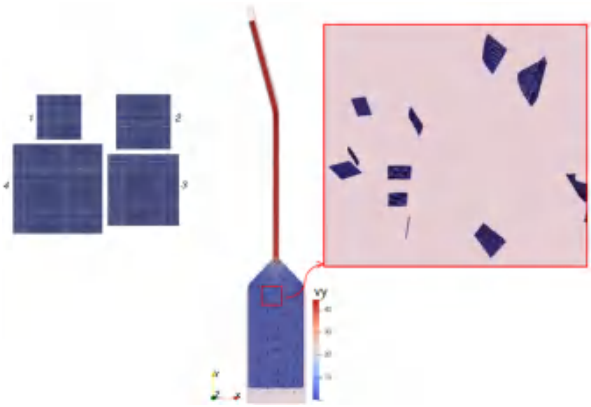
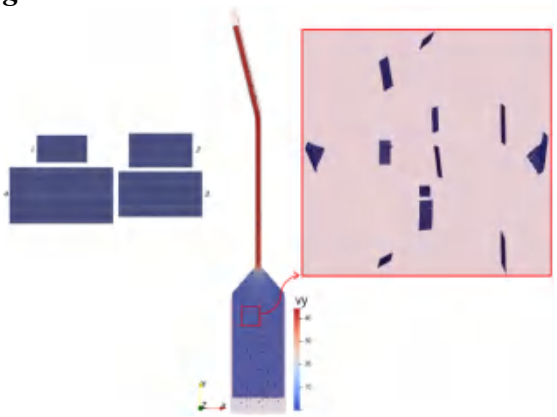


Figure 1 Square flake particle model (left) and its simulation results in a two-dimensional fluidized bed (right)

Table 2 Construction Information of the Rectangular Flake Particle Model

Particle chain number	1	2	3	4
Thickness (mm)	0.2	0.2	0.2	0.2
Area (mm²)	20.0	30.0	50.0	80.0
Length	30	38	50	62
Width	15	19	25	31
Number of particles per chain	450	722	1250	1922
Particle chain mass (g)	0.0021	0.0033	0.0058	0.0089
Distribution ratio (%)	40	35	20	5



Particle chain number	1	2	3	4
Thickness (mm)	0.2	0.2	0.2	0.2
Area (mm²)	20.0	30.0	50.0	80.0
Diameter	25	30	39	50
Number of particles per chain	457	656	1137	1884
Particle chain mass (g)	0.0021	0.003	0.0052	0.0087

Figure 2 Rectangular flake particle model (left) and its simulation results in a two-dimensional fluidized bed (right)

Distribution ratio (%)	40	35	20	5

Table 3 Construction Information of the Circular Flake Particle Model

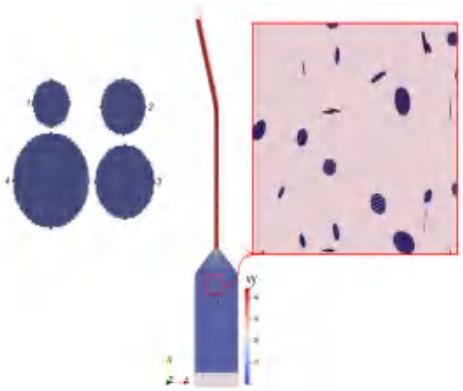


Figure 3 Circular flake particle model (left) and its simulation results in a two-dimensional fluidized bed (right)

Conclusions

The domain decomposition method was used for parallel computing, dividing the two-dimensional fluidized bed model into four regions along the height direction. Each region was allocated a CPU core and a GPU card. The simulation considered different shapes (square, rectangular, circular) of tobacco particle models to realistically reflect the shape and motion of the tobacco. Through the simulation of the laboratory two-dimensional fluidized bed device, material was provided for the verification of the correctness of the two-phase flow model and program.

Reference

[1] E.Q. Zhang, J.S. Du, J.W. Jiang, W. Zhang, B. Li, W.K. Zhu, Large-scale parallel computing based on OpenFOAM for numerical simulation of gas-solid flow in tobacco airflow drying devices, Tobacco Science and Technology, 2017(4).

[2] J. Xu, L.Q Lu, W. Ge, J.H. Li, Discrete simulation based on the EMMS paradigm and its chemical engineering applications, Journal of Chemical Engineering of China, 2015, 66(1).

[3] N. Yang, J.H. Li, Mesoscale science in chemical engineering and virtual process engineering: Analysis and prospects, Journal of Chemical Engineering of China, 2014, 65(7).

[4] J. Wang, P. Zhao, B. Zhao, Testing CFD-DEM method with a stochastic drag formulation using particle-resolved direct numerical simulation data as benchmark, Chem.Eng.Sci., 2021, 240.

Numerical simulation of particle behavior under two-phase impinging jet erosion

Haoyu Liu, Yanlin Zhao, Jun Yao
China University of Petroleum (Beijing), Beijing, China

Abstract
In present work, large eddy simulation is used to simulate the continuous phase and the Lagrange tracking method is coupled to study the particle motion. The flow characteristics, particle behavior and erosion morphology caused by particles in the two-phase impinging jet flows are studied. Small particles tend to generate *W*-shaped wall and large particles tend to generate *U*-shaped wall. Impinging on the *W*-shaped wall, particles approach the wall and the central axis are less affected by the normal deceleration from the local flow. Compared *W*-shaped wall with the flat wall, particle distribution is more uniform in the normal direction, less distribution near the wall and more distribution away from the wall. Impinging on the U-shaped wall, the inner annular high-vorticity region becomes wider and more concentrated, while the outer annular high-vorticity region becomes sparser and more dispersed. Particle distribution as particle-*U*-shaped-wall impact is more even than that as particle-flat-wall impact.

Keywords: Two-phase impinging jet; Particle-wall impact; Erosion morphology; Large eddy simulation; Turbulence

Introduction

The erosion occurred in a multiphase flow can be widely found as solid particles carried by the fluid impact walls. [1-3] On the one hand, the erosion could have a beneficial application. For example, impinging jet mixing high-speed flows with particles and gas is used to cut, deburr, and clean the workpiece. [1] It can also be used to clean chemical equipments such as heat exchanger, pipeline by sandblasting. [2] On the other hand, there must be disadvantages to wear. In the case of buried transportation pipelines, as the buried pipes leak and form a liquid-sand jet through the soil environment, the impinging jet may affect the adjacent pipelines and cause another leakage. [3] In present work, In order to predict the effect of erosion on the wall, LES was used to study two-phase impinging jet coupled with Lagrange particle tracking technology and combined with particle-wall collision and erosion models.

Methodology

The model is used to evaluate the erosion caused by particle-wall collision. Such model is based on experimental work [4] that aims to clarify the effect of particle size, particle shape, impact target material on the erosion rate. Given the impact angle at 90°, E_{90} as a reference, the erosion rate *ER* and the rebounded angle $h(\beta)$ can be calculated by Eq. (1)-(4).

$$ER = h(\beta)E_{90} \tag{1}$$

$$h(\beta) = \sin\beta^{n_1}\left(1 + H_v \cdot (1 - \sin\beta)\right)^{n_2} \tag{2}$$

$$E_{90} = K \cdot (H_v)^{k_1}\left(\frac{V_p}{V'}\right)^{k_2}\left(\frac{D_p}{D'}\right)^{k_3} \tag{3}$$

$$n_1 = s_1(H_v)^{q_1}, n_2 = s_2(H_v)^{q_2}, k_2 = 2.3(H_v)^{0.038} \tag{4}$$

the erosion depth Δh can be obtained by Eq. (5).

$$\Delta h = \frac{ER \cdot T}{\rho_w} \tag{5}$$

LES was used to study two-phase impinging jet coupled with Lagrange particle tracking technology and combined with particle-wall collision and erosion models. Particle distribution in the impinging jet and the erosion appearance was studied.

Results and discussion

In a particulate multiphase flow system, the working mechanisms of particle distribution can be mainly summarized as centrifugal, inertial and vortex mechanisms. [5] The distribution of large particle is mostly dominated by the inertia while that of small particle is dominated by vortex. Fig. 1. shows the two-dimensional contour of instantaneous longitudinal vorticity superimposed with sized particles distribution within $0<y/D<2.0$. It is seen that the free jet has the high vorticity concentrates in an elongated area ($0.6<y/D<2$) near the outer edge and dominate most particle distribution in it. In the impinging jet area ($0<y/D<0.6$ and $0<r/D<0.7$), the flow changes from the normal direction to the radial direction and particles carried by the fluid have to pass through these high vorticity zones from the free jet to the wall jet, where particle trajectory mainly depends on centrifugal and inertial effect. In the process of changing the direction of particle motion, particle-wall impact mostly occurs in the area of the impinging jet ($0<y/D<0.6$ and $0<r/D<0.7$). In the area of wall jet ($r/D>0.7$) two areas with fairly high vorticity can be found $1.0<r/D<1.4$ and $2.0<r/D<2.6$, which does affect particle distribution.

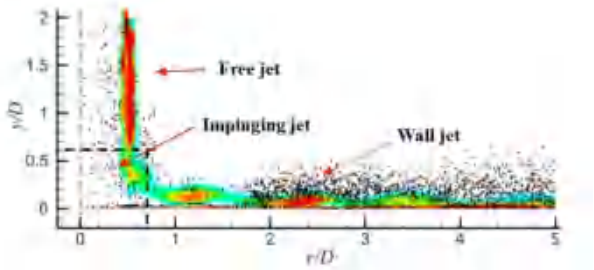


Figure 82 Contour of instantaneous longitudinal vorticity superimposed with particle distribution

Fig. 2. shows the instantaneous contour of radial vorticity superimposed with particle distribution near the target wall ($y/D=0.125$) for three sized particles, where particles are sampled in the area of $0<y/D<0.25$. For the smallest particle with St=1.56, an annular particle belt with high concentration can be found outside of the area $r/D=2.4$ (②), which is consistent with Fig.1. This is mainly due to the effect of high vorticity on particle behavior.

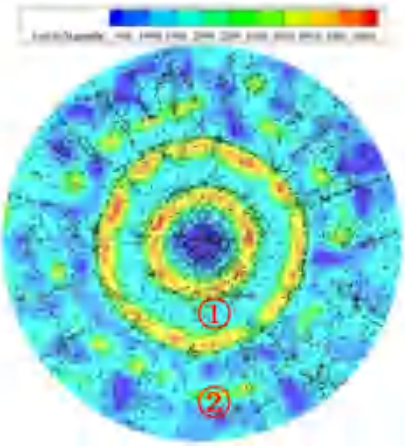


Figure 2 Contour of instantaneous radial vorticity superimposed with particle distribution near the target wall

Conclusions

The following results can be obtained from this three-dimensional finite element simulation study.

(1) Particle-wall impact angle increases with particle size. Along the radial direction, particle-wall impact angle decreases with *r/D* increasing and such trend decreases with increasing particle size.
(2) Regarding the distance from the impinging jet center axis, the particle-wall impact position increases with decreasing particle size as well as the position of the maximum N/N_0. The impact density increases with particle size and the trend of its decline with *r/D* also increases with particle size.
(3) For the erosion caused by particle-wall impact, the outer dimensionless contour radius of the erosion morphology decreases with increasing particle size but the maximum erosion depth increases with particle size. Small particles tend to generate *W*-shaped wall and large particles tend to generate *U*-shaped wall.

References

[1] T. Kuriyagawa, T. Sakuyama, K. Syoji, H. Onodera, A new device of abrasive jet machining and application to abrasive jet printer, Key Eng. Mater. 196 (2001) 103-110.
[2] Y.F. Wang, Discussion on off-line cleaning of petrochemical equipment, Cleaning World 34 (2018) 16-19.
[3] G. Chen, Z. Guo, Q. Zhou, Z. Chen, Z. Yuan, The reliability of adjacent gas pipeline under the erosion action of water-sand jet, Oil & Gas Storage and Transportation 10 (2019) 1095-1103.
[4] Y.L. Oka, K. Okamura, T. Yoshida, Practical estimation of erosion damage caused by solid particle impact: Part 1: Effects of impact parameters on a predictive equation. Wear 259 (2005) 95-101.
[5] M. Liu, J. Yao, Y.L. Zhao, The dispersion of particles in turbulent semi-circular duct flows. Petrol. Sci. 18(2021) 1240-1255.

Charged multiphase flow-based suppression of fugitive dust and application

ZUO Ziwen1 , WANG Junfeng2 , XU Haojie1 , ZHANG wei1 .
1. School of Energy and Power Engineering, Jiangsu University, Zhenjiang, Jiangsu, China
2. School of Energy and Power Engineering, Chongqing University, Chongqing, China

Abstract

Particulate matter (PM) is the primary pollutant in the global atmospheric environment directly affecting human health and socio-economic development. As one of the main sources of particulate pollution, fugitive dust is widely present in the environment such as power plants. The research has broken through the bottleneck that fine particulate matter is difficult to capture under the condition of fugitive emission. The multiphase flow theory and methodology of particle diffusion and capture under multi-field coupling are established. The key technology and equipment of dust suppression based on charged multiphase flow are innovated.

The basic theory of formation and control of fugitive dust pollution were constructed. The mechanisms of charged water mist capturing fine particles were clarified. The mechanisms of charged droplets improving the capture efficiency of fine particles under multi-field coupling were revealed. A new solution of fugitive dust suppression based on charged multiphase flow was proposed. The problem of low removal efficiency of fine particles by conventional water mist dust removal method was resolved. The removal efficiency of fine particulate matter (PM2.5) by electrostatic spray can be increased by more than 7 times.

A new scheme of multi-technology fugitive dust suppression based on charged multiphase flow was firstly proposed. A twin-fluid electrostatic spray system was invented, which broke through the technical bottleneck of low charging effect of highspeed jet droplets in high humidity environment. The universal problem of excessive fugitive dust emission with high concentration and strong shear was resolved. The dust suppression system for ship unloader has been developed to reduce the daily TSP concentration in the environment to less than 0.15 mg / m3 during coal transportation.

Keywords: Fugitive dust emission; Charged multiphase flow; Particle removal; Power plant.

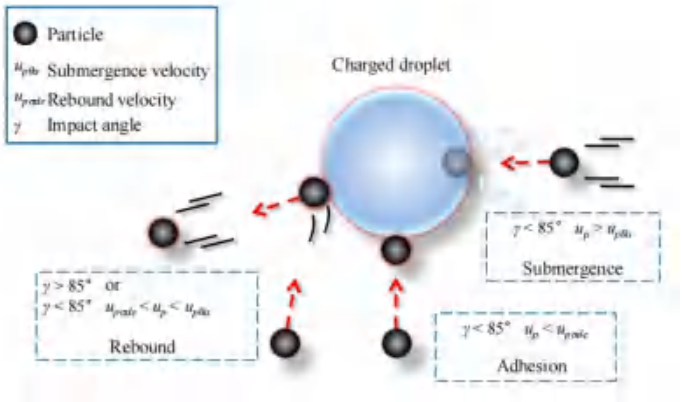


Figure 1 - Critical conditions of particle impact

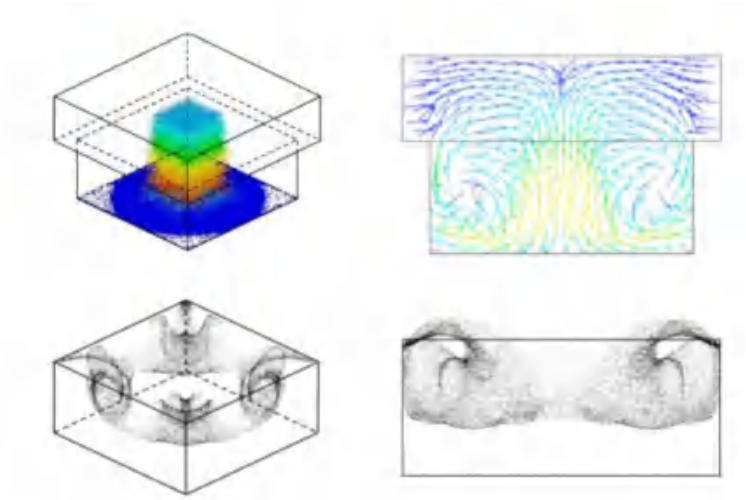


Figure 2 - Fugitive dust triggered by coal fall



Figure 3 - Dust suppression system of ship unloader Up：Original system Down：new system